

Lecture Notes in Mechanical Engineering

Puneet Verma

Olusegun D. Samuel

Tikendra Nath Verma

Gaurav Dwivedi *Editors*


Advancement in Materials, Manufacturing and Energy Engineering, Vol. II

Select Proceedings of ICAMME 2021

 Springer


Lecture Notes in Mechanical Engineering

Series Editors

Francisco Cavas-Martínez , Departamento de Estructuras, Universidad Politécnica de Cartagena, Cartagena, Murcia, Spain

Fakher Chaari, National School of Engineers, University of Sfax, Sfax, Tunisia

Francesca di Mare, Institute of Energy Technology, Ruhr-Universität Bochum, Bochum, Nordrhein-Westfalen, Germany

Francesco Gherardini , Dipartimento di Ingegneria, Università di Modena e Reggio Emilia, Modena, Italy

Mohamed Haddar, National School of Engineers of Sfax (ENIS), Sfax, Tunisia

Vitalii Ivanov, Department of Manufacturing Engineering, Machines and Tools, Sumy State University, Sumy, Ukraine

Young W. Kwon, Department of Manufacturing Engineering and Aerospace Engineering, Graduate School of Engineering and Applied Science, Monterey, CA, USA

Justyna Trojanowska, Poznan University of Technology, Poznan, Poland

Lecture Notes in Mechanical Engineering (LNME) publishes the latest developments in Mechanical Engineering—quickly, informally and with high quality. Original research reported in proceedings and post-proceedings represents the core of LNME. Volumes published in LNME embrace all aspects, subfields and new challenges of mechanical engineering. Topics in the series include:

- Engineering Design
- Machinery and Machine Elements
- Mechanical Structures and Stress Analysis
- Automotive Engineering
- Engine Technology
- Aerospace Technology and Astronautics
- Nanotechnology and Microengineering
- Control, Robotics, Mechatronics
- MEMS
- Theoretical and Applied Mechanics
- Dynamical Systems, Control
- Fluid Mechanics
- Engineering Thermodynamics, Heat and Mass Transfer
- Manufacturing
- Precision Engineering, Instrumentation, Measurement
- Materials Engineering
- Tribology and Surface Technology

To submit a proposal or request further information, please contact the Springer Editor of your location:

China: Ms. Ella Zhang at ella.zhang@springer.com

India: Priya Vyas at priya.vyas@springer.com

Rest of Asia, Australia, New Zealand: Swati Meherishi at swati.meherishi@springer.com

All other countries: Dr. Leontina Di Cecco at Leontina.dicecco@springer.com

To submit a proposal for a monograph, please check our Springer Tracts in Mechanical Engineering at <https://link.springer.com/bookseries/11693> or contact Leontina.dicecco@springer.com

Indexed by SCOPUS. All books published in the series are submitted for consideration in Web of Science.

More information about this series at <https://link.springer.com/bookseries/11236>

Puneet Verma · Olusegun D. Samuel ·
Tikendra Nath Verma · Gaurav Dwivedi
Editors

Advancement in Materials, Manufacturing and Energy Engineering, Vol. II

Select Proceedings of ICAMME 2021

 Springer

Editors

Puneet Verma
School of Earth and Atmospheric Science
Queensland University of Technology
Brisbane, QLD, Australia

Olusegun D. Samuel
Department of Mechanical Engineering
Federal University of Petroleum Resource
Effurun, Nigeria

Tikendra Nath Verma
Department of Mechanical Engineering
Maulana Azad National Institute
of Technology
Bhopal, India

Gaurav Dwivedi
Energy Centre
Maulana Azad National Institute
of Technology
Bhopal, India

ISSN 2195-4356

ISSN 2195-4364 (electronic)

Lecture Notes in Mechanical Engineering

ISBN 978-981-16-8340-4

ISBN 978-981-16-8341-1 (eBook)

<https://doi.org/10.1007/978-981-16-8341-1>

© The Editor(s) (if applicable) and The Author(s), under exclusive license to Springer Nature Singapore Pte Ltd. 2022

This work is subject to copyright. All rights are solely and exclusively licensed by the Publisher, whether the whole or part of the material is concerned, specifically the rights of translation, reprinting, reuse of illustrations, recitation, broadcasting, reproduction on microfilms or in any other physical way, and transmission or information storage and retrieval, electronic adaptation, computer software, or by similar or dissimilar methodology now known or hereafter developed.

The use of general descriptive names, registered names, trademarks, service marks, etc. in this publication does not imply, even in the absence of a specific statement, that such names are exempt from the relevant protective laws and regulations and therefore free for general use.

The publisher, the authors and the editors are safe to assume that the advice and information in this book are believed to be true and accurate at the date of publication. Neither the publisher nor the authors or the editors give a warranty, expressed or implied, with respect to the material contained herein or for any errors or omissions that may have been made. The publisher remains neutral with regard to jurisdictional claims in published maps and institutional affiliations.

This Springer imprint is published by the registered company Springer Nature Singapore Pte Ltd. The registered company address is: 152 Beach Road, #21-01/04 Gateway East, Singapore 189721, Singapore

Preface

This book presents a collection of research and review articles on different aspects of science and engineering of advance materials from the International Conference on Advancement in Materials, Manufacturing, and Energy Engineering (ICAMME), which was organized by the Department of Materials and Metallurgical Engineering in association with Energy Centre and Department of Mechanical Engineering, Maulana Azad National Institute of Technology, Bhopal, Madhya Pradesh, India, from 18th to 20th February 2021. The conference aims to provide a platform for academicians, scientists, and researchers across the globe to share their scientific ideas and vision in the areas of Materials and Metallurgical Engineering, Energy Efficient Systems, Nanomaterials, Composites, Process metallurgy, Extractive metallurgy, Physical metallurgy, mechanical behavior of materials, and other related fields of Materials Science. The ICAMME-2021 conference played a key role in setting up a bridge between academicians and industry. Due to the COVID-19 outbreak around the world, the meetings and gatherings were banned, besides a strict immigration policy. Based on most authors' appeal and health considerations, after careful discussion, the conference committee changed this event to an online conference.

The conference presented more than 100 participants to interchange scientific ideas. During the three days of the conference, researchers from educational institutes and industries offered the most recent cutting-edge findings, went through several scientific brainstorming sessions, and exchanged ideas on practical socio-economic topics. This conference also provided an opportunity to establish a network for collaboration between academicians and industry. The major emphasis was given on the recent developments and innovations in various fields of Materials Science and Metallurgy technologies through plenary lectures. This book presents various chapters addressing the science and engineering of various advance materials and technologies in the form of mathematical and computer-based methods and models for designing, analyzing, and measuring the characterization of material processing. The book brings together different aspects of engineering design and will be useful for researchers and professionals working in this field.

The editors would like to acknowledge all the participants who have contributed to this volume. We also deeply express our gratitude to the generous support provided

by MANIT, Bhopal. The editors also thank the publishers and every staff and student volunteer of the departments and institute who has directly or indirectly assisted in accomplishing this goal. Finally, the editors would also like to express their gratitude to the Respected Director of MANIT, Dr. N. S. Raghuwanshi, for providing all kinds of support and blessings.

Despite sincere care, there might be typos and always a space for improvement. The editors would appreciate any suggestions from the reader for further improvements to this book.

Brisbane, Australia
Effurun, Nigeria
Bhopal, India
Bhopal, India
April 2021

Puneet Verma
Olusegun D. Samuel
Tikendra Nath Verma
Gaurav Dwivedi

Contents

Investigation of Rare Earth Element Inclusion on the Structural and Magnetic Properties of Barium Ferrites	1
Mallika Chugh and Deepak Basandrai	
Computational Fluid Dynamic Analysis of Cyclone Separator for Flue Gas Cleaning by Using Standard k-Epsilon Model	25
Jaishree Chauhan, B. L. Salvi, M. S. Khidiya, and Chitranjan Agrawal	
Identification of Lubricant Contamination in Journal Bearings Using Vibration Signature Analysis	35
Ambuj Pateriya, N. D. Mittal, and M. K. Pradhan	
Mechanical Alloying of γ TiAl-Based Powder of Ti-46Al-1B (at%) Composition	45
Mrigesh N. Verma and Vijay N. Nadakuduru	
A Review on Development and Applications of Solar Dish Stirling System	57
Deepak Kumar and Meena Agrawal	
Physical Properties of Amorphous Nanosilica from Rice Husk (Agriculture Waste) and PVA Composite, Prepared Using Green Approach for Its Applications	71
Anurag Kumar, Rakesh Kumar Singh, Nishant Kumar, Atul Jyoti, and Prem Kumar	
Antibacterial Property of Biologically Synthesized Iron Nanoparticles Against <i>Staphylococcus aureus</i>	85
Satyam Sangeet, Arshad Khan, Sarit Prabha, and Khushhali M. Pandey	
Fabrication of Composite Phase Change Material: A Critical Review	97
P. Das, R. Kundu, S. P. Kar, and R. K. Sarangi	

Air Quality Assessment During Lockdown for Jaipur City	107
Darshan Mishra, Kaushiki Sharma, and Sohil Sisodiya	
Micellar Potentiometric Determination of Stability Constant and Antibacterial Investigations on Complexes of Cu (II) with 3, 4, 5-Trimethoxybenzaldehyde Thiosemicarbazone	123
Uma Rathore, Raja Ram, Kamal Kishor Verma, and N. Bhojak	
Aging of a Thermoplastic Polymer Under the Combined Effect of Ultraviolet Ray and Temperature	135
Sonya Redjala, Said Azem, and Nourredine Ait Hocine	
Effects of Additives and Treatment on Fly Ash-Based Polymer Composites	147
Sushant Patel, G. L. Devnani, and Deepesh Singh	
Powder Mixed Electrical Discharge Machining of EN 31 Steel	155
Rakesh Kumar Patel and M. K. Pradhan	
Simulation and Analysis of Hybrid Energy Resources in Chennai Using Homer Software	163
P. Abirami, M. Pushpavalli, V. Geetha, P. Sivagami, and R. Harikrishnan	
EDM Process Optimization of Machining Parameters for Through Hole Making on HCHCR AISI-D7 Steel Using RSM	179
Amit Kumar and Mohan K. Pradhan	
Improving the Performance of Supply Chain Through Industry 4.0 Technologies	197
Mohd Ammar, Abid Haleem, Mohd Javaid, Shashi Bahl, and Devaki Nandan	
Significant Applications of Composite and Natural Materials for Vibration and Noise Control: A Review	211
Kartikay Singh Pawar, Ashok Kumar Bagha, Shashi Bahl, and Devaki Nandan	
Digital Management Systems in Manufacturing Using Industry 5.0 Technologies	221
Nadia Fazal, Abid Haleem, Shashi Bahl, Mohd Javaid, and Devaki Nandan	
Mathematical and Computational Analysis of Shell and Tube Heat Exchanger on Varying Tube Patterns in Excel[®] and Ansys[®]	235
Ranjeet Prasad, Ajay Gupta, Pankaj Kumar, and Amit Kumar Mishra	
Design Analysis of Robotic Arm	247
Mahesh T. Kanojiya, Nitin K. Mandavgade, Chandrasekhar Padole, and Dipak Gulhane	

Pine Oil Extraction and Characteristics of Engine Using Pine Oil 263
 Uddeshya Kumar and Siddharth Jain

Microstructure Tribological Characterization of Copper Metal Matrix Reinforced with Cerium Oxide 273
 Vivek Pandey, Tushar Choudhary, and Anup Bajpai

Investigation on Vibration of Crankshaft in Reciprocating Engine 287
 Abhishek Gattlewar, Dipak Gulhane, Vijay Kalbande, Nitin K. Mandavgade, Rupesh Khorgade, and Mahesh T. Kanojiya

Comparative Thermodynamic Analysis of Simple Gas Turbine Fueled with Renewable Fuel 299
 Abhinav Anand Sinha, Tushar Choudhary, and Mohd. Zahid Ansari

Solar Thermal Receivers—A Review 311
 Manish Saini, Abhishek Sharma, Varun Pratap Singh, Gaurav Dwivedi, and Siddharth Jain

Powder Mixed Electric Discharge Drilling of Aluminum Based Metal Matrix Composite 327
 Pabitra Kumar Sahu and Sabindra Kachhap

Investigating the Change in Water Characteristics and Scale Formation Under the Varying Turbulent Flow 339
 Amrit Anand Dosar and Vivek Srivastava

A Study on Post-harvest Loss Reduction with Solar Dryer 351
 Ajay Vishwakarma, Sunanda Sinha, and Prashant Malik

Energetic and Exergetic Comparison of Opaque and Semi-transparent PVT Arrays Under Natural Convection Mode for Building Integration 361
 Amit Sharma, Ravi Kumar, C. S. Rajoria, and Sathans Suhag

Fabrication of IoT System for Structural Health Monitoring Considering Maintenance 4.0 375
 Priyank Srivastava, Anoop Kumar Shukla, Krishna Mohan Agarwal, Sanjeev Kumar Sharma, and Shubham Sharma

Effect of Biodiesel on Engine Performance and Emissions 383
 Anna Raj Singh, Sudhir Kumar Singh, and Siddharth Jain

Jatropha: A Sustainable Source of Transportation Fuel in India 395
 Rahul Chamola, Nitin Kumar, and Siddharth Jain

Morphological and Nanostructural Characteristics of Diesel Exhaust Soot Particles at Different Engine Operating Conditions 409
 Priyanka Arora, Puneet Verma, Faisal Lodi, Mohammad Jafari, Ali Zare, Svetlana Stevanovic, Timothy A. Bodisco, Richard J. Brown, and Zoran Ristovski

Design and Simulation Study of a Piezoelectric Microcantilever-Based Energy Harvester for Ambient Vibrations	419
Vinod Belwanshi, Vishnuram Abhinav, and Vibhor Kumar	
Utilization of Local Riverbed Sand in Green Sand Mould Casting—A Study	431
Jatin Sadarang, Ramesh Kumar Nayak, and Isham Panigrahi	
Ferrochrome Slag as an Alternative Mould Material for Green Sand Mould Casting—A Study	439
Jatin Sadarang, Ramesh Kumar Nayak, and Isham Panigrahi	
Evaluation of Compactibility and Shear Strength of Sand-Less Casting Mould for Sand Casting Process	449
Jatin Sadarang, Ramesh Kumar Nayak, and Isham Panigrahi	
A Study on the Design and Fabrication of Dry Cell Electrolysis Setup for Hydrogen Generation	459
Kamaraj Nithyanandhan, S. Ranjithkumar, Gaurav Dwivedi, and Somasundaram Periasamy	
A Short Review on Biped Robots Motion Planning and Trajectory Design	471
Kunchala Balakrishana Reddy, Gamini Suresh, Ravi Kumar Mandava, and T. Ch. Anil Kumar	
Optimization of Machining Process Parameters Using Grey Fuzzy Method	481
Vajrala Venkata Reddy, Ravi Kumar Mandava, and K. Srunivasulu Reddy	
Energy Analysis of R1234yf/R134a as Replacement of R134a in a Domestic Refrigerator	495
P. Saji Raveendran, P. C. Murugan, T. Darwin, Godwin Glivin, and Gaurav Dwivedi	
Effect of Na₂O Content on Ground Granulated Blast Furnace Slag Incorporated Fly Ash-Based Geopolymer Pastes	503
Rohit Kumar and Mayengbam Sunil Singh	
Performance and Emissions Characteristics of Diesel Engine Run on Citrullus Colocynthis Biodiesel with Zinc Oxide Additive	513
K. Logesh, M. Karthick, S. Baskar, and Abhishek Sharma	
Performance and Emission Characteristics of Single-Cylinder Diesel Engine Fueled with Biodiesel Derived from Cashew Nut Shell ...	521
M. Karthick, K. Logesh, S. Baskar, and Abhishek Sharma	

Investigation of Heat Transfer Characteristics in Double Tube Heat Exchanger with Helical Turbulator Using CFD 531
 S. Padmanabhan, M. Selvamuthukumar, S. Ganesan, S. Baskar, and Abhishek Sharma

AHP-based Identification of Tools for Sustainable Product Development 543
 Chinmay Saraf, Sachin Agrawal, Dharmesh Barodiya, Pankaj Shrivastava, and Tikendra Nath Verma

Design and Optimisation of Annulus Combustion Chamber of Gas Turbine Engine: An Analytical and Numerical Approach 553
 Ramakrishna Balijepalli, Abhishek Dasore, Upendra Rajak, Y. Siva Kumar Reddy, and Tikendra Nath Varma

Thermo-Economic Optimization of Spiral Plate HX by Means of Gradient and Gradient-Free Algorithm 569
 Musunuru Hari Krishna, Abhishek Dasore, Upendra Rajak, Ramakrishna Konijeti, and Tikendra Nath Verma

Numerical Investigation to Study the Effect of Inlet Inclination on the Turbulence Intensity of the Naturally Ventilated Room Using CFD 583
 Ghogare Abhijeet Ganesh, Shobha Lata Sinha, Tikendra Nath Verma, and Satish Kumar Dewangan

Analysis of Solar Photovoltaic-Based Water Pumping System in Sehore, India 591
 Shubham Mishra, Shrey Verma, Ambar Gaur, Subhashree Mohapatra, Subhankar Chowdhury, and Gaurav Dwivedi

Vibro-Acoustics of a Mandar 603
 Pradip Gorai, Pankaj Kumar, N. P. Choudhry, and Ajay Kr. Gupta

About the Editors

Dr. Puneet Verma has worked on wide areas of biodiesel, environmental science, air quality, and diesel particulate matter. He has completed his bachelor's degree in mechanical engineering from Punjab Technical University and M.Tech from IIT Roorkee under the umbrella of MHRD fellowship, India. He was awarded QUTPRA Scholarship for his Ph.D. in environmental engineering, Queensland University of Technology (QUT), Australia. Currently, he is working as Air Quality Scientist, ASK Consulting Engineers, Brisbane, Australia, where he has delivered multiple projects of emission, odor, noise, and dust monitoring at industrial and construction sites. He has also worked as Quality Control Chemist and HSE Specialist, Intertek Testing Services, Australia, and Environmental Research Intern, Puma Energy, Australia. He has published more than 33 research articles in international journals and conferences. He is Member of Clean Air Society of Australia and New Zealand, The American Association for Aerosol Research and Professional Mechanical Engineer (Engineers Australia).

Dr. Olusegun D. Samuel is Full-Time Lecturer and Research Fellow in the Department of Mechanical Engineering, Federal University of Petroleum Resources, Effurun, Delta State, Nigeria. He does research in the process intensification of biofuel production, upgrading of pyrolytic bio-oil and its efficacy of soft computing in its modelling, techno-economic analysis, and general mechanical engineering. He has trained many students in areas of production, renewable energy, tribology, diesel engine performance and emission parameter optimization techniques, degradation of elastomers in alternate fuel, corrosion of automotive parts in biodiesel-based fuel, biogas, residual stress, energy conversion, renewable energy, and thermo-fluids. Their current project is entitled "CFD studies and exergetic analysis of mechanical systems, and techno-economic and sustainability assessments of various combustion-related energy technologies." He has published more than 70 papers in reputed journals and two chapters in Nova Science Publishers and one in Intech Open. He has widely participated at national and international seminars as keynote and invited speakers and as an external examiner of Ph.D./M.Sc. thesis. He serves as Reviewer to Elsevier (*Energy, Journal of Cleaner Production, Fuel, etc.*) and Taylor and Francis. He is

the editorial board member of reputed journals published by Springer and other SCI indexed Journals.

Dr. Tikendra Nath Verma received his Bachelor of Engineering (B.E.) degree in mechanical engineering with securing first division from Pt. R. S. U. Raipur (C.G.) in 2006. He did his master's degree in thermal engineering in 2009 from the Department of Mechanical Engineering, Maulana Azad National Institute of Technology Bhopal (M.P.). He has obtained his Ph.D. degree from National Institute of Technology, Raipur (Chhattisgarh). He joined National Institute of Technology Manipur as Assistant Professor in September 2015. Presently, he is working as Assistant Professor (Grade—I) in the Department of Mechanical Engineering, Maulana Azad National Institute of Technology Bhopal. His areas of interest include computational fluid dynamics, heat and mass transfer, renewable energy, and alternative fuels in internal combustion engines. He has published more than 65 papers in SCI and Scopus indexed journals. He has published ten chapters with reputed publishers. He also serves as a potential reviewer for various journals such as *Energy*, *Energy Conversion and Management*, *Applied Energy*, *Fuel*, *Journal of Cleaner Production*, *Journal of Building Engineering*, *Waste Management*, *Journal of Hazardous Material*, etc. (Elsevier); *Journal of Thermal Analysis and Calorimetry* (Springer), *International Journal of Ambient Energy* (Springer); and *Journal of Thermal Engineering* (Begell House Journals).

Dr. Gaurav Dwivedi has completed his B.Tech in mechanical engineering from IKGPTU Jalandhar, M.Tech in energy systems from IIT Roorkee, and Ph.D. in the field of renewable energy (biofuel) from IIT Roorkee, India. He has 8 years of teaching experience in the field of mechanical and energy engineering and taught various subjects like IC engine, thermodynamics, fluid machinery, bioenergy, and others at various institutes like VIT University Vellore and Amity University Noida. Currently, he is working as Assistant Professor in the Energy Centre at Maulana Azad National Institute of Technology Bhopal, India. His area of interest is biodiesel production methodology, enhancement in fuel properties, and application of biofuel on engine operation. He has published more than 85 papers in various international journals and conferences. He has published more than 50 papers in SCI and Scopus indexed journals. He has published one book with International Publisher; along with that, he has contributed five chapters. He got Young Scientist Award at NIT Trichy for his contribution in the field of renewable energy. He is Active Member of Institution of Engineers (India) and Solar Energy Society of India and IEEE. He also served as Guest Editor for *Materials Today proceedings* and *Journal of Traffic and Transportation*.

Investigation of Rare Earth Element Inclusion on the Structural and Magnetic Properties of Barium Ferrites



Mallika Chugh and Deepak Basandrai

1 Introduction

Ferromagnetic oxide or ferrite is an expression that is contributed to the stuff containing oxides of metal and iron both as their mainstay [1]. Ferrites are mostly dark gray or black in their physical appearance and are also very hard and brittle. They are used thoroughly in various electric and magnetic areas as permanent magnets. Ferrites have various advantages such as wide frequency range (10 kHz to 50 MHz) [2]. They are highly resistible and temperature stable [2]. Moreover, ferrites are available at very low and reasonable cost which is one of the reasons that they are proved as commercially effective ceramic materials. Ferrite cores are widely used in toroidal inductors, cores of transformers, quality filters, transducers, memory chips and other very high operating devices [3]. Due to their low electrical conductivity and ohmic losses, they prevent eddy currents [1].

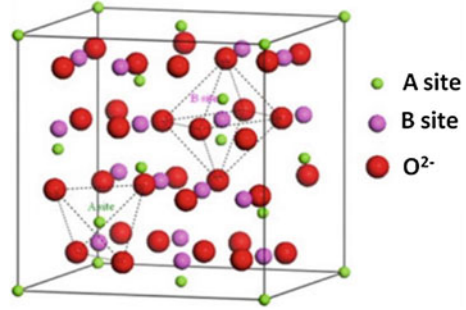
A lot of magnetic materials shows electromagnetic wave absorption owes to magnetic losses, but ferrites have been found to show considerably less losses at ferromagnetic resonance [3]. Below Curie temperature, ferromagnetic oxides manifest high-quality magnetic properties along with high intrinsic resistivity [2]. They are also used in the field of telecommunication, low-level applications and electromagnetic interference (EMI) suppression.

In addition to magnetic properties, dielectric properties are also revealed by ferrites. Ferrites are extensively owned by variety of electronic appliances. Due to their relevant conductivity, they work as electrodes in areas like chromium plating. Ferrites retaining DC resistivity of the value 10^9 or larger acquire very shallow losses which are not up to the mark of satisfying the needs for microwave applications.

M. Chugh · D. Basandrai (✉)

Department of Physics, School of Physical Sciences and Chemical Engineering, Lovely Professional University, Phagwara, Punjab 144411, India

Fig. 1 Structure of spinel ferrites



Ferrites are of two types (hard ferrites and soft ferrites), both having their own advantages. Hard ferrites are also known as ceramic magnets. Hard ferrites possess high coercivity and high remanence and are mainly used in small electric motors, loudspeakers, etc. The greatest magnetic field achieved by them is nearly 0.35 T [2].

Soft ferrites possess low coercivity; hence, they can alter their magnetization easily. They are worn by switched-mode power supply (SMPS) because of their low losses at high frequencies [2]. They are quite helpful in microwave applications, radio frequency circuits, rod antennas, high-frequency digital tapes, etc.

On the basis of the crystal structure, ferrites can be divided into different categories that are spinel ferrites, hexagonal ferrites and garnet ferrites.

Spinel ferrites are the ionic compounds whose physical and chemical effects can be dogged by the cation concentration at the tetrahedral and octahedral sites. Spinel structure (Fig. 1) is closed packed layout of oxygen atoms. Smallest repeating unit of spinel ferrites is made up of 32 oxygen ions [4].

Garnet ferrites have cubic symmetry as shown in Fig. 2. There are three types of cation sites, i.e., tetrahedral (fourfold), octahedral (sixfold) and dodecahedral (eightfold). They have large importance in the field of nanofluids, color imaging and electromagnetic shielding materials [4].

Hexagonal structure of ferrites known as hexaferrites tends to have crystalline structure due to close packing of oxygen ion layers. Their structure can be portrayed on the basis of fundamental structural blocks that are S, R and T [4].

But among all these types of ferrites, hexaferrites are in spotlight as they have emerged gracefully for vast scientific and technological advancement. Hexagonal

Fig. 2 Structure of garnet ferrites

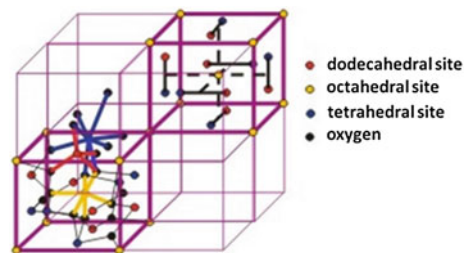
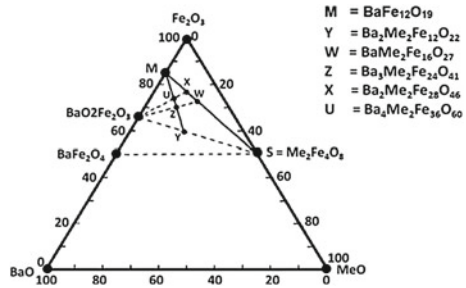


Fig. 3 Composition of hexagonal ferrites



structure of ferrites is best known for their huge role in microwave applications and in magnetic recording media due to their marvelous coercivity, Curie temperature, saturation magnetization, uniaxial magneto-crystalline anisotropy [5, 6]. Because of enormous magneto-crystalline anisotropy and chemical stability of hexaferrites, they are evaluated as preferable electromagnetic absorber in GHz frequencies [7, 8]. Hexagonal ferrites are considered to have self-biasing nature and narrow ferromagnetic resonance line width [6]. Figure 3 shows composition of hexagonal ferrites.

These ferrites are difficult to be replaced as they are comparably best magnetic material than others because they are relatively inexpensive and more stable. Spinel ferrites work under the range of 3 GHz, whereas the application range of hexagonal ferrites is felicitous for whole gigahertz zone because of their intrinsic anisotropy conduct [4].

The classification of hexagonal ferrites can be done further on the account of their chemical configuration.

That can be given as follows:

- M-type: [BaFe₁₂O₁₉]
- Y-type: [Ba₂Me₂Fe₁₂O₂₂]
- W-type: [BaMe₂Fe₁₆O₂₇]
- Z-type: [Ba₃Me₂Fe₂₄O₄₁]
- X-type: [Ba₂Me₂Fe₂₈O₄₆]
- U-type: [Ba₄Me₂Fe₃₆O₆₀]

M-type hexagonal ferrites—M-type hexaferrites (MeFe₁₂O₁₉) are cheaper to produce by using different methods for synthesis. They possess high electrical resistivity and intense magnetic uniaxial anisotropy across the c-axis. Saturation magnetization of M-type hexaferrites is low than the existing alloy magnets. Various features like high coercive force and chemical stability make these ferrites excellent permanent magnets [9].

Y-type hexagonal ferrites—These ferrites have acquired much more attention due to its multiferroic qualities [9]. Standard formula for Y-type hexagonal ferrites will be given as (A₂Me₂Fe₁₂O₂₂) where A = Sr²⁺, Ba²⁺, Pb²⁺, La²⁺ and Me = bivalent transition metal. In Y-type hexagonal structure, two tetrahedral sites and four octahedral sites inhabited small cations [10]. These ferrites are handed down in

electronic transmissions and microwave elements [9]. Different properties of Y-type hexaferrites can be affected by different factors such as synthesis methods, amount of substitution, sintering temperature and time and chemical composition.

W-type hexagonal ferrites—These ferrites have general formula $AMe_2Fe_{16}O_{27}$. These ferrites are hard magnetic materials and can be used effectively as nonconductive permanent magnets and in microwave region. Like M-type hexagonal ferrites, they also show uniaxial anisotropy along c-axis [9], but saturation magnetization possessed by W-type hexaferrites is relatively more than that of M-type hexaferrites.

Z-type hexagonal ferrites—Chemical framework of Z-type hexagonal ferrites is $A_3Me_2Fe_{24}O_{41}$ where $A = Pb^{2+}, Ba^{2+}, La^{2+}, Sr^{2+}$. The Z-type hexaferrites are found generally to be the sum of M-type and Y-type units of hexagonal ferrites. They are of great importance in radar-absorbing materials (RAMs) [9].

X-type hexagonal ferrites—These types of ferrites were known near about 50 years ago. Standard formula for X-type hexagonal ferrites is $A_2Me_2Fe_{28}O_{46}$ where $A = Pb^{2+}, Ba^{2+}, La^{2+}, Sr^{2+}$. We mostly get these X-type phases blended with phases of M-type and W-type, and it is quite tough to split them [9].

U-type hexagonal ferrites—The chemical composition for such compounds is $A_4Me_2Fe_{36}O_{60}$ where $A = Ba^{2+}, Sr^{2+}, La^{2+}, Pb^{2+}$. One Y-block and two M-blocks along the c-axis are superimposed for this structure. They have complex structure that is why they are hard to produce. They are beneficial in millimeter wave applications [9].

Barium hexaferrite is one of the chemically stable hexagonal structures acquiring admirable corrosion resistance. Barium ferrites are long-lasting magnet material which are formed on the basis of iron oxide (Fe_2O_3) and barium carbonate ($BaCO_3$). They have very low electrical conductivity, high Curie temperature and moderate permittivity. Barium hexaferrites are also chemically compatible with biological tissues; hence, they have a lot of importance in biomedical applications [11]. They have high microwave magnetic loss. There are different methods to produce barium ferrites such as hydrothermal, sol-gel combustion, spray pyrolysis, citrate precursor, co-precipitation and ball milling. Barium ferrites having morphology like platelet are considered best microwave absorbing material [8].

The plethora of dopants were used to alter the properties of barium hexaferrites. But the substitution of rare earth dopants such as dysprosium (Dy), terbium (Tb), erbium (Er), europium (Eu), holmium (Ho), etc., had tailored the properties of ferrites in a very appreciable manner. Rare earth elements were first spotted in the 1960s. They have illustrative hold on structural and magnetic properties of barium ferrites. These rare earth elements can be used widely in intensifying the coercive field and magnetization [12, 13]. They can also work as inhibition agent in mechanism of grain growth at high temperature. The analysis of the electrical resistivity and dielectric consequences on addition of doping of rare earth elements unfolds relevant data regarding the functioning of free electrical and localized charge bearers which gives us better understanding of the mechanism of electrical conduction.

2 Literature Review

2.1 Wang Jing et al. (2006)

Dysprosium (Dy), neodymium (Nd) and praseodymium (Pr) were switched in the sample of W-type barium ferrites of composition $\text{Ba}(\text{MnZn})_{0.3}\text{Co}_{1.4}\text{R}_{0.01}\text{Fe}_{15.99}\text{O}_{27}$. This whole procedure was done using chemical co-precipitation method. After examination, it was clear that the Fe^{3+} could be replaced by some RE^{3+} and modify the hyperfine variables. The loss in reflection and matching thickness of single-layered ferrite absorber was measured. There was a keen decrease in complex permittivity, and in addition to this, high-frequency relaxation and natural resonance frequency were increased. If the ferrite material is substituted with the rare earth element, dysprosium, then it gives out remarkable microwave absorption effects. At the value of 2.1 nm, the matching thickness value reaches up to -51.92 dB. The bandwidth touches the value greater than 8.16 GHz, and frequency starts with 9.9 GHz [14].

2.2 M. A. Ahmed et al. (2007)

A configuration of W-type barium hexagonal ferrite was prepared with composition of $\text{Ba}_{0.95}\text{R}_{0.05}\text{Mg}_{0.5}\text{Zn}_{0.5}\text{CoFe}_{16}\text{O}_{27}$ substituted with rare earth ions like Y, Er, Ho, Sm, Nd, Gd and Ce. This was done by double sintering ceramic process. X-ray diffraction specimens were used to characterize the structural properties of the sample and proved the existence of secondary phase. On increasing the ionic radius of rare earth ions, the strength of secondary phase also increases. The value of curie temperature also increases with the increase in concentration of rare earth ions samarium up to 1.04 angstrom and after that it starts decreasing after touching the maximum value. Faraday's method was implemented to study the discrepancy in magnetic susceptibility in temperature range 300–750 K at various amounts of magnetic field applied (1280, 1733, 2160 Oe) [12].

2.3 Aria Yang et al. (2007)

M-type hexagonal ferrite ($\text{BaFe}_{12-x}\text{Sc}_x\text{O}_{19}$) was made by substituting scandium. The method for this preparation was conventional ceramic technique. The values for anisotropy and magnetization both reduced on addition of scandium. It was concluded that bipyramidal sites were strongly preferred by scandium addition. Microwave and DC effects were studied extensively in this research [15].

2.4 *M. A. Ahmed et al. (2009)*

The effect of various rare earth dopants in the form of R_2O_3 where $R = Y^{3+}$, Er^{3+} , Ho^{3+} , Sm^{3+} , Nd^{3+} , Gd^{3+} and Ce^{3+} ions in chemical composition $Ba_{0.95}R_{0.05}Mg_{0.5}Zn_{0.5}CoFe_{16}O_{27}$ on electrical properties of W-type hexaferrite had been investigated. The results concluded that on introduction of R_2O_3 alteration of both physical and structural properties can be achieved. Samarium (Sm^{3+}) has highest values of dielectric constant (ϵ') and dielectric loss factor (ϵ'') and AC conductivity, but these factors decrease with increase in frequency. Semiconducting properties were indicated for these samples where AC conductivity increases with increase in temperature. Majority charge carriers were found to be electrons except in the case of Er^{3+} and Y^{3+} ions. Increase of charge carrier's concentration (n) was there with the substitution of Ba^{2+} ions by R^{3+} ions [16].

2.5 *Ji-Jing Xu et al. (2009)*

By using sol-gel method, Z-type ferrites doped with La^{3+} with composition $Ba_{3x}La_xCo_2Fe_{24}O_{41}$ ($x \frac{1}{4} 0.00-0.30$) were synthesized. And the influence of La^{3+} being a rare earth dopant on the different properties' composition was being characterized. The result of magnetic data resulted that increasing the concentration on La^{3+} ions from 0.0 to 0.3 makes the ferrite a better soft magnetic material. It is because of increase of magnetization and decrease of coercivity [17].

2.6 *Huang Xiaogu et al. (2010)*

By polymer adsorbent combustion method, W-type barium ferrites having chemical composition $Ba_{1-x}Er_x(Zn_{0.3}Co_{0.7})_2Fe_{16}O_{27}$ ($x = 0.00, 0.05, 0.10, 0.15, 0.20$) were synthesized by substituting Er^{3+} . X-ray diffraction analysis (XRD), X-ray fluorescence (XRF) and scanning electron microscopy (SEM) were done to characterize the crystal structure, surface morphology and electromagnetic properties. On doping content of 0.10 Er^{3+} ions, electromagnetic properties were quite improved [18].

2.7 *Imran Khan et al. (2011)*

By using simple chemical co-precipitation method, W-type strontium hexagonal ferrites having chemical composition $Sr_{1-x}Ce_xCo_2Mn_yFe_{16-y}O_{27}$ ($x = 0.00, 0.02, 0.04, 0.06$ and $y = 0.0, 0.2, 0.4, 0.6$) have been synthesized. The influence of rare earth dopant Ce at Sr and Mn at Fe site on the structural, magnetic and electrical

properties had been characterized. Different properties such as saturation magnetization, remanence, squareness ratio and coercivity were observed using hysteresis loop concluding at room temperature resistivity decreases with increasing content of Ce^{3+} and Mn^{2+} ions. It can be due to the fact that the substitution of Ce^{3+} at Sr^{2+} site increases the concentration of Fe^{2+} ions at octahedral site. There is increase in saturation magnetization and remanence and coercivity with Ce–Mn ion concentration. Hence, it can be used in high-density recording media [19].

2.8 Faiza Aen et al. (2011)

W-type hexagonal ferrites having a composition of $\text{BaHo}_x\text{Fe}_{16-x}\text{O}_{27}$ ($x = 0.0, 0.2, 0.4, 0.6, 0.8, 1.0$) were conducted using co-precipitation technique at high temperature of 1320°C . Single phase of ferrites was observed by XRD. On substituting the amount of Ho, magnetization increases. It is due to the difference in ionic radii of Ho^{3+} , that is, 0.901 \AA , and Fe^{3+} , that is, 0.67 \AA . Because of separation between grains, it was observed that DC resistivity increases on increasing concentration of Ho^{3+} at room temperature. And DC electrical resistivity works as a function of temperature; it expresses the semiconducting behavior [20].

2.9 Fengying Guo et al. (2012)

W-type hexaferrites, $\text{Ba}_{0.9}\text{RE}_{0.1}\text{Co}_2\text{Fe}_{16}\text{O}_{27}$ sample, were made with the substitution of rare earth ions (La^{3+} , Nd^{3+} , Sm^{3+}). The method used for this preparation was solid-state reaction method at the temperature of 1250°C for time period of 5 h. X-ray diffraction and scanning electron microscopy technique were used to explore the microstructure. As an outcome, single phase of W-type barium ferrite emerged as platelet-type shape. There was a gradual decrease in lattice parameter ‘a’ and ‘c’ with the decrease in the ionic radius of rare earth dopant. Vector network analyzer counted the complex permittivity and complex permeability from the scale of $0.5\text{--}18.0 \text{ GHz}$. Also, the microwave absorbing properties of the sample were highly increased in super-high frequency. Highest value of the dielectric loss tangent angle (0.75) at 16 Hz frequency was given by La-doped ferrite [8].

2.10 Irshad Ali et al. (2013)

Nanostructure Tb–Mn-substituted Y-type hexaferrites having single phase with chemical formula $\text{Sr}_2\text{Co}_{2x}\text{Mn}_x\text{Tb}_y\text{Fe}_{12y}\text{O}_{22}$ ($x = 0.0\text{--}1, Y = 0.0\text{--}0.1$) were prepared using micro-emulsion method. Polaron hopping is the conduction mechanism in

the ferrite system as the content of Tb–Mn increases the DC electrical conductivity. The samples which are having high conductivity have low activation energy. Maxwell–Wagner model and Koop’s phenomenological theory were used to explain the frequency-dependent AC conductivity. High value of quality factor is obtained, and Tb–Mn substitution helps to alter and improve electric and dielectric properties [21].

2.11 S. Cai et al. (2013)

Various rare earth elements such as lanthanum (La), dysprosium (Dy), neodymium (Nd), praseodymium (Pr), samarium (Sm), gadolinium (Gd) and ytterbium (Yb) $M = \text{Zn}^{2+}$, Mn^{2+} , $\text{Mn}_{0.5}^{2+}$, $\text{Zn}_{0.5}^{2+}$ were doped in the composition of M-type barium hexaferrite powders ($\text{Ba}_{0.95}\text{Re}_{0.05}\text{Fe}_{12}\text{O}_{19}$ and $\text{Ba}_{0.95}\text{Re}_{0.05}\text{M}_{0.05}\text{Fe}_{12}\text{O}_{19}$) with sol–gel self-combustion method. X-ray diffraction (XRD) and vibrating sample magnetometer (VSM) techniques were helpful for determining the structural composition of phase sample and magnetic effects. The average diameter of the magnetoplumbite of the sample was known to be 45 nm. Magnetic saturation was not altered by magnetic moments of rare earth ions. On decreasing the concentration of rare earth ions, there was also decrease in saturation magnetization except the Sm^{3+} and Gd^{3+} . Also based on anisotropy, when orbital quantum numbers for ions except Sm^{3+} and Gd^{3+} increased, H_C firstly increased and then decreased [22].

2.12 Irshad Ali (2014)

Y-type hexagonal ferrites with composition of $\text{Ba}_2\text{Zn}_2\text{Tb}_x\text{Fe}_{12x}\text{O}_{22}$ (0.6×6.0) were prepared using sol–gel auto-combustion method. Maxwell–Wagner type of interfacial polarization and the exchanging of charge carrier between Fe^{2+} and Fe^{3+} ions result in the dispersion of dielectric constant and dielectric loss at low temperature. The dielectric permittivity decreases with Tb^{3+} ion addition. The DC resistivity increased from 7.29×10^7 to 4.73×10^8 ohm cm because of unavailability of Fe^{3+} ions at octahedral sites. These properties are suitable for fabricating multi-layer chip inductors (MLCIs) with low eddy current losses and surface effect of materials [23].

2.13 Shihai Guo et al. (2014)

X-ray diffractometer and scanning electron microscopy were used to characterize the Sm^{3+} -doped Co Z-type hexagonal ferrite structures which were prepared by conventional ceramic method. After that, the effect on magnetic and different properties on that composition was observed on addition of Sm^{3+} ions. The hysteresis loop

expressed that the saturation magnetization for Sm^{3+} doped was more than that of undoped. After sintering at temperature of 1250 °C, samarium-doped Co Z-Type hexagonal ferrites show good high-frequency properties [24].

2.14 Ali Sharbati et al. (2015)

W-type of hexagonal ferrite with composition of $\text{BaNi}_2\text{Dy}_x\text{Fe}_{16-x}\text{O}_{27}$ ($x = 0-0.9$) was examined with the substitution of dysprosium. Citrate precursor method was preferably used during the preparation of the sample. Different properties like morphology, DC resistivity, crystalline structure and magnetic properties were investigated by using various techniques like X-ray diffraction (XRD), transmission electron microscopy (TEM), vibrating sample magnetometer (VSM) and vector network analyzer (VSA). The sample was kept heated at the temperature of 1250 °C for 4 h in the air. The hysteresis loop traced provided the increasing values of coercivity with addition of dysprosium (530–560 Oe). The saturation magnetization was decreasing on increasing the content of dysprosium and other magnetic effects. But DC resistivity took its value from 0.83×10^7 to 6.92×10^7 cm with increasing value of the dopant. The reason for this was that there were no Fe^{3+} ions present. Microwave properties of the sample reside between the range of 12 and 20 GHz. Minimum reflection loss (40 dB) was noticed at 16.2 GHz at $x = 0.6$ for 1.7-mm-thick layer [25].

2.15 Javed Rehman et al. (2016)

Single-phase terbium (Tb)-doped X-type hexagonal nano-ferrites having chemical composition $\text{Sr}_2\text{NiCoTb}_x\text{Fe}_{28x}\text{O}_{46}$ ($x = 0.00, 0.05, 0.1, 0.15, 0.2$) were synthesized with micro-emulsion method. Hexaferrites were confirmed by the spectral bands. The dielectric constant was found to be 12.5 at low frequency, while it decreased to 6.5 at high frequency. Introducing terbium reduced the saturation magnetization from 76 to 54 emu/g. Remanence was lowered from 27 to 21 emu/g. On increasing terbium, the coercivity was increased from 610 to 747 Oe [26].

2.16 Muhammad Irfan et al. (2016)

A composition of strontium hexaferrite as $\text{Sr}_2\text{MnNiFe}_{12}\text{O}_{22} + x\text{Y}_2\text{O}_3$ ($x = 0-5$ wt.%) was synthesized and proceeded with different processes like X-ray diffraction (XRD), scanning electron microscopy (SEM) and dielectric spectroscopy for observation. Doping of yttrium reduced the growth of grain. Low saturation magnetization and

high coercivity were indicated after yttrium doping to hexaferrites which are quite good magnetic properties [27].

2.17 Kush Rana et al. (2016)

Barium and cobalt used hexagonal ferrite with configuration of $\text{BaCo}_{0.8}\text{Sm}_x\text{Fe}_{(11.2-x)}\text{O}_{19}$ where $X = 0.2, 0.4$ and 0.6 with substitution of samarium was produced with the help of citrate precursor technique. Various characterization methods were implemented to look over the sample. Emergence of M phase with average crystalline proportions of 35–45 nm was examined by XRD. Transmission electron microscopy and field emission scanning electron microscopy were also drawn for the material sample. During vibrating sample magnetometer (VSM), field of 22,000 Oe was put in at the room temperature and then B–H loops were traced. It was noticed that as samarium ions are increased, there is decrease in retentivity, coercivity and specific saturation magnetization. The best values for coercivity and squareness ratio were found at the 0.2 value of x . These values are 2690.20 Oe and 0.5619, respectively [5].

2.18 Maria Zahid et al. (2017)

Y-type hexaferrites with chemical composition $\text{Ba}_2\text{NiCoDy}_x\text{Fe}_{12-x}\text{O}_{22}$ ($x = 0.00, 0.05, 0.01, 0.15, 0.20, 0.25$) were synthesized using sol–gel auto-combustion method. As frequency is increased, there is a decrease in electrical permittivity. It can be due to interfacial polarization which can be described with the help of Maxwell–Wagner model. Magnetization decreases because of segregation of Dy at grain boundaries. And coercivity also decreases on increasing the content of Dy due to exchange coupling effect between neighboring domains [3].

2.19 Anum Zafar (2017)

Magnetic and electrical properties of M-type barium hexaferrites were discovered. The sample was prepared by hydrothermal technique with substitution of Eu at 0, 0.02, 0.04, 0.08 and 0.10. The single phase of M-type hexagonal structure was proved by the XRD and FTIR which was done at the range of 40–100 MHz. The increased conductive behavior was shown by dielectric constant at low frequency. There was an increase in saturation magnetization from 30.49 to 54.27 emu/g and in coercivity 3.03–8.73 KOe with doping of the Eu [28].

2.20 Vipul Sharma et al. (2018)

M-type hexagonal barium ferrite is a kind of magnetic material which gives a lot of information about electromagnetic wave propagation in different microwave devices. They have large magnetization. Ferromagnetic resonance study of rare earth elements such as neodymium (Nd) and samarium (Sm), taking cobalt (Co) as base, doped hexaferrite nanoparticles. Different techniques such as X-ray diffraction, vibrating sample magnetometer (VSM) and ferromagnetic resonance (FMR) were used to check the structure and magnetic properties of doped hexaferrite nanoparticles. Substituting different rare elements like Nd and Sm has a great effect on electromagnetic properties of hexaferrites. Hydrothermal method is one of the best method for the synthesis of rare earth (Nd and Sm) doped M-type hexaferrites. Magnetization saturation was going down from 73.2 emu/g for (S1) pure BaM to 45.4 emu/g for $S_3(\text{BaCo}_{0.5}\text{Nd}_{0.3}\text{Fe}_{11})$. The doped samples showed resonance behavior lesser than the pure phase from 16 to 30 GHz [11].

2.21 Muhammad Faisal et al. (2018)

Different compositions of nano-crystalline M-type barium hexagonal ferrites with cobalt–samarium doping $\text{BaFe}_{12-2Z}\text{Co}_Z\text{Sm}_Z\text{O}_{19}$ were analyzed at ($Z = 0.0, 0.2, 0.4, 0.6$). This sample was prepared with WOWS sol–gel method without using water and surfactants. XRD patterns were examined to give out lattice constant, crystal size, porosity and theoretical density. LCR meter surveyed the dielectric specifications. Material morphology was discovered by scanning electron microscopy. Temperature was set up to 100–400 °C to verify the DC electrical resistivity. Large values of Curie temperature, magnetization, magneto-crystalline anisotropy and dielectric effects were unfolded. XRD concluded the hexagonal structure. The size of sample material was spilled about 295 nm to 440 nm by SEM. The ferromagnetic effect was elucidated at 25 °C by the hysteresis loop. The nano-crystalline structure was confirmed by the coercivity displayed by Sm^{3+} and Co^{2+} ions [7].

2.22 Safia Anjum et al. (2019)

$\text{Ba}_{1-x}\text{La}_x\text{Fe}_{12}\text{O}_{19}$ ($x = 0.0, 0.1, 0.2, 0.3, 0.4, 0.5$) which is a M-type barium hexaferrite was prepared through conventional ceramic route to know the effect of La^{3+} ions on various properties like structural, dielectric, optical and magnetic properties. Hexagonal structure of La^{3+} -doped Ba hexaferrites was confirmed by XRD. Stretching vibration of oxygen and metal (Fe–O) might be resulted that the bands are in the range 500–600 cm^{-1} confirmed by FTIR. Lanthanum substituted in M-type barium hexaferrite confirms the magnetoplumbite structure of La^{3+} ions which was

confirmed by XRD and FTIR. With increase in concentration of La^{3+} ions, band gap energy decreases, while the coercivity increases with the La^{3+} ion substitution because of ordering of paramagnetic La^{3+} at A-site which suppresses the ferromagnetic order. On increasing amount of lanthanum in M-type barium hexaferrite, the tangent loss decreases and AC conductivity increases at high frequency [6].

2.23 J. Mohammed et al. (2019)

$\text{Cu}^{3+}\text{-Er}^{3+}$ -substituted M-type strontium hexaferrites having chemical formula $\text{Sr}_{1-x}\text{Cu}_x\text{Fe}_{12-y}\text{Er}_y\text{O}_{19}$ ($x = 0.0, 0.1, 0.2$, and $y = 0.0, 0.4, 0.5$) were prepared using sol-gel auto-combustion method which was pre-sintered at 300 for 3 h and then after sintered at 1000 for 6 h. XRD gives the sample structure to be pure crystalline with the absence of magnetite ($\alpha\text{-Fe}_2\text{O}_3$) and other secondary phases. Band gap increases with the content of $\text{Cu}^{3+}\text{-Er}^{3+}$ calculated by UV-Vis NIR spectroscopy. Given samples show low dielectric loss with dielectric constant at high frequency. Ferromagnetic behavior was expressed by magnetization loop. Magnetic properties decrease with increase by substituting $\text{Cu}^{3+}\text{-Er}^{3+}$ [29].

2.24 İsa Araz (2019)

$\text{Ba}_{0.5}\text{Ce}_{0.5}\text{Fe}_{11}\text{CoO}_{19}$ chemical composition of barium hexaferrite with substitution of Ce-Co was prepared by ceramic technique. Dual phase was characterized by XRD grain size around 66.55 nm. The magnetizations were decreased with increase in Ce^{3+} ions. In the ferrite structure, more addition of Ce^{3+} ions gives rise to the conversion of some Fe^{2+} ions at the tetrahedral site from Fe^{3+} ions at octahedral sites to Fe^{2+} ions at the tetrahedral site. The spectrum of the complex intrinsic parameters and the electromagnetic wave absorbing was of range in between 2.0 and 18.0 GHz frequency range. Ce substitution to the barium hexaferrite was quite helpful in improving the electromagnetic wave absorbing ability. It can be considered quite efficient material for shielding and absorption application in microwave field [30].

2.25 Mohammad K. Dmour et al. (2019)

Using the famous preparation method of sol-gel, a complex configuration $\text{Ba}_{1-x}\text{Re}_x\text{Co}_2\text{Zn}_x\text{Fe}_{16-x}\text{O}_{27}$ was made and the few rare elements containing lanthanum (La), neodymium (Nd) and praseodymium (Pr) were mixed in the composition as ($x = 0.0, 0.1, 0.2$). It was then sintered at the temperature of 1250 °C for near about 2 h. Electromagnetic and microstructural effects were perceived. XRD technique gave the traces for pure W-type hexaferrite phase for all samples leaving

neodymium–zinc at $x = 0.2$ that was mixed with M-type phase in addition to W-type. Beneath the temperature of 300 °C, spin reorientation transformation was disclosed by the thermomagnetic curves. Magnetic transition was on the scale of 461–481 °C. It was also divulged that as RE–Zn concentration is made higher, there is a gradual increase in magneto-crystalline anisotropy field. This increase was given as (6.30–9.23 KOe). At the temperature values of 505–516 °C, weak magnetic phase transitions were revealed with cobalt-rich impurity magnetic phase [31].

The observed values of structural and magnetic parameters obtained from the literature review are summarized in Tables 1 and 2.

Transformation of abundant barium hexaferrites treated with rare earth elements like dysprosium, terbium, erbium, holmium, samarium and many others was registered down. Change in magnetic properties was noted with altering values of saturation magnetization, retentivity and coercivity. Semiconducting properties changed with growth in AC conductivity on increasing temperature. Elements like lanthanum, neodymium and samarium increased the magnetization saturation, retentivity and coercivity values influencing the magnetic properties. In some of the compositions, addition of cerium decreased the values of magnetization saturation, retentivity and coercivity. But on the average, net enhancement in electromagnetic properties of rare earth doped hexaferrites has been observed which increase their utility in high-frequency operating devices.

3 Synthesis Techniques Used to Prepare the Rare Earth-Doped Samples

Rare earth-doped hexaferrites can be prepared using various synthesis methods as shown in Fig. 4.

3.1 Sol–gel

This process emerged in the year 1921. It is a chemical method for preparing ceramic powders, gels and glasses. During this process, gels can be broken into granules when they are in the drying state. The materials required in this process are of inorganic configuration having various properties like superconductivity and ferroelectricity. It comprises various steps like solution, gelation, drying and densification. Firstly, a silicate solution is prepared in this process and then gel formation takes place. A sol is prepared with dispersion of colloidal particles (crystalline and amorphous). After this, a dry gel is obtained which is made up of 3-D network of silica. In this drying process, remaining solvent is removed. And after that final sintering, densification and grain growth mechanism are done to enhance the mechanical properties and the stability of the structure. Refer Fig. 5 for stepwise procedure of sol–gel method.

Table 1 Observed values of structural parameters

Composition	a (Å)	c (Å)	c/a (Å)	Reference no.
Ba(MnZn) _{0.3} Co _{1.4} REO _{0.01} Fe _{15.99} O ₂₇ (RE = Dy ³⁺ , Nd ³⁺ , Pr ³⁺)	5.90719–5.9028	32.92385–32.92554	–	[14]
BaCo ₂ La _x Fe ₂₄ O ₄₁ (x = 0.0–0.3)	5.883–5.96	5.2311–5.2548	8.892–8.852	[17]
Sr _{1-x} Ce _x Co ₂ Mn _y Fe _{16-y} O ₂₇ (x = 0.0–0.06, y = 0.0–0.6)	5.83–5.89	33.30–33.94	–	[19]
BaHo _x Fe _{16-x} O ₂₇ (x = 0.0 = 1.0)	5.86–5.91	32.6–33.45	5.55–5.66	[20]
Ba _{0.9} RE _{0.1} Co ₂ Fe _{16-x} O ₂₇ (RE = La ³⁺ , Nd ³⁺ , Sm ³⁺)	5.896 ± 0.0011–5.889 ± 0.0013	32.025 ± 0.0001–32.805 ± 0.0002	–	[8]
Ba ₂ Zn ₂ Tb _x Fe _{12-x} O ₂₂ (x = 0.00–0.10)	5.85–5.91	43.45–44.31	7.41–7.49	[23]
BaNi ₂ Dy _x Fe _{16-x} O ₂₇ (x = 0–0.9)	0.5866–0.5877	3.3261–3.3273	5.670–5.661	[25]
Sr ₂ NiCoTb _x Fe _{28-x} O ₄₆ (x = 0.00–0.2)	5.283–5.282	83.720–83.726	15.847–15.851	[26]
Ba ₂ NiCoDy _x Fe _{12-x} O ₂₂ (x = 0.00–0.25)	5.87–5.88	43.87–43.97	7.47–7.48	[3]
BaFe _{12-2x} Co _x Sm _x O ₁₉ (x = 0.0–0.6)	5.883 ± 0.500–5.864 ± 0.500	23.037 ± 0.500–22.998 ± 0.500	3.915–3.922	[7]
La _x Ba _(1-x) Fe ₁₂ O ₁₉ (x = 0.0–0.5)	5.8609–5.8655	23.0239–22.8198	3.92–3.88	[6]
Sr _(1-x) Cu _x Fe _{12-y} Er _y O ₁₉ (x = 0.0–0.2, y = 0.0–0.5)	5.91–5.87	23.27–23.15	3.937–3.943	[29]

(continued)

Table 1 (continued)

Composition	a (Å)	c (Å)	c/a (Å)	Reference no.
BaCe _x Fe ₁₁ CoO ₁₉ (x = 0-0.5)	5.893-5.892	23.185-23.183	3.9343-3.9356	[30]
Ba _(1-x) RE _x Co ₂ Zn _x Fe _{16-x} O ₂₇ (x = 0.0-0.2)	5.90-5.89	32.89-32.83	-	[31]

Table 2 Observed values of magnetic parameters

Composition	M_s (emu/g)	M_r (emu/g)	H_c (Oe)	Reference no.
$Ba_{3-x}Co_2La_xFe_{24}O_{41}$ ($x = 0.0-0.3$)	61.36–77.31	5.682–5.556	45.68–35.51	[17]
$BaHo_xFe_{16-x}O_{27}$ ($x = 0.0 = 1.0$)	3.648–31.831	1.334–14.492	1041.7–1709.6	[20]
$Ba_{0.9}RE_{0.1}Co_2Fe_{16-x}O_{27}$ (RE = La^{3+} , Nd^{3+} , Sm^{3+})	82.06–82.70	10.02–11.63	747.0–854.3	[8]
$BaNi_2Dy_xFe_{16-x}O_{27}$ ($x = 0-0.9$)	74–53	–	530–560	[25]
$Sr_2NiCoTb_xFe_{28-x}O_{46}$ ($x = 0.00-0.2$)	76–54	27–21	610–747	[26]
$BaCo_{0.8}Sm_xFe_{11.2-x}O_{19}$ ($x = 0.2-0.6$)	32.55–21.36	18.25–10.65	2690.20–2407.52	[5]
$Eu_xBa_{1-x}Fe_{12}O_{19}$ ($x = 0-0.10$)	30.49–54.27	–	3030–8730	[28]
$BaCo_xFe_{12}O_{19}$ ($x = 0-0.5$)	77–63.3	–	5200–2360	[11]
$BaFe_{12-2x}Co_xSm_xO_{19}$ ($x = 0.0-0.6$)	$62 \pm 0.5-61 \pm 0.5$	$40 \pm 0.5-35 \pm 0.5$	$5267 \pm 10-3087 \pm 10$	[7]
$La_xBa_{(1-x)}Fe_{12}O_{19}$ ($x = 0.0-0.5$)	–	2.085–1.515	409.08–590.18	[6]
$Sr_{(1-x)}Cu_xFe_{12-y}Er_yO_{19}$ ($x = 0.0-0.2$, $y = 0.0-0.5$)	59.41–51.84	34.07–29.27	6031.74–4962.09	[29]

(continued)

Table 2 (continued)

Composition	M_s (emu/g)	M_r (emu/g)	H_c (Oe)	Reference no.
$BaCe_xFe_{11}CoO_{19}$ ($x = 0-0.5$)	60-42.4	26.42-12.5	1159-462	[30]
$Ba_{(1-x)}RE_xCo_2Zn_xFe_{16-x}O_{27}$ ($x = 0.0-0.2$)	$73.03 \pm 0.09-74.60 \pm 0.08$	$11.42 \pm 0.50-6.26 \pm 0.60$	$95 \pm 5-80 \pm 5$	[31]

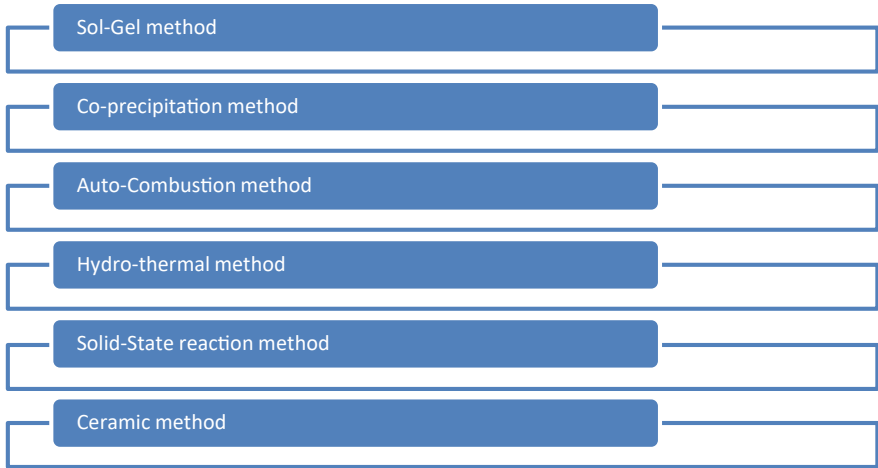
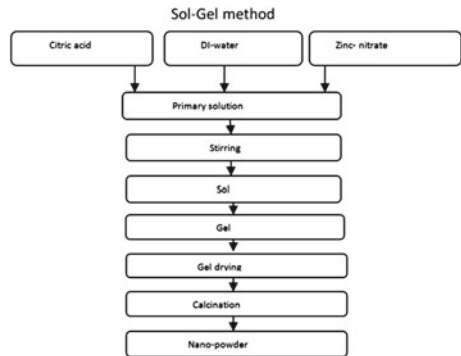


Fig. 4 Different synthesis techniques for preparing rare earth-doped samples

Fig. 5 Sol-gel method



3.2 Co-precipitation

It is a method in which a solute is precipitated out by some of the forces but normally that solute remains dissolved in the solution. This is facilitated by some of the chemical reaction made in the laboratories. The imperative forces pull out the solute from the dispersed medium. In this method, magnetic stirring at the temperature of 70 °C is done; after that in centrifugation process, particles are cleared by the deionized water, and in the last step, the resulted part is dried. In Fig. 6, various steps involved in the process of co-precipitation method are shown.

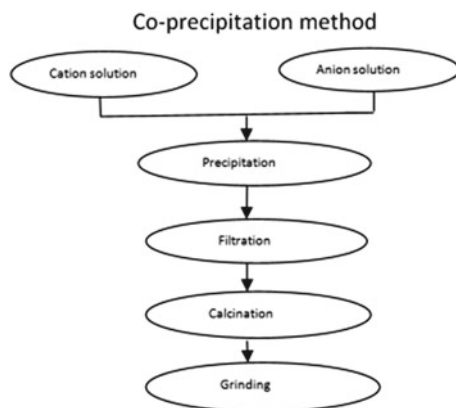


Fig. 6 Co-precipitation method

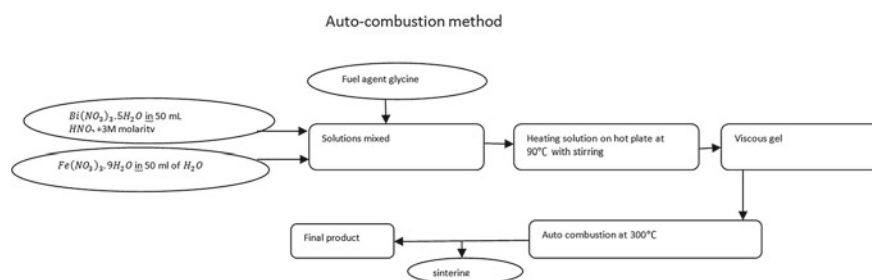


Fig. 7 Auto-combustion method

3.3 Auto-combustion Method

In this method, the solution of ammonia, citric acid and salts is set up to pH value of 7, and then on a dry plate, they are evaporated. Carbon dioxide gas is given out when polymerization of the citric acid takes place. Cations are changed into the barium carbonate and oxides of iron. Small grain-sized sample is obtained which is in last auto-combusted in the microwave oven to get the nano-powder. Auto-combustion method is described in Fig. 7.

3.4 Hydrothermal Method

It is a process in which single crystals (nanoparticles) are synthesized depending on the solubility of the minerals in the hot water. Crystal growth is taken out in a steel vessel called autoclave at high pressure. Temperature is kept constant in this process.

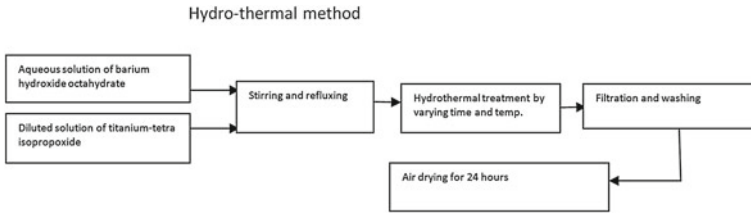


Fig. 8 Hydrothermal method

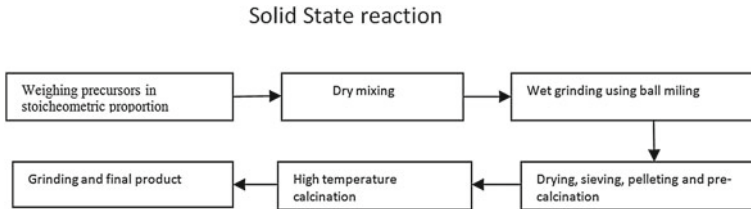


Fig. 9 Solid-state reaction

It is an effective method for preparing those crystalline phases which are not so much stable at higher temperature. Figure 8 shows the process of hydrothermal method.

3.5 Solid-State Reaction Method

As shown in Fig. 9, it is the simplest method for producing the single crystals and polycrystalline powders of phosphates and arsenates of transition metals and monovalent cations. In this process, required amount of precursors is taken and then they are grinded. The resulted powder is then heated at 350–400 °C resulting in the removal of ammonia, carbon dioxide, water and other nonvolatile substances. After that, grain size is decreased. Cation migration is then done at the high temperature, and then, crystals are separated by boiling water.

3.6 Ceramic Method

In this method, barium oxides and carbonate powders are heated to get the hexagonal ferrites. Because of low reactivity of the starters, high temperature is required in this process. Extrusion, slip casting, pressing, tape casting and injection molding are some of the most common ceramic forming methods. Figure 10 shows how the ceramic method is used to prepare the rare earth-doped barium hexaferrites.

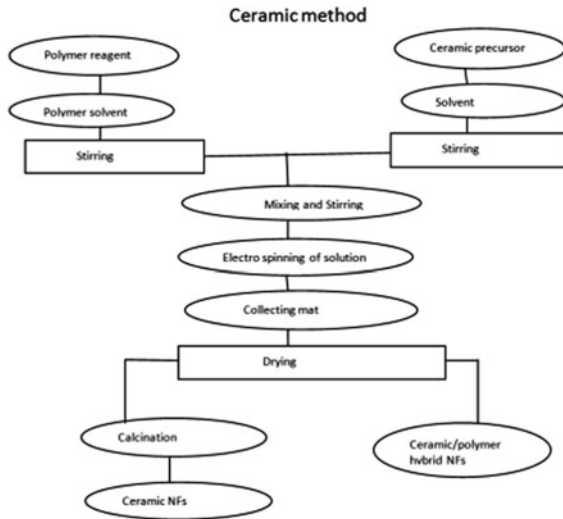


Fig. 10 Ceramic method

4 Conclusion

This paper lays out the detailed data about the verified upgrowth of the barium hexaferrites introduced with rare earth elements. Different types of ferromagnetic oxides with their application areas are discussed. According to the Literature review, the rare earth doped barium ferrites best supports for the enlightenment of electromagnetic properties. Various operating procedures including X-ray diffraction, scanning electron microscopy, etc., provided the useful information about the composition, crystallographic structure, surface topography of the sample, its chemical properties and much more. For various M-type barium hexaferrites, lanthanum ions increase the coercivity and AC conductivity at high frequency. Elements like cerium were used to improve the ability of the sample for absorbing electromagnetic waves. In few of the Y-type barium hexaferrites, DC electrical conductivity grows on addition of terbium like rare earth element. But for strontium hexaferrites, addition of terbium reduced the saturation magnetization and made an increase in coercivity. Samarium, holmium and erbium showed the best high-frequency dielectric properties which made them quite useful for application areas like semiconducting and other high-frequency operating devices. Magnetic properties talk about the most increase in magnetic saturation and coercivity that helps them being useful in field of recording media as permanent magnets, multilayered inductors and chips, etc.

References

1. Shah S, Pandey OP, Mohammad J, Srivastava AK, Gupta A, Basandrai D (2020) Reduced graphene oxide (RGO) induced modification of optical and magnetic properties of M-type nickel doped barium hexaferrites. *J Sol-Gel Sci Technol* 93:579–586. <https://doi.org/10.1007/s10971-019-05210-0>
2. Srivastava R, Yadav BC (2013) Ferrite materials: introduction, synthesis techniques, and applications as sensors. *Int J Green Nanotechnol.* <https://doi.org/10.1080/19430892.2012.676918>
3. Maria Zahid MU, Islam MS, Awan M, Ashiq N, Naseem S, Ali I, Iftikhar A, Ahmad M, Kamran Z (2017) Effect of dysprosium on structural and physical properties of $\text{Ba}_2\text{NiCoFe}_{12}\text{O}_{22}$ Y-type hexaferrites, *J Aust Ceram Soc.* <https://doi.org/10.1007/s41779-017-0101-3>
4. Robert C (2012) Pullar, hexagonal ferrites: a review of synthesis, properties and applications of hexaferrites ceramics. *Progress Mater Science* 57:1191–1334
5. Rana K, Thakur P, Thakur A, Tomar M, Gupta V, Luc Mattei J, Queffelec P (2016) Influence of samarium doping on magnetic and structural properties of M type Ba-Co hexaferrites. *Ceramics Int*
6. Anjum S, Seher A, Mustafa Z (2019) Effect of La^{3+} ions substituted M-type barium hexa-ferrite on magnetic, optical, and dielectric properties. *Appl Phys A* 125:664. <https://doi.org/10.1007/s00339-019-2937-6>
7. Faisal M, Saeed A, Larik FA, Ghumro SA, Rasheed S, Channar PA (2018) WOWS Sol-Gel based synthesis and structural, morphological, electrical and magnetic characterization of Co-Sm doped M-type barium hexaferrite materials. *J Electr Mater.* <https://doi.org/10.1007/s11664-018-6628-4>
8. Guo F, Ji G, Xu J, Zou H, Gan S, Xu X (2011) Effect of different rare-earth elements substitution on microstructure and microwave absorbing properties of $\text{Ba}_{0.9}\text{RE}_{0.1}\text{Co}_2\text{Fe}_{16}\text{O}_{27}$ ($\text{RE}=\text{La}$, Nd, Sm) particles. *J Magnet agnetic Mater* 324(2012):1209–1213,
9. Jotania RB, Virk HS (2012) Y-type hexaferrites: structural, dielectric and magnetic properties. *Solid State Phenomena* 189(2012):209–232
10. Kouril K, Chlan V, Stepankova H, Telfah A, Novak P, Knizek K, Hiraoka Y, Kimura T (2010) Distribution of Zn in magnetoelectric Y-type hexaferrite. *Acta Physica Polonica A* 118(5)
11. Sharma V, Kumari S, Kuanr BK. Rare earth doped M-type hexaferrites: ferromagnetic resonance and magnetization dynamics. *Am Inst Phys.* <https://doi.org/10.1063/1.5007297>
12. Ahmed MA, Okasha N, Kershi M (2007) Influence of rare-earth ions on the structure and magnetic properties of barium W-type hexaferrites. *J Magnet Magnet Mater* 320(2008):1146–1150
13. D'souza A, Deepak Kumar M, Chatim M, Naik V, Naik PP, Tangsali RB (2016) Effect of rare-earth doping on magnetic and electrical transport properties of nanoparticle Mn-Zn ferrite. *Adv Sci Lett.* <https://doi.org/10.1166/asl.2016.6966>
14. Jing W, Hong Z, Shuxin B, Ke C, Changrui Z (2006) Microwave absorbing properties of rare-earth elements substituted W-type barium ferrite. *J Magnet Magnet Mater* 324(2012):1209–1213
15. Yang A, Chen Y, Chen Z, Vittoria C, Harris VG (2008) Magnetic and atomic structure parameters of Sc-doped barium hexagonal ferrites. *J Appl Phys* 103:07E511
16. Ahmed MA, Okasha N, Kershi RM (2009) Extraordinary role of rare-earth elements on the transport properties of barium W-type hexaferrites. *Mater Chem Phys* 113:196–201
17. Ji-Jing Xu, Yang C-M, Zou H-F, Song Y-H, Gao G-M, An B-C, Gan Shu Cai (2009) Electromagnetic and microwave absorbing properties of Co_2Z -type hexaferrites doped with La^{3+} . *J Magn Magn Mater* 321:3231–3235
18. Xiaogu H, Jing Z, Hongzhou W, Shaoteng Y, Lixi W (2010) Er^{3+} -substituted W-type barium ferrite: preparation and electromagnetic properties. *J Rare Earths* 28(6):940
19. Khan I, Sadiq I, Ashiq MN, Rana M-U-D (2011) Role of Ce–Mn substitution on structural, electrical and magnetic properties of W-type strontium hexaferrites. *J Alloys Compounds* 509:8042–8046

20. Aen F, Niazi SB, Islam MU, Ahmad M, Rana MU (2011) Effect of holmium on the magnetic and electrical properties of barium based W-type hexagonal ferrites. *Ceram Int* 37:1725–1729
21. Ali I, Islam MU, Ashiq MN, Iqbal MA, Khan HM, Karamat N (2013) Effect of Tb–Mn substitution on DC and AC conductivity of Y-type hexagonal ferrite. *J Alloys Compounds* 579:576–582
22. Cai S, Xin PH, Wang PF, Zhang BB, Han YB, Peng XL, Hong B, Jin HX, Gong J, Jin DF, Ge HL, Wang XQ, Zhang J (2013) The sol-gel synthesis of rare—earth ions substituted barium hexaferrites and magnetic properties. *Modern Phys Lett B*, 27(26):1350192. <https://doi.org/10.1142/S0217984913501923>
23. Ali I, Shaheen N, Islam MU, Irfan M, Ashiq MN, Iqbal MA, Iftikhar A (2014) Study of electrical and dielectric behavior of Tb⁺³ substituted Y-type hexagonal ferrite. *J Alloys Compounds* 617:863–868
24. Guo S, Zhang Y, Wang Y, An J, Zhao D (2014) Microstructures and high frequency properties of Sm doped Co₂ Z-type hexagonal ferrites as anti-EMI magnetic bead materials. *IEE Trans Magnet* 50(1)
25. Sharbati A, Mola J, Khani V, Amiri GR, Mousarezafi R (2014) Influence of dysprosium addition on the structural, morphological, electrical and magnetic properties of nano-crystalline W-type hexaferrites. *Bull Mater Sci* 38(1)
26. Rehman J, Khan MA, Hussain A, Iqbal F, Shakir I, Murtaza G, Niaz Akhtar M, Nasar G, Warsi MF (2016) Structural, magnetic and dielectric properties of terbium doped NiCoX strontium hexagonal nano-ferrites synthesized via micro-emulsion route. *Ceramics Int*
27. Irfan M, Elahi A, Shakoor A (2016) Hysteresis and electric modulus analysis of Y³⁺ doped MnNi-Y-Type hexagonal ferrite. *Ceram-Silik* 60(2):34–40
28. Zafar A, Rahman A, Shahzada S, Anwar S, Khan M, Nisar A, Ahmad M, Karim S (2017) Electrical and magnetic properties of nano-sized Eu doped barium Hexaferrites. *J Alloys Compounds* 727:683e690
29. Mohammed J, Hafeez HY, Tekou T, Carol T, Ndikilar CE, Sharma J, Maji PK, Godara SK, Srivastava AK. Structural, dielectric, and magneto-optical properties of Cu²⁺–Er³⁺ substituted nanocrystalline strontium hexaferrite. *Mater Res Express*. <https://doi.org/10.1088/2053-1591/ab063b>
30. Araz I (2019) The effect of Ce–Co substitution on the structural and the electromagnetic properties of barium hexaferrites. *J Mater Sci Mater Electron*. <https://doi.org/10.1007/s10854-019-00811-5>
31. Dmour MK, Al-Hwaitat ES, Bsoul I, Mahmood SH (2019) Structural and magnetic properties of Ba_{1-x}Re_xCo₂Zn_xFe_{16-x}O₂₇ W-type hexaferrites prepared by sol–gel auto-combustion. *J Supercond Novel Magnet*. <https://doi.org/10.1007/s10948-019-05213-6>

Computational Fluid Dynamic Analysis of Cyclone Separator for Flue Gas Cleaning by Using Standard k-Epsilon Model



Jaishree Chauhan, B. L. Salvi, M. S. Khidiya, and Chitranjan Agrawal

1 Introduction

Cyclonic separation is a method for separating different fluid phases (different densities) or separating solid particles of a particular size from a gas stream. Cyclone separators or simply cyclones are separation devices that use the centrifugal forces, gravity and principle of inertia to remove particulate matter from gases [1]. Cyclone separators are used as a solution for eliminating particulates from air or other fluid streams with ease, at low expense, and these devices need comparatively low maintenance.

Flue gases are a resultant of combustion products and consist of water vapor, carbon dioxide, particulates, heavy metals and acidic gases. Cyclone separators are a low-cost method for refining these gases for particulates [2].

1.1 Working Principle

A cyclone separator is based on centrifugal principle in which particulates because of their mass are pushed to the outer edges as a result of the inertial force acting on them due to the rotational motion of the cyclonic flow. The model being studied here is that of a reverse flow cyclone separator, which consists of cylindrical top part called as barrel and a conical bottom part called as cone. The gas enters at the top of the body through an inlet at the top, flows downward and then upward and is then discharged through an outlet at the top (Fig. 1).

J. Chauhan (✉) · B. L. Salvi · M. S. Khidiya · C. Agrawal
Department of Mechanical Engineering, College of Technology and Engineering, MPUAT,
Udaipur, Rajasthan 313001, India

© The Author(s), under exclusive license to Springer Nature Singapore Pte Ltd. 2022
P. Verma et al. (eds.), *Advancement in Materials, Manufacturing and Energy Engineering*,
Vol. II, Lecture Notes in Mechanical Engineering,
https://doi.org/10.1007/978-981-16-8341-1_2

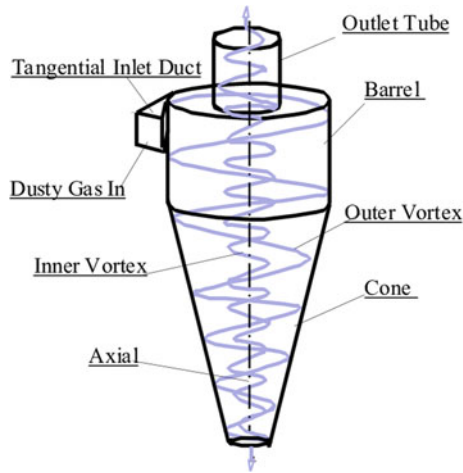


Fig. 1 Schematic diagram of reverse flow cyclone separator

A high-speed rotating flow in a helical pattern is established within the container which is introduced through an inlet tangential to barrel. Air flows in a spiral pattern, beginning at the barrel end of the cyclone and ending at the conical end before exiting the cyclone in a straight stream through the outlet at the top of the cyclone in the center of the separator [3]. Bigger and denser particles in the flowing stream have too much inertia to follow the tight curve of the helical flow and strike the outer wall, landing then to the end of the conical section of the cyclone where they can be collected and removed. In the cyclone separator, the spiral flow moves down toward the conical end of the device where the rotational radius of the stream is reduced, increasing the inertial forces on the particles in the flow, thus separating smaller particles [4].

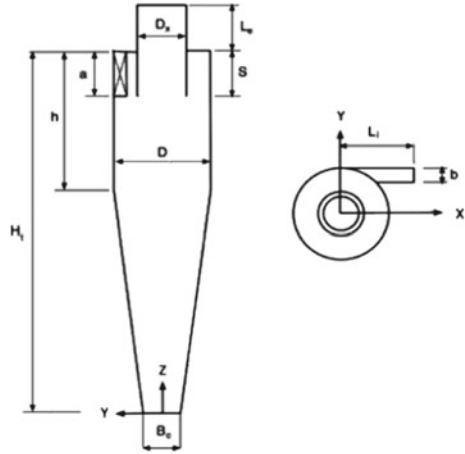
Swirl and turbulence are the two competing phenomena in the separation process: The swirl induces a centrifugal force on the solid phase which is the driving force behind the separation; turbulence disperses the solid particles and enhances the probability that particles get caught in the exit stream and both phenomena are related to the particle size and the flow conditions in the cyclone [5].

The cyclone geometry is described by seven geometrical parameters, viz. the inlet height a , width b , the vortex finder diameter D_x , length S , cylinder height h , cyclone total height H_t and cone tip diameter B_c (Fig. 2) [6, 7].

2 Materials and Methodologies

In this study, the cyclone separator is simulated using a standard k- ϵ model for the CFD using Ansys Fluent programming. The data obtained then is compared using velocity and pressure contour charts for different particles. The accuracy of the

Fig. 2 Cyclone separator geometry



simulation is dependent on the efficacy of the numerical model used to simulate the turbulence and the assumptions made during the process. Efficiency of the separator is calculated using Eq. (1), in which particle tracking data can be used from the simulation.

$$\text{Efficiency} = \frac{\text{particles trapped}}{\text{particles tracked}} * 100 \tag{1}$$

2.1 Standard *k-Epsilon* Model

It is the most common model used for simulation of turbulence in the system for computational fluid dynamics. It is a two-equation model which estimates the turbulence by using two transport equations (PDE). The first equation is for turbulence energy (*k*), and second is for dissipation of turbulent epsilon energy (*ε*). In this model, it is assumed that flow is completely turbulent and the effects of molecular viscosity are negligible [8, 9].

Governing Equation

The exact *k-ε* equations contain unknown and incalculable terms. So, for practical purposes we are using the standard *k-ε* turbulence model which minimizes the unknowns and presents set of equations which can be applied to a large number of turbulent applications.

For turbulent kinetic energy *k*,

Table 1 Measurements of separator

Parameters	Symbol used in the diagram	Value (mm)
Inlet height	a	100
Inlet width	b	50
Vortex diameter	D_x	100
Length	S	125
Cylinder height	h	400
Total height	H_t	800
Cone tip diameter	B_c	50

$$\frac{\partial(\rho k)}{\partial t} + \frac{\partial(\rho k u_i)}{\partial x_i} = \frac{\partial}{\partial x_j} \left[\frac{\mu_t}{\sigma_k} \frac{\partial k}{\partial x_j} \right] + 2\mu_t \alpha_{ij} \alpha_{ij} - \rho \varepsilon \quad (2)$$

For dissipation of energy,

$$\frac{\partial(\rho k)}{\partial t} + \frac{\partial(\rho k u_i)}{\partial x_i} = \frac{\partial}{\partial x_j} \left[\frac{\mu_t}{\sigma_\varepsilon} \frac{\partial \varepsilon}{\partial x_j} \right] + A_{1\varepsilon} \frac{\varepsilon}{k} 2\mu_t \alpha_{ij} \alpha_{ij} - A_{2\varepsilon} \rho \frac{\varepsilon^2}{k} \quad (3)$$

where

u_i represents velocity component in corresponding direction

A_{ij} represents component of rate of deformation

μ_t represents eddy viscosity

$\sigma_\varepsilon, \sigma_k, A_{1\varepsilon}, A_{2\varepsilon}$ are constants whose value is calculated using various iterations of data fitting for turbulent flow.

3 CFD Analysis Procedure Using Ansys Fluent

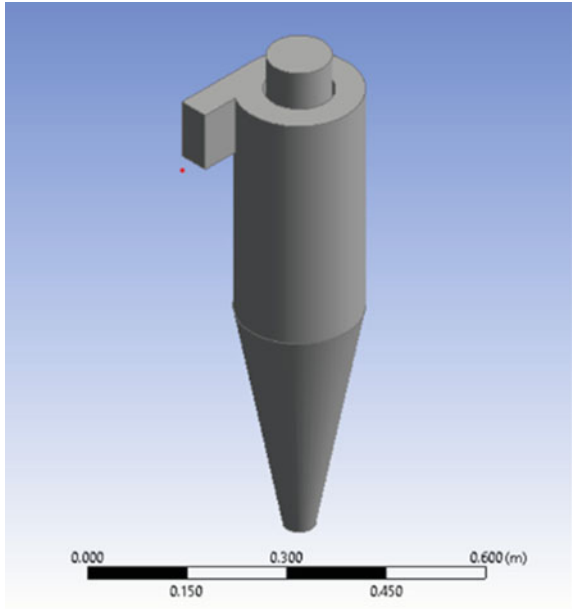
3.1 Input Parameters for the Modeling

For the study, we have used the geometrical measurements of the separator given in Table 1 to design the model in the design modeler of fluid flow. The symbols used can be referred from Fig. 2.

3.2 Modeling in Ansys Fluent for *k*-Epsilon Model

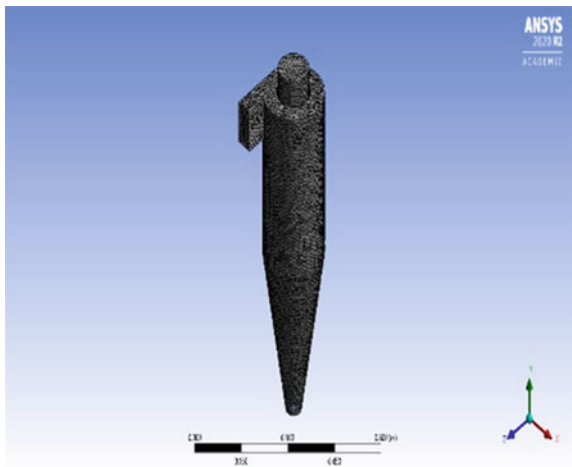
CFD analysis study is performed using Ansys Fluent system in the workbench of the program. The design for cyclone separator is created in the design modeler according to the dimensions mentioned in Table 1. For the resulting model (Fig. 3), the named selections for the inlet, outlet and Outlet_particles are created for the

Fig. 3 Cyclone separator model



relevant faces. Meshing is done for the model, the patch conforming method is used, tetrahedron type is used for the mesh, and element size is kept 0.001 m. Resulting mesh contains 93,606 elements and 18,888 nodes (Fig. 4) [10]. The mesh quality check is performed using the orthogonality metric and skewness; for orthogonality, the average value is 0.77, and for skewness, average value is 0.22. Both of these values make it a good-quality mesh.

Fig. 4 Meshing of the model



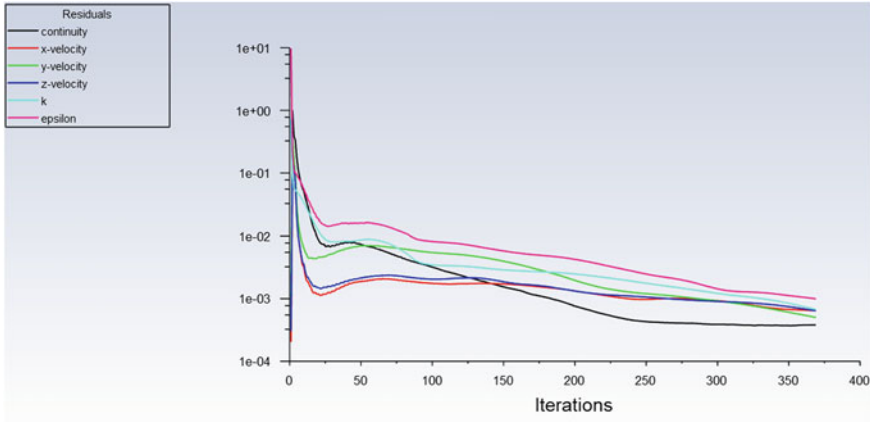


Fig. 5 Residuals chart

Simulation conditions are given in the Fluent setup to set and simulate the conditions for model. Simulation is done using realizable k -epsilon (2eqn) model with enhanced wall treatment and discrete phase modeling for the system. The boundary conditions are specified for the inlet with velocity of 8.0 m/s and dpm condition reflect, for outlet at the top dpm conditions are escape and for the outlet of particles at the bottom has the dpm condition as trap. Particle size is given as 5, 10, 15 μm of type ash particles in the air flow. Under the solution tab, the SIMPLE scheme is selected and changes are made for turbulent kinetic energy and turbulent dissipation rate to second-order upwind. The solution using standard initialization is initialized, and option for compute from inlet velocity is selected. The simulation was run for 500 iterations and find convergence occurs at 369 and particle history data is obtained and residual charts are created (Fig. 5) [11].

4 Results and Discussion

4.1 Analysis of Collection Efficiency

In the CFD analysis study, the particle size was varied from 5 to 15 μm and the particles were tracked in the simulation study to find the number of trapped and escaped particles. Collection efficiency is calculated by the data given by simulation using Eq. (1). Total particles tracked in simulation were 3900 in each case, and result is shown in Table 2. From the data, it is observed that as the particle size increases efficiency increases and a near-perfect collection can be seen for the 15 μm size particles, thus making cyclone separator as a good method for the filtration of the particle size of 10 μm and higher.

Table 2 Particle data

Particle size (μm)	Particles trapped	Efficiency (%)
5	3048	78.15
10	3628	93.03
15	3896	99.89

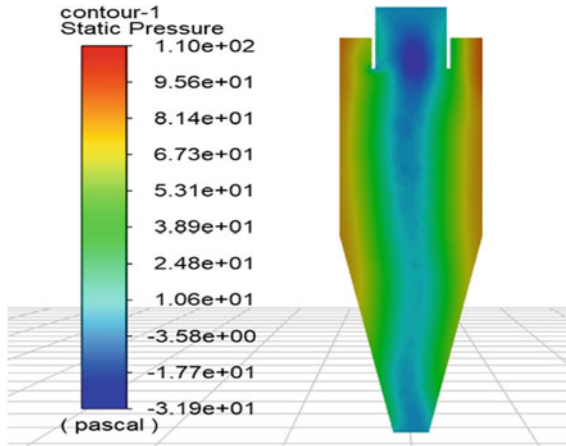


Fig. 6 Pressure contour chart

4.2 Analysis of Static Pressure and Wall Shear Stress

The static pressure for the separator is charted in a contour chart for the plane $x = 0$ which shows maximum pressure values at the outer edges of the separator (Fig. 6), thus showing that outer walls of the device are most susceptible to the abrasions. This contour also shows the low-pressure helical pattern in the center which is in agreement with the physics of cyclone formation. The wall shear stress for the separator is shown in Fig. 7, and the maximum value of 0.0531 Pascal is found at corner of the inlet where it meets the cylinder; since this value is very small, chances of fracturing are very low but this does give us an indication that abrasive action can occur at that spot.

4.3 Analysis of Radial Velocity and Turbulence

The radial velocity contour plotted on plane $x = 0$ (Fig. 8) shows us that maximum radial velocity is in the vortex finder where the concentration of particulates is least and fluid stream has been filtered. The turbulent intensity contour (Fig. 9) shows the opposite trend, and intensity is highest at bottom where inner vortex is being

Fig. 7 Wall shear stress contour

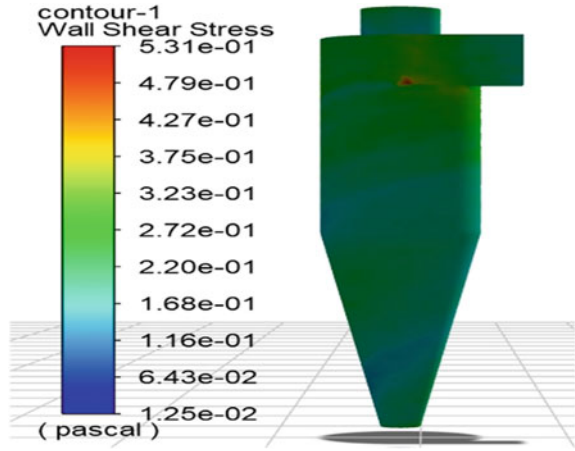
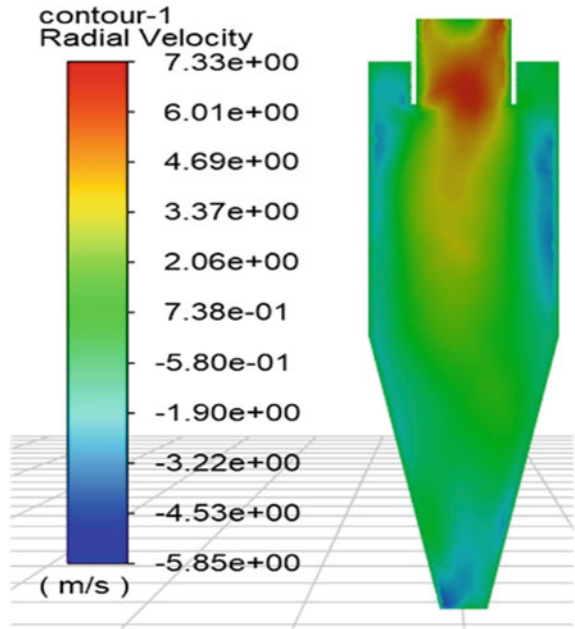
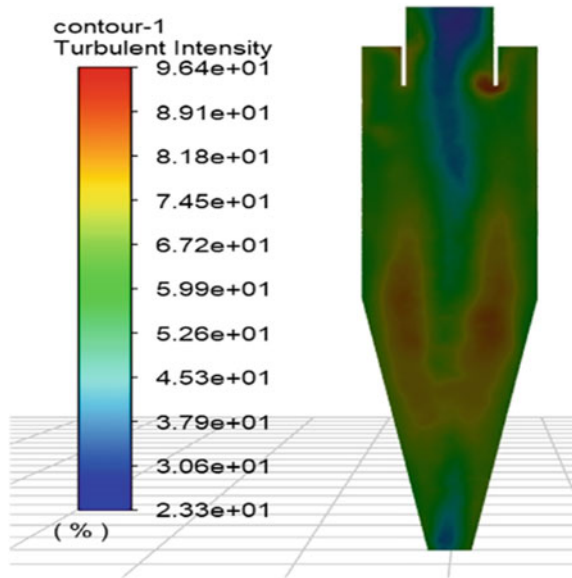


Fig. 8 Radial velocity contour



formed as well as at the corner of inlet where shear stress is highest. At the bottom where turbulent intensity is highest, the centrifugal velocity is pushing the particles toward boundary and gravity is dragging particles toward the bottom which is causing turbulence in the system.

Fig. 9 Turbulent intensity contour



5 Conclusions

The computational fluid dynamics (CFD) analysis was carried out for flow analysis and particle separation in a cyclone separator for flue gas cleaning. The study was carried out for ash particle size with uniform diameter of 5, 10, 15 μm . From the CFD analysis, it was found that separation efficiency increases with increase in particle size from 5 μm and is nearly 100% for larger particulates of 15 micrometer, thus making it a very good solution for filtration for larger particles before passing flue gases through finer filters for further separation and protecting them from abrasions.

Furthermore, the wall shear stress on the joint of inlet and the cylinder is highest and it should be braced with extra support to increase hardness and protect it from fracture. The CFD simulation and contour charts help to better visualize the complete particle separation procedure and give a better understanding for further optimization of the cyclone separator. Multiple iterations can be performed with the help of software, and parametric study in variables like inlet speed and particle sizes can be done. This would eliminate the need for actual fabrication of devices, time and cost saving in optimization of the cyclone separator.

Acknowledgments The authors are grateful to Scientific and Engineering Research Board, DST, New Delhi, India for providing financial support to conduct this work under grant number EEQ/2019/000339.

References

1. Muschelknautz U, Muschelknautz E (1999) Separation Efficiency of Recirculating Cyclones in Circulating Fluidized Bed Combustions. *VGB Power Tech: Essen, Germany* 79:48–53
2. Lee KW, Park SH, Xiang R (2001) Effects of cone dimension on cyclone performance. *J Aerosol Sci* 32:549–561
3. Dirigo J, Leith D (1985) Performance of theoretically optimized cyclones. *Filtr Sep* 119–125
4. Cortés C, Gil A (2007) Modeling the gas and particle flow inside cyclone separators. *Prog Energy Combust Sci* 33:409–452
5. Hoekstra AJ, Derksen JJ, Van Den Akker HEA (1999) An experimental and numerical study of turbulent swirling flow in gas cyclones. *Chem Eng Sci* 54:2055–2065
6. Hoffmann A, van Santen A, Allen R, Clift R (1992) Effects of geometry and solid loading on the performance of gas cyclones. *Powder Technol* 70:83–91
7. Stairmand CJ (1951) The design and performance of cyclone separators. *Trans Inst Chem Eng* 356–383
8. Wang HG, Shi S (2003) Application and comparison of different turbulence models in the three-dimensional numerical simulation of cyclone separators. *J Eng Therm Energy Power* 338–342
9. Narasimha M, Sripriya R, Banerjee PK (2005) CFD modelling of hydro cyclone—prediction of cut size. *Int J Miner Process* 53–68
10. Cortés C, Gil A (2007) Modeling the gas and particle flow inside cyclone separators. *Prog Energy Combust Sci* 409–452
11. Vaitiekunas P, Jakštoniene I (2010) Analysis of numerical modelling of turbulence in a conical reverse-flow cyclone. *J Environ Eng Landsc Manag* 321–328

Identification of Lubricant Contamination in Journal Bearings Using Vibration Signature Analysis



Ambuj Pateriya, N. D. Mittal, and M. K. Pradhan

1 Introduction

Industrial lubrication systems are often subject to different types of contaminations which are very damaging and sometimes fatal for certain components such as bearings or pumps. More than 70% of machine components such as journal bearing where lubricant plays a critical role failed due to lubricant contamination [1]. Water in the lubricant, along with solid particles, is one of the most well-known contamination problems in industrial applications [2]. Indeed, this type of contamination has a significant impact on the flow characteristics within the thickness of the film, resulting in unexpected behavior or damage to the bearing. The consequences can be catastrophic.

Journal slides within the bearing, trails lubricant, and generates hydrodynamic lift force by creating wedge flow motion. Oil film formed between the journal and bearing separates them as shown in Fig. 1. The clearance in between the journal and bearing is in order of microns. It is in the clearance space that contaminants get entrapped and result in bearing surface wear. The rise in friction due to the interaction of the bearing particle will cause localized heating which may lead to wiping and brushing of the surface [3]. Added to this, the absorbed contaminating particles increase the generation of internal particles, thus obstructing the lubrication system and generating starvation leading to failure [4]. The particle contaminant in a bearing is of two types: external ingested particles which are sand, dust, and grit, and internal ingested particle which is generated due to wear and corrosion [5]. Previous research showed that, by attacking the bearing base metal and other elements of the circuit, or by mixing with the lubricant itself, water contamination can lead to lubrication failure [6]. In both situations, oil contamination with polluted water is

A. Pateriya (✉) · N. D. Mittal · M. K. Pradhan
Department of Mechanical Engineering, Maulana Azad National Institute of Technology, Bhopal
462003, India

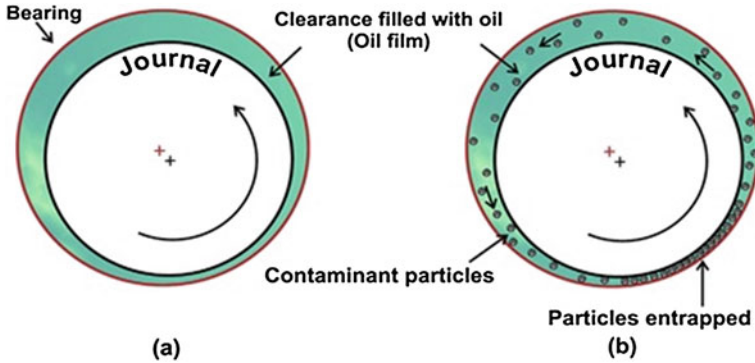


Fig. 1 Schematic diagram: **a** basic fluid film bearing and **b** entrapped foreign particles in bearing [8]

inherently unsafe and strategies need to be sought to ensure better working conditions and longer life of bearings [7].

Among the major detrimental effects of water, water mainly causes the lubricant to degrade itself, to resurface in a rust environment, and to reduce the boundary layer and hydrodynamic shielding [9, 10]. Water may also lead to different types of damage to the journal-bearing surfaces from corrosion to cavitation [11]. In the presence of hydrogen and oxygen, the Babbitt bearings, which consist mainly of lead and tin, can easily be oxidized. Vapor cavitation linked to implosion of water vapor and can cause comblike pitting on bearing surfaces [12]. Vibration analysis is a popular technique in the field of condition monitoring of machines. Monitoring of vibration signature has been widely used to gather information regarding the performance of bearings. Some fault detection analysis of bearings, such as oil whirl instability, oil whip, rubbing, and excessive preload, can be gathered from vibration signals [13]. Wear can also be predicted in bearing surface by use of the vibration signal. The existence of the 1X component is a significant feature of bearing wear [14]. The purpose of this article is to examine particulate contamination and water contamination in a journal-bearing lubricant (common sand particles of various sizes and weights as contaminants) by vibration techniques. Variation in the amplitude of vibration for different cases involving particle size, concentration and water type are experimentally shown in the amplitude vs frequency graphs. Features of the vibration signals such as peaks in terms of amplitude versus frequency and spectrum gave results for the condition monitoring of bearing [15].

Table 1 Specification of journal bearing

Outer diameter	62 mm
Inner diameter	25.4 mm
Diametric clearance	0.035 mm
Effective length	15 mm
L/D ratio	0.6
Bearing material	Phosphor bronze

Table 2 Specification of shaft and oil

Shaft material	Stainless steel
Density	7800 kg/m ³
Modulus of elasticity	210 GPA
Lubricant oil	Mineral oil
Oil supply	110 mLmin ⁻¹

2 Methodology and Sample Preparation

2.1 Methodology

Vibration data of healthy bearing without contamination were first measured, and after that, vibration data of contaminated bearings were taken using an accelerometer which was mounted on the housing of the bearing; two oil grooves were there at an angle of 30 degrees to each other. Vibration data were obtained in the form of amplitude versus frequency graphs. The intensity of the vibrations relies on the tally of these faults and their concentrations and sizes. It should be in mind that multiple defects in various areas of the bearing surface generate the same frequency but different phases of vibration [16].

To scrutinize how the particles of various sizes and different concentrations interact with the bearing surfaces and produce vibration signals, sand particles of various sizes 10, 15, 20, 25, and 40 μm and water contamination with soap, mineral, and saltwater were selected. The size of the biggest particle was not greater than 40 microns due to the clearance of the bearing; otherwise, the particle would accumulate in the oil grooves at the entry point of the bearing. Table 1 represents the specification of journal bearing, and Table 2 shows specification of shaft and oil.

2.2 Sample Preparation

Sand particles of various sizes and concentrations and water of three types were mixed with the lubricant in the stirrer in a variable volume percentage of grease, the stirrer speed was 1000 RPM for 10 min to make it a homogeneous mixture, and the

dissolved air was removed by rotating mixer at 1500 for 2 min before any sample preparation, from different solid and liquid contamination variations [17]. Figure 2a shows solid contaminants of different sizes and concentrations, and Fig. 2b shows the saltwater used.

The following is Table 3 for samples:

Tests were performed for clean oil without contamination and for five separate contamination cases.

Case 1—Lubricant oil with particulate contaminant (sand) concentration of 0.75 gm and size 10 μm as listed in Table 3.

Case 2—Lubricant oil with 20 μm particle size contaminant at 1 gm concentration.

Case 3—Oil with 40 μm particulate contaminant at a concentration of 1.25 gm.

Case 4—Water contamination by mineral water mixing 10% by volume in oil.

Case 5—Water contamination by mixing saltwater 10% by volume in oil.

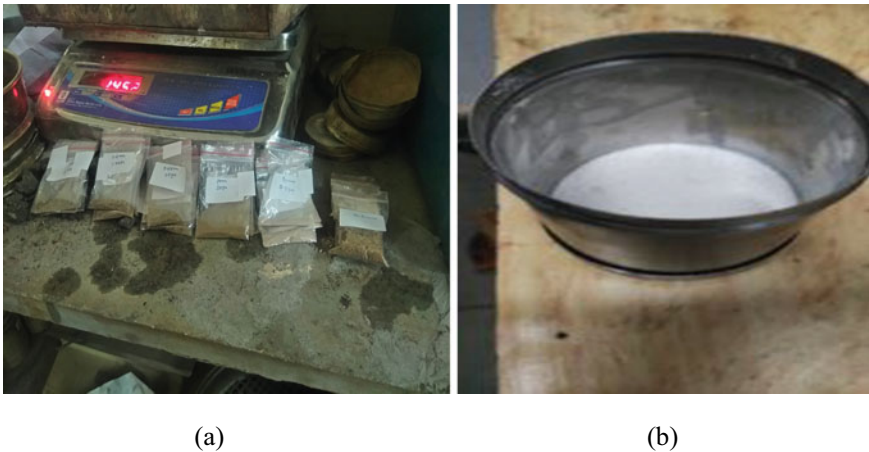


Fig. 2 a Solid contaminants of different sizes and concentration and b saltwater

Table 3 Sample preparation

Particle size (micron)	Weight of sand (grams)	Type of water	% of water (ml per ml of lubricant)
10	0.75	Salt	10
15		Soap	
20	1	Rain	15
25		Mineral	
40	1.25		

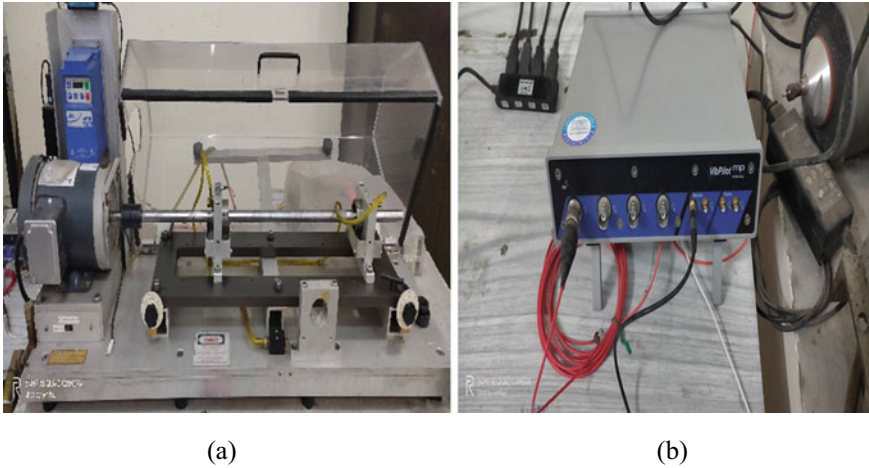


Fig. 3 Photograph of test rig: **a** Mfs-rds setup and **b** SO analyzer

3 Experimental Setup

The test rig was a machine fault simulator–rotor dynamics simulator, and it has been extensively used for fault detection in machines like misalignment, unbalance, and oil whirl [18]. The setup consists of two journal bearings, shaft, coupling, 0.5 kw motor, and accelerometer. Other accessories include an RPM calculation tachometer, a bearing oil temperature sensor, and a speed controller for the motor. To mitigate the addition of external noise in the measuring signal, rubber insulation pads were mounted under the motor, support bearing blocks, and loading lever. The photograph of the test setup is shown in Fig. 3a.

The accelerometer is connected to the SO analyzer (Fig. 3b) which analyzed the data and transferred to the computer; the computer processed the data in smart office software and gave a result in the form of amplitude versus frequency graphs.

4 Result and Discussion

4.1 Particle Size Effect

The peak of vibration in the normal operation without contamination is due to the friction of the fluid as shown in Fig. 4a, b, but with the particle contamination in the oil amplitude of vibration tends to increase because the friction of oil and abrasion of particle play a significant role as shown in Fig. 5.

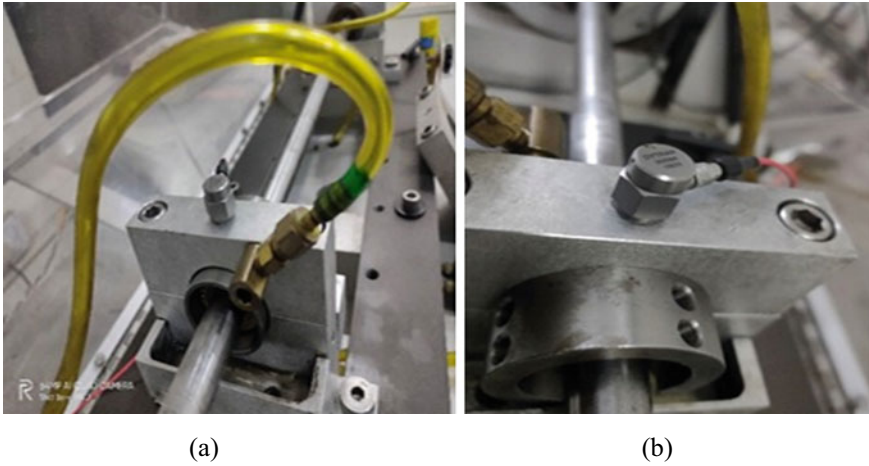


Fig. 4 Photograph of **a** lubricant oil supply in bearing and **b** DYTRAN accelerometer

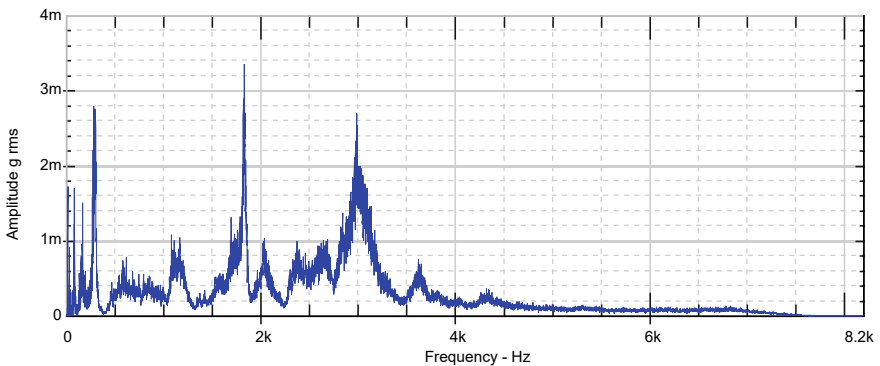


Fig. 5 Graph of amplitude versus frequency for clean oil

The amplitude of vibration in case 1 is high as compared to the healthy bearing as shown in Figs. 4 and 5; vibration levels are twice as in case 1 as compared to the clean oil case which depicts that particle contamination causes abrasion.

Case 2. Herein, contaminant particles of size 20 micron and concentration of 1 gm have been used as the particle size of 20 micron is less than the bearing clearance space that is why particle of this size is easily settled inside the clearance space; however, it increases the viscosity of the oil which increases the friction caused by oil, as shown in Fig. 6.

Case 3. The effect of the contaminant concentration on vibration was different from that of the particle size in case 3; particle sizes of 40 microns and concentrations of 1.25 gm were used. The degree of vibration increased with concentration, as shown in Fig. 7, which tends to stabilize to a maximum. On the other side, the vibration

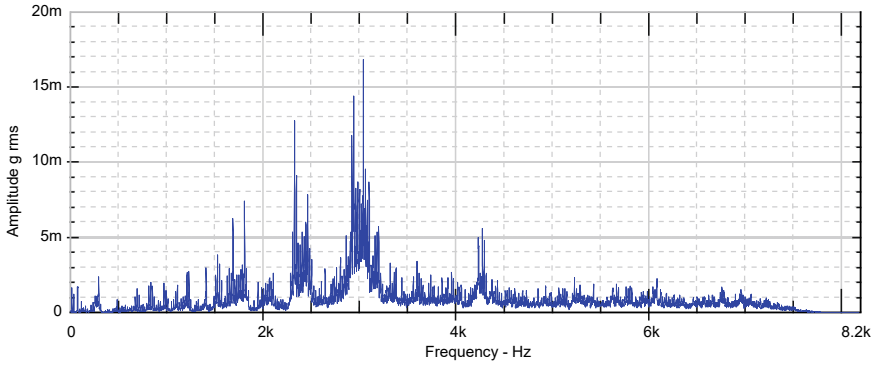


Fig. 6 Graph of amplitude versus frequency for case 1

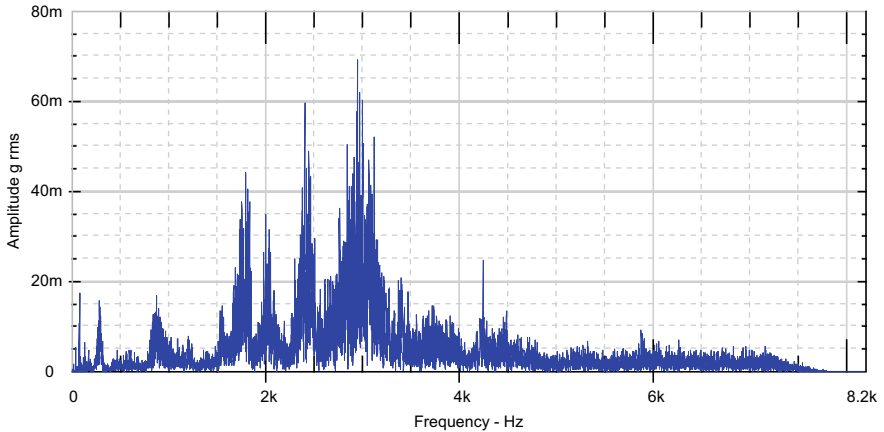


Fig. 7 Graph of amplitude versus frequency for case 2

frequency first increased and then decreased as the particle size increased (Fig. 8). The probable factor for vibration-level reduction was the particle settling effect.

4.2 Water Contamination Effect

In journal-bearing hydrodynamic oil, the film is weakened by water in oil, which in turn contributes to excessive wear. As little as 1% of the water will decrease bearing output. Significantly, under certain conditions water is converted into its constituent element, i.e., hydrogen and oxygen [19]. Hydrogen being the small ion can absorb on the bearing surface resulting in a phenomenon called hydrogen embrittlement [20]. Water causes damage to the bearing surface by corrosion in very little time. In case

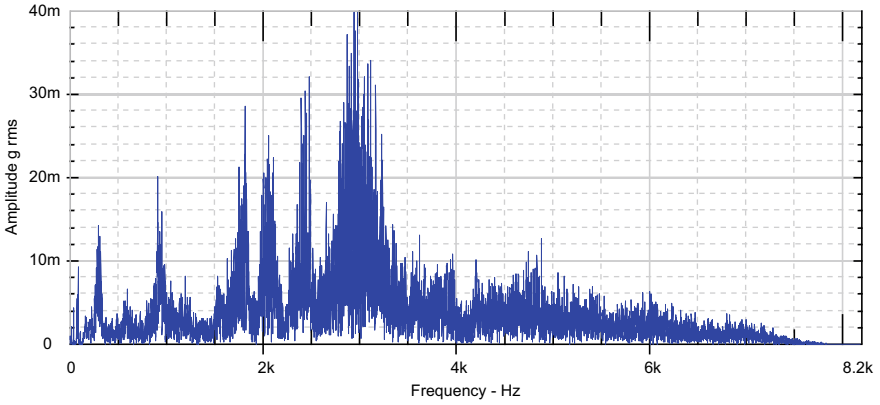


Fig. 8 Graph of amplitude versus frequency for case 3

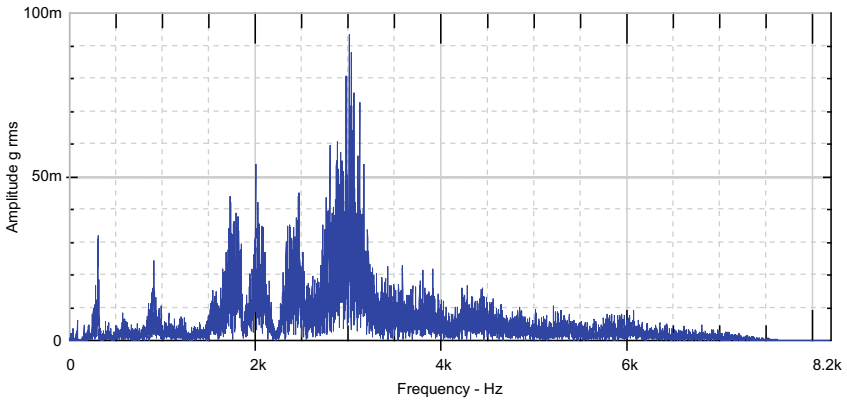


Fig. 9 Graph of amplitude versus frequency case 4

4 (Fig. 9) and case 5 (Fig. 10), mineral water and saltwater have been used; from the experimental data and graph, it is found out that extreme bearing damage is caused by saltwater than mineral water.

5 Conclusions

Vibration analysis is a predictive maintenance method which allows early problem detection in machines. Vibration signature analysis in both frequency and time domains can give useful results pertaining to the journal-bearing health monitoring. Vibration analysis in the frequency domain may predict that whether increased vibrations are due to sole bearing defect or due to other external sources. Increase in the

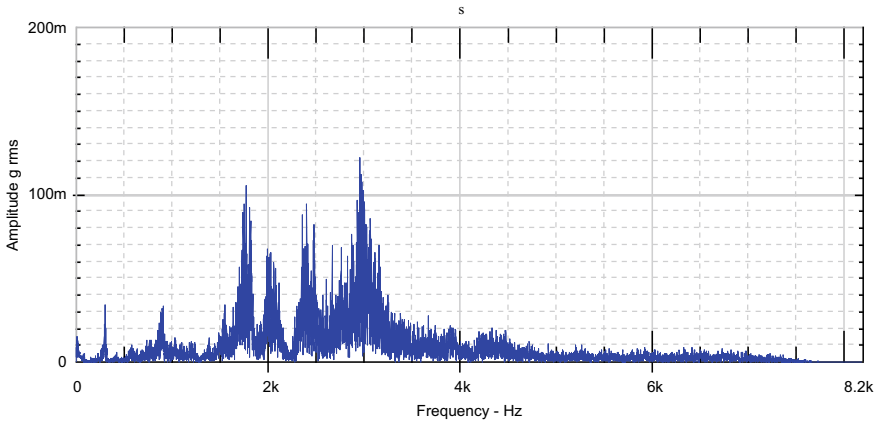


Fig. 10 Graph of amplitude versus frequency case 5

vibration energy at the attributed bearing frequencies can also indicate the progress of that particular fault.

Particle contamination and water contamination have been studied using vibration signature analysis. The study was carried out for five particle sizes and concentration and three types of water contamination. The following conclusion is made from the study.

- The amplitude of vibration first increases with an increase in particle size, but after 30 microns it tends to decrease, particle size greater than 30 microns cannot move inside the bearing clearance, and it gets crushed into small particles.
- Water contamination also causes major damage to the bearing surface by corrosion, rubbing phenomenon also started due to corrosion, and it is visible in the graphs where multiple peaks are appearing frequently.
- Particle concentrations have a distinct effect compared to the size of the particle but when both are combined, the vibration level increased to a dangerous level and may cause jamming of the machine.
- Multiple peaks in the graph of water contamination with higher acceleration amplitude are due to rusting. Bearing wear is more significant in bearing with saltwater and least with mineral water. Saltwater increases the corrosion rate rapidly which ultimately increases the internal ingested particles.

References

1. Wikström V, Höglund E, Larsson R (1993) Wear of bearing liners at low speed rotation of shafts with contaminated oil. *Wear* 162–164(PART B):996–1001
2. Ronen A, Malkin S (1982) Investigation of friction and wear of dynamically loaded hydrodynamic bearings with abrasive contaminants 82

3. Khonsari MM, Wang SH (1990) On the role of particulate contamination in scuffing failure. *Wear* 137(1):51–62
4. Wang Q (1997) Seizure failure of journal-bearing conformal contacts. *Wear* 210(1–2):8–16
5. Gangsar P, Tiwari R (2020) Signal based condition monitoring techniques for fault detection and diagnosis of induction motors: a state-of-the-art review. *Mech Syst Signal Process* 144:106908
6. Dadouche A, Conlon MJ (2016) Operational performance of textured journal bearings lubricated with a contaminated fluid. *Tribol Int* 93:377–389
7. Khonsari MM, Booser ER (2006) Effect of contamination on the performance of hydrodynamic bearings. *Proc Inst Mech Eng Part J J Eng Tribol* 220(5):419–428
8. Poddar S, Tandon N (2019) Detection of particle contamination in journal bearing using acoustic emission and vibration monitoring techniques. *Tribol Int* 134(February):154–164
9. Harika E, Bouyer J, Fillon M, Hélène M (2013) Effects of water contamination of lubricants on hydrodynamic lubrication: Rheological and thermal modeling. *J Tribol* 135(4):1–10
10. Harika E, Helene M, Bouyer J, Fillon M (2011) Impact of lubricant contamination with water on hydrodynamic thrust bearing performance. *Mec Ind* 12(5):353–359
11. Ma J, Zhang H, Shi Z, Kontogiorgos V, Gu F, Ball A (2018) Vibration analysis of journal bearings under water contaminated lubrication. ICAC 2018–2018 24th IEEE international conference on automation and computing improvement on products through automation computer, pp 6–7
12. Liu H et al (2009) The influence of sea water in oil emulsion on bearing performance. *Proc Inst Mech Eng Part J J Eng Tribol* 223(3):457–468
13. Kalkat M, Yıldırım Ş, Uzmay I (2003) Rotor dynamics analysis of rotating machine systems using artificial neural networks. *Int J Rotating Mach* 9(4):255–262
14. Machado TH, Alves DS, Cavalca KL (2019) Investigation about journal bearing wear effect on rotating system dynamic response in time domain. *Tribol Int* 129(May 2018):124–136
15. Maru MM, Castillo RS, Padovese LR (2007) Study of solid contamination in ball bearings through vibration and wear analyses. *Tribol Int* 40(3):433–440
16. Hase A, Mishina H, Wada M (2016) Fundamental study on early detection of seizure in journal bearing by using acoustic emission technique. *Wear* 346–347:132–139
17. Koulocheris D, Stathis A, Costopoulos T, Tsantiotis D (2014) Experimental study of the impact of grease particle contaminants on wear and fatigue life of ball bearings. *Eng Fail Anal* 39:164–180
18. Lee J, Park B, Lee C (2020) Fault diagnosis based on the quantification of the fault features in a rotary machine. *Appl Soft Comput* 97:106726
19. Lugt PM (2016) Modern advancements in lubricating grease technology. *Tribol Int* 97:467–477
20. Robertson IM et al (2015) Hydrogen embrittlement understood. *Metall Mater Trans B Process Metall Mater Process Sci* 46(3):1085–1103

Mechanical Alloying of γ TiAl-Based Powder of Ti–46Al–1B (at%) Composition



Mrigesh N. Verma and Vijay N. Nadakuduru

1 Introduction

Gamma (γ) titanium aluminide (TiAl)-based alloys have shown promising and attractive properties for such applications where the instruments need to work at high temperatures and show high efficiencies, and also, it is a suitable replacement for nickel-based superalloys [1, 2]. These favourable properties of TiAl like low density, high temperature strength, burn resistance and significant oxidation resistance make them a suitable material as replacement of superalloys in use. On account of such properties, research work with a focus on the development of these alloys has received a stimulus and can prove worthwhile [3, 4]. In the development of TiAl powder metallurgy has played a vital role and in particular mechanical alloying route due to its ease of synthesizing varying chemical composition even those which are not at all feasible by ingot metallurgy [5]. From all the available mechanical alloying process, high-energy ball milling is most attractive because of its processing speed.

Ingot metallurgy suffers from issues such as not only infeasibility of developing variable compositions but as well as rapid oxidation during processing. As opposed to ingot metallurgy, mechanical alloying in powder metallurgy uses elemental powders [6], which significantly eliminates the former's disadvantages such as distinct segregation, poor reproducibility, rapid oxidation and expensive processing equipment. Mechanical alloying when carried utilising ball milling has an added advantage of refining the grain size simultaneously as it creates the metal powder. Ball milling has a limitation of formation of agglomeration, but this also can be kept in check by utilisation of addition of process control agent like toluene, stearic acid and methanol [7]. Such additions come with its own disadvantage of contamination in the form

M. N. Verma · V. N. Nadakuduru (✉)

Department of Metallurgical and Materials Engineering, Malaviya National Institute of Technology Jaipur, Jaipur, Rajasthan, India

e-mail: vijay.meta@mnit.ac.in

of carbon, hydrogen and oxygen as all the process control agents used are organic in nature, but the contamination is in trace amount and can be overseen over the advantage it tends to provide to the process. Mechanical alloying is very well suited for high-energy ball milling and formation of alloys with hard to form compositions. This is possible, as the limitations of phase diagrams do not apply to mechanical alloying. Mechanical alloying also has its own hidden advantage as in the form of capability to form a fine-grained powder which can further be used as starting material for bulk formation giving superior mechanical properties [8]. Also, the particle size distribution is quite narrow in mechanically alloyed powder which gives better control in the compaction process.

The present work focuses on the same direction of synthesis of titanium aluminide alloy powder in ultrafine range using high-energy ball milling with starting materials as pure elemental powders [9, 10]. Also, work focuses on the grain refinement achieved during ball milling with the addition of boron, suggested as a grain refining additive [11–14].

2 Experimental

The following powder, along with particle size and purity as mentioned in Table 1, was mechanically alloyed to achieve a nominal composition of Ti–46Al–1B (at%). Retsch Planetary Ball Mill, model PM 100, was used to perform the alloying using a 500 ml vial and 12 mm balls, both made of stainless steel. Toluene was added to each batch as a process control agent (PCA) to prevent cold welding between the balls, vial and metal powders, which may lead to the formation of agglomerates, as well as provide a reducing media for the milling.

The powder sample was collected after mixing for 5 h at 100 RPM without interruption. After that, the milled powder was again sampled after every 3 h of net milling, carried out at 30 min of milling with 30 min of break at 400 RPM, for a cumulative milling time of 15 h. The break period is required to allow the entire set-up to cool down to room temperature.

The samples of the milled powder at different stages were characterised by an X-ray diffractometer (XRD), model Malvern PANalytical X'pert Pro, with Cu-K α source ($\lambda = 154.0598$ pm) radiation. A scanning electron microscope (SEM), model Nova Nano FE-SEM 450 (FEI), was deployed to carry out the morphological analysis of the powder samples. The samples recovered at different stages of milling were characterised by a transmission electron microscope (TEM), model Tecnai G² 20 (FEI) S-Twin operated at 20 kV. TEM images and selected area diffraction pattern

Table 1 Details of elemental powder

Element	Titanium	Aluminium	Boron
Purity	>99.9%	>99.9%	>99%
Particle size	50–60 μ m	20–25 μ m	200 mesh

(SAED) were recorded. TEM samples were prepared by agitating the powder samples in an ethanol medium for 60 min using a probe sonicator. The particle agglomerates were allowed to settle down for 10 min. Then, the sample from the upper layers of the dispersion was extracted using a micro-pipette and spread onto a carbon-coated copper grid. An energy-dispersive spectroscopy (EDS) device by Bruker Corp. attached to the TEM instrument was used to perform the compositional analysis. For the thermal behaviour analysis, milled samples at various stages were analysed using differential scanning calorimetry (DSC) with a Netzsch 404 f3 calorimeter, for a temperature up to 1000 °C with a heating rate set at 10 °C/min.

3 Results and Discussion

3.1 Results

The following graph (Fig. 1) shows the XRD peaks of the samples that were collected after the initial 5 h mixing period and after every 3 h interval of milling. The PANalytical X'pert Highscore software is used to analyse the peaks for all phases of respective constituents. The plot at the lowermost portion represents the sample after

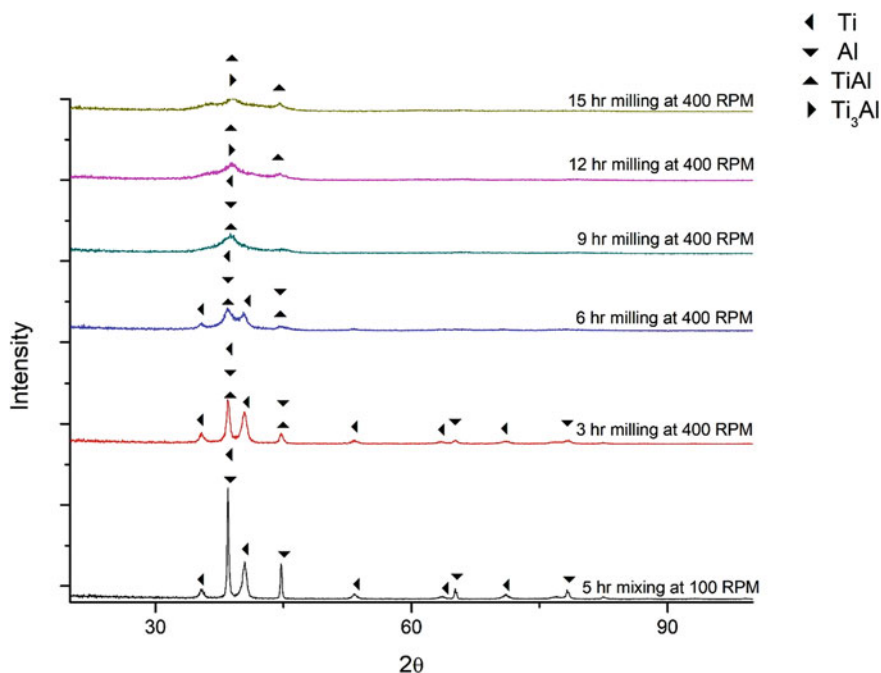


Fig. 1 XRD plots at various stages of milling

only mixing the powders showing only peaks of titanium and aluminium individually, indicating the absence of any alloying. As time is allowed for milling, we see that the natural peaks corresponding to elemental powders shift slightly and decrease in intensity. This signifies the partial dissolution of the elements and the commencement of alloyed compounds. Peaks corresponding to TiAl and Ti₃Al become relatively prominent in the graph post 6 h of milling, whereas the natural peaks of elements are barely visible. Milling for 9–12 h confirms the presence of only TiAl and Ti₃Al in the samples, with negligible traces of elemental peaks of Ti and Al. Further milling shows that peaks have broadened which indicate refinement of grain size and homogeneity in the sample. XRD plots show that TiAl and Ti₃Al start to form after 9 h of milling, where the minute elemental phase still remains in the sample at 9 h milled stage, but TiAl and Ti₃Al are the only phases present after milling time 12 h and more. Approximately 75% of TiAl is present after a milling time of 12 h milled stage. With further milling, it is observed that the percentage of TiAl drops with an increase in the percentage of Ti₃Al.

Figure 2a–f shows SEM images of the milled powder at different stages, with magnification set to 200X; it is evident that powders are breaking down into increasingly finer sizes and more uniform distribution of the elements, as milling time increases. Figure 3a–f shows particle size and morphology at successive stages of milling, with the magnification set at 10000X. Final particle size is observed majorly approximately 1 μm. At some locations, large particles are present as agglomerates as observed during SEM analysis, but the quantity of such agglomerates is low enough that they will not interfere in the alloy formation process. These agglomerates are formed of finer particles. As suggested by Opoczky [15], the milling results into three different stages, which explains a possible mechanism of these agglomerate formations. The first stage is Rittinger, second stage aggregation and the third stage being agglomeration which are characterised by increased interparticle interaction, in which particles in localised regions tend to adhere to each other leading to increase in size. As mentioned earlier, toluene was added to powder mixture for decreasing the rate of agglomerate formation, which is indeed working satisfactorily, as evident by a very low number of agglomerates present in the milled powder even after 15 h of net milling at which point the probabilities of interparticle interactions are highest. Particle size analysis had shown that the particle size distribution is quite close to that observed in SEM as shown in Fig. 4. The size distribution at 12 h milled stage is near approximately 1 μm, and further milling resulted in further reduction of particle size to 0.5 μm.

Grain size or diffusion couples present in particles of the milled powder at different stages of milling are observed by bright field imaging mode of TEM. These are shown in Fig. 5a–f. ImageJ was used to perform analysis on these images, and it was determined that grain sizes are occurring around an average value of 90 nm after 15 h of milling. This is further indicative of the internal grain sizes of 20–100 nm at the nano-crystalline level. A higher grain size of 115 nm is observed after net milling of 12 h. Individual and separate grains are not visible at the milling time of 9 h; however, distinct contrasting phases are still visible suggesting there may be presence of diffusion couples of the elemental phases. The SAED pattern (Fig. 6b)

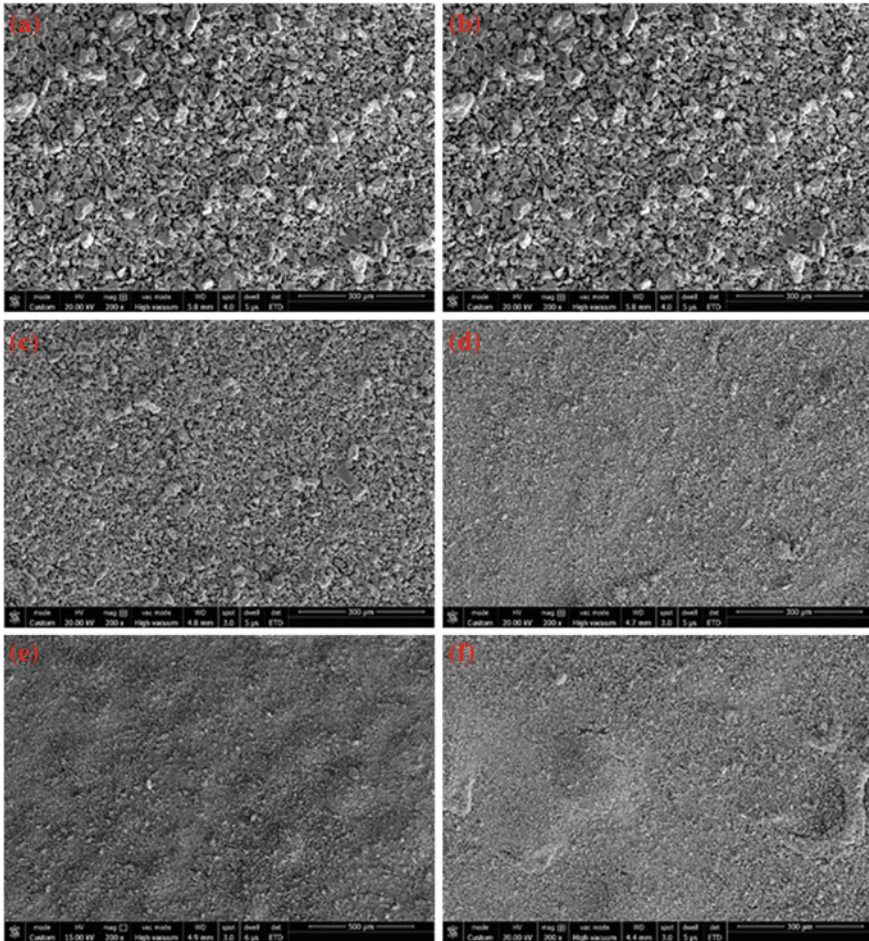


Fig. 2 SEM image of TiAl powder at 200X magnification: **a** as mixed, **b** 3 h milled, **c** 6 h milled, **d** 9 h milled, **e** 12 h milled, **f** 15 h milled

of the 15 h milled powder reflects the crystalline phase as there are distinct and clear diffraction spots present. Figure 6a represents the corresponding TEM bright field image. Thus, clearing the confusion from XRD analysis of amorphous phase being present or grain refinement, the peak broadening was quite surely because of grain refinement.

The EDS analysis (Fig. 7) is carried out with TEM imaging of powders after the final stages of milling showing composition close to the expected composition and in range of formation of gamma TiAl. These values are sufficiently close to the formation range of γ -TiAl and the expected compositional range of the required synthesis. There is presence of iron and chromium as trace amounts with the expected traces of carbon these came from the contamination from the stainless steel vial and

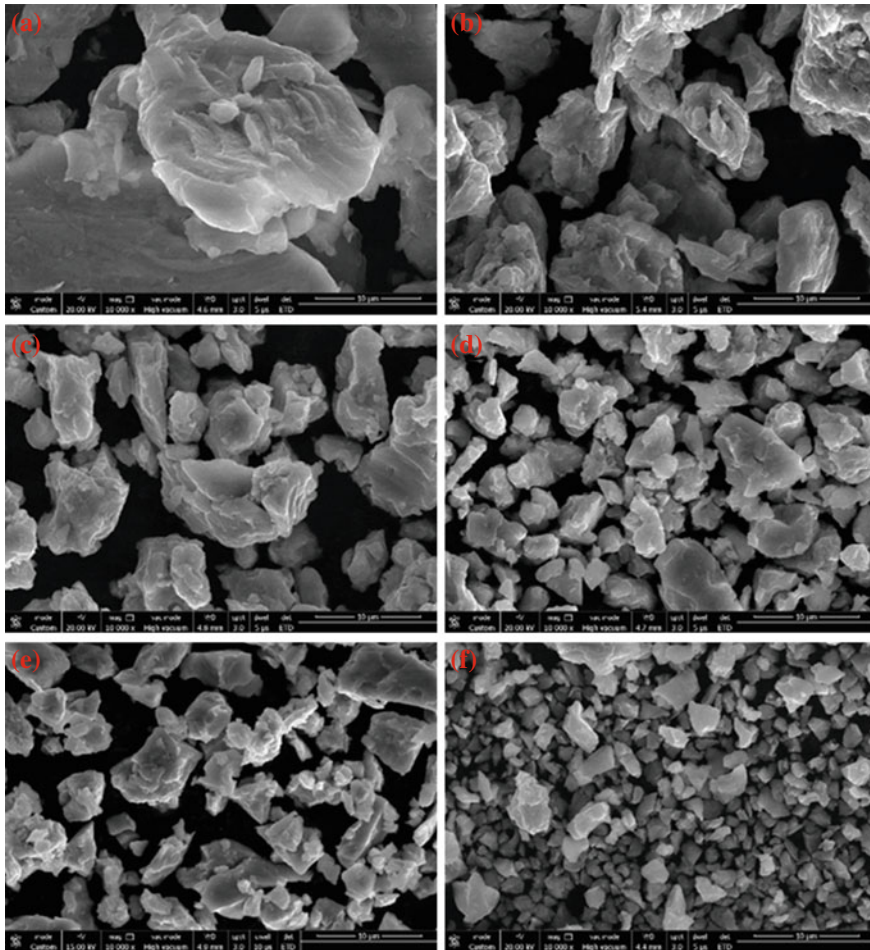


Fig. 3 SEM image of TiAl powder at 10000X magnification: **a** as mixed, **b** 3 h milled, **c** 6 h milled, **d** 9 h milled, **e** 12 h milled, **f** 15 h milled

process control agent respectively. The result corroborates the XRD peak pattern showing TiAl and Ti_3Al as the dominant phases of the sample. Boron concentration is relatively low and was not found to be uniform, as well as being undetectable in certain locations, aided by the lack of homogeneity.

DSC curves of ball-milled powder at various stages are represented in Fig. 8. At the as mixed stage, the powder shows a strong endothermic peak at approximately $665\text{ }^\circ\text{C}$, which is the aluminium melting peak. Further, there is a small exothermic peak at approximately $750\text{ }^\circ\text{C}$ which is as a result of reaction happening between titanium and aluminium forming the intermetallic TiAl and Ti_3Al . As the powder is milled, the melting peak almost vanishes, conforming that the majority of aluminium is consumed in the reactions that happen during milling. It is well known that the

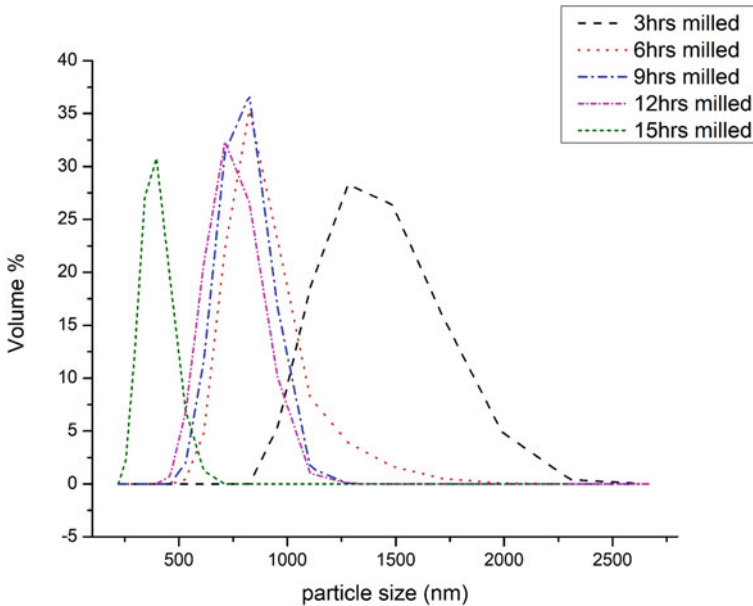


Fig. 4 Particle size distribution

formation of Al_3Ti or TiAl solid solution is dependent on the scale of Ti–Al diffusion couples by the first reaction between Ti and Al in the Ti–Al powder formed [16]. TiAl is formed by a reaction between Al_3Ti or $\text{Al}(\text{Ti})$ and Ti [16–18]. If all the Ti is now used up, it tends to react with TiAl and form Ti_3Al . Observing DSC of further milled powder did not show any peak related to aluminium melting which is of a significant importance from the powder metallurgical point of view. This is because if melting of aluminium occurs it will result in a porous structure in the sintered component [19, 20]. As the milling time progresses, the reaction peak representing reaction between Al and Ti tends to shift towards lower temperature. This happens because of the increase in the entropy of the powder due to the stress generated during the milling process. Thus, this extra energy is readily available for reaction, and as we approach near to the temperature, it helps to trigger the reaction early. Higher the entropy, earlier the reaction, and same is visible from the DSC curves of 3 h, 6 h and 9 h milled powder. With further milling, i.e. 12 h, this reaction peak vanishes which suggests that there are no free elements for reaction to happen; hence, alloying is complete by this stage of milling. Similar results are present in XRD results also.

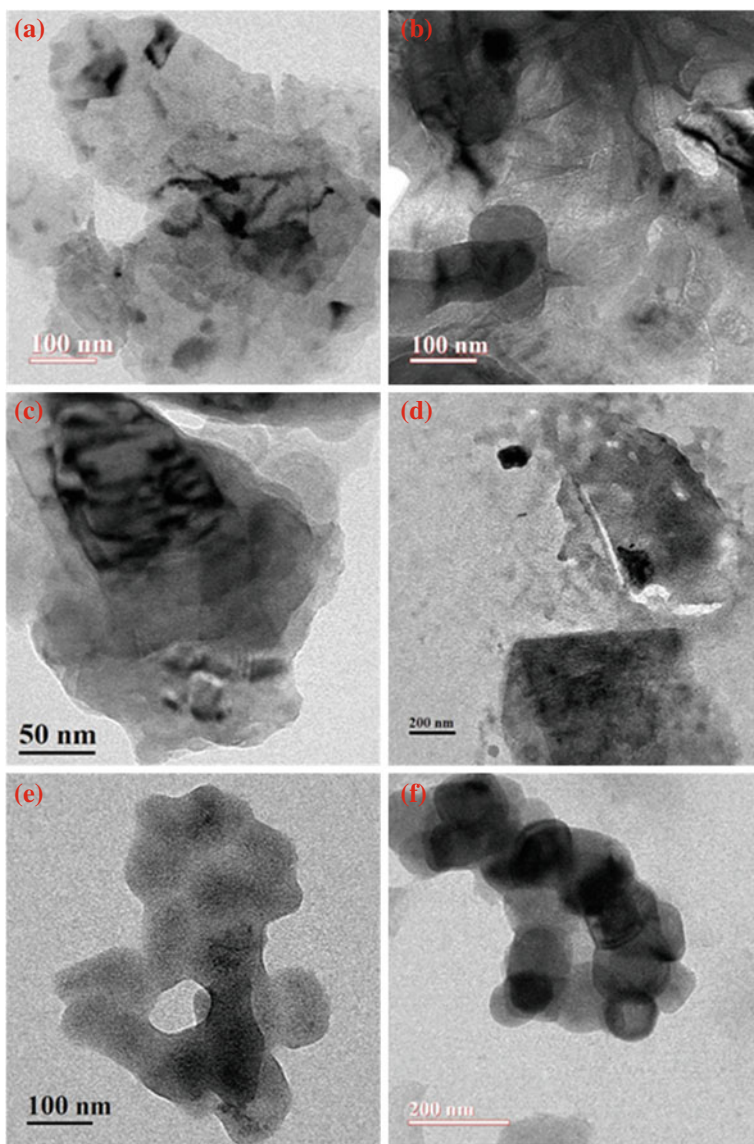


Fig. 5 TEM bright field image of TiAl powder: **a** as mixed, **b** 3 h milled, **c** 6 h milled, **d** 9 h milled, **e** 12 h milled, **f** 15 h milled

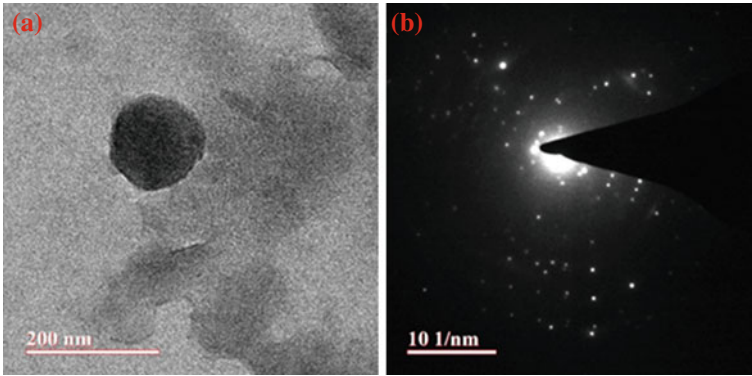


Fig. 6 a TEM bright field image and b corresponding SAED pattern

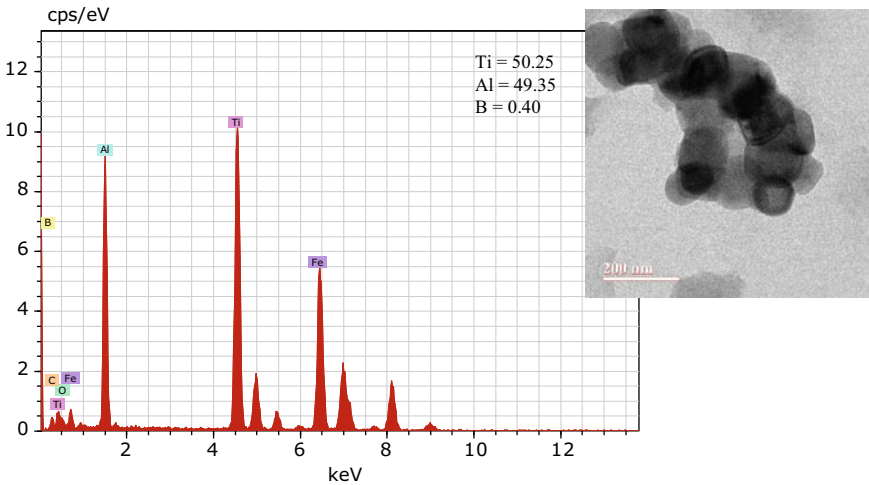


Fig. 7 EDS analysis of the region of bright field TEM image shown in right

3.2 Discussion

The mechanical alloying of powder, when studied using a combination of morphological characteristics, phase evolution and thermal analysis, provides an effective means towards the understanding of solid-state reactions and mechanisms that metal powders undergo during mechanical alloying. SEM imaging revealed refinement in particle shape and size along with increased homogeneity as the milling progresses. Particles change into irregular angular shapes, as they are repeatedly subjected to cold welding, severe plastic deformation and eventual fracture under severe load conditions [21]. These phenomena including the formation of fine-sized particles

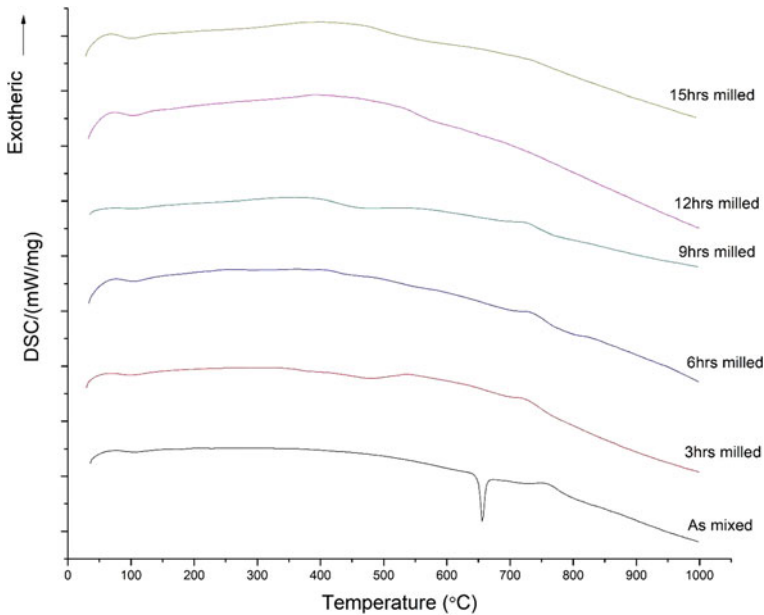


Fig. 8 DSC curves of powder at different milling stages

and elemental couples are well understood to occur during mechanical alloying by high-energy ball milling [16].

In the initial stages of milling, XRD analysis shows micrometre-sized couples, in a distinct phase, whereas the DSC analysis shows a distinct point corresponding to melting of elemental aluminium. The present study thus resembles the work of Li-Juan [22] and Mao [23]. As the milling time increases, the elemental layers start reducing in size down to nanometre ranges, while crystal imperfections and structural defects such as grain boundaries and dislocations start appearing [16], as confirmed by XRD results. When considering the XRD patterns of the as mixed and 3 hours milled powders, which showed strong elemental peaks. These peaks start to disappear with the progressive milling stages indicating that the aluminium and titanium are being consumed and getting transformed to solid solution during the course of milling. This behaviour is frequently reported for ball-milled powders. The chemical analysis made available via the EDS on the TEM confirms a composition that is sufficiently close to the intended result.

XRD results coupled with TEM results of milling show that milling post 12 h mainly contributes to grain refinement, as observed by broadening peaks in XRD plot and grains observed in TEM results. XRD analysis fairly matches the work presented by Yu [24], showing the formation of γ -TiAl and α_2 -Ti₃Al. Prior to milling for 12 h, all samples showed the presence of multiple phases, most of which are plausibly diffusion couples and are visible in TEM images. At the 12 h milled stage, only particles with ultrafine grains are observable. XRD plots at the 12 h and 15 h

milled stages show significant noise, usually indicative of non-crystalline matter, or amorphous phase; however, the presence of sharp peaks and spot SAED patterns of powder in TEM rules out probabilities of amorphous phases existing in the mixture to a great extent.

4 Conclusion

Formation of alloy started from the 9 h milling stage and is complete by the end of 12 h milling stage; further milling has only the grain refinement effect. The optimum results of mechanically alloying were after milling for 12 h. The grain size of 12 h milled powder is in the ultrafine range, and further milling (up to 15 h) further refined the grain size but at the cost of increased concentration of Ti_3Al phase as compared to that in 12 h milled powder. XRD and TEM observations revealed that the grains are at ultrafine level after 12 h of milling.

Acknowledgements We would like to thank the Department of Science and Technology, Science and Engineering Research Board, India, for providing financial support.

References

1. Lipsitt HA (1985) Titanium aluminide—an overview. *Mater Res Soc* 39
2. Kim Y-W (1989) Intermetallic alloys based on gamma titanium aluminide. *Jom* 41:24–30
3. Dimiduk D (1999) Gamma titanium aluminide alloys—an assessment within the competition of aerospace structural materials. *Mater Sci Eng A* 263:281–288
4. Yamaguchi M, Inui H, Kishida K, Matsumuro M, Shirai Y (1995) gamma titanium aluminide alloys. *Mater Res Soc Symp Proc* 364:3–16
5. Shahzad A, Zadorozhnyy VY, Pavlov MD, Zheleznyi MV, Chirkov AM, Zagrebin DS, Semenov DV, Khasenova RS, Kaloshkin SD (2018) Deposition of the Ti-Al coatings on different metallic substrates by mechanical alloying and subsequent laser treatment. *J Alloys Compd* 731:1295–1302
6. Long Y, Wang T, Zhang HY, Huang XL (2014) Enhanced ductility in a bimodal ultrafine-grained Ti–6Al–4V alloy fabricated by high energy ball milling and spark plasma sintering. *Mater Sci Eng A* 608:82–89
7. Nouri A, Hodgson PD, Wen CE (2010) Effect of process control agent on the porous structure and mechanical properties of a biomedical Ti–Sn–Nb alloy produced by powder metallurgy. *Acta Biomater* 6:1630–1639
8. Shanmugasundaram T, Guyon J, Monchoux JP, Hazotte A, Bouzy E (2015) On grain refinement of a γ -TiAl alloy using cryo-milling followed by spark plasma sintering. *Intermetallics* 66:141–148
9. Nadakuduru VN, Cao P, Zhang DL, Gabbitas B (2007) Ultrafine grained Ti–47Al–2Cr (at%) alloy prepared by high energy mechanical milling and hot isostatic pressing. *Adv Mater Res* 29–30:139–142
10. Nadakuduru VN, Zhang DL, Cao P, Chiu YL, Gabbitas B (2011) The mechanical behaviour of an ultrafine grained Ti–47Al–2Cr (at%) alloy in tension and compression and at different temperatures. *Mater Sci Eng A* 528:4592–4599

11. Hu D (2002) Effect of boron addition on tensile ductility in lamellar TiAl alloys. *Intermetallics* 10:851–858
12. Cheng TT (2000) Mechanism of grain refinement in TiAl alloys by boron addition—an alternative hypothesis. *Intermetallics* 8:29–37
13. Luo JS, Voisin T, Monchoux JP, Couret A (2013) Refinement of lamellar microstructures by boron incorporation in GE-TiAl alloys processed by spark plasma sintering. *Intermetallics* 36:12–20
14. Amherd Hidalgo A, Frykholm R, Ebel T, Pyczak F (2017) Powder metallurgy strategies to improve properties and processing of titanium alloys: a review. *Adv Eng Mater* 19:1–14
15. Opoczky L (1977) Fine grinding and agglomeration of silicates. *Powder Technol* 17:1–7
16. Zhang DL, Ying DY (2001) Solid state reactions in nanometer scaled diffusion couples prepared using high energy ball milling. *Mater Sci Eng A* 301:90–96
17. Oehring M, Klassen T, Bormann R (1993) The formation of metastable Ti–Al solid solutions by mechanical alloying and ball milling. *Mater Sci Soc* 8:2819–2829
18. Fan GJ, Quan MX, Hu ZQ (1995) Supersaturated Al(Ti) solid solution with partial L12 ordering prepared by mechanical alloying. *Scr Metall Mater* 33:377–381
19. Yang JB, Teoh KW, Hwang WS (1996) Solid-state hot pressing of elemental aluminum and titanium powders to form TiAl ($\gamma+\alpha_2$) intermetallic microstructure. *J Mater Eng Perform* 5:583–588
20. Wenbin F, Lianxi H, Wenxiong H, Erde W, Xiaoqing L (2005) Microstructure and properties of a TiAl alloy prepared by mechanical milling and subsequent reactive sintering. *Mater Sci Eng A* 403:186–190
21. Fang WB, Li XW, Sun HF, Ding YF (2011) Characterization of Ti-50Al composite powder synthesized by high energy ball milling. *Trans Nonferrous Met Soc China (English Ed)* 21:s333–s337
22. Xu LJ, Xiao SL, Chen YY, Wang J (2012) Microstructure and mechanical properties of Ti–43Al–9V alloy fabricated by spark plasma sintering. *Trans Nonferrous Met Soc China (English Ed)* 22:768–772
23. Mao SX, McMinn NA, Wu NQ (2003) Processing and mechanical behaviour of TiAl/NiAl intermetallic composites produced by cryogenic mechanical alloying. *Mater Sci Eng A* 363:275–289
24. Yu HB, Zhang DL, Chen YY, Cao P, Gabbitas B (2009) Synthesis of an ultrafine grained TiAl based alloy by subzero temperature milling and HIP, its microstructure and mechanical properties. *J Alloys Compd* 474:105–112

A Review on Development and Applications of Solar Dish Stirling System



Deepak Kumar and Meena Agrawal

1 Introduction

The most important renewable energy source is solar energy. The thermal power generation is from solar energy that utilizes the concentration of the solar irradiation. This solar irradiation drives a heat engine and rotates the prime mover so that electrical energy can be generated. Hence, it becomes a conventional kind of electrical power generation system which generates electrical energy from thermal energy by converting thermal energy into mechanical energy first. At the present time, a total four kinds of systems [1] that can utilize the solar power [2] to generate electricity and they are:

- (a) Parabolic trough systems,
- (b) Solar tower systems,
- (c) Stirling solar dish systems, and
- (d) Linear Fresnel systems.

Out of these four systems, our study is focused on Stirling solar dish system. In this system, the receiver receives the solar radiation by tracking the sun and focuses on a point where Stirling unit is located. Due to several design limitations, the Stirling engine system is utilized in relatively low power applications and also due to the wind load effect on concentrator dish. But a large amount of power can be generated by integrating each unit into a dish farm. The applications of this system include:

- (a) Electrical power generation [4–15],
- (b) Cooking [16–25],

D. Kumar (✉) · M. Agrawal
Energy Centre, Maulana Azad National Institute of Technology, Bhopal, Madhya Pradesh
462003, India

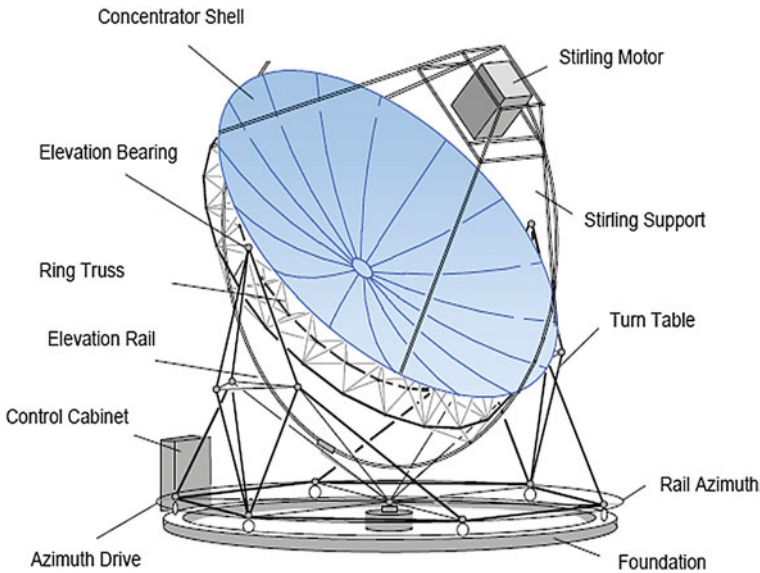


Fig. 1 Structural model of dish Stirling system (EURODISH system) [3]

- (c) Heating water [26–29],
- (d) Land irrigation [30, 31], and
- (e) Desalination and distillation of water [32, 33].

The structural model for Stirling system [34] is represented in Fig. 1 [3]. In this model, two-axis tracking system by using Azimuth angle control mechanism is used.

1.1 Stirling Engine

The first Stirling engine was developed by Robert Stirling in 1816. It works on the mechanical/physical phenomena of working fluid. This working fluid bears hydrogen, nitrogen, argon, and air [35–37]. It has great flexibility in activation but difficult in development and commercialization due to its high manufacturing cost, the very high difficulty of sealing its working chamber. By the way for the importance of energetic and low emission Philips research laboratory started to work with it [38], the application of the Stirling engine is in aerospace in various ways [39, 40].

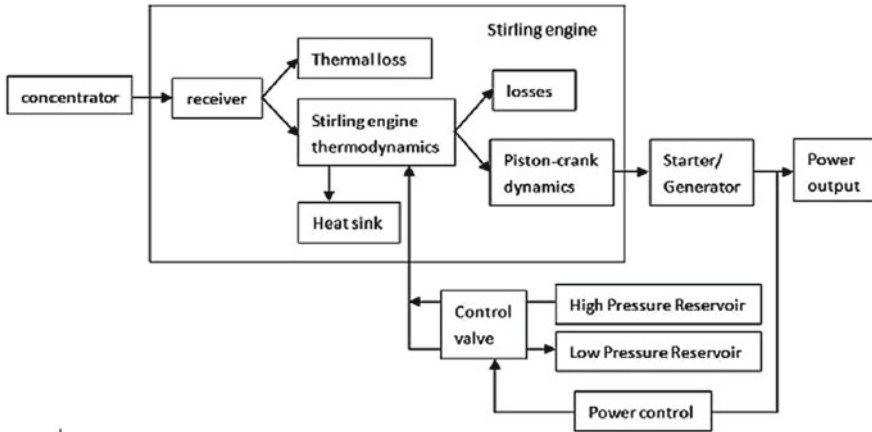


Fig. 2 Block model for dish Stirling engine system [41]

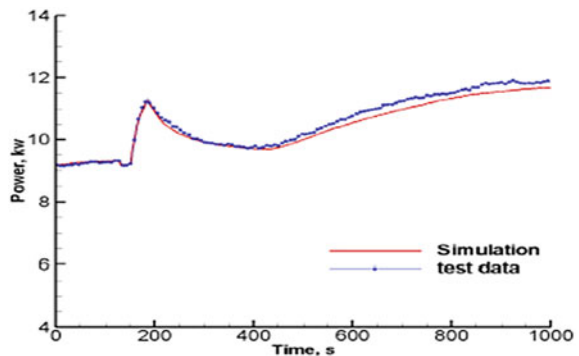
1.2 Model of Stirling Engine System

The energy transfer in concentrator (parabolic) and receiver, thermodynamic cycle, the flow of heat, and dynamics in the mechanical and electrical system (like Stirling engine and generator) are included in the complete model, as shown in Fig. 2 [41].

1.3 Dynamic Analysis

The following graph (Fig. 3) [41] is a representation of simulated and test data between output power and time during operation.

Fig. 3 Output power during operation [41]



2 Design Analysis Factors and Specifications of Solar Dish Technologies for Different Systems and Applications

As there are the many parts of a Stirling system, concentrator receiver, and engine, this review shows the main technical aspects and their performance parameters as given in Table 1. Because of the different applications of the Stirling engine, there are different design factors and technologies that are being adopted. These design factors include solar radiation falling at the concentrator, the material of the reflector, diameter and aperture of the concentrator shape, focal length of parabolic dish geometric concentration ratio rim angle, etc. Here some of the solar dishes which are implemented worldwide are given.

The following Table 2 gives you an idea about its feasibility, and it also investigates the applications of different kinds of technology in dish systems in the world.

3 Dish Stirling System Using Humidification–Dehumidification Desalination Cycle in Zero Energy Building

Due to many issues, we are facing an increase in energy demand. The solar dish Stirling system can be utilized as one of the sustainable solutions. This system is used in zero energy building (ZEB) as shown in Fig. 4 [72]. One of the promising solutions is to counter the environmental change and its issues by reducing load demand and greenhouse gages (GHG) [73, 74].

The solar dish system is used in a building to provide electricity and cooling. This can be done by using Stirling motor.

There are four different thermodynamical cycle/processes that are followed in the Stirling system. These four consecutive steps are:

- (a) The isothermal process in which the fluid gets compressed and heat is extracted for the desalination process. From Fig. 4, the heat sink temperature rises to TL2 from TL1 after the isothermal process (1–2).
- (b) After step 1, the regenerator receives the fluid and its temperature rises to Th. This process is called the isochoric process (2–3).
- (c) Now in step (3–4), an irreversible heat transfer occurs in the isothermal process, and this transfer happens between the thermal absorber to the heat sink at temperature TH (constant). Due to the heat transfer, the temperature falls from TH1 to TH2, and the working fluid expands. This process is called the isothermal heat addition process. And at this stage, the power can be generated by the Stirling cycle.
- (d) At stage (4–1), the working fluid rejects the heat to the regeneration, called the isochoric heat rejection process.

Table 1 Latest research data for the development of components of solar dish system

Specification	Authors	Research data	Study	References
Diameter of concentrator	Ramos	With 7.5 m in diameter of parabolic dish produces 9000 W in Mexico City	T	[42]
	Srithar et al.	Diameter of dish concentrator of parabolic shape is 1.25 m	E	[43]
	Hijazi et al.	Three different diameters of parabolic dish are 5, 10, and 20 m	T	[44]
	Lovegrove et al.	Construction of dish in spherical shape of 25 m in diameter	E	[45]
	Li and Dubowsky	Designing of one large and one small dish of 30 m and 56 cm in diameter	E	[46]
	Schertz et al.	Demonstration of a parabolic dish of 3.6 m diameter the design structure of parabolic dish is stretched-membrane optical facet type	E	[47]
	Xu et al.	In this design, ray tracing simulation and calculation are performed for a dish of 12.6 m at high temperature	T	[48]
	Arulkumaran and Christraj	Designing of 2.7 m parabolic dish without any tracking	E	[49]
	Nazemi and Boroushaki	Estimation of aperture diameter of the dish is 8.5913 m	T	[50]
Area and depth of dish concentrator	El-Kassaby	Designing of a square solar dish in a parabolic structure cooker has aperture area is of 1.96 m ²	T	[51]
	Lovegrove et al.	Designing and construction of concentrator solar dish of 500 m ² in area	E	[45]

(continued)

Table 1 (continued)

Specification	Authors	Research data	Study	References
	Li and Dubowsky	Designing of large and small parabolic mirrors with 3.107 m and 5.8 cm dish depth	E	[46]
	Senthil and Cheralathan	Designing of Scheffler parabolic dish of 16 m ²	E	[52]
	Johnston	At Australian National University (ANU), a 400 m ² concentrator is simulated	T	[53]
Reflector material and shape	Ramos	With the efficiency of 86% and consisting 12 facets made of aluminum sheet and fiber glass, respectively	T	[42]
	Alarcón et al.	Construction of a polished parabolic dish made of stainless steel	E	[11]
	El-Kassaby	Designing of a solar cooker with 0.5 mm thickness reflector surface made of polished stainless steel	T	[51]
	Lovegrove et al.	Designing and construction of 380 identical spherical of 1.17 m mirror panels	E	[45]
	Ma et al.	Designing of a solar concentrator for energy collection based on triangular membrane facets (600) which is supported by deployable perimeter truss structure	T	[54]
	Li and Dubowsky	Construction of a large dish mirrors in parabolic shape where it is constructed of high reflective surfaces in flate	E	[46]
	Schertz et al.	Demonstration of parabolic dish in stretched-membrane optical facet consisting of 12 facets identical	E	[48]

Table 2 Various design specifications of Solar dish Stirling systems

Name of the system	Year	Electrical power (kW)	Total efficiency (%)	References
Vangaurd	1984	25	29.4	[55–57]
McDonnell Douglas Astronautics Company	1984_88	25	29–30	[58–60]
German/Saudi	1984_88	52.5	23.10	[61, 62]
Schlaich Bergermann und Partner, Inc	1991	9	20.30	[61–63]
CPG 7.5-kW	1992	7.5	19	[64, 65]
Aisin/Miyako	1992	8.5	16	[64, 65]
STM Solar PCS	1993	25	N/A	[64, 65]
Science Applications International Corp /STM	N/A	22.9	20	[66, 68–71]
Schlaich Bergermann und Partner, Inc	N/A	8.5	19	[61, 62, 68–71]
Stirling Energy Systems, Inc	N/A	25.3	29.4	[68–70]
Wilkinson, Goldberg and associates, inc (mod1)	N/A	11	24.5	[67,04,05,06,7]
Wilkinson, Goldberg and associates, inc (mod2)	N/A	8	22.5	[67–71]
Dish Stirling Almeria, Spain I	1992	40	N/A	[68–71]
Dish Stirling Almeria, Spain II	1997	50	18	[68–71]

3.1 Humidification–Dehumidification (HDH) Desalination Unit

For the pure water production, a system called the HDH desalination cycle is simulated which is based on air cooler water heater. The main outputs are pure water and brine under the HDH process. The preheated gross water receives heat from humid hot air in the dehumidifier heat exchanger with mass flow m_w and the temperature is $T_{w,6}$.

In the humidifier exchanger, the working fluid of the Stirling engine reheats the warm water at temperatures $T_{w,7}$, and at temperature $T_{w,8}$, the hot water transfers the heat to the dry air. With mass flow rate m_{da} and temperature $T_{a,10}$, the humidifier passes the cooler air, and heat of the water called brine is out with mass flow rate m_b and temperature $T_{b,9}$. The seawater takes the heat from the hot air to make it dry air

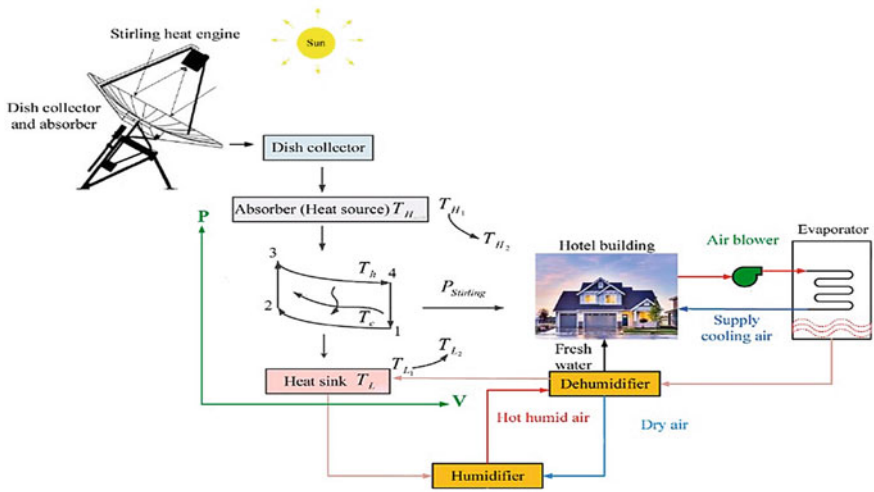


Fig. 4 A proposed model for ZEB using SDS system [72]

at temperature $T_{a,11}$ and form a complete cycle. And finally, at the temperature of $T_{a,12}$ the system produces drinking water [75].

Figure 5 [72] shows the mass flow rate for various fluids under operation in ZEB.

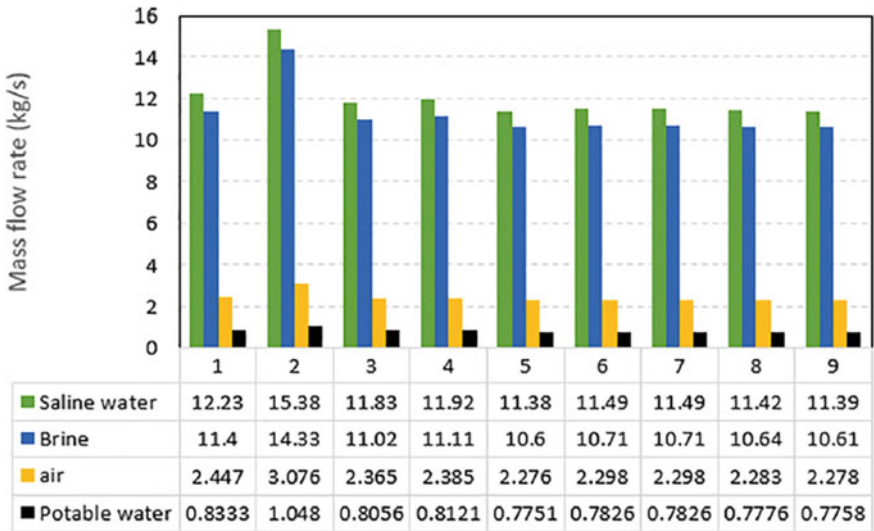


Fig. 5 Mass flow rates of various fluids [72]

4 Dish Stirling (DS) System Using Doubly Fed Induction Generator (DFIG) System

Solar dish Stirling engine has a great speed controlling mechanism so that can be utilized to harness the maximum power from the sun by creating and analyzing a dynamic model. This is to be done by proposing another coupled system called doubly fed induction generator by all means of harnessing maximum power by using maximum power point tracking (MPPT) because of the variation in solar insolation. For this power generation scheme (the DS solar–thermal power generation scheme) [76–78], mechanical energy is developed by using DS solar system from solar energy. And further this mechanical energy is used to drive a constant speed IG.

In the interconnection of DFIG, there are some other power converters that are connected in between to establish the dynamic model. They are:

- (a) Back-to-back converter
- (b) Rotor side converter
- (c) Grid side converter
- (d) DC link with LC filter

The back-to-back converter connected to the DFIG at rotor side with all other converters is given in Fig. 6 [79].

4.1 The Relationship of Optimal Engine Speed and Solar Insolation Under Steady-State Condition and Their Region of Operation

It is possible that, if the variation in insolation I is constant, then the operation of DFIG under dish Stirling system will work properly.

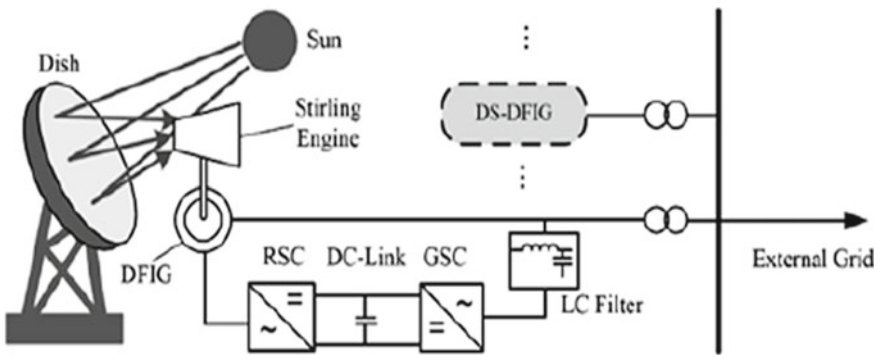


Fig. 6 Schematics of DS-DFIG system [79]

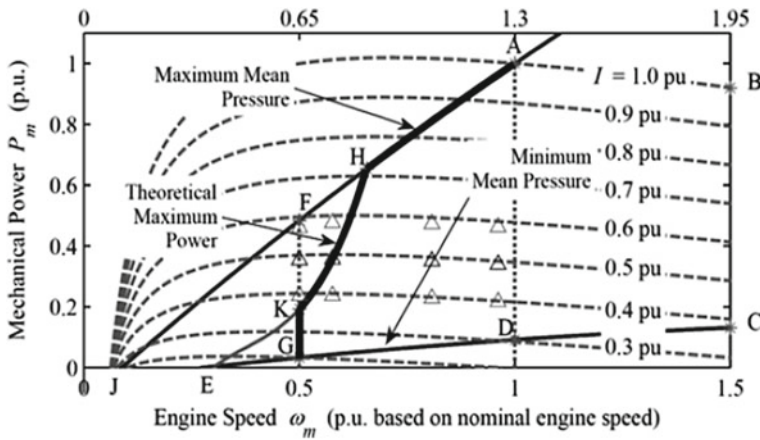


Fig. 7 Region of operation of DS-DFIG using MPPT [79]

The energy that is, maximum in nature can be harness from the DS-DFIG proposed model. The area A–D–G–F–A represents the feasible operation of the DFIG generator. Here in Fig. 7 [79], line A–H–K–G represents the MPPT locus.

5 Conclusion

This paper reviews about the development of Stirling system over the years to achieve maximum output energy by using MPPT technique. Also, it includes the development of the components of the solar dish Stirling system. The Stirling engine has a special character to share with the world and that character is to generate electricity also can be utilized as heat source, i.e., co-generation at high temperature with maximum efficiency by using various types of working fluids. The behavior of the Stirling system under various applications is steady. And in the future, there is a bright scope in Stirling system.

References

1. Dwivedi A, Bari A, Dwivedi G (2013) Scope and application of solar thermal energy in India—a review. *Int J Eng Res Technol* 315–322
2. Verma S et al (2020) Solar PV powered water pumping system—a review. *Mater Today Proc.* <https://doi.org/10.1016/j.matpr.2020.09.434>
3. Lemmer V (2014) Comparative market analysis and economic simulation for Morocco of the parabolic trough and dish CSP technologies. <http://hdl.handle.net/10451/12381>
4. Wu SY, Xiao L, Cao Y, Li YR (2010) A parabolic dish/AMTEC solar thermal power system and its performance evaluation. *Appl Energy* 87(2):452–462

5. Kleih J (1991) Dish-stirling test facility. *Sol Energy Mater* 24(1):231–237
6. Nepveu F, Ferriere A, Bataille F (2009) Thermal model of a dish/Stirling systems. *Sol Energy* 83(1):81–89
7. <http://www.nrel.gov/csp/solarpaces/>
8. Snidvongs S (2005) The structure and foundation design for small solar thermal dish stir-ling10kW power plant for Thailand soft land and poor isolation nature. In: ASME 2005 international solar energy conference. American Society of Mechanical Engineers, pp 729–35
9. Ramos C (2004) Design and construction of a parabolic dish in Mexico. In: ISEC 2004-65045, international solar energy conference, Portland, Oregon
10. Zang C, Li B, Li X, Zheng F, Li, A (2004) Structural design and analysis of the dish solar thermal power system. In: 2nd international energy conversion engineering conference
11. Alarcón JA, Hortúa JE, Lopez A (2013) Design and construction of a solar collector parabolic dish for rural zones in Colombia. *Tecciencia* 7(14):14–22
12. Hartenstine J, Dussinger P (1994) Development of a solar and gas fired heat pipe receiver for the Cummins Power generation 7.5kWe dish/Stirling system. *Intersoc Energy Conv Eng Conf*
13. Li Y, Choi SS, Yang C (2014) An average-value model of kinematic Stirling engine for the study of Variable speed operations of dish stirling solar thermal generating system. In: Control and automation (ICCA), 11th IEEE international conference, pp 1310–1315
14. Poullikkas A, Kourtis G, Hadji Paschalis I (2010) Parametric comparative study for the instal-lation of solar dish technologies in Cyprus. In: Power generation, transmission, distribution and energy conversion (MedPower2010), 7th Mediterranean conference and exhibition, pp 1–8
15. Moreno J, Rawlinson S, Andraka C, Mehos M, Bohn MS, Corey J (1999) Dish/Stirling hybrid receiver sub-scale tests and full-scale design (No. 1999-01-2561). SAE Technical Paper
16. Balzar A, Stumpf P, Eckhoff S, Ackermann H, Grupp M (1996) A solar cooker using vacuum-tube collectors with integrated heat pipes. *Sol Energy* 58(1):63–68
17. Grupp M, Balmer M, Beall B, Bergler H, Hancock D, Schröder G (2009) Online recording of solar cooker use rate by an ovel metering device: prototype description and experimental verification of output data. *Sol Energy* 83(2):276–279
18. Muthusivagami RM, Velraj R, Sethumadhavan R (2010) Solar cookers with and without thermal storage - a review. *Renew Sustain Energy Rev* 14(2):691–701
19. Badran AA, Yousef IA, Joudeh NK, Al Hamad R, Halawa H, Hassouneh HK (2010) Portable solar cooker and water heater. *Energy Convers Manag* 51(8):1605–1609
20. Raturi MP, Deolal MH, Grover J, Kumar A (2014) Parabolic dish type solar cooking system with gravity based solar tracking system. *IOSR J Mech Civ Eng* 11(3):34–6
21. Agrawal H, Yadav V, Kumar Y, Yadav A (2014) Comparison of experimental data for sensible and latent heat storage materials for late evening cooking based on a dish type solar cooker. *Int J Energy a Clean Environ* 15(1):47–72
22. Rao KS, Rao BJM (2007) Innovative solar cooking vessel design. In: 5th international energy conversion engineering conference and exhibit (IECEC), St. Louis, Missouri, pp 25–27
23. Lokeswaran S, Eswaramoorthy M (2012) Experimental studies on solar parabolic dish cooker with porous medium. *Appl Sol Energy* 48(3):169–174
24. Aidan J (2014) Perform Evala Parabol Sol Dish Cooker Yola, Niger *IOSRJAP* 6(5):46–50
25. Panwar NL, Kaushik SC, Kothari S (2012) Experimental investigation of energy and exergy efficiencies of domestic size parabolic dish solar cooker. *J Renew Sustain Energy* 4(2):023111
26. Mohammed IL (2012) Design and development of a parabolic dish solar water heater. *Int J EngRes Appl* 2:1
27. Manukaji JU, Akinbode FO (2002) Design and performance analysis of a solar cooker using fresnel reflectors. *Spectrum* J 9:1
28. Dafle VR, Shinde NN (2012) Design, development & performance evaluation of concentr-ating Monoaxial Scheffler technology for water heating and low temperature industrial steam application. *Int J Eng Res Appl (IJERA)* 2(6):848–52
29. Sakhare V, Kapatkar VN (2014) Experimental analysis of parabolic solar dish with copper helical coil receiver. *International. J Innov Res Adv Eng (IJIRAE)* 1:8
30. Habib-agahi H, Jones SC. Irrigation market for solar-thermal parabolic-dish systems

31. Saini A, Kohli S, Pillai AJ (2013) Solar powered Stirling engine driven water pump. *IJRET* 02(11):615–20
32. Srithar K, Rajaseenivasan T, Karthik N, Periyannan M, Gowtham M (2016) Standalone triple basin solar desalination system with cover cooling and parabolic dish concentrator. *Renew Energy* 90:157–165
33. El-Kassaby MM (1991) New solar cooker of parabolic square dish: design and simulation. *Renew Energy* 1(1):59–65
34. Hafez A, Soliman A, El-Metwally K, Ismail I (2017) Design analysis factors and specifications of solar dish technologies for different systems and application. *Ren Sust Ene Rev* 67:1019–1036
35. Bert J, Chrenko D, Sophy T, Le Moyne L, Sirot F (2014) Simulation, experimental validation and kinematic optimization of a Stirling engine using air and helium. *Energy* 78:701–712
36. Chen M, Ju Y (2015) Effect of different working gases on the performance of a small thermoacoustic Stirling engine. *Int J Refrig* 51:41–51. <https://doi.org/10.1016/j.ijrefrig.2014.12.006>
37. Kazimierski Z, Wojewoda J (2014) Comparison of the externally heated air valve engine and the helium Stirling engine. *Energy Convers Manag* 80:357–362. <https://doi.org/10.1016/j.enconman.2013.12.055>
38. Martini W (1983) Stirling engine design manual. DOE/NASA/3152-78/1, NASA, CR-13518
39. Fan S, Li M, Li S, Zhou T, Hu Y, Wu S (2017) Thermodynamic analysis and optimization of a Stirling cycle for lunar surface nuclear power system. *Appl Therm Eng* 111:60–67. <https://doi.org/10.1016/j.applthermaleng.2016.08.053>
40. Kobayashi M, Hasebe N, Hiramoto T, Miyachi T, Murasawa S, Okada H, Okudaira O, Yamashita N, Berezhnoy A, Shibamura E, Takashima T, D'uston C, Narasaki K, Tsurumi K, Kaneko H, Nakazawa M, Mori K, Fujii M (2005) Germanium detector with Stirling cryocooler for lunar gamma-ray spectroscopy. *Nucl Instrum Methods Phys Res Sect A Accel Spectrometers, Detect Assoc Equip* 548:401–410
41. Li M, Dong J (2012) Modeling and simulation of solar dish-Stirling systems. 2012 Asia-Pacific Power Energy Eng Conf. <https://doi.org/10.1109/APPEEC.2012.6307165>
42. Ramos C (2004) Design and construction of a parabolic dish in Mexico. In: ISEC2004-65045, international solar energy conference, Portland, Oregon
43. Srithar K, Rajaseenivasan T, Karthik N, Periyannan M, Gowtham M (2016) Stand-alone triple basin solar desalination system with cover cooling and parabolic dish concentrator. *Renew Energy* 90:157–165
44. Hijazi H, Mokhiamar O, Elsamni O (2016) Mechanical design of a low-cost parabolic solar dish concentrator. *Alex Eng J* 55(1):1–11
45. Lovegrove K, Burgess G, Pye J (2011) A new 500 m² paraboloidal dish solar concentrator. *Sol Energy* 85(4):620–626
46. Li L, Dubowsky S (2011) A new design approach for solar concentrating parabolic dish based on optimized flexible petals. *Mech Mach Theory* 46(10):1536–1548
47. Schertz PT, Brown DC, Konnerth III A (1991) Facet development for a faceted stretched-membrane dish by Solar Kinetics, Inc (No. SAND-91-7009). Sandia National Labs., Albuquerque, NM (United States); Solar Kinetics, Inc., Dallas, TX (United States)
48. Xu G, Wang Y, Quan Y, Li H, Li S, Song G, Gao W (2015) Design and characteristics of a novel tapered tube Bundle receiver for high-temperature solar dish system. *Appl Therm Eng* 91:791–799
49. Arulkumaran M, Christraj W (2012) Experimental analysis of non-tracking solar parabolic dish concentrating system for steam generation. *Eng J* 16(2):53–60
50. Nazemi SD, Boroushaki M (2016) Design, analysis and optimization of a solar dish/Stirling system. *Int J Renew Energy Dev* 5(1):33–42
51. El-Kassaby MM (1991) New solar cooker of parabolic square dish: design and simulation. *Renew Energy* 1(1):59–65
52. Senthil R, Cheralathan M (2016) Effect of the PCM in a solar receiver on thermal performance of parabolic dish collector. *Therm Sci* 007–7

53. Johnston G (1995) Flux mapping the 400 m² “Big Dish” at the Australian National University. *J Sol Energy Eng* 117(4):290–293
54. Ma H, Jin G, Zhong X, Xu K, Li Y (2012) Optical design of a solar dish concentrator based on triangular membrane facets. *Int J Photo* 2012:1–5
55. Droher JJ, Squier SE (1986) Performance of the Vanguard solar dish Stirling engine module, Technical Report EPRIAP-4608. Palo Alto, CA: Electric Power Research Institute
56. Grasse W, Hertlein HP, Winter CJ (1991) Thermal solar power plants experience. In: Plants CJ, Winter RL, Sizmann, VantHull LL (eds) *Solar power*, pp 215–282. Springer, Berlin
57. Schiel W (1999) Dish/Stirling systems. Solar thermal electricity generation. Co-lección Documentos CIEMAT. Madrid, pp 209–250. CIEMAT, Spain
58. Lopez C, Stone K (1992) Design and performance of the Southern California Edison Stirling dish. *Solar Eng Proc ASME Int Solar Energy Conf* 945–952
59. Mancini T, Heller P, Butler B, Osborn B, Schiel W, Goldberg V, Buck R, Diver R, Andracka C, Moreno J (2003) Dish-Stirling systems: an overview of development and status. *Int J Sol Energy Eng* 125:135–151
60. Stone K, Leingang E, Rodriguez G, Paisley J, Nguyen J, Mancini T, Nelving H (2001) Performance of the SES/Boeing dish Stirling system. In: Kleis SJ, Bingham CE (eds) *Proceedings of solar forum 2001 solar energy: the power to choose*, pp 21–27, New York, USA
61. Schiel W, Keck T, Kern J, Schweitzer A (1994) Long term testing of three 9 kW dish/Stirling systems. *ASME 1994 Solar Eng Conf* 541–550
62. Schiel W, Schweitzer A, Stine W (1994) Evaluation of the 9-kWe Dish/Stirling system of Schlaich Bergermannund partner using the proposed IEA Dish/Stirling performance analysis guidelines. *Intersoc Energy Conv Eng Conf* 4:1725–1725
63. Romero Alvarez M, Zarza E (2007) Concentrating solar thermal power. *Handbook of energy efficiency and renewable energy*
64. Stine WB, Diver RB (1994) *A compendium of solar dish/Stirling technology*
65. Crawford SM (1996) *A comparative analysis of viable solar thermal technologies for solar field development and commercialization (Doctoral dissertation)*. University of Nevada, Las Vegas
66. Mayette J, Davenport R, Forristall R (2001) The salt river project sun dish dish-Stirling system. In: Kleisand SJ, Bingham CE (eds) *Proceedings of solar forum 2001 solar energy: the power to choose*, pp 19–31, New York, USA
67. Diver R, Andracka C, Rawlinson K, Thomas G, Goldberg V (2001) The advanced dish development system project. In: Kleisand SJ, Bingham CE (eds) *Proceedings of solar forum 2001 solar energy: the power to choose*, pp 341–351, New York, USA
68. Monne C, Bravo Y, Alonso S, Moreno F, Munoz M (2013) Developments for future implementation in dish-Stirling technology. *Stroj: časopis za Teori Praks - U Stroj* 55(1):35–44
69. Kalt schmitt M, Streicher W, Wiese A (2007) *Renewable energy: technology, economics and environment*. Springer Science & Business Media
70. Fraser PR (2008) *Stirling dish system performance prediction model. (Doctoral dissertation)*. University of Wisconsin Madison
71. Poullikkas A, Kourtis G, Hadji PI (2010) Parametric analysis for the installation of solar dish technologies in Mediterranean regions. *Renew Sustain Energy Rev* 14(9):2772–2783
72. Jabari F, Nazari-heris M, Mohammadi-ivatloo B, Asadi S, Abapour M (2020) A solar dish Stirling engine combined humidification-dehumidification desalination cycle for cleaner production of cool, pure water, and power in hot and humid regions. *Sustain Energy Tech Assessments* 37:100642
73. Karji A, Woldesenbet A, Khanzadi M, Tafazzoli M (2019) Assessment of social sustainability indicators in mass housing construction: a case study of Mehr housing project. *Sustain Cities Soc* 50:101697
74. Yi H, Srinivasan RS, Braham WW, Tilley DR (2017) An ecological understanding of net-zero energy building: evaluation of sustainability based on emergy theory. *J Cleaner Prod* 143:654–671

75. Jabari F, Mohammadi-ivatloo B, Ghaebi H, Bannae-sharifian MB (2019) Biogas fueled combined cooling, desalinated water and power generation systems. *J Cleaner Prod* 219:906–924
76. Li Y, Choi SS, Yang C (2014) Dish-Stirling solar power plants: modelling, analysis and control of receiver temperature. *IEEE Trans Sustain Energy* 5(2):398–407
77. Howard DF, Liang J, Harley RG (2010) Control of receiver temperature and shaft speed in dish-Stirling solar power plants to meet grid integration requirements. In: *Proceedings of IEEE Energy Conversion Congress Exposition, Atlanta, GA, USA*, pp 398–405
78. Howard D, Harley RG (2010) Modelling of dish-Stirling solar thermal power generation. In: *Proceedings IEE power energy society general meeting, Minneapolis, MN, USA*, pp 1–7
79. Li Y, Choi S, Yang C, Wei F (2015) Design of variable-speed dish-Stirling solar-thermal power plant for maximum energy harness. *IEEE Trans Energy Convers* 30(1):394–403

Physical Properties of Amorphous Nanosilica from Rice Husk (Agriculture Waste) and PVA Composite, Prepared Using Green Approach for Its Applications



Anurag Kumar, Rakesh Kumar Singh, Nishant Kumar, Atul Jyoti, and Prem Kumar

1 Introduction

Rice husk is agricultural waste. India being the second largest producer of rice and being a staple food here every year 120 million tons of paddy are produced alone, where total production of rice in world is 7.0×10^8 m tons/year. Rice husk contains about 75% of organic matter that evaporates while burning of husk, and the residue is named as rice husk ash [1]. Its absorbent and insulating properties are used as a strengthening agent in building materials [2, 3]. Uses of rice husk have been limited to low added value such as fertilizers and land-filling and for a developing nation like will act as a boon to industries. Rice husk is used as soil ameliorant. An ameliorant is a chemical that is applied to improve the quality of the soil and thereby improves plant growth [4]. In the present study, rice husk is used for extraction of nanosilica by applying leaching method with HCL. Leaching with HCL produces a high surface area of amorphous nanosilica in the comparison of other acids such as nitric acid and sulfuric acid [5]. In this method, no harmful chemical or gases are emitted. Therefore, this ecofriendly approach may be support conversion of agriculture waste in silica materials. Nanosilica is mostly used in drug delivery system, paint, ceramic, polymer, electronics, and automobile sectors [6–10]. It is the abundance of rice husk in rice producing countries that has led the researchers to look for innovative ideas to make use of this waste to create wealth and knowledge. Polyvinyl alcohol (PVA) is a synthetic polymer, which is most commonly used in biomedical application

A. Kumar · R. K. Singh (✉) · N. Kumar · A. Jyoti
Aryabhata Center for Nanoscience and Nanotechnology, Aryabhata Knowledge University,
Patna, India

P. Kumar
Sarvajanik Interstarie Vidyalaya, Sarvodaya Nagar, Banka, Bihar 813102, India

and microorganism immobilization due to its excellent biocompatibility, biodegradability, non-toxicity [11–15]. In this present study, sol–gel citrate precursor method is used for preparation of PVA/SiO₂ composite. Sol–gel citrate precursor is most reliable and convenient technique for preparation of polymer composite materials [16–18]. PVA/SiO₂ composite is widely used in various applications such as optical material, sensor, catalysis, enzyme encapsulation, and adsorption due to its bioactive and excellent mechanical properties [19–21].

2 Experimental: Materials and Method

Materials:

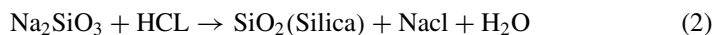
Rice husk is taken from rice mill, Fatehpur, Patna, Bihar, India. Polyvinyl alcohol (PVA) is a synthetic polymer that was taken from Sigma Aldrich, which is used for preparation of PVA/nanosilica composite material.

2.1 Synthesis of Nanosilica

The amorphous nanosilica was extracted from rice husk by using eco-friendly leaching method. During synthesis of nanosilica, firstly proper cleaning of rice husk is with demineralized water for removing dust particles and then dried in hot air oven at 40 °C up to dry it. After drying, rice husk is burnt in muffle furnace at 600 °C for 2 h. Then obtained rice husk ash (RHA) is treated with 2.5 N NaOH. It is an exothermic reaction. Then mixture is heated on magnetic stirrer hot plate at temperature 60 °C for 3 h. The lid of the flask is covered with a glass stopper, and the stirrer speed is optimized. The solution was filtered by using warm deionized water and grade 1 filter paper to wash the alkali and was then left to dry. The yield of this reaction was sodium meta-silicate (Na₂SiO₃) using Eq. 1.



Then, rice husk ash (RHA) is leached with 1N HCl for 2 h. This drastic pH shift results in the formation of nanosilica from microphase silica (Eq 2). The solution is washed thoroughly by using deionized water. The filtrate was left to dry in the hot air oven at 90 °C for 24 h. The oven-dried RHA was again heated in high-temperature furnace at 600 °C for 2 h with a constant ramp rate of 6 °C/min. The nanosilica obtained as shown by simple mechanism in Fig. 1 was characterized using characterization tools XRD, SEM, HR-TEM, and FTIR for structural properties.



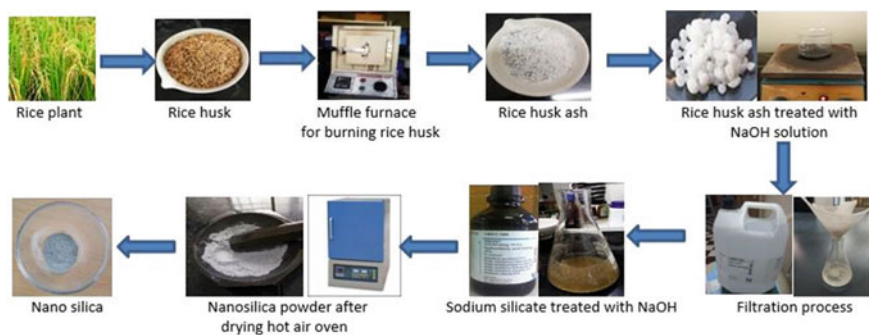


Fig. 1 Schematic diagram of synthesis process of amorphous nanosilica

After burning at this temperature, obtained rice husk ash is annealed at different temperature for different time. The first sample is annealed at 400 °C for 2 h, second sample is annealed at 500 °C for 2 h, and third sample is annealed at the temperature of 600 °C for 2 h.

2.2 Preparation of SiO_2 -PVA Composite Materials

Preparation of SiO_2 -PVA (polyvinyl alcohol) composite materials by using sol-gel citrate precursor method and preparation method is shown in Fig. 2 as schematic diagram. During preparation, polyvinyl alcohol of 5.8 g and silicon dioxide 0.2 g are taken and a solution is made with 50 ml distilled water in a beaker and mixed on the magnetic stirrer for 1 h by the help of magnetic bead. In second step after 1 h silicon dioxide which is amorphous having annealed at the temperature 600 °C in the beaker was allowed and left for 24 h. After 24 h gel is formed of polyvinyl alcohol and silicon dioxide, third step is to put it in the glass petri dish and then dry it in air oven up to dry it of 100 °C. After drying the gel, a SiO_2 -PVA composite was obtained. Present research work describes the results obtained from the characterization studies

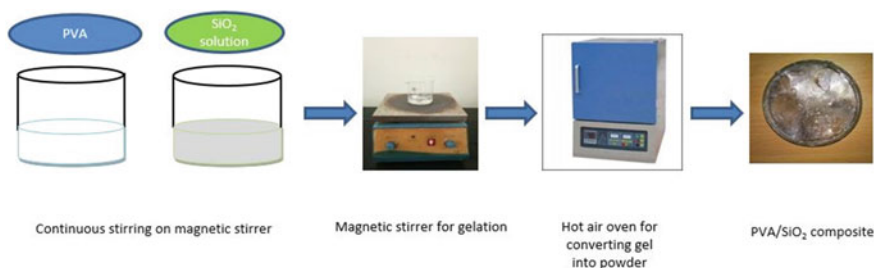


Fig. 2 Schematic diagram of preparation of PVA- SiO_2 composite material

of the synthesized amorphous nanosilica and its composite materials (SiO_2 -PVA). This deals with the studies of structural and microstructural and photoluminescence properties of materials using X-ray diffractometer (XRD), Fourier transform infrared spectroscopy (FTIR), scanning electron microscope (SEM), and photoluminescence spectrometer (PL).

3 Results and Discussions

3.1 X-Ray Powder Diffraction Measurement

The XRD patterns of the obtained amorphous nanosilica powder were leached with 1 N hydrochloric acid (HCl) for various temperatures as shown in Fig. 3. In all cases, broad peak zone was obtained at near $2\theta = 22^\circ$ and signifies the amorphous nature of silica-based materials [22]. The peak obtained in XRD analysis shows that nanomaterial prepared by RHA is amorphous in nature [23]. These materials are prepared by annealing the silica materials at 400°C for 2 h, 500°C for 2 h, and at 600°C for 2 h in muffle furnace. Synthesized nanosilica from rice husk remains amorphous up to about 600°C . It is clear that when annealing temperature is below the temperature of 600°C then the nanosilica also obtained is amorphous in nature. Further the size was calculated using HR-TEM and was found to be $8(\pm 1\text{ nm})$, shown in Fig. 4d.

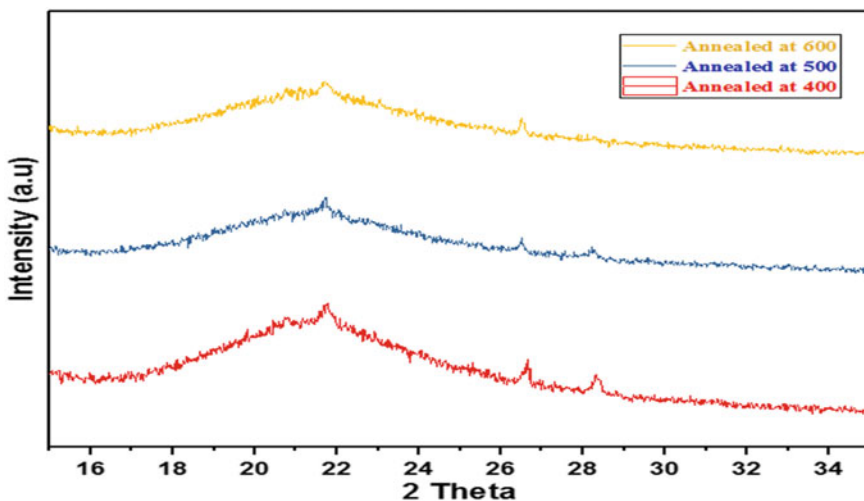


Fig. 3 XRD spectrum of amorphous nanosilica annealed at temperature 400°C , 500°C , and 600°C

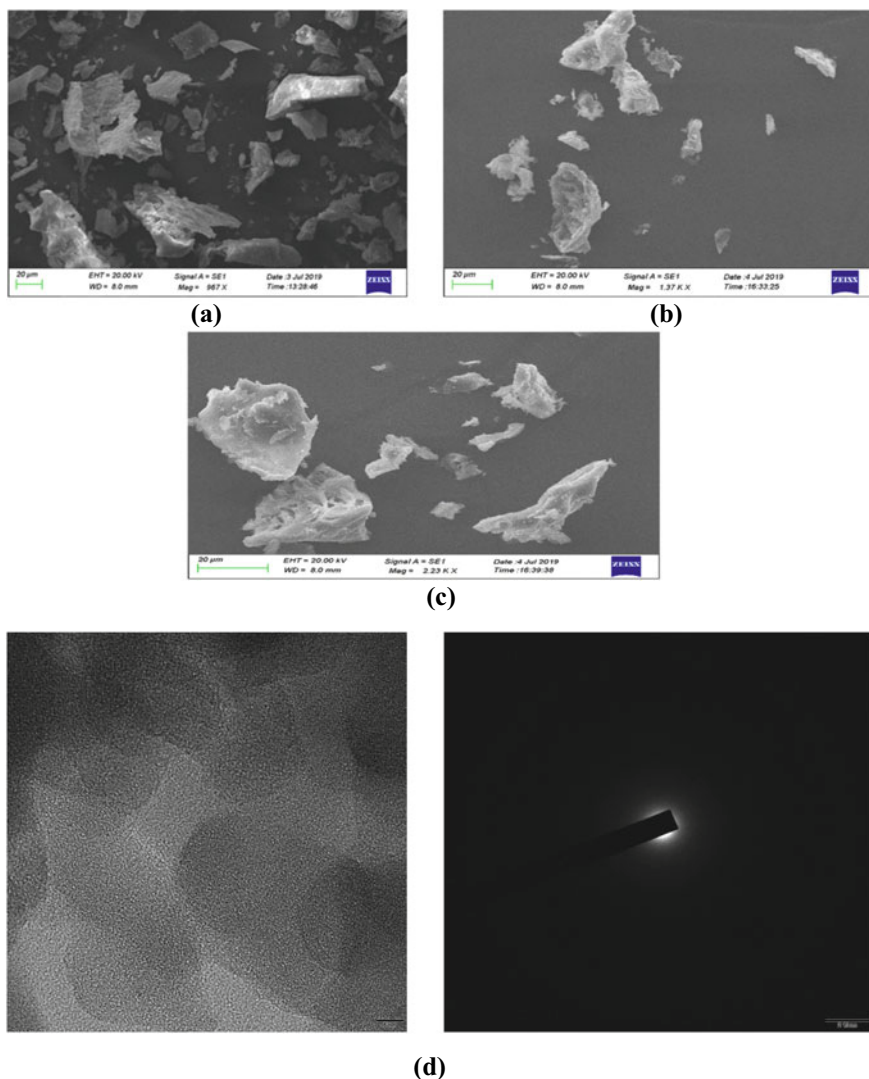


Fig. 4 SEM images of the sample, prepared at annealed temperature of **a** 400 °C, **b** 500 °C, **c** 600 °C, **d** TEM images of amorphous nanosilica

3.2 Scanning Electron Microscope Measurement

The SEM image of all the three samples annealed at different temperature and time is shown in Fig. 4a–c. Silica is an insulating material; therefore, analysis of morphological properties and sample has been coated with gold for conductivity of electron. Figure 4a–c shows the SEM images of nanosilica particles obtained under

20 kV resolution with 967, 1.97 K, and 2.23 K magnification, respectively. From this SEM image, arrangement of the silica can be noticed agglomeration in irregular shape formed which might be due to different annealing temperature which leads to different growth of crystal. This agglomeration shows porosity also. This porosity is found very much important for rice husk nanosilica particle for various applications [24, 25].

4 TEM Measurement

Further to investigate the size of amorphous nature of the prepared material, HRTEM and SAED pattern analysis were performed, which are shown in Fig. 4d. The study shows that size of the prepared nanomaterial is approximately 8 nm (± 1 nm). Further to confirm the amorphous nature of the prepared material, small angle electron diffraction (SAED) pattern shows no concentric circle and no bright spot. Thus, as concentric circle has no interplanar distance, i.e., hkl space, there is no spacing in the prepared material. Thus, TEM analysis confirms small-sized nanosilica materials from rice husk, which is reported by research group [26].

5 FTIR Measurement

FTIR results, shown in Fig. 5, show that the peak numbers are almost at the same position which is annealed at different temperature, hence confirmed that same material (i.e., nanosilica). The peak numbers near 3300–3450 cm^{-1} show the presence of silanol–OH bond and absorbed water. The transmittance peak at 985 cm^{-1} is due to the presence of siloxane bonds, i.e., Si–O–Si bond is also present in all of three samples. The presence of Si–OH and other silicone bond stretching vibrations is also present. The peaks between 1000 and 900 cm^{-1} are attributed to the stretching vibrations of C–H and C–Cl bonds. The FTIR graph confirms the presence of silica and is similar to the FTIR of nanosilica obtained by some research group works [5, 22]. Thus, FTIR measurement shows that annealing temperature cannot change the internal bonding nature of amorphous silica, while their surface morphology was found to change.

5.1 Photoluminescence Measurement

Figure 6 shows the photoluminescence spectrum of a pure amorphous nanosilica powder excited by radiation of wavelength of 200 nm. Luminescence properties may be due to energy band gap, defects in the crystal, types of element present, and the wavelength of incident radiation. The prominent luminescence peaks are present

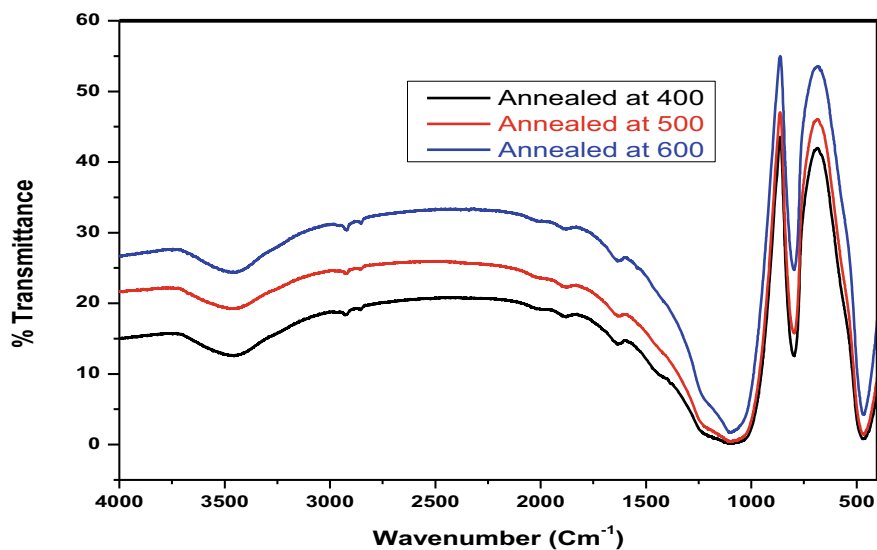


Fig. 5 FTIR of nanosilica annealed at 400 °C, 500 °C, and 600 °C

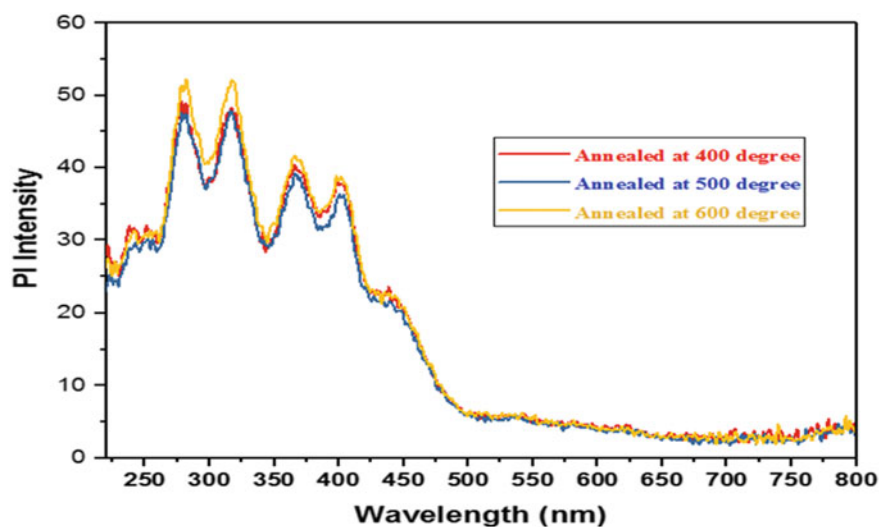


Fig. 6 Photoluminescence (PL) spectrum of amorphous nanosilica

in the UV regions and may be attributed due to the presence of various type of defects in as-synthesized nanosilica. The probable defects can be situated in Si or O₂, silica vacancy, or chemical bonding that is occupied in oxygen molecule. Luminescence feature also depends on other crucial factors which include solvent, atmosphere, temperature, etc., during synthesis process. Figure 6 shows that a wide emission band

was absorbed in the silica sample with a maximum intensity at range between 250 and 325 nm and some peaks at ranges between 350 and 425 nm. Photoluminescence spectrum showed wide emission in a UV range [27, 28]. Thus, natural silica materials prepared using green approach may have some applications in silicon industry and cement industries.

6 Studies on Nanosilica–PVA Composite Materials

The nanosilica-based composite is prepared using amorphous nanosilica and polyvinyl alcohol (PVA). Polyvinyl alcohol (PVA) is a water-soluble polymer having molecular formula $[\text{CH}_2\text{CH}(\text{OH})]_n$. PVA is colorless materials having high susceptible to water and this shows hygroscopic property. Due to higher humidity, more water is absorbed. The water of PVA acts as a plasticizer.

6.1 XRD measurement of Composite material (SiO_2 –PVA)

The XRD patterns of PVA–nanosilica composites are shown in Fig. 7. We have chosen nanosilica prepared at 600 °C annealing temperature for composite preparation. An intense peak of nanocomposite is observed at 19.5 degree that shows (1 1 0) plane. This looks like semi-crystalline. Major peak of amorphous nanosilica is obtained about 23 degree. The intensity of the (1 1 0) plane PVA is comparatively higher and which may be due to hydroxyl group (O–H) present in inside chains [29]. The mixing of nanosilica into PVA do not show any changes in the intensity of the (1 1 0) plane. The intensity peak for the nanosilica composite system is slight better than that of the

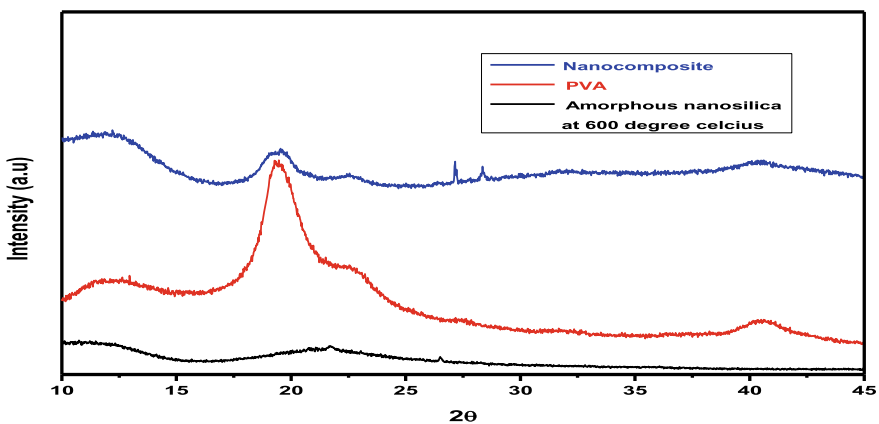


Fig. 7 XRD image of composite material of SiO_2 –PVA

PVA, while we have used of 0.2 wt.% of nanosilica in PVA composite crystallinity of nanosilica composite further increased. The actual cause for such changes is future research plan. Similar behavior was also reported by some researcher [30, 31]. The average crystalline size of PVA, amorphous nanosilica, and composite was found to be 9 nm, 21 nm, and 13 nm, respectively.

6.2 SEM Measurement of Composite material of SiO₂-PVA

The pure PVA and nanomaterials-reinforced PVA composite films are examined using SEM as shown in Fig. 8. Compared to pure PVA film, morphology of PVA nanosilica composites can be easily identified. After amorphous nanosilica is added into the PVA matrix, this protrusion explains the deterioration of the elongation at break of PVA composites compared to pure PVA. A homogenous distribution is observed in the PVA composite with the introduction of 0.2 wt.% of nanosilica as shown in above Fig. 8. Silica interaction at surface becomes more compact in composite materials. This may be useful better mechanical properties as multifunction properties [32, 33]. Further studies of mechanical properties are required, and this is our future work.

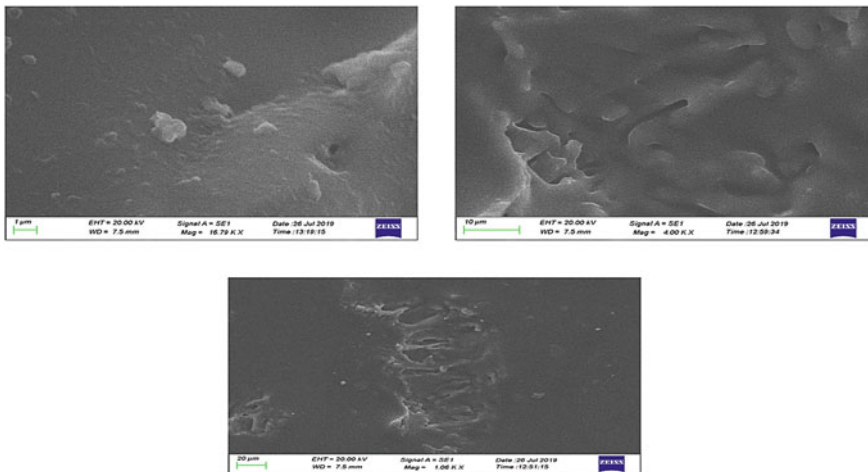


Fig. 8 SEM images of composite material of SiO₂-PVA

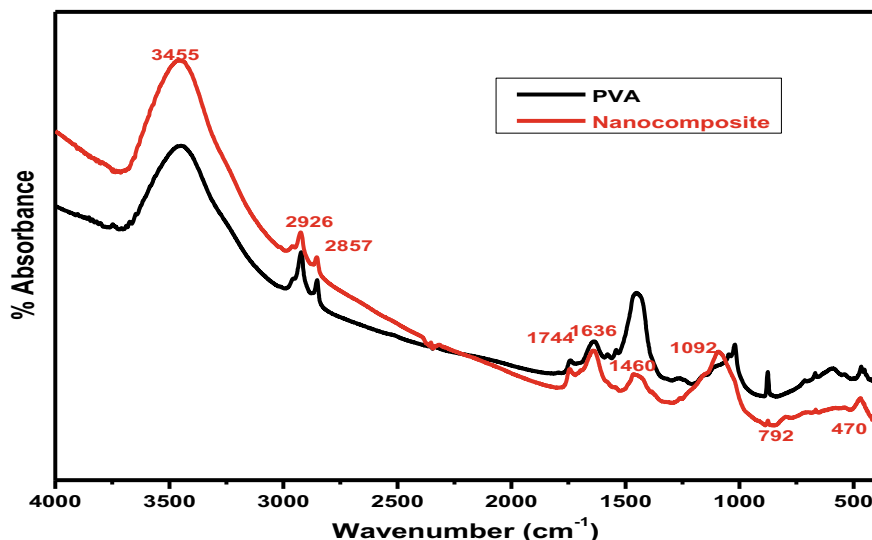


Fig. 9 FTIR spectrum of nanocomposite material of SiO_2 -PVA

6.3 FTIR Measurement of Composite material of SiO_2 -PVA

The FTIR spectrum of SiO_2 -PVA nanocomposite is shown in Fig. 9. The absorption peaks are almost looking at the same position, which shows homogeneity of the organic-inorganic molecule. The H-bonding may be a possible reason for such homogenous behavior. The important interactions may occur due to the presence of silanol groups of SiO_2 nanoparticle and hydroxyl groups of PVA. Due to such interactions, stress and interatomic force affected the behavior of the composite. Such changed properties in such composite materials were reported [34]. The FTIR data supports SEM measurement. Due to strong Si-O bond, silica-based mesoporous nanoparticles are more stable to external response such as degradation and mechanical stress as compared to niosomes, liposomes, and dendrimers which inhibit the need of any external stabilization in the synthesis of mesoporous silica nanoparticles. Mesoporous silica has been widely used as a coating material.

6.4 Photoluminescence Measurement of Composite material

Figure 10 shows of a composite materials SiO_2 -PVA amorphous nanosilica powder excited using radiation wavelength of 200 nm. The addition of nanosilica reduces the PL intensity of the PVA matrix. The PL intensity of amorphous nanosilica is almost near about PVA, while the intensity of the nanocomposite is lower than PVA. Thus, luminescence intensity of nanocomposite reduces, which may be due to

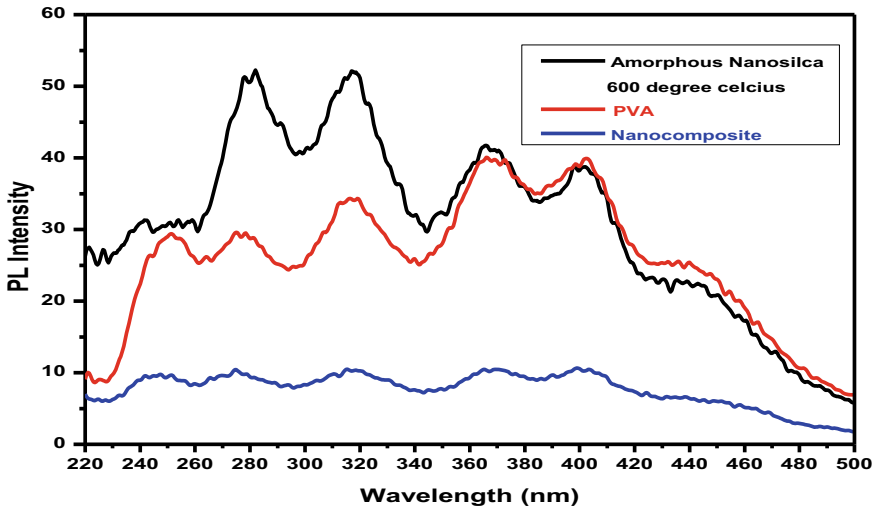


Fig. 10 Photoluminescence (PL) spectrum of SiO₂-PVA composite material

agglomeration of nanosilica that behaves like a barrier to the penetration of light. The other possible reason may be explored. This is our future work. The intensity of light is further reducing with addition of 0.2 wt.% of nanosilica into the PVA composite. The addition of nanomaterials increased the probability of the nanomaterials to interact and aggregate with the PVA, which leads to reduction in light transmission [35].

Thus in nutshell, present research may provide some technical and knowledge support to different industries. Since several industries such as electronics, cement, rubber, drug delivery, and related sectors are highly dependent on silica, this is a growing concern because of the environmental impact of sourcing and refining of silica. Thus, a green source of silica is of vital importance to meet the growing demand for silicon in the industry. Composite of amorphous silica with magnetic materials may be useful to prepare magnetic polymer, which was reported [26].

7 Conclusions

The small-sized amorphous nanoscale silica materials from rice husk were prepared using low-cost ecofriendly approach. Structural properties that prepared silica materials were determined using XRD, TEM, and SEM. TEM measurement shows size of about 8 nm. Broad XRD peak zone was obtained at near $2\theta = 22^\circ$ that indicates the amorphous nature of silica materials. Surface morphology measurement of silica depends on temperature and shows agglomerated porous structure. Photoluminescence spectra measurement represent wide emission in UV region. PVA/SiO₂

composite was also prepared ecofriendly using low-cost chemical method. Functional group of silica and its composite was measured using FTIR and shows the presence of hydrogen bonded silanol group that increases the densification of composite. The luminescence emissions of radiations in composite materials are also in UV range but intensity height decreases considerably. Physical properties measurement of present research open a new window for electronics, cement, medicine industries, and for its use as raw materials or composite materials. Since several industries such as electronics, cement, rubber, drug delivery, and related sectors are highly dependent on silica, a green source of silica is of vital importance to meet the growing demand for silicon in the industry.

Acknowledgements Authors are also grateful to Department of Education, Govt. of Bihar and Aryabhata Knowledge University, Patna which has been very supportive in establishment and functioning of the Aryabhata Center for Nanoscience and Nanotechnology, Aryabhata Knowledge University, Patna, Bihar, India.

References

1. Real C, Alcalá D, María C, José M (2008) *J Am Ceram Soc* 79:2012–2016
2. Givi AN, Rashid SA, Aziz FNA, Salleh MAM (2010) *Compo Part B: Engg* 41:673–677
3. Tangchirapat W, Buranasing R, Jaturapitakkul C, Chindaprasirt P (2008) *Constr Build Mater* 22:1812–1819
4. M.Dominic CD, Begum PMS, Joseph R, Joseph D, Kumar P, Ayswarya EP (2013) *I J Sci Env Tech* 2:1027–1035
5. Yuvakumar R, Elango V, Rajendran V, Kannan N (2012) *J Exp Nanosc* 1–10
6. Liu YL, Hsu CY, Hsu KY (2005) *Polymer* 46:1851–1856
7. Shin Y, Lee D, Lee K, Ahn KH, Kim B (2008) *J Ind Eng Chem* 14:515–519
8. Lakshmi UR, Vimal Chandra S, IndraDeo M, Lataye DH (2009) *J Environ Manage* 90:710–720
9. Jang HT, Park Y, Ko YS, Lee JY, Margandan B (2009) *Int J Greenhouse Gas Control* 3:545–549
10. Sun L, Gong K (2001) *Ind Eng Chem Res* 40:5861–5877
11. Li X, Hu A, Ye L (2011) *J Polym Environ* 19:398–404
12. Feng S, Chen H, Liu Y, Huang Z, Sun X, Zhou L (2013) *Sci Rep* 3:1838
13. Zhang Y, Ye L (2011) *Polym-Plast Techno* 50:776–782
14. Ionita M, Iovu H (2012) *Compos B Eng* 43:2464–2470
15. Li Z, Zhang J, Du J, Han B, Wang J (2006) *Colloids Surf A Physicochem Eng Aspect* 286:117–120
16. Song YH, Zheng Q, Lai ZZ (2008) *Chinese. J Polym Sci* 26:631–638
17. Zheng JZ, Zhou XP, Ying JR, Xie XL, Mai YW (2009) *Chinese. J Polym Sci* 27:685
18. Liu AX, Wei JC, Chen XS, Jing XB, Cui Y, Liu Y (2009) *Chinese. J Polym Sci* 27:415–426
19. Singh V, Singh D (2013) *Process Biochem* 48:96–102
20. Tong HW, Utlu BR, Wackett LP, Aksan A (2013) *Mater Lett* 111:234–237
21. Cheng Q, Pan F, Chen B, Jiang Z (2010) *J MembrSci* 363:316–325
22. Thuadajj N, Nuntiya A (2008) *Chiang Mai. J Sci* 35:206–211
23. Amutha K, Ravibhaskar R, Sivakumar G (2010) *I J Nanotech Appl* 4:61–66
24. Liou TH (2004) *Mat Sci Eng: A* 364:313–323
25. Carmona VB, Oliveria RM, Silva WTL, Mattoso LHC (2013) *Indus. Crops. Prod* 43:291–296
26. Jyoti A, Singh RK, Kumar N, Aman AK, Kar M (2021) *Mat Sci Eng: B* 263:114871
27. Slowing II, Trewyn BG, Giri S, Lin VS-Y (2007) *Adv Func Mater* 17:1225–1236

28. Aboshi A, Kurumoto N, Yamada T, Uchino T (2007) *A J Phys Chem C* 111:8483–8488
29. Saheb DN, Jog JP (1999) *Adv Poly Tech* 18:351–363
30. Zhu YS, Wang XJ, Hou YY, Gao XW, Liu LL, Wu YP, Shimizu M (2013) *Electroch Acta* 87(2013):113–118
31. Peng Z, Kong LX, Li SD (2005) *Polymer* 46:1949–1955
32. Yang J, Chen JR, Song JH (2009) *Vib Spectrosc* 50:178–184
33. Kim OH, Lee K, Kim K, Lee BH, Choe S (2006) *Polymer* 47:1953–1959
34. Costa HS, Rocha MF, Andrade GI, Barbosa-Stancioli EF, Pereira MM, Orefice RL, Vasconcelos WL, Mansur HS (2008) *J Mater Sci* 43:494–502
35. Karthikeyan B, Hariharan S, Sasidharan A, Gayathri V, Arun T, Madhumitha C (2019) *Opt Mat* 90:139–144

Antibacterial Property of Biologically Synthesized Iron Nanoparticles Against *Staphylococcus aureus*



Satyam Sangeet, Arshad Khan, Sarit Prabha, and Khushhali M. Pandey

1 Introduction

Oral illnesses represent a significant health trouble for some nations and influence individuals all through their lifetime, causing torment, distress, and distortion. It is assessed that oral maladies influence about 3.5 billion individuals around the world [1]. More than 300 known types of microorganisms are found in oral cavity [2]. *Staphylococcus aureus* is one of the major bacteria found in oral sepsis. There are different medications available to treat the pathogenicity of this bacteria. With the constantly uprising impact of multi-drug resistance (MDR), it gets imperative to investigate new territories to attempt to focus on the pathogenicity of *S. aureus*. Various forms of complications can be brought about by this microorganism going from gentle skin contaminations to perilous sicknesses, such as oral mucositis [3], angular cheilitis [4], osteomyelitis [5] and bacteremia [6]. There are various virulence factors via which *S. aureus* spreads its infections such as CHIP, SCIN [7], etc. Both these virulence proteins attack the complement pathway of immune response of the host. SCIN is an inhibitor of the C3 convertase enzyme that blocks the conversion of C3b on the bacterial surface, thus resulting in the human neutrophil lose its ability to phagocytose *S. aureus* [8]. On the other hand, CHIP is a chemokine receptor modulator. It is responsible for the gradual response loss of the peptide receptors of neutrophils and the C5a receptor (C5aR). This process halts the chemotaxis of neutrophil, thereby halting its activation in response to formylated peptides and C5a [9–12].

Until now, prescriptions accessible to control *S. aureus* contaminations have been different anti-toxins, for example, flucloxacillin [3], erythromycin, vancomycin and fusidic acid [13]. Some inorganic modulators have been accounted for to repress

S. Sangeet (✉) · A. Khan · S. Prabha · K. M. Pandey
Department of Biological Science and Engineering, Maulana Azad National Institute of
Technology, Bhopal, Madhya Pradesh, India

the development of *S. aureus* [2]. Thus, there is a growing need to synthesize new medications to target the virulence of *S. aureus*. Natural blend of metal nanoparticles utilizing diverse plant parts [14], microorganisms [9, 15] and enzymes [16] is gaining lot of attention. Nanoscale size of nanoparticles provides them large surface area that ultimately increases their reactivity [17]. Also, utilizing nanoparticles can provide good results as they have been giving positive response in various fields, viz. biomedical, pharmaceuticals, etc. [18–20].

Iron nanoparticles have received a lot of attention because of their highly interactive behavior with other molecules, thereby increasing their antibacterial activity as well as overall efficiency. Physical and chemical methods including sodium borohydride reduction [21], mechanical milling [22], etc., are utilized for FeNPs synthesis. FeNPs synthesized by these methods are relatively unstable and, consequently, hazardous for environment [23, 24]. Biosynthesis of iron nanoparticles via different plants extracts has been reported in past and includes *Syzygium aromaticum* (clove) [25], *Musa ornata* (banana) [26], brown sea weed *Dictyota dicotoma* [27], *Eriobotrya japonica* (loquat) [28], *Ageratum conyzoides* [29]. Iron nanoparticles produced via plant extracts are ecofriendly, less expensive, biocompatible and highly stable [26]. FeNPs are produced when the plant metabolites reduce the iron ion from Fe^{3+} to Fe^0 state [26, 30, 31]. The plant metabolites act as reducing agents and support material for iron nanoparticle synthesis [32].

The present work focusses on the biological synthesis of FeNPs from two plant sources: Pan (*Piper betel*) and clove (*S. aromaticum*). The crystalline structure of FeNPs was studied using the XRD analysis, and the surface topology of FeNPs was analyzed using SEM. Molecular docking analysis was performed between the synthesized iron nanoparticles and the chemotaxis inhibitory protein (CHIP) to understand if the synthesized nanoparticles interacted with the virulence protein of *S. aureus* and thus acted as potential natural inhibitors. This work aims at exploring the possibility of a natural inhibitor of *S. aureus*, thereby acting as natural medication for oral sepsis.

2 Materials and Methodology

2.1 Chemicals and Reagents

Ferric chloride was obtained from Himedia (Mumbai, India) and concentration 0.5 M and 0.001 M was prepared by using double distilled water.

2.2 Preparation of Aqueous Extract

Fresh Pan (*Piper betel*) leaves collected from local market, Bhopal, were washed thoroughly with de-ionized water. The leaves were then subjected to a drying process

for 2–3 days at 22°–25 °C. To prepare the aqueous extract of *Piper betel* leaves, the leaf powder and double distilled water were taken in the ratio of 1 g:100 ml. The resultant solution was then transferred to a water bath for 15 min. The solution obtained was then filtered followed by a centrifugation process at 6000 rpm to collect the supernatant for further experimental procedures. Clove (*S. aromaticum*) extract preparation was done using the Soxhlet apparatus [33].

2.3 Synthesis of Iron Nanoparticles (FeNPs)

The *Piper betel* extract was diluted to 1:8 ratio with double distilled water. Diluted *Piper betel* extract was then treated with 0.5 M FeCl₃ (Himedia pvt. Ltd.) in 2:1 ratio to synthesize FeNPs. Subsequently, color change of mixture was observed. Synthesis of FeNPs using clove (*S. aromaticum*) extract was carried out [33].

2.4 Characterization of Iron Nanoparticles (FeNPs)

Characterization of the bio-synthesized FeNPs was carried out using SEM and XRD. Scanning electron microscopic (SEM) analysis was performed to characterize the surface topology of the nanoparticles. X-ray diffraction (XRD) pattern was recorded at XRD system operating at 40 kV to confirm the presence of crystalline iron nanoparticles implemented.

2.5 Molecular Docking Studies

PatchDock server was employed to explore the docking analysis of the natural ligand, eugenol, α -linalool, β -caryophyllene, eugenol-FeNP, α -linalool-FeNP and β -caryophyllene-FeNP with chemotaxis inhibitory protein (CHIP). The crystallographic structure of CHIP was obtained from the protein data bank (PDB ID: 1XEE). The compound α -linalool (PubChem ID: 69016), β -caryophyllene (PubChem ID: 5281515), eugenol (PubChem ID: 3314), and iron ion was downloaded from PubChem database. Eugenol, α -linalool and β -caryophyllene were modified to add Fe ion in order to create the nanoparticle conjugate in ChemOffice [34]. Chem3D was used for the ligand energy minimization, and CHIP energy minimization was carried out using Chimera [35]. Protein file was optimized by deleting the native ligands and the water molecules. The results obtained were then analyzed using Discovery Studio.

2.6 Molecular Simulation Studies

Molecular simulations were performed on the CABS-flex 2.0 online server. The distance restraints and the simulation options were kept at default. The fluctuation data obtained were saved and the corresponding fluctuation curves were drawn using the Jupyter Notebook and Python's matplotlib package.

3 Results and Discussion

3.1 Iron Nanoparticle (FeNPs) Synthesis

Biological synthesis of FeNPs was done using the leaf extract of Pan (*Piper betel*). The plant extract of Pan was treated with 0.5 M FeCl_3 . A drastic color change was observed from light brown to deep black. This color change was an indication for the formation of FeNPs as shown in Fig. 1a–c. Biological synthesis of FeNPs was also mediated using clove (*S. aromaticum*) bud extract. FeCl_3 was added in the bud extract in the ratio of 1:1. A typical color change occurred from pale brownish to deep black. This color change indicated the formation of FeNPs as shown in Fig. 2a, b.

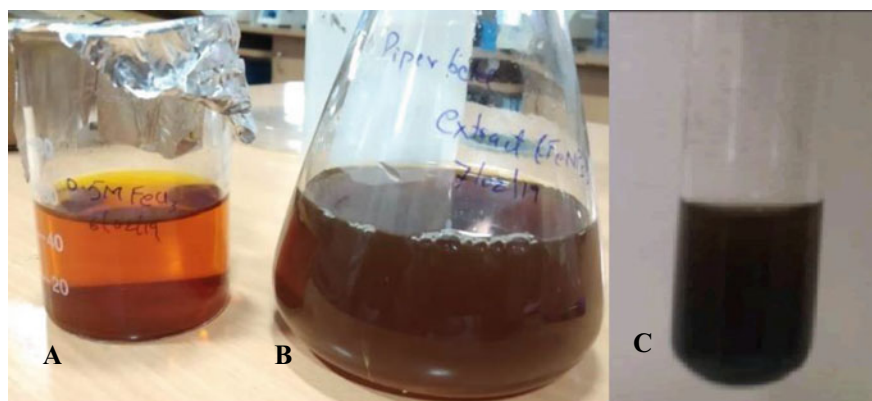


Fig. 1 Iron nanoparticles synthesized from *Piper betel* **a** Ferric chloride, **b** *Piper betel* extract, **c** Iron nanoparticles (Pb-FeNP)

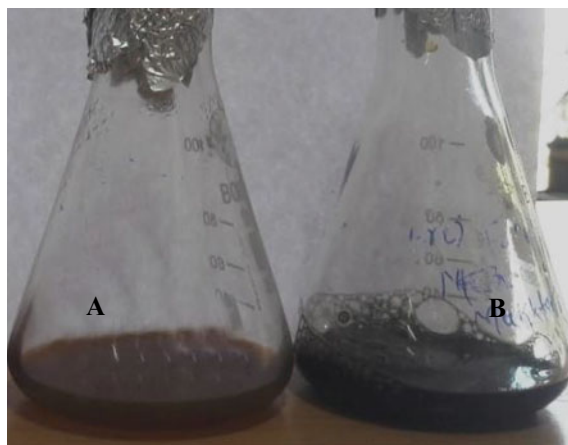


Fig. 2 Iron nanoparticles synthesized from clove (*S. aromaticum*) **a** Clove extract, **b** Iron nanoparticles (Clove-FeNP)

3.2 Characterization of Silver Nanoparticles

SEM analysis was performed for morphological examination of iron nanoparticles synthesized from *Piper betel* and clove. SEM examination showed poly-scattered Pb-FeNP nanoparticles with almost spherical shape nanoparticles in the size range of 1–100 nm (Fig. 3a). The SEM analysis of iron nanoparticles synthesized from clove showed the surface topology of the nanoparticles to be in the range of 1–100 nm (Fig. 3b). XRD analysis was performed to confirm the iron nanoparticle crystallinity in *Piper betel* sample (Fig. 4a, b). The intensity of diffraction was measured between a 2θ value of 20° – 80° . The XRD curve gave the 2θ peaks at 33.50° , 42.32° , 49.54° and 53.95° arrangements of lattice planes which correspond to (104), (124), (024) and (116) features of a hexagonal rhomb-centered structure for α - Fe_2O_3 . Results

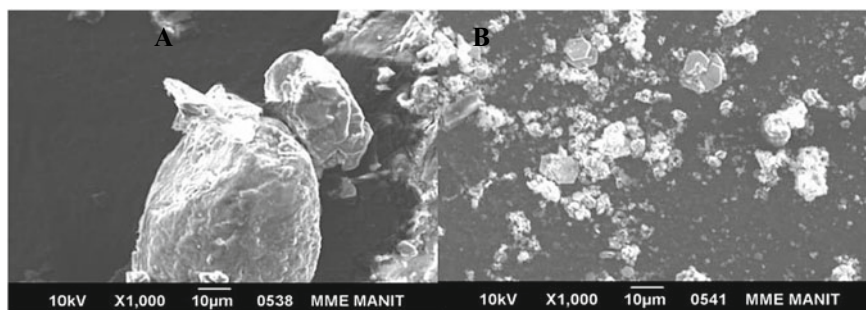


Fig. 3 SEM analysis **a** Iron nanoparticles synthesized from *Piper betel*, **b** Iron nanoparticles synthesized from clove (*S. aromaticum*)

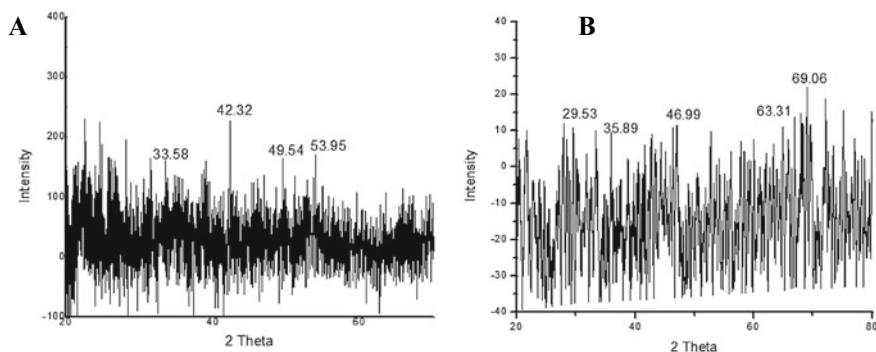


Fig. 4 X-ray diffraction analysis **a** Iron nanoparticles from *Piper betel*, **b** Iron nanoparticles from clove (*S. aromaticum*)

are as per the standard document no. 72-0469 of the Joint Committee on Powder Diffraction. The result suggested that the bio-synthesized FeNPs were crystalline in nature and were in agreement with previous findings [36].

3.3 Molecular Docking

GC-MS studies on the leaf extract of *Piper betel* reveal that eugenol is one of the main phytochemicals present along with α -linalool [37]. Also, the GC-MS studies of the bud extract of clove reveal that eugenol is one of the main phytochemicals along with β -caryophyllene [38]. Current study focusses on docking of the natural ligand, eugenol, α -linalool, β -caryophyllene and FeNP with the virulence protein, chemotaxis inhibitory protein (CHIP), of *S. aureus*. The amino acids which are involved in interaction of ligand, docking score and desolvation energy, are given in Table 1.

Table 1 Interaction between CHIP and corresponding ligands with PatchDock Score and ACE value

Protein	Ligand	PatchDock score	Atomic contact energy (ACE) (kcal/mol)
CHIP	C5aR	6652	-11.12
CHIP	Iron	952	21.41
CHIP	Eugenol	3322	-135.10
CHIP	Eugenol + Fe	3488	-83.86
CHIP	α -linalool	3016	-119.58
CHIP	α -linalool + Fe	3800	-73.29
CHIP	β -caryophyllene	3658	-164.05
CHIP	β -caryophyllene + Fe	3788	-178.68

Docking analysis of CHIP and *Piper betel*. CHIP is responsible for providing virulence to the *S. aureus* by explicitly hindering the C5a- and formylated-MLP initiated reactions of neutrophils and monocytes [10]. The docking of CHIP with its natural ligand C5aR shows hydrogen bonding interaction between the amino acids of *N*-terminal of C5aR and CHIP. Acidic aspartic acid of *N*-terminal C5aR, Asp10, Asp15 and Asp18 showed electrostatic bonding with Lys92, carbon hydrogen bonding with Asn31 and interactions with Ser32 and Pro113, respectively (Fig. 5a). The involvement of Asp10, Asp15 and Asp18 of *N*-terminal of C5aR with CHIP is in agreement with previous findings [39]. Fe showed metal acceptor bonding with Asn31 (Fig. 5b). Docking of CHIP with eugenol showed carbon hydrogen bonding with Leu34 and hydrophobic interactions with Leu41, Met93 and Pro113 with a score of 3322 and an ACE value of -131.10 kcal/mol (Fig. 5c). Docking result of α -linalool with CHIP showed carbon hydrogen bonding with Pro113 and hydrophobic interaction with Met93 and Leu41 with a score of 3,016 and ACE of -119.53 kcal/mol (Fig. 5d), whereas docking result of CHIP with eugenol + Fe showed a better result as compared with eugenol alone, with a docking score of 3488 and ACE of -83.86 kcal/mol. Moreover, the complex showed restricted interaction

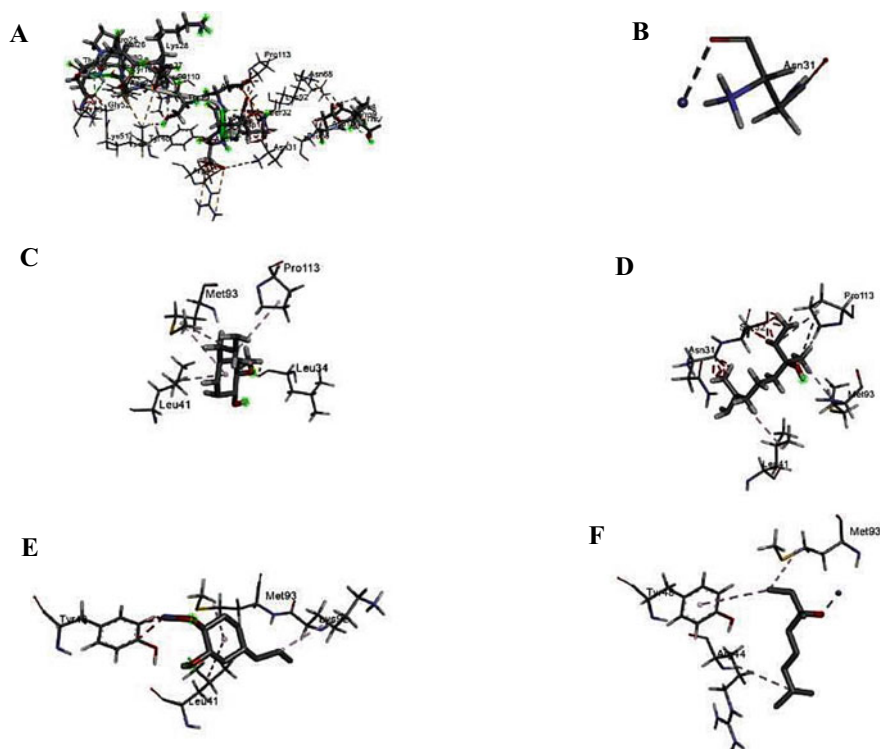


Fig. 5 MD analysis of CHIP with **a** C5aR, **b** Iron (Fe), **c** Eugenol, **d** α -linalool, **e** Eugenol + Fe, **f** α -linalool + Fe

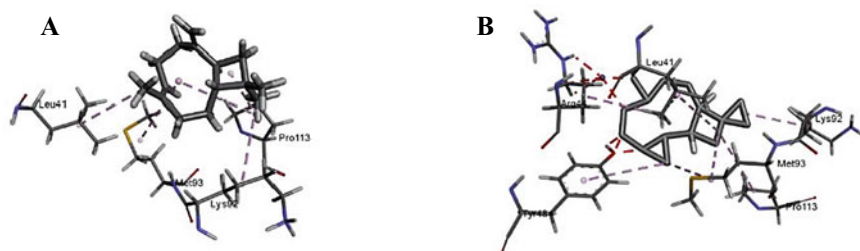


Fig. 6 Molecular docking analysis of CHIP with **a** β -caryophyllene, **b** β -caryophyllene + Fe

with Tyr48 and hydrophobic interactions with Met93, Lys92 and Lys41 (Fig. 5e). The molecular docking of α -linalool-Fe with CHIP revealed hydrophobic interaction with Met93, Arg44 and Tyr48 with a docking score of 3,800 and an ACE of -73.29 kcal/mol (Fig. 5f) which was far better as compared to α -linalool alone. Thus, this study suggests that since the active site of CHIP while binding with its natural ligand C5aR involves Asn31, Ser32, Pro35, Arg44, Tyr48, Lys92 and Pro113 as a major amino acid; the synthesized iron nanoparticles from Piper betel also interacted with the amino acids of active site of the CHIP virulence protein of *S. aureus*. This finding suggests that the synthesized iron nanoparticles from Piper betel can act as a natural inhibitor for CHIP.

Docking Analysis of CHIP and Clove (*S. aromaticum*). Molecular docking of CHIP with the leaf extract of clove and conjugated iron nanoparticles were carried out. Eugenol along with β -caryophyllene are found to be the major phyto-chemicals in the extract of clove bud. Docking of CHIP with β -caryophyllene showed hydrophobic interactions with Leu41, Met93, Lys92 and Pro113 with a score of 3658 and an ACE value of -164.05 kcal/mol (Fig. 6a), whereas docking result of CHIP with β -caryophyllene + Fe showed better results as compared with β -caryophyllene alone with a docking score of 3,788 and ACE of -178.68 kcal/mol. Moreover, the complex showed hydrophobic interactions with Arg44, Met93, Lys92, Leu41 and Pro113 (Fig. 6b). This study, therefore, suggests that since the active site of CHIP while binding with its natural ligand C5aR involves Arg44, Tyr48, Lys92 and Pro113 as a major amino acid, the synthesized iron nanoparticles from clove (*S. aromaticum*) also interacted with the amino acids of active site of the CHIP virulence protein of *S. aureus*. This suggests that the synthesized iron nanoparticles from clove can act as a natural inhibitor for CHIP as well.

3.4 Molecular Simulation Studies

Molecular simulation studies provided a comparative analysis between the root mean square fluctuations (RMSF) values of the individual amino acid residues of the phytochemicals and their nanoparticle conjugates. From the graph (Fig. 7), it can be

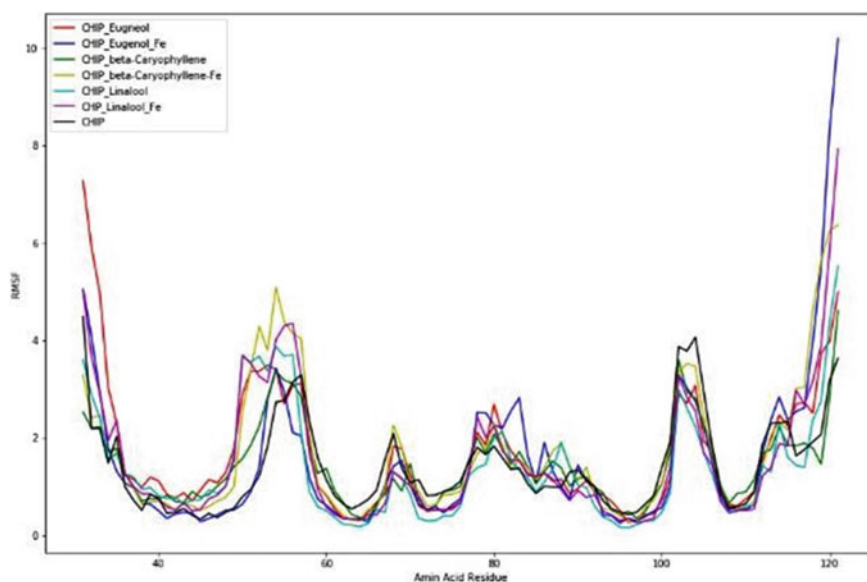


Fig. 7 Molecular simulation curve of CHIP with phytochemicals and nanoparticles

observed that the RMSF curve of CHIP- β -caryophyllene-Fe and CHIP- α -linalool-Fe shows close relation with that of RMSF curve of CHIP. On exploring the fluctuation plot, it can be seen that the Pro111 residue in CHIP- α -linalool-Fe has a lower RMSF value than the Pro113 residue of CHIP and CHIP- β -caryophyllene-Fe. This result is also supported by the high PatchDock score of CHIP- α -linalool-Fe. Thus, it can be suggested that the iron nanoparticle conjugate of α -linalool shows better interaction and may have the potential to act as a natural inhibitor against the *S. aureus* virulence.

4 Conclusion

FeNP's antibacterial properties have gained so much attention in the recent past. The profundity of the iron nanoparticles and their wide scale application has opened up an unexplored area to see whether these nanoparticles can be exploited for their potential use against multi-drug resistance bacteria and viruses as well. *S. aureus* is a clinically and epidemiologically important bacteria. Therefore, it is of utmost importance that we target the bacteria and restrict its activity. One of the ways to do so is by targeting its virulence system. This study focused on treating the virulence system of the bacteria with biologically synthesized iron nanoparticles (FeNPs) from *Piper betel* and clove. *S. aureus* infects the host via its virulence chemotaxis inhibitory protein (CHIP). Molecular docking was performed between CHIP (major virulence proteins of *S. aureus*) with synthesized nanoparticles. Eugenol, α -linalool

were found to be the major phytochemicals in the *Piper betel* leaf extract and Eugenol, β -caryophyllene were identified as the important phytochemicals in the bud extract of clove. Chem3D was used to prepare iron nanoparticle complex of Eugenol, α -linalool and β -caryophyllene and target the virulence protein CHIP. The docking studies were performed with CHIP. The interaction between the synthesized iron nanoparticles and the active amino acids of the virulence protein. Molecular simulation studies also support the results obtained, indicating that the iron nanoparticle conjugate of α -linalool shows better interaction with the virulence protein than the other phytochemical nanoparticle conjugate. This study may open up a new front for targeting the virulence proteins of *S. aureus*. Further experimental work is required to confirm the computational results and take the investigations forward.

5 Conflict Declaration

No potential conflicts.

Acknowledgements The authors express their gratitude towards Maulana Azad National Institute of Technology for the support and facilities extended.

References

1. Metrics GH (2019) Global, regional, and national incidence, prevalence, and years lived with disability for 354 diseases and injuries for 195 countries and territories, 1990–2017: a systematic analysis for the global burden of disease study 2017, 1990–2017. [https://doi.org/10.1016/S0140-6736\(18\)32279-7](https://doi.org/10.1016/S0140-6736(18)32279-7)
2. Fang M, Chen J, Xu X, Yang P, Hildebrand HF (2006) Antibacterial activities of inorganic agents on six bacteria associated with oral infections by two susceptibility tests. *Int J Antimicrob Agents* 27:513–517. <https://doi.org/10.1016/j.ijantimicag.2006.01.008>
3. Bagg J, Sweeney MP, Wood KH, Wiggins A, Sweeney MP, Wood KH, Role AWP (2009) Microbial ecology in health and disease possible role of *Staphylococcus aureus* in severe oral Mucositis among elderly dehydrated patients. 2235. <https://doi.org/10.3109/08910609509141382>
4. Oza N, Doshi JJ (2017) Angular cheilitis: a clinical and microbial study, pp 661–665. <https://doi.org/10.4103/ijdr.IJDR>
5. Olson ME, Horswill AR (2013) Previews *Staphylococcus aureus* osteomyelitis: bad to the bone. *CHOM* 13(6):629–631. <https://doi.org/10.1016/j.chom.2013.05.015>
6. Fowler VG, Olsen MK, Corey GR, Cheng AC, Dudley T, Oddone EZ (2015) Clinical identifiers of complicated, p 163
7. Wamel WJB, Van Rooijackers SHM, Ruyken M, Van Kessel KPM, Van Strijp JAG (2006) The innate immune modulators staphylococcal complement inhibitor and Chemotaxis inhibitory protein of *Staphylococcus aureus* are located on β -hemolysin-converting bacteriophages 188(4):1310–1315. <https://doi.org/10.1128/JB.188.4.1310>
8. Rooijackers SHM, Ruyken M, Roos A, Daha MR, Presanis JS, Sim RB et al (2005). Immune evasion by a staphylococcal complement inhibitor that acts on C3 convertases 6(9):920–927. <https://doi.org/10.1038/mi1235>

9. Gaikwad S, Ingle A, Gade A, Rai M, Falanga A, Inconrato N, Russo L, Galdiero S, Galdiero M (2013) Antiviral activity of mycosynthesized silver nanoparticles against herpes simplex virus and human parainfluenza virus type 3. *Int J Nanomed* 8:4303–4314
10. De Haas CJC, Veldkamp KE, Peschel A, Weerkamp F, Van Wamel WJB, Heezius ECJM et al (2004) Chemotaxis inhibitory protein of *Staphylococcus aureus*, a bacterial antiinflammatory agent 199(5). <https://doi.org/10.1084/jem.20031636>
11. Postma B, Kleibeuker W, Poppelier MJG, Boonstra M, Van Kessel KPM, Van Strijp JAG, De Haas CJC (2020) Residues 10–18 within the C5a Receptor N terminus compose a binding domain for chemotaxis inhibitory protein of *Staphylococcus aureus* 280(3):2020–2027. <https://doi.org/10.1074/jbc.M412230200>
12. Postma B, Poppelier MJ, Van Galen JC, Prossnitz ER, Van Strijp JAG, De Haas CJC, Van Kessel KPM (2004) Chemotaxis inhibitory protein of *Staphylococcus aureus* binds specifically to the C5a and formylated peptide receptor
13. Jackson MS, Bagg J, Gupta MN, Sturrock RD (1999) Oral carriage of staphylococci in patients with rheumatoid arthritis 54(mean 32):572–575
14. Gade A, Gaikwad S, Tiwari V, Yadav A, Ingle A, Rai M (2010) Biofabrication of silver nanoparticles by *Opuntia ficusindica*: In vitro antibacterial activity and study of the mechanism involved in the synthesis 370–375
15. Konishi Y, Ohno K, Saitoh N, Nomura T (2007) Bioreductive deposition of platinum nanoparticles on the bacterium *Shewanella algae* 128:648–653. <https://doi.org/10.1016/j.jbiotec.2006.11.014>
16. Willner BI, Baron R (2006) Growing metal nanoparticles by enzymes**, 1109–1120. <https://doi.org/10.1002/adma.200501865>
17. Herberts CA, Hagens WI, Oomen AG, Heugens EHW, Roszek B, Bisschops J et al (2009) Nano-silver a review of available data and knowledge gaps in human and environmental risk assessment 3(June). <https://doi.org/10.1080/17435390902725914>
18. Chari N, Felix L, Davoodbasha M, Sulaiman A (2017) Biocatalysis and agricultural biotechnology In vitro and in vivo antibiofilm effect of copper nanoparticles against aquaculture pathogens, 10(November 2016), pp 336–341. <https://doi.org/10.1016/j.bcab.2017.04.013>
19. Taylor P, Lewisoscar F, Mubarakali D (2015) Biofouling: the journal of bioadhesion and biofilm one pot synthesis and anti-biofilm potential of copper nanoparticles (CuNPs) against clinical strains of *Pseudomonas aeruginosa* (August). <https://doi.org/10.1080/08927014.2015.1048686>
20. Shafreen RB (2017) Inhibitory effect of biosynthesized silver nanoparticles from extract of *Nitzschia palea* against curli-mediated biofilm of *Escherichia coli*. <https://doi.org/10.1007/s12010-017-2503-7>
21. Woo H, Park J, Lee S, Lee S (2014) Chemosphere Effects of washing solution and drying condition on reactivity of nano-scale zero valent irons (nZVIs) synthesized by borohydride reduction. *Chemosphere* 97:146–152. <https://doi.org/10.1016/j.chemosphere.2013.11.010>
22. Karimi EZ, Zebarjad SM, Bataev IA, Bannov AG (2014) A novel method for fabrication of Fe catalyst used for the synthesis of carbon nanotubes 37(5):1031–1038
23. Huang G, Wang M, Hu Y, Lv S, Li C (2017) Debromination reactivity of cellulose-tetrabromodiphenyl ether 1–17
24. Stankic S, Suman S, Haque F, Vidic J (2016) Pure and multi metal oxide nanoparticles: synthesis, antibacterial and cytotoxic properties. *J Nanobiotechnol* 14:1–20. <https://doi.org/10.1186/s12951-016-0225-6>
25. Pattanayak M, Mohapatra D, Nayak PL, Mahaviyalaya M (2013) Green synthesis and characterization of zero valent iron nanoparticles from the leaf extract of *Syzygium aromaticum* (clove) 18(5):623–626. <https://doi.org/10.5829/idosi.mejsr.2013.18.5.11729>
26. Makarov VV, Makarova SS, Love AJ, Sinitsyna OV, Dudnik AO, Yaminsky IV et al (2014) Biosynthesis of stable iron oxide nanoparticles in aqueous extracts of *Hordeum vulgare* and *Rumex acetosa* Plants
27. Chandran M, Yuvaraj D, Christudhas L, Kv R (2016) Bio-synthesis of iron nano-particles using the Brown Seaweed, *Dictyota dicotoma*. 12

28. Onal ES, Yatkin T, Aslanov T, Erg M, Ozer A (2019) Biosynthesis and characterization of iron nanoparticles for effective adsorption of Cr (VI). 2019(Vi)
29. Shigwenya E, Patrick M, Kareru G, Gachui E, Augustine M, Nyabola O et al (2019) Biosynthesis of iron nanoparticles using *Ageratum conyzoides* extracts, their antimicrobial and photocatalytic activity. SN Applied Sciences, (January). <https://doi.org/10.1007/s42452-019-0511-7>
30. Phan CM, Nguyen HM (2017). Role of capping agent in wet synthesis of nanoparticles. <https://doi.org/10.1021/acs.jpca.7b02186>
31. Sebastian A, Nangia A, Prasad MNV (2017) SC. J Clean Prod. <https://doi.org/10.1016/j.jclepro.2017.10.343>
32. Herlekar M, Barve S, Kumar R (2014) Plant-mediated green synthesis of iron nanoparticles
33. Kasthuri G, Reddy AN, Roopa PM, Zamare DK (2017) Application of green synthesized iron nanoparticles for enhanced antimicrobial activity of selected traditional and commonly exploited drug amoxicillin against *S treptococcus mutans*, 14(September), 1135–1141
34. ChemOffice, 7.0.1. 2002. CambridgeSoft, Corporation, Cambridge, MA
35. UCSF Chimera (2004) A visualization system for exploratory research and analysis. Pettersen EF, Goddard TD, Huang CC, Couch GS, Greenblatt DM, Meng EC, Ferrin TE, J Comput Chem 25(13):1605–1612
36. Indian Journal of Science Green Synthesis and Characterization of Iron Oxide Nanoparticles from the Leaf Extract of Piper betle (2018) (August)
37. Madhumita M, Guha P, Nag A (2019) Industrial crops & products extraction of betel leaves (Piper betle L.) essential oil and its bio-actives identification: process optimization, GC-MS analysis and anti-microbial activity. Ind Crops Prod 138(July):111578. <https://doi.org/10.1016/j.indcrop.2019.111578>
38. Srivastava AK, Srivastava SK, Syamsundar KV (2005) Bud and leaf essential oil composition of *Syzygium aromaticum* from India and Madagascar 1(May 2004):51–53. <https://doi.org/10.1002/ffj.1364>
39. Liu Z, Yang Y, Jiang L, Xu Y, Wang A, Du G, Gao J (2011) Tyrosine sulfation in N-terminal domain of human C5a receptor is necessary for binding of chemotaxis inhibitory protein of *Staphylococcus aureus*. Nat Publ Group 32:1038–1044. <https://doi.org/10.1038/aps.2011.53>

Fabrication of Composite Phase Change Material: A Critical Review



P. Das, R. Kundu, S. P. Kar, and R. K. Sarangi

1 Introduction

In the present situation, due to rapid growth in population, energy shortage has become very common. Use of electricity consumption is increasing every year in India. Energy requirement is increasing in our day to day life with requirement for improvement in living standards of the current population. To solve the demand and supply issue, it has become necessary to find a suitable alternative. Oil is always an important source of energy. However, the major issues like depletion of fossil fuel and huge processing cost has become a limitation for its use. Therefore, in the last few years, inclination toward renewable energy sources has increased. Solar PV has been one of such option for generation of electricity and for thermal requirements. Here, it is clear that the amount of energy production by solar PV is less as compared to the other power sources. Energy requirements in the form of heat or electricity requires modern technologies to improve their efficiency and reduce the energy losses. Therefore, several researches are going on in finding an alternative solution for energy storage. Thermal energy storage is one of the most useful method to store energy and it plays a vital role in efficient utilization at various industrial systems. Several devices and components of TES has been integrated at different networks of and used for dynamic optimization. Challenges are faced in such as poor thermal conductivity, life of the thermal storage material, range of operation of the material, storing density, mechanical strength and cost effectiveness [1]. The use of phase change material can be a solution in direction to solve the drawback of thermal energy storage materials. Phase-changing material (PCM) has drawn serious attention by enhancing the ability of thermal storage devices with reduced variation in temperature from energy storage to release, good density for storage and reutilizing properties. Addition of composite phase change materials has been effective in

P. Das · R. Kundu · S. P. Kar (✉) · R. K. Sarangi
Kalinga Institute of Industrial Technology, Deemed to be University, Bhubaneswar, Odisha, India

solving several challenges such as enhancing thermal conductivity, thermal stability, chemical stability and better surface finish of the materials. For thermal conductivity enhancement, composite phase change material (CPCM) generally has a skeleton material and a thermal conductivity enhancing material (TCEM) [2]. Selections of materials, manufacturing processes, chemical and physical properties are to be taken into account while selecting a phase change material.

2 Composite Phase Change Materials (CPCMs)

2.1 Selection of the Material

Material selection is an important aspect of CPCMs formation for a specific purpose and application. The selected materials should meet all the requirements with a competitive and minimized cost. When the material is being chosen for an application such as thermal energy storage, then it must have high thermal conductivity, good melting point and high latent heat. Energy storage depends upon its charging and discharging period and should be able to transfer heat at desirable rate. Apart from these, some of the other factors to be taken into consideration are the stability of the material, durability, environmental impacts, chemical hazards, etc.

2.2 Fabrication

Some of the methods in which composite materials can be fabricated based on their purpose of utilization. Some of the key processes followed are direct impregnation, vacuum impregnation, melting impregnation, magnetic stirring, etc. For preparing composite phase-changing material with metal foam, impregnation method can be used to insert metal foam into composite phase-changing material. Direct impregnation process may face issues in immersing metal foam into composite phase-changing material. Due to lack of vacuum, air gets trapped in the pores of the phase-changing material which causes difficulty in impregnating the metal form. These lead to low quality of PCM and also poor heat transfer. Zuo et al. [3] fabricated paraffin and carbon-coated nano scroll by vacuum impregnating method. It was found from the analysis that at 600 °C calcination of the composite phase change material achieved an optimum loading of 60.63%, 63.14% and 59.99% at 600 °C, 700 °C and 800 °C, respectively. The thermal conductivity was found to be 0.51 W/m K, 0.50 W/m K and 0.52 W/m K at 600 °C, 700 °C and 800 °C, respectively. Form-stable phase change material (FSPCM) was found to be chemically stable and good reliability. Li et al. [4] experimentally prepared composite PCM using lauric acid and stearic acid as PCM. Diatomic as supporting material for enhancing the loading capacity and expanded graphite was used in thermal conductivity. It was found from the study that the loading

capacity of raw diatomite and microwave acid-treated diatomite were 70.36% and 107.04%, respectively. Higher crystallization was obtained due to better surface and pore structure. Thermal conductivity was improved by addition of expanded graphite and the value of lauric acid–stearic acid–diatomic–expanded graphite got increased by 3.2 times that of lauric acid–stearic acid–diatomic. Wang et al. [5] prepared a composite pcm using Cetyl palmitate by using binary 1-hexadecanol (HD) and palmitic acid as starting material without taking any catalyst. After the preparation of Cetyl palmitate, it is melted by infiltration with nickel foam different pore sizes (70, 90 and 110PPI) in order to increase the thermal conductivity. The latent heat of fusion and melting temperature was found to be 180.9 J/g and 52.3 °C, respectively. As compared to pure Cetyl palmitate the thermal conductivity was found to be increased by 1.88, 2.02 and 4.86 times for pore sizes of 70, 90 and 110 PPI, respectively. Mhiri et al. [6] prepared composite PCM using paraffin, graphite and carbon foam in vacuum impregnation process. Graphite was used as a thermal conductivity enhancer. It was found from the experimentation that the melting was enhanced by 21% as compared to pure paraffin. Melting process was increased by 31% in case of carbon foam-paraffin. Paneliya et al. [7] prepared composite phase change material experimentally by considering paraffin as phase change material and silica shell as the supporting material. It was found from the study that silica shell reduces the flammability and has a better thermal stability. At an encapsulation ratio of 79.89%, the phase change material melts completely at 54.2 °C with a latent heat of 151.12 J/g, and it solidifies at 52.09 °C with a latent heat of 100.16 J/g. The composite phase-changing material showed good capability to store latent heat and improved thermal stability. Zou et al. [8] considered polyethylene glycol as phase-changing material and *N*-methyl acrylamide as supporting material by emulsion polymerization process. It was found from the experimentation that the composite phase change material melted at 26.24 °C having a latent heat of fusion of 106.5 J/g, and it solidifies at a temperature of 32.56 °C having latent heat of solidification of 104.9 J/g. Latent heat changed by 5% after thermal cycling which is a small amount. Shi and Li [9] fabricated a composite phase-changing material using polyethylene glycol and attapulgite as supporting matrix for improving the thermal properties. There was an increase in latent heat of polyethylene glycol-modified attapulgite form-stable composite phase change material by 86.7% as compared to polyethylene glycol raw attapulgite form-stable composite phase change material. Wang et al. [10] experimentally investigated capric acid as phase-changing material and disodium hydrogen phosphate dodecahydrate as supporting matrix for fabricating composite phase-changing material by sol–gel method. Theoretical results showed that the phase change temperature of the fabricated composite was found to be 33.8 °C, melting enthalpy of phase change was 168.8 J/g, and the degree of super cooling was 0.9 °C and thermal conductivity was 0.468 W/m K. Experimental results showed that composite phase-changing material had poor super cooling degree of 95.6% compared to the pure form of disodium hydrogen phosphate dodecahydrate. Thermal conductivity was found to be improved by 1.96% as compared to the pure form. Tan and Xie [11] fabricated a composite phase-changing material capric–palmitic acid eutectic mixture and silica xerogel exfoliated graphite nanoplatelets by solution gel method for enhancing

thermal conductivity. It was found from the result that CA-PA and silica form-stable composite exhibited good form stability characteristics and achieved 75 wt%. Capric-palmitic-silica-xGnP xerogel form stable phase-changing materials had good stability at 85 wt% during the addition of 6 wt% graphite nanoplatelets. The melting enthalpy was found to be 123.1 J/g with more thermal stability and having thermal conductivity 0.70 W/m K that was 218% higher than normal capric-palmitic. Chen et al. [12] investigated experimentally polyethylene glycol and cellulose nanofiber sponge coated with polypyrrole to fabricate composite phase-changing material by impregnation. It was found from the study that the efficiency of electric to heat conversion was up to 85.1%. The composite phase-changing material has high loading of 94 wt% with a phase changing enthalpy of 169.7 J/g. Higher speed of heat releasing and storing was found for thermal conductivity which symbolizes the material is suitable for latent heat storage. Jin et al. [13] prepared composite pcm sodium acetate trihydrate-potassium urea and chloride-urea expanded graphite by melt blending method. From the result, it was found that the temperature and enthalpy of composite phase-changing material was 47.5 °C and 200.3 kJ/kg, respectively. Thermal conductivity of the composite was 1.48 W/m K. The phase-change time of the SAT-KCl-urea/EG CPCM was reduced by approximately 30% for sodium acetate trihydrate-potassium urea and chloride-urea and expanded graphite (SAT-KCl-urea/EG) CPCM as compared to that of the SAT-KCl-urea composite salt. Phase-change temperature of SAT-KCl-urea/EG CPCM was found to be stable at 45.9 °C and very little degree of supercooling of 1.56 °C after 100 melting and solidification cycling time. Chriaa et al. [14] investigated experimentally a composite phase-changing material using hexadecane as phase-changing material and the low-density polyethylene LDPE-tri-block copolymer-styrene ethyleneco-butylene styrene (SEBS) as supporting material. Expanded graphite was added as thermal conductivity enhancer. The composite was fabricated by sonication method. It was found from the result that composite with 10 wt% expanded graphite and 75 wt% hexadecane was able to successfully prevent leakage. By using 75 wt% of hexadecane, an improvement in thermal conductivity intensification was found and by adding 5-15 wt% of expanded graphite, thermal conductivity got increased from 38 to 277%. With 20 wt% of expanded graphite and 4 wt% of hexadecane, optimum amount of thermal conductivity intensification was found. Yu et al. [15] prepared a composite using eutectic nitrate (NaNO₃)-KNO₃ as phase-changing material, nano-SiO₂ and expanded graphite as additives by mechanical dispersion method. Expanded graphite had been used in various quantities of (5, 10, 15 and 20 wt%). It was found from the results that by addition of nano-SiO₂ and expanded graphite the specific heat was 3.92 J/g K at 15 wt% of expanded graphite and 1 wt% of SiO₂ nanoparticles. At 15 wt% of expanded graphite the composite had highest thermal conductivity when 1 wt% of nano-SiO₂ had been considered which is equal to 8.47 W/m K. There is an increase in specific heat from 3.77 to 3.82 J/g K after 100 heating-cooling cycles. The composite at 400 °C had better thermal stability. Dongmei Han et al. [16] experimentally investigated a composite phase-changing material using chloride salts (MgCl₂ KCl:NaCl) as base salt and Al₂O₃, CuO and ZnO nanoparticles by solution evaporation method. It was found from the result that there was a decrease by 2.4-7.6% in phase change latent heat,

and there was an increase in sensible heat by 3.9–13.7%. There was an improvement in thermal conductivity and diffusivity by 48% and 61.97%, respectively, by using AL_2O_2 . The doping of AL_2O_2 results in higher thermal stability at 820 °C. Xia et al. [17] experimentally investigated a composite phase-changing material using polyethylene glycol and 4,4'-diphenylmethan diisocyanate as the cross-linking agent and graphene oxide by two-step polymerization process. From the study, it was found that it had good thermal stability, and there was little change in latent heat and phase change temperature. The composite phase-changing material maintains temperature during the heating process at 50–57 °C for 410 s. Because of the presence of graphene oxide, the thermal conductivity increases of the composite. The composite had high phase change latent heat. Jia et al. [18] fabricated polyethylene glycol and boron nitride-chitosan by vacuum impregnation method. It was found from the result that at 27.01 wt% of Boron, the composite phase-changing material had higher thermal conductivity 2.78 W/m K which was 804% higher than pure polyethylene glycol. Suitable thermal storage density of 136 J/g was found with good thermal stability and ability to be reused was found after 50 thermal cycles. Li et al. [19] fabricated stearic acid and graphite sheet for preparing composite phase-changing material by centrifuging method. It was found from the result that ultrathin graphite sheets (UGS-5000) having centrifugation at 5000 rpm had superior loading capacity of 171.5% and crystallization ratio (F_c) of 94.02% as compared ultrathin graphite sheets (UGS-3500) having centrifugation at 3500 rpm. UGS 5000 had good enthalpy values for solidification and melting was 113.7 J/g and 112.9/g, respectively. It displayed excellent thermal stability and had thermal conductivity 10.08 times higher than stearic acid. Mengdi Yuan et al. [20] experimentally investigated the composite pcm using erythritol as phase-changing material and expanded graphite (EG) as the supporting matrix by impregnation, compression and sintering for mid-temperature thermal energy storage. In the study, five samples having different expanded graphite content of 5, 8, 10, 12 and 15 wt% had been analyzed. It was found from the results that the freezing temperature and thermal conductivity was enhanced by addition of expanded graphite as well as there was declination in latent heat, melting temperature and degree of supercooling. With 10wt% of expanded graphite, higher thermal conductivity of 12.51 W/mK than pure erythritol by 17.38 times and 212.5 J/g of latent heat was recorded. 10wt% of expanded graphite had reduced charging time of 59.4% than pure erythritol. Degree of supercooling can be reduced by using 10 wt% of expanded graphite from 39.5% to 19.5% and remains stable. Gu et al. [21] prepared a composite phase-changing material using Palmitic acid and graphite powder by facile direct impregnation method for improving overall thermal conductivity. It was found from the result that the melting and solidifying latent heat was 52.5 J/g and 51.5 J/g, respectively, solidifying and melting temperature was 58.4 °C and 64.3 °C, respectively. Using 5 wt% of graphite powder resulted in increase in thermal conductivity by 86%. Sari et al. [22] fabricated a composite pcm using mystiric acid and silica fume by direct impregnation method. It was found from the result that the prepared composite phase-changing material had excellent heat capabilities ranging from 87 to 91 J/g. The composite was found to be thermally and chemically stable up to temperature of 175 °C. From the study, it was noted that 1 wt% carbon nano

tube doped sample had improved thermal conductivity property with good cooling and heating time. Zhang et al. [23] experimentally investigated the preparation of composite pcm using lauric–stearic acid Eutectic mixture and carbonized biomass waste corn cob by vacuum impregnation method for building energy storage. It was found from the result that the composite was structurally and chemically stable. The thermal conductivity of prepared composite was 0.441 W/m K was found to be 1.93 times higher than lauric–stearic acid by 0.228 W/m K. Zhang et al. [24] fabricated a composite PCM using lauric–myristic–stearic acid eutectic mixture and TiO_2 -TiC-C loaded expanded vermiculite by vacuum impregnation. It was found from the results that the thermal conductivity of lauric–myristic–stearic acid eutectic mixture expanded vermiculite additional acid treated was 0.676 W/m K and lauric–myristic–stearic acid eutectic mixture expanded vermiculite without additional acid treatment lauric–myristic–stearic acid eutectic mixture expanded vermiculite (0.694 W/m K) that was 51.2% and 55.3% higher than that of lauric–myristic–stearic acid eutectic mixture expanded vermiculite (0.447 W/m K). From the study, the melting latent heat found lauric–myristic–stearic acid eutectic mixture expanded vermiculite was 115 J/g and lauric–myristic–stearic acid eutectic mixture expanded vermiculite was 105.8 J/g that are 45.2% and 32.7% higher than lauric–myristic–stearic acid eutectic mixture expanded vermiculite which had 79.7 J/g. Jianguyun Zhang et al. [25] experimentally investigated composite phase-changing material prepared by using paraffin as phase-changing material and expanded graphite, epoxy resin, aluminum nitride additives by magnetic stirring to improve the battery heat dissipation. Different percentage of aluminum nitride as 0 wt%, 5 wt%, 10 wt%, 15 wt%, 20 wt% and 25 wt% were used in composite and had been analyzed. It was found from the experiment that the prepared composite PCM that had aluminum nitride less than 25% had better thermal conductivity, volume resistivity and mechanical strength. Composite using 20 wt% aluminum nitride had highest electric insulating, thermal and mechanical property. There was an improvement in thermal conductivity from 1.48 W/m K to 4.331 W/m K at 50 °C. From the study, it was found that an increase in bending, impact and tensile strength by 67.6%, 38.1% and 164.2%. The volume resistivity also improved by $26.62 \times 10^{11} \Omega \text{ cm}$ which was 14.94% higher than paraffin and expanded graphite composite. The battery module with composite phase-changing material had higher heat dissipation and maximum temperature was reduced by 19.4%. Cheng et al. [26] fabricated a composite PCM using form-stable tetradecanol as PCM and expanded perlite as supporting material and addition of copper powder and carbon fiber as thermal conductivity enhancer by vacuum impregnation. The composite was prepared in two parts: (i) tetradecanol copper powder expanded perlite and (ii) tetradecanol carbon fiber expanded perlite by weighing copper powder, carbon fiber expanded perlite and tetradecanol in a ratio from 0 to 4%. It was found from the results that tetradecanol copper powder expanded perlite melted at 35.5 °C having phase change enthalpy of 156.7 kJ/kg and had an enthalpy of 156.1 kJ/kg for freezing at 36.1 °C. Thermal conductivity was improved from 0.481 W/m K to 1.463 W/m K. Chen et al. [27] experimentally investigated composite pcm prepared using paraffin as phase-changing material and CuO nanopowders by sonicating with an ultrasonic cell crusher for solar thermal storage and thermoelectric application.

Maximum of 2.3% of pure paraffin was added for preparing the composite. It was found from the result that addition of CuO powder could efficiently receive solar energy and efficiently convert it to thermal energy. In the study, it was found that an improvement in solar thermoelectricity by 0.1% which was 1.8 times that of pure paraffin. Wu et al. [28] fabricated composite phase change material taking paraffin as PCM and carbon nanotubes as thermal conductivity enhancer. With increase in mass fraction of carbon nano tubes melting and solidification, latent heat decreases gradually. Phase change latent heat of melting and solidification were lower than pure paraffin by 8.9% and 9.3%. There was an increase in thermal conductivity of solid and liquid state of phase change material by adding 3% of carbon nano tube were higher than pure paraffin by 30.3% and 28.5%, respectively. Li et al. [29] fabricated a composite phase change material using stearic acid and expanded graphite by melting impregnation. Expanded graphite had been used in different mass fractions of 2 wt%, 6 wt% and 10 wt%. It was found from the result that at 6 wt% of expanded graphite the thermal conductivity reached to 2.5 W/m K that was 9.6 times more than pure stearic acid having latent heat of melting of 163.5 J/g. The melting time at 6 wt% of EG was 2900 s that was 63.3% quicker than pure stearic acid and had the shortest heat release time of 876 s. Ren et al. [30] investigated experimentally the preparation of composite phase change material using binary eutectic salt $\text{Ca}(\text{NO}_3)_2\text{-NaNO}_3$ and expanded graphite as supporting material and thermal conductivity enhancer by impregnation and sintering. It was found from the result that 7 wt% of EG the composite had good shape stability without any leakage or crack, and the thermal conductivity was increased from 0.681 to 5.66 W/m K. There was negligible change in melting temperature after 500 cycles for 7 wt% of EG. Sciacovelli et al. [31] fabricated a composite phase change material taking high-density polyethylene (HDPE) and graphite using single-screw continuous-extrusion device for thermal energy storage. By addition of composite graphite, a visible increase in thermal diffusivity can be seen up to 70% and by using 10% composite graphite, latent heat decreases by 10%. Using 5% composite graphite results in low extrusion speed of 5 rpm, and using 10% composite graphite results in low extrusion speed of 20 rpm. Zhao et al. [32] investigated experimentally a composite phase change material having modified sodium acetate trihydrate (SAT) aluminum alloy and copper foam by vacuum impregnation method for thermal energy storage. It was found from the result that modified SAT additives of 2 wt% carboxyl methyl cellulose and 2wt% disodium hydrogen phosphate dodecahydrate (DHPD) had best performance and degree of supercooling was 4.6 °C. Modified SAT had phase change enthalpy of 253.6 J/g. Wang et al. [33] fabricated composite phase change material using erythritol as phase-changing material and alumina by ultraviolet-assisted hydrolysis method. The fabrication process is carried in two steps: first, hydrolysis and secondly, directional adsorption and condensation. It was found from the result that at 60 °C, the degree of supercooling was decreased by 18.9 °C and with the rise in heat release performance from 44.5% to 96.7% by adding impurity and encapsulation. The thermal conductivity of the composite was 0.84 W/m K at 25 °C and increased by 29.2% than pure erythritol. From the study, it was found that there was negligible variation in chemical structure, thermal behavior and thermal durability.

Xiang composite pcm using myristol alcohol (MA), copper foam and nickel foam by vacuum melting infiltration method. It was found from the result that thermal conductivity of MA and nickel foam composite of 40 PPI and MA and copper foam composite of 40 PPI had increased by 1.80 and 7.51 times, respectively. The thermal conductivity was higher at smaller size of pore for both nickel and copper foam. Karthik et al. [34] experimentally investigated composite pcm using paraffin wax and graphite foam by impregnation method. The sample prepared was maintained at 75 °C for 1 month. It was found from the result that there was no chemical reaction between them paraffin wax and graphite foam. It had a higher compressive strength by five times more than graphite foam. There was reduction in charging and discharging time and the thermal conductivity paraffin wax and graphite foam was better as compared to pure paraffin wax.

3 Conclusions

For using TES technology, several challenges are faced regarding its material selection, fabrication process and its analysis. Emphasis must be given to find the optimized techniques to meet a solution that can reduce the previously existing drawbacks. In order to choose a composite phase-changing material, selection of material is a vital factor for finding the right fit according to the characterization and purpose. The results showed that the most common used phase-changing material is paraffin; however, due to its low conductivity, it has to be paired with a supporting material for improving its performance. Different techniques of fabrication have been taken into account, and it was found that vacuum impregnation technique was the most cost-effective method to prepare a CPCM. Analysis has been the core pillar to support the theory.

References

1. Zhao B, Li C et al (2016) Heat transfer performance of thermal energy storage components containing composite phase change materials. *IET Renew Power Gener* 10(10):1515–1522
2. Karaman S, Ali K et al (2011) Polyethylene glycol (PEG)/diatomite composite as a novel form-stable phase change material for thermal energy storage. *Solar Energy Mater Solar Cells* 95(7):1647–1653
3. Zuo X, Li J et al (2020) Emerging paraffin/carbon-coated nanoscroll composite phase change material for thermal energy storage. *Renew Energy* 152:579–589
4. Li, Chuanchang, Wang M., et. al. “Enhanced properties of diatomite-based composite phase change materials for thermal energy storage.” *Renewable Energy* 147, 265–274 (2020).
5. Wang C, Wang T et al (2020) Facile synthesis and thermal performance of cetyl palmitate/nickel foam composite phase change materials for thermal energy storage. *J Energy Storage* 28:101179
6. Mhiri H, Jemni A, Sammouda H (2020) Numerical and experimental investigations of melting process of composite material (nanoPCM/carbon foam) used for thermal energy storage. *J Energy Storage* 29:101167

7. Paneliya S, Khanna S et al (2020) Core shell paraffin/silica nanocomposite: a promising phase change material for thermal energy storage. *Renew Energy*
8. Zou X, Zhou W et al (2020) Preparation and characterization of poly (N-methylol acrylamide)/polyethylene glycol composite phase change materials for thermal energy storage. *Solar Energy Mater Solar Cells* 205:110248
9. Shi J, Li M (2020) Synthesis and characterization of polyethylene glycol/modified attapulgite form-stable composite phase change material for thermal energy storage. *Sol Energy* 205:62–73
10. Wang P, Feng X et al (2020) Preparation and thermal properties of colloidal mixtures of capric acid and $\text{Na}_2\text{HPO}_4 \cdot 12\text{H}_2\text{O}$ as a phase change material for energy storage. *Solar Energy Mater Solar Cells* 215:110636
11. Tan N, Xie T (2020) Preparation and characterization of capric-palmitic acids eutectics/silica xerogel/exfoliated graphite nanoplatelets form-stable phase change materials. *J Energy Storage* 102016
12. Chen L, Lv J et al (2020) A shape-stable phase change composite prepared from cellulose nanofiber/polypyrrole/polyethylene glycol for electric-thermal energy conversion and storage. *Chem Eng J* 400:125950
13. Jin X, Xiao Q et al (2020) Thermal conductivity enhancement of a sodium acetate trihydrate–potassium chloride–urea/expanded graphite composite phase–change material for latent heat thermal energy storage. *Energy Build* 110615
14. Chriaa I, Karkri M et al (2020) The performances of expanded graphite on the phase change materials composites for thermal energy storage. *Polymer* 123128
15. Yu Q, Lu Y et al (2020) Preparation and thermal properties of novel eutectic salt/nano- SiO_2 /expanded graphite composite for thermal energy storage. *Solar Energy Mater Solar Cells* 215:110590
16. Han D, Lougou B et al (2020) Thermal properties characterization of chloride salts/nanoparticles composite phase change material for high-temperature thermal energy storage. *Appl Energy* 264:114674
17. Xia Y, Zhang H et al (2019) Graphene-oxide-induced lamellar structures used to fabricate novel composite solid-solid phase change materials for thermal energy storage. *Chem Eng J* 362:909–920
18. Jia X, Li Q et al (2020) High thermal conductive shape-stabilized phase change materials of polyethylene glycol/boron nitride@ chitosan composites for thermal energy storage. *Compos Part A Appl Sci Manuf* 129:105710
19. Li C, Xie B et al (2019) Ultrathin graphite sheets stabilized stearic acid as a composite phase change material for thermal energy storage. *Energy* 166:246–255
20. Yuan M, Ren Y et al (2019) Characterization and stability study of a form-stable erythritol/expanded graphite composite phase change material for thermal energy storage. *Renew Energy* 136:211–222
21. Gu X, Liu P et al (2019) Enhanced thermal conductivity of palmitic acid/mullite phase change composite with graphite powder for thermal energy storage. *Renew Energy* 138:833–841
22. Sari A, Al-Ahmed A et al (2019) Investigation of thermal properties and enhanced energy storage/release performance of silica fume/myristic acid composite doped with carbon nanotubes. *Renew Energy* 140:779–788
23. Zhang W, Zhang W et al (2019) Lauric-stearic acid eutectic mixture/carbonized biomass waste corn cob composite phase change materials: preparation and thermal characterization. *Thermochim Acta* 674:21–27
24. Zhang J, Wang Z et al (2020) Novel composite phase change materials with enhancement of light-thermal conversion, thermal conductivity and thermal storage capacity. *Sol Energy* 196:419–426
25. Zhang J, Li X et al (2020) Characterization and experimental investigation of aluminum nitride-based composite phase change materials for battery thermal management. *Energy Convers Manag* 204:112319
26. Cheng F, Zhang X et al (2019) Thermal conductivity enhancement of form-stable tetrade-canol/expanded perlite composite phase change materials by adding Cu powder and carbon fiber for thermal energy storage. *Appl Therm Eng* 156:653–659

27. Chen M, He Y et al (2019) Solar thermal conversion and thermal energy storage of CuO/Paraffin phase change composites. *Int J Heat Mass Transf* 130:1133–1140
28. Wu X, Wang C et al (2019) Experimental study of thermo-physical properties and application of paraffin-carbon nanotubes composite phase change materials. *Int J Heat Mass Transf* 140:671–677
29. Li C, Zhang B et al (2019) Stearic acid/expanded graphite as a composite phase change thermal energy storage material for tankless solar water heater. *Sustain Cities Soc* 44:458–464
30. Ren Y, Xu h et al (2018) Ca(NO₃)₂-NaNO₃/expanded graphite composite as a novel shape-stable phase change material for mid- to high-temperature thermal energy storage. *Energy Convers Manag* 163:50–58
31. Sciacovelli A, Navarro M et al (2018) High density polyethylene (HDPE)—graphite composite manufactured by extrusion: a novel way to fabricate phase change materials for thermal energy storage. *Particuology* 40:131–140
32. Zhao L, Xing Y et al (2018) Thermal performance of sodium acetate trihydrate based composite phase change material for thermal energy storage. *Appl Therm Eng* 143:172–181
33. Wang Y, Li S et al (2017) Supercooling suppression and thermal behavior improvement of erythritol as phase change material for thermal energy storage. *Sol Energy Mater Sol Cells* 171:60–71
34. Karthik M, Faik A et al (2017) Graphite foam as interpenetrating matrices for phase change paraffin wax: a candidate composite for low temperature thermal energy storage. *Sol Energy Mater Sol Cells* 172:324–334

Air Quality Assessment During Lockdown for Jaipur City



Darshan Mishra, Kaushiki Sharma, and Sohil Sisodiya

1 Introduction

Air pollution!! One of the critical terms that we hear in our regular daily schedule, articles, news, etc. The populace development, metropolitan turn of events and vehicular blast have decayed the encompassing air quality in late mechanical time. Gaseous pollutants and particulate matter pollutants of significant general health concerns represent a genuine danger to human wellbeing [1]. In this speedily developing urbanization and industrialization, one life saver that is being overlooked persistently is environment and perhaps the most basic term go under this is air quality. Street residue and auxiliary particles radiated from different sources are the essential patrons of contamination in the public capital, as indicated by a draft report by IIT Kanpur [2]. These exercises for the most part defile the air which influence medical condition to the occupant and polluting the climate. The consolidated impacts of outside and family unit air pollution kill an expected 7,000,000 individuals worldwide consistently; 9 out of 10 individuals inhale air that surpasses WHO rule limits containing elevated levels of toxins (WHO 2020). Non-integrated baseline data predominantly proved to be inadequate to portray a clear picture of the adjacent environment [3]. The remarkable inescapable of the COVID-19 have made it a worldwide pandemic that has prompted noxious outcomes in different pieces of the world. To check the spread of this profoundly infectious illness and limit the casualty, various nations have received extreme yet significant measures to diminish collaboration among people, forbidding huge scope public and private get-togethers, forcing a time limitation, controlling transportation, advancing social distancing,

D. Mishra · K. Sharma · S. Sisodiya (✉)
University Department of Civil Engineering, Rajasthan Technical University, Kota, India
e-mail: ssisodiya.npiu.ce@rtu.ac.in

© The Author(s), under exclusive license to Springer Nature Singapore Pte Ltd. 2022
P. Verma et al. (eds.), *Advancement in Materials, Manufacturing and Energy Engineering*,
Vol. II, Lecture Notes in Mechanical Engineering,
https://doi.org/10.1007/978-981-16-8341-1_9

among every one of these measures, the compelling and significant factor is LOCK-DOWN which demonstrated unexpected improvement in nature of air and overall environmental conditions during the respective period.

In the midst of the COVID-19 pandemic, a cross country lockdown is forced in India from March 24th to April 14th and extended up to May 3, 2020. The current study approaches to relate the effect of COVID-19 lockdown with the air quality of Jaipur, considering the air pollutants (PM_{10} , $PM_{2.5}$, NO_2 , SO_2) during pre-lockdown and the lockdown period. The study also compares the air quality of lockdown period of 2020 with the same period of 2019. CPCB-the Central Pollution Control Board of India is a legal association under the Ministry of Environment, Forest, and Climate Change which was originated in 1974 under the Water (prevention and pollution control) act. It is a summit association in the field of pollution control. These ground checking stations are overseen under the authority of CPCB (Central Pollution Control Board) [4].

Jaipur, one of the most polluted city of Rajasthan, says WHO report as other urban areas would end up subject to various wellsprings of pollution. The one that would be the most 'encompassing' out of every one of them would be discharges from vehicles, industries. With vehicles being an integral part of air deterioration in enormous urban communities, auxiliary poisons, for example, nitrogen dioxide (NO_2) would end up in high amount noticeable all around. With large number of vehicles, motorbikes and trucks, the air will quite often show raised readings of nitrogen dioxide. Additionally, PM can be named essential particles which are produced into the air through modern exercises, street traffic, street dust, ocean shower and windblown soil; they likewise contain carbon and a natural compound, metals and metal oxides and particles [5]. There are numerous examples of the huge waste disposal piles in the city bursting into flames. At the point when this happens, the vapor from consumed plastic, wood and dead natural material would deliver a lot of materials, for example, dark carbon and unstable natural mixes into the air, making gagging exhaust, and smoke discover its way into the homes and roads of Jaipur's inhabitants.

1.1 Air Pollutants and Their Adverse Effects

Main air toxins that are harmful for the natural and human health hazards are particulate matter (PM), carbon monoxide, sulfur dioxide, nitric oxide, ozone and so on. Their sources and risks are shown in (Table 1). Particulate matter includes tiny solids along with tiny droplets that are extremely less in measurement which may genuinely influence when get breathed in. Particles under $10\ \mu\text{m}$ size (PM_{10}) can get profound into your lungs and some may even get into your circulation system. Wherever, particles of size under $2.5\ \mu\text{m}$, otherwise called fine particles or $PM_{2.5}$, represent the most serious danger to wellbeing. At the point when contrast with human hair that is $50\text{--}70\ \mu$ in distance across, PM_{10} (dia@ $10\ \mu\text{m}$) and $PM_{2.5}$ (dia@ $2.5\ \mu\text{m}$) particles are 5–7 times and 20–30 times less while looking at PM_{10} and $PM_{2.5}$, $PM_{2.5}$ is four times less than PM_{10} (Fig. 1). This shows how harmful these particles are

Table 1 Air pollutants and their adverse effects

Pollutant	Source	Environmental risks	Human health risks
Carbon monoxide (CO)	Auto discharges, mechanical processes, fires, etc.	Adds to exhaust smog arrangement	Compounds manifestations of coronary illness, for example, chest torment; may mess vision up and diminish physical and mental abilities in sound individuals
PM _{2.5} and PM ₁₀	Sources of essential particles incorporate flames, smokestacks, building destinations, and unpaved streets while sources of auxiliary particles incorporate responses between vaporous synthetics radiated by automobiles and power plants	Adds to development of haze and acid rain, hence changes the pH equilibrium of streams and harms structures, landmarks and foliage	Unpredictable heartbeat, disturbance of breathing sections, exacerbation of asthma
Nitrogen dioxide (NO ₂)	Power generation, automobile emissions, industrial processes	Harm to foliage; adds to brown haze formation	Disturbance of breathing sections and inflammation
Ozone (O ₃)	Unpredictable natural mixes (VOCs) and nitrogen oxides (NO _x) from industrial and vehicle emanations, electrical utilities, compound solvents and fuel fumes	Interferes with the capacity of specific plants to breathe, prompting expanded weakness to other natural stressors (e.g., infection, brutal climate)	Diminished lung work, aggravation of breathing areas and irritation
Sulfur dioxide (SO ₂)	Power generation, modern cycles, fossil-fuel combustion, vehicle emanations	Significant reason for dimness, adds to acid rain, harms foliage, responds to shape particulate issue, structures and landmarks	Breathing troubles, especially for individuals with asthma and coronary illness

Source U.S. Environmental Protection Agency

to the human organs. These would incorporate issues such as respiratory problems, for example, emphysema, bronchitis, exasperated asthma attacks and whatever other condition that falls under the pneumonic infection section. With the unfathomably little size of PM_{2.5} being a factor, it can infiltrate profound into the tissue of the lungs, where it can go into the alveoli. Sulfur dioxide (SO₂) vapid gas with a sharp, aggravating smell shaped because of consuming of powers and by the purifying of

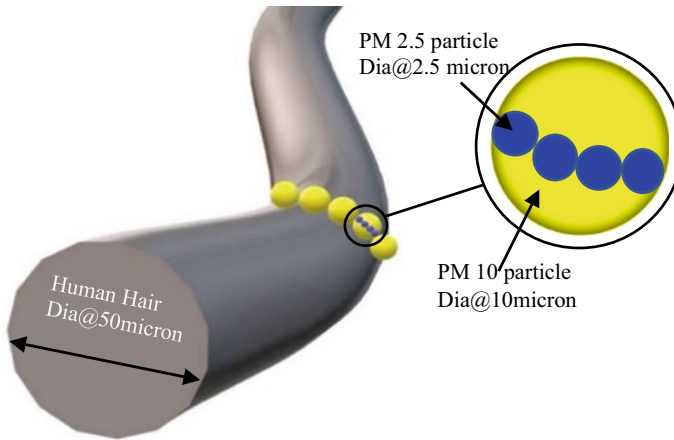


Fig. 1 Particle size comparison

mineral metals that contain sulfur. Sources incorporate force plants, metals handling and smelting facilities and vehicles. Nitrogen-dioxide (NO_2) shapes because of start of non-sustainable power sources such as gas, oil, coal especially fuel used in vehicles. It is similarly made from making nitric destructive, refining of oil and metals, welding and using explosives, business collecting and food creating.

2 Study Area

Jaipur is the capital and the biggest city of the Indian province of Rajasthan having absolute zone of 11,143 km^2 , situated in the north-western piece of the nation (Fig. 2). The latitude of Jaipur is 26.9124 °N and the longitude is 75.7873 °E with rise 431 m (1417 ft.) above sea level. Starting at 2011, Jaipur was the 10th most crowded city in country with population around 3.1 million in 2011. The general population thickness is resolved to be 598 individuals for each square kilometer. It has a rainstorm-impacted hot semi-bone-dry atmosphere with precipitation around 650 mm consistently with a moist atmosphere. In the significant stretches of April, May, June and July, the ordinary consistently temperature of the district is around 30 °C (86 °F). By and large, the normal month to month wind speed shifts in the middle of 2.5 and 10.0 km/h with most extreme during summer (6–10 km/h) and storms (7–8 km/h) and least in winters [6]. Jaipur city is quite possibly the most westernized ones in the country. It has six sectors including the focal and the edges locale. Jaipur is a gigantic urban heat island zone with including natural temperatures sporadically falling under freezing in winters.

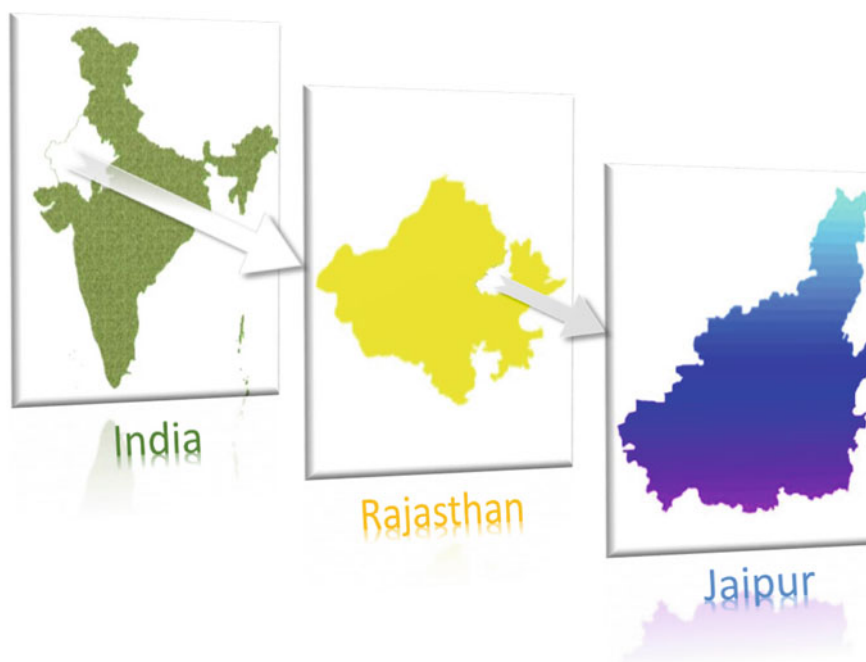


Fig. 2 Location map of study area

3 Methodology

The advantage study was completed to evaluate the effect of lockdown on the air quality in Jaipur city; the everyday (24 h) air pollutant concentration data for three air quality checking stations in city were gathered from Rajasthan State Pollution Control Board for the period from March 25 to May 3, 2019 and the lockdown period from March 25 to May 3, 2020 to give an itemized investigation of the air quality under the national ambient air quality standards (NAAQS).

3.1 Air Quality Index (AQI)

AQI is utilized to report day by day air quality conditions; it is a device utilized by different offices to give data on nearby air quality and whether air pollutants levels. AQI concept changes weighted estimations of individual air pollutants into a single number or set of numbers which might be generally used [7]. The AQI estimations incorporate particulate issue ($PM_{2.5}$ and PM_{10}), ground-level ozone (O_3), nitrogen

dioxide (NO₂), sulfur dioxide (SO₂) and carbon monoxide (CO) emanations. In the current investigation, three unique strategies used to ascertain AQI are as per the following.

3.2 Air Quality Index by Oak Ridge

The Oak Ridge Air Quality Index (ORAQI) method was developed by Oak Ridge National Laboratory. ORAQI is a nonlinear index having exponential function with coefficient with other nonlinear relationship [8].

$$\text{ORAQI} = \left[39.02 \sum (C_i/C_s) \right]^{0.967}$$

where

C_i Monitored concentration of pollutant 'i'

C_s National ambient air quality standard (NAAQS) for pollutant 'i'.

3.3 Air Quality Index by Alternative Method

The determination of AQI using the alternative methodology uses the following expression [9].

$$\text{AQI} = 1/4 [I_{\text{PM}_{10}}/S_{\text{PM}_{10}} + I_{\text{PM}_{2.5}}/S_{\text{PM}_{2.5}} + I_{\text{SO}_2}/S_{\text{SO}_2} + I_{\text{NO}_2}/S_{\text{NO}_2}] * 100$$

where

I_i Monitored concentration of pollutant 'i'

S_i National ambient air quality standard (NAAQS) for pollutant 'i'.

3.4 Air Quality Index by CPCB Method

The sub-index (I_p) of individual pollutant is obtained by physically measuring pollutants, e.g., PM_{2.5}, PM₁₀, SO₂ and NO₂ [10].

$$I_p = \{[(I_{\text{HI}} - I_{\text{LO}})/(B_{\text{HI}} - B_{\text{LO}})] * (C_p - B_{\text{LO}})\} + I_{\text{LO}}$$

where

I_p sub-index for P pollutant

B_{HI} Breakpoint concentration greater or equal to given concentration

B_{LO} Breakpoint concentration smaller or equal to given concentration

- I_{HI} AQI value corresponding to B_{HI}
- I_{LO} AQI value correspond to B_{LO}
- C_p measured concentration of P pollutant.

4 Observations

Ambient air quality is determined and Box plots of PM_{10} , $PM_{2.5}$, SO_2 , NO_2 concentrations are shown in Figs. 3, 4, 5 and 6, respectively, for three air monitoring stations of Jaipur. Further, change in ratio of $PM_{2.5}$ and PM_{10} for March 25–May 3, 2019 and lockdown 2020 is shown in Fig. 7.

- The average concentration of PM_{10} particle at station 1, 2 and 3 are $150.658 \mu\text{g}/\text{m}^3$, $137.88 \mu\text{g}/\text{m}^3$ and $154.87 \mu\text{g}/\text{m}^3$, respectively, in selected period for 2019, while the reduced average concentration during lockdown 2020 for three stations are $74.49 \mu\text{g}/\text{m}^3$, $62.21 \mu\text{g}/\text{m}^3$ and $77.42 \mu\text{g}/\text{m}^3$, respectively.
- The average concentration of $PM_{2.5}$ particle at station 1, 2 and 3 are $46.08 \mu\text{g}/\text{m}^3$, $41.99 \mu\text{g}/\text{m}^3$ and $66.09 \mu\text{g}/\text{m}^3$, respectively, in selected period for 2019, while the reduced average concentration during lockdown 2020 for three stations are $27.59 \mu\text{g}/\text{m}^3$, $22.003 \mu\text{g}/\text{m}^3$ and $32.36 \mu\text{g}/\text{m}^3$, respectively.
- The average concentration of SO_2 at station 1, 2 and 3 are $16.57 \mu\text{g}/\text{m}^3$, $11.85 \mu\text{g}/\text{m}^3$ and $13.86 \mu\text{g}/\text{m}^3$, respectively, in selected period for 2019, while the reduced average concentration during lockdown 2020 for three stations are $15.004 \mu\text{g}/\text{m}^3$, $11.015 \mu\text{g}/\text{m}^3$ and $12.50 \mu\text{g}/\text{m}^3$, respectively.

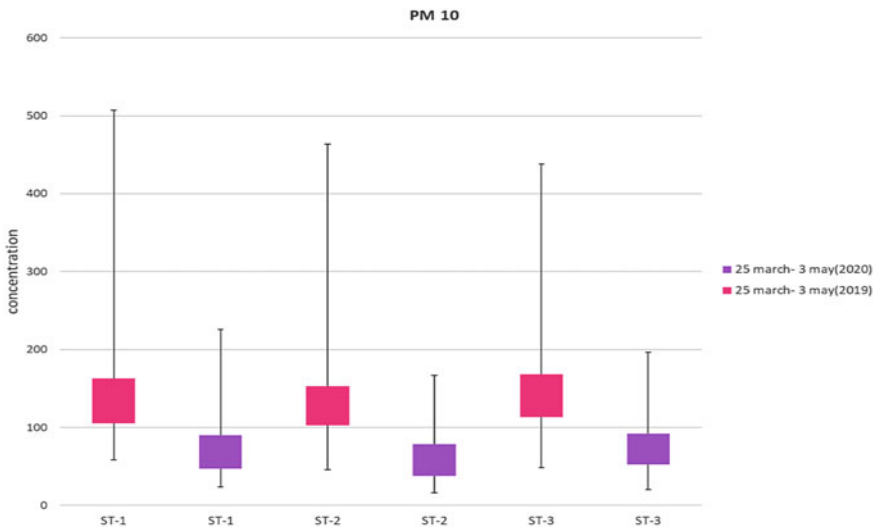


Fig. 3 Box plot for PM_{10} concentration during March 25–May 3, 2019 and lockdown 2020

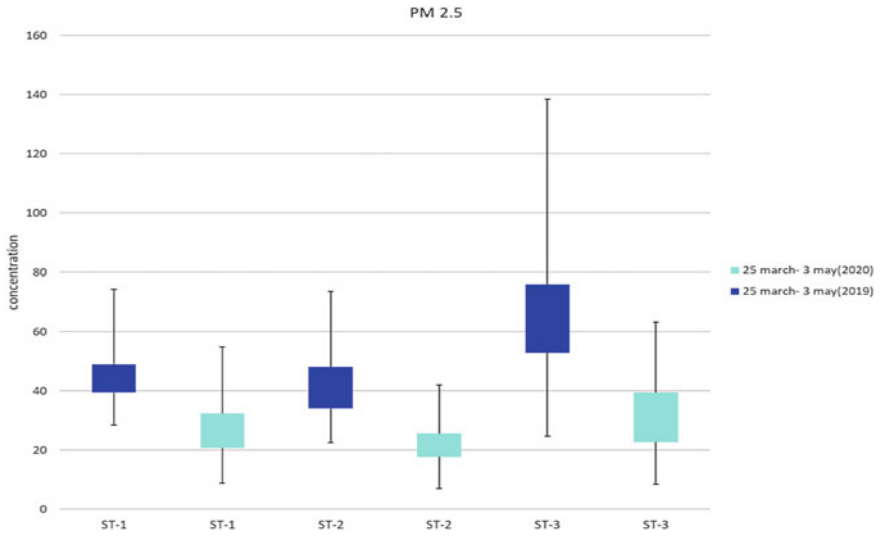


Fig. 4 Box plot for PM_{2.5} concentration during March 25–May 3, 2019 and lockdown 2020

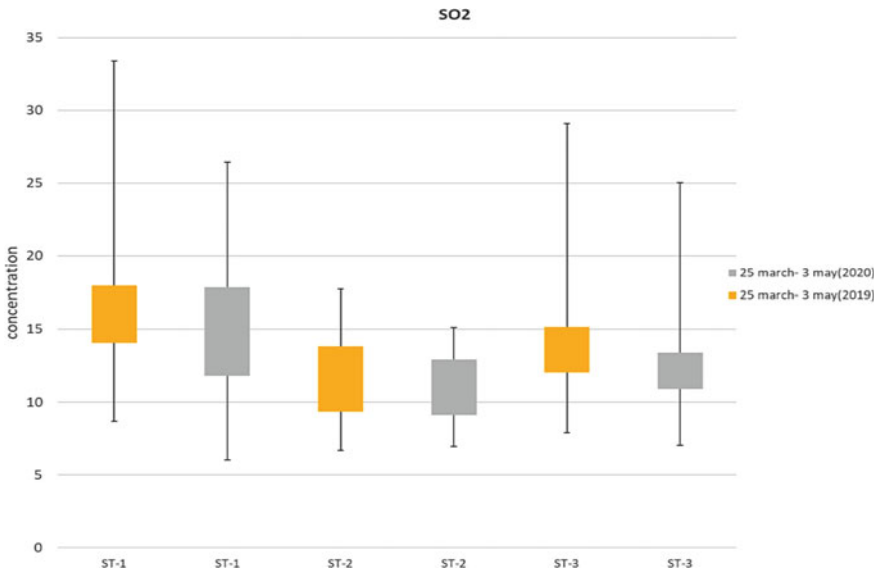


Fig. 5 Box plot for SO₂ concentration during March 25–May 3, 2019 and lockdown 2020

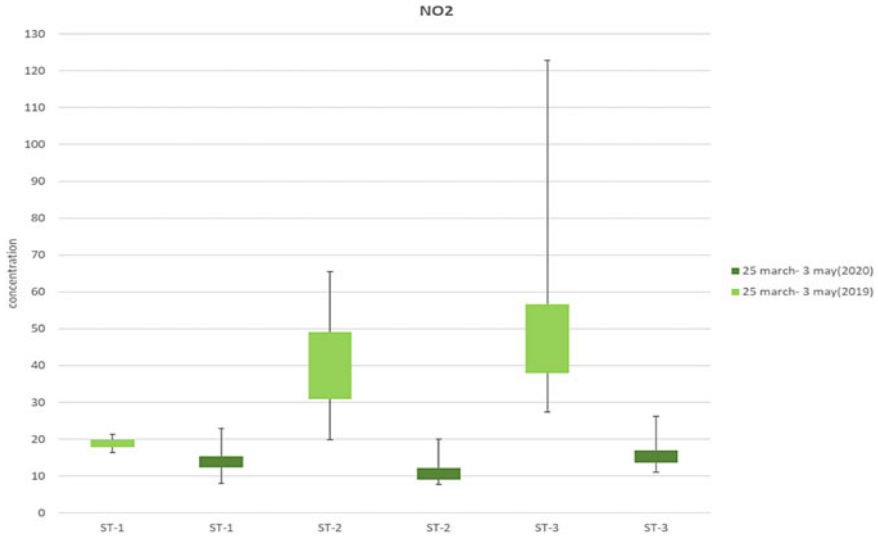


Fig. 6 Box plot for NO₂ concentration during March 25–May 3, 2019 and lockdown 2020

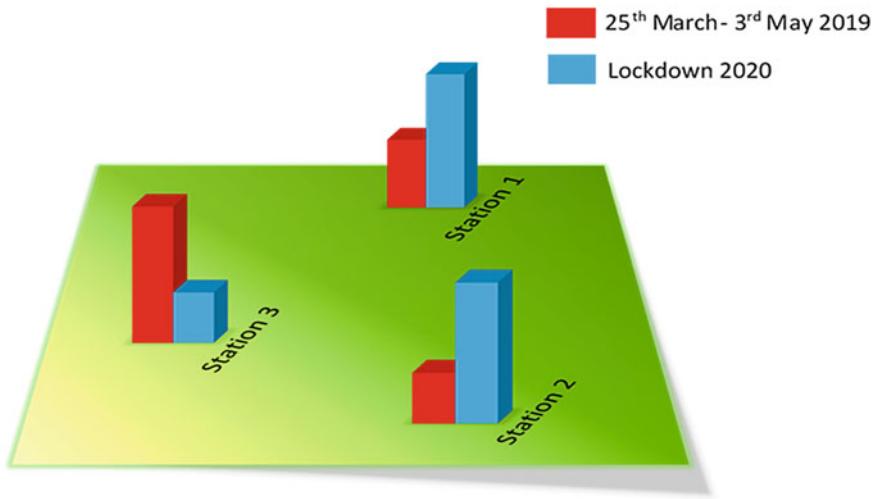


Fig. 7 Change in PM_{2.5}/PM₁₀ ratio during March 25–May 3, 2019 and lockdown 2020

- The average concentration of NO₂ at station 1, 2 and 3 are 18.78 $\mu\text{g}/\text{m}^3$, 39.92 $\mu\text{g}/\text{m}^3$ and 48.94 $\mu\text{g}/\text{m}^3$, respectively, in selected period for 2019, while the reduced average concentration during lockdown 2020 for three stations are 13.95 $\mu\text{g}/\text{m}^3$, 11.19 $\mu\text{g}/\text{m}^3$ and 15.62 $\mu\text{g}/\text{m}^3$, respectively.

5 Results and Discussion

To check the air quality of Jaipur city, data obtained from all three monitoring stations at residential sites is used to calculate Air Quality Index by different AQI methods.

The results of AQI for three monitoring stations during lockdown 2020 with comparison to same period in 2019 are shown in Figs. 8, 9, 10, 11, 12 and 13, result shows the decline in pattern of AQI during lockdown when contrasted and a similar time of 2019 (Table 2).

It is observed that average AQI during 25th march to 3rd may 2019 for monitoring stations-1, 2 and 3 is 138.025, 126.825 and 144.625 respectively (by CPCB method) which is a clear sign of moderate air pollution while average AQI values during lockdown period 2020 for monitoring stations-1, 2 and 3 is 72.275, 60.875 and 75.525 respectively (by CPCB method) shows a significant decrement as compare to year 2019, which is a sign of satisfactory or fair air quality (Table 2). As far as rate, Shastri Nagar, Jaipur (ST-1) shows all in all decrement observable all-around quality document between 37 and 48% when thought about between lockdown 2020 and same time of 2019. While Adarsh Nagar, Jaipur (ST-2) and Police Commissionerate, Jaipur (ST-3) has 47-55% declination perceptible all-around quality record. The proportion of $PM_{2.5}$ and PM_{10} during the lockdown time frame when contrasted with the relating time frame in 2019 increased. It shows that limitations during lockdown prompted better control on PM_{10} at Shastri Nagar, Jaipur (ST-1) and Adarsh Nagar, Jaipur (ST-2) while Police Commissionerate, Jaipur (ST-3) show decrease in ratio as compared to design period of 2019 which might be because of more noticeable effect of restricted residue lifting on streets of Jaipur during the lockdown time frame. As due to restrictions of various activities which are responsible for PM_{10} concentration, levels of PM_{10} decreased during lockdown. Apparently coarser portion has diminished at a quicker rate in areas with huge traffic.

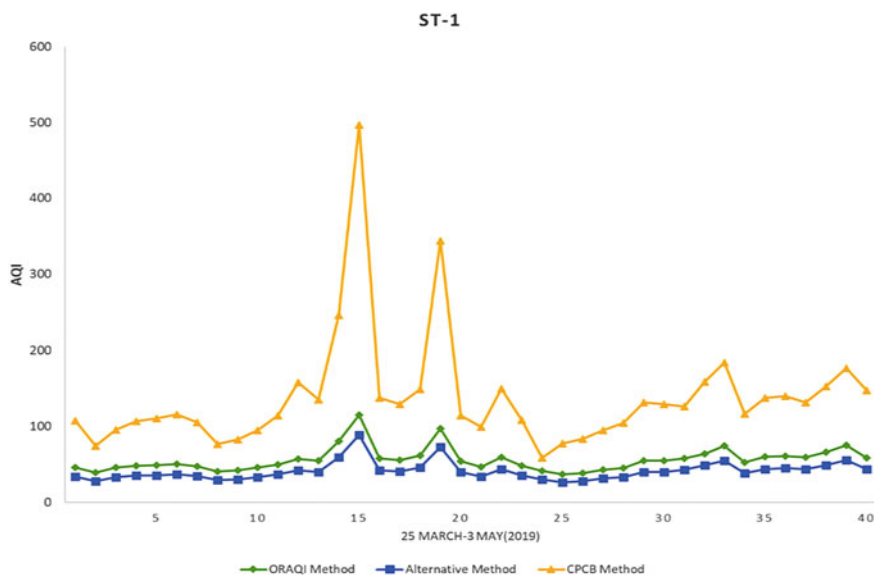


Fig. 8 AQI of station 1 during March 25–May 3, 2019

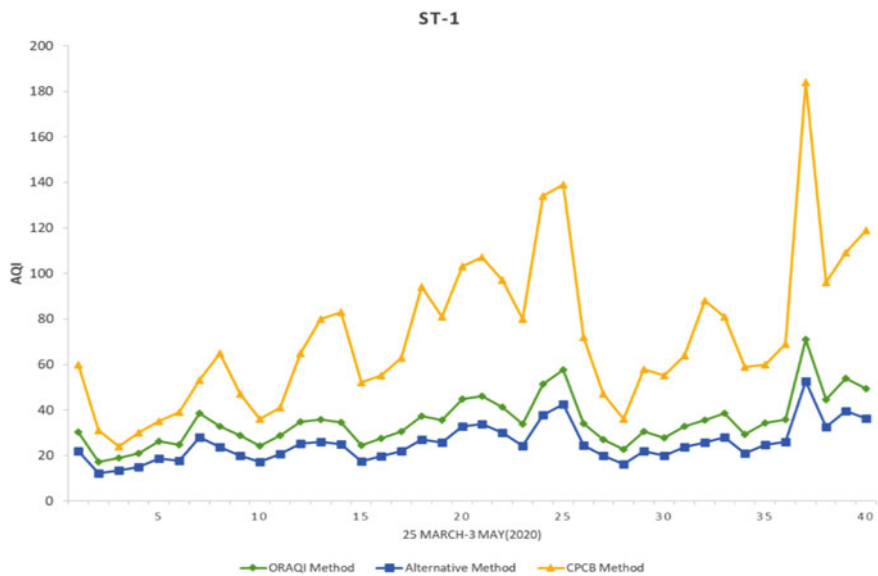


Fig. 9 AQI of station 1 during lockdown 2020

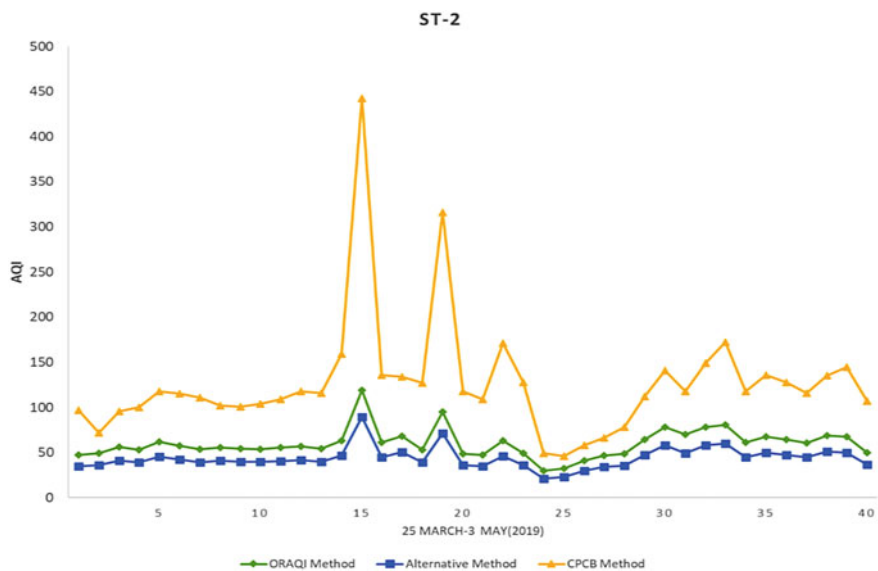


Fig. 10 AQI of station 2 during March 25–May 3, 2019

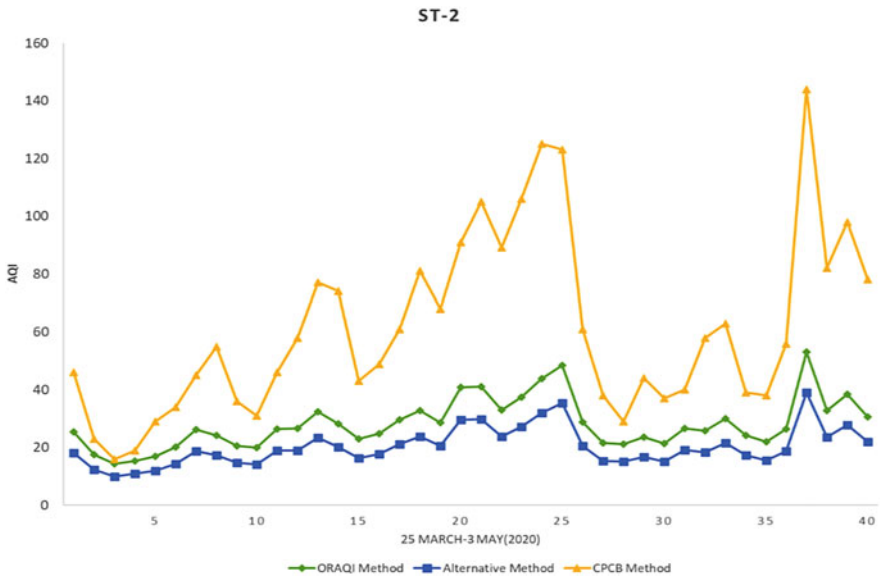


Fig. 11 AQI of station 2 during lockdown 2020

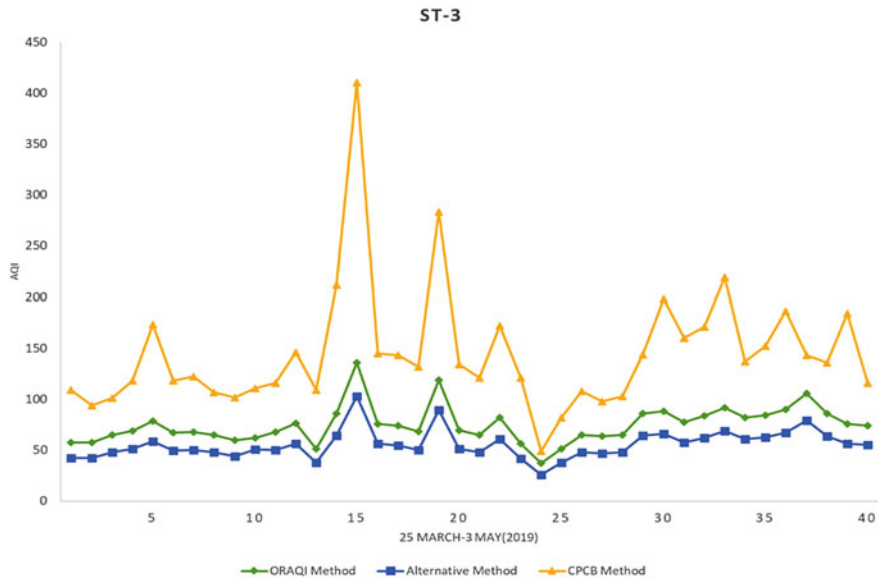


Fig. 12 AQI of station 3 during March 25–May 3, 2019

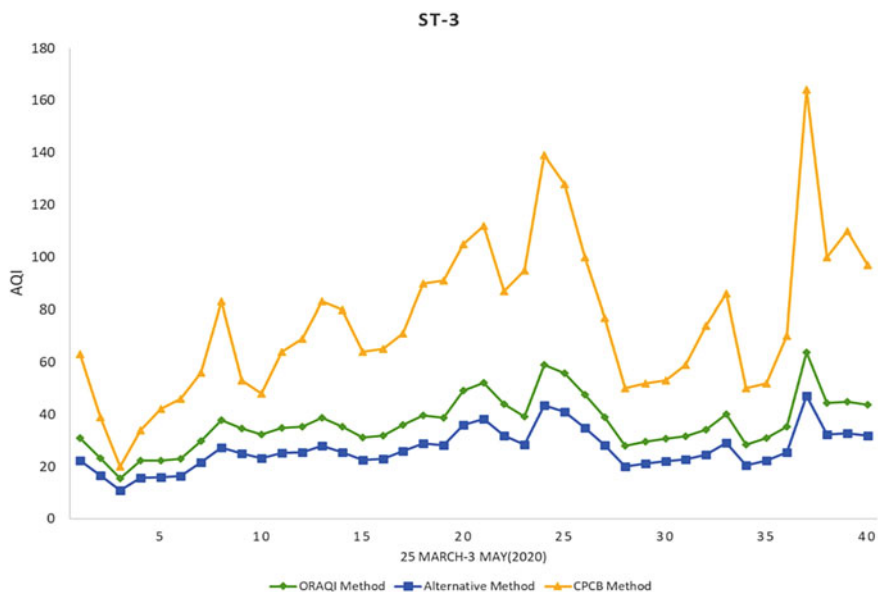


Fig. 13 AQI of station 3 during lockdown 2020

Table 2 Classification of AQI used for comparative study

AQI (ORAQI)	AQI (alternative method)	AQI (CPCB, 2014)
Excellent = 0–20	Clean air = 0–25	Good (0–50)
Good = 21–39	Light air pollution = 26–50	Satisfactory (51–100)
Fair = 40–59	Moderate air pollution = 51–75	Moderately polluted (101–200)
Poor = 60–79	Heavy air pollution = 76–100	Poor (201–300)
Bad = 80–99	Sever air pollution = 100 and above	Very Poor (301–400)
Dangerous = 100 and above		Severe (401–500)

6 Conclusion and Future Approach

An immense decrease in the concentration of NO₂ is seen at station 2 (72%) and station 3 (68%) during lockdown against 2019 concentrations of the same period. Though, particulate matter diminished by half during lockdown with a little abatement in SO₂ levels, i.e., 7–9% in comparison with 2019 period. This is because of the traffic limitations and impeded business regions during lockdown. Furthermore, during lockdown period all checking stations was in acceptable and great level.

At the point when metropolitan super centers have been running consistently for financial improvement without thinking about the constraints of common assets,

measures like impermanent lockdown may arise as a powerful answer for control natural awkwardness. Another telling statistic that illustrates the level of traffic congestion in Jaipur is that 60% of the city roads are used for parking—the highest in any city in India. The increment in private vehicular rush hour gridlock is answerable for quite a bit of this as per the report. Very much built streets, traffic guidelines and utilization of cleaner powers will help in additional decreasing vehicular outflows and clearly the lockdown ends up being a significant advance for improving air quality.

Jaipur has been communicated as the capital which could in a general sense increases vehicular people heading to extended toxins focuses or pollutant. Further, it is a standard spot of vacationer interest and besides being considered as savvy city, typical checking of air quality and estimation of AQI is crucial for screen any abrupt changes in air quality in the city.

7 Credit Author Statement

Kaushiki Sharma: Methodology, Writing-Original Draft, Writing-Review and Editing, **Darshan Mishra:** Formal analysis, Writing-Review and Editing, **Sohil Sisodiya:** Writing-Review and Editing.

References

1. Patel JA, Prajapati BI, Panchal V (2017) Assessment of ambient air quality and air quality index (AQI) in Dahej Area, Gujarat, India. *Nat Environ Pollut Technol* 16(3):943–945. <https://doi.org/10.20546/ijemas.2017.606.323>
2. Aishwarya Paradkar M, Rutika Nanivadekar M, Gharad P (2015) “Research report on Delhi air pollution,” no. December, pp 563–569 [Online]. Available: http://www.ijstm.com/images/short_pdf/1459435749_1200B.pdf
3. Agarwal P, Melkania U (2018) Assessment of the ambient air quality at the industrial area using the air quality index method (AQI), vol 11, no. April, p 30954. <https://doi.org/10.30954/0974-1712.04.2018.2>
4. Sikarwar A, Rani R (2020) Assessing the immediate effect of COVID-19 lockdown on air quality: a case study of Delhi, India, pp 1–19. <https://doi.org/10.21203/rs.3.rs-31822/v1>
5. Abulude FO (2016) Particulate matter: an approach to air pollution, pp 1–14. <https://doi.org/10.20944/preprints201607.0057.v1>
6. Dadhich AP, Goyal R, Dadhich PN (2018) Assessment of spatio-temporal variations in air quality of Jaipur city, Rajasthan, India. *Egypt J Remote Sens Sp Sci* 21(2):173–181. <https://doi.org/10.1016/j.ejrs.2017.04.002>
7. Gowtham Sarella MDAKK (2015) Ambient air quality analysis using air quality index—a case study of Vapi. *Int J Innov Res Sci Technol* 1(10):68–71
8. Nigam S, Rao BPS, Kumar N, Mhaisalkar VA (2015) Air quality index—a comparative study for assessing the status of air quality. *Res J Eng Technol* 6(2):267. <https://doi.org/10.5958/2321-581x.2015.00041.0>

9. Ganguly R (2019) Indexing method for assessment of air quality, pp 68–85. <https://doi.org/10.4018/978-1-5225-7289-3.ch003>
10. Nihalani S, Kadam S (2019) Ambient air quality assessment for Vadodara City using AQI and exceedence factor. SSRN Electron J 838–846. <https://doi.org/10.2139/ssrn.3464926>

Micellar Potentiometric Determination of Stability Constant and Antibacterial Investigations on Complexes of Cu (II) with 3, 4, 5-Trimethoxybenzaldehyde Thiosemicarbazone



Uma Rathore, Raja Ram, Kamal Kishor Verma, and N. Bhojak

1 Introduction

Thiosemicarbazone and their metal complexes have a great verity of biological activity. Medicinal study has been done of this class of compounds against tuberculosis, leprosy, psoriasis, rheumatism, trypanosomiasis, and coccidiosis [1]. Various drugs containing thiosemicarbazone moiety like Triapine has paid important role in the treatment of solid tumors and hematological malignancies. It also has exhibited property of radiosensitizer [2–4] and also has shown lesser antitumor activity and selectivity than di-2-pyridylketone thiosemicarbazone [5, 6].

In this paper, we are reporting the stability constant and antimicrobial activity of Cu (II) complexes with thiosemicarbazide-based ligand: 3, 4, 5-Trimethoxybenzaldehyde thiosemicarbazone as shown in Fig. 1.

2 Materials and Methods

All the chemicals used were of AR grade and procured from Himedia. Metal salt was purchased from E. Merck and was used as received. All solvents used were of standard/spectroscopic grade. Ligand 3, 4, 5-Trimethoxybenzaldehydethiosemicarbazone was synthesized by condensation reaction of thiosemicarbazide with 3, 4, 5-Trimethoxybenzaldehyde in presence of

Present Address:

U. Rathore (✉) · R. Ram · N. Bhojak
GCRC, P.G. Department of Chemistry, Govt. Dungar College (NAAC Grade-A), Bikaner,
Rajasthan 334003, India

K. K. Verma
S.R.L.S. Govt. P.G. College Kaladera, Jaipur, Rajasthan, India

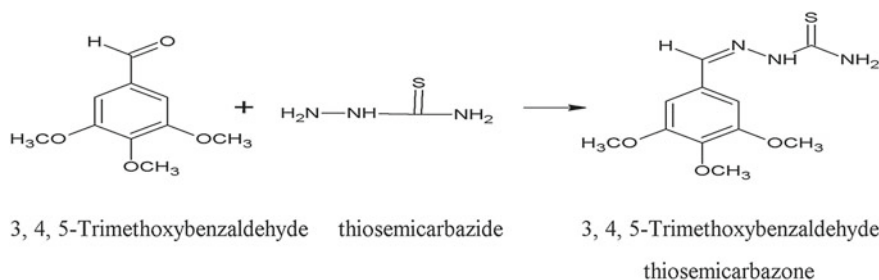


Fig. 1 Chemical reaction 3, 4, 5-Trimethoxybenzaldehyde with thiosemicarbazone

methanol according to the literature [7]. Metal ligand complexes were formed by potentiometrically. All biological activities have been carried out by disk diffusion method under horizontal laminar. The Digital pH meter 335 is used to observe the pH values of various solutions in present study.

3 Procedure

Potentiometric Study

Potentiometric study has been conducted in non-micellar (alcohol and water) and in micellar medium (HTAB, SDS and TX-100). Three sets of titrations were prepared for comparison. Volume of all the system was made up to 25 ml using 60% ethanol. Titration of the three sets of mixtures has been carried out against a standard alkali given by Irving and Rossotti method [8].

Biological Study

Biological investigation has been carried out by disk diffusion method. The agar was prepared in plate, and microorganisms were cultivated on to the surface of the agar plate. Broth was applied on agar plate; then filter paper disks, impregnated with different types of sample, were placed on the agar. After incubation of the plates, the diameter of the zone of inhibition (ZI) of microorganism growth around each disk was measured [9, 10].

4 Results and Discussion

Potentiometric Study

Proton-ligand Stability Constants (pK):

The proton–ligand formation curves were estimated by plotting graphs between the values (\bar{n}_A) Vs pH readings. This curve indicates average number of hydrogen ions (\bar{n}_A) attached to a ligand. The value of pH where $\bar{n}_A = 1.5$ and $\bar{n}_A = 0.5$ corresponds to the values of pK1 and pK2, respectively. The proton-ligand formation numbers (\bar{n}_A) were calculated by Irving and Rossotti method [8].

$$\bar{n}_A = Y - \frac{(V_1 - V_2)(N^o + E^o)}{(V^o + V_1)T_{CL}^o} \quad (1)$$

where V^o = Initial volume of solution (25 ml), E^o = Initial concentration of free acid (HNO_3), Y = Number of dissociable protons from ligand, T_{CL}^o is concentration of ligand in solution, and $(V_1 - V_2)$ = Volume of alkali (KOH) consumed by acid and ligand on the same pH [11].

Metal ligand Stability Constant (log K):

Metal ligand stability constant ($\log K$) was determined by metal complex formation curve, and this curve indicated average number of ligand (\bar{n}) attached to metal ion. Metal ligand stability constant ($\log K$) was determined by the half integral method by plotting \bar{n} versus pL

$$\bar{n} = \frac{(V_3 - V_2)(N^o + E^o)}{(V^o + V_1)(\bar{n}_A)T_{CM}^o} \quad (2)$$

$$pL = \log_{10} \frac{\sum_{n=0}^n \beta_n^H \cdot \frac{1}{(\text{anti log pH})^n}}{T_{CL}^o - \bar{n}T_{CM}^o} \times \frac{V^o + V_3}{V^o} \quad (3)$$

V_3 is the volume of KOH added in the metal ions titration to attain the given pH reading and T_{CM}^o total concentration of metal present in solution. (pL) is free ligand exponent function. $\log K_1$ and $\log K_2$ were calculated from the formation curve by the known value of pL at which $(\bar{n}) = 0.5$ and $(\bar{n}) = 1.5$ corresponding to the values of $\log K_1$ and $\log K_2$, respectively [12].

The values of \bar{n}_A and pH of ligand in non-micellar medium and micellar medium have been reported in Tables 1 and 2. The \bar{n} and pL values of ligand 3, 4, 5-TBT with Cu (II) metal in non-micellar and micellar medium have been reported in Tables 3, 4, 5, 6, and 7.

Figures 2, 3, 4, 5, and 6 show plots between and pL values of ligand 3, 4, 5-TBT with Cu (II) in Alc. + water, alcohol, HTAB, SDS, and TX-100 medium, respectively.

Table 1 \bar{n}_A and pH values of Ligand 3, 4, 5-TBT in alcohol and alcohol + water

\bar{n}_A and pH value of ligand 3, 4, 5-TBT in alcohol			\bar{n}_A and pH value of ligand 3, 4, 5-TBT in alcohol + water		
Sr. No.	pH	\bar{n}_A	Sr. No.	pH	\bar{n}_A
1	4.4	1.03455	1	4.4	1.10368
2	4.65	0.97411	2	4.65	1.22459
3	4.9	1.0259	3	4.9	1.28498
4	5.15	1.03453	4	5.15	1.28923
5	5.4	1.03452	5	5.4	1.31511
6	5.65	1.0302	6	5.65	1.33666
7	5.9	1.01725	7	5.9	1.34527
8	6.15	1.01725	8	6.15	1.35389
9	6.4	1.01725	9	6.4	1.36249
10	6.65	1.02156	10	6.65	1.36679
11	6.9	1.02156	11	6.9	1.3754
12	7.15	1.02156	12	7.15	1.384
13	7.4	1.02587	13	7.4	1.39262
14	7.65	1.02587	14	7.65	1.41417
15	7.9	1.02587	15	7.9	1.41412
16	8.15	1.02586	16	8.15	1.42705
17	8.4	1.03017	17	8.4	1.43997
18	8.65	1.03448	18	8.65	1.44425
19	8.9	1.03448	19	8.9	1.43988
20	9.15	1.03448	20	9.15	1.43981
21	9.4	1.03447	21	9.4	1.43976
22	9.65	1.03016	22	9.65	1.4354
23	9.9	1.03447	23	9.9	1.42671
24	10.15	1.02585	24	10.15	1.43097
25	10.4	1.02154	25	10.4	1.43517
26	10.65	1.03876	26	10.65	1.43505
27	10.9	1.0646	27	10.9	1.50387
28	11.15	1.08612	28	11.15	1.42601
29	11.4	1.08609	29	11.4	1.32648
30	11.65	1.14199	30	11.65	1.22295
31	11.9	1.1591	31	11.9	1.14535
32	12.15	1.40372			

Table 2 \bar{n}_A and pH values of Ligand 3, 4, 5-TBT in HTAB, SDS and TX-100 medium

HTAB			SDS			TX-100		
Sr. No.	pH	\bar{n}_A	Sr. No.	pH	\bar{n}_A	Sr. No.	pH	\bar{n}_A
1	4.4	1.14255	1	4.4	1.14255	1	4.15	1.10796
2	4.65	1.1382	2	4.65	1.1382	2	4.4	1.082
3	4.9	1.11225	3	4.9	1.11225	3	4.65	1.07766
4	5.15	1.082	4	5.15	1.082	4	4.9	1.06902
5	5.4	1.0302	5	5.4	1.0302	5	5.15	1.08195
6	5.65	1.02157	6	5.65	1.02157	6	5.4	1.08194
7	5.9	1.01725	7	5.9	1.01725	7	5.65	1.08193
8	6.15	1.02588	8	6.15	1.02588	8	5.9	1.07761
9	6.4	1.02156	9	6.4	1.02156	9	6.15	1.08192
10	6.65	1.03019	10	6.65	1.03019	10	6.4	1.08192
11	6.9	1.02587	11	6.9	1.02587	11	6.65	1.08191
12	7.15	1.03018	12	7.15	1.03018	12	6.9	1.08622
13	7.4	1.03018	13	7.4	1.03018	13	7.15	1.07759
14	7.65	1.03449	14	7.65	1.03449	14	7.4	1.07758
15	7.9	1.03449	15	7.9	1.03449	15	7.65	1.08189
16	8.15	1.03449	16	8.15	1.03449	16	7.9	1.08188
17	8.4	1.04311	17	8.4	1.04311	17	8.15	1.09049
18	8.65	1.04311	18	8.65	1.04311	18	8.4	1.09911
19	8.9	1.05604	19	8.9	1.05604	19	8.65	1.09909
20	9.15	1.06035	20	9.15	1.06035	20	8.9	1.1077
21	9.4	1.06897	21	9.4	1.06897	21	9.15	1.11631
22	9.65	1.07758	22	9.65	1.07758	22	9.4	1.12061
23	9.9	1.0862	23	9.9	1.0862	23	9.65	1.13783
24	10.15	1.08189	24	10.15	1.08189	24	9.9	1.15505
25	10.4	1.11637	25	10.4	1.11637	25	10.15	1.16796
26	10.65	1.15511	26	10.65	1.15511	26	10.4	1.24545
27	10.9	1.1809	27	10.9	1.1809	27	10.65	1.3099
28	11.15	1.30141	28	11.15	1.30141	28	10.9	1.63231
29	11.4	1.33574	29	11.4	1.33574			
30	11.65	1.43892						

Biological Investigations

Study of ligand and metal complexes has been carried out against *Escherichia coli*, *Staphylococcus aureus*, and *Bacillus subtilis* bacterial strain as shown in Fig. 7. By applying disk diffusion method, following results have been found [13].

Table 3 \bar{n} and pL values of Ligand 3, 4, 5-TBT with Cu (II) in alcohol

Sr. No.	pH	pL	\bar{n}
1	4.4	4.4868107	0.3195978
2	4.65	4.2609902	0.3649481
3	4.9	3.9967165	0.337658
4	5.15	3.7326064	0.3102307
5	5.4	3.4687181	0.2827896
6	5.65	3.2141635	0.2736236
7	5.9	2.9688398	0.282688
8	6.15	2.7235565	0.2917836
9	6.4	2.4736139	0.2917603
10	6.65	2.237801	0.3191001
11	6.9	2.0070459	0.3555403
12	7.15	1.7668527	0.3737433
13	7.4	1.5317474	0.4010744
14	7.65	1.3019717	0.4375007
15	7.9	1.0779026	0.4830352
16	8.15	0.8654858	0.5468104
17	8.4	0.6321628	0.5741051
18	8.65	0.4163853	0.6287567
19	8.9	0.1959426	0.674265

5 Conclusion

The values of log K are determined by potentiometrically and found greater than zero which clearly indicates the formation of complex between metal ion and thiosemi-carbazones ligand. The antibacterial properties of the ligands and its complexes were studied against *E. coli*, *S. aureus*, and *B. subtilis* bacteria. The result shows that all the Cu(II) complexes have moderate antibacterial activities against these bacteria. Antibacterial activity of ligand screened in alcohol: water medium has been reported highest against *S. aureus*.

Table 4 \bar{n} and pL values of Ligand 3, 4, 5-TBT with Cu (II) in alcohol + water

Sr. No.	pH	pL	\bar{n}
1	4.4	4.4801728	0.430544
2	4.65	4.1274677	0.2327738
3	4.9	3.8370127	0.1478531
4	5.15	3.5838412	0.1406337
5	5.4	3.3174715	0.1050328
6	5.65	3.0639467	0.0968726
7	5.9	2.8108415	0.0898289
8	6.15	2.5695255	0.1083793
9	6.4	2.3164084	0.1013519
10	6.65	2.0780982	0.1262862
11	6.9	1.8367029	0.1443137
12	7.15	1.5893726	0.1496406
13	7.4	1.344942	0.1611015
14	7.65	1.0881805	0.1464365
15	7.9	0.8440843	0.1586261
16	8.15	0.6198842	0.2115928
17	8.4	0.4174451	0.3055417
18	8.65	0.2446311	0.4479593

Table 5 \bar{n} and pL values of Ligand 3, 4, 5-TBT with Cu (II) in HTAB

Sr. No	pH	pL	\bar{n}
1	4.4	4.3807527	0.2010965
2	4.65	4.0944541	0.1238031
3	4.9	3.8625744	0.1619522
4	5.15	3.6278206	0.1935017
5	5.4	3.4011435	0.2408027
6	5.65	3.1555055	0.2492664
7	5.9	2.9268087	0.2913428
8	6.15	2.6967479	0.3296539
9	6.4	2.4582473	0.351294
10	6.65	2.2157494	0.3651476
11	6.9	1.9732291	0.3789075
12	7.15	1.7348384	0.4001118
13	7.4	1.4991081	0.4259305
14	7.65	1.2516322	0.4302488
15	7.9	1.0144085	0.4528618
16	8.15	0.7720571	0.4661816
17	8.4	0.536105	0.4905489
18	8.65	0.3038378	0.5207001

Table 6 \bar{n} and pL values of Ligand 3, 4, 5-TBT with Cu (II) in SDS

Sr. No	pH	pL	\bar{n}
1	4.15	4.6533016	0.296045
2	4.4	4.4030557	0.2950866
3	4.65	4.1456334	0.2801811
4	4.9	3.896935	0.282414
5	5.15	3.6373472	0.2630728
6	5.4	3.3995522	0.2869673
7	5.65	3.1619244	0.3108583
8	5.9	2.9293617	0.344101
9	6.15	2.6871618	0.358643
10	6.4	2.4500653	0.3825243
11	6.65	2.2087977	0.3984493
12	6.9	1.9623296	0.4047581
13	7.15	1.7318869	0.4399649
14	7.4	1.4864474	0.4479489
15	7.65	1.2399982	0.4540968
16	7.9	0.9991157	0.4699953
17	8.15	0.7562055	0.4820707
18	8.4	0.5223417	0.5095949
19	8.65	0.2910322	0.5409172
20	8.9	0.1527159	0.7155896

Table 7 \bar{n} And pL values of Ligand 3, 4, 5-TBT with Cu (II) in TX-100

Sr. No	pH	pL	\bar{n}
1	4.4	4.3516715	0.1209872
2	4.65	4.0950195	0.1062395
3	4.9	3.8606959	0.1397405
4	5.15	3.6316069	0.1834835
5	5.4	3.4148978	0.251231
6	5.65	3.1917471	0.3039875
7	5.9	2.964608	0.3476486
8	6.15	2.7311103	0.3783573
9	6.4	2.5097855	0.4305816
10	6.65	2.2719462	0.452093
11	6.9	2.0471427	0.4959913
12	7.15	1.8206339	0.5357724
13	7.4	1.5858077	0.5608433
14	7.65	1.3446059	0.5751775
15	7.9	1.1101103	0.6001621
16	8.15	0.8706056	0.6168094
17	8.4	0.6174987	0.6116873
18	8.65	0.3832954	0.6364367

Fig. 2 Formation curve b/w \bar{n} and pL in alc. + water medium

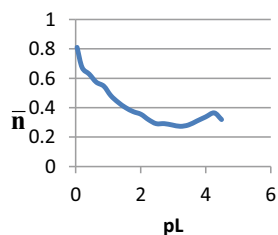


Fig. 3 Formation curve b/w \bar{n} and pL in alcoholic medium

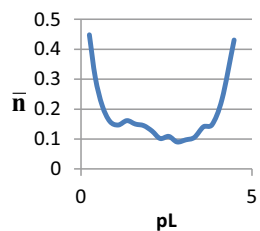


Fig. 4 Formation curve b/w \bar{n} and pL in HTAB medium

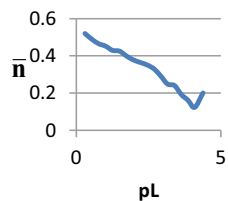


Fig. 5 Formation curve b/w \bar{n} and pL in SDS medium

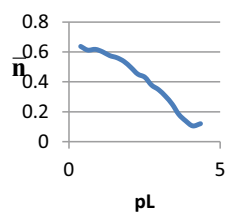
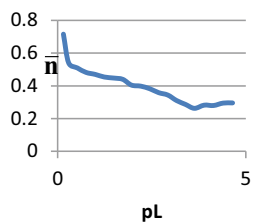


Fig. 6 Formation curve b/w \bar{n} and pL in TX-100 medium



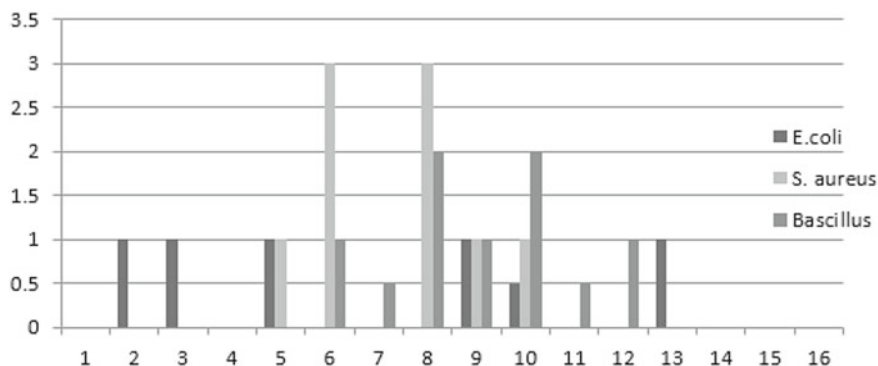


Fig. 7 Biological activity of thiosemicarbazone ligand and metal complexes

References

- Demertzi DK, Domopoulou A, Demertzis MA, Valle G, Papageorgiou AJ (1997) Palladium(II) complexes of 2-acetylpyridine N(4)-methyl, N(4)-ethyl and N(4)-phenyl-thiosemicarbazones. Crystal structure of chloro(2-acetylpyridine N(4)-methylthiosemicarbazonato) palladium(II). Synthesis, spectral studies, in vitro and in vivo antitumour activity. *Inorg Biochem* 68:147–155
- Ratner ES, Zhu YL, Penketh PG, Berenblum J, Whicker ME, Huang PH, Lee Y, Ishiguro K, Zhu R, Sartorelli AC, Lin Z (2016) Triapine potentiates platinum-based combination therapy by disruption of homologous recombination repair. *Br J Cancer* 114:777–786
- Nutting CM, Van LH, Miah AB (2009) Phase II study of 3-AP triapine in patients with recurrent or metastatic head and neck squamous cell carcinoma. *Ann Oncol* 20:1275–1279
- Ma B, Goh BC, Tan EH (2008) A multicenter phase II trial of 3-aminopyridine-2-carboxaldehyde thiosemi-carbazone (3-AP, triapine) and gemcitabine in advanced non-small-cell lung cancer with pharmacokinetic evaluation using peripheral blood mononuclear cells. *Invest New Drugs* 26:169–173
- Yuan J, Lovejoy DB, Richardson DR (2004) Novel di-2-pyridyl-derived iron chelators with marked and selective antitumor activity: in-vitro and in-vivo assessment. *Blood* 104:1450–1458
- Whitnall J, Howard P, Ponka Richardson DR (2006) A class of iron chelators with a wide spectrum of potent antitumor activity that overcomes resistance to chemotherapeutics. *Proceeding of national academy of sciences*, vol 103, pp 14901–14906
- Lobana TS, Sanchez A, Casas JS (1997) Synthesis, characterization, and in vitro cytotoxic activities of benzal-dehyde thiosemicarbazone derivatives and their palladium (II) and platinum (II) complexes against various human tumor cell lines. *J Chem Soc* 22:4289–4300
- Irving HM, Rosstti HS (2009) The calculation of formation curves in mixed solvents. *J Chem Soc* 2904–2910
- Mohammadzadeh T, Sadjjadi SM, Habibi P, Sarkari B (2012) Comparison of agar dilution, broth dilution, cylinder plate and disk diffusion methods for evaluation of anti-leishmanial drugs on leishmania promastigotes. *Iran J Parasitol* 7(3):43–47
- Singh BK, Mishra P, Prakash A, Bhojak N (2012) Spectroscopic electrochemical and biological studies of the metal complexes of the Schiff base derived from pyrrole-2-carbaldehyde and ethylenediamine. *Arab J Chem* 10:S472–S483
- Pund DA, Bhagwatkar RA, Tavade DT, Rathod DB (2009) Studies on interaction between La (ii), and Nd (iii) metal ions and 1-(4-hydroxy-6-methyl pyrimidino)-3-substituted thicarbamide at 0.1 M ionic strength pH metrically. *Rasayan J Chem* 2(3):246–249

12. Janrao DM, Pathan J, Kayande DD, Mulla JJ (2014) An over view of potentiometric determination of stability constants of metal complexes. *Sci Rev Chem Commun* 4(1):11–24
13. Gakkhar N, Bhatia, Bhojak N (2015) Comparative study on physiochemical properties of various milk samples. *Int J Recent Sci Res* 6(6):4436–4439

Aging of a Thermoplastic Polymer Under the Combined Effect of Ultraviolet Ray and Temperature



Sonya Redjala, Said Azem, and Nourredine Ait Hocine

1 Introduction

The PC is appreciated for its properties such as transparency, impact resistance and ease of processing. It is used in several applications such as vehicle components, displays as well as in construction and greenhouses. However, its exposure to bad weather triggers physical [1] and chemical [2] aging mechanisms. As a result, these mechanisms cause structural changes and alter its various properties over time [3–5].

In this article, we have studied mixed aging, which consists of exposure of polycarbonate samples to a combined action of UV and temperature. For this, aging under UV-C ($\lambda = 253$ nm) combined with isothermal treatments at 40, 80 and 120 °C for 72, 144 and 216 h were carried out on the polycarbonate of bisphenol A. Observations under an optical microscope, physico-chemical and thermal analyses were then carried out in order to demonstrate the effects of aging on the various properties.

2 Experimental Techniques

2.1 Aging

The polycarbonate samples were aged in a heating chamber with UV lamps made of aluminum with dimensions of $50 \times 20 \times 40$ cm³. This is equipped with two Philips-type UV lamps producing radiation with a wavelength of 253 nm and energy

S. Redjala (✉) · S. Azem
Department of Mechanical Engineering, Mouloud Mammeri University of Tizi-Ouzou, Tizi Ouzou, Algeria

N. A. Hocine
Institute of Applied Sciences of Tours (INSA), Lyon, France

of 4.3 eV. They are mounted under the vault with ventilation to prevent degradation under the effect of heat. Inside the enclosure, an electrical resistance is used to heat the samples to a controlled temperature. A sheet is installed above the resistance to properly distribute the heat in the enclosure. The samples are placed on a metal grid allowing rapid homogenization of the temperature. A sensor records the temperature in the vicinity of the specimens and transmits the information to a Eurotherm type regulator which allows the heating rate to be controlled and the set temperature to be maintained by means of a power dimmer. Thermal insulation is provided by a layer of alumina wool placed on the walls and floor of the enclosure. Note that only one side of the samples is directly exposed to UV radiation.

2.2 *Different Analyses Used*

Characterization by optical microscopy (OM). Micrographs of virgin and aged PC were obtained using an Olympus BX60 type optical microscope (MO) which can magnify the image up to 1000 times.

X-ray diffraction (XRD). XRD analyses were carried out on samples aged under UV combined with temperature, which revealed a change in crystallinity caused by the aging of this material.

A Brucker D8 Advance type X-ray diffractometer, with a θ - 2θ assembly was used for this purpose. It is equipped with a 40 kV high voltage generator, which accelerates the electrons in copper anode X-ray tube with a $K\alpha$ line of 1.54 Å. The scan interval was set from 5 to 60° with a step of 0.02° and an exposure time of one second per step. The software driving the device is Spectrum V5.3.1. The tube remains stationary while the detector is stepping while the sample is rotating. When the sample forms an angle θ with the incident beam, the detector moves to 2θ to record the diffracted radiation.

The $1 \times 1 \text{ cm}^2$ surface sample is placed on a hollow sample holder so that the surface to be analyzed is at the same level as the reference surface of the sample holder in order to avoid line shifts. The sample holder is then fixed in its housing by a magnetization system provided for this purpose.

Differential thermal and thermogravimetric analysis (DTA/TGA). Differential thermal analysis (DTA) consists of recording the endothermic and exothermic effects, which are the consequences of reaction or transformation taking place in the material during a thermal cycle. To do this, the sample is placed in a boat next to a second boat containing a reference sample (alumina powder). The two nacelles are arranged on two thermocouples mounted in opposition so as to be able to record the TDA signal which is the difference between the signals of the two thermocouples. Thus, any release or absorption of heat by the sample will be recorded. This manifests itself on the TDA curve as an exothermic or endothermic peak. This analysis therefore allows the detection of any transformation that is accompanied by a thermal effect such as,

for example, melting and crystallization, which are, respectively, endothermic and exothermic.

Thermogravimetric analysis (TGA) is the instantaneous measurement of the variation in the mass of a sample as it is heated. The curves reveal the temperatures of certain phenomena, which are accompanied by changes in mass, such as for example oxidation, decomposition, etc.

The sample, weighed beforehand, is placed in a basket placed at the end of a ceramic rod. A silicon carbide (SiC) resistor furnace is used to heat the sample at a controlled rate. The rod is mounted on an analytical balance to note, via a sensor, any change in the mass of the sample during heat treatment. In this way, it is possible to determine the temperature of the phenomenon, which is at the origin of the change in mass. The signal of the derivative of the TGA “d (TGA)” makes it possible to precisely identify this temperature.

The device used is of the PERKEN ELMER Diamond TGA/DTA type. The 10 mg sample is heated up to 800 °C with a heating rate of 10 °C/min. This device records the thermal effects of reactions or transformations that take place during heating of the sample. At the same time, the mass is weighed instantly, by an analytical balance, which allows a recording of any change in the mass of the sample. In order to avoid oxidation of the sample, we performed our tests in a dynamic nitrogen atmosphere.

The samples for thermal analyses were obtained by cutting strips of one millimeter thick and a few milligrams from the face exposed directly to UV radiation using a wire cutter. These samples are weighed using an analytical balance.

3 Results and Discussions

3.1 *Metallographic Observations*

We note the presence of cracks on the surface of the sample aged for 216 h under the combined action of UV and the temperature of 40 °C (Fig. 1a). Micrographs of samples aged at 80 and 120 °C show cavities and particles, respectively, as well as surface waves as shown in Fig. 1b, c, respectively.

3.2 *X-ray Diffraction*

Aging under UV combined at a temperature of 40 °C. Figure 2 shows diffractograms of PC aged under UV combined at the temperature of 40 °C for 72, 144 and 216 h. It appears that the intensity of the diffraction peak changes with the duration of aging. An increase in this intensity is observed at the same level for aging times of 72 and 216 h. On the other hand, for 144 h, there is a decrease in intensity to a value lower than that of the virgin material accompanied by a shift of the line toward the

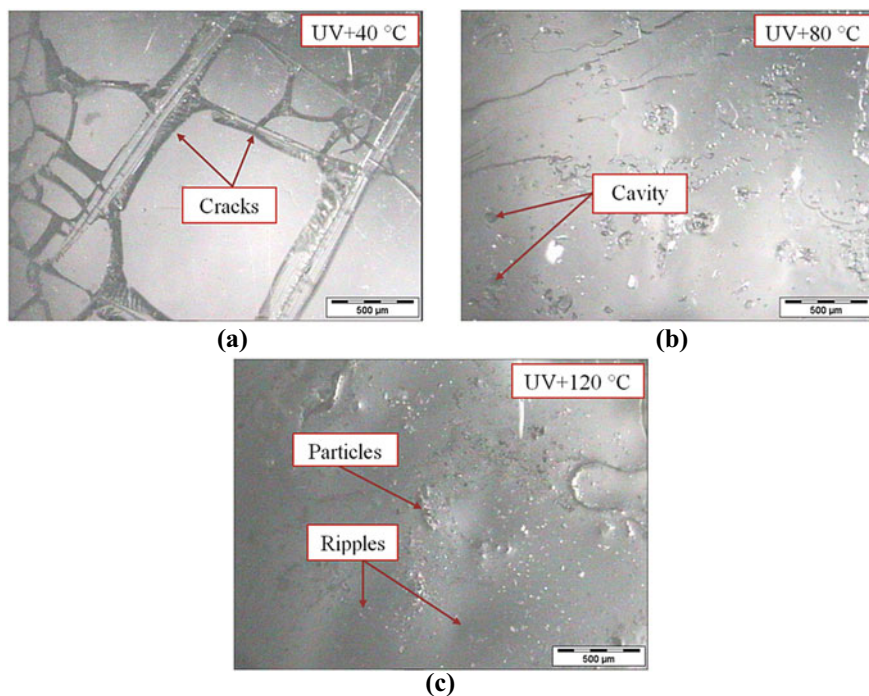
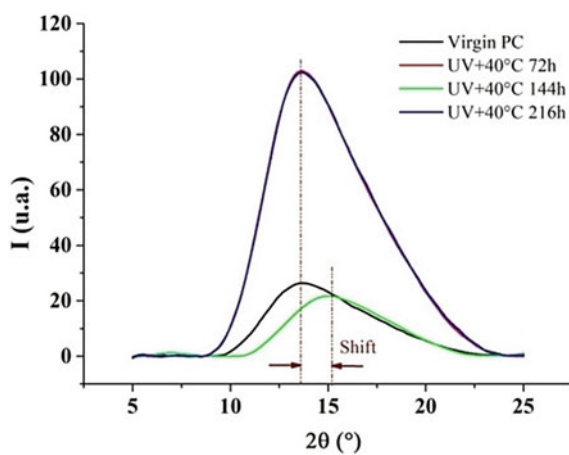


Fig. 1 Optical micrographs of the PC aged under UV combined at **a** 40, **b** 80 and **c** 120 °C for 216 h

Fig. 2 XRD of PC aged with UV combined at 40 °C for 72, 144 and 216 h



large angles of diffraction. The increase in intensity corresponds to an increase in the rate of crystallinity while its decrease reflects an amorphization of the material. Indeed, at short times, the material begins to undergo the phenomenon of physical aging under the effect of UV and temperature [1, 2]; the molecular chains become mobile and rearrange themselves more in the crystalline areas. When the duration is medium (144 h), the more vulnerable bonds begin to break, which disturbs the order in the crystallites. This then results in a decrease in the intensity of the diffraction peak with a shift corresponding to a tightening of the molecular chains in the crystallites. Over a longer period (216 h), the free radicals, formed by bond breakage, undergo a crosslinking phenomenon which again increases the crystallinity which manifests itself by an increase in the intensity of the diffraction peak [6]. Thus, it seems that the phenomena of bond breaking and crosslinking are successive and contribute to a modification of the structure as a function of the aging period.

UV aging combined at a temperature of 80 °C. When the temperature increases to 80 °C, the increase in diffraction intensity, for 72 h, is relatively smaller than that observed for a temperature of 40 °C (Fig. 3). For 144 h of aging, there is also an amorphization which results in a relatively greater decrease in the intensity of the diffraction peak. We observe a shift of the peak toward the large angles, which is the greater the longer the duration.

UV aging combined at a temperature of 120 °C. Thus, it appears that the increase in temperature disrupts the order in the crystallites for aging times of 72 and 144 h. For the duration of 216 h, the intensity increases again due to the phenomenon of crosslinking favorable to the increase in the rate of crystallinity [7].

Aging at 120 °C causes a gradual increase in crystallinity for 72 and 144 h of aging. On the other hand, for a period of 216 h of aging, the material is strongly amorphized. This is evidenced by the diffractogram of Fig. 4 which shows a strong attenuation of the intensity of the diffraction peak.

Fig. 3 XRD of the PC aged with UV combined 80 °C for 72, 144 and 216 h

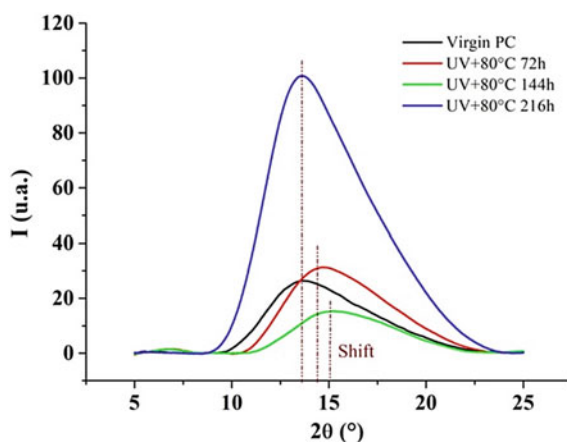
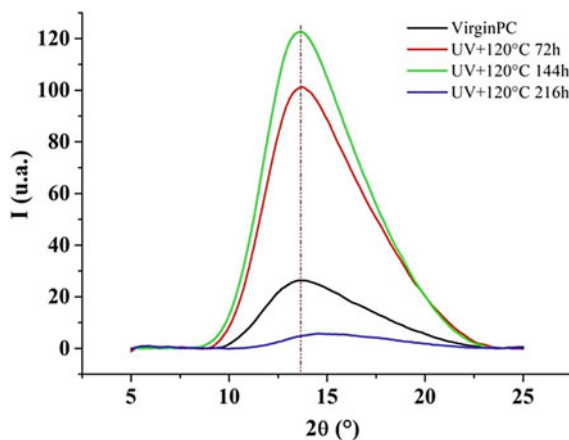


Fig. 4 XRD of the combined UV aged PC at the temperature of 120 °C for 72, 144 and 216 h



3.3 Thermal Degradation

Thermogravimetric and differential thermal analysis. Figure 5a–c shows the thermogravimetric curves of virgin and UV aged PC combined at temperatures of 40, 80 and 120 °C, for periods of 72, 144 and 216 h, respectively. These curves all reveal a reduction in the mass of the samples, which reflects a decomposition of material by the release of volatile products; in this case, carbon monoxide and carbon dioxide, as well as water vapor [8]. It can be seen that these curves have different slopes depending on the aging parameters. The rate of degradation corresponds to the slope of the TG curve.

Figure 6a–c shows the derivatives of the thermogravimetry curves of virgin and UV aged PC combined at the temperatures of 40, 80 and 120 °C for periods of 72, 144 and 216 h, respectively. The peak of the derivative corresponds to the temperature at which the rate of degradation is maximum (zoom of Fig. 6).

Figure 7a, b shows the variations of the temperature of the onset of degradation and of the average rate of degradation of the PC as a function of the aging time under UV combined at the temperatures of 40, 80 and 120 °C (Table 1).

This figure shows that the temperature at the start of degradation decreases at the short durations (72 h) of aging of the PC then increases at the long and medium durations for temperatures of 40 and 80 °C. On the other hand, for the aging temperature of 120 °C, the temperature at the start of degradation decreases at low and medium aging times. However, it grows over long durations while remaining less than that of the virgin PC. Thus, it seems that aging under UV combined with a temperature of 40 °C increases thermal stability especially at long periods. On the other hand, as soon as the aging temperature becomes high (120 °C), the thermal stability is affected regardless of the aging period. When UV rays are accompanied by heating at low temperature, the PC undergoes physical aging which makes it more stable at

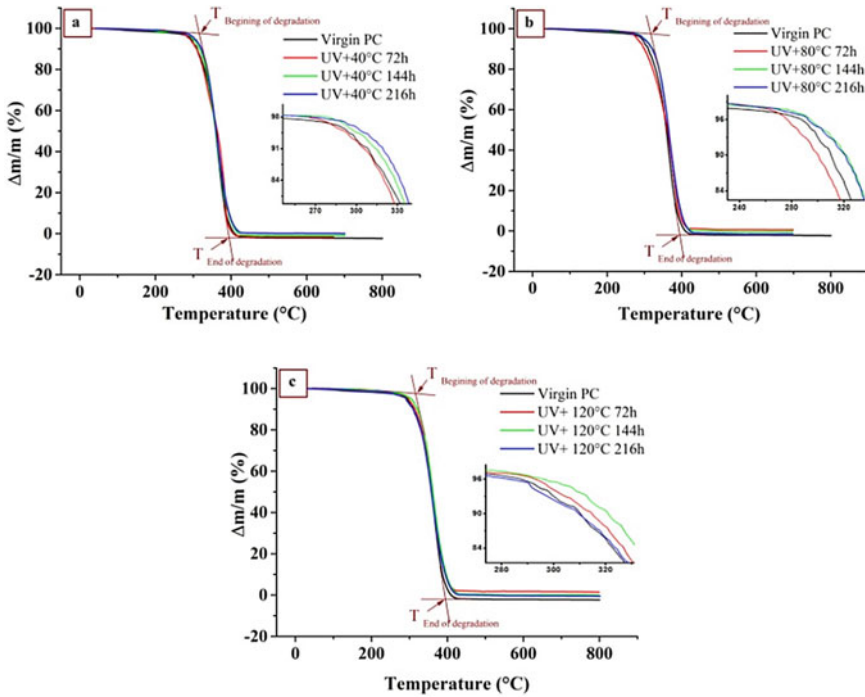


Fig. 5 Thermograms (TG) of virgin and UV aged PC combined at temperatures: **a** 40 °C; **b** 80 °C; **c** 120 °C, for 72, 144 and 216 h

temperature, but as soon as the aging temperature increases, bond breaks are possible which favors the reduction of thermal stability aged material [7].

It is noted that the degradation rate follows the same pattern as the temperature at the start of degradation as a function of the duration of mixed aging (UV + T).

Differential thermal analysis. Figure 8a–c shows the differential thermal analysis (DTA) curves of virgin and UV aged PC combined at temperatures of 40, 80 and 120 °C for periods of 72, 144 and 216 h, respectively. These curves reveal two endothermic peaks (denoted by 1 and 2) for the samples aged independently of the aging temperature. In contrast, the virgin material shows a single endothermic peak of ATD. A third endothermic peak (denoted by 3) is observed only for aging at 40 and 80 °C for 72 h. These endothermic peaks reflect decomposition phenomena that take place by breaking of bonds under the effect of temperature and UV. The surfaces of these peaks correspond to the energies brought into play during the various decompositions.

Note that these peaks have different surfaces, which explains why the decomposition reactions require relatively lower energy when some of the bonds concerned are already broken during aging. On the other hand, when during aging, there is formation of a new substance by crosslinking and oxidation. It will take more energy to

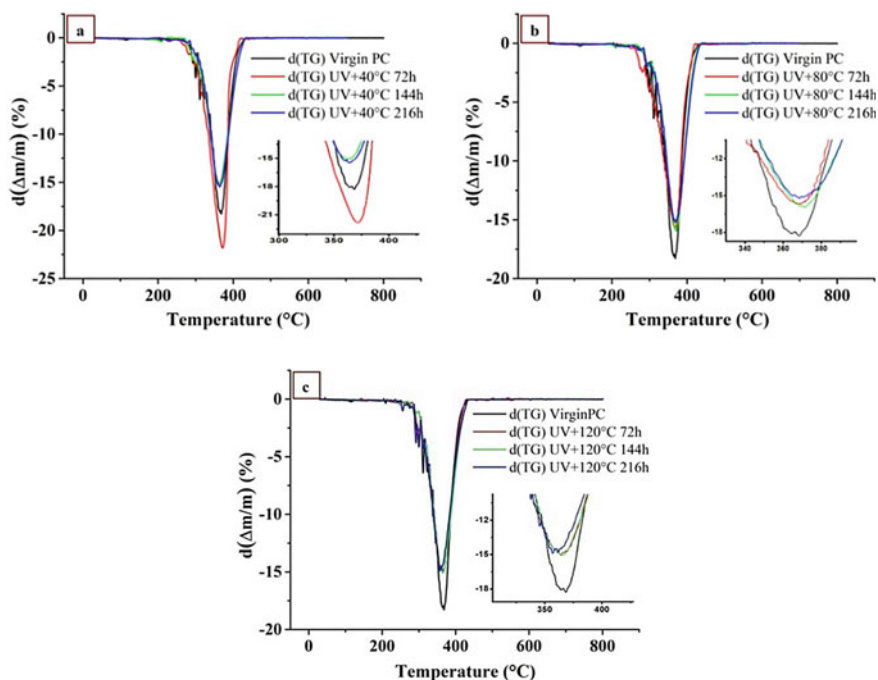


Fig. 6 TG derivatives of virgin and UV aged PC combined at: **a** 40 °C; **b** 80 °C; **c** 120 °C for 72, 144 and 216 h

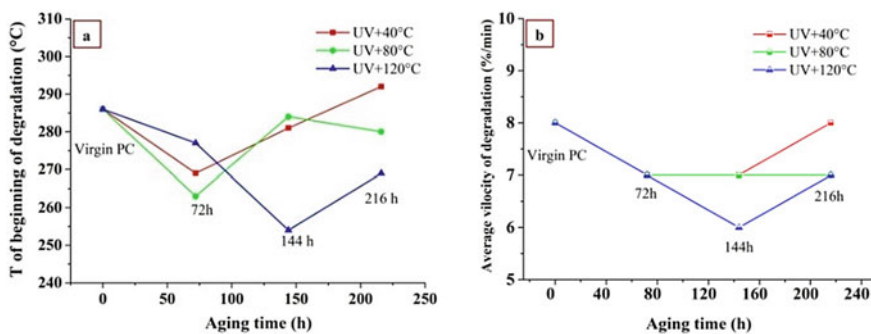


Fig. 7 **a** Temperatures at the start of degradation and **b** Average speeds as a function of time and temperature of aging

ensure its decomposition; in this case, the corresponding ATD peak will have a larger surface as shown in Fig. 8. In addition, the shift of peak 1 toward low temperatures shows that the structure of the material has undergone changes during aging.

The decomposition temperatures corresponding to the various peaks are reported in Table 2 as a function of the aging temperatures and the exposure times.

Table 1 Average speed (V_{avg}) and temperature interval of the start and end of degradation as a function of the aging time of virgin PC and aged under UV combined at 40, 80 and 120 °C

Times (h)	$T_{\text{Beginning of degradation}} (^\circ\text{C})$	$T_{\text{End of degradation}} (^\circ\text{C})$	Average rate (%/mn)
UV + 40 °C			
0	286	410	8
72	269	408	7
144	281	418	7
216	292	415	8
UV + 80 °C			
Times (h)	$T_{\text{Beginning of degradation}} (^\circ\text{C})$	$T_{\text{End of degradation}} (^\circ\text{C})$	Average rate (%/mn)
0	286	410	8
72	263	413	7
144	284	420	7
216	280	421	8
UV + 120 °C			
Times (h)	$T_{\text{Beginning of degradation}} (^\circ\text{C})$	$T_{\text{End of degradation}} (^\circ\text{C})$	Average rate (%/mn)
0	286	410	8
72	277	417	7
144	254	423	6
216	269	419	7

4 Conclusion

PC subjected to the combined action of UV and temperature undergoes a significant deterioration of its properties. The modification of these properties is a consequence of the splitting of molecular chains induced by the action of UV energy and temperature and the appearance of surface damage is presented by ripples revealed by optical microscopy.

Ordered areas after aging are evidenced by increased intensities of the X-ray diffraction peaks as well as an increase in crystal volumes is revealed by a shift in the diffraction peaks of aged materials. On the other hand, there is an amorphization of the PC as a function of the aging time, revealed by DRX.

An increase in thermal stability, due to the physical aging of the material, signifies a delay in the thermal degradation of the PC which has been demonstrated by thermogravimetry and by differential thermal analysis. Additionally, ATD shows that exposure of the PC to high temperatures results in breaks in the chemical bonds of the material indicated by decreasing peaks in ATD curves, meaning that the aged material requires less energy than the reference material.

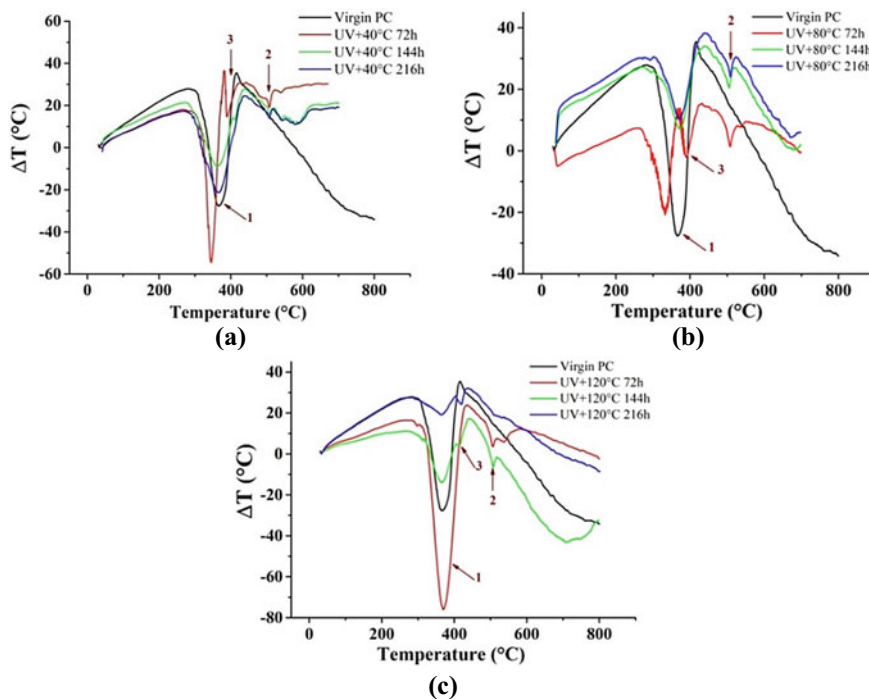


Fig. 8 TDA curves of virgin PC and aged under UV combined at **a** 40, **b** 80 and **c** 120 °C for 72, 144 and 216 h

Table 2 Decomposition temperatures

Times (h)	Peak 1 (°C)	Peak 2 (°C)	Peak 3 (°C)
UV + 40 °C			
0	360	/	/
72	345	508	390
144	363	508	409
216	366	507	404
UV + 80 °C			
Times (h)	Peak 1 (°C)	Peak 2 (°C)	Peak 3 (°C)
0	360	/	/
72	334	508	387
144	371	505	/
216	368	508	/
UV + 120 °C			
Times (h)	Peak 1 (°C)	Peak 2 (°C)	Peak 3 (°C)
0	360	/	/
72	371	506	418
144	365	506	413
216	363	508	/

References

1. Ho CH, Vu-Khanh T (2003) effects of time and temperature on physical aging of polycarbonate. *Theoret Appl Fract Mech* 39(2):107–116
2. Schnell H (1964) *Chemistry and physics of polycarbonate*, inter-science, New York
3. Sharma T, Aggarwal S, Sharma A, Kumar S, Mittal VK, Kalsi PC, Manchanda VK (2008) Modification of optical properties of polycarbonate by gamma irradiation. *Radiat Eff Defects Solids* 163(2):161–167
4. El-Ghazaly M, ShAydorous A, Al-Thomali TA (2013) Ultraviolet radiation of short wavelength (UVC) induced-modifications in optical properties of PADC. *Life Sci J* 10(4):2446–2450
5. Gogotov IN, Barazov SKh (2012) the effect of ultraviolet light and temperature on the degradation of composite polypropylene. *PLAST Massy* 12:55–58
6. Claude B, Gonon L, Duchet J, Verney V, Gardette JL (2004) Surface cross-linking of polycarbonate under irradiation at long wavelengths. *Polym Degradation Stab* 83:237–240
7. Diepens M, Gijssman P (2009) Outdoor and accelerated weathering studies of bisphenol A polycarbonate. *Polym Degrad Stab* 96:649–652
8. Yan Ch, Jian H, Zhang J, Zhao F, Liu Ch, Shen Ch (2016) The influence of sub-Tg annealing on environmental stress cracking resistance of polycarbonate. *Polym Test* 56:364–368

Effects of Additives and Treatment on Fly Ash-Based Polymer Composites



Sushant Patel, G. L. Devnani, and Deepesh Singh

1 Introduction

Fly ash which is also called fuel ash is result of burning of coal used in thermal power plants for the generation of electrical energy. In modern era, thermal power plants are mostly operated on burning of coal and the resulted fly ash is captured with the help of electrostatic precipitators or other equipment such as particle filtration. The coal is extracted from various parts of land not from one particular part; therefore, its composition varies depending upon the place from where it is extracted. But all types of coal contain some amount of silicon dioxide, aluminium oxide and calcium oxide which all are found in fly ash when the coal is burned. In early days when coal was first used power plants, fly ash that was produced was dumped into land near the power plants. In the beginning, people did not noticed that it was harmful to humans as well as environment. But when it was noticed, various laws were passed to contain the unsafe dumping of fly ash. It was advised to use various equipment which were helpful in pollution control. Therefore, disposal and utilization of fly ash is a major issue observed by academicians and researchers. Reinforcement in various polymer matrix to form composites is an option which can give a new way of sustainable development and diversity of applications in the field of material science and composites. Nowadays, concrete is mostly used in construction works, and binding material is mainly cement. But using cement is also a problem because it results in emission of 8% of global carbon dioxide. Therefore, many studies suggest that if we use geopolymer concrete than normal concrete, than it can lower the emission of carbon dioxide as its binding material consists fly ash [1]. Due to this reason, almost 15% of fly ash produced in India is used to manufacture the concrete. In

S. Patel (✉) · D. Singh
Civil Engineering Department, HBTU, Kanpur, India

G. L. Devnani
Chemical Engineering Department, HBTU, Kanpur, India

year 2012–2013 in India, 163.56 million tone of fly ash was generated in comparison with year 1996–1997 in which 68.88 million tone was generated, out of which 63.17% of ash was utilized [2]. Composition of fly ash varies in different ways as bituminous fly ash contains SiO_2 (20–60%), Al_2O_3 (5–35%), Fe_2O_3 (10–40%), CaO (1–12%), LoI (0–15%). Similarly subbituminous fly ash contains silica oxide (40–60%), Al_2O_3 (20–30%), Fe_2O_3 (4–10%), CaO (5–30%), LoI (0–3%), and lignite fly ash contains SiO_2 (15–45%), Al_2O_3 (20–25%), Fe_2O_3 (4–15%), CaO (15–40%), LoI (0–5%) [3]. Fly ash can also be used for making bricks. Normally clay is used to make bricks, but if used fly ash, then it can help in removing fly ash from open grounds or dumpsters. As dumping of fly ash also results in ground pollution. If we use 25% fly ash in making bricks, it can help in reduction of weight by 18%, but it will not affect the strength of bricks [4]. Utilization of fly ash in geopolymer composites increases its strength, but if it is exposed to sulphuric acid, then it does not help much but if we use some amount of OPC in it, then it can further increase its strength. Because OPC can resist sulphuric acid greatly [5].

2 Fly Ash Composites

A composite is a material which is formed by combining two or more materials having separate physical and chemical properties. When the two materials are mixed, it is done with the purpose of creating a material to complete a specific task, such as to make a material stronger than usual, or lighter or immune to electric currents. Most of the composite materials are mixture of two materials only. One of which is the matrix or also known as binder. Purpose of the binder is to bind or surround the fibres or particles of other material. The other material is called reinforcement. The first composite material formed in modern time was fibreglass. There are various reasons to use composite materials. One of the main reasons to use composite materials is because of its unique properties such as its ability to save its weight in relative stiffness and strength. Reinforcement of fly ash in polymer matrix can not only serve the purpose of its disposal and at the same time can provide distinct properties as compared to individual phase. These polymer matrix may be thermoset or thermo polymer depending on the requirement of application. Some widely used polymer matrix in which reinforcement of fly ash has been applied is discussed below.

2.1 HDPE Based Composites

HDPE is the most common and important thermoplastic product made from petroleum, and it is in high demands in recent times due to its high strength, toughness, cost-effective nature; less permeable to moisture and other oxidizing agents; fine elongation property; and its ability to remain unaffected for surface impacts. It can also be used for various applications such as packaging or other commercial

purposes. If we melt down fly ash and mix with HDPE, it will increase its flexural property [6]. If we further study three other methods to study the impact fly ash composites such as Maleic Anhydride grafting method of matrix, electron beam irradiation method and irradiation method of fly ash/ nano-fly ash separately then out of these three methods we will find that electron beam irradiation of HDPE–fly ash/nano-fly ash results in tremendous increase in physio-mechanical, thermal and dynamic mechanical properties [7]. These results are the proof that fly is very useful reinforced filler material for HDPE and its reduced size, i.e. nano-level is further more useful for future applications [8].

2.2 LDPE Based Composites

These days composites are most commonly used attributes because of its differentiable characteristic which is acquired by the mixing of components. As we spend more time on this planet, this planet or the people are moving towards the direction in which we will be using green technology. Nowadays, fly ash-based polymers are used as filler materials for producing LDPE based fly ash composites. Now if we increase the filler loading in these composites, it will increase its tensile strength as well as it will also increase its modulus of elasticity, but it will also decrease the percentage of elongation [9].

2.3 Epoxy-Based Composites

Epoxy-based composites are low molecular weight pre-polymer or high molecular weight polymers containing at least two epoxide groups. They are mainly used for surface coatings. Liquid epoxy composites have extraordinary ability of mixing and processing with the reinforcement materials in granular form or fibre form [10]. But the overall outcome depends on the combined effort of the materials. Metallic filled composites are mostly deployed in moulds manufacturing, so that small parts of plastics can be manufactured. These mixtures of fibres and aluminium are used for optimizing mechanical and thermal properties of composites for rapid tooling applications [11]. There are various researches done on the epoxy-based composites due to its lightweight and other significant properties in one of these types of studies it is shown that even if we use nano-filler material in smallest ratio possible it will improve the mechanical and thermal property of fly ash-based composites [12]. It was also noted that if we use 5 wt% of fly ash and 2.5 wt% of graphene as filler materials in the manufacturing of composites, then these composites have higher hardness value compared to other fly ash-based composites [13].

2.4 *PLA Based Composites*

PLA {poly lactic acid} is a matrix material which is used in composites to hold the reinforcing fibres. It is biodegradable in nature; therefore, it is used for making biocomposite materials. In last few decades, PLA based polymer composites are being studied and researched because of the unique properties of these composites such as biocompatibility or biodegradability. Therefore, in one of these researches, electrical and thermal conducting polymer composites were developed on their biodegradable PLA basis [14]. Later, it was found that if we add 1% CNT, then thermal conductivity of ternary PLA composites will increase by at least by 40% compared to binary PLA composites.

In one of the other studies, it was concluded that heat or ionizing radiation-based adhesive composites formulation can offer sufficient strength comparable to shear stress and degree of substrate failure {50–90%} for a variety of adhesive loading in the range of 95 g/m² and 300 g/m² [14].

2.5 *PVA Based Composites*

Polyvinyl alcohol is a colourless usually non-toxic thermoplastic adhesive prepared by polymerization of vinyl acetate. Polyvinyl alcohol is a synthetic polymer and is also considered as true biodegradable product as it is superbly hydrophilic and biocompatible. Many researches are being done to review mechanical and water absorption property of PVA bases composites [15]. There are many researches or studies done on PVA mainly to study the effect on mechanical properties of PVA based composites while using fibres as reinforcing materials to manufacture PVA blend films. It was found that one of the serious disadvantages of PVA based composites was its high usage or its high solubility in water. Researches are being done to nullify this disadvantage as well as other disadvantages such as high cost, high water absorption. So that PVA based composites can have a further applications in different fields [16]. Table 1 presents the brief compilation and key findings of fly ash-based polymer composites.

3 Conclusion

Fly ash is a very useful material to be reinforced in various polymer matrix. Optimization of loading and treatment method is very important to get superior results. Proper combination of matrix, fly ash additive and treatment methodology can give promising results and improve the quality of composites. It also helps us in recycling of fly ash because if it is not recycled then it causes health-related problems to humans and other environmental problems [20].

Table 1 Fly ash reinforced different polymer composites

S. no.	Matrix used	Composition	Key result	References
1	HDPE	15–20% fly ash	At 20% by weight flexural strength of the composites is maximum, flexural modulus is also maximum (1260 MPa)	[6]
2	LDPE	20–30% fly ash	At 25% by weight compressive strength improved by 1.44 times and flexural strength improved by 2.16 times	[9]
3	PVA	0.5% crosslinking glyoxal and PVA	It resulted in swelling power decreased from 105.6% to 78.3%	[16]
4	PLA	1.0 wt% of CNT	It was noticed that by adding 1.0% weight of CNT thermal conductivity increased from 10 to 40%	[14]
5	Epoxy	10% fly ash	Stability of blend increased with increase in fly ash content in epoxy	[12]
6	Epoxy	Fly ash volume fraction (10–50%)	It is shown that if the volume fraction is 50%, then the compressive strength is 165.6 MPa which is highest	[6]
7	Epoxy-based composites	NaOH solution 5%, 6% and 10%	It was observed that 10% solution flexural strength of fibre composites was highly improved	[17]
8	PVA based composites	Synthesization of PVA & MXenes	It was observed on their synthesization that thermal conductivity of PVA based polymer composites was highly improved to 47.6 W/(mK), which is higher than some metals	[18]
9	PLA based composites	Helical carbon nanotubes (HCNTs) interacted with PLA matrix	When the procedure was complete, the impact strength value was improved 30%	[19]

- It was noticed that fly ash-based modified epoxy composites with surface treatment have greater impact strength.
- Compressive strength of fly ash composites was found to be improved.
- Flexural strength was also improved.
- It also solves the environmental pollution problem.

References

1. Cai J, Pan J, Li X, Tan J, Li J (2020) Electrical resistivity of fly ash and metakaolin based geopolymers. *Constr Build Mater* 234:117868. <https://doi.org/10.1016/j.conbuildmat.2019.117868>
2. Yao ZT, Ji XS, Sarker PK, Tang JH, Ge LQ, Xia MS et al (2015) A comprehensive review on the applications of coal fly ash. *Earth-Sci Rev* 141:105–121. <https://doi.org/10.1016/j.earsci.2014.11.016>
3. Chou M (2012) IM. Fly ash fly ash. *Encycl Sustain Sci Technol* 2012:3820–3843. https://doi.org/10.1007/978-1-4419-0851-3_121
4. Abbas S, Saleem MA, Kazmi SMS, Munir MJ (2017) Production of sustainable clay bricks using waste fly ash: mechanical and durability properties. *J Build Eng* 14:7–14. <https://doi.org/10.1016/j.jobbe.2017.09.008>
5. Mehta A, Siddique R (2017) Sulfuric acid resistance of fly ash based geopolymer concrete. *Constr Build Mater* 146:136–143. <https://doi.org/10.1016/j.conbuildmat.2017.04.077>
6. Satapathy S, Nando GB, Nag A, Raju KVS (2013) HDPE-fly ash/nano fly ash composites. *J Appl Polym Sci* 130. <https://doi.org/10.1002/app.39733>
7. Kumar B, Garg R, Singh U (2012) Utilization of flyash as filler in Hdpe/flyash polymer composites: a review. *Int J Appl Eng Res* 7
8. Satapathy S, Kothapalli RVS (2018) Mechanical, dynamic mechanical and thermal properties of banana fiber/recycled high density polyethylene biocomposites filled with flyash cenospheres. *J Polym Environ* 26. <https://doi.org/10.1007/s10924-017-0938-0>
9. Authors F. Akhilendra Kumar Singh (2016)
10. Abdellaoui H, Raji M, Bouhfid R, Qaiss A el kacem (2018) Investigation of the deformation behavior of epoxy-based composite materials. *Fail Anal Biocompos Fibre Reinf Compos Hybrid Compos* 2018:29–49. <https://doi.org/10.1016/B978-0-08-102293-1.00002-4>
11. Sim J, Kang Y, Kim BJ, Park YH, Lee YC (2020) Preparation of fly ash/epoxy composites and its effects on mechanical properties. *Polym (Basel)* 12:1–12. <https://doi.org/10.3390/polym12010079>
12. Tiwari S, Srivastava K, Cl G, Srivastava D (nd) Epoxy/fly ash from thermal power plant/nanofiller nanocomposite: studies on mechanical and thermal properties : a review 1–16. <https://doi.org/10.35248/2252-5211.20.10.375>
13. Jena PC (2019) Mechanical properties of fabricated CFRP with filler 1886–1892. <https://doi.org/10.35940/ijeat.E7166.088619>
14. Lebedev SM, Gefle OS, Amitov ET, Berchuk DY, Zhuravlev DV (2017) Poly(lactic acid)-based polymer composites with high electric and thermal conductivity and their characterization. *Polym Test* 58. <https://doi.org/10.1016/j.polymertesting.2016.12.033>
15. Ling Y, Wang K, Li W, Shi G, Lu P (2019) Effect of slag on the mechanical properties and bond strength of fly ash-based engineered geopolymer composites. *Compos Part B Eng* 164. <https://doi.org/10.1016/j.compositesb.2019.01.092>
16. Jain N, Singh VK, Chauhan S (2017) A review on mechanical and water absorption properties of polyvinyl alcohol based composites/films. *J Mech Behav Mater* 26:213–222. <https://doi.org/10.1515/jmbm-2017-0027>

17. Sood M, Dwivedi G (2018) Effect of fiber treatment on flexural properties of natural fiber reinforced composites: a review. *Egypt J Pet* 27:775–783. <https://doi.org/10.1016/j.ejpe.2017.11.005>
18. Liu R, Li W (2018) High-thermal-stability and high-thermal-conductivity Ti₃C₂T_x MXene/poly(vinyl alcohol) (PVA) composites. *ACS Omega* 3:2609–2617. <https://doi.org/10.1021/acsomega.7b02001>
19. Wang Y, Mei Y, Wang Q, Wei W, Huang F, Li Y et al (2018) Accepted manuscript
20. Wee LS, Lian OC (2019) Zain MRM. Mechanical properties of engineered cementitious composites using local ingredients. *J Mech Eng* 16

Powder Mixed Electrical Discharge Machining of EN 31 Steel



Rakesh Kumar Patel and M. K. Pradhan

1 Introduction

Machining of complex shape in difficult to machine material such as EN 31 (HRC 62) is troublesome by using conventional machining process. For machining of these difficult to machine material, advanced machining process such as ECM, LBM, EBM or EDM process, etc., can be used. In the advanced machining process, EDM gives better geometrical variation and good surface finish [1]. It uses short time multiple discharge of high-density current between tool and workpiece to remove the material [2, 3]. It can machine any electrically conductive material regardless of its physical properties. It is generally use in making mold, die, aerospace, automobile components, etc. The use of EDM is limited due to its low material removal rate (MRR), high surface roughness and high tool wear. To overcome these limitations, researchers had tried mixing of conducting and non-conducting powder particle in the dielectric fluid which increase the stability of the machining process and improves the EDM performance.

Powder mixed EDM (PMEDM) firstly invented in 1970 and first publication came in 1981 [1]. By adding conductive powder particle in the dielectric fluid, it helps in breakdown of dielectric, i.e., dielectric strength decreases due to decrease in dielectric strength the gap between the tool and workpiece increase [2–4] due to increase in inter electrode gap proper flushing take place and also due to adding of powder particle energy per pulse distributed in multiple discharges, so it creates shallow cavity and surface roughness (SR) decreased [5, 6] used graphite powder, peak current, pulse on time, voltage taken as input parameter and for experimentation uses response surface methodology to analyze the MRR and SR [7] added SiC powder and uses graphite and copper tool electrode and found better machining performance and decrease in white

R. K. Patel (✉) · M. K. Pradhan
Maulana Azad National Institute of Technology, Bhopal 462003, India

recast layer thickness [8] added multi walled carbon nano tube mixed dielectric for machining of aluminum metal matrix composite and get improved MRR and reduced SR.

In the present study, an attempt is made to machine EN31 steel alloy with advanced machining process PMEDM with two different tool material copper and brass electrode with peak current, pulse on time and concentration of micron size powder particle as input parameter and MRR, TWR and SR determined to the find the effect of input parameter.

2 Experimental Investigation

EN 31 steel used as a workpiece material. The hardness of the steel is measured using digital hardness tester and found the hardness value 63 HRC. Tool material solid copper and brass of circular shape 14 mm diameter used. EDM oil used as a dielectric fluid and SiC of micron size 45–50 μm used as additives. Attachment of PMEDM made on Electronica S-50 CNC machines as shown in Figs. 1 and 2. Machining of EN 31 with Cu in reverse polarity (workpiece positive, electrode negative) found difficulty so we have chosen normal polarity for Cu electrode and reverse polarity for brass electrode as shown in Fig. 3. Experiments are plan using Taguchi DOE L18 orthogonal array [9]. Table 1 shows the input parameter with its level used in experiment and Table 2 shows the Experimental plan and experimental results.

Fig. 1 Attachment of powder mixed EDM



Fig. 2 Attachment in EDM machine



Fig. 3 Machined workpiece



Table 1 Input parameters

Parameter	Low level	Medium level	High level
I_p (A)	5	15	25
T_{on} (μ sec)	100	200	300
Conc. (g/l)	0	5	10
Tool material	Cu	Brass	–

Table 2 Experimental results

Run	Tool	Ton (μ sec)	Ip (A)	Conc. (g/l)	MRR (mm^3/min)	TWR (mm^3/min)	Ra (μm)
1	Cu	100	5	0	5.2847	0.0309	5.7600
2	Cu	100	15	5	15.2474	0.9959	6.8016
3	Cu	100	25	10	17.1031	1.7579	7.8473
4	Cu	200	5	0	4.9465	0.0087	6.1210
5	Cu	200	15	5	20.8094	0.6239	9.2554
6	Cu	200	25	10	13.9874	0.6174	7.5099
7	Cu	300	5	5	4.3746	0.0233	5.7658
8	Cu	300	15	10	8.1980	0.0370	6.9728
9	Cu	300	25	0	38.8383	2.5319	11.3132
10	Brass	100	5	10	7.9361	0.6366	6.9915
11	Brass	100	15	0	4.0602	2.6050	9.9604
12	Brass	100	25	5	19.1141	5.0580	8.2221
13	Brass	200	5	5	6.3503	1.6319	6.9163
14	Brass	200	15	10	10.0403	0.2594	7.1491
15	Brass	200	25	0	16.6114	3.7899	11.0158
16	Brass	300	5	10	3.7550	0.3812	6.5702
17	Brass	300	15	0	6.5476	1.7270	12.1290
18	Brass	300	25	5	6.7339	0.5852	6.8851

3 Results and Discussion

MRR—Larger is better (Table 3)

TWR—Smaller is better (Table 4)

Surface roughness (SR)—Smaller is better (Table 5)

Figure 4 shows the effect of input parameter on MRR. From the graph and the calculated value of S/N ratio, it shows that all four parameters significantly influence the MRR. But peak current is more influencing input parameter. Figure 5 shows the effect of input parameter on TWR, and current is more influencing parameter.

Table 3 MRR response table for signal to noise ratios

Level	Tool	Ton	Ip	Conc
1	17.85	19.76	14.45	18.84
2	20.98	20.61	19.47	20.18
3		17.88	24.33	19.23
Delta	3.13	2.73	9.88	1.34
Rank	2	3	1	4

Table 4 TWR response table for signal-to-noise ratios

Level	Tool	Ton	Ip	Conc
1	-1.588	1.145	18.681	6.450
2	14.225	7.564	5.237	3.848
3		10.246	-4.963	8.656
Delta	15.813	9.102	23.644	4.808
Rank	2	3	1	4

Table 5 SR response table for signal-to-noise ratios

Level	Tool	Ton	Ip	Conc
1	-18.30	-17.49	-16.03	-19.08
2	-17.28	-17.88	-18.60	-17.18
3		-17.99	-18.73	-17.10
Delta	1.02	0.51	2.70	1.98
Rank	3	4	1	2

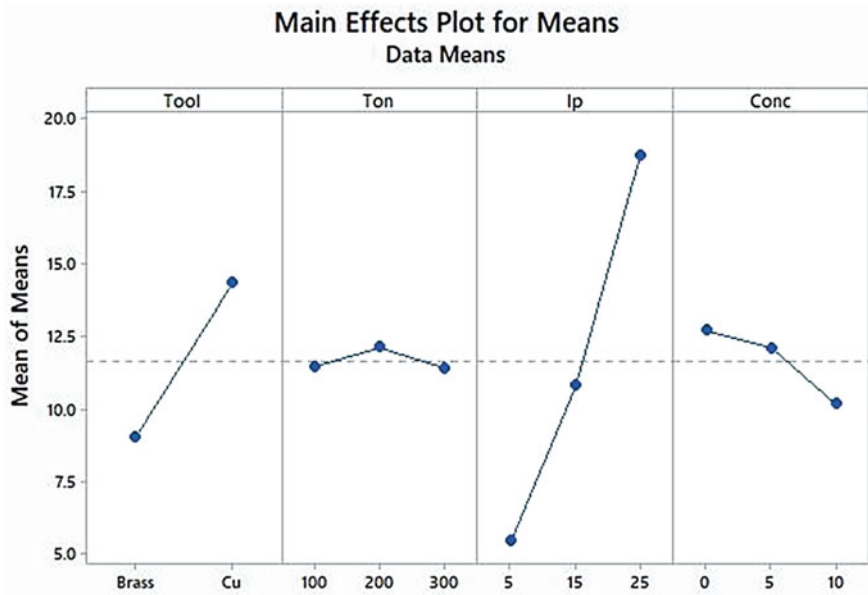


Fig. 4 Main effect plot for MRR

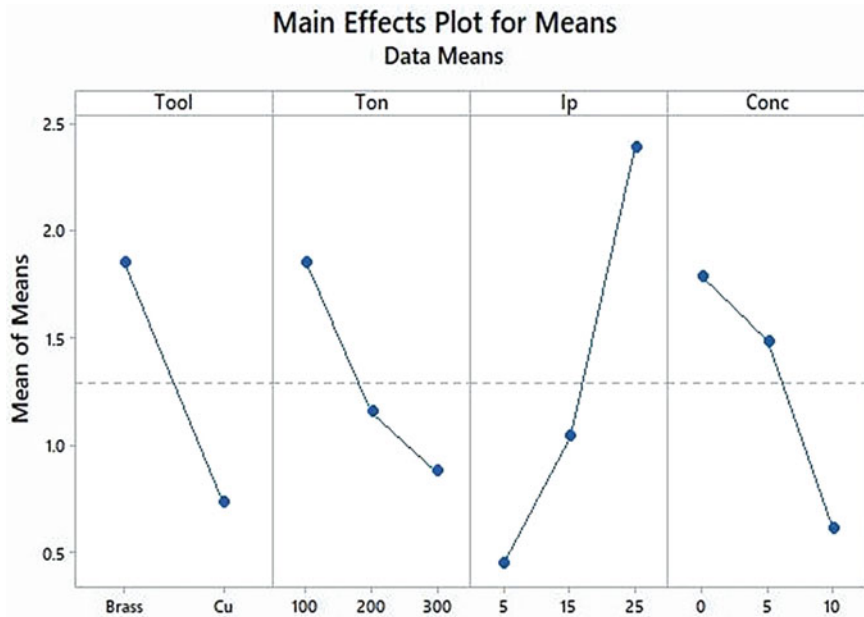


Fig. 5 Main effect plot for TWR

Figure 6 shows the effect of input parameters on the surface roughness. And all the input parameters significantly affect the SR concentration of the powder particle highly parameter compared to others. Figure 7 shows the Cu material tool electrode give better performance, i.e., higher MRR and lower TWR and SR as compared to brass tool electrode.

4 Conclusion

From the Taguchi analysis, peak current is highly influencing parameter for all the responses. Tool material also affects all the responses significantly. From the above experiment, it is found that tool is different for both the cases. For brass tool, material reverse polarity, i.e., tool negative and workpiece positive is giving good responses and for copper tool material normal polarity, i.e., tool positive and workpiece negative give better responses. By increasing the concentration of SiC powder, all the responses values are decreasing, so the surface quality improved, but the machining efficiency is not that much increased. So, for improving the surface characteristics, powder particle can be used in the dielectric.

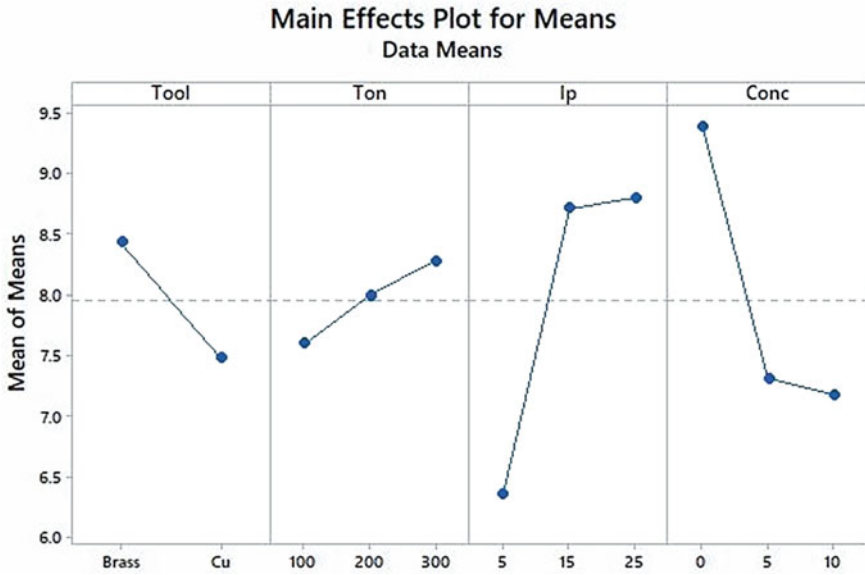


Fig. 6 Main effect plot for SR

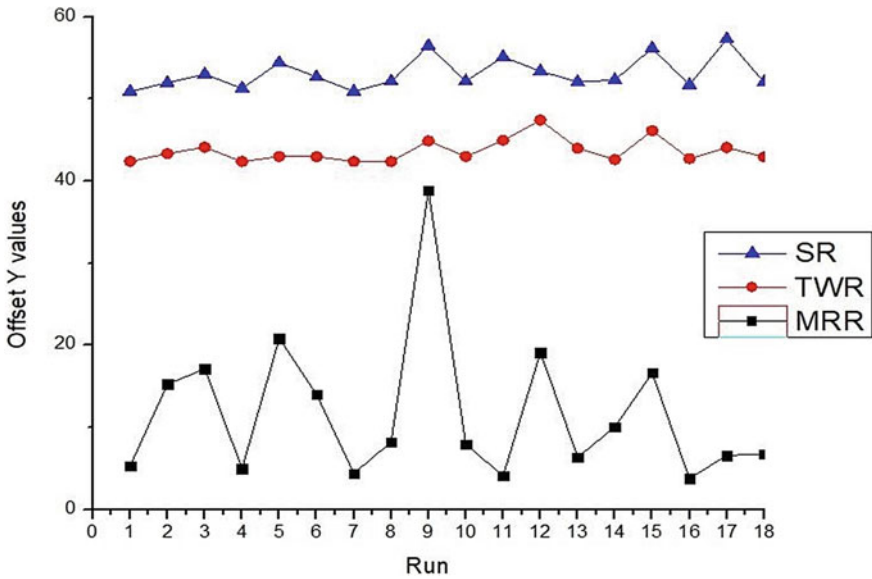


Fig. 7 Comparison of performances (Run 1–9—Cu Tool and 10–18—brass Tool)

References

1. Erden A, Bilgin S (1981) Role of impurities in electric discharge machining. *Proc Int Mach Tool Des Res Conf* 4:345–350. https://doi.org/10.1007/978-1-349-05861-7_45
2. Tzeng YF, Lee CY (2001) Effects of powder characteristics on electrodischarge machining efficiency. *Int J Adv Manuf Technol* 17(8):586–592. <https://doi.org/10.1007/s001700170142>
3. Mohri N, Saito N, Higashi M, Kinoshita N (1991) A new process of finish machining on free surface by EDM methods. *CIRP Ann Manuf Technol* 40(1):207–210. [https://doi.org/10.1016/S0007-8506\(07\)61969-6](https://doi.org/10.1016/S0007-8506(07)61969-6)
4. Kansal HK, Singh S, Kumar P (2007) Effect of silicon powder mixed EDM on machining rate of AISI D2 die steel. *J Manuf Process* 9(1):13–22. [https://doi.org/10.1016/S1526-6125\(07\)70104-4](https://doi.org/10.1016/S1526-6125(07)70104-4)
5. Ming QY, He LY (1995) Powder-suspension dielectric fluid for EDM. *J Mater Process Tech* 52(1):44–54. [https://doi.org/10.1016/0924-0136\(94\)01442-4](https://doi.org/10.1016/0924-0136(94)01442-4)
6. Mohanty G, Mondal G, Surekha B, Tripathy S (2018) Experimental investigations on graphite mixed electric discharge machining of En-19 alloy steel. *Mater Today Proc* 5(9):19418–19423. <https://doi.org/10.1016/j.matpr.2018.06.302>
7. Al-Khazraji A, Amin SA, Ali SM (2016) The effect of SiC powder mixing electrical discharge machining on white layer thickness, heat flux and fatigue life of AISI D2 die steel. *Eng Sci Technol Int J* 19(3):1400–1415. <https://doi.org/10.1016/j.jestch.2016.01.014>
8. Mohal S, Kumar H (2017) Study on the multiwalled carbon nano tube mixed EDM of Al-SiC p metal matrix composite. *Mater Today Proc* 4(2):3987–3993. <https://doi.org/10.1016/j.matpr.2017.02.299>
9. Pradhan MK (2010) Modeling and simulation of thermal stress in electrical discharge machining process. In: 4th international conference on advances in mechanical engineering, September 2010, pp 1–6

Simulation and Analysis of Hybrid Energy Resources in Chennai Using Homer Software



P. Abirami, M. Pushpavalli, V. Geetha, P. Sivagami, and R. Harikrishnan

1 Introduction

Our globe gets polluted due to industrialization and automation. The emission of gases from conventional energy sources is also a cause for polluting nature. The nature can be saved by using renewable sources in power generation. Though, many renewable sources are available solar power is one of the most widely used powers to supply a specific load. If a single PV source is supplying a load, then it is required to increase the size of system. To avoid complexities solar, wind, and battery storage systems are connected together to form hybrid energy sources. The resources are interconnected in order to track maximum energy from them. HRES can be able to supply the load continuously in both standalone and grid connected modes. The main motto in designing a hybrid system is to reduce the cost of design as well as to obtain efficient solutions. Still, researches are carried out to select a best methodology to achieve this. Among these methodologies, HOMER Pro is an efficient simulation software which is used to analyze both on grid and off grid hybrid systems. For computing, simulating, and optimizing hybrid systems HOMER software is introduced by National Renewable Energy Laboratory. Both technological and economic analysis is successfully simulated using HOMER PRO.

Rohit [1] explains about the energy needs of remote villages in India. HOMER software results are compared with conventional grid extension which concludes that the integration of sources without grid location is a cost-effective method. Singh et al. [2] designed a hybrid energy system to satisfy the load demand of MANIT Bhopal. Okedu and Uhunmwangho [3] computed the efficiency of renewable energy using HOMER Pro. Here, a system consists of different sources is investigated and finally

P. Abirami (✉) · M. Pushpavalli · V. Geetha · P. Sivagami
Sathyabama Institute of Science and Technology, Chennai, India

R. Harikrishnan
Symbiosis Institute of Technology, Symbiosis International Deemed University, Pune, India

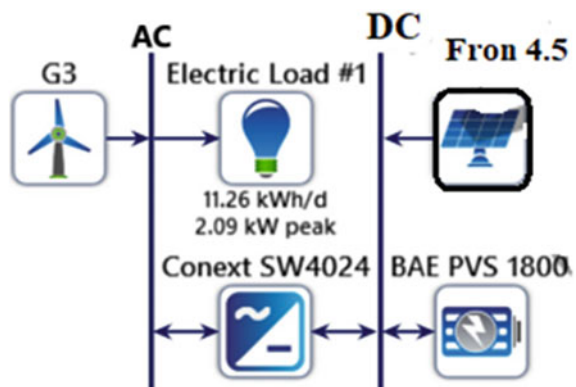
concluded that the model considered is best suitable for load variations. Jin et al. [4] conducted a case study of economic assessment process in South Korea where the carbon emission is reduced by avoiding the usage of fossil fuels. Manmadharao et al. [5] discussed the integrated-on grid solar system to supply the load in Vijayawada. From the results, he finalized that the operating cost and losses of the proposed system are reduced. Now a days advanced software technology has been developed mainly to perform design and cost analysis of renewable resources [6–8]. From literature survey outcome HOMER is a desired simulation software to analyze and implement hybrid resources at Chennai location. Initially, research was carried out for hybrid sources. In the future, based on location the performance improvement of individuals will be carried out for meeting the load demands.

2 Proposed System Description

Figure 1 represents the design of proposed system. It is designed for the altitudes ($13^{\circ}5.0'N$, $80^{\circ}16.2'E$) at Chennai in India shown in Fig. 2. It is a off grid hybrid power system modeled to supply 11.26 kWh/d electric load. The peak load considered is 2.09 kW. The resources used here are G3 generic wind source, From 4.5 Solar source, Storage Unit, and a Connext Converter.

Table 1 represents the components utilized in the proposed system design. The components are PV with Maximum Power Point Tracking of 4.4 kW, Generic Wind Turbine of 3 kW, Storage Battery connected as 15 Strings and Connext converter of 1.92 kW rating.

Fig. 1 Schematic of proposed system



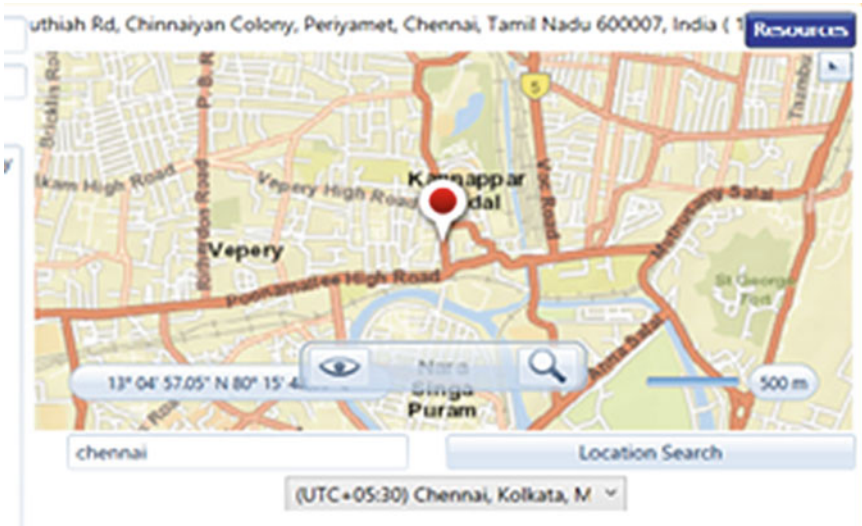


Fig. 2 Location of Chennai. Source HOMER

Table 1 Component history

S.No.	Component	Size	Unit
1	PV-(MPPT)	4.40	kW
2	G3—generic wind turbine	3	kW
3	Storage—BAE Secura Solar 12 PVS 1800	15	Strings
4	Schneider conext SW4024	1.92	kW

2.1 Load Detail

Figure 3 represents the scheduled load profile of proposed system. From the diagram, it is clear that peak load is required mostly in the summer months.

Figure 4 shows electric load details of the proposed system. Here, the daily, seasonal and yearly requirement of the load is given.

2.2 Solar Panel Detail

Figure 5 represents the PV radiation and clearness index of Solar Source from National renewable energy lab database. The lifetime of solar panels taken is around 15 years. In the solar system, MPPT algorithm is implemented to get the maximum output from PV. The output of PV is calculated by using the following formula in HOMER Pro as referred from [9].

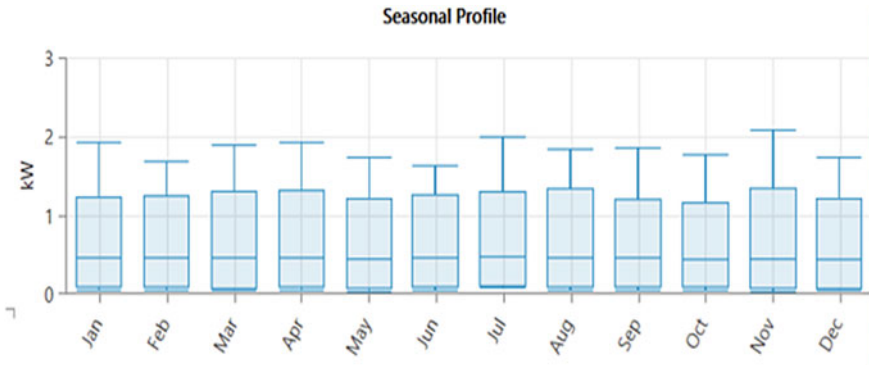


Fig. 3 Scheduled load profile

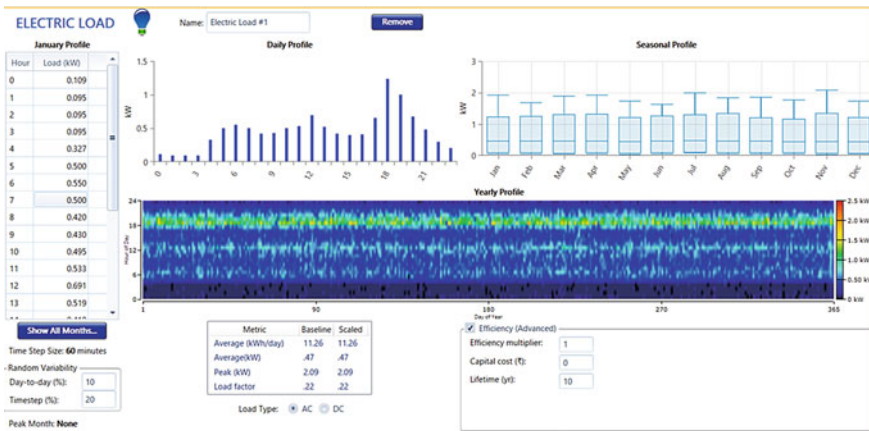


Fig. 4 Electric load

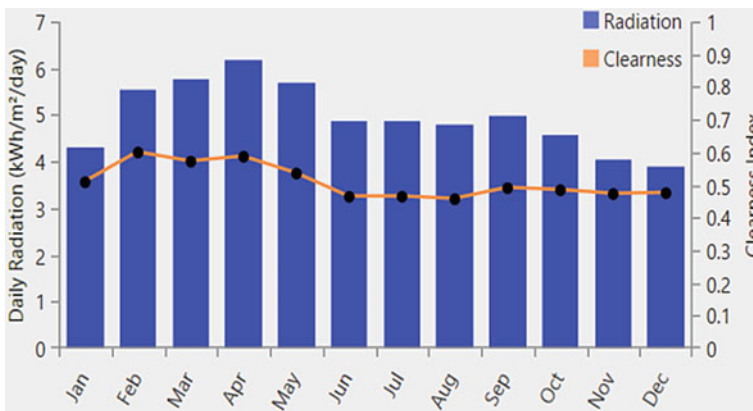


Fig. 5 PV radiation and clearness index. Source HOMER

$$\begin{aligned}
 PV(O/P) &= \text{Rated Capacity of PV} * PV \text{ Derating Factor} \\
 &* \left(\text{Solar Radiation Incident on PV} / \text{Incident Radiation at } 1 \text{ kW/m}^2 \right) \\
 &* \left(1 + \text{Temperature Coefficient of PV} (\text{PV Cell Temperature} - \text{PV Cell Temperature at } 25^\circ\text{C}) \right).
 \end{aligned}$$

2.3 Wind Source

Figure 6 gives the detail of average wind speed (m/s) for a year. The detailed graph is taken from NASA meteorology above 50 m from earth. The wind speed is calculated by the following formula as referred from [9].

$$\begin{aligned}
 &\text{Wind turbine speed at hub height} \\
 &= \text{Wind speed at anemometer height} * (\text{hub height of wind turbine} / \text{anemometer height})^{\text{power law constant}}
 \end{aligned}$$

From Table 2 various power outputs for corresponding wind speed are discussed. It is clear that the maximum output is obtained at the speed of 14 and 15 m/s.

The graphical representation of Table 2 is shown in Fig. 7. The graph is plotted between wind speed and power output. The peak power output 3 kW is attained at a wind speed of 14 to 15 m/s.

Figure 8 gives us the specification of wind turbine implemented in the system. The lifetime is taken as 20 years and the hub height (17 and 20 m) is taken for sensitivity analysis.

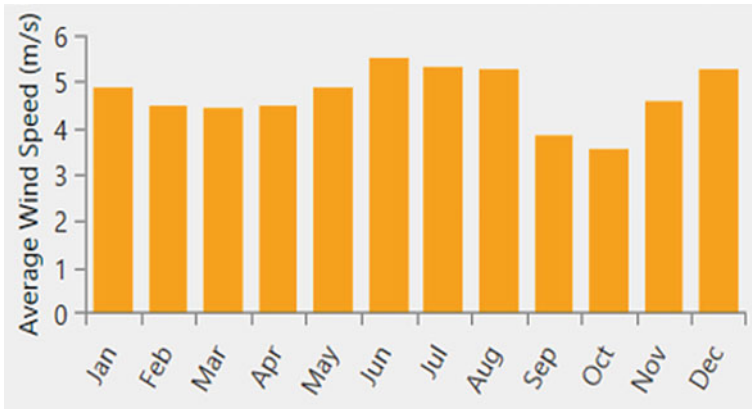
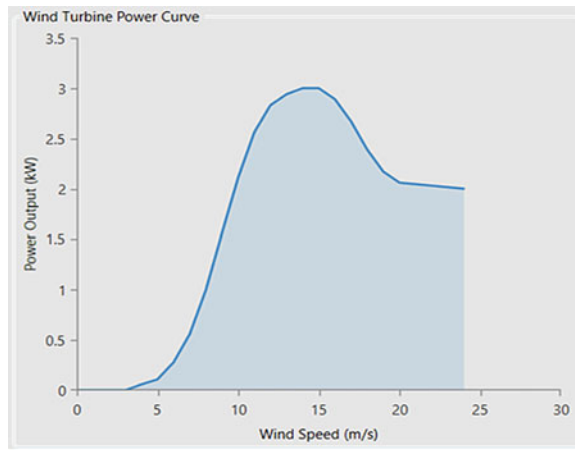


Fig. 6 Wind resource. Source HOMER

Table 2 Wind speed and power output

Wind speed (m/s)	Power output (kW)
0	0
3	0
4	0.06
5	0.11
6	0.28
7	0.56
8	1
9	1.56
10	2.11
11	2.56
12	2.83
13	2.94
14	3
15	3

Fig. 7 Wind turbine power curve



2.4 Storage Unit

Here, BAE solar 12 PVS 1800 battery is used for storage unit with 15 strings connected in parallel each carries 2 V.

A connext converter is acting as both rectifier and inverter when required.

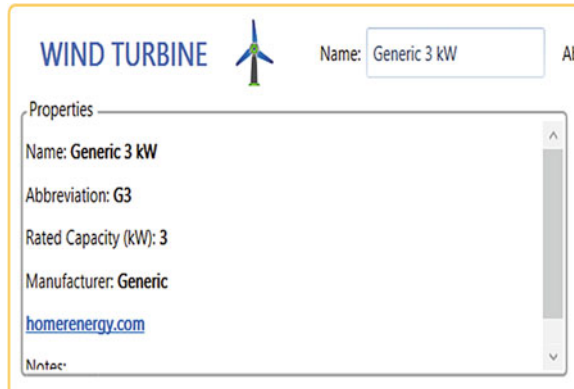


Fig. 8 Wind turbine specification

3 Simulation Results

The proposed model system is simulated by using calculator button in the software. After simulation, various outputs can be obtained and the tabulation of optimization results and sensitivity analysis has been displayed in Fig. 9. Here three types of

Sensitivity Cases											
Sensitivity		Architecture									
Fron4.5 Derating (%)	G3 Hub Height (m)	Fron4.5 (kW)	Fron4.5-MPPT (kW)	G3	BAE PVS 1800	Conext SW4024 (kW)	Efficiency1	Dispatch	NPC (₹)		
80.0	17.0	4.65	4.40	17	1.85	0	CC	₹28,142			
80.0	20.0	4.65	4.40	17	1.85	0	CC	₹28,142			
90.0	17.0	4.35	4.40	15	1.92	0	CC	₹26,502			
90.0	20.0	4.35	4.40	15	1.92	0	CC	₹26,502			

Optimization Results											
Architecture										Cost	
Fron4.5 (kW)	Fron4.5-MPPT (kW)	G3	BAE PVS 1800	Conext SW4024 (kW)	Efficiency1	Dispatch	NPC (₹)	₹30 (₹)	Operating cost (₹/yr)		
4.65	4.40	17	1.85	1.00	CC	₹28,142	₹0.530	₹490.83			
4.65	4.40	17	1.85	1.00	LF	₹28,142	₹0.530	₹489.87			
4.65	4.40	17	1.85	0	LF	₹28,142	₹0.530	₹489.87			
4.65	4.40	17	1.85	0	CC	₹28,142	₹0.530	₹489.87			
4.64	4.40	17	1.86	0	CC	₹28,151	₹0.530	₹490.83			
4.64	4.40	17	1.86	0	LF	₹28,151	₹0.530	₹490.83			
4.64	4.40	17	1.86	1.00	LF	₹28,151	₹0.530	₹490.83			
4.64	4.40	17	1.86	1.00	CC	₹28,151	₹0.530	₹490.83			
4.65	4.40	17	1.84	0	LF	₹28,151	₹0.530	₹489.36			
4.65	4.40	17	1.84	1.00	LF	₹28,151	₹0.530	₹489.36			

Fig. 9 Results and sensitivity analysis

outputs can be compared. They are summary, tables, and graphs of the simulation. From these results we can conclude at the Net Present Cost of the design.

Figure 10 represents the Net Present Cost of hybrid system. The cost is estimated based on derating factor of pv and hub height of wind source. The cost is varying uniformly around Rs. 26,000 to Rs. 28,500.

The detailed cost summary for different units is explained in Fig. 11. Among these capital cost for PV source is higher when compared with other components. Red color part indicates connext converter cost, light blue color meant for PV and wind source cost and violet color shows the battery amount. In this summary capital, operating, replacement and salvage costs for different unit is discussed.

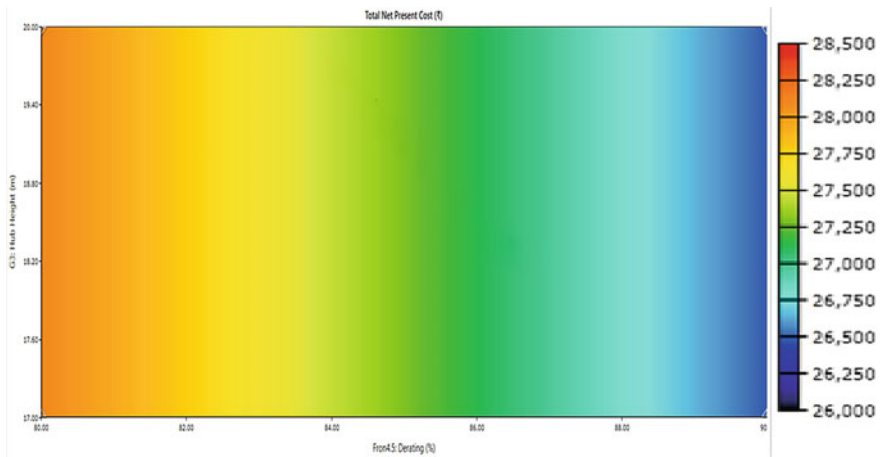


Fig. 10 NPC of the system

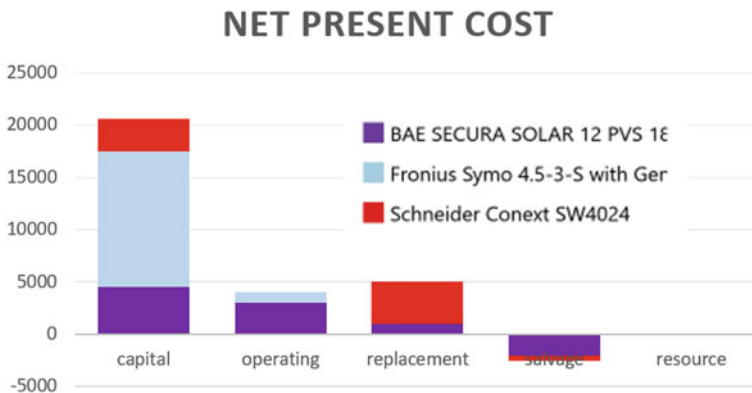


Fig. 11 Cost summary

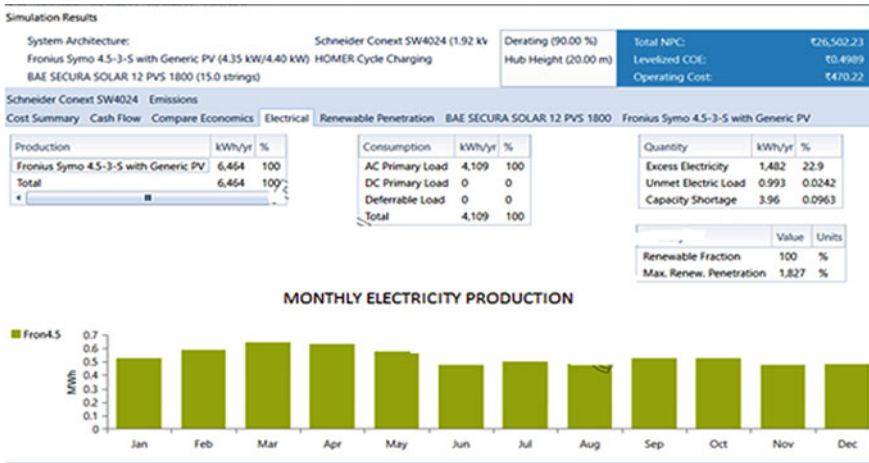


Fig. 12 Electrical production of PV

Figure 12 gives us the monthly electric production of PV in MWhr. Also the consumption of load, excess electricity production, unmet electric load, and storage capacity details are provided here.

Figure 13 yields the yearly production of PV. From the fig, the mean output is nearly 17.7 kWh/d. The efficiency of PV is 17%. Total generation of power is 6464 kWh/year.

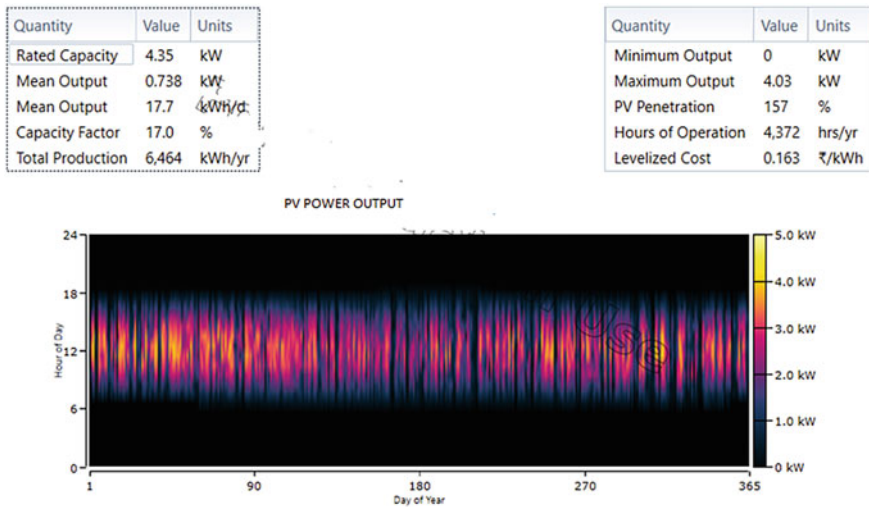


Fig. 13 Yearly production of PV

The SOC of battery is given in Figs. 14 and 15 batteries are connected in 15 parallel strings each battery with a voltage of 2 V. The parameters covered here are autonomy, storage wear cost, nominal capacity of the battery and annual throughput details, etc.

Figure 15 indicates time series analysis of ambient temperature. Temperature is maximum in the month of May, June, July, and August.

Time series analysis of total electrical load met in 12 months and 24 h/day in a month is displayed in Fig. 16.

Daily profile of AC primary load is indicated in Fig. 17. Here, it shows that almost the load gets energized completely by the sources throughout the year.

Figure 18 represents the monthly profile of unmet electrical load. From the diagram, it is clear that all demands of the load have been met successfully. Only in the month of December 0.01 kW of load is not met.

Cumulative Distributive analysis of renewable output is represented in Fig. 19. The graph is plotted between total renewable output and cumulative frequency. Only at 50% of CF, the renewable sources deliver power gradually to the load.

Figure 20 represents the CDF of net electrical load served to the system. The graph is plotted between cumulative frequency and total electrical load served in kW. The peak demand of the load is achieved at 100% cumulative frequency.

4 Conclusion

Thus, from the simulation results and cost analysis, it is proved that the load is supplied continuously by the sources which represent that the optimal solution of proposed system is obtained. Also, cost analysis is carried out for sensitivity cases like derating factor of PV and different hub heights of wind turbine. So, it is proved that the proposed simulation technique is an optimized and cost-effective methodology for implementing hybrid renewable resources. The optimal cost of the system is around Rs. 26,000 to Rs. 28,500. Capital cost, operating cost, and replacement cost analysis gives us better idea to design a system without any losses. Here, a small unit is designed to supply a load of 11.26 kW. In the future, a domestic utility in Chennai can be analyzed and optimized.

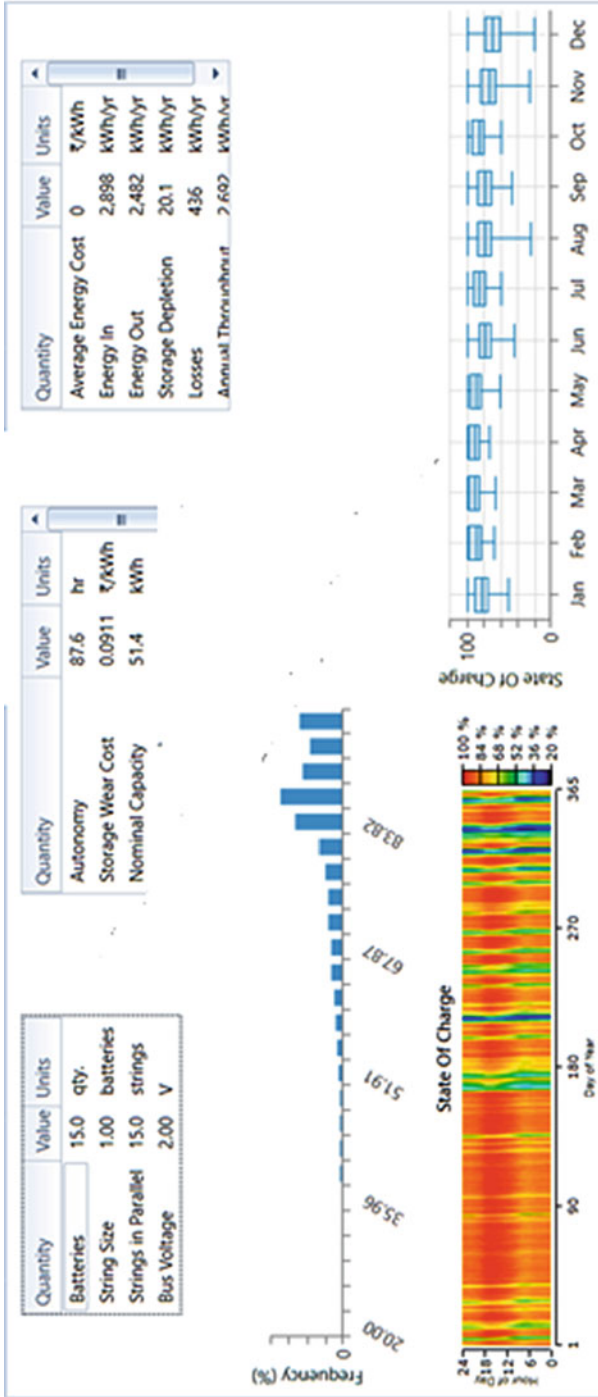


Fig. 14 SOC of battery

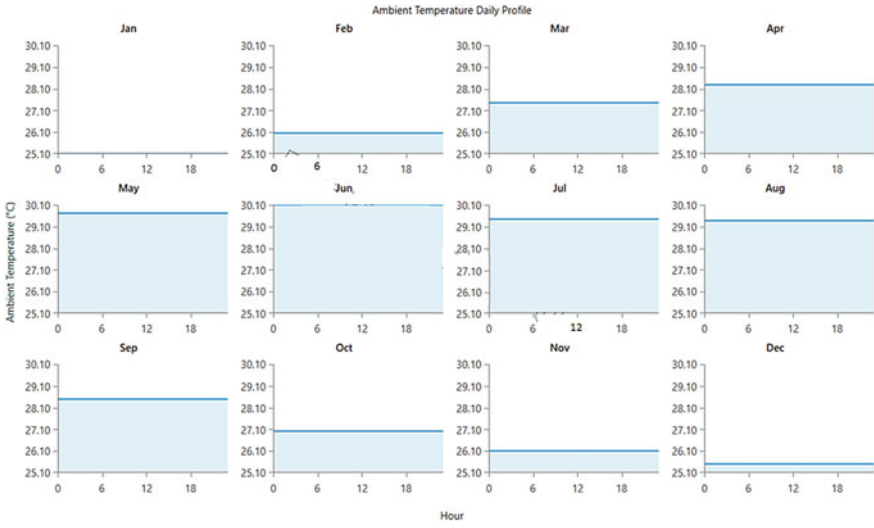


Fig. 15 Ambient temperature profile

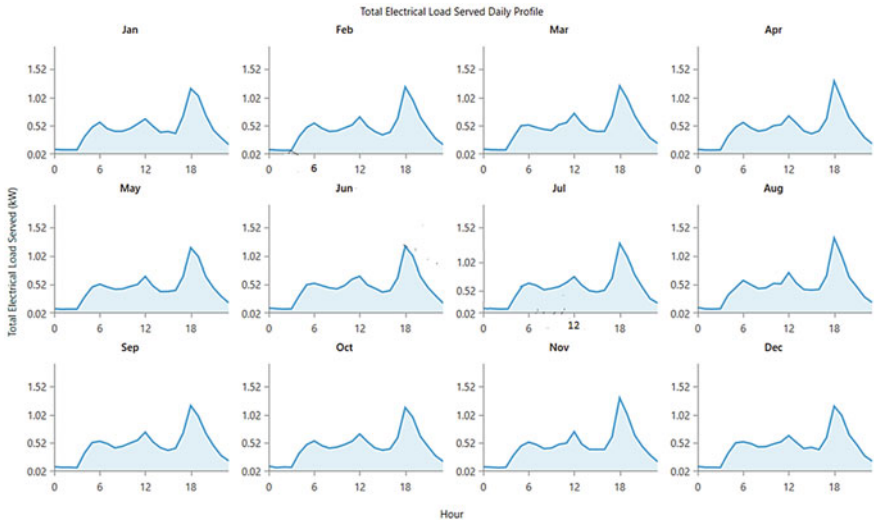


Fig. 16 Total electrical load met

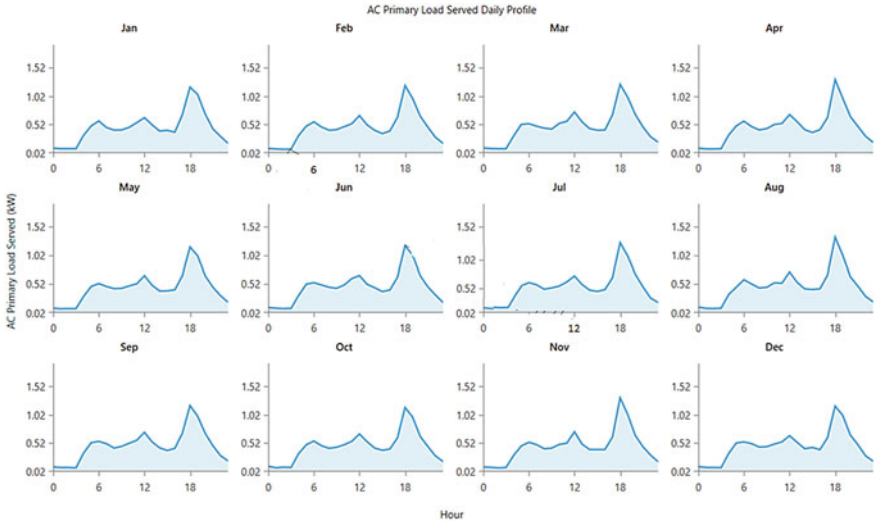


Fig. 17 Daily profile of AC primary load

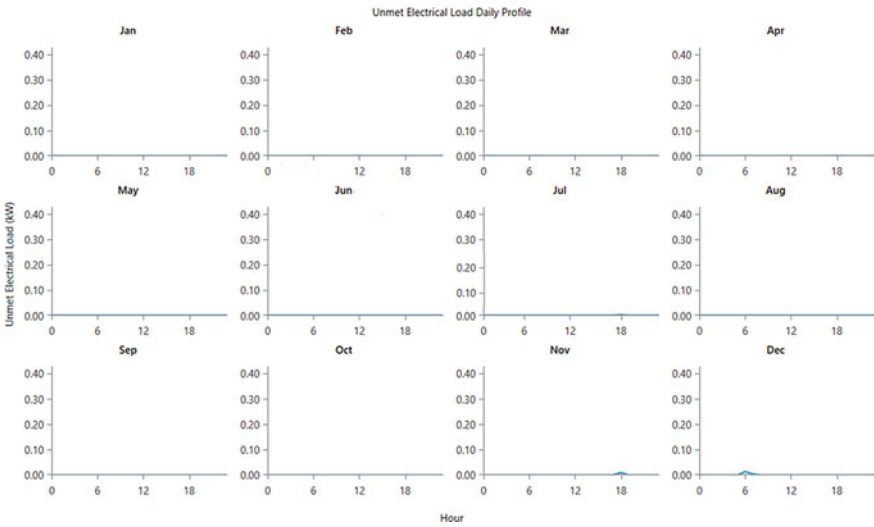


Fig. 18 Monthly profile of unmet electrical load

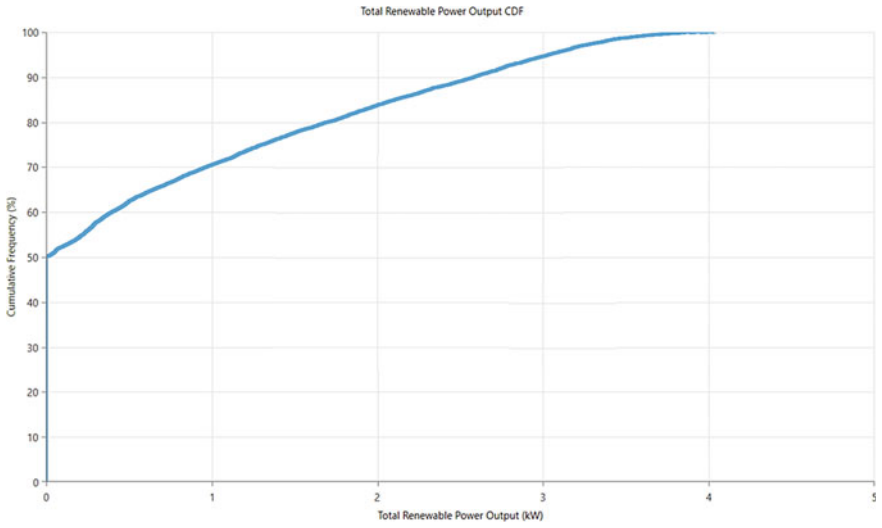


Fig. 19 CDF of Renewable Output

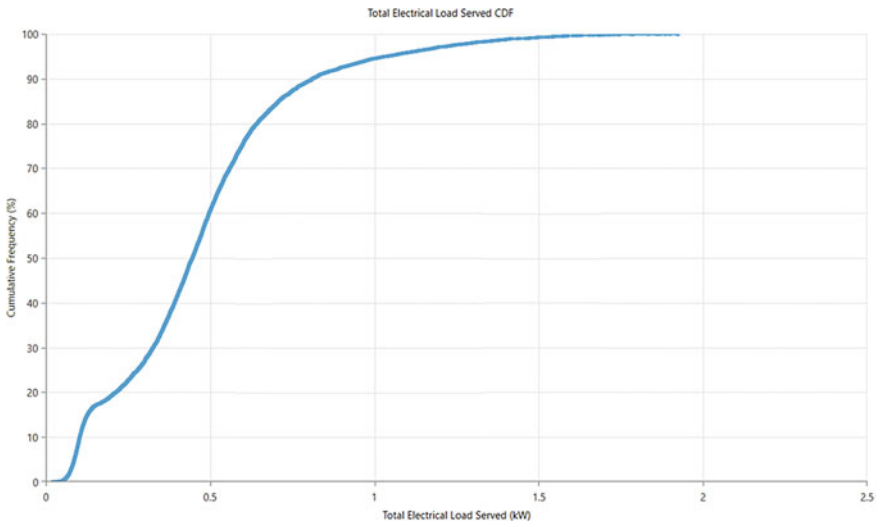


Fig. 20 Total electrical load served analyzed using CDF

References

1. Sen R, Bhattacharyya SC (2014) Off-grid electricity generation with renewable energy technologies in India: an application of HOMER. *Renew Energy* 1(1):388–398
2. Singh A, Baredar P, Gupta B (2015) Computational simulation and optimization of a solar, fuel cell and biomass hybrid energy system using HOMER Pro software. *Proc Eng* 2(5):743–750
3. Okedu KE, Uhumwangho R (2014) Optimization of renewable energy efficiency using HOMER. *Int J Renew Energy Res* 4(2):1–8
4. Jin S, Kim H, Kim TH, Shin H, Kwag K, Kim W (2018) A study on designing off-grid system using HOMER pro—a case study. *IEEE* 1(6):1851–1855
5. Manmadharao S, Chaitanya SNVSK, Venkateswara rao B, Srinivasarao G (2019) Design and optimization of grid integrated solar energy system using HOMER GRID software. *IEEE* 19(1):1–5
6. Nurunnabi Md, Roy NK (2015) Grid connected hybrid power system design using HOMER. *IEEE* 15(2):18–21
7. Ghose S, El Shahat A, Haddad RJ (2017) Wind-solar hybrid power system cost analysis using HOMER for Statesboro Georgia. *IEEE* 3(1):1–3
8. Divya Navamani J, Lavanya A, Prahadheeshwar CM, Mohammed Riyazudeen S (2019) Hybrid power system design using Homer Pro. *Int J Recent Technol Eng (IJRTE)* 8(1S4)
9. <https://www.homerenergy.com>

EDM Process Optimization of Machining Parameters for Through Hole Making on HCHCR AISI-D7 Steel Using RSM



Amit Kumar and Mohan K. Pradhan

1 Introduction

The effect of EDM parameters on responses namely TWR, MRR, ROC, and Ra through the machining of HCHCr AISI D7 steel was investigated in the current research. Due to difficulty to cut these hard materials, non-conventional machining like EDM, electrochemical machining, ultrasonic machining, etc. are generally preferred to get better machining characteristics [1]. EDM is the most common and generally appropriate machining method among these non-traditional machining processes for such type of material. Also, it is suitable for any material with exceptional machining accuracy in terms of surface quality as long as the material is conductive [2]. EDM is a non-traditional electrothermal machining technique used usually for hard-to-cut materials. It is also used in the processing of components with complex profiles by sparks between the electrode and the workpiece with fair precision [3]. In a dielectric fluid, EDM tool and workpiece were submerged which helps to remove debris as well as cool the work material and tool. The restriction of the spark is one of the key functions of the dielectric in order to provide a greater energy density which results in higher performance [4]. A substantial flushing pressure is needed to set in EDM machine to take away the debris between the work material and tool. Abnormal discharge such as arcing and short circuiting can occur for inadequate flushing pressure, which may lead to process instability [5]. It has been seen that over cut is a common problem in EDM while machining. The process parameters to be correctly selected to increase MRR and precession. Simultaneously to reduce overcut, tool wear, and surface roughness, this is the researchers' main topic of recent years. The researchers are still attempting to select the best setting in this direction to obtain better machining characteristics. Weighted based TOPSIS method along with Shannon's Entropy for optimization, $I_p = 10$ A, $\tau = 90\%$, T_{on}

A. Kumar (✉) · M. K. Pradhan
Maulana Azad National Institute of Technology, Bhopal 462003, India

= 100 μ s and $V = 40$ V are the optimum operating conditions recognized by gray relational analysis [6]. During the electrical discharge drilling phase with different parameter settings. Hammed [7] has seen the effect on surface roughness and wear ratio of discharge current and T_{on} of SS AISI 304 in EDM process with copper rectangular shape tool. It was found that R_a enhances by reducing the peak current. TWR was increased with the rise in the current Values. $I_p = 21$ A, $T_{off} = 15$ μ s, $T_{on} = 90$ μ s, and tool rotation = 600 rpm were recommended to reduce TWR and optimize MRR by using electrical discharge drilling system with multi-objective parametric optimization. It was based on pulse component analysis and gray relational analysis [8]. In order to investigate the variation in input parameters of EDM on the radial overcut response, a model based on artificial neural network has been proposed. The accuracy and precision of the object are greatly influenced by the radial overcut. In the EDM process, a multi optimal combination of process parameters for the responses is difficult to find, as these parameters affect them differently [9]. After many literature surveys, it was found that hollow (tubular) electrodes for EDM route towards through hole making has rarely been studied on HCHCr AISI D7 steel (hard-to-cut materials), The above-mentioned hole making process can reduce the work material's consumption and waste can also further utilize. The aims of the current work have been defined that to prospect analysis of EDM on HCHCr AISI D7 steel using hollow copper tool electrode by hole making. To find the effects on different machining performance measurements namely MRR, TWR, ROC, and R_a of EDM parameters I_p , T_{on} , and V during through hole made on the above material. To use the Response Surface Method (RSM) in design expert software to find the best process parameter for smooth hole making.

2 Methodology and Experimental Procedure

2.1 Material Details

AISI D7 steel having many areas of application like mold liners for bricks industries, lining equipment for shot blasting equipment, powder compaction tooling, flattening rolls, ceramic extrusion, and molding tools. A $65 \times 32 \times 6$ mm³ rectangular plate has been used and the pictorial view and CAD diagram depicted in Figs. 1 and 2. HCHCr AISI D7 steel consists of highest percentage of chromium in AISI group so it is having high resistance to corrosion. Chemical composition of AISI D7 steel work material and its properties has been depicted in Tables 1 and 2 respectively. For machining such type of hard material, a suitable conductive tool is required. So, hollow shape tool made of pure electrolytic copper was used. Selection of pure copper as electrode is due to its exceptional resistance to wear characteristics. For machining intricate shapes with better surface finish, wear resistance is very much required. The dimension of tubular electrode and its CAD diagram have been depicted in Figs. 3 and 4. In Table 3, the properties of pure copper were described. Due to these

Fig. 1 Work material for EDM machining



Fig. 2 CAD diagram of specimen

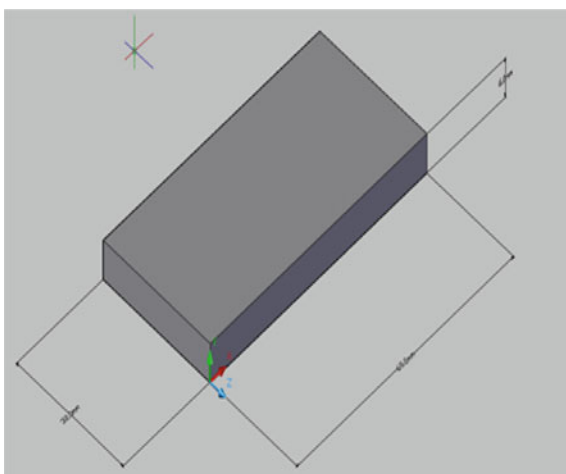


Table 1 Composition of HCHCr AISI D7 steel

Element	Fe	C	Mn	Si	P	Cr	S	Ni	V	Mo	Cu	W
Content (%)	78.27	2.35	0.6	0.6	0.03	12.6	0.03	0.30	3	1.2	0.02	1.00

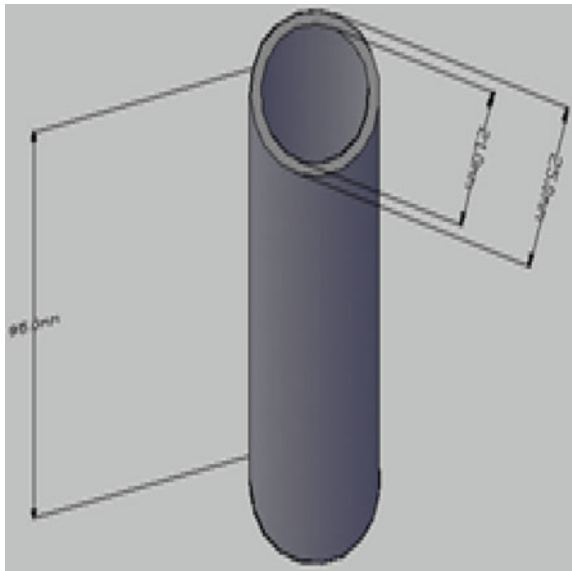
Table 2 Mechanical properties of HCHCr AISI D7 steel

Properties	Unit
Elastic modulus	$180\text{--}210 \times 10^9 \text{ pa}$
Poisson's ratio	0.26–0.30
Rockwell hardness C	62.5

Fig. 3 Hollow shape copper tool



Fig. 4 CAD diagram of tool electrode



advantages, the copper electrode has been selected for the steel work material of hole making. The hollow shape electrode was machined by turning on the lathe, followed by grinding to bring it to the required dimension and prepared for machining.

Table 3 Properties of pure copper

Physical properties	Value
Density (g/cc)	8.89
Specific gravity at 20C (g/cc)	8.9
Electrical resistivity ($\mu\Omega/cm$)	1.96
Thermal conductivity (W/m K)	268.389
Melting point ($^{\circ}C$)	1083

Table 4 Control parameters and their level

Variants	Unit	Notation	Level of variation		
			1	2	3
Current (Ip)	A	A	6	8	10
Pulse on time (Ton)	μs	B	100	150	200
Voltage (Vg)	V	C	50	60	70

2.2 Selection of Parameters and Design of Experiment for Processes

For effective study, it is necessary to select suitable parameters with their range. Based on the various trials and literature survey three electrical process parameters were selected while machining on EDM, i.e., Ip, Ton, and V. Duty factor and flushing pressure, other than these electrical parameters, were fixed to see how they affect EDM responses such as MRR, TWR, ROC, and Ra. Using central composite design, experiments were planned according to RSM with randomized subtype, no blocks, reduced cubic. By applying these parameters in RSM, a total 15 number of experiments was designed with various combination of all three parameters in Design Expert 11 software. In which Ip, Ton, and Voltage had 3 levels and their ranges were decided on various trial experiments by considering constraints of machine tools. All the control parameters and their levels have mentioned in Table 4.

2.3 EDM Experimentation

A Die sinking EDM machine (Electronica S50 CNC EDM) has been used for experimentation. Electra EDM oil used during machining has good dielectric strength and high flash point. It is totally safe from fire hazards. An arrangement of tool and work-piece in EDM machine as shown in Fig. 5. All 4 responses for 15 no. of experiments are recorded in Table 5. The machined surface and the removed material have shown in Figs. 6 and 7.

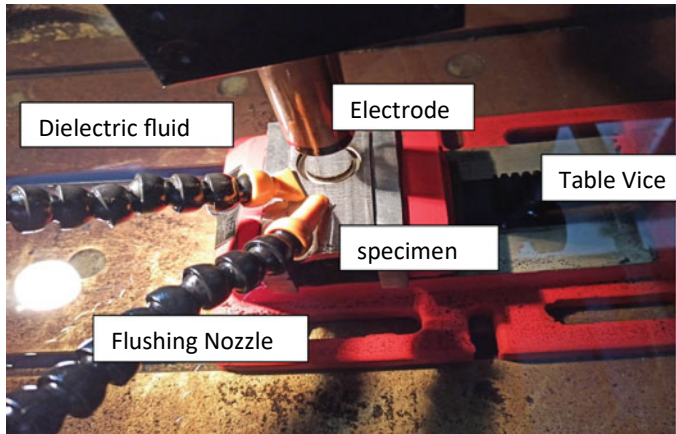


Fig. 5 Tool and workpiece arrangement in EDM

Table 5 Experimental results on EDM

Run	Ip (A)	Ton (μ s)	Voltage (V)	MRR (mm^3/min)	TWR (mm^3/min)	ROC (mm)	Ra (μm)
1	8	150	60	10.7227	0.696924	0.407833	6.46533
2	8	200	60	13.7056	0.778823	0.431	4.586
3	8	150	70	12.6803	0.843703	0.772333	6.49067
4	8	100	60	10.42049	0.688153	0.467833	4.42667
5	10	200	50	16.9423	1.255	0.312167	4.25433
6	6	100	50	6.38301	0.126735	0.1916	5.432583
7	10	100	50	13.7256	1.34483	0.197667	4.64933
8	10	200	70	18.9136	1.47637	0.648833	4.798
9	8	150	50	11.9436	0.628153	0.194167	6.33367
10	10	100	70	15.5494	0.954831	0.6015	4.74467
11	6	200	70	9.07301	0.371634	0.690367	4.95633
12	6	100	70	7.86775	0.22738	0.8815	4.89846
13	6	150	60	8.90179	0.333171	0.37833	6.28767
14	6	200	50	7.9028	0.48123	0.1185	5.989633
15	10	150	60	17.9533	1.12182	0.3315	6.78936



Fig. 6 EDMed removed work surface



Fig. 7 EDMed hole of work material

3 Result and Discussion

3.1 Analysis of Variance (ANOVA)

The different performance parameters and the corresponding ANOVA test were performed using Design Expert 11 software. For identification of statistically specified process parameters, there was a need for broad variance analysis called ANOVA test. The ANOVA analysis is intended to determine the significance of the process parameters that influence the response of the EDM. In this analysis, p -values were used to verify the interpretation of the coefficients required to explain the pattern of variables' interactions. The lower the p -value, the higher the coefficient of meaningful correlation. A t -test with 95% confidence was performed by ANOVA to get the value of the regression coefficient. The determination coefficient (R^2) articulates

the excellence of the model equation fit, and an F-test evaluated its statistical significance [10]. The mathematical model developed by ANOVA according to fit statistics are linear for MRR, TWR, and quadratic for ROC, Ra respectively written as Eqs. 1, 2, 3, and 4;

$$\text{MRR} = -13.09269 + 2.14779 * A + 0.025182 * B + 0.071868 * C \quad (1)$$

$$\text{TWR} = -1.41895 + 0.230635 * A + 0.002042 * B + 0.000380 * C \quad (2)$$

$$\begin{aligned} \text{ROC} = & -0.575481 + 0.348426 * A - 0.005863 * B - 0.022808 * C \\ & + 0.000533 * A * B - 0.003258 * A * C - 0.000046 * B * C \\ & - 0.015079 * A^2 + 0.000014 * B^2 + 0.000680 * C^2 \end{aligned} \quad (3)$$

$$\begin{aligned} \text{Ra} = & +6.17347 - 1.83779 * A + 0.222857 * B \\ & - 0.286501 * C - 0.001196 * A * B + 0.013790 * A * C \\ & - 0.000013 * B * C + 0.067080 * A^2 - 0.000706 * B^2 + 0.001420 * C^2 \end{aligned} \quad (4)$$

where A, B, C denote input parameters such as peak current, pulse time, and voltage respectively.

3.2 Impact on MRR of Process Parameters

It is always required to achieve higher MRR for any machining process to get maximum productivity. The gap between the workpiece and the electrode also partly affects EDM and also depends on the size of the eroding surface under the machining condition. MRR can be calculated from the relation written in Eq. 5.

$$\text{MRR}(\text{mm}^3/\text{min.}) = \frac{\text{Loss in weight (gm)} \times 60}{\text{The density of specimen (gm/mm}^3) \times \text{Machining Time (sec.)}} \quad (5)$$

From Table 6, the MRR linear model in which the F -value of 90.77 directs the model is important. Because of noise, there is just a 0.01% chance that such a high F -value would occur. P -values lower than 0.0500 mean that the terms of the model are significant. A is a substantial model term in this section. Values greater than 0.1000 mean the terms of the model are not important. If there are a lot of negligible model terms, model reduction can be done to enhance this model (not counting those needed to facilitate hierarchy). The 0.9354 expected R^2 is in fair agreement with the 0.9506 modified R^2 ; i.e., the difference is less than 0.2. As shown in the main effect plot of Fig. 8a–c, the direct effect of all three process parameters on MRR. The increase in MRR with an increase in I_p and T_{on} occurs. It is due to the fact that the energy

Table 6 ANOVA results for MRR

Source	Sum of squares	df	Mean square	F-value	p-value	
Model	205.54	3	68.51	90.77	<0.0001	Significant
A- <i>I_p</i>	184.52	1	184.52	244.45	<0.0001	
B- <i>T_{on}</i>	15.85	1	15.85	21.00	0.0008	
C-voltage	5.16	1	5.16	6.84	0.0240	
Residual	8.30	11	0.7548			
Cor total	213.84	14				

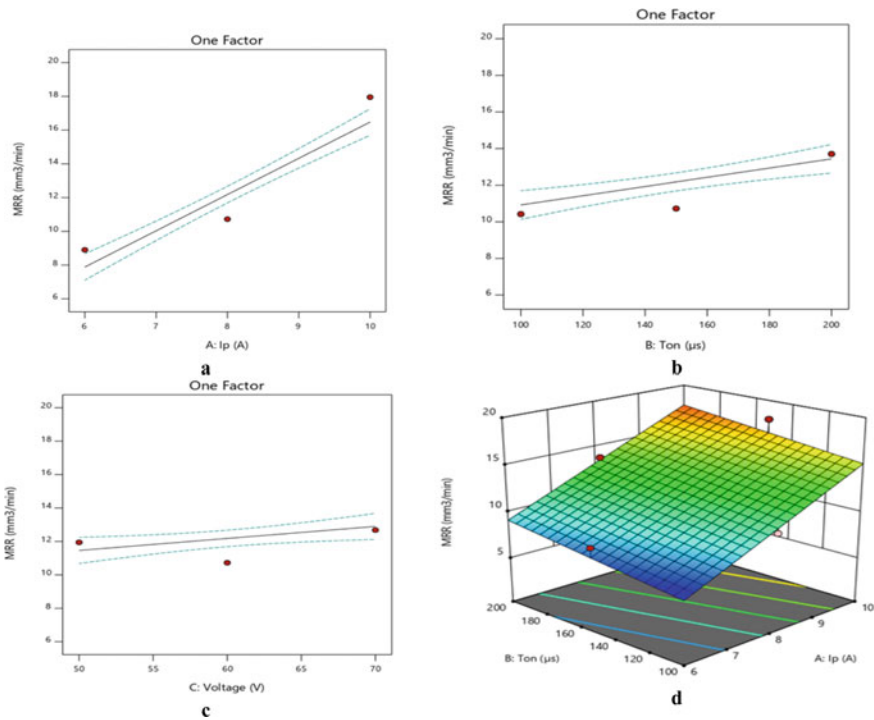


Fig. 8 Effect of process parameters **a** *I_p*, **b** *T_{on}*, **c** *V* (main effect plot) and **d** 3D response surface plot of *I_p* and *T_{on}* on MRR

of the discharge is increased to facilitate melting and vaporization and to promote the impulse's large ionization in the spark gap [11]. At high current, however, the MRR is larger and the debris at the electrode gap is larger and more centered. Large debris accumulation will cross the gap between the electrodes and reduce the MRR by subsequent short circuiting [12]. Also, MRR first decreases from 50 to 60 V, and then it increases till 70 V when increasing the voltage. It can be seen from Fig. 8d, the MRR increases suddenly with *I_p* and *T_{on}* changes for any voltage value. This is

because of their superior control of the input energy [13]. The voltage is, therefore, an irrelevant parameter of the MRR, while the Ton is an important parameter. The maximum and minimum MRR can be seen from 3D surface Fig. 8d that MRR was found maximum at $I_p = 10$ A, $T_{on} = 200$ μ s and voltage = 60 V and minimum at $I_p = 6$ A, $T_{on} = 100$ μ s, and voltage = 60 V respectively.

3.3 Impact on TWR of Process Parameters

The tool electrode wear is influenced simultaneously by multiple parameters with varying input values. The tool's wear rate directly affects dimensional accuracy and the shape generated which makes TWR another important factor in the analysis of EDM. TWR is expressed as the ratio of the difference in weight of the instrument prior, and after machining to the process time of the material. That can be explaining by Eq. 6.

$$TWR = \frac{\Delta V}{t} = \frac{\Delta W}{\rho * t} \quad (6)$$

where ΔV is the electrode volumetric loss, ΔW is the electrode's weight loss, t is the machining time, and ρ is the electrode's density. The linear model for TWR was proposed as shown in Table 7, where the F -value of 49.31 means that the model is relevant and because of noise, there is a 0.01% risk that an F -value high will occur. TWR increases drastically as I_p increases, as seen in Fig. 9a, while T_{on} and V have only a minor effect on TWR, as shown in Fig. 9b, c, respectively. High pulse current and voltage, therefore, produce high discharge energy and generate a large TWR. While T_{on} showed decreasing trends of TWR up to 150 μ s and then it abruptly increases till 200 μ s. The probability of electrode surface deposition of carbon appears to increase overall T_{on} , lower I_p , and lower voltage, which helps to reduce electrode wear [14]. It means current affect more causing tool wear. As can be seen from Fig. 9d, the TWR is more of a higher T_{on} value, while for any voltage value, the TWR rises with respect to I_p . For TWR, thus, voltage is an insignificant

Table 7 ANOVA results for TWR

Source	Sum of squares	df	Mean square	F -value	p -value	
Model	2.23	3	0.7440	49.31	<0.0001	Significant
A- I_p	2.13	1	2.13	141.01	<0.0001	
B- T_{on}	0.1043	1	0.1043	6.91	0.0235	
C-Voltage	0.0001	1	0.0001	0.0096	0.9239	
Residual	0.1660	11	0.0151			
Cor Total	2.40	14				

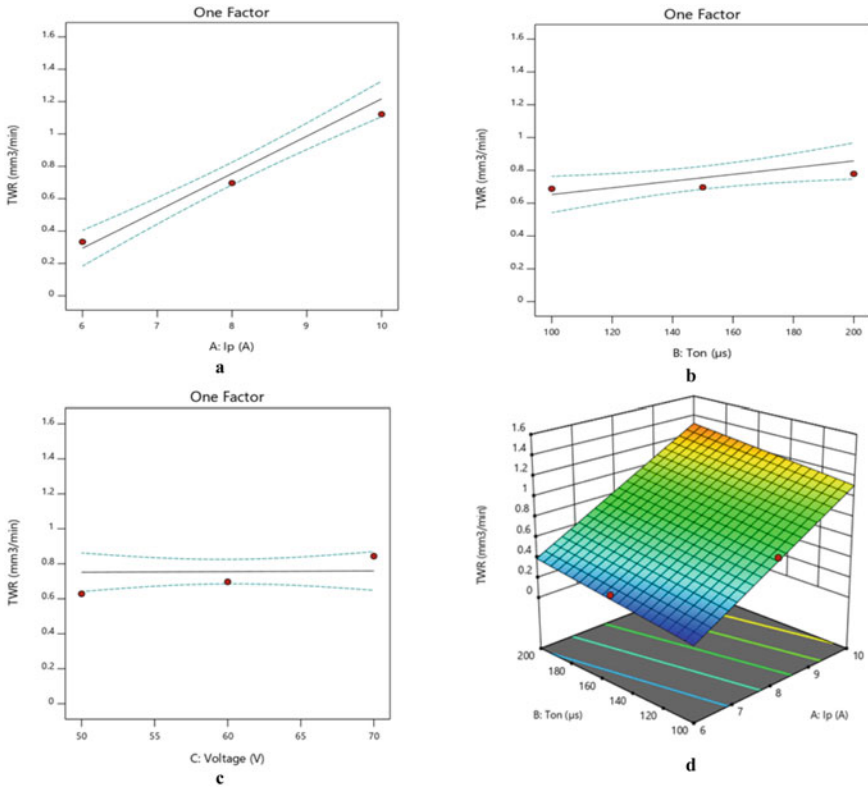


Fig. 9 Effect of process parameters **a** Ip, **b** Ton, **c** V (main effect plot) and **d** 3D response surface plot of Ip and Ton on TWR

parameter, while the key parameters are Ton and Ip. The 3D response surface graph said that the minimum tool wear occurs at Ip = 6 A, Ton = 100 µs, and voltage = 50 V.

3.4 Impact on ROC of Process Parameters

The ROC arising from the electrode wear and discharge gap significantly affects the dimensional accuracy of EDM. It can be calculated on the basis of tool maker microscope data by Eq. 7.

$$ROC = \frac{D1 - D2}{2} \tag{7}$$

Table 8 ANOVA results for ROC

Source	Sum of squares	df	Mean square	F-value	p-value	
Model	0.7528	9	0.0836	142.29	<0.0001	Significant
A-Ip	0.0028	1	0.0028	4.84	0.0792	
B-Ton	0.0019	1	0.0019	3.30	0.1291	
C-Voltage	0.6659	1	0.6659	1132.74	<0.0001	
AB	0.0227	1	0.0227	38.60	0.0016	
AC	0.0340	1	0.0340	57.78	0.0006	
BC	0.0043	1	0.0043	7.29	0.0428	
A ²	0.0094	1	0.0094	15.91	0.0104	
B ²	0.0030	1	0.0030	5.11	0.0733	
C ²	0.0119	1	0.0119	20.24	0.0064	
Residual	0.0029	5	0.0006			
Cor total	0.7557	14				

where, $D1$ = Reading on right-side of the optical micrometer, and $D2$ = Reading on left side of the optical micrometer. For this Quadratic model was suggested by ANOVA. The 142.29 model F -value means that the model is relevant, as shown in Table 8. There is just a 0.01% chance of a high F -value due to noise. In this analysis p -values lower than 0.0500 suggest important model terms. Figure 10a depicted that when I_p increase then ROC is first increasing then decreases as opposite to T_{on} shows the trends in Fig. 10b. In the main effect plot shown in Fig. 10c, voltage has a significant impact on ROC, which rises as voltage increases from 50 to 70 V. As shown in Fig. 10d, the maximum ROC was located at $I_p = 8$ A and $T_{on} = 200$ μ s. There is an average increase in ROC when it comes to gap voltage. Using low I_p and low V the top radial could be minimized as shown in Fig. 10e, f. The requirement of minimum ROC value which can be seen from the response plot, at $I_p = 6$ A, $T_{on} = 100$ μ s and Voltage = 50 V.

3.5 Impact on Ra of Process Parameters

Surface roughness is a calculation of the product's technical consistency which mostly affects the cost of the product's production. The name of the surface roughness tester used to measured was SurfTest SJ-210. As indicated by the quadratic model is significant in Table 9, the F -value of 7.2 means that there is only a 2.18% probability that noise will trigger this high F -value to occur. On the machined surface, the high energy pulse creates craters that lead to poor quality of the surface finish. The approximate responses for the R_a in relation to the I_p are shown in Fig. 11a. It depicts that with an increase in I_p , the R_a increases drastically and hits the peak value. Large I_p and voltage, therefore, produce large discharge energy and cause a

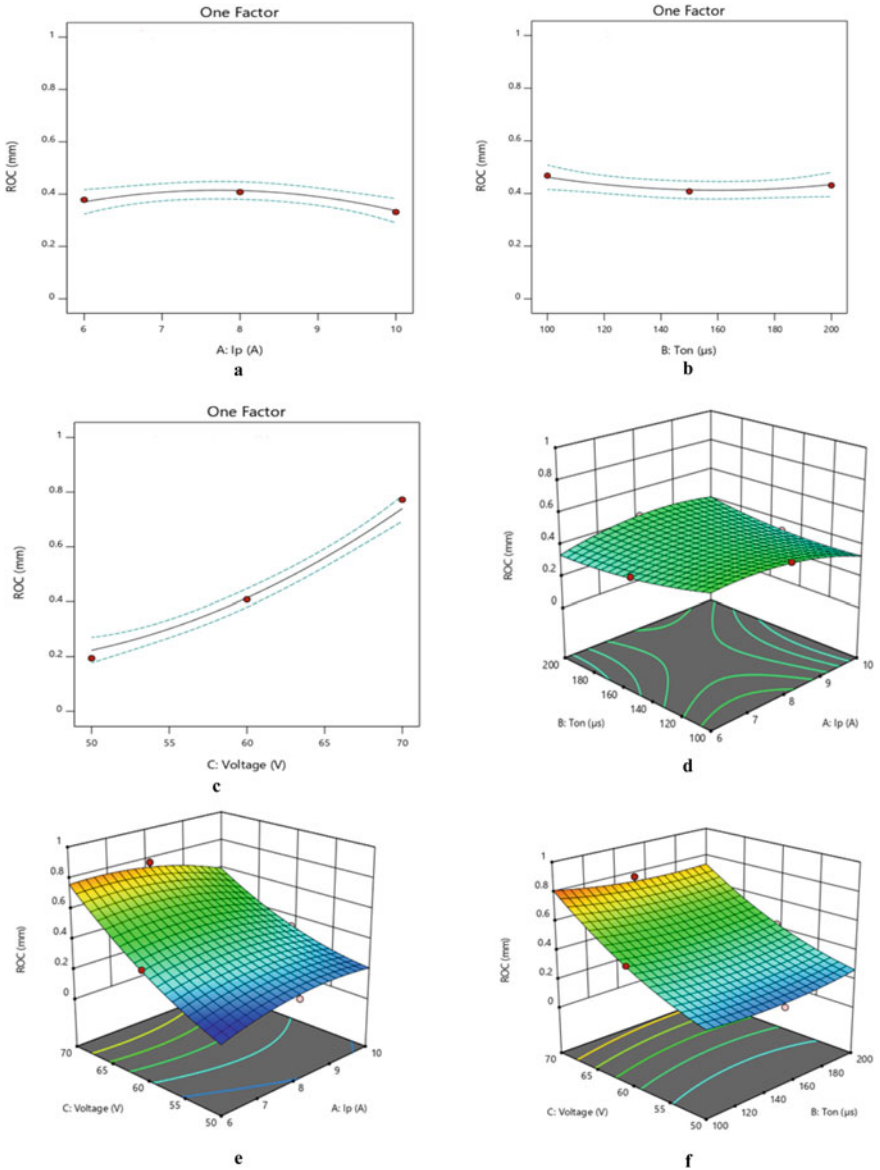


Fig. 10 Effect of process parameters **a** Ip, **b** Ton, **c** V (main effect plot) and 3D response surface plot of **d** Ip and Ton, **e** Ip and V, **f** Ton and V on ROC

Table 9 ANOVA results for Ra

Source	Sum of squares	df	Mean square	F-value	p-value	
Model	10.19	9	1.13	7.12	0.0218	Significant
A-Ip	0.5424	1	0.5424	3.41	0.1241	
B-Ton	0.0187	1	0.0187	0.1176	0.7456	
C-Voltage	0.0595	1	0.0595	0.3741	0.5675	
AB	0.1144	1	0.1144	0.7190	0.4352	
AC	0.6085	1	0.6085	3.83	0.1079	
BC	0.0003	1	0.0003	0.0020	0.9658	
A ²	0.1851	1	0.1851	1.16	0.3299	
B ²	8.00	1	8.00	50.29	0.0009	
C ²	0.0518	1	0.0518	0.3258	0.5928	
Residual	0.7954	5	0.1591			
Cor total	10.99	14				

larger crater to result in higher Ra on the workpiece surface. From Fig. 11b, it can be seen that when Ton increases from 100 to 150 μ s then Ra increases after that it decreases up to 200 μ s. Voltage affects slightly similar to Ip as shown in Fig. 11c. It has been seen that the minimum surface roughness from the 3D response graph of Fig. 11d is about 4.5 μ m at Ip = 8 A and Ton = 150 μ s. Similarly, it can be seen from Fig. 11e the minimum value of Ra is at Ip = 8 A and V = 70 V and from Fig. 11f the minimum value of Ra at Ton = 100 μ s and V = 60 V.

3.6 Optimization of EDM Parameters

Using an numerical optimization tool, RSM is used to achieve the best optimal values of the process parameters. It is an interaction of mathematical and statistical methods that combine independent quantitative variables to model and optimize response variables. To optimize the process parameters, based on the model developed and plots of contours and 3D response surface graphs, Design expert software is used. The optimum MRR, TWR, ROC, and Ra on the EDM machining of HCHCr AISI D7 steel material is exhibited by the peak of response surface as shown in Figs. 8, 9, 10 and 11 it was found the one optimum solution out of 51 solutions is MRR = 12.7516 mm³/min, TWR = 0.917112 mm³/min, ROC = 0.234904 mm and Ra = 4.56426 μ m corresponding to control parameters' Ip = 9.159A \approx 10 A, Ton = 100 μ s and Voltage = 50.8296 V \approx 50 V respectively at 0.629 desirabilities.

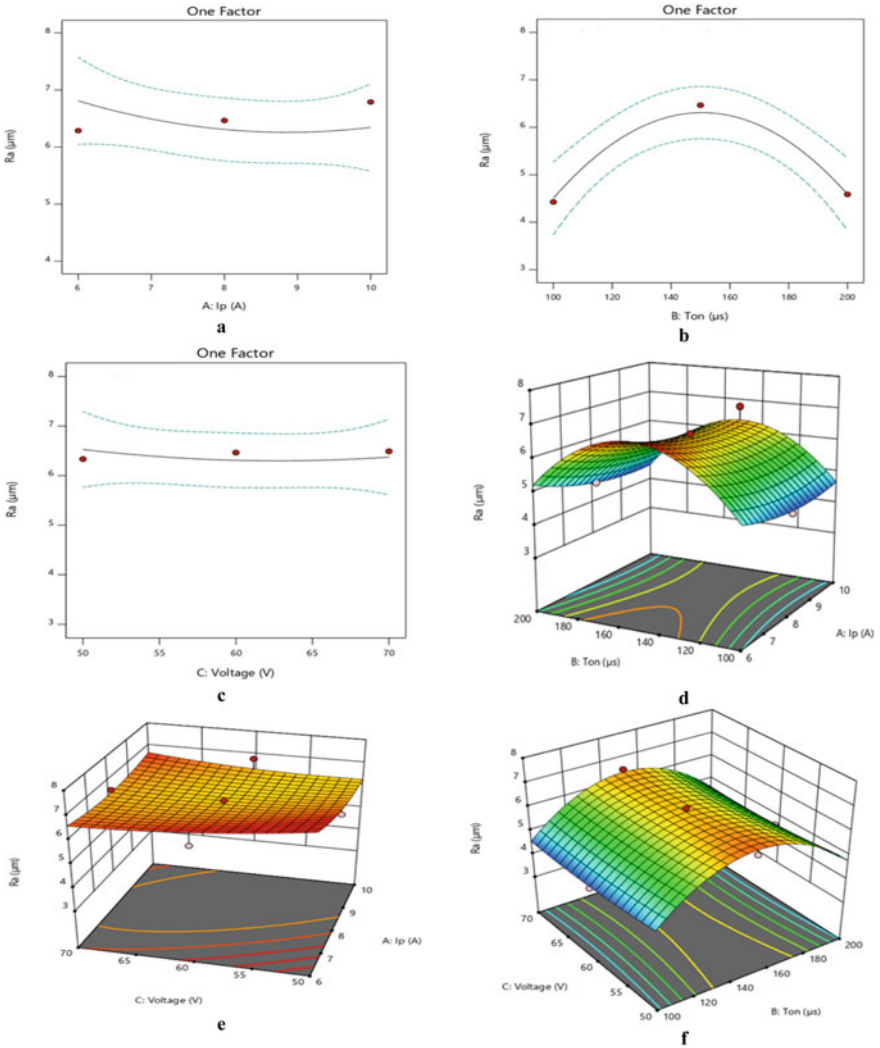


Fig. 11 Effect of process parameters **a** Ip, **b** Ton, **c** V (main effect plot) and 3D response surface plot of **d** Ip and Ton, **e** Ip and V, **f** Ton and V on Ra

4 Conclusion

An experimental study has been performed on electrical discharge machine of HCHCr AISI D7 steel material. Experiments were done based on different combinations of machining parameters. It was seen that this hole making process reduced the work material's consumption and waste also further utilized by using hollow shape tool. A mathematical model was created using the analysis of ANOVA in Design

Expert software to demonstrate the relation between the control factor and response parameters. The influence on EDM responses of all three process parameters has been observed. The expected values correspond relatively well with R^2 to the experimental values for MRR, ROC, TWR, and Ra respectively. The most significant factor was found to be peak current, Influencing all four performance characteristics. With an increase in I_p and T_{on} for any voltage value, the TWR increases. Better ROC and Ra were found at lower peak current. Application of RSM methodology has identified numerical optimal configuration of process parameters as: $I_p = 9.159 \text{ A} \approx 10 \text{ A}$, $T_{on} = 100 \text{ } \mu\text{s}$, and Voltage = $50.8296 \text{ V} \approx 50 \text{ V}$ at 0.629 desirabilities.

References

1. Ho KH, Newman ST (2003) State of the art electrical discharge machining (EDM). *Int J Mach Tools Manuf* 43(13):1287–1300. [https://doi.org/10.1016/S0890-6955\(03\)00162-7](https://doi.org/10.1016/S0890-6955(03)00162-7)
2. Aggarwal V, Khangura SS, Garg RK (2015) Parametric modeling and optimization for wire electrical discharge machining of Inconel 718 using response surface methodology. *Int J Adv Manuf Technol* 79(1–4):31–47. All the control parameters and their levels like the table shown 4 <https://doi.org/10.1007/s00170-015-6797-8>
3. Rajesha S, Sharma AK, Kumar P (2012) On electro discharge machining of inconel 718 with hollow tool. *J Mater Eng Perform* 21(6):882–891. <https://doi.org/10.1007/s11665-011-9962-8>
4. Leão FN, Pashby IR (2004) A review on the use of environmentally-friendly dielectric fluids in electrical discharge machining. *J Mater Process Technol* 149(1–3):341–346. <https://doi.org/10.1016/j.jmatprotec.2003.10.043>
5. Jeswani ML (1979) Small hole drilling in EDM. *Int J Mach Tool Des Res* 19(3):165–169. [https://doi.org/10.1016/0020-7357\(79\)90006-4](https://doi.org/10.1016/0020-7357(79)90006-4)
6. Pradhan MK (2018) Optimisation of EDM process for MRR, TWR and radial overcut of D2 steel: a hybrid RSM-GRA and entropy weight-based TOPSIS approach. *Int J Ind Syst Eng* 29(3):273. <https://doi.org/10.1504/ijise.2018.10013960>
7. Hammed S (2020) Effect of current and pulse-on time on surface roughness and wear ratio of stainless steel aisi 304 in electrical pulse-on time on surface roughness and wear ratio of stainless steel AISI 304 in electrical discharge machining, no. June, 2020
8. Kumar P, Yadav SKS (2019) Multi-objective optimization of electrical discharge drilling (EDD) process using PCA based grey relational analysis. *Mater Today Proc* 26(xxxx):2013–2020. <https://doi.org/10.1016/j.matpr.2020.02.438>
9. Pradhan MK (2012) Determination of optimal parameters with multi response characteristics of EDM by response surface methodology, grey relational analysis and principal component analysis. *Int J Manuf Technol Manag* 26(1–4):56–80. <https://doi.org/10.1504/IJMTM.2012.051435>
10. Pradhan MK (2013) Optimization of MRR, TWR and surface roughness of EDMed D2 Steel using an integrated approach of RSM, GRA and Entropy measurement method. 2013 *Int Conf Energy Effic Technol Sustain ICEETS 2013*:865–869. <https://doi.org/10.1109/ICEETS.2013.6533499>
11. Kuppan P, Rajadurai A, Narayanan S (2008) Influence of EDM process parameters in deep hole drilling of Inconel 718. *Int J Adv Manuf Technol* 38(1–2):74–84. <https://doi.org/10.1007/s00170-007-1084-y>
12. Kumar H, Davim JP (2011) Role of powder in the machining of Al-10%SiCp metal matrix composites by powder mixed electric discharge machining. *J Compos Mater* 45(2):133–151. <https://doi.org/10.1177/0021998310371543>

13. Chiang KT (2008) Modeling and analysis of the effects of machining parameters on the performance characteristics in the EDM process of Al₂O₃+TiC mixed ceramic. *Int J Adv Manuf Technol* 37(5–6):523–533. <https://doi.org/10.1007/s00170-007-1002-3>
14. El-Taweel TA (2009) Multi-response optimization of EDM with Al-Cu-Si-TiC P/M composite electrode. *Int J Adv Manuf Technol* 44(1–2):100–113. <https://doi.org/10.1007/s00170-008-1825-6>

Improving the Performance of Supply Chain Through Industry 4.0 Technologies



Mohd Ammar, Abid Haleem, Mohd Javaid, Shashi Bahl,
and Devaki Nandan

1 Introduction

Worldwide technologies from Industry 4.0 are now being adopted. In almost all sectors, these innovations have tremendous potential and have brought positive changes. According to a study published by Markets and Markets, Industry 4.0's current market share may surpass USD 71.7 billion and is expected to be more than USD 150 billion by 2024. A report published by PricewaterhouseCoopers (PwC) on the growth of Industry 4.0 says that 33% of the surveyed companies are digitizing their supply chains, and 72% of the companies, who had not planned to digitize their supply chain in the next five years, have also started the digitization. It also said that enterprises with highly digitized supply chains and activities could anticipate 4.1% annual productivity gains while rising sales by 2.6% a year. Because of the COVID-19 pandemic, this technology's adoption rate has increased, and market share might also be higher than expected. We require a proper management system for such an immersive use of these advanced technologies [1, 2].

This paper focuses on the technology of Industry 4.0 for the proper management system of the supply chain. Technologies like Data Processing, Cyber Protection, Industrial Internet of Things (IoT), Advanced Robotics, and Additive Manufacturing (AM) are being used in the manufacturing industry. This industry has

M. Ammar · A. Haleem · M. Javaid
Department of Mechanical Engineering, Jamia Millia Islamia, New Delhi 110025, India

S. Bahl (✉)
Department of Mechanical Engineering, I.K. Gujral Punjab Technical University Hoshiarpur
Campus, Hoshiarpur 146001, India
e-mail: shashi.bahl@ptu.ac.in

D. Nandan
Department of Industrial and Production Engineering, G.B. Pant, University of Agriculture and
Technology, Pantnagar 263145, India

changed tremendously and, in the days to come, it is predicted to change further [3, 4]. With all the latest emerging technologies, it is important to maintain a proper management structure to handle them appropriately. These inventions can be used to the best of their ability with properly designed management systems. The applications of Industry 4.0 technologies are in taking challenges of COVID-19 pandemic. These technologies fulfill the global medical supply chain crisis during COVID-19 pandemic [5–12]. This paper's primary research objectives are to study in brief about smart supply chain, discuss significant characteristics of smart supply chain processes, discuss the major role of Industry 4.0 technologies for smart supply chain, and study digital supply chain using Industry 4.0 technologies.

2 Smart Supply Chain

Supply chain networks have existed for ages now. With time, there are new developments in every technology. With the advent of technologies like Internet of Things, Augmented Reality, Advanced Robotics, and many more in Industry 4.0, supply chain networks have become smarter [13, 14]. Figure 1 shows the characteristics of smart supply chain processes. Integration of Industry 4.0 technologies in the supply



Fig. 1 Six characteristics of smart supply chain processes

chain networks has resulted in huge benefits. Though smart supply chain development is a complex process, it is still being developed and used quickly [15, 16]. Despite the difficulties, this is still done because the benefits obtained are higher and more profitable than the time invested and the challenges faced. An improved supply chain results in an improved business process, ultimately providing quicker response and higher efficiency. Moreover, in smart supply chain networks, machinery costs are also low, and most of the processes are operated with smart devices [17].

3 Significant Characteristics of Smart Supply Chain Processes

Smart supply chains are now being developed and implemented across industries. It has various advantages and helps in increasing the profits of various industries. Instrumented, Interconnected, Intelligent, Automated, Integrated, and Innovative are six main characteristics in a supply chain [18–21]. Table 1 discusses the significant characteristics of the smart supply chain processes.

Table 1 Significant characteristics of smart supply chain processes

S. No.	Characteristics	Description
1	Instrumented	The information collected in the smart supply chain is very much dependent on machines. It relies on sensors, meters, RFIDs, and other such devices. These devices provide more accurate information and are more reliable
2	Interconnected	This kind of supply chain network is designed so that all the entities and assets are interconnected. Thus in a smart supply chain, all the IT systems, business entities, products, and other smart objects are connected
3	Intelligent	To optimize the performance of a smart supply chain, they make comprehensive optimal decisions
4	Automated	Most of the processes in Smart Supply chains are automated. This is done to achieve higher efficiency and to minimize the chances of errors. Low-efficiency resources such as manually operated machines and even labors are avoided as much as possible
5	Integrated	The collaboration of the supply chain at all stages is very important. In a smart supply chain, it is made sure that most of the processes like joint decision making, information sharing, etc. are all integrated
6	Innovative	Requirements keep on increasing, and it is important to keep pushing our systems for more and hence innovation is needed everywhere. In smart supply chain, innovation is needed to meet the new requirements, improve existing needs, or inarticulate needs

4 Major Role of Industry 4.0 Technologies for Smart Supply Chain

Industry 4.0 technologies play an essential role in developing the smart supply chain. With the use of predictive analytics methods, organizations could condense forecasting errors to nearly half [22, 23]. The demand of medical supply chain during COVID-19 pandemic can be fulfilled by Industry 4.0 technologies. These are helpful to smartly track the products during COVID-19 pandemic [24–36]. Table 2 discusses the major role of Industry 4.0 technologies for the smart supply chain.

Industry 4.0 technologies are helpful for the effective management of the smart supply chain. These are being used for tracking of inventory for the smooth manufacturing processes [37–42]. Figure 2 shows the effective management of a smart supply chain.

- *Better Collaboration*: A big problem for businesses is information flow. Integrated software systems reduce bottlenecks and allow information to be seamlessly exchanged, providing a large-scale view of the supply chain from end-to-end [43, 44].
- *Shipping Optimization*: Shipping optimization has become a challenge for supply chain executives because of the rising prices. Identifying the most effective shipping strategies for small shipments, large bulk orders and other shipping situations helps businesses get orders to consumers quicker while reducing costs [13, 16, 45].
- *Improved Quality Control*: Enhanced quality management benefits businesses that have better control over their direct suppliers, and the suppliers of their suppliers. For example, enforcing uniform minimum quality standards allows direct suppliers to recognize and collaborate with secondary suppliers that fulfill those requirements [46–48].
- *Improved Cash Flow*: Disruptions in the supply chain have a domino effect, affecting every juncture in the supply chain, but the same applies to the positive: successful management of the supply chain has direct and indirect effects that facilitate the reliable, smooth flow of information, products, and services from procurement to final delivery. Enforcing standardized minimum quality standards, for instance, encourages direct suppliers to identify and cooperate with secondary suppliers that meet those criteria. Working with reputable vendors, for example, not only means fewer delays and more happy clients, but it also increases cash flow by enabling earlier invoicing [49, 50].
- *Keeping up with Demand*: Bullwhip effect-This phenomenon is mostly due to delays in disclosing supply and demand changes. To avoid obstacles like the bullwhip effect, supply chain leaders with access to real-time, reliable information, and integrated data can provide better forecast demand and react quickly to changing market conditions [41, 51, 52].
- *Improved Risk Mitigation*: Granular supply chain data analysis may reveal potential threats, allowing businesses to implement contingency plans to adapt quickly to unforeseen circumstances. Companies may prevent negative impacts by taking

Table 2 Major role of Industry 4.0 technologies for smart supply chain

S. No.	Role	Description
1	Enhanced transparency and precision and improved lead times in such situations	Internationally established supply chain networks involve numerous suppliers operating within the same network. Using IoT for live tracking and end-to-end transparency helps prevent supply chain disruptions
2	Predict obstructions in operations	A smart supply chain is often self-organizing and self-optimizing, and therefore the real-time data from the sensors connected across the factory are often integrated with the data as per the choice of an individual user. Smart systems can predict a possible operational problem arising from a process. Pre-fixing this sort of issue will streamline the system and stop waste from excess production. It will enable leaner manufacturing and operational efficiency
3	Data analytics for demand prediction	Using machine learning, we can predict the demand for a specific item more precisely by analyzing data. As compared to providing a single forecast number, we can also get the values of probability distributions of the expected demand volume. Through this, businesses may also quantify the possible risks involved in the supply chain and plan accordingly
4	Augmented reality in inventory and stock management	Many supply chain networks use augmented reality to carry out various processes in the warehouse. It helps in reducing inventory time. Using smart glasses, RFID, barcodes, sensors, it becomes easier to locate the stock and check the quantity. The user on the warehouse floor with the AR device can easily navigate the stocks and perform the required task without much training
5	Augmented reality for product delivery	Delivering products to the end-user consumes a considerable amount of time. Instead of struggling for parcels to be delivered or searching for the right building, delivery personnel can depend on AR for identification and location

(continued)

Table 2 (continued)

S. No.	Role	Description
6	Mixed reality for remote collaboration	With MR, digital collaboration and specialized assistance for maintenance and troubleshooting have become possible. It saves time and is economically more feasible for the company. This technology is not new but has gained its importance, especially during COVID lockdown. As new safety guidelines were issued, it became an urgent requirement to solve this issue
7	Product tracking	Using Barcode/RFID: all the parcels now have a barcode attached to them. It contains the order information about the package. The user gets the update at every step of the delivery. It is a prevalent method and is being widely used by almost every advanced logistics network Using GPS: some shipments contain costly and valuable items. For such kinds of shipments, a GPS tracking device is kept with the package. It provides a real-time location of the package. Since this method is very costly, it is used only with costly shipments
8	Specialized Freight handling	Various industries have specific handling functionality, e.g., in cold chain logistics; it is necessary to transport perishable foods to specific standards. By integrating smart devices with the existing cold chain, companies have developed technologies to verify the quality of transported food products and medicines, if they are being kept at the right temperature and conditions until the last mile delivery
9	Supplier management	This technology allows for understanding the contribution of each supplier in the company's business model. It also helps to understand the relationship of the company with the supplier. Supplier management is an essential part of a supply chain. With these technologies, decision-makers can be more confident while managing a supplier

(continued)

Table 2 (continued)

S. No.	Role	Description
10	Collaboration portals	This is one of the best uses of cloud computing in the supply chain. These kinds of portals allow companies and suppliers to collaborate. It has helped in overcoming various collaboration challenges faced in the industry. Using these portals, both company and supplier have access to information like order forecasts, purchase orders, production progress, shipment history, and other relevant details

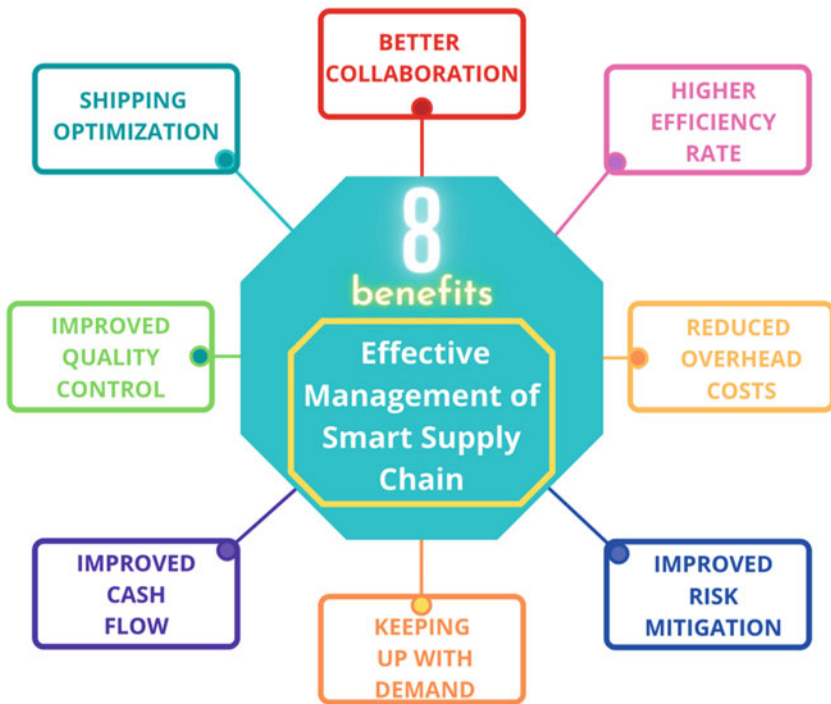


Fig. 2 Eight benefits of effective management of smart supply chain

preventive steps, rather than responding to supply chain delays, quality control problems, or other issues when they occur [53–55].

- *Reduced Overhead Costs:* Companies will minimize the overhead costs associated with storing slow-moving inventory by stocking less low-velocity inventory with more reliable demand forecasts to make room for higher-speed,

revenue-producing inventory. Another method of achieving leaner operations is to recognize excessive expenditures [56].

- *Higher Efficiency Rate*: With real-time details on the availability of raw materials and production delays, businesses may introduce contingency plans, such as sourcing materials from a backup provider, to avoid further delays. Implementing smart automation systems also results in higher performance [4, 57].

5 Digital Supply Chain Using Industry 4.0 Technologies

In Industry 4.0, when implementing technology and smart factory implementation, there is a new paradigm change due to which many new technologies have been introduced in the supply chain industry [54, 58]. Like enabling IoT in manufacturing and production has helped in the creation of the cyber-physical environment. It focuses mainly on smart factories' global networks that can share and monitor information [59–61]. The smart factory will function autonomously with this cyber-physical system. Disruptive revolutions are transforming the environment and business models of many industries. Analytics and supply chains are also critical segments influenced by the fourth industrial revolution due to the increased introduction of digitalized processes and impressive data growth as shown in Fig. 3.

- *Faster*: With Industry 4.0 in the Supply Chain, product distribution processes have evolved mainly, resulting in reduced delivery time and improved inventory management systems. Digitization has made it possible to use advanced forecasting methods, such as predictive internal data analytics (e.g., demand) and external data (e.g., industry dynamics, etc.), to ensure that customers are served



Fig. 3 Advantages of digitalization in supply chain

by their needs and met in advance. For example, Amazon ships the goods before the customer, and the last orders make an order is matched with shipment already in the distribution network and is sent to the customer's location.

- *Supple*: The Digital Supply Chain process manages real-time planning that enables businesses to respond to changes in demand or supply flexibly and durably, thereby reducing planning cycles. Planning becomes a continuous process due to sudden changes in demand and can respond dynamically to changing requirements or constraints.
- *Drilled Down*: The demand of today's time is customization as per the need of the person. Industry 4.0 in the supply chain helps businesses handle demand at a much worse level through micro-segmentation, niche market description, mass customization, and a more appropriate scheduling process for more individualization of the goods.
- *Efficient*: The days are gone where it was just a physical Endeavor to get goods down to end customers. There is the automation of both physical activities and technology participation with digitization that improves supply chain productivity. Technology such as robotics, AI, and computer advances effectively handles material handling, automating receiving/unloading, choosing, packaging, and even shipping final goods. Even transport with an automated transport system for prompt and non-failure delivery has been upgraded.

6 Limitations and Future Scope

Because of the lockdown during the COVID-19 pandemic, no physical survey could be carried out. In certain places, there were very few papers available, so we had to use business reports and online communications. Work can be conducted in the future on how to reduce supply chain accidents and mishappening by using Industry 4.0. There has been no automation of various warehouse processes; research must find solutions for those processes. The autonomy of these supply chains is also an environment that will change in the future. There is much work required for automation in the logistics segment of the supply chain industry.

7 Conclusion

Supply chain networks have simplified than earlier, but many processes need automation. Much work has been done in the delivery line area, but this network's transportation line has not changed much and needs to be focused on. There are three main primary enablers of digital supply chain conversion: a consistent plan, new skills, and an advanced climate. The digital supply chain begins with an understanding of the digital waste of the current operation, the lack of information sometimes leads to a failed path, and it is necessary to encapsulate the technological innovations.

Digitization technologies must then be generated with preparation. Implementation of an innovative technical solution is the final prerequisite. This completely blends with the advancements that contribute to a digitally fitted, creative world ready for the end customers to enter every segment in and out.

References

1. Alicke K, Rachor J, Seyfert A (2016) Supply chain 4.0—the next-generation digital supply chain. McKinsey & Company
2. Bharmal A (2019) Industry 4.0 market by technology and geography—global forecast to 2024. Markets and Markets
3. Fatorachian H, Kazemi H (2021) Impact of Industry 4.0 on supply chain performance. *Prod Plan Control* 32(1):63–81. <https://doi.org/10.1080/09537287.2020.1712487>
4. Xie Y, Yin Y, Xue W, Shi H, Chong D (2020) Intelligent supply chain performance measurement in Industry 4.0. *Syst Res Behav Sci* 37(4):711–718. <https://doi.org/10.1002/sres.2712>
5. Singh RP, Javaid M, Haleem A, Vaishya R, Bahl S (2020) Significance of health information technology (HIT) in context to COVID-19 pandemic: potential roles and challenges. *J Ind Integr Manag* 5(4):427–440. <https://doi.org/10.1142/s2424862220500232>
6. Sharma A, Bahl S, Bagha AK, Javaid M, Shukla DK, Haleem A (2020) Multi-agent system applications to fight COVID-19 pandemic 17(5):41–43. <https://doi.org/10.4103/am.am>
7. Rizvi AT, Haleem A, Bahl S, Javaid M (2021) Artificial intelligence (AI) and its applications in Indian manufacturing: a review. In: Acharya SK, Mishra DP (eds) *Current advances in mechanical engineering*. Lecture notes in mechanical engineering. Springer Nature
8. Iyengar KP, Vaishya R, Bahl S, Vaish A (2020) Impact of the coronavirus pandemic on the supply chain in healthcare. *Br J Healthc Manag* 26(6):1–4. <https://doi.org/10.12968/bjhc.2020.0047>
9. Haleem A, Gupta P, Bahl S, Javaid M, Kumar L (2020) 3D scanning of a carburetor body using COMET 3D scanner supported by COLIN 3D software: issues and solutions. *Mater Today Proc*. <https://doi.org/10.1016/j.matpr.2020.07.427>
10. Bahl S, Singh RP, Javaid M, Khan IH, Vaishya R, Suman R (2020) Telemedicine technologies for confronting COVID-19 pandemic: a review. *J Ind Integr Manag* 5(4):547–561. <https://doi.org/10.1142/S2424862220300057>
11. Bahl S et al (2020) Biosensors applications in fighting COVID-19 pandemic. *Apollo Med* 17(3):221–223. https://doi.org/10.4103/am.am_56_20
12. Bahl S, Iyengar K, Bagha AK, Jaly I, Jain V, Vaishya R (2021) Bioengineering technology in context to COVID-19 pandemic: potential roles and applications. *J Ind Integr Manag Innov Entrep*. <https://doi.org/10.1142/S2424862221500056>
13. Kumar SR, Pravin K, Mahesh C (2019) Evaluation of supply chain coordination index in context to Industry 4.0 environment. *Benchmarking Int J*. <https://doi.org/10.1108/BIJ-07-2018-0204>
14. Tortorella GL, Miorando RF, Fries CE, Vergara AMC (2018) On the relationship between lean supply chain management and performance improvement by adopting Industry 4.0 technologies. *Proc Int Conf Ind Eng Oper Manag* 2475–2484
15. Strandhagen JW, Buer S-V, Semini M, Alfnes E, Strandhagen JO (2020) Sustainability challenges and how Industry 4.0 technologies can address them: a case study of a shipbuilding supply chain. *Prod Plan Control* 1–16. <https://doi.org/10.1080/09537287.2020.1837940>
16. Garay-Rondero CL, Martinez-Flores JL, Smith R, Neale S, Morales OC, Aldrette-Malacara A (2019) Digital supply chain model in Industry 4.0. *J Manuf Technol Manag* 31(5):887–933. <https://doi.org/10.1108/JMTM-08-2018-0280>
17. Lifang W, Xiaohang Y, Alan J, YDC (2016) Smart supply chain management: a review and implications for future research. *Int J Logist Manag* 27(2):395–417. <https://doi.org/10.1108/IJLM-02-2014-0035>

18. Mangla SK, Kusi-Sarpong S, Luthra S, Bai C, Jakhar SK, Khan SA (2020) Operational excellence for improving sustainable supply chain performance. *Resour Conserv Recycl* 162:105025. <https://doi.org/10.1016/j.resconrec.2020.105025>
19. Liu B, De Giovanni P (2019) Green process innovation through Industry 4.0 technologies and supply chain coordination. *Ann Oper Res*. <https://doi.org/10.1007/s10479-019-03498-3>
20. Dalenogare LS, Benitez GB, Ayala NF, Frank AG (2018) The expected contribution of Industry 4.0 technologies for industrial performance. *Int J Prod Econ* 204:383–394. <https://doi.org/10.1016/j.ijpe.2018.08.019>
21. Yadav G, Kumar A, Luthra S, Garza-Reyes JA, Kumar V, Batista L (2020) A framework to achieve sustainability in manufacturing organisations of developing economies using industry 4.0 technologies' enablers. *Comput Ind* 122:103280. <https://doi.org/10.1016/j.compind.2020.103280>
22. Isaksen O (2020) The use of augmented reality in supply chain management: what it means for you. ENAVATE
23. Verma P (2018) 13 essential types of supply chain management tools for 2021. SelectHub
24. Jaly I, Iyengar KP, Bahl S, Jain V, Vaishya R (2020) COVID-19 pandemic and debates on the design of operating theatre ventilation systems in healthcare facilities. *J Ind Integr Manag Innov Entrep* 1–22. <https://doi.org/10.1142/S2424862221500093>
25. Gupta N, Bahl S, Bagha AK, Vaid S, Javaid M, Haleem A (2020) Nanomedicine technology and COVID-19 outbreak : applications and challenges. *J Ind Integr Manag Innov Entrep* 1–22. <https://doi.org/10.1142/S2424862221500123>
26. Ashima R, Haleem A, Bahl S, Javaid M, Mahla SK, Singh S (2021) Automation and manufacturing of smart materials in additive manufacturing technologies using internet of things towards the adoption of Industry 4.0. *Mater Today Proc*. <https://doi.org/10.1016/j.matpr.2021.01.583>
27. Fatma N, Haleem A, Bahl S, Javaid M (2021) Prospects of jewelry designing and production by additive manufacturing. In: Acharya SK, Mishra DP (eds) *Current advances in mechanical engineering*. Lecture notes in mechanical engineering. Springer Nature
28. Bahl S, Goyal T (2020) Corona warriors under risk during COVID-19 pandemic. *Curr Med Res Pract* 10(6):314–315. https://doi.org/10.4103/cmrrp.cmrrp_69_20
29. Jaly I, Iyengar K, Bahl S, Hughes T, Vaishya R (2020) Redefining diabetic foot disease management service during COVID-19 pandemic. *Diabetes Metab Syndr Clin Res Rev* 14(5):833–838. <https://doi.org/10.1016/j.dsx.2020.06.023>
30. Vaishya R, Bahl S, Singh RP (2020) Letter to the editor in response to: Telemedicine for diabetes care in India during COVID19 pandemic and national lockdown period: Guidelines for physicians. *Diab Metab Syndr Clin Res Rev* 14(4):687–688. <https://doi.org/10.1016/j.dsx.2020.05.027>
31. Suman R, Javaid M, Haleem A, Vaishya R, Bahl S, Nandan D (2020) Sustainability of coronavirus on different surfaces. *J Clin Exp Hepatol* 10(4):386–390. <https://doi.org/10.1016/j.jceh.2020.04.020>
32. Iyengar K, Bahl S, Vaishya R, Vaish A (2020) Challenges and solutions in meeting up the urgent requirement of ventilators for COVID-19 patients. *Diab Metab Syndr Clin Res Rev* 14(4):499–501. <https://doi.org/10.1016/j.dsx.2020.04.048>
33. Javaid M, Haleem A, Vaishya R, Bahl S, Suman R, Vaish A (2020) Industry 4.0 technologies and their applications in fighting COVID-19 pandemic. *Diab Metab Syndr Clin Res Rev* 14(4):419–422. <https://doi.org/10.1016/j.dsx.2020.04.032>
34. Sharma A, Bahl S, Bagha AK, Javaid M, Shukla DK, Haleem A (2020) Blockchain technology and its applications to combat COVID-19 pandemic. *Res Biomed Eng*. <https://doi.org/10.1007/s42600-020-00106-3>
35. Kushwaha S et al (2020) Significant applications of machine learning for COVID-19 pandemic. *J Ind Integr Manag* 5(4):453–479. <https://doi.org/10.1142/S2424862220500268>
36. Softa A, Bahl S, Bagha AK, Sehgal S, Haleem A, Javaid M (2020) Tissue engineering and its significance in healthcare during COVID-19 pandemic : potential applications and perspectives. *J Ind Integr Manag Innov Entrep* 1–21. <https://doi.org/10.1142/S242486222150007X>

37. Sajid S, Haleem A, Bahl S, Javaid M, Goyal T, Mittal M (2021) Data science applications for predictive maintenance and materials science in context to Industry 4.0. *Mater Today Proc.* <https://doi.org/10.1016/j.matpr.2021.01.357>
38. Fatima S, Haleem A, Bahl S, Javaid M, Mahla SK, Singh S (2021) Exploring the significant applications of internet of things (IoT) with 3D printing using advanced materials in medical field. *Mater Today Proc.* <https://doi.org/10.1016/j.matpr.2021.01.305>
39. Bahl S, Bagha AK, Rab S, Javaid M, Haleem A, Singh RP (2020) Advancements in biosensor technologies for medical field and COVID-19 pandemic. *J Ind Integr Manag Innov Entrep* 1–24. <https://doi.org/10.1142/S2424862221500081>
40. Ammar M, Haleem A, Javaid M, Walia R, Bahl S (2021) Improving material quality management and manufacturing organizations system through Industry 4.0 technologies. *Mater Today Proc.* <https://doi.org/10.1016/j.matpr.2021.01.585>
41. da Silva VL, Kovaleski JL, Pagani RN (2019) Technology transfer in the supply chain oriented to industry 4.0: a literature review. *Technol Anal Strateg Manag* 31(5):546–562. <https://doi.org/10.1080/09537325.2018.1524135>
42. Mattos NDL et al (2019) Exploring Industry 4.0 technologies to enable circular economy practices in a manufacturing context: a business model proposal. *J Manuf Technol Manag* 30(3):607–627. <https://doi.org/10.1108/JMTM-03-2018-0071>
43. Bhaveshkumar DSKM, Pasi N, Rane SB (2020) Smart supply chain management: a perspective of Industry 4.0. *Int J Adv Sci Tech* 29(05) SE-Articles 3016–3030
44. Abhijeet G, Merve EK, Hamid M, Mohit G (2020) The impact of Industry 4.0 implementation on supply chains. *J Manuf Technol Manag* 31(4):669–686. <https://doi.org/10.1108/JMTM-10-2019-0368>
45. Manavalan E, Jayakrishna K (2019) A review of internet of things (IoT) embedded sustainable supply chain for industry 4.0 requirements. *Comput Ind Eng* 127:925–953. <https://doi.org/10.1016/j.cie.2018.11.030>
46. Mastos TD et al (2020) Industry 4.0 sustainable supply chains: an application of an IoT enabled scrap metal management solution. *J Clean Prod* 269:122377. <https://doi.org/10.1016/j.jclepro.2020.122377>
47. Ivanov D, Dolgui A, Sokolov B (2019) The impact of digital technology and Industry 4.0 on the ripple effect and supply chain risk analytics. *Int J Prod Res* 57(3):829–846. <https://doi.org/10.1080/00207543.2018.1488086>
48. Erik H, Henrik S, Haozhe C, Alexander P, Günter P (2019) Supply chain management and Industry 4.0: conducting research in the digital age. *Int J Phys Distrib Logist Manag* 49(10):945–955. <https://doi.org/10.1108/IJPDLM-11-2019-399>
49. Lorenzo A, Messeni PA, Umberto P, Claudio GA (2019) Towards Industry 4.0: Mapping digital technologies for supply chain management-marketing integration. *Bus Process Manag* J 25(2):323–346. <https://doi.org/10.1108/BPMJ-04-2017-0088>
50. Jayaram A (2016) Lean six sigma approach for global supply chain management using industry 4.0 and IIoT. In: 2016 2nd international conference on contemporary computing and informatics (IC3I), pp 89–94. <https://doi.org/10.1109/IC3I.2016.7917940>
51. Kumar P, Singh RK, Kumar V (2021) Managing supply chains for sustainable operations in the era of industry 4.0 and circular economy: analysis of barriers. *Resour Conserv Recycl* 164:105215. <https://doi.org/10.1016/j.resconrec.2020.105215>
52. FGF, Arturo G-RJ, Anthony A, Vikas K (2019) Supply chain 4.0: concepts, maturity and research agenda. *Supply Chain Manag Int J* 25(2):262–282. <https://doi.org/10.1108/SCM-09-2018-0339>
53. Michael W, Sobhan A, WLC, Bill W (2020) Logistics innovation capability and its impacts on the supply chain risks in the Industry 4.0 era. *Mod Supply Chain Res Appl* 2(2):83–98. <https://doi.org/10.1108/MS CRA-07-2019-0015>
54. Esmaeilian B, Sarkis J, Lewis K, Behdad S (2020) Blockchain for the future of sustainable supply chain management in Industry 4.0. *Resour Conserv Recycl* 163:105064s. <https://doi.org/10.1016/j.resconrec.2020.105064>

55. Zheng T, Ardolino M, Bacchetti A, Perona M (2020) The applications of Industry 4.0 technologies in manufacturing context: a systematic literature review. *Int J Prod Res* 1–33. <https://doi.org/10.1080/00207543.2020.1824085>
56. Francisco FG, Arturo G-RJ, Anil K, Vikas K (2020) Performance measurement for supply chains in the Industry 4.0 era: a balanced scorecard approach. *Int J Prod Performance Manag*, vol ahead-of-p, no. ahead-of-print. <https://doi.org/10.1108/IJPPM-08-2019-0400>
57. Balan S, Rukshanda K, Piyush M, Vipul J (2019) Designing a hybrid cloud for a supply chain network of Industry 4.0: a theoretical framework. *Benchmarking Int J*, vol ahead-of-p, no. ahead-of-print. <https://doi.org/10.1108/BIJ-04-2018-0109>
58. Caiado RGG, Scavarda LF, Gavião LO, Ivson P, de Nascimento DL, Garza-Reyes JA (2021) A fuzzy rule-based industry 4.0 maturity model for operations and supply chain management. *Int J Prod Econ* 231:107883. <https://doi.org/10.1016/j.ijpe.2020.107883>
59. Dossou P-E (2018) Impact of sustainability on the supply chain 4.0 performance. *Procedia Manuf* 17:452–459. <https://doi.org/10.1016/j.promfg.2018.10.069>
60. Chetna C, Amol S (2019) A review of Industry 4.0 in supply chain management studies. *J Manuf Technol Manag* 31(5):863–886. <https://doi.org/10.1108/JMTM-04-2018-0105>
61. Andrea P, Federica C, Margherita P (2020) Industry 4.0 and supply chain process re-engineering: a coproduction study of materials management in construction. *Bus Process Manag J* 26(5):1093–1119. <https://doi.org/10.1108/BPMJ-04-2019-0147>

Significant Applications of Composite and Natural Materials for Vibration and Noise Control: A Review



Kartikay Singh Pawar, Ashok Kumar Bagha , Shashi Bahl ,
and Devaki Nandan

1 Introduction and Literature Review

Increasing environmental consciousness and demands more sustainable product has pushed the manufacture to consider the removal of traditional composite which uses synthetic fiber as reinforcement such as glass, carbon or kevlar. For this reason, the substitution of conventionally used synthetic fiber materials by natural fibers has become an emerging area of interest. Natural fibers fiber based composite have lower cost as compared to synthetic fiber; they are biodegradable and cause less pollution and minimal health hazards. These renewable materials could be used to replace new conventional composite. The use of composite materials in structural components requires better understanding of static and dynamic properties of the fiber and matrix. The dynamic properties, damping, and sound absorption are important factors in many industrial applications, especially, for automotive industry. The composite structures could improve the vibration damping since the energy dissipation of composite materials is much better than the convention structure and hence is a better alternative.

Composites reinforced with natural fiber such as sisal, jute, and kenaf have recently drawn a lot of attention from researchers due to their good mechanical properties,

K. S. Pawar · A. K. Bagha

Department of Mechanical Engineering, Dr. B.R. Ambedkar National Institute of Technology,
Jalandhar 144011, India

S. Bahl (✉)

Department of Mechanical Engineering, I.K. Gujral Punjab Technical University Hoshiarpur
Campus, Hoshiarpur 146001, India
e-mail: shashi.bahl@ptu.ac.in

D. Nandan

Department of Industrial and Production Engineering, G.B. Pant University of Agriculture and
Technology, Pantnagar 263145, India

light weight, environmentally friendly, and sustainability. Composite reinforced with sisal has shown potential for structural application at low economic cost [1]. Natural fiber has good potential. They have many advantages such as low density and cost and sustainability. The product derived from natural fiber reinforced composite can be reused or incinerated and do not have to be land filled as other synthetic fiber [2]. Composites reinforced with natural have better acoustic performance and vibration damping properties over synthetic fiber based composites [3, 4]. Natural fiber based composite flax-PP found widespread uses especially in the automotive sector with Polypropylene (PP) be most widely used matrix with natural fiber [5, 6].

Hadiji et al. [7] has analyzed the composite of the flax-PP, hemp-PP, kenaf-PP, and glass-PP with nonwoven fabrics and influencing factors such as type of fiber used, the volume fraction of fiber/matrix, the fiber orientation, and the porosity content, on the damping behavior of these composites is analyzed and compared with the convention glass fiber-PP composite. Free flexural vibration test is conducted with different fiber orientations and porosity (4–64%). It also shows as the porosity is increased the loss factor is also increased at 64% porosity the increase in loss factor by 108.7%. Thus porosity can play a vital role in increasing the damping property of the composite. Merotte et al. [8] has analyzed the effect of porosity content of flax-PP composite and how it affects the acoustical and mechanical properties of the composite. It explores the compaction rate during the manufacturing which directly affects the porosity and at which porosity we get the best sound absorption without sacrificing other mechanical properties. The porosity content varies from (0–70%). When the porosity is 60% the porous network is tortuous, the sound wave spread through the network due which the fiber rub against each other which eventually dissipate the energy into heat.

Mamtaz et al. [9] studied factors such as bulk density, fiber finesse, grain size, sample size thickness, and granular size in sound absorption of the composite. Fiber size can increase the sound adsorption at lower frequency levels. Authors also investigated the fibrogranular composites which have better sound absorption than conventional fiber composite, the granular size granulates of grain sizes between (0.71–1) mm and consolidated material of grain size less than 2 mm contribute higher to the flow resistivity and hence increases the sound absorption of the composite, it also states that the bulk density also increase the sound absorption of the composite in medium and high frequency range, increasing the sample thickness increases sound absorption at low frequency region but not at high frequency region. Rahman [10] studied damping mechanism which is present in composite. It shows results regarding fiber aspect ratio, volume fraction, fiber orientation, polymer material (viscoelastic nature), and effect of frequency on the damping of the composite. The increase in volume fraction of fiber increases the vibration damping in spite of the decrease of the viscoelasticity at it increases overall interface area, with more area there is more energy dissipating site so the vibrating damping increase. With the decrease of fiber aspect ratio there is the interface area also increases thus more vibration damping. Fiber orientation also play role in vibration damping with different matrix and fiber material there is different orientation of the fiber at which the vibration damping is maximum.

Nor et al. [11] has investigated different factors that affect the sound absorption of coir fiber based composites the factor such as bulk density, fiber diameter, and layer thickness of the coir fiber based composite it has also compared the fresh coir fiber with industrial coir fiber. It has shown that fresh coir fiber has better sound adsorption than industrial fiber, comparison of coir fiber with different diameters has shown that fiber with fewer diameters has better sound absorption. Composite with more bulk density has better sound absorption. Increasing the thickness of the composite has improved the sound adsorption at lower frequency without much change in the value of sound absorption. Koizumi et al. [12] has investigated the bamboo fiber and analyses factors such as fiber diameter, thickness, and density which affect the sound adsorption. The reduced fiber diameter has shown an increase in the sound adsorption, the thickness increased has shown an increase in sound adsorption at low level of frequency range. Increased density has also shown increased sound absorption. Porous material gives sound absorption over broadband range of frequency. Senthil Kumar et al. [13] has investigated the vibration damping of randomly oriented banana and sisal fiber in polymer matrix and observed with the increase of the fiber content there is an increase in the natural frequency of the composite of all length thus increase in the stiffness of the material has impact on the natural frequency of the composite. Banana fiber based composite shows with the decrease in the fiber content the damping should increase due to viscoelasticity of the polymer matrix. However, for sisal based fiber composite it shows reverse trend which may due to the interface stiffness and thickness as banana fibers are having smaller diameters which can cause thicker interface and thus increasing the damping of the composite.

Muller et al. [14] has investigated the acoustical property of cotton based composite in thermoset and thermoplastic matrices. Hybrid fleece with phenolic resin binder and fleece with epoxy binder are compared. Phenolic binder has shown better results than the epoxy based binder in higher frequency range of above 2 kHz. The sound adsorption is better with lower degree of compression. The higher compression rate results in lower sound adsorption at every frequency range. Cotton based composite shows good sound adsorption because of high fibrous structure. But fibrous structure has low stiffness thus cannot be used as structural member. Cotton fiber has also been used with other fibers and with different blending ratios. This affects the sound absorption coefficient on different frequency range [15, 16]. Zhang et al. [17] has investigated the sound and vibration damping of PLA fiber with natural fiber. Equal weight of PLA fiber with natural fiber is carded and blended together forming a nonwoven homogeneous mat which is further processed to form a composite panel. The acoustic performance is measured with the help wave number. Cotton-PLA and hemp-knead-PP composites have similar acoustic behavior with coincidence frequency at 2170 Hz and 2134 Hz respectively; as hemp kenaf-PP composite has been used in the automobile industry thus cotton-PLA gives a good alternative. Hu et al. [18] has investigated the damping characteristic of composite from the viewpoint of micromechanical analysis and purposed two damping models, the viscoelastic damping model, and specific damping capacity model. The author also compares the model's result with the experimental data and found considerable agreement between both.

Melo and Radford [19] has investigated fiber reinforced composites with the DMA and has shown trend in which there is an increase in damping loss factor as temperature increases. Senthil Kumar et al. [20] has investigated the effect of layering pattern and chemical treatment on the static and dynamic characteristic of banana and coconut sheath reinforced hybrid composite. The dynamic characteristics are studied with the help of impulse hammer technique layering pattern coconut sheath-banana-coconut sheath layering pattern showing better result the other layering pattern. Sargianis et al. [21] has studied the vibration and sound damping characteristics of natural material based composites and compared with synthetic fiber based composite with the help of wave number. The loss factor is determined by the frequency response function for each composite. Le Guen et al. [22] new has investigated the effect of adding polyglycerol on the flax fiber reinforced composite and has found that at polyol loading under 5 wt% the damping coefficient of the composite was improved by 15–25% when compared to flax fiber composite which is not impregnated by polyol. Talib et al. [23] has investigated the PLA composites with randomly oriented kenaf fiber with different volume fractions of the fiber on DMA at 1 Hz and has concluded that damping peak with more than 50 wt% of fiber has reduced amplitude with respect to neat PLA. Wielage et al. [24] has studied the PP composites reinforced with flax fiber, hemp fiber, and glass fiber with different volume fractions, they concluded that as the fiber content increased the loss factor decreases.

2 Composite and Natural Fibers for Noise and Vibration Absorption

In this section, we have discussed chemical treatment of the fiber which improves the properties of the natural fiber. Treatment of the fiber plays a vital role in many properties of the composite. It cleans the surface of the fiber, reduces the diameter, stops moisture absorption, modifies the surface of the fiber, and improves the adhesion between the fiber and matrix [25–33]. It can also increase the strength of the natural fiber as in case of ramie fiber which went under alkali treatment and register increase in strength of about 4–18% more than the untreated fiber [34]. Alkali treatment also called mercerization reduces the diameter of the fiber. Clean the surface of the fiber and overall produces higher quality fiber [33]. Concentration of NaOH affects the reduction in diameter as shown in Fig. 1. A number of coupling agents such as saline coupling agents can be used to enhance the interfacial bonding between the fiber and matrix and thus improving properties of the composite [35]. Alkalinization also improves the fiber-matrix bonding [36].

Theoretical calculations of sound absorption coefficient can be obtained by the predictions of the Delany-Bazley and the Garai-Pompoli models. The acoustic absorption coefficient of fibrous materials is usually determined by porosity, thickness and pore size, etc. The sound absorption coefficient can be measured with the

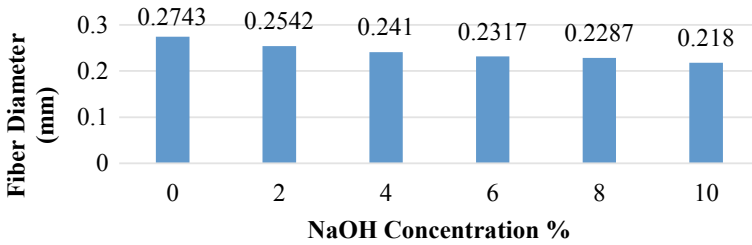


Fig. 1 Effect of NaOH concentration on fiber diameter of the natural fiber [33]

help of an impedance tube tester according to the ASTM standard E 1050 [37]. Schematic diagram of impedance tube MIC1 and MIC2 is shown in Fig. 2.

Three processes constitute the absorption of sound energy in the fibrous material. Initially, when the sound waves hit the fiber the sound wave transmits into the fibers, and due to viscous effect between the fiber frame and air cavities the energy is converted into heat. The heat will be further dissipated due to the temperature gradient between different fibers. The vibration of fiber will also happen due vibration of air in the bulk of the material [38]. Factors such as porosity, bulk density, fiber diameter, grain size, sample size thickness, granular size, and fiber size affect the sound adsorption in the composite material [7, 9]. The sound absorption of any composite material can be increased with more tortuous path. This provides more flow resistivity to the sound wave traveling. This can be achieved by reducing the diameter of the composite, this allows more fibers to be in the unit volume which increases the flow resistivity [39]. Noise reduction coefficient gives value for easy comparison between comparing the acoustic behavior of various materials [36]. Noise reduction coefficient (NRC) can be defined as the arithmetic mean of sound absorption coefficients at 250, 500, 1000, and 2000. NRC values are used as indexes of the sound absorbing efficiency of the material.

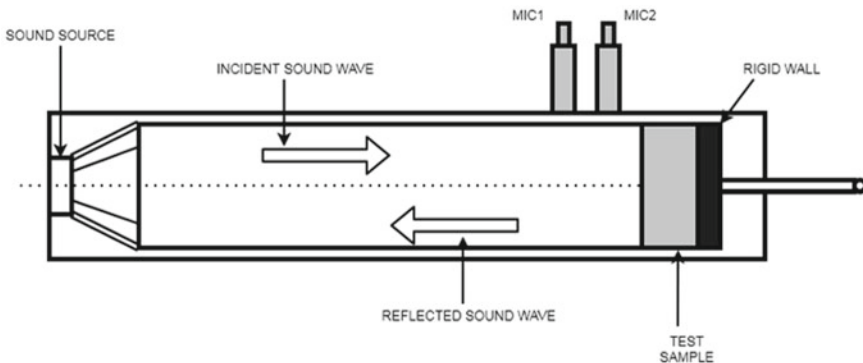


Fig. 2 Schematic diagram of Impedance tube MIC1 and MIC2 denote two microphones [37]

Damping can be categorizing into two groups: material damping and structural damping. Material damping is due to the energy dissipated from the volume of the material and structural damping is due to the relative motion between the different components which causes rubbing [40]. Mechanism of damping in composite differs considerably from the conventional material. Viscoelasticity of the composites plays an important role in the vibration damping of the material. Composites with materials having viscoelasticity can improve the vibration damping of a composite without reducing strength and stiffness of the composite material [41–49]. The viscoelastic layers are very effective in improving the damping (loss factor) of the structure [50, 51]. Vibration damping is caused due to interphase. Interphase is the region between fiber and matrix and is along the fiber length. Interphase properties differ from both matrix and fiber. The properties of interphase play an important role in vibration damping of the composite. Vibration damping is caused due to damage. It is mainly of two types: damping due to energy dissipation and frictional damping. Damping due to energy dissipation is caused due damage to the matrix and fiber which causes crack in matrix and damage the fiber. It causes energy dissipation due to friction at cracks and delamination sites [52, 53]. Frictional damping is caused due to interface slip between unbound regions between fiber and matrix in composite interface. Frictional sliding between the matrix and the nanotubes in the nanocomposite is the main source of dissipation of energy and causes damping [54].

There are numerous ways by which we can measure damping such as logarithmic decrement, the damping ratio, the specific damping capacity, quality factor, loss factor, and specific damping capacity [55]. Loss factor can be easily being calculated from the dynamic mechanical analyzer by which we can estimate the damping of the composite. DMA cannot be used for material with high modulus however it measurements are still important to validate the damping in material [54]. Figure 3 shows the comparison in approximate value of loss factor between the natural and synthetic fiber with natural showing better damping characteristics. Finite element method can also be used to find the damping factor of the composite.

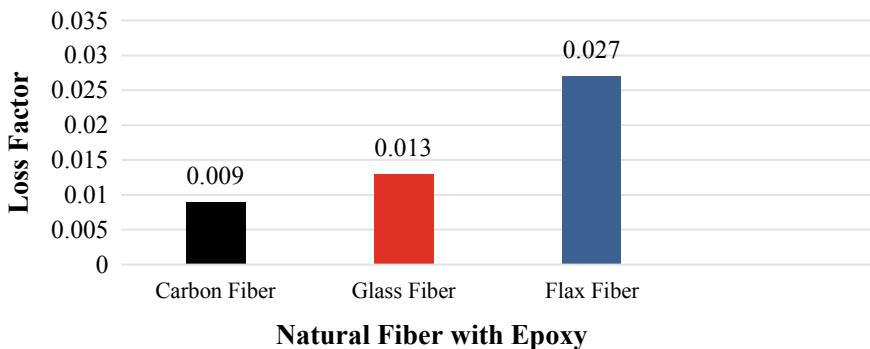


Fig. 3 Comparison of loss factor between the synthetic fiber (GF and CF) reinforced epoxy and natural fiber (FF) reinforced epoxy [56]

3 Conclusions

Natural fibers are already replacing common synthetic fibrous materials for acoustic absorption and vibration damping as in case of automotive industry where natural based composites are becoming more widespread. The use of chemical treatment such as alkali treatment cleans the fiber, reduces the fiber diameter, improves fiber matrix adhesion, and increases the quality of the natural fiber. Porosity of the composite which can be controlled during the fabrication of the composite can increase both vibration damping and acoustic performance of the fiber. More fibrous fiber such as cotton material can also increase the vibration damping and acoustic performance of the fiber however it reduces mechanical strength of the fiber by using hybrid composite of two natural fibers with different bends we can mitigate this issue. Viscoelasticity of the matrix and aspect ratio of the fiber surface influence the vibration damping and acoustic performance of the composite. The properties of the interphase which can change by the chemical treatment also affect the vibration and acoustic performance of the composites. Fiber reinforced PLA composite and bio composite a good alternative to conventional natural fiber based composite as the matrix used is also biodegradable plastic which is even more sustainable.

References

1. Li Y, Mai Y-W, Ye L (2000) Sisal fibre and its composites: a review of recent developments. *Compos Sci Technol* 60:2037–2055. [https://doi.org/10.1016/S0266-3538\(00\)00101-9](https://doi.org/10.1016/S0266-3538(00)00101-9)
2. Witayakran S, Smitthipong W, Wangpradid R, Chollakup R, Clouston PL (2017) Presented at the natural fiber composites: review of recent automotive trends. <https://doi.org/10.1016/B978-0-12-803581-8.04180-1>
3. Flynn J, Amiri A, Ulven C (2016) Hybridized carbon and flax fiber composites for tailored performance. *Mater Des* 102:21–29. <https://doi.org/10.1016/j.matdes.2016.03.164>
4. Rueppel M, Rion J, Dransfeld C, Fischer C, Masania K (2017) Damping of carbon fibre and flax fibre angle-ply composite laminates. *Compos Sci Technol* 146:1–9. <https://doi.org/10.1016/j.compscitech.2017.04.011>
5. Arbelaz A, Fernández B, Cantero G, Llano-Ponte R, Valea A, Mondragon I (2005) Mechanical properties of flax fibre/polypropylene composites. Influence of fibre/matrix modification and glass fibre hybridization. *Compos Part A Appl Sci Manuf* 36:1637–1644. <https://doi.org/10.1016/j.compositesa.2005.03.021>
6. Zhang L, Miao M (2010) Commingled natural fibre/polypropylene wrap spun yarns for structured thermoplastic composites. *Compos Sci Technol* 70:130–135. <https://doi.org/10.1016/j.compscitech.2009.09.016>
7. Hadji H, Assarar M, Zouari W, Pierre F, Behloul K, Zouari B, Ayad R (2020) Damping analysis of nonwoven natural fibre-reinforced polypropylene composites used in automotive interior parts. *Polym Testing* 89:106692. <https://doi.org/10.1016/j.polymertesting.2020.106692>
8. Merotte J, Le Duigou A, Bourmaud A, Behloul K, Baley C (2016) Mechanical and acoustic behaviour of porosity controlled randomly dispersed flax/PP biocomposite. *Polym Test* 51:174–180. <https://doi.org/10.1016/j.polymertesting.2016.03.002>
9. Mamtaz H, Fouladi MH, Al-Atabi M, Narayana Namasivayam S (2016) Acoustic absorption of natural fiber composites. *J Eng* 2016:5836107. <https://doi.org/10.1155/2016/5836107>

10. Rahman MZ (2021) Mechanical and damping performances of flax fibre composites—a review. *Compos Part C Open Access* 4:100081. <https://doi.org/10.1016/j.jcomc.2020.100081>
11. Nor MJM, Ayub M, Zulkifli R, Amin N, Fouladi MH (2010) Effect of different factors on the acoustic absorption of coir fiber. *J Appl Sci* 10:2887–2892. <https://doi.org/10.3923/jas.2010.2887.2892>
12. Koizumi T, Tsujiuchi N, Adachi A (2002) The development of sound absorbing materials using natural bamboo fibers. *High Perform Struct Mater* 59:157–166. <https://doi.org/10.2495/HPS020161>
13. Senthil Kumar K, Siva I, Jeyaraj P, Winowlin Jappes JT, Amico SC, Rajini N (2014) Synergy of fiber length and content on free vibration and damping behavior of natural fiber reinforced polyester composite beams. *Mater Des* 1980–2015(56):379–386. <https://doi.org/10.1016/j.matdes.2013.11.039>
14. Mueller DH, Krobjilowski A (2003) New discovery in the properties of composites reinforced with natural fibers. *J Ind Text* 33:111–130. <https://doi.org/10.1177/152808303039248>
15. Küçük M, Korkmaz Y (2012) The effect of physical parameters on sound absorption properties of natural fiber mixed nonwoven composites. *Text Res J* 82:2043–2053. <https://doi.org/10.1177/0040517512441987>
16. Zhu W, Nandikolla V, George B (2015) Effect of bulk density on the acoustic performance of thermally bonded nonwovens. *J Eng Fibers Fabr* 10:39–45. <https://doi.org/10.1177/155892501501000316>
17. Zhang J, Khatibi AA, Castanet E, Baum T, Komeily-Nia Z, Vroman P, Wang X (2019) Effect of natural fibre reinforcement on the sound and vibration damping properties of bio-composites compression moulded by nonwoven mats. *Compos Commun* 13:12–17. <https://doi.org/10.1016/j.coco.2019.02.002>
18. Hu B-G, Dokainish MA (1993) Damped vibrations of laminated composite plates—modeling and finite element analysis. *Finite Elem Anal Des* 15:103–124. [https://doi.org/10.1016/0168-874X\(93\)90059-Y](https://doi.org/10.1016/0168-874X(93)90059-Y)
19. Melo JDD, Radford DW (2005) Time and temperature dependence of the viscoelastic properties of CFRP by dynamic mechanical analysis. *Compos Struct* 70:240–253. <https://doi.org/10.1016/j.compstruct.2004.08.025>
20. Senthil Kumar K, Siva I, Rajini N, Winowlin Jappes JT, Amico SC (2016) Layering pattern effects on vibrational behavior of coconut sheath/banana fiber hybrid composites. *Mater Des* 90:795–803. <https://doi.org/10.1016/j.matdes.2015.11.051>
21. Sargianis JJ, Kim H-I, Andres E, Suhr J (2013) Sound and vibration damping characteristics in natural material based sandwich composites. *Compos Struct* 96:538–544. <https://doi.org/10.1016/j.compstruct.2012.09.006>
22. Le Guen M-J, Newman RH, Fernyhough A, Staiger MP (2014) Tailoring the vibration damping behaviour of flax fibre-reinforced epoxy composite laminates via polyol additions. *Compos A Appl Sci Manuf* 67:37–43. <https://doi.org/10.1016/j.compositesa.2014.08.018>
23. Talib RA, Tawakkal ISMA, Khalina A (2011) The Influence of Mercerised Kenaf Fibres reinforced polylactic acid composites on dynamic mechanical analysis. *Key Eng Mater* 471–472:815–820. <https://doi.org/10.4028/www.scientific.net/KEM.471-472.815>
24. Wielage B, Lampke T, Utschick H, Soergel F (2003) Processing of natural-fibre reinforced polymers and the resulting dynamic–mechanical properties. *J Mater Process Technol* 139:140–146. [https://doi.org/10.1016/S0924-0136\(03\)00195-X](https://doi.org/10.1016/S0924-0136(03)00195-X)
25. Bahl S, Bagha AK, Sehgal S (2021) Experimental investigations into sound transmission loss by different materials at aircraft noise. *Mater Today Proc.* <https://doi.org/10.1016/j.matpr.2020.12.153>
26. Chhipa SM, Kumar P, Bagha AK, Bahl S (2020) Removing uncertainty in the boundary condition of five degree of freedom spring mass vibratory system using direct updating method. *Mater Today Proc.* <https://doi.org/10.1016/j.matpr.2020.08.803>
27. Bahl S, Bagha AK (2020) Finite element modeling and simulation of the fiber–matrix interface in fiber reinforced metal matrix composites. *Mater Today Proc.* <https://doi.org/10.1016/j.matpr.2020.06.160>

28. Bagha AK, Bahl S (2020) Finite element analysis of VGCF/pp reinforced square representative volume element to predict its mechanical properties for different loadings. *Mater Today Proc.* <https://doi.org/10.1016/j.matpr.2020.06.108>
29. Bahl S, Dolma J, Jyot Singh J, Sehgal S (2020) Biodegradation of plastics: a state of the art review. *Mater Today Proc.* <https://doi.org/10.1016/j.matpr.2020.06.096>
30. Bahl S (2020) Axisymmetric finite element analysis of single fiber push-out test for stainless steel wire reinforced aluminum matrix composites. *Mater Today Proc* 28:1605–1611. <https://doi.org/10.1016/j.matpr.2020.04.848>
31. Bahl S, Cambow R, Kumar Bagha A (2020) An experimental study to measure the acoustical properties of natural fibers at real case broadband excitations. *Mater Today Proc* 28:1279–1284. <https://doi.org/10.1016/j.matpr.2020.04.228>
32. Bahl S, Singh T, Kumar V, Sehgal S, Bagha AK (2021) A systematic review on recent progress in advanced joining techniques of the lightweight materials. *AIMS Mater Sci* 8:62–81. <https://doi.org/10.3934/matserci.2021005>
33. Kalia S, Kaith BS, Kaur I (2009) Pretreatments of natural fibers and their application as reinforcing material in polymer composites—a review. *Polym Eng Sci* 49:1253–1272. <https://doi.org/10.1002/pen.21328>
34. Goda K, Sreekala MS, Gomes A, Kaji T, Ohgi J (2006) Improvement of plant based natural fibers for toughening green composites—effect of load application during mercerization of ramie fibers. *Compos A Appl Sci Manuf* 37:2213–2220. <https://doi.org/10.1016/j.compositesa.2005.12.014>
35. Xie Y, Hill CAS, Xiao Z, Militz H, Mai C (2010) Silane coupling agents used for natural fiber/polymer composites: A review. *Compos A Appl Sci Manuf* 41:806–819. <https://doi.org/10.1016/j.compositesa.2010.03.005>
36. Van de Weyenberg I, Chi Truong T, Vangrimde B, Verpoest I (2006) Improving the properties of UD flax fibre reinforced composites by applying an alkaline fibre treatment. *Compos A Appl Sci Manuf* 37:1368–1376. <https://doi.org/10.1016/j.compositesa.2005.08.016>
37. ASTM C384-04(2016): Standard test method for impedance and absorption of acoustical materials by impedance tube method. ASTM International, West Conshohocken, PA
38. Allard JF, Atalla N (2009) Propagation of sound in porous media: modelling sound absorbing materials. Wiley. <https://doi.org/10.1002/9780470747339>
39. Tang X, Yan X (2017) Acoustic energy absorption properties of fibrous materials: a review. *Compos Part A Appl Sci Manuf* 101:360–380
40. Kulkarni P, Bhattacharjee A, Nanda BK (2018) Study of damping in composite beams. *Mater Today Proc* 5:7061–7067. <https://doi.org/10.1016/j.matpr.2017.11.370>
41. Bahl S, Nagar H, Singh I, Sehgal S (2020) Smart materials types, properties and applications: a review. *Mater Today Proc* 28:1302–1306. <https://doi.org/10.1016/j.matpr.2020.04.505>
42. Kesharwani A, Bedi R, Kumar Bagha A, Bahl S (2020) Experimental study to measure the sound transmission loss of natural fibers at tonal excitations. *Mater Today Proc* 28:1554–1559. <https://doi.org/10.1016/j.matpr.2020.04.839>
43. Suman R, Nandan D, Haleem A, Bahl S, Javaid M (2020) Experimental study of electroless plating on acrylonitrile butadiene styrene polymer for obtaining new eco-friendly chromium-free processes. *Mater Today Proc.* <https://doi.org/10.1016/j.matpr.2020.04.843>
44. Kumar Bagha A, Bahl S (2020) Strain energy and finite element analysis to predict the mechanical properties of vapor grown carbon fiber reinforced polypropylene nanocomposites. *Mater Today Proc.* <https://doi.org/10.1016/j.matpr.2020.09.034>
45. Bahl S (2020) Numerical simulation of the debonding behavior of fiber reinforced metal matrix composites. *Mater Today Proc* 28:1328–1334. <https://doi.org/10.1016/j.matpr.2020.04.598>
46. Bahl S (2020) Fiber reinforced metal matrix composites—a review. *Mater Today Proc.* <https://doi.org/10.1016/j.matpr.2020.07.423>
47. Kumar Saini M, Kumar Bagha A, Kumar S, Bahl S (2020) Finite element analysis for predicting the vibration characteristics of natural fiber reinforced epoxy composites. *Mater Today Proc.* <https://doi.org/10.1016/j.matpr.2020.08.717>

48. Suman R, Nandan D, Haleem A, Bahl S, Javaid M (2020) Comparative study of silicon dioxide and kaolinite ratio for temperature and humidity variations of earth energy enabled cooling system and traditional cooler. *Mater Today Proc.* <https://doi.org/10.1016/j.matpr.2020.04.847>
49. Rao MD, Echempati R, Nadella S (1997) Dynamic analysis and damping of composite structures embedded with viscoelastic layers. *Compos B Eng* 28:547–554. [https://doi.org/10.1016/S1359-8368\(96\)00073-X](https://doi.org/10.1016/S1359-8368(96)00073-X)
50. Beane SM, Marchi MM, Snyder DS (1995) Utilizing optimized panel damping treatments to improve powertrain induced NVH and sound quality. *Appl Acoust* 45:181–187. [https://doi.org/10.1016/0003-682X\(94\)00040-3](https://doi.org/10.1016/0003-682X(94)00040-3)
51. Makhecha DP, Ganapathi M, Patel BP (2002) Vibration and damping analysis of laminated/sandwich composite plates using higher-order theory. *J Reinf Plast Compos* 21:559–575. <https://doi.org/10.1177/0731684402021006833>
52. Lai J-Y, Young K-F (1995) Dynamics of graphite/epoxy composite under delamination fracture and environmental effects. *Compos Struct* 30:25–32. [https://doi.org/10.1016/0263-8223\(94\)00017-4](https://doi.org/10.1016/0263-8223(94)00017-4)
53. Tenek LH, Henneke EG, Gunzburger MD (1993) Vibration of delaminated composite plates and some applications to non-destructive testing. *Compos Struct* 23:253–262. [https://doi.org/10.1016/0263-8223\(93\)90226-G](https://doi.org/10.1016/0263-8223(93)90226-G)
54. Gibson RF (2016) Principles of composite material mechanics. CRC Press, Boca Raton. <https://doi.org/10.1201/b19626>
55. Kinra VK (1992) M3D: mechanics and mechanisms of material damping. American Society for Testing & Materials
56. Duc F, Bourban PE, Plummer CJG, Manson J-AE (2014) Damping of thermoset and thermoplastic flax fibre composites. *Compos A Appl Sci Manuf* 64:115–123. <https://doi.org/10.1016/j.compositesa.2014.04.016>

Digital Management Systems in Manufacturing Using Industry 5.0 Technologies



Nadia Fazal , Abid Haleem , Shashi Bahl , Mohd Javaid ,
and Devaki Nandan

1 Introduction

Industrial revolutions are meant to segregate man's and machine's work and hand over jobs to robots that are difficult and dangerous for the workforce. Due to the significant impact of machines on society, it is crucial to understand their relation [1]. The first industrial revolution can be traced back to 1780s, which started off, with the generation of power from water, steam, and fossil fuels. The second industrial revolution started in the 1870s, which led to electrification and mass production. With the arrival of electronics and information technology, the third industrial revolution started with automation in the 1970s. The development of new technologies paved the way for the fourth industrial revolution, which started in 2011 by the German Federal government but is still unknown and not yet well grown. This utilizes cloud computing and the Internet of Things (IoT) to establish cyber-physical systems (CPS). This CPS will deploy digital twin technologies to increase the level of digitization in every industry [2]. Digital technologies are used during the COVID-19 pandemic to create significant advancements in healthcare. These technologies can digitally store the patient data, which helps for proper monitoring and treatment process [3–12].

With growing technologies, another industrial revolution is bound to happen in the future, which will be the industrial revolution 5.0, better known as Industry

N. Fazal · A. Haleem · M. Javaid
Department of Mechanical Engineering, Jamia Millia Islamia, New Delhi 110025, India

S. Bahl (✉)
Department of Mechanical Engineering, I.K. Gujral Punjab Technical University Hoshiapur
Campus, Hoshiarpur 146001, India
e-mail: shashi.bahl@ptu.ac.in

D. Nandan
Department of Industrial and Production Engineering, G.B. Pant University of Agriculture and
Technology, Pantnagar 263145, India

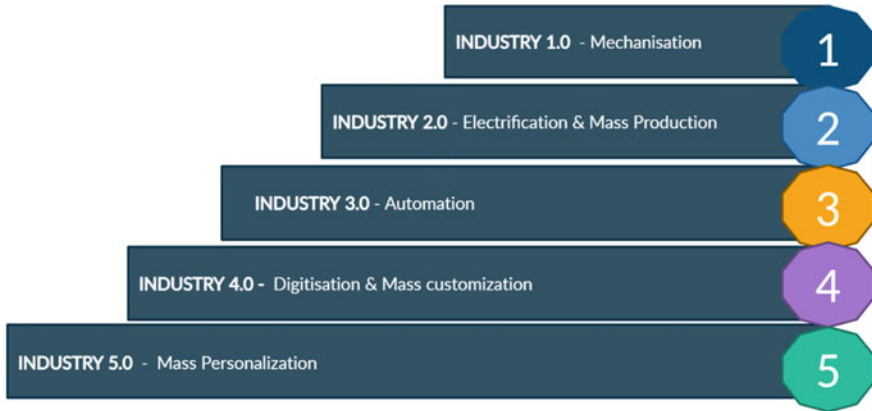


Fig. 1 Summary of Industrial revolutions, their period, and their characteristics

5.0. Researchers have already started talking about industry 5.0, based on learning human behavior with artificial intelligence (AI) [13]. Figure 1 depicts the summary of industrial revolutions, their period, and their characteristics. This paper aims to establish various technological advancements in the upcoming revolution and how these can prove beneficial to the manufacturing industry in solving their problems.

2 Industry 5.0

The term Industry 5.0 was first published in an article on LinkedIn by Michael Rada on December 1, 2015. The implementation of this revolution is meant for solving industrial and social problems related to industrialization [13]. Industry 4.0 is all about increasing the process's efficiency by automating manufacturing processes ignoring all other aspects like employment and environmental pollution. Industry 5.0 will create a smart manufacturing system and smart supply chains which will use data intelligently. Smart factories will provide greater flexibility to communicate among themselves [14]. The transition from Industry 4.0 to Industry 5.0 will create better ideas with humans' brainpower [15]. Industry 4.0 brought mass customization, but Industry 5.0 will bring mass personalization according to the customer's needs. It focuses on continuous development, value-added activities, and less waste generation [16].

3 Need for the Study and Research Objectives

Today, quintillion bytes of data are created every day by technology like IoT. This has imposed many severe challenges. The need to leverage Big Data has become of utmost importance for every manufacturing industry. The unstructured data needs to be structured in order to get useful business insights. Industrial manufacturers can use this data to optimize resources' cost and consumption by creating a digital management system driven by industry 5.0 technologies [17, 18]. These new technologies' help can easily tackle the problem of waste generation and pollution. This paper addresses the following primary research objectives:

- To identify major technologies of Industry 5.0.
- To explore challenges faced by the contemporary manufacturing industries with Industry 4.0.
- To understand the digital connectivity of manufacturing systems by using Industry 5.0 technologies.
- To identify the application of Industry 5.0 technologies in managing manufacturing industries.

4 Advancements in Industry 5.0 as Compared to Industry 4.0

Industry 4.0 focuses on mass customization and provides better coordination between machines and information technology. The main idea of Industry 4.0 is to fulfill individual customer requirements through smart manufacturing. This revolution deals with intelligent devices and systems for creating digital factories [14]. The important drivers of Industry 4.0 are the Internet of Things (IoT), Industrial Internet of Things (IIoT), Cloud computing, Cybersecurity, Big Data, and Smart manufacturing [19]. Industry 5.0 will emerge as the age of augmentation when humans and machines will reconcile and work together. Unlike Industry 4.0, this paradigm will combine both humans' strength and the Cyber-Physical Production System (CPPS) [20]. This efficient relationship will solve all the problems of the economy, ecology, and social world. They will impact the environment in the field of reducing waste materials that may also reduce the material cost, thereby decreasing the social impact of industrial processes [21].

5 Major Technologies of Industry 5.0

5.1 Collaborative Systems and Other Smart Systems

Cobots are different from robots in industries as they are equipped with susceptible smart sensors for assembling products. They work alongside humans in order to enhance personalization in products. This will save time and can be produced in large quantities. Unlike industrial robots, these systems are designed not to harm the workers working along with them [22].

5.2 Digital Twin

In today's world, where everything is now on a virtual platform, manufacturers also need to adopt this concept to reduce the cost of collecting data. Its adoption requires integrating other technologies like Big Data analytics, smart sensors, and other IoT technologies. In manufacturing industries, it becomes necessary to clarify the product's specifications to optimize the final product. The solution provided by the digital twin can be used in this process [23].

5.3 Smart Manufacturing Through Exoskeletons

With increasing social distancing rules and a need for a safer work environment, an advanced robotic technology called exoskeletons can help humans assist them in various manufacturing industries activities. These are a bit different from collaborative robots as humans must be present in the environment while wearing them. Exoskeletons can be an asset to the industry if it incorporates technologies like virtual reality (VR) and machine learning (ML) [24].

5.4 Smart Materials

With the advent of new, advanced materials and structures, smart materials have been recently engineered. Light, reactive smart materials have the potential to be used in the 4D printing method. The use of polymeric composite materials in producing arms of cobots will increase production performance in manufacturing industries. Intelligent materials, on the other side, are more sophisticated and responsible than smart materials. Research is being carried on this topic to employ them in manufacturing industries for smarter production [25].

5.5 Advanced Implementation of AI, IoE, and Cloud Computing

As we proceed to the next industrial revolution, advancements in various technologies like IoT and AI will occur. With time IoT will transform into IoE (Internet of Everything), which will connect the physical assets and various other intangible assets. Advances in intelligent CPS will prove to be an emergent technology in the Fifth industrial revolution [26]. These technologies are also applicable in healthcare during COVID-19 pandemic. The successful implementation of these technologies is helpful to reduce the load of healthcare workers [27–35].

5.6 4D Printing

For manufacturing products that are more creative and personalized, the 4D printing technique will be inaugurated in the fifth industrial revolution, focusing on the design process. 4D printing technology will require different smart materials that are flexible and adaptable in nature, like Shape memory alloys (SMA) and Shape memory polymers (SMP) [36]. 4D printed structures can significantly reduce the volume of storage in industries. These materials can self-adapt and self-repair, which can prove advantageous to the manufacturing industries [37]. Figure 2 shows significant technologies of Industry 5.0 used to create the manufacturing system smarter and intelligent.

6 Personalization in Industry 5.0

The customer's ever-growing demands and the basic human urge cannot be neglected, which has led to personalization. Industry 5.0 will provide technologies that will enhance customers' personalization experience, thereby increasing affordability and comfortability. Such high quality and unique products are possible because of the cyber-physical systems driven by mass customization, making them affordable. This symbiotic relationship between man and machine working together improves efficiency and uniqueness [26]. It is only possible because robots can do repetitive and tedious jobs while humans can have more out of the box thinking.

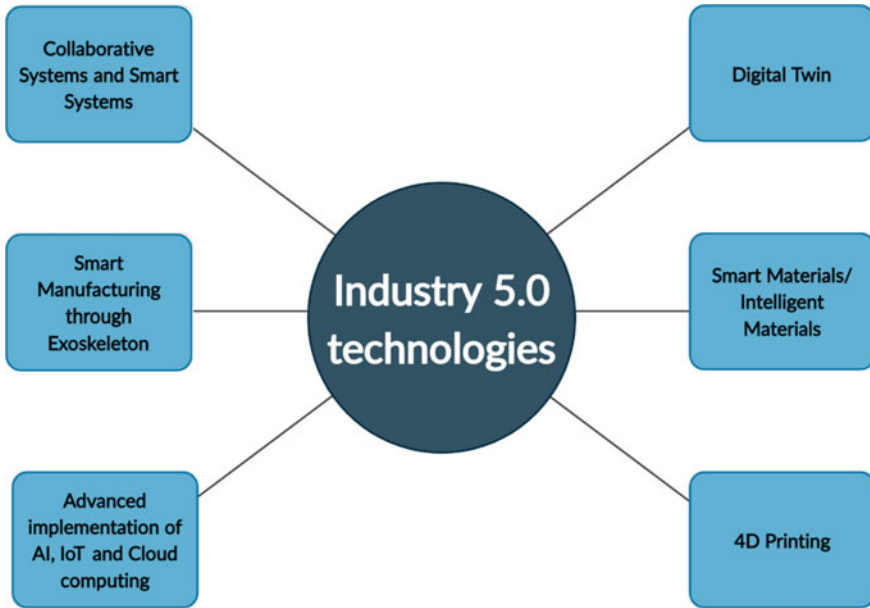


Fig. 2 Significant technologies of the fifth industrial revolution to create the manufacturing system smarter and intelligent

7 Digital Management System

A digital management system benefits from leveraging digital technologies to improve a physical operation's efficiency and performance. With the increase in technologies and resources, manufacturers need to optimize their production, logistics, supply chain, and various other domains. Digital transformation will lead to disruption, which is a necessary disruption. So, the manufacturers need to automate and digitalize their management system for the upcoming changes in technology.

8 Challenges to Contemporary Manufacturing Industries

Manufacturers need to identify the technical, social, and environmental barriers which can hamper their productivity and profitability. The future of manufacturing industries depends on the decisions and actions and is thus required to provide a solution. Table 1 discusses major challenges to manufacturing Industries which are to be taken care of by Industry 5.0 technologies. These challenges need to be addressed in order to find effective ways to solve a manufacturer's problem. Reducing the quality of the manufactured product will not help increase the manufacturing industry's

Table 1 Challenges to contemporary manufacturing industries

Sr. No.	Challenges	Description	References
1	COVID-19 Pandemic	COVID-19 pandemic has severely impacted the manufacturing industries and is causing disruptions to economic activity. Most of the manufacturers must revamp their raw material stock and production capacity. This pandemic has slowed down trade between different countries, thereby disrupting the supply chain	[38–43]
2	Globalization	Globalization is the worldwide exchange of technologies or trade. However, along with these come great challenges. This has led to the concentration of capital in the developed countries or countries which are developing at a high pace	[44]
3	Automation	Automation is considered one of the biggest challenges for the manufacturing industries. With an increased demand for customization and personalization of products, manufacturers need flexible automation tools. Manufacturers need to shift quickly to modular, flexible, and collaborative automation system	[45]
4	Manufacturing skills	These days most of the manufacturing sector is transforming itself according to the technologies. Lack of digital skills and less software knowledge hampers the firm’s growth. As the industries are becoming data-driven, a highly skilled workforce is essential	[46]
5	Supply chain	The manufacturing sector generates a massive amount of real-time Big Data from sensors, machines, and digital devices. Good supply chain management must be carried out in order to enhance visibility throughout the process. Also, this will reduce the wastage of resources during the procedure	[47]
6	Environmental challenges	Due to industrialization, a major part of climate change can be attributed to the manufacturing industries. Global warming is one of the most critical issues that need to be taken seriously. There is considerable pressure on the government and the manufacturing sectors to ensure that the environment is protected. Combining robust green products and clean production will help the manufacturers attain sustainable growth	[48]

(continued)

Table 1 (continued)

Sr. No.	Challenges	Description	References
7	Digital transformation	In today's competitive landscape, manufacturers need to gear up for the changing industrial environment. For a smooth transition, every industry must ensure that they are technically, intellectually, and strategically available. Manufacturers have to adapt their business to the digital world. For this ample number of resources are required	[49]

production or profit. Therefore, technologies associated with the fifth industrial revolution will help them cope with the challenges, further increase profit and production, and maintain their quality.

9 Significant Management Areas in Manufacturing Industries Using Industry 5.0 Technologies

The technologies associated with the fifth industrial revolution can solve various contemporary manufacturing industries' problems in different domains [22, 50]. Figure 3 shows the interconnection of a different area where Industry 5.0 technologies are helpful in manufacturing. With proper implementation, these are used to improve the efficiency and productivity of the industry.

Table 2 discusses the significant management areas in manufacturing industries that would be extensively using Industry 5.0 technologies.

10 Limitation and Future Scope of the Study

This study is purely theoretical, and the ideas proposed by this paper have not been practically implemented. Any reliable statistics or surveys are not available. As Industry 5.0 is yet to arrive, it is in the conceptual state; not much research is available on this topic, and manufacturing industries are trying to find solutions to their problems with the implementation of Industry 3.0 and Industry 4.0. Extensive research needs to be done on developing the right set of skills among the workforce for the upcoming transition.

The paper mainly focused on the components and technologies associated with Industry 5.0, challenges and issues associated with the manufacturing industries, and its application in manufacturing industries by creating an efficient digital management system. As the implementation of Industry 5.0 increases, new research streams should be discovered. Differences and disputes can appear between man



Fig. 3 Areas in the manufacturing industry where Industry 5.0 technologies can be applied

and machines. It must be minimized in the future. Risks and challenges that may come with this new revolution have to be determined as technology comes with great power.

11 Conclusion

The Fifth Industrial revolution is supposed to bring mass personalization along with smoother production and higher efficiency. It is also expected to positively impact our environment, which is being gradually declining due to industrialization. This revolution uses smart machines with intelligence to automate manufacturing processes. The new technologies in Industry 5.0 enhance not only efficiency but also the interaction between humans and robots. Contrary to the assumption that people would lose

Table 2 Significant management areas in manufacturing industries need Industry 5.0 technologies

S. No.	Management areas	Description
1	Manufacturing	On the whole, manufacturing becomes less sophisticated with introducing technologies like AI, IoE, Cobots, etc. Products manufactured are less defective, more personalized, as well as cost-effective. Repetitive and arduous tasks can be performed by exoskeletons and robots, while humans can do the intellectual and creative part [51, 52]
2	Finance	For transparency in transactions and exchanging data securely, manufacturers can leverage IoT and Blockchain concepts. These can help secure transactions within the manufacturing sector. With the help of a digital assistant, invoices and expenditures can be calculated intelligently saving time [53, 54]
3	Processes	With the help of more advancement in collaborative robots, automation in the industry will indeed occur. With the help of IoT and AI, manufacturing processes can be interlinked with each other so that real-time data can be transferred, leading to higher efficiency in production and more outstanding quality [55, 56]
4	Quality	Industry 5.0 technologies not improve the quality of life but also maintain the quality of the product. By the use of the concept of smart manufacturing, they can optimize the workflow and other processes. Mass personalization is achievable by employing the correct business strategy in these industries. This revolution puts much focus on the design and manufacturing of products [57]
5	Supply	Technologies like cobots, AI, wearable exoskeletons can transform the traditional supply chain into a smart supply chain leading to robust logistics. This will reduce supply risks and increase customization, which in turn lead to customer satisfaction. It will help us gain business insights which will help in gaining enormous profits [58]
6	Inventory	By using correct techniques and technology in the manufacturing industry, a vast amount of resources can be saved in inventory management. There is a need to balance the right amount of inventory in the warehouse for a smooth supply chain. This kind of inventory management software is available like warehouse management software and RFID and barcode scanners for orders [59]
7	Transportation	Intermodal transportation can help save time in the supply chain process also save much money. Manufacturers can pool their resources and use sophisticated Transport Management Systems (TMS) for reducing their costs. It will effectively manage the massive amount of data generated from the supply chain and take care of how much resources are being spent anywhere [60, 61]

(continued)

Table 2 (continued)

S. No.	Management areas	Description
8	Workforce	Collaborative robots will work along with humans to perform hazardous and repetitive jobs in order to improve efficiency. Cobots are installed with GPS, AI, and smart sensors to learn behavior, while humans can use their innovative ideas for smart production. Industry 5.0 will produce different roles like Chief Robotics Officer (CRO) in the manufacturing industry, which will require new skills to learn in the coming future [62]

jobs, we see that this revolution will create different roles that will indeed differ from today's workforce. The government, industry, and researchers will have to make sure that they are relevant in the future by investing in them.

References

- Demir KA, Döven G, Sezen B (2019) Industry 5.0 and Human-Robot Co-working. *Proc Comput Sci* 158:688–695. (2019). <https://doi.org/10.1016/j.procs.2019.09.104>
- Nahavandi S (2019) Industry 5.0—a human-centric solution. <https://doi.org/10.3390/su11164371>
- Sajid S, Haleem A, Bahl S, Javaid M, Goyal T, Mittal M (2021) Data science applications for predictive maintenance and materials science in context to Industry 4.0. *Mater Today Proc.* <https://doi.org/10.1016/j.matpr.2021.01.357>
- Bahl S, Iyengar K, Bagha AK, Jaly I, Jain V, Vaishya R (2021) Bioengineering technology in context to COVID-19 pandemic: potential roles and applications. *J Ind Integr Manag Innov Entrepreneurship.* <https://doi.org/10.1142/S2424862221500056>
- Bahl S, Bagha AK, Rab S, Javaid M, Haleem A, Singh RP (2020) Advancements in biosensor technologies for medical field and COVID-19 pandemic. *J Ind Integration Manag Innov Entrepreneurship* 1–24. <https://doi.org/10.1142/S2424862221500081>
- Rizvi AT, Haleem A, Bahl S, Javaid M (2021) Artificial intelligence (AI) and its applications in Indian manufacturing: a review. In: Acharya SK, Mishra DP (eds) *Current advances in mechanical engineering. Lecture notes in mechanical engineering.* Springer Nature. https://doi.org/10.1007/978-981-33-4795-3_76
- Bahl S, Singh RP, Javaid M, Khan IH, Vaishya R, Suman R (2020) Telemedicine technologies for confronting COVID-19 pandemic: a review. *J Ind Integr Manag* 5:547–561. <https://doi.org/10.1142/S2424862220300057>
- Haleem A, Gupta P, Bahl S, Javaid M, Kumar L (2020) 3D scanning of a carburetor body using COMET 3D scanner supported by COLIN 3D software: issues and solutions. *Mater Today Proc.* <https://doi.org/10.1016/j.matpr.2020.07.427>
- Bahl S, Javaid M, Bagha AK, Singh RP, Haleem A, Vaishya R, Suman R (2020) Biosensors applications in fighting COVID-19 pandemic. *Apollo Med* 17:221–223. https://doi.org/10.4103/am.am_56_20
- Sharma A, Bahl S, Bagha A, Javaid M, Shukla D, Haleem A (2020) Multi-agent system applications to fight COVID-19 pandemic. *Apollo Med* 17:S41–S43. https://doi.org/10.4103/am.am_54_20
- Singh RP, Javaid M, Haleem A, Vaishya R, Bahl S (2020) Significance of health information technology (HIT) in context to COVID-19 pandemic: potential roles and challenges. *J Ind Integr Manag* 5:427–440. <https://doi.org/10.1142/S2424862220500232>

12. Fatima S, Haleem A, Bahl S, Javaid M, Mahla SK, Singh S (2021) Exploring the significant applications of internet of things (IoT) with 3D printing using advanced materials in medical field. *Mater Today Proc.* <https://doi.org/10.1016/j.matpr.2021.01.305>
13. Martynov VV, Shavaleeva DN, Zaytseva AA (2019) Information technology as the basis for transformation into a digital society and industry 5.0. In: 2019 International conference “quality management, transport and information security, information technologies” (IT&QM&IS), pp 539–543. <https://doi.org/10.1109/ITQMIS.2019.8928305>
14. Javaid M, Haleem A (2020) Critical components of Industry 5.0 towards a successful adoption in the field of manufacturing. *J Ind Integr Manag.* <https://doi.org/10.1142/S2424862220500141>
15. Aslam F, Aimin W, Li M, Ur Rehman K (2020) Innovation in the Era of IoT and Industry 5.0: absolute innovation management (AIM) framework. <https://doi.org/10.3390/info11020124>
16. Mekkunel F (2019) Industry 5.0: man-machine revolution 1–63
17. ElFar OA, Chang C-K, Leong HY, Peter AP, Chew KW, Show PL (2020) Prospects of Industry 5.0 in algae: customization of production and new advance technology for clean bioenergy generation. *Energy Convers Manag X* 100048. <https://doi.org/10.1016/j.ecmx.2020.100048>
18. Özdemir V, Hekim N (2018) Birth of Industry 5.0: making sense of big data with artificial intelligence, “the internet of things” and next-generation technology policy. *OMICS J Integr Biol* 22:65–76. <https://doi.org/10.1089/omi.2017.0194>
19. Vaidya S, Ambad P, Bhosle S (2018) Industry 4.0—A Glimpse. *Proc Manuf* 20:233–238. <https://doi.org/10.1016/j.promfg.2018.02.034>
20. Longo F, Padovano A, Umbrello S (2020) Value-oriented and ethical technology engineering in Industry 5.0: a human-centric perspective for the design of the factory of the future. <https://doi.org/10.3390/app10124182>
21. Paschek D, Mocan A, Draghici A (2019) Industry 5.0—the expected impact of next industrial revolution. *Manage Knowl Learn Int Conf* 125–132
22. George AS, George H (2020) Industrial revolution 5.0 : the transformation of the modern manufacturing process to enable man and machine to work hand. *J Seybold Rep* 15:214–234
23. FutureBridge: Application of digital twin in industrial manufacturing. <https://www.futurebridge.com/industry/perspectives-mobility/application-of-digital-twin-in-industrial-manufacturing/>. Last accessed 2021/01/17
24. Cobots and Exoskeletons: When Robots and human beings interact with each other. <https://norlean.com/en/blog/cobots-and-exoskeletons-when-robots-and-human-beings-interact-with-each-other/>. Last accessed 2021/01/17
25. Osada Y (1993) Smart materials and structures. Gandhi MV, Thompson BS (eds) Chapman and Hall, London 1992, 310 p, hardback, ISBN 0-412-37010-7. *Adv Mater* 5:313–314 (1993). <https://doi.org/10.1002/adma.19930050427>
26. Pathak P, Pal PR, Shrivastava M, Ora P (2019) Fifth revolution: applied AI and human intelligence with cyber physical systems. *Int J Eng Adv Technol* 8:23–27
27. Bahl S, Goyal T (2020) Corona warriors under risk during COVID-19 pandemic. *Curr Med Res Pract* 10:314–315. https://doi.org/10.4103/cmrr.cmrr_69_20
28. Jaly I, Iyengar K, Bahl S, Hughes T, Vaishya R (2020) Redefining diabetic foot disease management service during COVID-19 pandemic. *Diab Metab Syndr* 14:833–838. <https://doi.org/10.1016/j.dsx.2020.06.023>
29. Vaishya R, Bahl S, Singh RP (2020) Letter to the editor in response to: telemedicine for diabetes care in India during COVID19 pandemic and national lockdown period: guidelines for physicians. *Diab Metab Syndr* 14:687–688. <https://doi.org/10.1016/j.dsx.2020.05.027>
30. Suman R, Javaid M, Haleem A, Vaishya R, Bahl S, Nandan D (2020) Sustainability of Coronavirus on different surfaces. *J Clin Exp Hepatol* 10:386–390. <https://doi.org/10.1016/j.jceh.2020.04.020>
31. Iyengar K, Bahl S, Raju V, Vaish A (2020) Challenges and solutions in meeting up the urgent requirement of ventilators for COVID-19 patients. *Diab Metab Syndr Clin Res Rev* 14:499–501. <https://doi.org/10.1016/j.dsx.2020.04.048>
32. Javaid M, Haleem A, Vaishya R, Bahl S, Suman R, Vaish A (2020) Industry 4.0 technologies and their applications in fighting COVID-19 pandemic. *Diab Metab Syndr Clin Res Rev* 14:419–422. <https://doi.org/10.1016/j.dsx.2020.04.032>

33. Sharma A, Bahl S, Bagha AK, Javaid M, Shukla DK, Haleem A (2020) Blockchain technology and its applications to combat COVID-19 pandemic. *Res Biomed Eng*. <https://doi.org/10.1007/s42600-020-00106-3>
34. Kushwaha S, Bahl S, Bagha AK, Parmar KS, Javaid M, Haleem A, Singh RP (2020) Significant applications of machine learning for COVID-19 pandemic. *J Ind Integr Manag* 5:453–479. <https://doi.org/10.1142/S2424862220500268>
35. Fatma N, Haleem A, Bahl S, Javaid M (2021) Prospects of jewelry designing and production by additive manufacturing. In: Acharya SK, Mishra DP (eds) *Current advances in mechanical engineering. Lecture notes in mechanical engineering*. Springer Nature. https://doi.org/10.1007/978-981-33-4795-3_80
36. FutureBridge: 4D Printing—The Technology of the Future. <https://www.futurebridge.com/industry/perspectives-mobility/4d-printing-the-technology-of-the-future/>. Last accessed 2021/01/17
37. Nkomo NZ (2018) A review of 4D printing technology and future trends. 11th South African conference on computational and applied mechanics, SACAM 2018, pp 202–211
38. Gupta N, Bahl S, Bagha AK, Vaid S, Javaid M, Haleem A (2020) Nanomedicine technology and COVID-19 outbreak : applications and challenges. *J Ind Integr Manag Innov Entrepreneurship* 1–22. <https://doi.org/10.1142/S2424862221500123>
39. Ashima R, Haleem A, Bahl S, Javaid M, Mahla SK, Singh S (2021) Automation and manufacturing of smart materials in additive manufacturing technologies using Internet of Things towards the adoption of Industry 4.0. *Mater Today Proc*. <https://doi.org/10.1016/j.matpr.2021.01.583>
40. Jaly I, Iyengar KP, Bahl S, Jain V, Vaishya R (2020) COVID-19 pandemic and debates on the design of operating theatre ventilation systems in healthcare facilities. *J Ind Integr Manag Innov Entrepreneurship* 1–22. <https://doi.org/10.1142/S2424862221500093>
41. Iyengar KP, Vaishya R, Bahl S, Vaish A (2020) Impact of the coronavirus pandemic on the supply chain in healthcare. *British J Healthc Manage* 26:1–4. <https://doi.org/10.12968/bjhc.2020.0047>
42. Ammar M, Haleem A, Javaid M, Walia R, Bahl S (2021) Improving material quality management and manufacturing organizations system through Industry 4.0 technologies. *Mater Today Proc*. <https://doi.org/10.1016/j.matpr.2021.01.585>
43. Softa A, Bahl S, Bagha AK, Sehgal S, Haleem A, Javaid M (2020) Tissue engineering and its significance in healthcare during COVID-19 pandemic : potential applications and perspectives. *J Ind Integr Manag Innov Entrepreneurship* 1–21. <https://doi.org/10.1142/S242486222150007X>
44. Stalker P (2000) *Workers without frontiers: the impact of globalization on international migration*/Peter Stalker. Lynne Rienner Publishers, Boulder, Colo. , London
45. Colombo AW, Harrison R (2008) Modular and collaborative automation: achieving manufacturing flexibility and reconfigurability. *Int J Manuf Technol Manage* 14:249–265. <https://doi.org/10.1504/IJMTM.2008.017726>
46. Raj A, Dwivedi G, Sharma A, Lopes de Sousa Jabbour AB, Rajak S (2020) Barriers to the adoption of industry 4.0 technologies in the manufacturing sector: an inter-country comparative perspective. *Int J Prod Econ* 224:107546. <https://doi.org/10.1016/j.ijpe.2019.107546>
47. Zhong RY, Newman ST, Huang GQ, Lan S (2016) Big data for supply chain management in the service and manufacturing sectors: challenges, opportunities, and future perspectives. *Comput Ind Eng* 101:572–591. <https://doi.org/10.1016/j.cie.2016.07.013>
48. Young P, Byrne G, Cotterell M (1997) Manufacturing and the environment. *Int J Advan Manuf Technol* 13:488–493. <https://doi.org/10.1007/BF01624609>
49. Gurbaxani V, Dunkle D (2019) Gearing up for successful digital transformation. *MIS Q Executive* 18:209–220. <https://doi.org/10.17705/2msqe.00017>
50. Stallard B (2021) Manufacturing transportation and logistics 101. <https://www.manufacturingtomorrow.com/article/2018/02/manufacturing-transportation-and-logistics-101/10996>. Last accessed 2021/01/17

51. Ozkeser B, Koluman OE (2018) Lean innovation approach in Industry 5.0. the Eurasia proceedings of science engineering and mathematics (EPSTEM), vol 2, pp 422–428
52. Sarfraz Z, Sarfraz A, Iftikar H, Akhund R (2021) Is COVID-19 pushing us to the fifth industrial revolution (Society 5.0)? Pak J Med Sci 37. <https://doi.org/10.12669/pjms.37.2.3387>
53. Massaro A, Galiano A (2020) Re-engineering process in a food factory: an overview of technologies and approaches for the design of pasta production processes. *Prod Manuf Res* 8:80–100. <https://doi.org/10.1080/21693277.2020.1749180>
54. Zambon I, Cecchini M, Egidi G, Saporito MG, Colantoni A (2019) Revolution 4.0: Industry vs. agriculture in a future development for SMEs. <https://doi.org/10.3390/pr7010036>
55. Basl J, Doucek P (2019) A Metamodel for evaluating enterprise readiness in the context of industry 4.0. <https://doi.org/10.3390/info10030089>
56. Clim A (2019) Cyber security beyond the industry 4.0 era. A short review on a few technological promises. *Inform Econ* 23:34–44. <https://doi.org/10.12948/issn14531305/23.2.2019.04>
57. Melnyk L, Dehtyarova I, Kubatko O, Karintseva O, Derykolenko A (2019) Disruptive technologies for the transition of digital economies towards sustainability. *Econ Annals-XXI* 179:22–30. <https://doi.org/10.21003/ea.V179-02>
58. Sharma I, Garg I, Kiran D (2020) Industry 5.0 and smart cities: a futuristic approach. *Eur J Mol Clin Med* 7:2750–2756
59. Ungureanu AV (2020) The transition from Industry 4.0 to Industry 5.0. The 4Cs of the global economic change. In: 16th economic international conference NCOE 4.0 2020, vol 13, pp 70–81. <https://doi.org/10.18662/lumproc/ncoe4.0.2020/07>
60. Gerrikagoitia JK, Unamuno G, Urkia E, Serna A (2019) Digital manufacturing platforms in the Industry 4.0 from private and public perspectives. <https://doi.org/10.3390/app9142934>
61. Semolic B, Steyn P (2018) Industry 4.0 collaborative research, innovation and development (RID) projects. *PM World J VII*:1–28
62. Zhou J, Li P, Zhou Y, Wang B, Zang J, Meng L (2018) Toward New-Gener Intel Manuf. *Engineering* 4:11–20. <https://doi.org/10.1016/j.eng.2018.01.002>

Mathematical and Computational Analysis of Shell and Tube Heat Exchanger on Varying Tube Patterns in Excel[®] and Ansys[®]



Ranjeet Prasad, Ajay Gupta, Pankaj Kumar, and Amit Kumar Mishra

1 Introduction

The HE (heat exchanger) is a thermal energy transferal device which exchange the heat between hot fluid and cold fluid (liquid, gas) without mixing of both fluid which take part in the HT (HT stands for heat transfer) since both fluids are maintained no contact with each other by help of a solid wall usually. There are some unique sorts of HE (HE stands for heat exchanger) that are utilized depending on the application. For instance, double pipe HE is used in chemical processes like condensing the vapour to the liquid. The size of material that wants to use must be considered since it affects the overall HTC (HTC stands for heat transfer coefficient) to make this type of HE. The outlet temperature for both hot and cold fluids obtained is assessed by using the best design for this type of heat exchanger. In process industries, heat exchanger has great value applications. Heat exchanger exchanges thermal energy between two bodies carrying flowing fluids. In any process which involves heat transfer (like condensation heating, cooling, boiling, etc.) demands a HE to attain thermal energy exchange. Heating and cooling of moving streams of fluids happens in initial stages and then phase transformation may take place on further heating or cooling. On the basis of purpose, a HE serves, those HE which is used for condensing are named condensers while those used for boiling fluid are named boilers. Amount of HT using minimal area for HT and pressure drop are a measure for calculating efficiency and performance. Overall HTC is an appropriate acquaintance for its efficiency calculations. Capital investment and energy pre-requisite (operating cost) of a HE can be estimated

R. Prasad (✉) · A. K. Mishra

Department of Mechanical Engineering, B.I.T Sindri, Dhanbad, Jharkhand, India

A. Gupta

Department of Mechanical Engineering, S.R.U, Raipur, Chhattisgarh, India

P. Kumar

Department of Mechanical Engineering, GMRIT, Rajam, India

by pressure drop and area requirement for desired amount of HT. Generally, a lot of theories and literature are available to draft a HE as indicated by the requirements.

Heat exchangers are an essential part of the industries such as: process industries, power plants, oil refining and so on. While the STHX (shell and tube heat exchangers) have almost 40% share in various applications in industries. So, it is essential to increase the performance of heat exchanger. Arrangement of Tubes effect on the performance of the shell and tube heat exchanger. Particularly, the very common type of problem in baffle segment that is fouling zone due to which high drop in pressure occurs in between the flow, another type of misshapen is due to flow vibration across the bundles of tube. The basic literature supports the present works represents against experimental data by Kern, Tinker and Delaware [1–3]. University of Delaware [3] carried out sixteen years of research on shell and tube heat exchanger (STHX) and the first report based on heat transfer and pressure drop presented in 1950, subsequently, four reports are presented on spacing, baffles and a number of new features are comprised. Bell [4, 5] designed a heat exchanger based on report given by Delaware University and present a comprehensive investigation report on program. In comparison of various methods in literature Palen and Taborek [6] provided the appropriate effects in comparison to other approaches in literature. The phenomenon of flow through shell and tube can be understood by numerical and experimental analysis. The structure, shape and configuration of tubes and cylinder of heat exchanger configuration was clarified by Gay and Mackley [7] (Bell 1963) who have given great effort in the of heat transfer, while Halle et al. and Pekdemir et al. [8] (Gay et al. 1976) examined drop in pressure during flow. These days, the numerical techniques have turned into an efficient option for the examination of STHX and through a complete stream design and a heat transfer field, it could be acquired with considerably less problematic explained by Seemawute and Eiamsaard [9], Rhodes and Carlucci [10].

In this research paper emphasized optimizing the heat transfer and fluid flow of water inside STHX by applying different shapes of segmental baffle and ribbed tube. Different shapes of ribbed tubes (Circular, triangular, zig-zag shape, plus shape) are used with STHX. The fluent part of work is simulated by fluent module in ANSYS's workbench (Ver. 17). All the desired results are compared with numerical and experimental data presented in the literatures.

2 Methodology and Numerical Analysis

Procedure/Steps in Conducting Project

- (1) Design Analytically heat exchanger coil.
- (2) Design Numerically heat exchanger coil through Ansys.
- (3) Analytical and Numerical design Validation.
- (4) Analytical optimization of parameters of heat exchanger.

1. Analytical Study

Equations (1) and (2) shown below can be used to calculate heat transfer in between fluid streams under steady-state conditions between the heat exchanger and its surroundings:

$$Q_h = (m.C_p)_h.(T_{h1} - T_{h2}) \tag{1}$$

$$Q_h = (m.C_p)_c.(T_{c1} - T_{c2}) \tag{2}$$

The heat transfer can be explained by LMTD, as the temperature difference varies locally on both sides of shell and tube in STHE.

$$Q = U.A.T_{lm} \tag{3}$$

where U in Eq. (3) represented overall coefficient of heat transfer considering fouling resistance, associate with heat transfer area and the LMTD evaluated on the basis of temperature of both sides of fluid.

$$\Delta T_{lm} = \frac{\Delta T_1 - \Delta T_2}{\ln\left(\frac{\Delta T_1}{\Delta T_2}\right)} \tag{4}$$

$$\frac{1}{U} = \frac{d_o}{d_i} \cdot \frac{1}{h_i} + \frac{d_o \cdot \ln\left(\frac{d_o}{d_i}\right)}{2K} + \frac{1}{h_o} \tag{5}$$

On the basis of the above Formulation. An excel sheet is prepared to determine the dimension of Heat exchanger as shown in Figs. 1 and 2. On that basics, four different design is prepared as shown in Figs. 3, 4, 5 and 6. It shows no error between numerical and analytical but further in Table 1 shows the deviation in effectiveness of numerical and analytical values under tolerance at different patterns and at different flow rates.

3 Numerical Design of the Heat Exchanger Coil Through Ansys

3.1 Geometry of the Studied Model

A three-dimensional, schematic of the shell and tube heat exchanger (STHE) system is depicted in Fig. 1 respectively. The dimension of the respective shell and tubes of STHE system are listed in Table 1. The dimensions of present model of shell and tubes are same for all models of STHE, only position of tubes are arranged in different

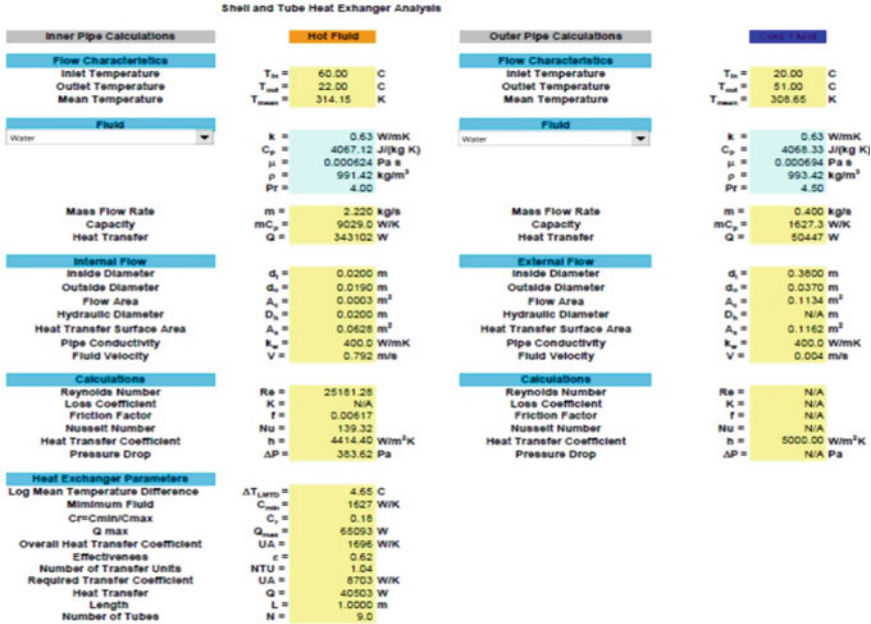


Fig. 1 Design analysis using excel

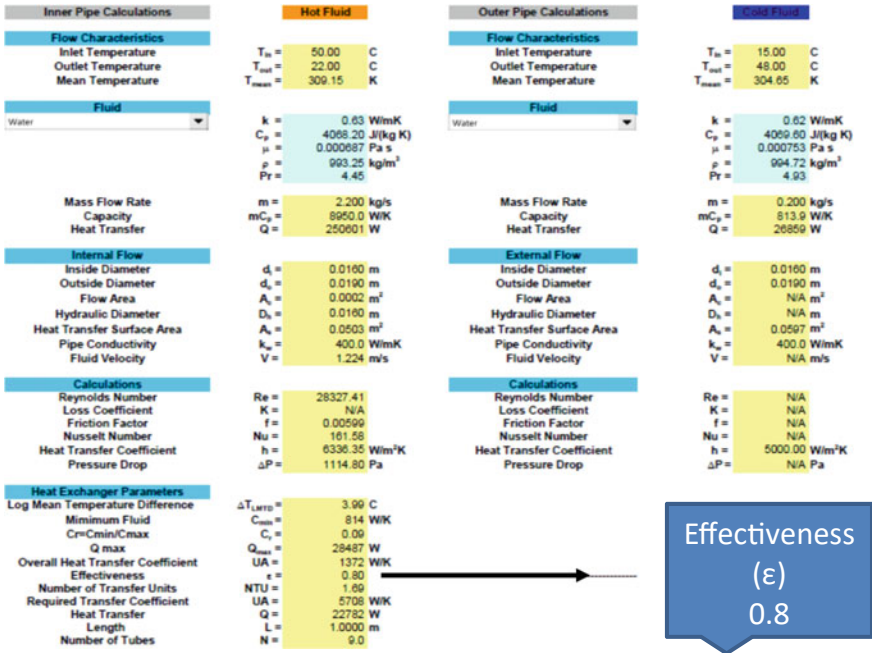


Fig. 2 Confirm the effectiveness (ϵ) similar as in numerical analysis

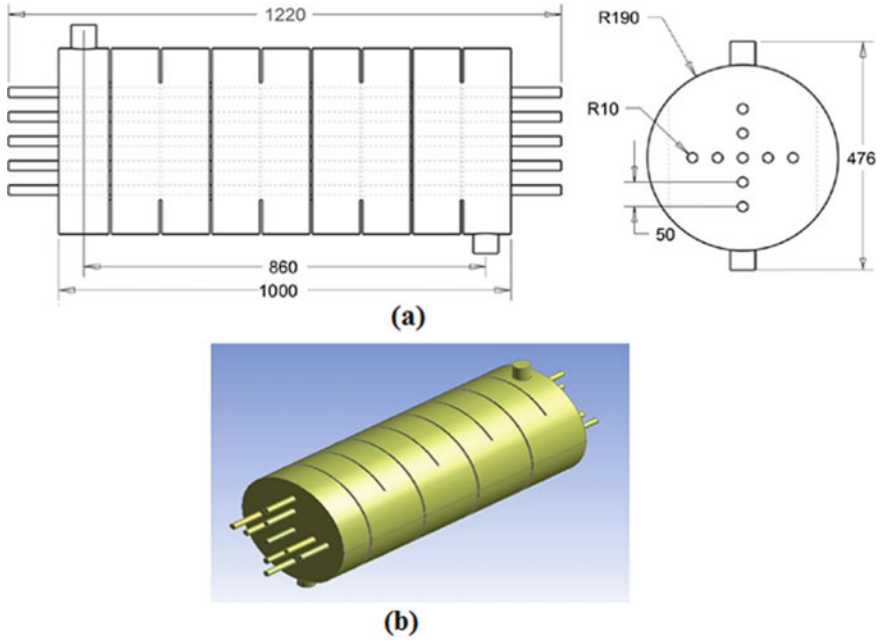


Fig. 3 a Front view and side view of plus (+) pattern, b 3D-view of STHE with plus pattern

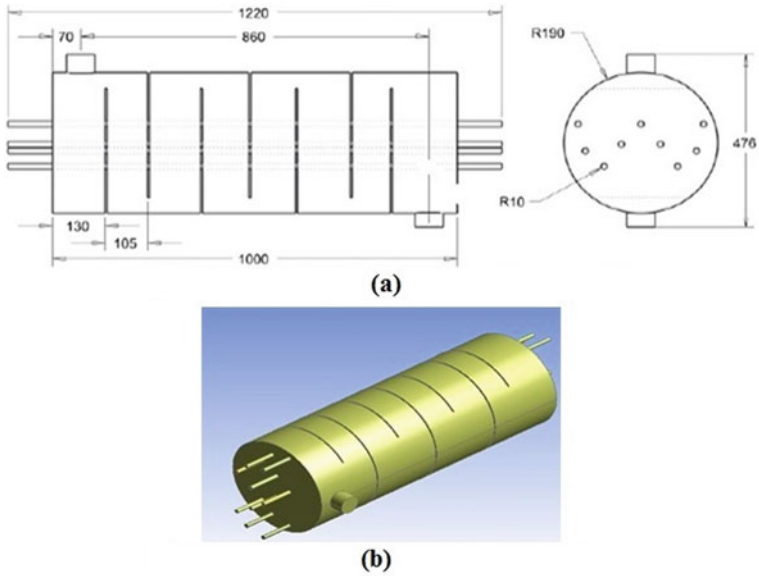


Fig. 4 a Front view and side view of zig-zag pattern, b 3D-view of STHE with Zig-zag pattern

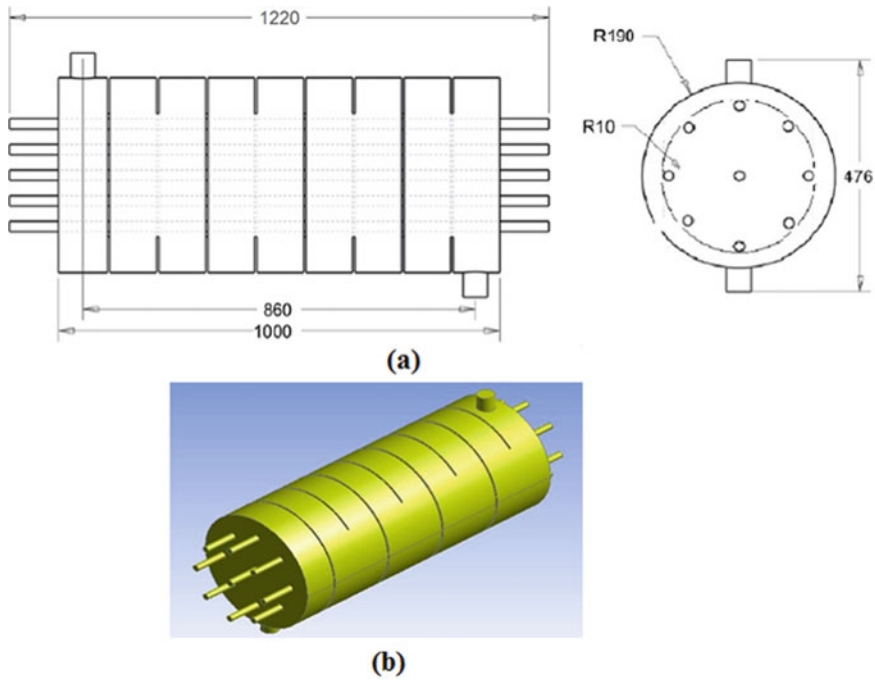


Fig. 5 a Front view and side view, b 3D-view of STHE with circular pattern

patterns like (triangular, circular, zig-Zac, etc.). To facilitate the Computational fluid dynamics (CFD) simulation process of the analysis, some assumption is considered.

- The system wall temperature was 400 K.
- There is no leak in between connection of shell and tube.
- Consider the thermal flux of shell is to be zero.
- Consider the fluid properties of the system to be kept as constant.

Shell and tube heat exchanger geometrical model is created in the ANSYS workbench in design module section. This heat exchanger (HE) is a counter flow HE and tube side is made with 10 different inlets comprising of 9 complete tubes with 1 half tube symmetry consideration. Outlet length of the shell is also greater than before to make easy modelling software to avoid or escape the back flow condition. That's given in Fig. 8, the simplified model or geometry can be seen with the original model or geometry.

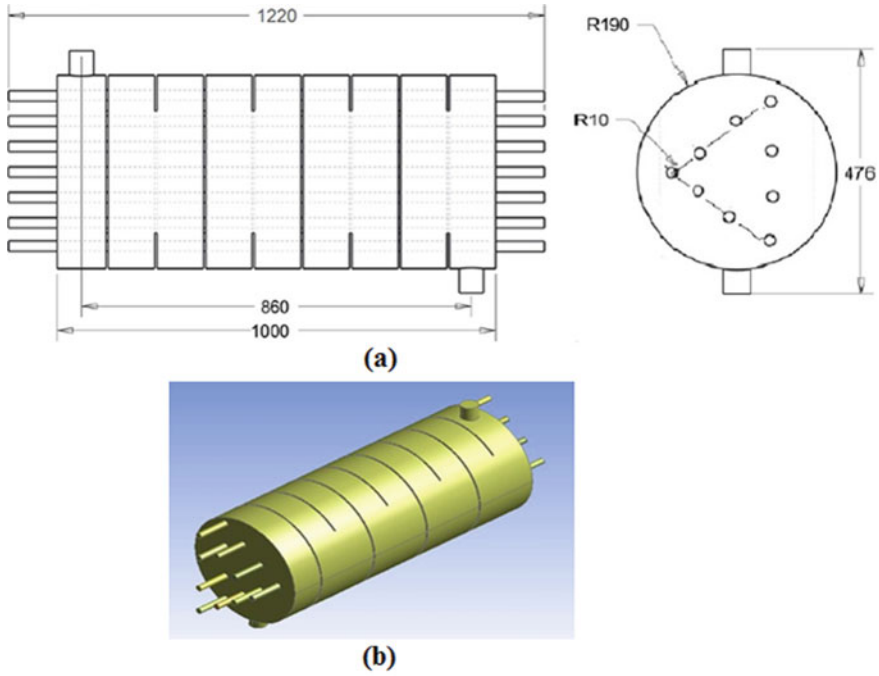


Fig. 6 a Front view and side view, b 3D-view of STHE with triangular pattern

Table 1 Boundary condition of STHE

	BC type	Shell	Tube
Inlet	Mass flow rate	10 kg/sec	5 kg/sec
Outlet	Pressure-outlet	0	0
Wall	Zero slip condition	Zero heat flux	Fixed
Turbulence	Intensity	3.5%	4.1%
Temperature	Temperature Inlet	300 K	500 K

3.2 Governing Equations

The $k - \epsilon$ turbulent model is taken for turbulent flow modelling in fluent for numerical simulation. In the computational domain, governing equations for continuity, energy and momentum are given below:

$$\frac{\partial}{\partial x_1}(\rho u_1) = 0 \tag{6}$$

$$\frac{\partial}{\partial x_1}(\rho u_1 T) = \frac{\partial}{\partial x_1} \left(\frac{\partial T}{\partial x_1} \frac{k}{c_p} \right) \tag{7}$$

$$\frac{\partial}{\partial x_1}(\rho u_1 u_k) = -\frac{\partial P}{\partial x_1} + \frac{\partial}{\partial x_1}\left(\mu \frac{\partial u_k}{\partial x_1}\right) \quad (8)$$

Inside the shell part of heat exchanger, fluid flow is taken as turbulent. Navier–Stokes equations are implemented for the simulation of fluid module, where time-averaged effects on flow parameters of flow turbulent in STHE are considered. The implemented model come across accuracy and reliability necessities in the considered heat transfer and fluid flow.

3.3 Heat Transfer and Pressure Drop

3.3.1 Heat Transfer Rate Inside Shell Fluid Flow in STHE is Given Below

$$\dot{Q} = \dot{m} C_{ps} (T_{s,in} - T_{s,out}) \quad (9)$$

3.3.2 Heat Transfer Coefficient Inside Shell Fluid Flow in STHE is Calculated Using the Following Equations

$$h_s = \frac{\dot{Q}}{A_0 \Delta T_m} \quad (10)$$

$$A_0 = N_t \cdot \pi d_0 L \quad (11)$$

$$\Delta T_m = \frac{\Delta T_{max} - \Delta T_{min}}{\ln(\Delta T_{max}/\Delta T_{min})} \quad (12)$$

$$\Delta T_{max} = T_{s,in} - T_w \quad (13)$$

$$\Delta T_{min} = T_{s,out} - T_w \quad (14)$$

where, A_0 is the outer area of tubes, N_t is no. of tubes, T_w is the temperature of tube walls and s and t represent shell and tube sides. To compare the fluid dynamics and thermal performance of STHE by using performance evaluation criteria index (PEC) which is prepared with new position or shape of tubes configuration to evaluate the heat transfer efficiency. Calculation is done by predicted friction factor and Nusselt numbers.

$$PEC = \frac{Nu/Nu_n}{(f/f_n)^{1/3}} \quad (15)$$

Table 2 Thermal properties of working fluid in shell side of STHE

ρ kg/m ³	μ * 103 Pa s	k W/m K	cp kJ/kg K	β * 106 K ⁻¹
997.0	0.855	0.613	4179	276.1

where Nu and Nu_n are the averaged Nusselt number for STHE. Also, f and f_n are the friction factor for STHE which is prepared with the new position or shape of tubes configuration, respectively.

4 Boundary Conditions

1. According to the need of the model, the boundary conditions are applied or used. The applied boundary condition for both heat transfers as well as fluid flow simulation is summarized as follows.
2. The turbulence BC have an infinitesimal or negligible effect over the solution and its result, after that it is seen that. With respective boundary conditions, the walls are individually specified 'No slip' condition for each and every wall. Excluding tube wall, zero heat flux condition is set for each wall. Tube walls are set to 'coupled' for transferring heat between shell sides stream of fluid and tube sides stream of fluid. In Table 3 all details about all BC can be seen.

4.1 Thermal Properties of Shell Side Fluid of STHE

The temperature of the fluid at inlet is at 300 K and the pressure side is at 100 kPa. In accumulation, the thermal properties of the shell fluid that is water are represented in Table 2.

4.2 Mesh Generation

Comparatively coarse mesh or grid is generated starting with, 1.825 Million cells. In this grid or mesh containing mixed cell (the cell type is mainly Hexahedral and Tetra cells) which having quadrilateral and triangular both faces at the boundaries as shown in Figs. 7 and 8. When using structured cells (Hexahedral cell), care is taken to as possible as, for that reason, geometry or model is divided into numerous fragments or parts for using the automatic methods existing in the ANSYS meshing. It is intended to diminish numerical dispersion as conceivable by structuring or generate the mesh in a proper way or method, for the most part, close to the wall region. After that, for mesh independent model, generate a fine mesh is with 5.6525 M cells. After the use

Table 3 Compression of analytical and numerical values

Pattern unit	Effectiveness CFD	Effectiveness analytical	Press. drop CFD	Press. drop analytical
Zig	0.8	0.8	219	278
Zig	0.55	0.58	229	308
Zig	0.66	0.45	224	348
Zig	0.76	0.65	241	389
Plus	0.3	0.4	152.4	255
Plus	0.32	0.25	161	326.1
Plus	0.4	0.55	298	329.6
Plus	0.31	0.2	278	333.1
Cir.	0.4	0.45	202	336.6
Cir.	0.43	0.46	275	340.1
Cir.	0.5	0.4	217	343.6
Cir.	0.24	0.3	290	347.1
Tri.	0.45	0.55	216	350.6
Tri.	0.35	0.34	223	354.1
Tri.	0.23	0.25	225	357.6
Tri.	0.3	0.44	215	361.1

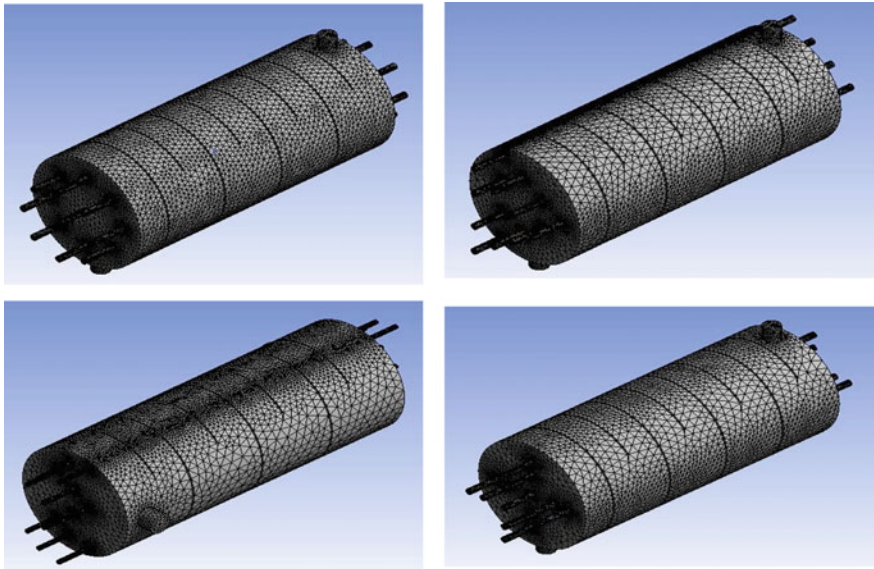


Fig. 7 Meshing of the different pattern of STHE

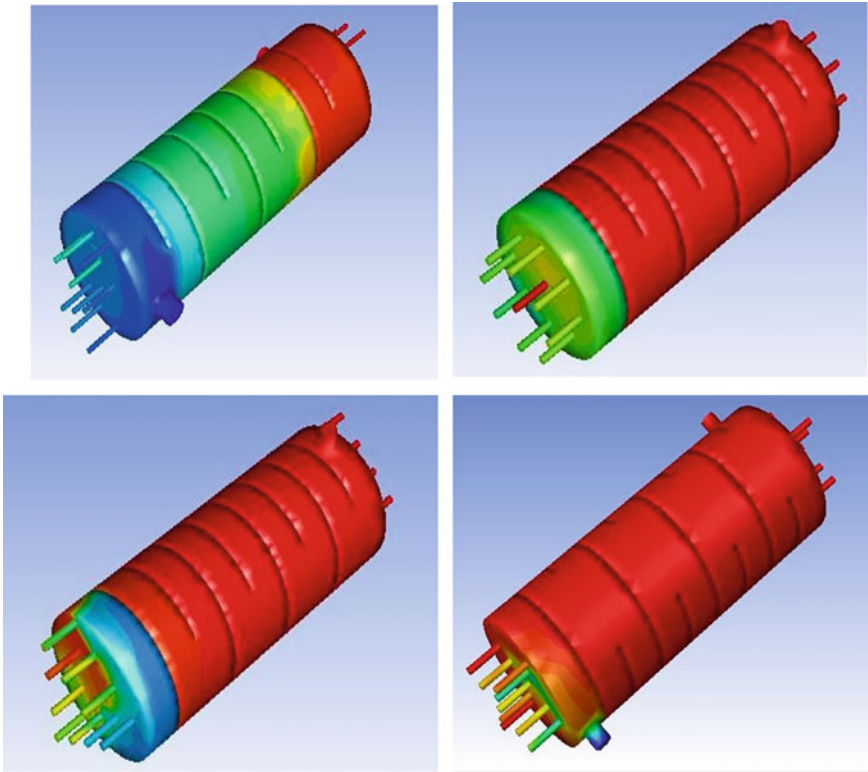


Fig. 8 Meshing of the different pattern of STHE

of fine mesh, the edges and region of high pressure and temperature gradients have finely meshed.

RESULT

Optimization Results

To optimize the given model, consider a set of 16 design points and optimal values are obtained from those design points which are well satisfying the constraints and minimizing the objective.

Final result of the project is shown in Table 3.

The table shows the effectiveness of the HE with respect to the different mass flow rates and temperatures. In the table, we can see the zig-zag pattern have better effects than others.

4.3 Conclusion

1. The objective of the present study is to provide a more complete understanding Flow maldistribution in tubular heat exchangers by studying area weighted and mass weighted temperature profiles for maldistribution without back flow and maldistribution with back flow.
2. Comparison of average temperature profiles of flow maldistribution with the average temperature profiles of uniform mass flow distribution.
3. The objective of this study is to develop a CFD simulation to predict heat Transfer in concentric tube heat exchangers by using different mass flow rates of fluid.
4. The obtained value of effectiveness through analytical shows the conformity result with numerical result within expectable uncertainty range as shown in Table 3.

References

1. A heat exchanger applications general (2011) http://www.engineersedge.com/heatexchanger/heat_exchanger_application.htm
2. Kakac S, Liu H (1998) Heat exchangers: selection, rating, and thermal performance
3. <http://www.wcr-regasketing.com>, "Heat exchanger applications." <http://www.wcregasketing.com/heat-exchanger-applications.htm>, 2010
4. Bell KJ (January 26, 2005) Heat exchanger design for the process industries. ASME J Heat Transfer. December 2004; 126(6):877–885
5. Panchal CB, Bell KJ (May 1, 1987) Simultaneous production of desalinated water and power using a hybrid-cycle OTEC plant. ASME J Sol Energy Eng 109(2):156–160
6. Ishihara K, Palen JW, Taborek J (1980) Critical review of correlations for predicting two-phase flow pressure drop across tube banks. Heat Transfer Eng 1(3):23–32
7. Gay B, Mackley NV (1976) Shell-side heat transfer in baffled cylindrical shell and tube exchangers—an electrochemical mass transfer modelling technique. Int J Heat Mass Transfer 19:995–1002
8. Bell, KJ (1963) Final report of the cooperative research programme on shell and tube heat exchangers, University of Delaware, Engineering Experimental Station, Bulletin No. 5. Google Scholar.
9. Thianpong C, Eiamsa-Ard P, Eiamsa-Ard S (2012) Heat transfer and thermal performance characteristics of heat exchanger tube fitted with perforated twisted-tapes. Heat Mass Transfer 48(6):881–892
10. Rhodes DB, Carlucci, LN (1984) Predicted and measured velocity distribution in a model heat exchanger. No. AECL–8271. Atomic Energy of Canada Ltd

Design Analysis of Robotic Arm



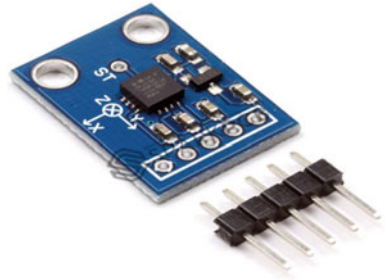
Mahesh T. Kanojiya , Nitin K. Mandavgade , Chandrasekhar Padole ,
and Dipak Gulhane 

1 Introduction

The robots are used in many industries. The purpose of the utilization of the robot is to reduce the error and improve the productivity. The robotic arm plays an important role in improving the productivity rate of the production industry [1]. The robotic arm consists of the hands, joints, end effectors, gripper, etc. Most of the robotic arm is operated by the electric motors. Various operating mechanisms are available for operation of the robotic arm; it includes hydraulic and pneumatic mechanism [2]. In hydraulic mechanism, the liquid is pressurized under the high pressure, and in pneumatic mechanism, the gases are pressurized. The hydraulic mechanisms are utilized for operating the heavy work, and pneumatic mechanism is used for precise work or light work. There are many ways to define the robot. It may be defined as the mechanical structure which is programmed for performing various functions as per the requirement. The definition adopted by International Standard Organization, ISO, and agreed upon by most of the users and manufacturers is “an industrial robot is an automatic, servo controlled, freely programmable, multipurpose manipulator with several areas, for handling of workpieces, tools or special devices”. Therefore, we can define an industrial robot a general-purpose, programmable machine possessing certain anthropomorphic characteristics. The most important characteristic of an industrial robot is its mechanical arm, which is supposed to perform various industrial tasks. Other humanlike characteristics are the robot capabilities to respond to sensory inputs and communicate with other machines among other, and these capabilities permit the robot to perform a variety of useful tasks [3].

M. T. Kanojiya · N. K. Mandavgade (✉) · C. Padole · D. Gulhane
Department of Mechanical Engineering, NIT, Nagpur, India

Fig. 1 Three-axis accelerometer



2 Objective of Work

The objectives of work are:

- Design of gesture-controlled arm operation.
- Fabrication of gesture-controlled robotic arm.
- Programming for controlling of robot.
- Simulation of the complete system.

3 Manufacturing Components

The basic components used in design and development of robotic arm are as follows.

3.1 Accelerometer

Accelerometer is used to give the desired motion to the robotic arm [4, 5]. In this project, 3 accelerometers are used for the motion of 6 motors (2 at the base and 4 in the arms). There are 5 pins in the accelerometer, viz. x, y, z, -ve and +ve, as shown in Fig. 1. The motion of the accelerometer gives the value of the voltages in the different planes.

3.2 Microcontroller

Microcontroller used in this system is AVR (ATmega32). As ADC is inbuilt in this, there is no need to use the extra ADC device. Two microcontrollers are used for the system, one for the transmitter and second for the receiver section. In this, there are four ports, viz. Port A, Port B, Port C and Port D. Each port contains eight pins [6]. There are totally 40 pins in the microcontroller as shown in Fig. 2.

Fig. 2 Microcontroller
ATmega32



- (a) 32 pins for the 4 ports (each port contains 8 pins).
- (b) Pin 10 and 31 for $-ve$ supply and 11 and 30 for the $+ve$ supply (4 pins).
- (c) Pin 9 for the RST and 12 and 13 is of XATL, and pin 32 is of ARED (4 pins).

The input can be taken from the Port A, and the output can be taken through any one of the three ports.

3.3 LCD Screen

LCD screen is used to display the values of analog signal of the accelerometer.

3.4 Encoder (HT12E)

The function of encoder is to encode the information received from the microcontroller and send it to the transmitter in the form of the binary signals [7]. There are 18 pins in the encoder (9 pins on either side) as shown in Fig. 3. $1\text{ M}\Omega$ resistance is connected across the pins 15 and 16. Transmitter is connected to the pin 17, and the pin 18 is of VCC. Input supply ($-$) is given to the pins 9 and 14.

3.5 Transmitter (315 MHz)

Transmitter is used to transmit the encoded information collected from the encoder to the receiving section (receiver) in the form of the analog signal [8]. There are four pins to the transmitter as shown in Fig. 4. The first pin is for the $-ve$ terminal, 2nd is connected to the pin 17 of the encoder, 3rd is for the $+ve$ terminal (VCC), and the 4th pin is connected to the antenna.

Fig. 3 Encoder

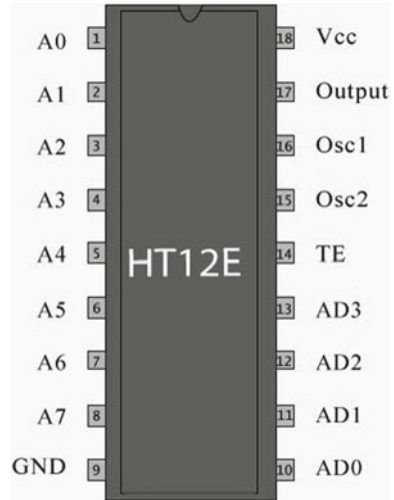


Fig. 4 Transmitter



3.6 Receiver

Receiver receives the information which is sent from the transmitter and passes it to the decoder [8]. There are 8 pins to the receiver. All these pins are shown in Fig. 5, respectively. Pin 1 is for the antenna, -ve supply is given to the pins 2, 3 and 8, and pins 4 and 5 are connected to the VCC (+ve). Pin 6 is connected to the pin 14 of the decoder [9].

Fig. 5 Receiver

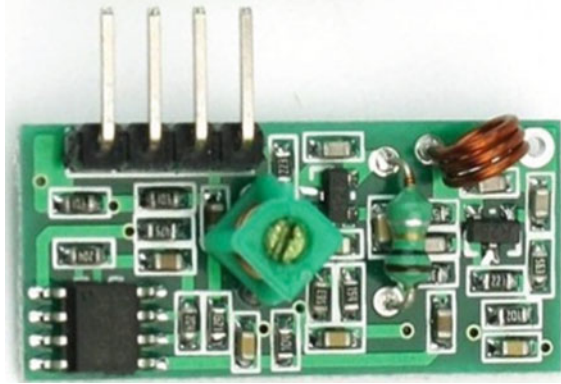


Fig. 6 Decoder



3.7 Decoder (HT12D)

Decoders decode the information collected from receiver into the original form (digital signal) and send it to the microcontroller. Decoder contains 18 pins. $-ve$ supply is given to the pins 9 and 18; also, resistance of $47\text{ K}\Omega$ is connected across the pins 15 and 16. LED is connected to the pin 17, and pins 10, 11, 12 and 13 are connected to the pins 40, 39, 38 and 37 of the microcontroller, respectively [6]. All these pins are shown in Fig. 6.

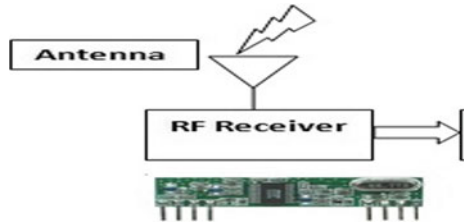
3.8 Amplifiers (L293D)

Amplifiers amplify the voltage and supply it to the motors. Generally, the amplifier is having 16 pins. 12 V power supply is directly given to the pin 8 from the battery, and $+ve\ 5\text{ V}$ is given to the pins 1, 9 and 16. $-ve$ supply is given to the pins 4, 5 and 12, 13. The output is taken from the pins 3, 6, 11 and 14. Pins 2, 7, 10 and 15 are connected to the Port D of the microcontroller. One amplifier can drive the two motors, so three amplifiers are used to drive six motors. The basic amplifier is shown in Fig. 7.

Fig. 7 Amplifier



Fig. 8 Voltage regulator



3.9 Battery

12 volt power supply battery is used for the operation of the overall system.

3.10 Voltage Regulator (7805)

As the whole system (escape motors) operates on the +5 V power supply, the voltage of the battery should have to reduce to +5 V. The voltage regulator is shown in Fig. 8. 7805 step-down voltage regulator was used. Last two digits in 7805 indicate the voltage which is needed for operating the system.

3.11 PCBs

PCB stands for the “printed circuit board,” which is used to mount the components on it. The software used for drawing and designing the PCB is “PCB Artist.”

3.12 Transmitter End

The transmitter module is shown in Fig. 9. The transmitters attached to various components are shown in Fig. 9.

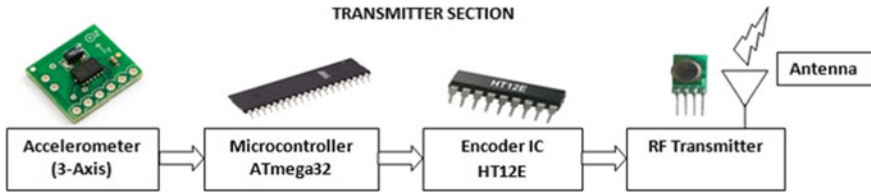


Fig. 9 Block diagram of the transmitter module

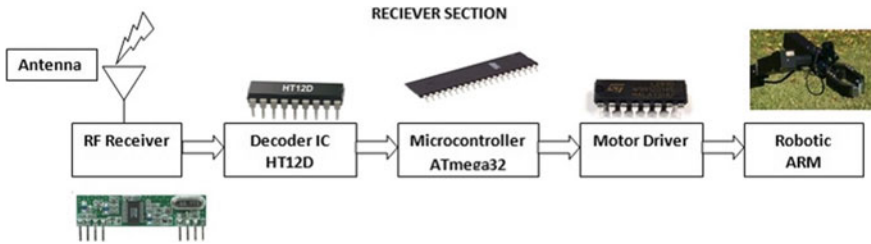


Fig. 10 Block diagram of the receiver module

3.13 Receiver End

In the receiver end, a receiver module is attached with the circuit which detects the signal transmitted from the transmitter end and sends to the decoder for decoding the signal into its original form [10, 11]. Now, decoder decodes the signal in the form of digital and sends it to the microcontroller for controlling the movement of the robotic arm. In electronic part of the project, the most important thing is printed circuit board (PCB) designing. The software used for the PCB designing is **PCB Artist**. This is the advanced software used to design the PCB. The working flow of the receiver is shown in Fig. 10.

4 Mechanical Designing and Fabrication

4.1 Mechanical Structure of Robotic Arm

Figure 11 shows the prototype of the robotic arm that is calibrated precisely and accurately. The complete structure is made up of aluminum.

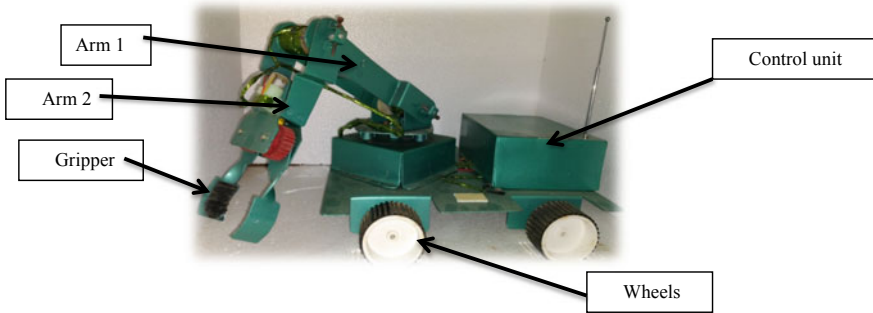


Fig. 11 Fabricated model

4.2 Design

Components designed:

1. End effector.
2. Base frame.
3. Robot arm.

4.3 End Effector

The end effectors are having the following specifications.

Weight of object to be lifted = 150 gm.

Dimensions of object: diameter of the ball (r) = 30 mm.

Material used for end effector is aluminum.

We select end effector by make or buy decision.

An end effector consists of gripper and gear mechanism.

4.3.1 Gripper

Gripper employs mechanical grasping for holding object.

Total length of gripper=17 cm.

There are various types of gripper:

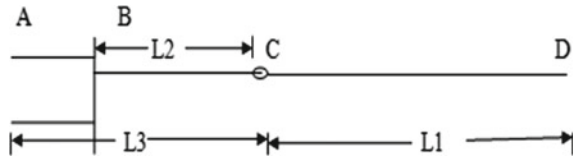
- (a) Flat-type gripper
- (b) V-block-type gripper
- (c) Circular arc-type gripper.

We are using circular arc gripper because it covers maximum circumferential area.

Size of gripper during relaxation = 10 mm

Size of gripper during opening = 118 mm

Length of link of gripper = 130 mm.

Fig. 12 Arm length

4.3.2 Gear

Gear is the mechanical element used for transmitting power and rotary motion from one shaft to another shaft. Gears used in designing of end effector are worm gear and spur gear.

4.4 Design of Base Frame

Design of base frame is considered from system layout.

Length = 13 cm; width = 13 cm; height = 6 cm.

4.5 Arm Design

4.5.1 Given Conditions

The arm has the following specification (Fig. 12):

$$BC = L_2 = 140 \text{ mm.}$$

$$CD = L_1 = 240 \text{ mm.}$$

$$AC = L_3 = 310 \text{ mm.}$$

AB—Length of gripper.

BC—Length of ARM 2.

CD—Length of ARM 1.

4.5.2 Force Analysis

Force on Gripper

Let

m = mass of object.

$m = 150 \text{ gm.}$

$m = 0.15 \text{ kg.}$

Therefore, the force acting on the object due to mass is

$F = m \times g$ where F is force acting on object and g is gravitational force [10]

$$F = 0.15 \times 9.81$$

$$F = 1.47 \text{ N}$$

There is some friction between the fingers of the end effector or gripper and the object.

Let, μ be coefficient of friction.

This friction is responsible for gripper to hold object exerting the force W .

Therefore, the friction force is as follows [10].

$$F = \mu \times N \times P_g \quad (1)$$

where

N no. of fingers

P_g gripping force

μ coefficient of friction.

But the capacity of the force increases due to incorporated safety by F.O.S.

Let, n be factor of safety (F.O.S).

Therefore, design force is as follows [10].

$$F_d = n \times W \quad (2)$$

From Eqs. (1) and (2),

Design force = friction force

$$N \times W = \mu \times N \times P_g$$

$$P_g = (n \times W) / \mu \times N$$

According to consideration

From design data book

From Table no. 1.20A

For electric motor and dynamic load with light shock

F.O.S, $n = 1.5$

$W = m \times g$, where W is dynamic load [10]

$$= 0.15 \times 9.81$$

$$W = 1.47 \text{ N}$$

$\mu = 0.3$ (generally)

$$N = 2$$

Put all the values in equation

$$P_g = (1.5 \times 1.47)/(0.3 \times 2)$$

$$P_g = 3.675$$

If we supplied 12 V (V) and 1 A current (I) and resistance (R) of dc motor having 10 rpm, can be calculated using Joules law as below.

By Joules law [10],

$$P = I \times I \times R$$

where P is power.

I is current supplied.

R is resistance.

Therefore, $V = R \times I$ (by Ohm's law)

where V is voltage

$$R = 12/1$$

$$R = 12 \Omega$$

$$P = 1 \times 1 \times 12$$

$$P = 12 \text{ W}$$

$$\text{But, } P = (2\pi NT)/60$$

$$12 = (2 \times 3.145 \times 10 \times T)/60$$

$$T = 11.46 \text{ N-m}$$

where T is torque on motor.

As $T = \text{force} \times \text{perpendicular distance}$ [10]

$$T = F \times r$$

where r is radius of ball as we have considered 3-cm diameter object.

For holding 3-cm diameter, so we take 8 cm distance between two jaws for relaxation.

$$11.46 = F \times 0.04$$

$$F = 286.5 \text{ N.}$$

For Relaxation

For gripping the 3-cm diameter part, the gripping length should be more than 3 cm; therefore, we are considering it as $L = 13 \text{ cm}$.

$$P_g = 0 \text{ and } L = 13 \text{ cm}$$

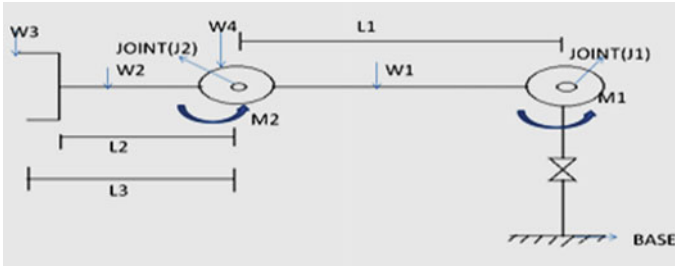


Fig. 13 Force analysis of arm

4.5.3 Force Analysis of Arm

Here,

$L1$ = Length of Arm 1.

$L2$ = Length of Arm 2.

$L3$ = Length from gripper and Arm 2.

The material of arm selected is aluminum (Fig. 13).

Consider:

Weight of object to be lift = 1500 gm.

Length of Arm 1 = 240 mm.

Length of Arm 2 = 140 mm.

Let

- Weight of Arm 1 ($W1$) = 80 gm
= $0.08 \times 9.81 = 0.7848$ N.
- Weight of Arm 2 ($W2$) = 60 gm
= $0.06 \times 9.81 = 0.6$ N.
- Weight of end effector ($W3$) = 100 gm
= $0.10 \times 9.81 = 0.981$ N.
- Weight at joint J2 ($W4$) = 150 gm
= $0.15 \times 9.81 = 1.47$ N.

After consideration, moment arm calculation is done by multiplying downward force and linkage length. In the above FBD, it has just two degree of freedom which is required for lifting.

$$\text{Moment of arm} = \text{downward force} \times \text{linkage length}$$

Torque about joint 1 [10, 12]

$$\begin{aligned} M1 &= L1/2 \times W1 + L1 \times W4 + (L1 + L2/2) \times W2 + (L1 + L3) \times W3 \\ &= 0.24/2 \times 0.7848 + 0.24 \times 1.47 + (0.24 + 0.14/2) \times 0.6 + (0.24 + 0.31) \times 0.981 \\ M1 &= 1.2 \text{ N - m} \end{aligned}$$

Torque about joint 2 [10]

$$\begin{aligned} M2 &= L2/2 \times W2 + L3 \times W3 \\ M2 &= 0.346 \text{ N - m} \end{aligned} \tag{3}$$

We know that

$$\sigma = \frac{P}{A}$$

where

- σ Stress developed at the end of the gripper.
- P Load at the end of the gripper.
- A Area of the object to be considered.

$$\begin{aligned} \sigma &= \frac{286}{\frac{\pi}{4}d^2} \\ \sigma &= \frac{286}{\frac{\pi}{4}30^2} \\ \sigma &= 0.404 \text{ N/mm}^2 \end{aligned}$$

Thus, the stress coming on the end of the grip, i.e., on the object to be hold, is 0.404 N/mm^2 . The analysis of the robotic arm was done using the Ansys software, and it has been found that the stress coming on the end of the gripper is 0.026 N/mm^2 as shown in Fig. 14. Comparing the stress value of the theoretical calculation and software-based result, it has been found that the stress which is at the end of the gripper is less; hence, the designed purpose is solved.

5 Conclusion and Future Scope

With the increasing demand to procure goods on time, with greater accuracy and perfection, the need to switch over to robotics seems imperative. The employment of robotics in the workstations will revolutionize the production process. The field therefore is very promising and offers vibrant scope and growth prospects. Generally,

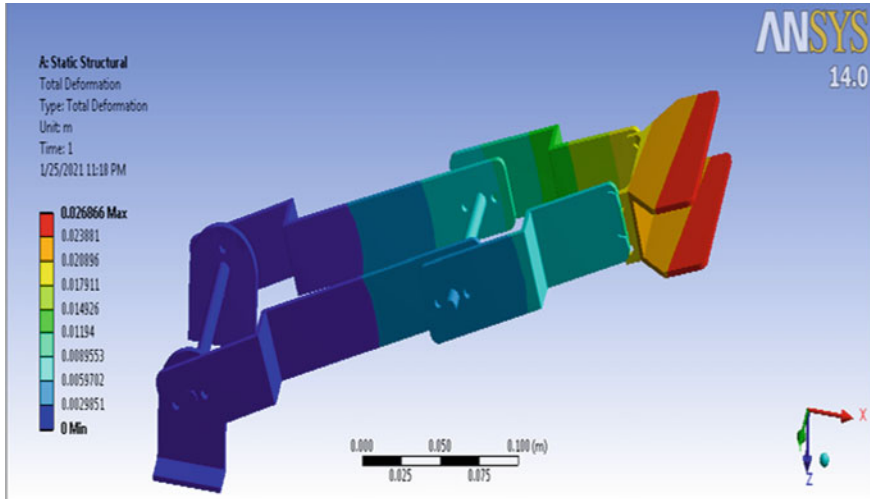


Fig. 14 Deformation analysis of arm

the robots manufactured have a fixed base but our robot possesses a unique feature; i.e., it has mobile base; with the help of its four-wheel drive, it can move right, left, forward, backward and complete 360 degrees of rotation. We have used aluminum links because of its higher strength and lightweight properties. We made use of square bar because that makes it easy to fit the nuts and bolts on a square bar than a round bar. Nylon gears have been made to reduce the weight of the assembly, and it also possesses characteristic like anti-corrosive which makes it unique in application. Metal shafts have been employed in place of nylon shafts to handle high torque transmission which could have not been possible using nylon shafts.

Microcontroller used was 8951 which is now replaced by AVR ATmega32 to incorporate the analog-to-digital converter. The 8951 microcontroller does not possess inbuilt ADC which otherwise should have to be installed separately but with the use of ATmega32, ADC is present inside it, so the problem was solved. Parallel communication was initially used for the system data transfer which is now replaced by serial data communication because in parallel communication only 16 combinations can be obtained which is not sufficient to accommodate all the features of the robot; also, it is one sided which is not adequate. Hence, it was replaced and now the robot functions properly.

Hence, the following conclusions can be drawn by:

- (a) The robot efficiently performs the task of detecting, picking and placing objects.
- (b) The infrared sensors and feedback sensory system operate effectively and efficiently maneuver the robot in the autonomous mode.
- (c) The use of ATmega32 was compatible with the system.

- (d) The robot can be used in arena, and without any human intervention, it can perform various tasks and can also be employed in similar assembly line.
- (e) The stress which is at the end of the gripper is less; hence, the designed purpose is solved.

References

1. Nair RS, Kumar S, Soumya N, Shanmugasundaram M (2018) A study on gesture controlled robotic arms and their various implementations. *Int J Mech Eng Technol (IJMET)* 9(3):425–434, Article ID: IJMET_09_03_042
2. Teli SN, Bhalerao A, Ingole S, Jagadale M, Kharat K (2017) Design and fabrication of pneumatic robotic arm. *Int J Sci Eng Res* 8(3)
3. Patidar V, Tiwari R, Survey of robotic arm and parameters. International conference on computer communication and informatics (ICCCI-2016), Coimbatore, India
4. Gautam PK, Pandey S, Nanda VK (2018) Robot control by accelerometer based hand gesture using Arduino microcontroller. *Int J Recent Technol Eng (IJRTE)* 7(4)
5. Bhojak V, Solanki GK, Daultani S, Gesture controlled mobile robotic arm using accelerometer. *Int J Innov Res Sci Eng Technol* 4(6)
6. Pawar V, Bire S, More S, More K, Mule R (2018) Review on design and development of robotic arm generation-1. *Int J Innov Sci Res Technol* 3(3)
7. Javanjal V, Kumar A, Korasawala D, Bari G, Narkhede A (2019) Design and development of gesture controlled robot. *Int Res J Eng Technol (IRJET)* 06(05)
8. Budheliya CS, Solanki RK, Acharya HD, Thanki PP, Ravia JK (2017) Accelerometer based gesture controlled robot with robotic arm. *Int J Innov Res Sci Technol* 3(10)
9. Zagade A, Jamkhedkar V, Dhakane S, Patankar V, Kasture A, Gaike V (2018) A study on gesture control Arduino robot. *Int J Sci Dev Res* 3(5):385–392
10. Wei AN, Voon QKL, Ismail MA, Mustaffa N, Ismail MH (2015) Design and development of a mechanism of robotic arm for lifting part1. 2nd integrated design project conference (IDPC). <https://www.researchgate.net/publication/289893486>
11. Sharma S, Sharma S, Yadav P (2017) Design and implementation of robotic hand control using gesture recognition. *Int J Eng Res Technol (IJERT)* 6(04):302–307
12. Elfasakhany A, Yanez E, Baylon K, Salgado R (2011) Design and development of a competitive low-cost robot arm with four degrees of freedom. *Mod Mechan Eng* 1:47–55. <https://doi.org/10.4236/mme.2011.12007> Published Online November 2011. <http://www.SciRP.org/journal/mme>

Pine Oil Extraction and Characteristics of Engine Using Pine Oil



Uddeshya Kumar and Siddharth Jain

1 Introduction

Pine oil is an oil which is obtained from different species of pines, mainly by *Pinus sylvestris*. It is obtained with the help of steam distillation of needles, stumps, and twigs of different kinds of pines. Pine oil is very popularly known as a Christmas tree. Historically pine tree is very much familiar for the mankind because its wood is very rich in resin which makes it ideal for the production of tar, turpentine and also proves its importance as use of fuel and products of pine oil are used in construction and painting industries. According to different mythologies, it is believed that pine tree refers to the reputation as it is always growing taller to catch the beams of sun, this is the reason that it is also known as a “The Master of Light” and “The Torch Tree.” Pine oil is traditionally used in medicals such as to prevent fungal infections, i.e., athlete's foot and it is also famous for its effectiveness against minor abrasions, such as bites, cuts, and scrapes from developing infections. When applied to the hair, Pine Oil is having a big reputation to exhibit an antimicrobial property that cleanses to remove bacteria as well as a build-up of excess oil, dead skin, and dirt [1–12]. But in this paper, we are focusing on the “Modification of pine oil to biodiesel with different experiments and Engine characteristics by using pine oil as a fuel”.

We know very well that for a country's growth its energy sector and transportation sector plays a vital role as same as a backbone of human body and fuel is the most important parameter for these sectors, here biodiesel provides us an advantage because now in this competitive world where every country wants to be superior to other, biodiesel shows us a path of sustainable development. As we know biodiesel is the near future as it is one of a few methods to reduce global warming as well as providing sufficient amount of fuel for mankind so that different power generation and other operations can be performed however right now the cost of biodiesel and

U. Kumar · S. Jain (✉)

Department of Mechanical Engineering, College of Engineering Roorke, Roorkee, India

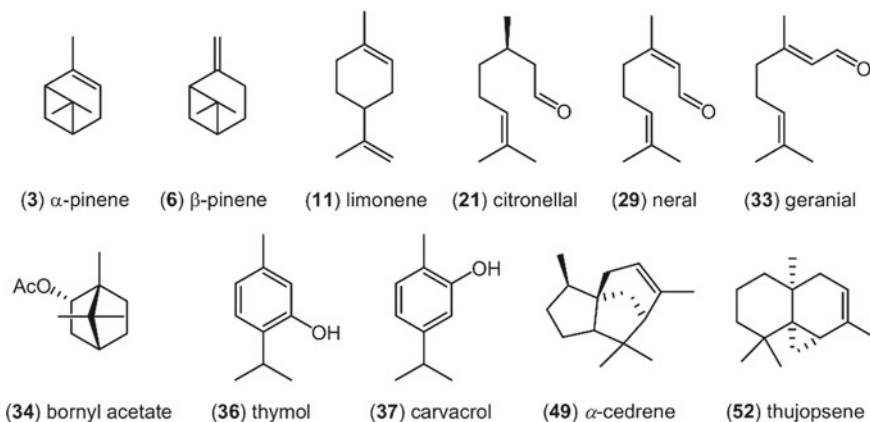


Fig. 1 Different types of indexes [19, 24]

its feasibility in the market is a big challenge but on the other hand it provides us an opportunity to develop in a manner of eco-friendly mankind and it also gives an advantage over other methods, i.e., biodiesel can run on the normal or current Diesel engines with slight modifications so it will not create a mess and challenge for the engine producing industries. In this world, with a pass of every second, the pollution level is increasing rapidly some persons know the effect of this pollution and some people don't know but this will harm us all, we can fulfill our needs from the conventional source of fuel (for example coal, wood) but for a long run, it will be dangerous for all of us in the world [9–33]. The use of renewable energy and production of energy from the waste biomass becomes a light of hope for all of us because it can change the future in a fruitful way. The amount of pollution varies from country to country and it is no longer a secret that we have only a few weapons like renewable energy to fight against this climate change, which is the biggest of the whole world. There are different types of indexes which are originated in order to rank different countries on the basis of their improvements in the renewable energy sector (fight against global warming) such as climate change performance index, environmental performance index, renewable energy country index, World Energy Council's energy trilemma index, population index, S&P Global Timber & Forestry Index, renewable energy country index and other (Fig. 1).

2 Transesterification

Transesterification is a reaction in which an Ester molecule reacts with an alcohol molecule in order to get a different ester molecule. Generally, it is also defined as the reaction of an Ester in order to convert one form of an ester into another form with the help of an acidic or basic catalyst/conditions in the presence of alcohol (Fig. 2).

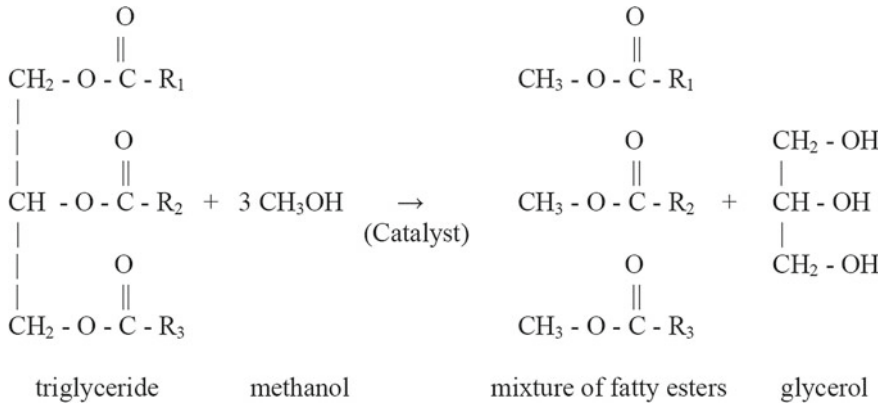


Fig. 2 Transesterification [1-4]

As we all know that biodiesel is another form of diesel fuel that is obtained from the long chain fatty acid esters, plants or animals by reacting them with alcohol by the application of transesterification process (the process of converting s animal or plant oil into biodiesel). The most common blend of biodiesel is B20 which shows the 20% volume of biodiesel and 80% volume of diesel, however, B5 is also a very common type of biodiesel blend which implies 5% of biodiesel and 95% of diesel in volume proportion.

3 Torrefaction

The torrefaction process is basically the carbonization of biomass in limited oxygen supply. In other words, it can also be defined as the thermal process to convert biomass into a coal like material, which will provide better fuel characteristics when compared to original biomass. Torrefaction is widely accepted and used method because of its advantages such as it makes biomass hydrophobic, transport and material handling is easier and less expensive, outdoor storage is possible, longer storage life without fuel degradation, smoke producing compounds removed, and more (Fig. 3).

4 Different Methods of Pine Oil Extraction

Pine oil extraction is carried out for many decades and for the extraction of this oil there are many conventional methods as well as some advanced methods. Very first method was the steam distillation method then Soxhlet extraction followed by solvent extraction, rectification and fractionation of solvent extracts, maceration, and presently techniques like accelerated solvent extraction, microwave hydro-diffusion

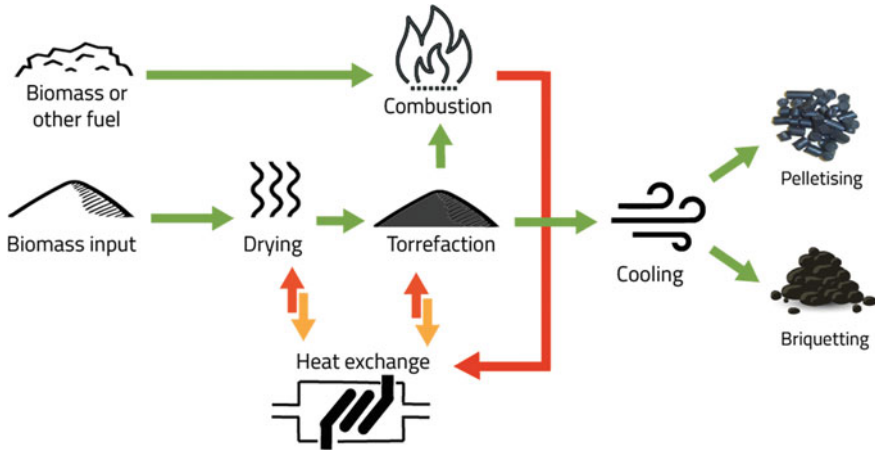


Fig. 3 Torrefaction [21]

and gravity method, supercritical fluid extraction method, extraction method assisted by ultrasound, solvent free microwave extraction and many more.

1. Steam distillation

This is one of the oldest methods used for the extraction of oil. In this method, steam generator is used to generate steam, which then passes through the plant material. The plant material is present in the apparatus, when vapors pass through it then they are condensed with the help of a condenser. Anhydrous Na_2SO_4 is used in order to dry the oil which is collected after condensation. In this method of oil extraction, extraction needs to be performed many a time (at least 3 times).

2. Solvent extraction method

It is a conventional extraction method that is employed for the extraction of oil from oilseeds with low oil content (<20%), like soybean. This method is most commonly used for the extraction of vegetable oil. Mr. Bhutiya researched the oil's extraction optimization, found out that solvent extraction method is a very effective method with high yield value along with a consistent performance but this method is costlier as compared to mechanical press method. One of the reasons for this higher cost is Solvent cost, which is used in this method of extraction. There are many solvents like diethyl ether, ethanol, and hexane, which can be used in this extraction method. Muzenda et al. [5] work on the optimization of process parameters for castor oil production suggested that solvent's ability during solvent extraction is improved with an increase in extraction time. Research work done by Ikya et al. [6] in 2013 on The effect of extraction methods on yield and quality characteristics of oils from shea nut shows that when Solvent extraction method is used then oil yield of 47.5% is obtained which is higher than the old traditional method of extraction having 34.1% of oil yield, also lower flash point, lower moisture content and lower fire point values are obtained

by employing solvent extraction method. According to Buenrostro and Munguia [7], this method has several disadvantages such as long extraction time, more requirement of energy, higher solvent consumption, volatile organic compound's emission into the atmosphere, due to high processing temperature it gives poor product quality and relatively higher number of processing steps.

3. Mechanical expression

It is as simple as its name, in this method pressure is applied to the oil material from which oil is to be extracted. This method of oil extraction is often used for vegetable oil when the quantity of oil content is greater than 20%. According to Mwithiga and Moriasi [17] oil yield increased linearly with compression pressure and they got the peak yield at about 75 °C where compression pressure was (40–80 kgf/m²), time duration of pressing (6–12 min) and increase in bulk temperature of preheated oilseeds takes place. After seeing the work of Oyinlola et al. [8], it is suggested that mechanical presses for small scale oil extraction are simpler, inhibit less steps, and are safer for use. Mainly there are two types of mechanical press methods, i.e., Cold press and Hot press. Hot press process is carried out at a higher pressure and at a higher temperature, whereas Cold press process is carried out at a lower pressure and a lower temperature (generally below 50 °C). Higher temperature press method increases the efficiency of the extraction process and yields up to a maximum of 80% but this higher temperature adversely affects the quality of oil. One of the reasons for high yield in hot press is the inverse relationship between the viscosity of oil and temperature.

4. Microwave assisted extraction

This is a modern technique for the extraction of oil from oilseeds, it is a simple and more efficient method for the extraction of vegetable oils as compared to other thermal extraction processes. MAE uses radio waves for the flow of energy and converts this energy of 300 MHz frequency–300 GHz frequency into heat energy. The study done by Damirichi et al. [9] shows that microwave radiation technique is very much useful in order to get higher extraction yield from oilseeds and improved mass transfer coefficient can be obtained.

Moreno et al. [10] also experimented with microwave pretreatment for the extraction of oil from avocado and found out that the efficiency from Soxhlet-hexane extraction of 54% is increased to the efficiency of 97% when Soxhlet-hexane extraction is coupled with microwave pretreatment. If we are concerned about the quality of oil obtained from microwave technique then we can refer Veldsink et al. [11], who reported that due to the increment in phenolic antioxidants, better oxidative stability is obtained.

5. Ultrasonic assisted extraction (UAE)

This is one of the most popular and innovative methods of oil extraction in which ultrasonic sound waves are used. In this method heat and vibration is produced by ultrasonic waves which result in the breakage of rigid cell walls of plant, thereby

increasing the contact between plant material and solvent. For the comparison of this UAE method with the Conventional solvent extraction, one can refer Samaram et al. [12] research work who employed both of these techniques for the production of oil from papaya seeds, they resulted that the conventional solvent extraction was lasted 12 h, whereas UAE method lasted for only 30 min, which makes this method more efficient in terms of reduced time lag and yield. Li et al. [13] also applied this UAE method for the production of oil from soybean by employing hexane as solvent, they suggested that UAE inhibits a better oil extraction efficiency and may impact significantly on the edible oil industry. There are certain advantages of UAE like Reduction in extraction time as studied by Stanislavjevic et al. [14] in 2007, Lower energy consumption and eco-friendly as suggested by Tian et al. [15] in 2013 and this UAE method also Increases extraction yield as mentioned by Takadas and Doker [16] in their research work.

6. Supercritical fluid extraction (SFE)

It is one of the special types of extraction method by using solvent which is in a gaseous form. Supercritical Fluid is also known as a dense gas. According to Schaneberg and Khan [23], most commonly used supercritical fluid for the extraction of oil is Carbon Dioxide, for the supercritical CO₂ extraction, temperature, and pressure are maintained above 304 K and 74 bar respectively. As suggested by them, we have to be very careful with the selection of temperature and pressure because supercritical fluid's properties can be altered by these parameters. This type of extraction process is not very efficient if we are considering economical methods due to the requirement of high pressure (cost is higher than conventional methods).

5 Pine Oil's Performance in Engine Experiments

Keivani et al. [21] and his research fellows done their research on the pine wood's torrefaction in a continuous system along with torrefaction conditions optimization. The torrefied red pine wood particles continuously in a screw conveyer reactor system having a capacity of 5 kg/hr. They obtained higher heating value of 26,761.9 kJ/kg, energy yield of 47.49%, hardgrove grindability index of 91.76, H/C ratio of 0.099, and O/C ratio of 0.312 and optimum bio coal yield of 56.59% at 299.71 °C and 28.4 min (approximately 300 °C and 30 min). They also concluded that bio coal prepared in this research work displays very similar properties as that of Turkish lignite. So, it is suggested that this bio coal can be used as a supplementary fuel in the coal fired combustion system for energy production.

Islam et al. [24] studied oil extraction from pine seed by the application of solvent extraction method and they gave several conclusions. Firstly, the extracted pine oil exhibits slightly greater density as compared to diesel fuel but lower than that from pyrolytic pine oil. Secondly, the extracted pine oil has a calorific value 34.65 MJ/kg, which is lower than that of diesel fuel but higher than pyrolytic pine oil. Lastly, the

extracted pine oil has 62% lower dynamic viscosity (8.74 centipois @30 °C) and 19% lower kinematic viscosity (10.43 centistoke @30 °C) than pyrolytic pine oil respectively.

Sendilvelan et al. [18] performed their experiments on the Analysis of Performance, Combustion and Emission Characteristics on Biofuel of Novel Pine Oil, with different parameters and load variations, they came to know a very unique result, i.e., In a Diesel engine, pine oil can be used directly without any transesterification process because of its unique chemical possessions. They came to know that thermal efficiency and consumption of 5% pine oil is very very close to that of diesel. From the emission report, it is clearly shown that emissions of CO & HC has been decreased significantly and an advanced level in emission of NO_x is obtained.

Research work done by Vallinayagam et al. [19] shows that there is a comparable calorific value between pine oil and diesel. They perform their experiments on a single cylinder 4 strokes direct injection Diesel engine with pine oil biofuel blends of 25, 50, and 75% with diesel and they came to know that at full load condition, 100% pine reduces CO emission by 65%, HC emission by 30% and Smoke emissions by 70% and also the maximum release rate of heat is increased by 27% with an increase in brake thermal efficiency of 5% hence it was clearly shown that 100% pine oil can be directly used in diesel engine and hidden advantages of pine oil can be utilized.

Kiran et al. [22] along with his fellows perform different experiments on the different blends of pine oil and use them as an input fuel for Diesel engines and their experiments are focused on the usefulness of biodiesel in compressed ignition engines. The biodiesel used by them for their experiments is obtained from the transesterification of pine seed oil and they blend it at different concentrations i.e, B10, B20, B30, and B100. Experiments and emission analyses were performed at different load conditions on a 4 stroke single cylinder engine. After the completion of analysis, it is concluded that B20 holds better potential to use as fuel in compressed ignition (CI) engines because B20 shows a significant reduction in pollutants of CO, CO₂ and HC while the mechanical efficiency and brake thermal efficiency of pine oil have increased by 4.85% and 23.2% respectively. This B20 blend also shown an increase in NO_x emission about 9.12%.

6 Conclusion

Researchers have done huge work to develop biodiesel from pine oil using various catalysts like heterogeneous and homogeneous catalysts. The present paper dealt with the fuel extraction methods from pine oil and a review on engine performance using the pine fuel. It was found that the biodiesel performance on engine is very good as compared to diesel.

References

1. Dwivedi G, Verma P, Sharma MP (2018) Optimization of storage stability for Karanja biodiesel using Box-Behnken design. *Waste Biomass Valorization* 9(4):645–655. <https://doi.org/10.1007/s12649-016-9739-2>
2. Dwivedi G, Jain S, Sharma MP (2011) Impact analysis of biodiesel on engine performance—a review. *Renew Sustain Energy Rev* 15(9):4633–4641. <https://doi.org/10.1016/j.rser.2011.07.089>
3. Chamola R, Khan MF, Raj A (2019) Verma M And Jain S: Response surface methodology based optimization of in situ transesterification of dry algae with methanol, H₂SO₄ and NaOH. *Fuel* 239:511–520
4. Kumar S (2017) Jain S And Kumar H: Process parameter assessment of biodiesel production from a Jatropha–algae oil blend by response surface methodology and artificial neural network. *Energy Res Part A* 39:2119–2125
5. Muzenda E, Kabuba J, Mdletye P, Belaid M (2012) Optimization of process parameters for castor oil production. *Proceeding of the world congress on engineering 2012 Vol. III WCE 2012*, July, 4–6, London, UK
6. Ikya JK, Umenger LN, Iorbee A (2013) Effects of extraction methods on the yield and quality characteristics of oils from shea nut. *J Food Res Sci* 2:1–12
7. Buenrostro M, Munguia CL (1986) Enzymatic extraction of avocado oil. *Biotechnol Lett* 8:505–506
8. Oyinlola A, Ojo A, Adokoya LO (2004) Development of a laboratory model screw press for peanut oil expression. *J Food Eng* 64:221–227
9. Damirichi A, Alirezalu SK, Achaclousi BF (2011) Microwave pretreatment of seeds to extract high quality vegetable oil. *Int J Nutriyion Food Eng* 5(9):508–511
10. Moreno AO, Dorantes L, Galindex J, Guzman RI (2003) Effect of different extraction methods on fatty acids, volatile compounds and physical and chemical properties of avocado (*Perseaamaricana* Mil) oil. *J Agr Food Chem* 51:2216–2221
11. Veldsink JW, Muuse BG, Meijer MMT, Cuperus FP, Van De Sande RLKM, Van Putte KPAM (1999) Heat pretreatments of oilseeds: effect on oil quality. *Fett/Lipid* 7:244248
12. Samaram S, Mirhosseini H, Tan CP, Ghazali HM (2014) Ultrasonic-assisted extraction and solvent extraction of papaya seed oil: crystallization and thermal behaviour, saturation degree, colour and oxidative stability. *Ind Crops Prod* 52:702–708
13. Li H, Pordesimo L, Weiss J (2004) High Intensity ultrasonic-assisted extraction of oil from soybeans. *Food Res Int* 37(7):731–738
14. Stanisavljevic IT, Lazic ML, Veljkovic VB (2007) Ultrasonic extraction of oil from tobacco (*Nicotiana tabacum* L.) seeds. *Ultrason Sonochem* 4(5):646–652
15. Tian Y, Xu Z, Zhang B, Lo YM (2013) Optimization of ultrasonic-assisted extraction of pomegranate (*Punicagranatum* L) seed oil. *Ultrason Sonochem* 20(1):202–208
16. Takadas F, Doker O (2017) Extraction method and solvent effect on safflower seed oil production. *Chem Process Eng Res* 51:9–17
17. Mwithiga G, Moriasi L (2007) A study of yield characteristics during mechanical oil extraction of pretreated and ground soybeans. *J Appl Sci Res* 3(10):1146–1151
18. Sendilvelan S, Bhaskar K, Prabu NM (2017) Analysis of performance, combustion and emission characteristics on biofuel of novel pine oil. *Rasayan J Chem* 10(3):873–880
19. Vallinayagam R, Vedharaj S, Yang WM, Roberts WL, Dibble RW (2015) *Renew Sustain Energy Rev* 51:1166
20. Yusuf AK (2018) A review of methods used for seed oil extraction. *Int J Sci Res (IJSR)* 7(12). <https://doi.org/10.21275/1121804>
21. Keivani B, Gultekin S, Olgun H, Atimtay AT Torrefaction of pine wood in a continuous system and optimization of torrefaction conditions. *Int J Energy Res*
22. Kiran CHR, Ramana CHV, Reddy BN, Rama Krishna VS (2021) Experimental investigation of performance and emission characteristics of diesel engine using pine oil blends. *AIP conference proceedings*, vol 2317, p 040006. <https://doi.org/10.1063/5.0036484>

23. Schaneberg BT, Khan IA (2002) Comparison of extraction methods for marker compounds in the essential oil of lemon grass by GC. *J Agric Food Chem* 50:1345–1349
24. Islam MN, Sabur A, Ahmmed R, Hoque ME (2014) Oil extraction from pine seed (*Polyalthia longifolia*) by solvent extraction method and its property analysis. In: 6th BSME international conference on thermal engineering (ICTE 2014)
25. Goyal P, Sharma MP, Jain S (2013) Optimization of transesterification of *Jatropha curcas* oil to biodiesel using response surface methodology and its adulteration with kerosene, material and environment science, vol 4, pp 277–284
26. Jain S, Sharma MP (2012) Oxidation thermal and storage stability studies of *Jatropha curcas* biodiesel, international scholarly research notice
27. Jain S, Sharma MP (2011) Oxidation and thermal behavior of *Jatropha curcas* biodiesel influenced by antioxidants and metal contaminants. *Int J Eng Sci Technol*
28. Narula V, Thankur V, Uniyal A, Kalra S, Jain S (2016) Process parameter optimization of low temperature transesterification of algae-jatropha curcas oil blend. *Energy* 119:983–988
29. Narula V, Khan MF, Negi A, Thankur A, Uniyal A, Kalra S, Jain S (2017) Low temperature optimization of biodiesel production from algal oil using CaO and CaO/AL₂O₃ as catalyst by the application of response surface methodology. *Energy* 140:884–9879
30. Jain S (2013) Sharma M P : Engine performance and emission analysis using oxidatively stabilized *Jatropha curcas* biodiesel. *Fuel* 106:152–156
31. Jain S, Sharma MP (2012) Correlation development between the oxidation and thermal stability of biodiesel. *Fuel* 102:354–358
32. Jain S (2011) Sharma MP: Study of oxidation stability of *Jatropha curcas* biodiesel/diesel blends. *Energy Environ* 2:533
33. Jain S, Sharma MP (2011) Power generation from MSW of Haridwar city: a feasibility study. *Renew Sustain Energy Rev* 15:69–90

Microstructure Tribological Characterization of Copper Metal Matrix Reinforced with Cerium Oxide



Vivek Pandey, Tushar Choudhary, and Anup Bajpai

Abbreviations

Cu	Copper
CeO ₂	Cerium oxide
UTM	Universal testing machine
SEM	Scanning electron microscopy
XRD	X-ray diffraction

1 Introduction

In the growing technology, most of the heavy mechanical industries are looking for new technologies to develop certain specific property combinations. Composite materials are produced by combining materials into a single material to better suit for a specific application than either of the original materials separately.

Ahmed et al. [1] investigated nanostructures which are made by semiconducting pure and Gd-doped cerium oxide (CeO₂) with application to gas sensors. After tested by X-ray diffraction, Raman spectroscopy and transmission electron microscope nanostructures with gas sensor have improved sensitivity, stability, and can operate in lower temperature. Elena et al. [2] investigated hot stamping process on boron steels; the dies are tested at conditions like adhesive wear, abrasion, thermal stresses, and fatigue. The results showed an increase of COF. Wear mechanism of

V. Pandey (✉)

Gyan Ganga Institute of Technology and Sciences, Jabalpur 482003, India

T. Choudhary · A. Bajpai

PDPM Indian Institute of Information Technology, Design and Manufacturing, Jabalpur 482005, India

coated and uncoated sample comes out as adhesive and oxidative when tested. Ali Mazahery et al. [3] investigated microstructure and tribological properties of SiC particles reinforce with Al-based composite on different size and volume fraction. Compcasting process is used for making composites. Pin-on-disk wear tester, hardness measurement, and SEM were used for microstructural characterization. Ana et al. [4] show that for improving surface properties of different steels and alloys plasma nitriding processes are widely used. Three nitride layers were cold rolled and then tested by SEM, XRD, and Rietveld method and hardness measurement. Result shows that as nitriding temperature increases the compound layer of Fe₂-3N increases and of Fe₄N decreases. Liu et al. [5] examined cerium oxide (CeO₂) nanoparticles by using ammonia water and oxalic acid from precipitation method. They were tested by X-ray, SEM, and FT-IR. The results showed that the average particle size and crystallite size increased with increasing the temperature. Kanwarje et al. [6] take P20 tool steel and develop coating from microwave hybrid heating process with addition of CeO₂ (modified coating) with varying wt%. On addition of CeO₂ (1 wt%), it improves microstructure pattern, hardness (30%), and wear behavior of coatings. Makoto et al. [7] examined cerium oxide and Cu-containing cerium oxide. The results show that presence of copper enhances reducibility and sulfidation in cerium oxide. Kenneth et al. [8] investigated the behavior of copper matrix composites when reinforced from chips of steel on wear and different properties of mechanical. Low porosity was found when steel chip was added as compared to addition of alumina chip in copper matrix. Wear resistance, mechanical properties hardness, and tensile strength are also improved. Ke-Chao et al. [9] investigated on samples of copper matrix composites reinforced by WC particle. Result indicated that addition of WC increases the hardness, coefficient of friction, and resistance against the scratch. As the normal load increases, material removal mechanism improves. Debalina et al. [10] investigate iron matrix composites which were reinforced by tungsten carbide on the dry sliding wear test at room temperature. Result shows that WC increases the microhardness, wear resistance and nanocomposites showed lower COF and surface roughness. Yusoff et al. [11] investigated the effect of copper tungsten and graphite manufactured by ball mill operation. XRD, SEM, hardness, and electrical conductivity were finding out. Increasing milling time shows increase in hardness of composite but reduction in electrical conductivity. Zhang et al. [12] used SiCp/Cu composite to investigate dry sliding wear behavior by using pin-on-disk tester. Volume loss gets starts with sliding distance and by application of load; this happens because of enlargement of mean free path between particles, and wear resistance is proportional to reinforcement particles. Deshpande et al. [13] investigated the effect of WC particle-reinforced copper matrix composites on wear behavior by using pin-on-disk tester against a sintered SiC abrasive disk. Tiwari et al. [14] quoted that the wear rate and friction coefficient depend on Cu part of mix, when applied with harder material. This is because of adhesive bonding and layer forming between particles. From the detailed literature review, it was found that no work was done to investigate the effect of cerium oxide on mechanical, wear, and microstructural property of copper metal powder. The purpose of the project is to find out the characterization of copper specimen with variable addition of cerium oxide in its

composition through various mechanical properties. The project will also help us to find out any abrupt changes in the properties of copper with changing percentage of cerium oxide on different sintering temperature.

2 Materials Selection

To obtain copper-based powder metallurgy specimens and study the effects of cerium oxide content and temperature on its microstructure properties, graphite powder is used as lubricant. The copper powder having purity of about 99.5% and cerium oxide of 99.95% are used. Graphite powder of 98% purity is used for lubrication purpose. All purchased from Qualikems Fine Chemicals Pvt. Ltd., Vadodara.

3 Methodology

3.1 Preparation of Specimen

The pin-on-disk machine has a pin holder of capacity varying from 6 to 12 mm. As the powder preforms should have sufficient contact area with the disk, the pin diameter was decided as 12 mm.

3.2 Design of Experiment

Sintering temperature (°C)	Cerium oxide content (weight percentage)
$T_1 = 900$	$(CeO_2)_1 = 0$
$T_2 = 950$	$(CeO_2)_2 = 0.2$
$T_3 = 1000$	$(CeO_2)_3 = 0.6$
	$(CeO_2)_4 = 1$

3.3 Process of Experiment

From preparing of specimen to examine them, it contains different stages of experiment. Flowchart of experiment is shown in Fig. 1.

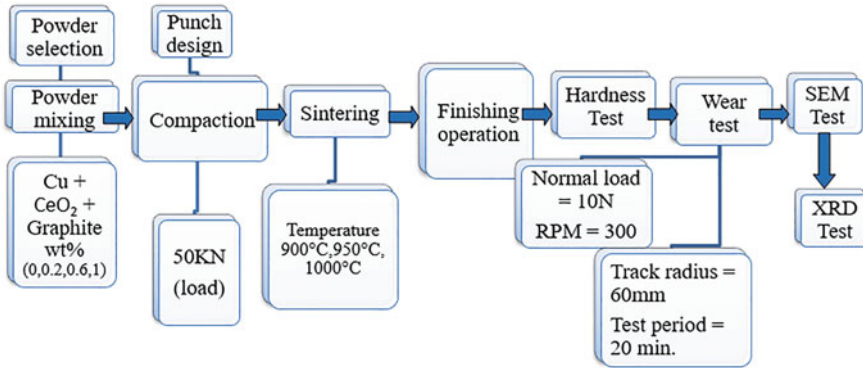


Fig. 1 Flowchart of experiment

Steps for making specimens.

1. Powder mixing
2. Cold compaction
3. Sintering process
4. Finishing operations

4 Test Performed

4.1 Hardness Test

The Vickers microhardness was calculated by a microhardness tester machine using a load of 50 gf. 20 readings were taken and average values were reported in the graph.

4.2 Wear Test

The samples formed are then being tested to analyze the wear behavior of the copper-cerium oxide powder performs in dry sliding condition of room temperature and humidity of 60–65%. This experimentation is being carried out on a pin-on-disk wear testing machine using samples of \varnothing 12 mm (avg. value) 15 mm in length (avg. value).



Fig. 2 Wear and friction tester, digital controller box, reading on MAGVIEW-2010

4.3 Wear Testing Operation

To study wear behavior of specimens to pin-on-disk type wear testing instrument (Model: DUCOM TR-20) having a hardened steel disk of diameter 160 mm \times 10mm thick, set required track radius 60 mm. Keep normal test weight of 10 N. The adjusted wear display is to be within $\pm 5 \mu\text{m}$. Select the mode of operation (time) 20 min distance traveled by sample about 2300 m. The setup is shown in Fig. 2.

Start push button on the controller front panel to commence the test. Set there required RPM by rotating the SET 300 RPM knob in clockwise direction. The test stops automatically after the complete of preset time.

4.4 SEM Test

The scanning electron microscope test of specimen was examined for microstructure conducted in the instrument model used for the SEM analysis which was JEOLJSM-6380A analytical scanning electron microscope device in IIITDM SEM, as shown in Fig. 3.

4.5 XRD Test

The experiment was conducted at Lab of Raja Ramanna Centre for Advanced Technology RRCAT, UGC-DAE Consortium for Scientific Research, Indore, India, on XRD machine which is D8Advance X-ray diffractometer (XRD) at an angle range of 200–950 range and wavelength of 1.54 nm. X-ray diffraction (XRD) is a high-tech, non-destructive technique for analyzing a wide range of materials. The machine setup is shown in Fig. 4. This XRD machine is capable to measure nine samples in a series. Samples in powder form and in thin film can be measured using this XRD machine. We have use thin-film coating in our study.



Fig. 3 JEOLJSM-6380A scanning electron microscope

Fig. 4 D8 Advance X-ray diffractometer (XRD) machine



5 Result and Discussion

5.1 *Effect of CeO₂% and Sintering Temperature on Hardness*

The increased hardness is attributed to the CeO₂ particles which act as barriers and prevents the movement of dislocations within the matrix. It was found that as CeO₂% increases hardness is also increases because CeO₂ increases density. It is verified by

Table 1 Average hardness (BH) at different sintering temperature and CeO₂ content

CeO ₂ content wt%	900 °C sintered temperature	950 °C sintered temperature	1000 °C sintered temperature
0	32	34	35
0.2	34	35	36
0.6	37.333	38	38.333
1	44	46.333	48

microstructure. As sintering temperature increases, the hardness shows the increasing trend because bonding increases with temperature. The same can be seen in Table 1. When sintering temperature increases densification is also increases and sample at 1000 °C shows maximum hardness and sample at 900 °C shows minimum hardness.

5.2 Effect of CeO₂% and Sintering Temperature on Density

Figure 5a shows the variation of density with respect to CeO₂ content (wt%). As CeO₂ content (wt%) increases, density is also increases from 0 to 1%. In 900 °C temperature by increasing the CeO₂%, from 0 to 0.2% density increases 1.34%, 0.2 to 0.6% it increases 0.646%, and from 0.6 to 1% it increases 1.12%. In 950 °C temperature by increasing CeO₂ from 0 to 0.2% density increases 0.22%, 0.2 to 0.6% it increases 1.23%, and from 0.6 to 1% it increases by 0.68%. In 1000 °C by increasing CeO₂ from 0 to 0.2% density increases 0.86%, 0.2% to 0.6% it increases 0.53%, and from 0.6 to 1% density increases by 0.85%. Sample at 1% shows dense structure, and sample at 0% shows minimum density.

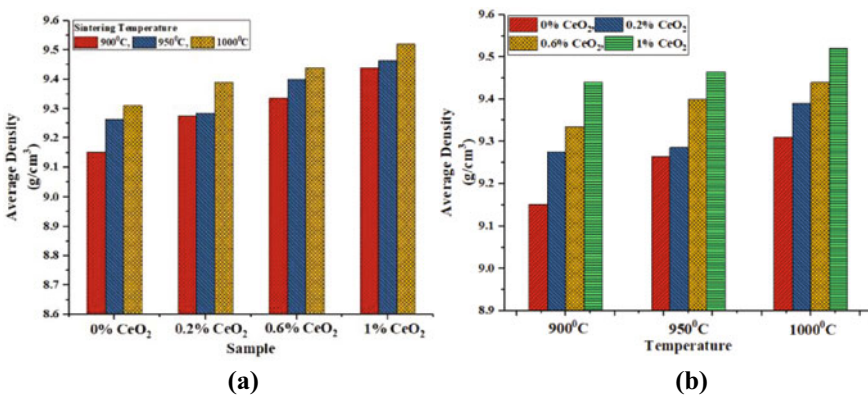


Fig. 5 a Effect of CeO₂% on density. **B** Sintering temperature on density

Figure 5b shows the variation of density with respect to sintering temperature. As sintering temperature increases, density also increases from 900 to 1000 °C. In 0% CeO₂ by increasing the temperature from 900 to 950 °C density increases 1.22% and from 950 to 1000 °C it increases 0.50%. In 0.2% CeO₂ by increasing the temperature from 900 to 950 °C density increases 0.10% and from 950 to 1000 °C it increases 1.13%. In 0.6% CeO₂ by increasing the temperature from 900 to 950 °C density increases 0.69% and from 950 to 1000 °C it increases 0.43%. In 1% CeO₂ by increasing the temperature from 900 to 950 °C density increases 0.26% and from 950 to 1000 °C it increases 0.59%. Sample at 1000 °C shows dense structure, and sample at 900 °C shows minimum density.

5.3 Effect of CeO₂% and Sintering Temperature on Wear

Pin-on-disk machine (Model: DUCOM TR-20 Bangalore, India) with ASTM-G99 standard was used for measuring the sliding wear. The following four combinations 0, 0.2, 0.6, and 1% cerium oxide were mixed with copper metal powder composite. 10 KN load was applied to investigate the wear performance. The wear is higher in 0% CeO₂, and it was minimum at 1% CeO₂ in copper metal powder matrix. The initial increase in wear loss was reduced after 500 s, beyond this wear loss curve followed moderately increase path. The high wear loss is in initial stage possibly due to high contact pressure between the sample and counter surface. After increasing the time, the real contact area between these two surfaces increases and adhesive wear takes place. A layer is formed between the sample and the counter surfaces which prevent the material loss so in later stage wear loss reduces. Figure 6a–d shows wear effect.

5.4 SEM Results

Figures 7, 8, 9, and 10 show the microstructure of 0% CeO₂, 0.2% CeO₂, 0.6% CeO₂, and 1% CeO₂ in copper metal powder matrix. There is large number of microcracks in the copper matrix, and the structure is porous because in 0% CeO₂ no cerium oxide is added and it start reduces up to 1% of CeO₂. Black patches represent the presence of CeO₂, and it is clearly seen where white patches represent the copper. It is seen that in 1% cerium oxide the structure is dense, very less microcrack occurs and it is also validated by hardness and wear resistance. At 1% cerium oxide, it shows the behavior of high hardness. It was also found that the CeO₂ is uniformly distributed in copper matrix. From analysis it has been observed that as the CeO₂ contain increases the black patches become more remarkable, on comparing Figs. 7, 8, 9, and 10.

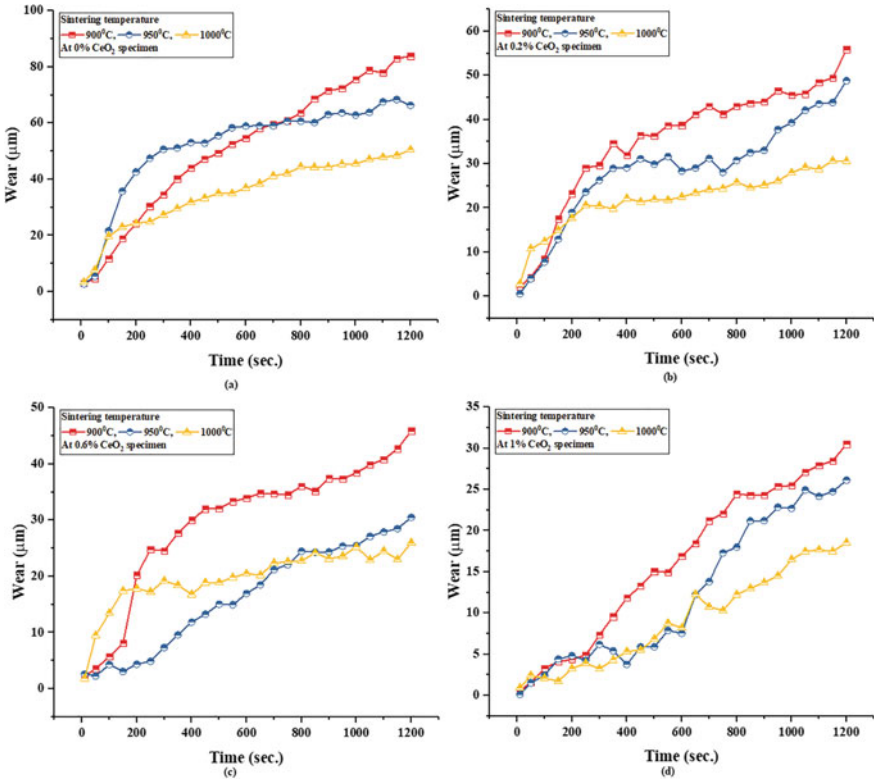


Fig. 6 Average wear (μm) with sintering temperature (in $^{\circ}\text{C}$) at 0–1% CeO_2 specimen

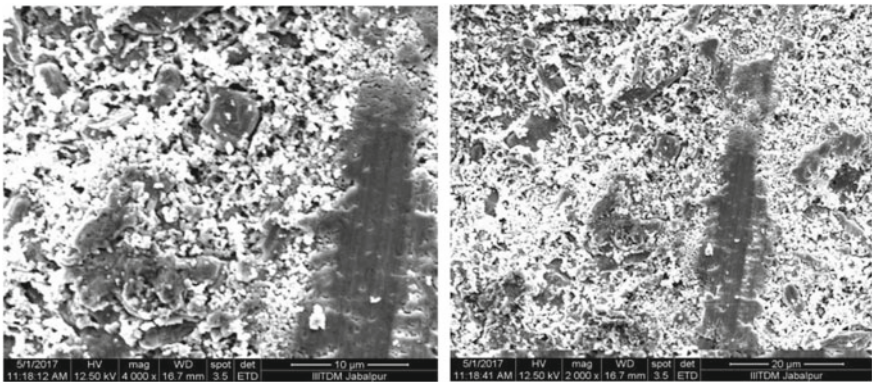


Fig. 7 SEM results for pure copper

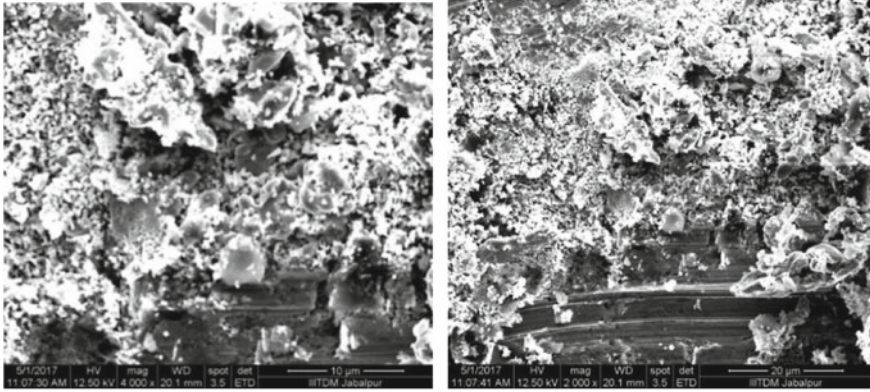


Fig. 8 SEM results for 0.2% cerium oxide

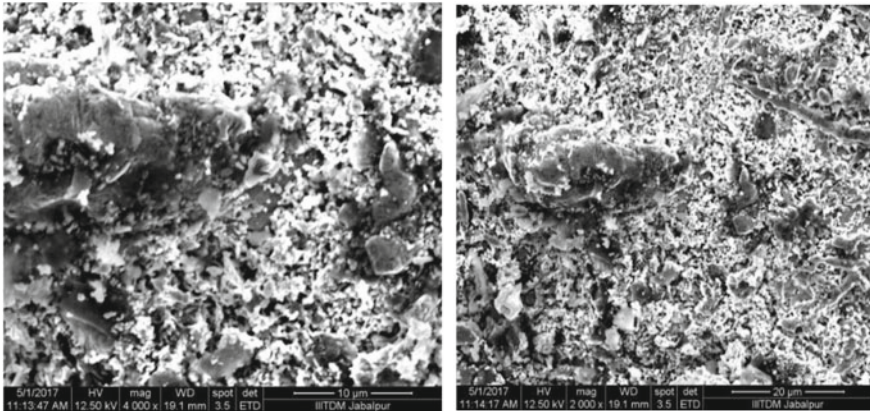


Fig. 9 SEM results for 0.6% cerium oxide

5.5 XRD Test

Figure 11 indicates the XRD diffraction pattern of 0, 0.2, 0.6, and 1% CeO_2 particle. Peaks found at angle $2\theta = 36,043'$, $43,032'$, $50,047'$, $74,015'$, and $89,093'$. In graphs, 1 shows CeO_2 and 2 as Cu. After addition CeO_2 from 0.2 to 1% no new peak was found in the diffraction pattern which indicates the good solubility of CeO_2 in copper matrix but a reduction of the peaks was also observed in the diffraction pattern that conforms the uniformly distribution of CeO_2 in copper matrix. It was also observed that peaks center shifted toward the smaller value. The result is stressed evaluation in the matrix which causes the reduction in the peaks intensity. It can be inferred that the addition of CeO_2 has fine microstructure.

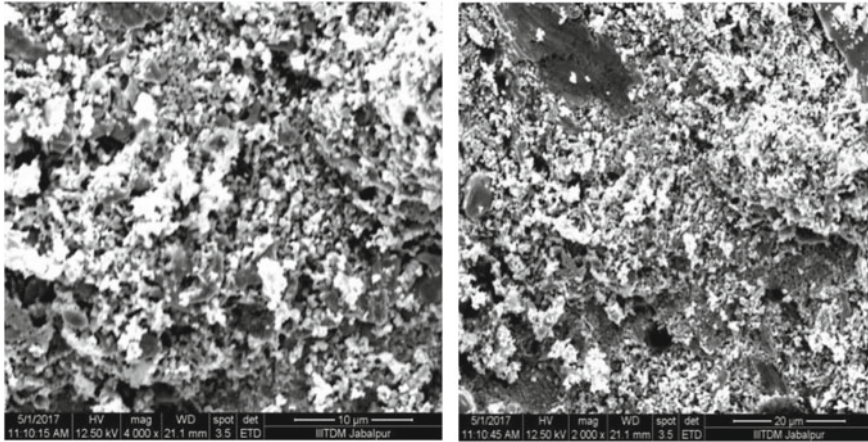


Fig. 10 SEM results for 1% cerium oxide

6 Conclusions

On the basis of the observations taken and result derived, the following conclusions can be made:-

1. The experiment shows that copper-cerium oxide specimen hardness increases with increase in sintering temperature and cerium oxide content. Although the rise was slower initially, the value of Brinell hardness number increased in the specimen with higher cerium oxide percentage at higher sintering temperature. So, it may be suggested that there should be some lattice modification at higher CeO_2 content.
2. A constant trend of increasing density was seen with increasing sintering temperature and cerium oxide content. The voids of the copper metal matrix are filled by progressive fusion of cerium oxide atoms with copper.
3. The specimen with highest cerium oxide content and sintering temperature has very less value of porosity in it.
4. Observing the wear trend of the copper composite specimen, it is clear that cerium oxide is providing good amount of wear resistance to copper as the wear of specimen with no cerium oxide was excessively high as compared to that with 0.2% CeO_2 and it decreased further as cerium oxide was added to 1%.
5. The SEM test showed that the addition of cerium oxide provided pitting corrosion and oxidation resistance to the copper composite samples as white flakes of copper can be seen in the image of 0% CeO_2 specimen cleaner surface that can be observed in the final image with 1% CeO_2 content.
6. XRD result indicated that addition of CeO_2 from 0.2% to 1% no new peak was found in the diffraction pattern which indicates that good solubility of CeO_2 in copper matrix but it was also observed that a reduction of the peaks in

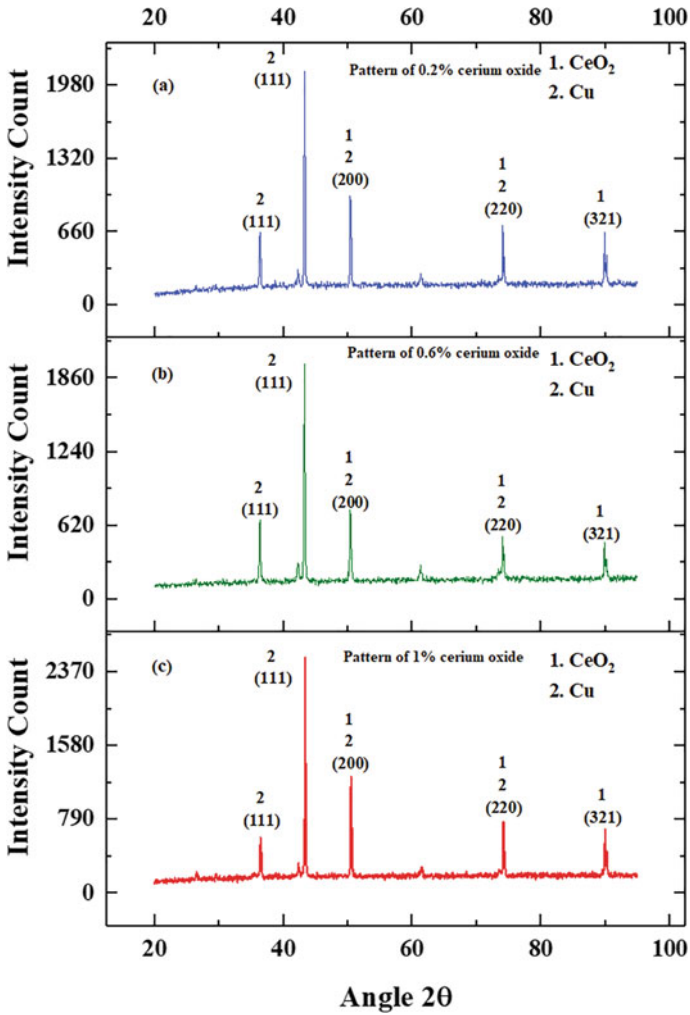


Fig. 11 XRD diffraction pattern for different % of cerium oxide

the diffraction pattern conforms the uniformly distribution of CeO_2 in copper matrix.

7. Thus copper composite using for engineering applications such as automobile, defence and shipping industries applications.

References

1. Aboud AA, Al-Kelesh H, El Rouby WMA, Farghali AA, Hamdedein A, Khedr MH (2017) CO₂ responses based on pure and doped CeO₂ nano-pellets. *JMR&T* 7(1):14–20
2. Gracia-Escosa E, García I, de Damborenea JJ, Conde A (2017) Friction and wear behavior of tool steels sliding against 22MnB5 steel. *JMR&T* 6(3):241–250
3. Mazahery A, OstadShabani M (2013) Micro structural and abrasive wear properties of SiC reinforced aluminum-based composite produced by compo casting. *Trans Nonferrous Met Soc China* 23(7):1905–1914
4. de Andrade Manfridini AP, de Godoy GCD, de Arruda Santos L (2016) Structural characterization of plasma nitride interstitial-free steel at different temperatures by SEM, XRD and Rietveld method. *JMR&T* 6(1):65–70
5. Liu YH, Zuo JC, Ren XF, Yong L (2014) Synthesis and character of cerium oxide (CeO₂) nanoparticles by the precipitation method. *Metallurgy* 53(4):463–465
6. Singh K, Sharma S (2018) Development of Ni-based and CeO₂ Modified Coatings by Microwave Heating. *Mater Manuf Processes* 33(1):50–57
7. Kobayashi M, Flytzani-Stephanopoulos M (2002) Reduction and sulfidation kinetics of cerium oxide and Cu-modified cerium oxide. *Ind Eng Chem Res* 41(13):3115–3312
8. Kanayo Alaneme K, UfuomaOdoni B (2016) Mechanical properties, wear and corrosion behaviour of copper matrix composites reinforced with steel machining chips. *Eng Sci Technol Int J* 19(3):1593–1599
9. Zhou K-C, Pei H-L, Xiao J-K, Zhang L (2015) Micro-scratch behaviour of WC particle-reinforced copper matrix composites. *Rare Met.* <https://doi.org/10.1007/s12598-015-0586-2>,(2015)
10. Bhattacharjee D, Muthusamy K, SarathiRamanujam EO, Composites L-R (2014) *Tribol Trans* 57:292–299
11. Yusoff M, Othman R, Hussain Z (2011) Mechanical alloying and sintering of nanostructure tungsten carbide-reinforced copper composite and its characterization. *Mater Des* 32(6):3293–3298
12. Zhang L, He XB, Qu XH, Duan BH, Lu X, Qin ML (2008) Dry sliding wear properties of high volume fraction SiCp/Cu composites produced by pressure less infiltration. *Wear* 265:1848–1856
13. Deshpande PK, Lin RY (2006) Wear resistance of WC particle reinforced copper matrix composites and the effect of porosity. *Mater Sci Eng A* 418(1):137–145
14. Tiwari AK, Mishra TK, Choubey M, Ranjan RK, Investigation of wear behaviour of Al +Cu powder performs. *IOSR J Eng (IOSRJEN)* 2. e ISSN: 2250-3021, p-ISSN: 2278-8719. www.iosrjen.org

Investigation on Vibration of Crankshaft in Reciprocating Engine



Abhishek Gatlewar , Dipak Gulhane , Vijay Kalbande ,
Nitin K. Mandavgade, Rupesh Khorgade , and Mahesh T. Kanojiya 

1 Introduction

Crankshaft dynamics has gradually become an activity of automobile companies, and the stab is constantly rising in the sense of noise, vibration, and roughness (NVH) [1]. The vibration and noise generated by the crank gearbox through high-speed software are the primary issues in dynamic research. The main difficulty in finding a crankshaft is related to the way the crankshaft wraps around the bearing and rotates uninterruptedly. This effect is called reciprocating rotation, and the influence between the crankshaft and the crankshaft jointly participates in the appearance of engine noise and vibration which determines the load capacity of the crankshaft and its bearing life [2].

Crankshafts are widely used in the automotive industry. It has been observed that everything from small-capacity laptops to machines with great potential is used correctly. During the operation of the notebook computer, the curved bearing is subjected to variable loads, which can cause variable anxiety. The connecting rod mechanism of the crank experiences various anxieties during the entire work cycle. Evidence shows that due to various load conditions, the crank itself vibrates that have hundreds of effects on its bearings, resulting in increase of the wear and tear of the crank [3]. Therefore, it is predictable that by estimating its vibration, the impact of various load regulations on a unique unit on its overall performance can be noted.

A. Gatlewar · D. Gulhane · V. Kalbande · N. K. Mandavgade (✉) · R. Khorgade · M. T. Kanojiya
Nagpur Institute of Technology, Nagpur 411501, India

2 Formulation of Present Work

Literature survey has shown that crankshaft plays a very important role in strengthening and motion transmission. Therefore, it is necessary to understand its dynamic behavior under operational situation. Due to its intricacy and the establishment of geometric shapes, it is difficult to use the analysis potential to evaluate the crankshaft. Therefore, in this research software platform methods to analyze the dynamic behavior of the crankshaft has been used. There are many software programs such as CATIA, HYPER MESH, ANSYS, and among others that are used to check the problems opposite to the improvement of stress, strain, etc. In fact, it provides the concept of the fatigue life cycle of the tested aspect. However, software platforms still face challenges; that is, how to truly announce the value of the parameter that the factor will work on. Therefore, it is difficult to confirm the existence range of the factor or point out the exact reason for its failure.

The results obtained from the software program depend on calculations performed with the aid of a software package manually entered by the programmer. The software program only indicates the effect saved in the memory and has nothing to do with the wise situation. Therefore, it is stated that analytical capabilities are as important as software platform. However, the final results obtained through the use of analytical skills are limited by the range of variables considered, and in the end no specific answers can be obtained.

The general techniques for evaluation are as follows:

1. Get the specific size of the thing to be tested.
2. Use any modeling software platform to create models.
3. Save the created model file so that it can be imported into evaluation software, ANSYS, Unigraphics, etc.
4. Open the file in the analysis software program [ANSYS] to perform static evaluation (using dynamic force as input) and model evaluation [vibration].
5. Apply the meshing situation. Since the difference between the real answer and the approximate answer depends on the mesh, we choose.
6. Get the value of stress, natural frequency, strain, and mode shape.

3 Model Analysis by Vibration

However, since there are unique strategies for performing model vibration evaluation, the following will introduce the step-by-step technique of the method used in the existing setup:

1. The body gadget [engine] is converted into a basic dynamic model. The dynamic model is a crank chain, assuming that the center of gravity of the engine in each phase is located at the geometric center.

2. The kinematics evaluation of the model is performed graphically. Under this evaluation, the speed and speeding up of the center of gravity of each hyperlink have been expected.
3. After the kinematics evaluation of the model, it will be regarded as a dynamic evaluation according to the regulations proposed by D'Alembert. Accordingly, when the inertial force generated due to the acceleration related to the hyperlink is considered on the link, the dynamic situation can be regarded as the static situation.
4. Calculate the load torque on the engine crankshaft when the crank rotates.

Finally, the calculated load torque is used to estimate the torsional amplitude of the shaft below the torsional vibration.

4 Slider–Crank Dynamic Analysis

The dynamic conduction of the reciprocating engine's crankshaft is shown in Fig. 1. The slider–crank associations and their centers of gravity are assumed to be concentrated in the core of each link. For evaluation purposes, the reciprocating engine is modeled as a simplified crank–crank combination, and the positions of the reciprocating engine cylinder, crank, connecting rod, and piston are represented as hyperlink 1, hyperlink 2, hyperlink 3, and hyperlink 4.

A. Estimate link power Start

In the above situation, the crank rotates in a counterclockwise path, and its angular displacement is 360° , so dynamic evaluations were performed on 400° , 112° , 256° , 328° , 400° , 472° , 616° , and 688° . At this time, the angle function of hyperlink 2 is 360° , and it appreciates hyperlink 1. Since all the hyperlinks of the mechanism move at a certain speed and acceleration, the inertial force related to the hyperlink cannot be ignored. Therefore, it is necessary to evaluate the kinematics of the link at each angular function. Tables 1 and 2 show all the calculated pace and acceleration values and plotted as shown in Figs. 2 and 3.

Fig. 1 Slider–crank arrangement

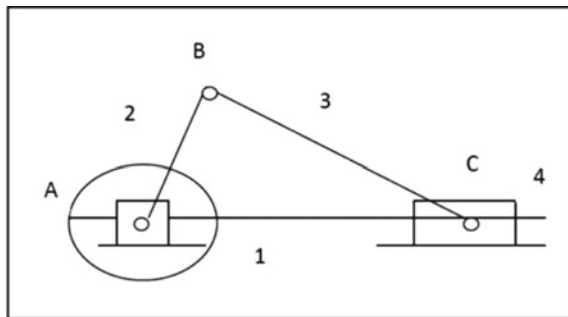


Table 1 Crankshaft velocity calculation

\emptyset	V2	V3	V4
40	95.24	82.66	85.84
112	95.24	32.41	79.52
256	95.24	35.55	76.38
328	95.24	82.84	85.80
400	95.24	32.41	79.52
472	95.24	35.55	76.38
616	95.24	35.55	76.38
688	95.24	82.84	85.80

Table 2 Crankshaft acceleration calculations

\ominus	a_{g2}	a_{g3}	a_{g4}
40	98,779.75	194,412.3	205,253.9
112	98,779.75	143,098.8	142,098.8
256	98,779.75	139,151.7	126,310.1
328	98,779.75	194,412.3	205,253.9
400	98,779.75	194,412.3	205,253.9
472	98,779.75	143,098.8	142,098.8
616	98,779.75	139,151.7	126,310.1
688	98,779.75	194,412.3	205,253.9

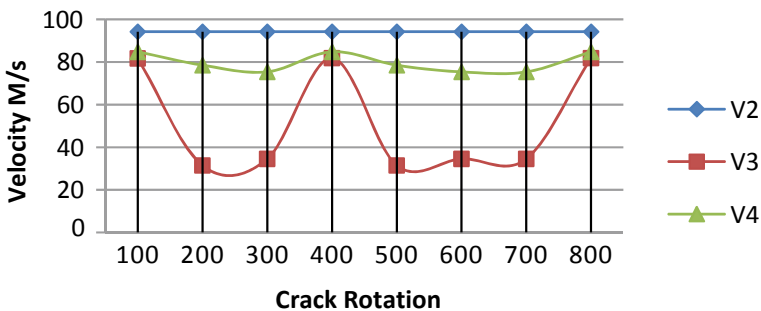


Fig. 2 Crank rotation versus velocity

As shown in Fig. 4, the dynamic evaluation of the slider–crank mechanism when $\theta = 328^\circ$. In this figure, we focus on the force applied to the connecting rod, crank, and slider. These forces are represented by $F_P, F_{14}, FW, F_{i4}, F_{i3}, F_{34}, F_{i2},$ and F_{23} where F_P is the stress pressure performed on the slider or piston due to the strength stroke at the coefficient C , and F_{14} is the daily response due to the pressure and the pressure generated. For the cylindrical inner wall, F_{i4} is the inertial pressure caused by the movement of the slider, FW is the pressure caused by the mass of the slider, and

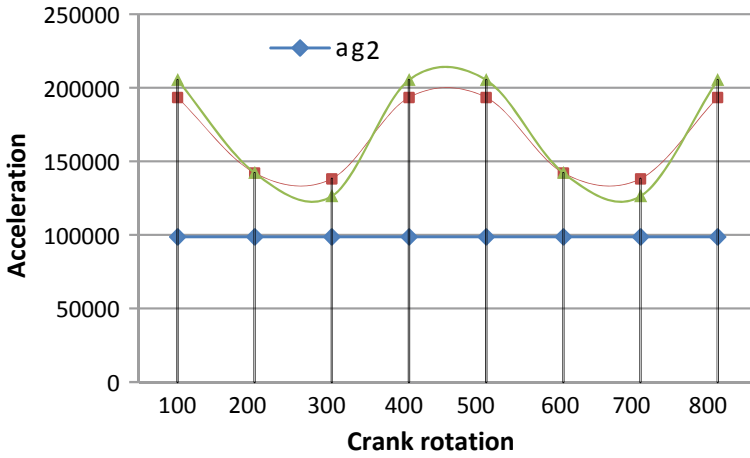


Fig. 3 Crank rotation versus acceleration

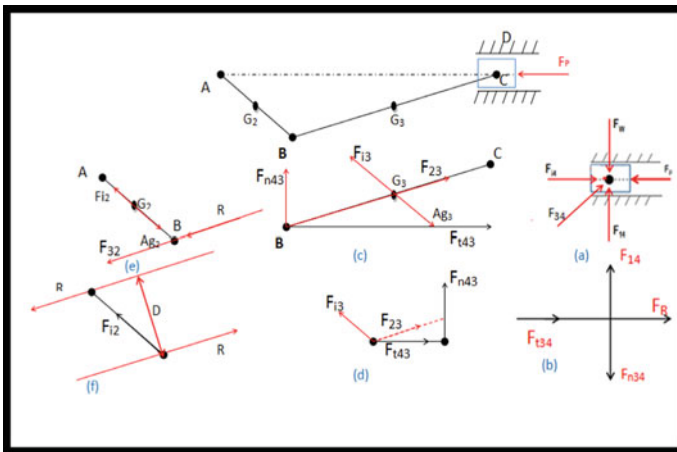


Fig. 4 Slider-crank schematic diagram at 328°

F_{34} is the pressure caused by the hyperlink 3 on the hyperlink four (i.e., the slider). But the F_{34} pressure is unknown, and the pressure F_{34} is calculated by decomposing the pressure F_{34} into two elements, namely $F_{34}(t)$ and $F_{34}(n)$. The position $F_{34}(t)$ represents the tangential factor $F_{34}(n)$ represents the everyday elements that appear perpendicular to the cylinder floor [4, 5].

In the same way, the forces exerted on the connecting rod and crank are $F_{43}(n)$, $F_{43}(t)$, F_{i3} , F_{23} and F_{32} , F_{i2} , respectively, which are proved in the determination standards 1.4(c) and (e), where $F_{43}(n)$ represents daily things appearing in the factor Con hyperlink 3, $F_{43}(t)$ represents the tangent factor of the hyperlink 3 on the floor

C, F_{i3} represents the inertial pressure appearing through the center of gravity of the hyperlink 3, and F_{23} is the hyperlink 2. The generated pressure is on the hyperlink 3; that is, from the crank to the connecting rod, F_{32} is the pressure caused by the hyperlink 3 on the hyperlink 2, and F_{i2} represents the inertial pressure performed through the center of gravity of the hyperlink 2. Forces F_p , FR, F_{i2} , F_{i3} , F_{i4} , and FR can be calculated using the following formula:

$$F_p = P \times \text{Area}, \left(\text{Area} = \frac{\pi}{4} * D^2 \right)$$

where P = Pressure.

D = Diameter of cylinder.

$$\text{FR} = F_p - F_{i4}$$

$$F_{i2} = m2 \times a_{g2}$$

$$F_{i3} = m3 \times a_{g3}$$

$$F_{i4} = m4 \times a_{g4}$$

where FR = Resultant force, Newton.

F_i = Inertial pressure, Newton.

m = Mass in kg.

a_g = Acceleration due to gravity, m/s^2 .

Among them, $m2$, $m3$, and $m4$ are the masses of the crank, connecting rod and slider. a_{g2} , a_{g3} , a_{g4} are acceleration caused by gravity. Further, R is the resultant force of force F_{32} and F_{i2} passing through point B as shown in Fig. 4. The forces calculated for links 2, 3, and 4 as shown in Table 3.

Thus, the load torque for each position is computed as shown in Table 4.

Table 3 Forces calculation

Link	Forces (N)
2	$F_{i2} = 12,777.87$ $F_{32} = 4,650,000$
3	$F_{i3} = 50,132.47$ $F_{i43} = 4,400,000$ $F_{n43} = 1,400,000$ $F_{23} = 46,500,000$
4	$F_{i4} = 4,454,000.9$ $F_p = 10,530$

Table 4 Torque calculation

Crank rotation (θ)	Load torque (K-Nm)
40	167.4
112	9.62
256	9.03
328	167.4
400	167.4
472	9.62
616	9.03
688	167.4

5 Crankshaft Vibration Analysis

The comparison of dynamic crankshaft was carried out, and it is concluded that the location a single-cylinder engine is a model as a simplified slider–crank affiliation which types the groundwork for vibration evaluation. Taking into consideration slider–crank affiliation, all the propagating forces by using the hyperlinks has been probable and quicker or later a load torque performing at crankshaft is calculated. This evaluation was conducted at different levels of crank rotation with an interval of 360° . The projected load torque is validated as shown in Fig. 5.

In the modern research, the crankshaft factors of the engine are selected for evaluation purposes. We can observe that the crankshaft is guilty for altering reciprocating motions of the slider piston into rotary motion of the gearbox. This problem appears a payload from the engine (developed interior cylinders) and a payload from the gearbox (because of the weight of the system). Consequently, crankshaft will carry torsional vibrations. At this, instant torsional vibrations related to crankshaft are noted in component in a piece of writing.

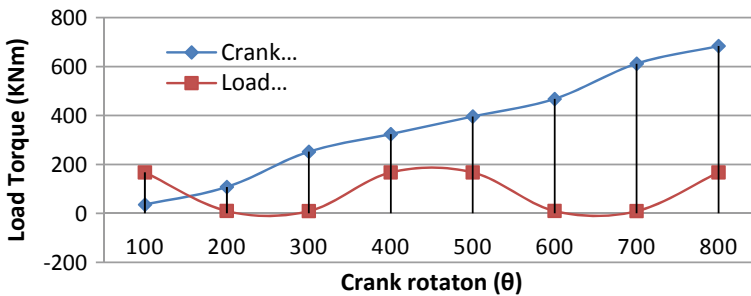


Fig. 5 Load torque versus crank rotation

6 Crankshaft Torsional Vibration

The crankshaft modeled as a single rotor shaft machine for study purposes is shown in Fig. 6. The piston and connecting rod of a crank assembly position changed by way of rotor and equal inertia computed I_0 is 753,798,081.2 kg-mm².

The equation of action for torsional vibrations thinking about a rotor of inertia, i.e., hooked up on the shaft of torsional stiffness k_t , the equation of motion used for torsional vibration of the shaft be able to write as:

$$I_0 \ddot{\theta} + k_t \theta = T(t) = 167.4 \cos \omega t \tag{1}$$

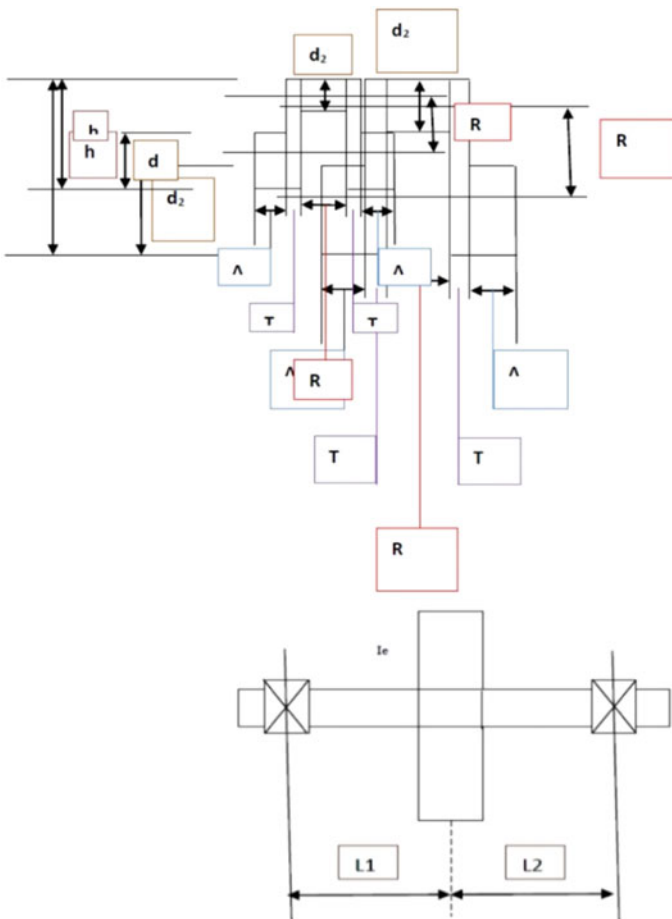


Fig. 6 Crankshaft of single cylinder

$$I_0 \frac{d^2\theta}{dt^2} + k\theta(t) = 167.4 \cos \omega t \quad (2)$$

$$\frac{d^2\theta}{dt^2} + \frac{k_t}{I_0} \theta(t) = \frac{167.4 \cos \omega t}{I_0} \quad (3)$$

$$\left(D^2 + \frac{k_t}{I_0} \right) \theta = \frac{167.4 \cos \omega t}{I_0} \quad (4)$$

$$\left(m^2 + \frac{k_t}{I_0} \right) = 0 \quad (5)$$

$$m = \pm \sqrt{\frac{k_t}{I_0}} \quad (6)$$

but

$$K_t = \frac{\pi}{32} X d^4 X \left(\frac{G}{L_e} \right) \quad (7)$$

$$I_0 \ddot{\theta} + k_t \theta = T(t) = 167.4 \cos \omega t$$

$$k_t = \frac{\pi}{32} \times 50^4 \times \left(\frac{79 \times 10^3}{50} \right)$$

$$k_t = 969,475,857.9$$

$$\frac{k_t}{I_0} = 1.28$$

$$m = \pm 1.28$$

$$\text{C.F.} = A \cos\left(\frac{k_t}{I_0} t\right) + B \sin\left(\frac{k_t}{I_0} t\right) \quad (8)$$

$$\text{C.F.} = A \cos(1.28t) + B \sin(1.28t) \quad (9)$$

$$\text{P.I.} = \frac{1}{D^2 + \frac{k_t}{I_0}} \times \frac{167.4 \cos \omega t}{I_0} \quad (10)$$

Replacing D^2 by $-\omega^2$

$$\text{P.I} = \frac{167.4}{I_0} \times \frac{1}{\left(-\omega^2 + \frac{k_t^2}{I_0}\right)} \cos \omega t$$

$$\text{P.I} = \frac{167.4}{I_0} \cos \omega t \frac{1}{\left(\frac{k_t^2}{I_0} - \omega^2\right)} \quad (11)$$

$$\theta(t) = \text{C.F.} + \text{P.I} \quad (12)$$

$$\theta(t) = A \cos\left(\frac{k_t}{I_0} t\right) + B \sin\left(\frac{k_t}{I_0} t\right) + \text{P.I}$$

$$\theta(t) = A \cos(1.28t) + B \sin(1.28t) + 2.22 \times 10^{-7} \cos(2094.36)t \times \frac{1}{(1.28^2 - 2094.36^2)}$$

$$\theta(t) = A \cos(1.28t) + B \sin(1.28t) - 5.06 \times 10^{-14} \cos(2094.36)t$$

By applying the boundary condition, we get

At $t = 0$, $\theta(t) = 0$

$$\theta(t) = A - 5.06 \times 10^{-14} = 0 \quad (13)$$

$$A = 5.06 \times 10^{-14}$$

At the value $t = 0.03$, then $\theta(t) = 0.628$ rad

$$\theta(t) = A \cos(1.28t) + B \sin(1.28t) - 5.06 \times 10^{-14} \cos(2094.36)t$$

$$0.628 = 5.06 \times 10^{-14} \cos(1.28 \times 0.03) + B \sin(1.28 \times 0.03)$$

$$- 5.06 \times 10^{-14} \cos(2094.36)0.03$$

$$B = 16.35$$

The solution can be written as

$$\theta(t) = 5.06 \times 10^{-14} \cos(1.28t) + 16.35 \sin(1.28t) - 5.06 \times 10^{-14} \cos(2094.36)t$$

The inertia force values are calculated as shown in Table 5.

From Fig. 7, the inertia forces of link 3 and link 4 do not exhibit as much variation as found in link 4 of inertia forces. The version of slider inertia stress may be demonstrated via a cosine that is the same to the version demonstrated through load torque with admire to the rotation of crank.

Figure 8 generates in MATLAB shows an evaluation of the slider-crank mechanism of an engine that helps to find the consequences of the evaluation.

Table 5 Inertia forces values

θ	F_{i2}	F_{i3}	F_{i4}
40	12,777.87	50,132.47	4,454,001
112	12,777.87	36,832.01	308,354.5
256	12,777.87	35,808.9	274,092.9
328	12,777.87	50,132.47	4,454,001
400	12,777.87	50,132.47	4,454,001
472	12,777.87	36,832.01	308,354.5
616	12,777.87	35,808.9	274,092.9
688	12,777.87	50,132.47	4,454,001

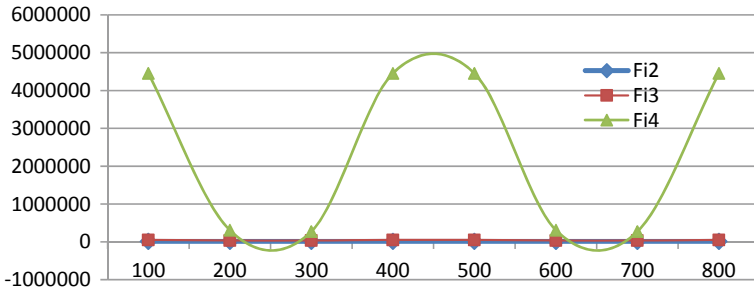


Fig. 7 Load torque and inertia forces

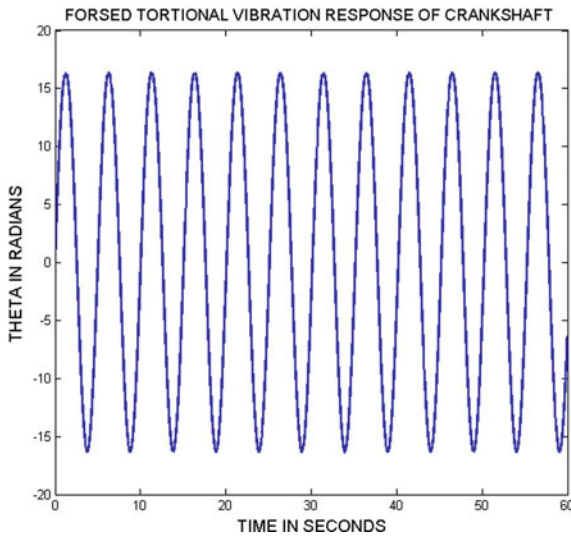


Fig. 8 Forced torsional vibration response of crankshaft

7 Conclusion

Vibrations including bending, torsion, and axial coupling have been observed to affect the crankshaft. Torsional vibration is responsible for crankshaft failure. The engine's inertia and combustion load sources produce bending and torsion loads on the crankshaft. The effect of modal evaluation is very important because it is the resonance frequency, or perhaps the frequency that provides the most vibration results. The present studies have also shown that deformation is usually located on the hyperlink between the bearing housing and the crankshaft pin. This helps predict the chance of interference between the crankshaft and different parts. Through the use of excellent shape maps, the resonant vibration of gadgets can be effectively avoided and the results provide a theoretical basis for the calculation of optimized formats and fatigue life styles. Vital places on the crankshaft structure are all placed on the clean areas due to the fact of high-stress gradient in these places; however, at the end it results in high-stress awareness factor.

References

1. Talikoti B et al (2015) *Int J Eng Res Appl* 5(12, Part-1):26–30
2. Talikoti BS, Kurbet SN, Kuppast VV (2015) A review on vibration analysis of crankshaft of internal combustion engine. *Int Res J Eng Technol (IRJET)* 02(09)
3. Balamurugan CM, Krishnaraj R, Sakthivel M, Kanthavel K, Marudachalam D, Palani MGR (2011) Computer aided modeling and optimization of crankshaft. *Int J Sci Eng Res* 2(8). ISSN 2229-5518
4. Desai HD (2009) Computer aided kinematic and dynamic analysis of a horizontal slider crank mechanism used for single-cylinder four stroke internal combustion engine. In: *Proceedings of the world congress on engineering 2009, vol II, WCE 2009, London, UK, 1–3 July 2009*
5. Brahmabhatt J et al (2014) Design and analysis of crankshaft for single cylinder 4-stroke diesel. *Int J Adv Eng Res Stud (IJETT)* V18(7):309–314
6. Montazersadgh FH, Fatem A (2007) Dynamic load and stress analysis of a crankshaft. SAE technical paper no. 010258. Society of Automotive Engineers
7. Patil AM, Desavale RG (2013) Theoretical and experiment analysis of torsional and bending effect on four cylinders engine crankshaft by using finite element approach. *Int J Eng Res* 2(6):379–385

Comparative Thermodynamic Analysis of Simple Gas Turbine Fueled with Renewable Fuel



Abhinav Anand Sinha, Tushar Choudhary, and Mohd. Zahid Ansari

1 Introduction

In the late 1930s, gas turbines, initially postulated and theoretically studied during the initial decade of the twentieth century, became a reality in engineering. The technology of aircraft gas turbine has evolved steadily and in a continuous manner over the last 50 years [1]. Energy is the main initiator of nearly everything, and it is important for our everyday lives and activities in different industries. Gas turbine (GT) power plants are commonly used for the generation of electricity worldwide, and natural gas is also used in such plants as a frequent fuel [2]. The increase in demand for energy typically contributes to an increase in global environmental issues [3]. Gas turbine (GT) output is affected by the quality of components and the working temperature of the turbine. The overall performance of the gas turbine cycle depends mainly on the compressor's pressure ratio (rp) [4].

Exergy-based optimization is considered one of the best methods for the assessment of the performance of power plant in this respect. The use of energy is very much governed by thermodynamic laws (majorly second law of thermodynamics) [5]. In thermodynamics, efficiency is one of the most commonly used concepts, and it demonstrates how well an energy transfer or method is done. In thermodynamics, efficiency is also one of the most widely misused words and is also a source of confusion [6]. Traditionally, efficiency has been mainly specified based on the first law (i.e., energy). Exergy research has found progressively more widespread acceptance in recent decades as a valuable method in the design, evaluation, optimization, and development of energy systems [7]. While the exergy analysis approach is often seen as a new method for the analysis of energy systems, the basic concepts were implemented as early as the 1940s. An exergy-based performance analysis overcomes the

A. A. Sinha (✉) · T. Choudhary · Mohd. Z. Ansari
Mechanical Engineering Department PDPM IIITDM, Jabalpur, MP 482005, India
e-mail: 20pmeo04@iiitdmj.ac.in

constraint of an energy-based analysis and utilizes second law of thermodynamics [8]. Whenever an irreversible process happens, energy is destroyed [9].

M. Fallahet has addressed simple gas turbine (SGT), steam injection gas turbine (STIG), gas turbine with evaporative inlet air cooler (EVGT), and steam injection gas turbine with evaporative inlet air cooler (ESTIG) in his paper and has done exergetic comparison between four different configurations. The results show that the precedence order for the optimization of system components varies when calculated with ESTIG [10]. In evaluating the efficiency of the Omotosho Phase I Gas Thermal Power Plant, this paper explains the use of exergy analysis and suggests solutions to decrease exergy destruction in power plants. As temperature of ambient rises in the plant and its components, the exergy effectiveness decreases and the efficiency of exergy destruction increases. To solve this problem, the turbine air inlet cooling system is therefore suggested for the plant [11]. Ali Mousafarash and Mohammad Ameri has conducted energy, exergy, and exergo-economic study of various working conditions of gas turbine power plant located near Tehran, the capital city of Iran and concluded that the finest working conditions that can be considered for the power plant are 100 MW load at 40 °C. An increase in temperature of ambient has a negative effect on the cycle's energy efficiency, so in order to counter this aspect this we can use cooling methods at gas turbine air inlet. The effects of pressure ratio (rp), compressor inlet temperature (CIT), and turbine inlet temperature (TIT) on the output parameters of open cycle gas turbines have been studied by Hüseyin Kurt et al. The result showed that a decrement in CIT and an increase in TIT and pressure ratio (rp) values improved the net power output and thermal efficiency. The CIT should be selected as low as possible, and the TIT should be selected as high as possible if it is intended to provide a high net power output and thermal efficiency for the turbine [12]. The cooling process of blade is studied in depth for reheating, as it is considered to be of critical importance for performance optimization [13]. In addition, Tushar Choudhary has worked on novel combination of high-temperature solid oxide fuel cell that is coupled with recuperative gas turbine-based hybrid power plant (SOFC-blade cooled GT). The suggested SOFC-blade cooled gas turbine hybrid has hybrid efficiency of 73.46% [14]. In another paper, author deals with the thermo-economic investigation of the gas turbine cycles with potential application as marine gas turbines. Appropriate objective function in a form of decision variables was considered to carry out the study. Fuel cost and investment cost both were combined and taken as objective function. The total cost flow rate for basic gas turbine (BGT), recuperated gas turbine (RcGT), and intercooled gas turbine (IcGT) has been found to be 0.37646 \$/s, 0.3518 \$/s, and 0.40791 \$/s, respectively [15]. This paper deals with computational fluid dynamics modeling of solid oxide fuel cell (SOFC) which is combined with cogeneration system. Commercial software COMSOL 4.3.1 has been used to carry out the CFD modeling of SOFC using finite volume approach. Performing parametric analysis was used to examine the performance characteristics of an SOFC. It has been witnessed that in terms of power supply and thermo-economics internal reforming is advantageous over the external reforming system [16].

A literature study indicates that all research papers used exergy analysis exploring gas turbine cycle irreversibilities. Many scientists are trying to work with various gas turbine configurations. In most cases, in the GT cycle, natural gas is the primary fuel for combustion. No detailed discussion on different fuels is obtained like Jatropha, Soybean, and coconut husk, and coconut shell. This paper shows the comparative analysis on the performance of gas turbine with different fuels and also shows the exergy analysis of system components with these fuels.

2 System Configuration

In BGT (Fig. 1), at ambient temperatures, fresh air enters into compressor (state 1), where the air is compressed and its pressure and temperature are increased (state 2). This air at high pressure and temperature enter into combustion chamber. Fuel (m_f) is introduced at this pressure and temperature in combustion chamber which increases the temperature of combustible gas (state 3) at constant pressure and then expands in gas turbine.

Conventionally, natural gas is used as combustible fuel in the simple gas turbine cycle. Most of the researchers' works are with natural gas. In this paper, four different fuels are used having calorific values as shown in Fig. 2 [17]. Most of the energy generated in the world is obtained from conventional fuel like oil, coal, and natural gas. Since these sources are limited and will deplete soon [18, 19], biodiesel is a future fuel that can replace the existing diesel made from nonconventional sources such as vegetable oils and animal fats. The use of biodiesel will allow the development of agriculture, economy, and environment.

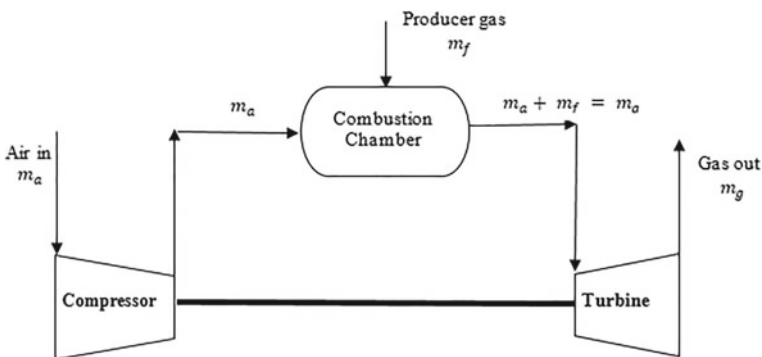


Fig. 1 Basic gas turbine cycle

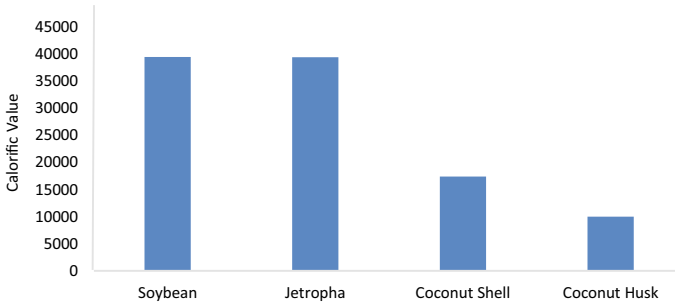


Fig. 2 Calorific value of different fuels

3 Mathematical Model

In the subsection, thermodynamic modeling of different components used in the previous section of the proposed cycles will be evaluated and analyzed as follows. The first and second laws of thermodynamics are taken into consideration over the entire calculation under steady flow assumptions. For the cycle, air is used as the main stream of working fluid and is believed to be the optimal gas for the various states. Compressor, gas turbine, combustion chamber, and recuperator are shown in Figs. 3, 4, 5, and 6, respectively.

The thermodynamic properties of air are taken into consideration and are modeled as follows: Touloukian and Tadash and Sahu [19, 20] discussed this polynomial function for specific heat of air is given as below.

$$C_{pa} = 1.023204 - 1.76021 \times 10^{-4}T + 4.0205 \times 10^{-7}T^2 - 4.87272 \times 10^{-11}T^3 \tag{1}$$

Polynomial equation for the specific heat of combustion gases has been modeled is [19]

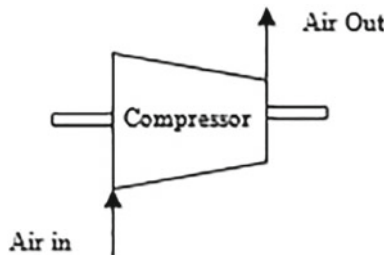


Fig. 3 Compressor

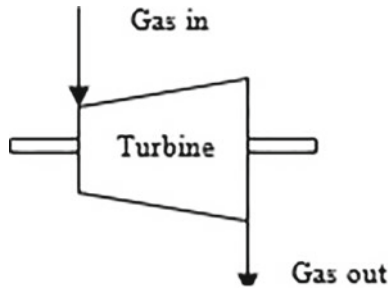


Fig. 4 Gas turbine

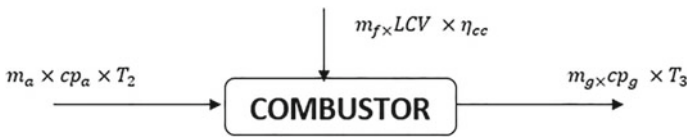


Fig. 5 Combustion chamber

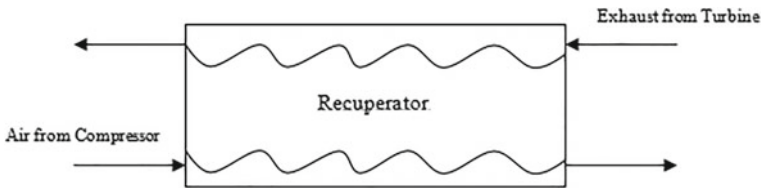


Fig. 6 Recuperator

$$C_{pg} = \left[15.276826 + 0.01005T - 3.19216 \times 10^{-6}T^2 + 3.48619 \times 10^{-10}T^3 + x_0(0.104826 + 5.54150 \times 10^{-5}T - 1.67585 \times 10^{-8}T^2 + 1.18266 \times 10^{-12}T^3) \right] / V \tag{2}$$

Thus, the enthalpy and entropy of the gas and air can be evaluated as follows

$$h = \int_{T_a}^T C_p(T) dT \tag{3}$$

$$\theta = \int_{T_a}^T C_p(T) \frac{dT}{T} \tag{4}$$

$$s = \theta - R \ln \frac{P}{P_{ambient}} \tag{5}$$

First law efficiency: It is defined as the ratio of the output energy to the input energy of a device, which is derived from the first law of thermodynamics, states that energy cannot be created nor be destroyed, it can be converted from one form to another. The first law is only concerned with the quantities of energy and disregards the form in which the energy exists.

$$\eta_I = \frac{W_{\text{net,out}}}{Q_{\text{in}}} \quad (6)$$

Second law efficiency: It is defined as the ratio of the minimum available energy (or exergy) which must be consumed to do a task divided by the actual amount of exergy consumed in performing the same task

$$\eta_{II} = \frac{W_{\text{out}}}{Ex_{\text{in}}} \quad (7)$$

Exergy is defined as the maximum amount of useful work that can be obtained theoretically from a system when it comes in equilibrium with its environment. It is shown by Eq. (8) where h_0 and s_0 are enthalpy and entropy taken at room temperature T_0 and at atmospheric pressure P_0 . In contrast to energy, exergy depends on the state of the system along with the state of the external environment.

$$ex_T = (h - h_0) - T_0(S - S_0) \quad (8)$$

$$dS = dh - vdp \quad (9)$$

$$s - s_0 = C_p \ln \frac{T}{T_0} - R \ln \frac{p}{p_0} \quad (10)$$

By using the mathematical definitions of enthalpy and entropy, Eq. 8 can be expressed as

$$e_x^T = C_p [T - T_0] - T_0 \left[C_p \ln \frac{T}{T_0} - R \ln \frac{P}{P_0} \right] \quad (11)$$

In finding out Gibbs function for fuels, the ratio (\emptyset) of chemical exergy, and “the change in the standard Gibbs function of reaction (kJ/kg) to the change in enthalpy of reaction (kJ/kg).”

$$\text{Total rate of exergy input} = -\Delta G_0 = \emptyset \times mf \times CV \quad (12)$$

Energy balance equations for various parts of gas turbine plant that are discussed in the previous section are as follows:

- Air compressor

Real temperature at the compressor exits:

$$T_e = T_i \left[1 + \frac{1}{\eta_{AC}} \left(r^{\frac{\gamma-1}{\gamma}} - 1 \right) \right] \quad (13)$$

Using SFEE balance equations for the system, the following equation for compressor work is.

$$W_c = m_a C_{pa} (T_e - T_i) \quad (14)$$

The specific exergy destruction in the compressor without bleeding of air for cooling is given by

$$m_a T_0 \left[C_{pa} \times \ln \frac{T_e}{T_i} - R \times \ln \frac{P_e}{P_i} \right] \quad (15)$$

- Combustion chamber

The working fluid of the cycle with the product gaseous fuel is burnt in the combustor,

Energy balance in combustor is given as follows

$$m_f \times LCV \times \eta_{cc} = m_e \times c_{pe} \times T_e - m_i \times c_{pi} \times T_i \quad (16)$$

And exergy loss in combustor is given by relation:

$$T_0 \left\{ \left[m_e C_{pa} \ln \frac{T_e}{T_0} - m_e R_e \ln \frac{P_e}{P_0} \right] - \left[m_i C_{pg} \ln \frac{T_i}{T_0} - m_i R_i \ln \frac{P_i}{P_0} \right] \right\} + T_0 \Delta S_0 \quad (17)$$

- Gas turbine

Actual temperature at the exit of turbine is

$$T_e = T_i \left[1 - \eta_{GT} \left(1 - r^{\frac{1-\gamma}{\gamma}} \right) \right] \quad (18)$$

The specific exergy destruction in the turbine

$$m_g \times T_0 \times \left[C_{pg} \times \ln \frac{T_e}{T_i} - R \ln \frac{P_e}{P_i} \right] \quad (19)$$

4 Results and Discussion

The influence of various operating parameters has been taken for operating conditions which are provided in Table 1. Figure 7 shows the comparison of fuel-wise mass flow rate for BGT and RGT cycles. It is clear from the results that less amount of mass flow rate of fuel is required as increases the pressure ratio (rp) of system. In Fig. 7, large amount of coconut husk is required to produce 80 kJ/kg as compared to other soybean, jatropha, and coconut shell. Soybean shows the same trend as jatropha, or it is clear from Fig. 7 which is soybean and jatropha overlaps each other. But either of these fuels show that initially that is at lower pressure ratio (rp) large amount of mass flow rate is required and it will reduce as increases the pressure ratio (rp). Network of the system initially increases but after attaining some peak it will reduce rapidly.

Table 1 Operating parameters

Cp for air (kJ/kg K)	1.005
Isentropic efficiency of compressor (%)	88
Air inlet temperature in compressor (K)	293
Pressure ratio (rp)	10
Turbine inlet temperature (TIT) (°C)	900
Isentropic efficiency of turbine (%)	90
Efficiency of combustion chamber (%)	98
Calorific value (kJ/kg)	Soybean—39,480 Jatropha—39,455 Coconut Shell—17,400 Coconut Husk—10,010

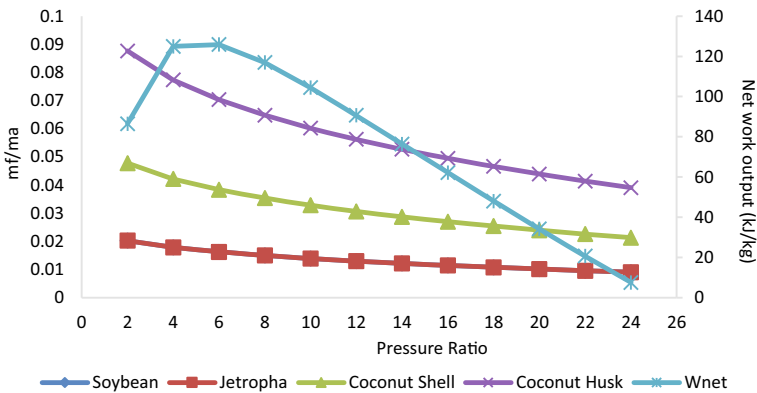


Fig. 7 Ratio of mass flow rate and network versus pressure ratio (rp)

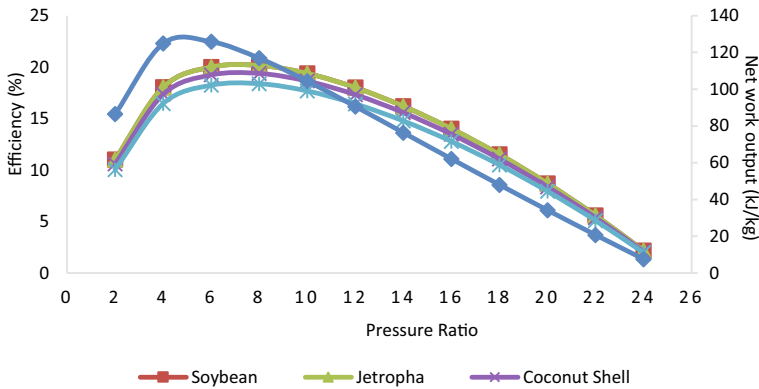


Fig. 8 Efficiency and network versus pressure ratio (rp)

This is just because of the exergy loss in the compressor increases. For producing 104.45 kJ/kg network, mass flow rate of fuel per kg of air required is 0.0139 kg/s for soybean and jatropha, 0.0328 kg/s for coconut shell, and 0.0602 kg/s for coconut husk.

Figure 8 shows the first law efficiency of system with different fuels. All four fuels show approximately same efficiency trend with pressure ratio (rp). Initially, it increases at lower pressure ratio (rp) and then decreases at higher pressure ratio (rp). Efficiency of soybean and jatropha overlaps each other and shows approximately the same values. This happens just because of its calorific value. Calorific value of soybean and jatropha is 39480 kJ/kg and 39,455 kJ/kg, respectively. Due to nearly the same calorific value, they have the same heating value. Therefore, the efficiency of system is same for both the fuels. Coconut husk has the lowest calorific value and therefore has lower heating value. From Figs. 7 and 8, it clearly shows that lower the mass flow rate higher the efficiency of the system. It means small amount of mass flow rate of fuel per kg of air is required to produce more amount of network at corresponding pressure ratio (rp).

Figure 9 shows that exergy destruction within the system components with different fuels. Combustion chamber has the largest exergy destruction as compared to other components. Turbine has the lowest exergy loss within the system. Considering four different fuels for comparing the exergy destruction of system components and with soybean and jatropha, compressor shows the same value of exergy destruction. The lowest exergy destruction in compressor is observed with the coconut husk and second lowest with coconut shells. Same as for turbine and combustion chamber is observed. In gas turbine system, the largest exergy loss is observed with soybean and then jatropha and then with coconut shell and the lowest with coconut husk.

First law efficiency gives the quantitatively approach to analyze the system but exergy efficiency provides a way to get the system performance qualitatively. Exergy efficiency is given an actual picture of system performance. Figure 10 shows that the thermal efficiency of the system with soybean and Jatropha is maximum and

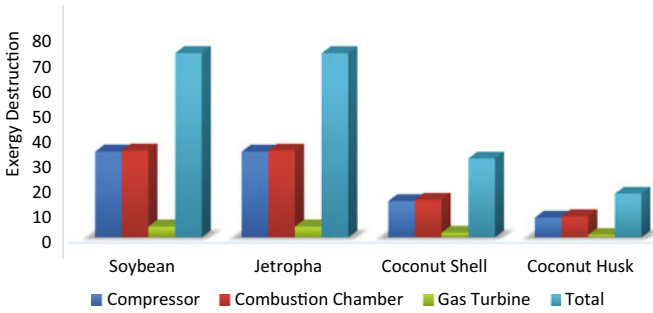


Fig. 9 Exergy destruction in system components

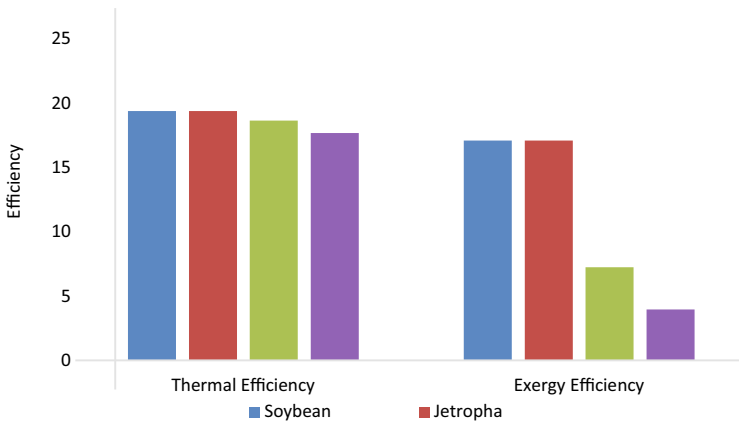


Fig. 10 Thermal and exergy efficiencies of the system with different fuels

decreases in order to coconut shell and coconut husk. While when considering the exergetic efficiency of the gas turbine cycle, the lowest exergy efficiency is observed with coconut husk and maximum with soybean and Jatropha. It means more energy is available for converting work into useful work with soybean and Jatropha as compared to coconut shell and coconut husk.

Figure 11 shows that the destruction of exergy within the system components with different types of fuels. Chamber of combustion has more exergy destruction as compared to other parts. Turbine has the lowest exergy loss within the system. Considering four different types of fuels for comparing the exergy destruction of system components, it was found that the compressor shows the same value of exergy destruction with Soybean and Jatropha. The lowest exergy destruction in compressor is observed with the coconut husk and second lowest with coconut shells. Same as for a turbine and combustion chamber is observed. In the gas turbine system, the largest exergy loss is observed in case of soybean and after that in case of Jatropha and then with coconut shell and at last lowest in case of coconut husk.

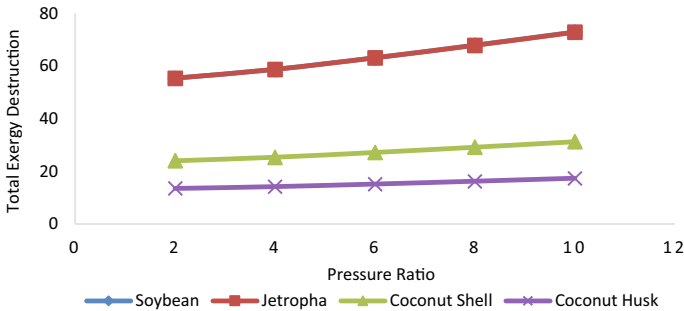


Fig. 11 Total exergy destruction in system with different fuels

5 Conclusions

In this paper, a thermodynamic model has been developed with the help of first and second laws of thermodynamics for each components of gas turbine cycle. Following conclusions are made from this study and are detailed below:

Lesser mass flow rate of fuel per kg of air is required as increases the pressure ratio (rp) of system. Soybean shows the same trend as jatropa, or it is clear from Fig. 8 is soybean and jatropa overlap each other. But either of these fuels show that initially that is at lower pressure ratio (rp), large amount of mass flow rate is required and it will reduce as increases the pressure ratio (rp).

Efficiency of soybean and jatropa overlaps each other and shows approximately the same values. This happens just because of its calorific value. Calorific value of soybean and jatropa is 39480 kJ/kg and 39,455 kJ/kg, respectively.

Combustion chamber has the largest exergy destruction as compared to other components.

References

1. Gupta AK (1997) Gas turbine combustion: prospects and challenges. *Energy Convers Manage* 38(10–13):1311–1318
2. Ahmadi P, Dincer I et al (2011) Thermodynamic and exergoenvironmental analyses, and multi-objective optimization of a gas turbine power plant. *Appl Therm Eng* 31:2529–2540
3. sahu M et al (2016) Thermoeconomic investigation of different gas turbine cycle configuration for marine application. SAE technical paper 2016-01-2228. <https://doi.org/10.4271/2016-01-2228>
4. Rahman MM et al (2011) Thermodynamic performance analysis of gas-turbine power-plant. *Int J Phys Sci* 6(14):3539–3550
5. Dincer I, Rosen MA (2007) *Exergy: energy, environment and sustainable development*. Elsevier
6. Kanoglu M et al (2007) Understanding energy and exergy efficiencies for improved energy management in power plants. *Energy Policy* 35:3967–3978
7. Ebadi MJ, Gorji-Bandpy M (2005) Exergetic analysis of gas turbine plants. *Int J Exergy* 2(1):31–39

8. Ofudu JC, AbamD SP (2002) Energy analysis of Afam thermal power plant. *NSE Tech Trans* 37(3)
9. Dincer I, Cengel YA (2001) Energy, entropy and exergy concepts and their roles in thermal engineering. *Entropy* 3:116–149
10. Fallah M et al (2017) Comparison of different gas turbine cycles and advanced exergy analysis of the most effective. *Energy* 116:701–715
11. Okechukwu EH, Imuentinyan OA (2013) Exergy analysis of Omotosho phase 1 gas thermal power plant. *Int J Energy Power Eng* 2(5):197–203
12. Kurt H et al (2009) Performance analysis of open cycle gas turbines. *Int J Energy Res* 33:285–294
13. Facchini B et al (2000) Exergy analysis of combined cycles using latest generation gas turbines. *J Eng Gas Turbines Power* 122(2):233–238
14. Coudhary T (2017) Thermodynamic assessment of advanced SOFC-blade cooled gas turbine hybrid cycle. *Int J Hydrogen Energy* 42(15):10248–10263
15. Sahu M, Choudhary T, Sanjay Y (2016) Thermo-economic investigation of different gas turbine cycle configurations for marine application. SAE technical paper 2016-01-2228
16. Choudhary T, Kumar Sahu M (2017) CFD modeling of SOFC cogeneration system for building application. *Energy Procedia* 109:361–368
17. Oliveira LE, Da Silva MLCP (2013) Comparative study of calorific value of rapeseed, soybean, jatropha curcas and crambe biodiesel. In: International conference on renewable energies and power quality. ISSN 2172-038 X, No.11, March 2013
18. Anawar F et al (2010) Okra seed oil for biodiesel production. *Appl Energy* 87:779–785
19. Demirbas A (2005) Biodiesel production from vegetable oil via catalytic and noncatalytic supercritical methanol transesterification methods. *Program Energy Combust* 31:466–487
20. Touloukian YS, Makita T (1970) Thermo-physical properties of matter. The TPRC data series. Vol-6 IFI/PLENUNM: New York, Washington

Solar Thermal Receivers—A Review



Manish Saini, Abhishek Sharma, Varun Pratap Singh, Gaurav Dwivedi,
and Siddharth Jain

1 Introduction

The energy requirements of today's world are fulfilled by the combustion of fossil fuels, which is not only limited and emits hazardous waste and environmental pollution. It is polluting the environment and causing climate change. To combat this, scientists are trying to phase out all fossil fuels in favour of natural resources such as light, water, and other non-traditional alternative sources. Such non-traditional renewable technologies have the opportunities to resolve energy crises. Renewable energy sources like biofuels [1–9], wind energy [10], and solar energy accounts for a sizable portion of non-traditional energy sources [11].

The tradition of regular use of solar power dates back to 1455 BC, but the comprehensive operation of this form of energy has yet to be achieved. The energy absorbed from the earth by the sun in a single hour is larger than the amount of energy consumed in a year. After passing through a series of atmospheric layers, solar radiation that strikes the Earth's surface reaches it either directly or indirectly. Solar energy's primary issue is its unusual nature, as well as the question of how to collect and store it. Even in small parts of the world, this tradition of using solar energy in everyday life experiences has not been possible old time. In an hour, the amount of energy absorbed by the earth's surface exceeds the amount spent in a year.

Solar radiation enters the Earth's surface direct or indirect, passing through a series of layers of the atmosphere. Solar energy's main challenge is the unpredictability of its supply, as well as its capture and storage. It also disseminates solar energy in small regions around the world [12].

M. Saini · A. Sharma · V. P. Singh
Solar Energy Centre, Department of Mechanical Engineering, College of Engineering Roorkee,
Roorkee, India

G. Dwivedi (✉) · S. Jain
Energy Centre, MANIT, Bhopal, India

Solar energy is used to switch to renewables in a variety of industries, including power generation, heating, agriculture, and industrial processes such as disinfection, refining, pasteurization, drying, cooling, and climate control, as well as distillation.

2 Solar Receivers

Solar power receivers are a specific type of heating systems that convert solar radiation into the heat capacity of the transport media. The major part of a solar-based system is a solar receiver, which collects solar energy, transforms it to the desired location, and transports that heat to a fluid passing through the collector (usually air, liquid, or oil). The solar energy received is transferred directly from fluid flowing to the warm water or air ventilating facilities, or to a heat storage reservoir, from which it could be obtained for use at nighttime and/or during overcast weather [13].

3 Receivers' Classification

3.1 Stationary Receivers

Solar energy receivers are essentially differentiated by their movement and stagnant nature, the axis of tracking, and the working temperature. In this study, researchers evaluate the solar receivers on stationary and working temperature bases. Those receivers remain fixed in place and, therefore, do not move with the sun. This classification includes three types of receivers:

1. Flat-plate receivers (FPR).
2. Static compound parabolic receivers (SCPR).
3. Evacuated tube receivers (ETR) (Table 1).

3.1.1 Flat-Plate Receivers (FPR)

Figure 1 depicts the basic flat-plate solar receiver. As sunlight strikes a blackened coated absorber surface with a high absorption coefficient via a transparent cover, a significant part of the energy is captured by the surface and transported to the transport medium throughout the fluid channels, where it is taken away for conservation or even use. FPRs have the benefits of being cheap to produce, collecting simultaneously beam and diffuse radiation, and being firmly fixed in place, requiring no sun monitoring.

The following are the primary parts of an FPR as shown in Fig. 2:

Upper Surface (Cover): Glass or other radiation-transmitting materials (one or more sheets).

Table 1 Solar energy receivers [14]

Movement	Receivers type	Receivers type	Concentration ratio (CR)	Temperature range (°C)
Stationary	Flat-plate receivers (FPR)	Flat	1.0	30–80
	Evacuated tube receivers (ETR)	Flat	1.0	50–200
	Static compound parabolic receivers (SCPR)	Tubular, Line focus	1.0–5.0	60–240
Single-axis tracking	Compound parabolic receivers (CPR)	Tubular, Line focus	5.0–15.0	60–300
	Linear Fresnel reflector (LFR)	Tubular, Line focus	10.0–40.0	60–250
	Cylindrical trough receivers (CTR)	Tubular, Line focus	15.0–50.0	60–300
	Parabolic trough receivers (PTR)	Tubular, Line focus	10.0–85.0	60–400
Two-axis tracking	Parabolic dish reflector (pdr)	Point focus	600.0–2000.0	100–1500
	Heliostat field receivers (hfr)	Point focus	300.0–1500.0	150–2000

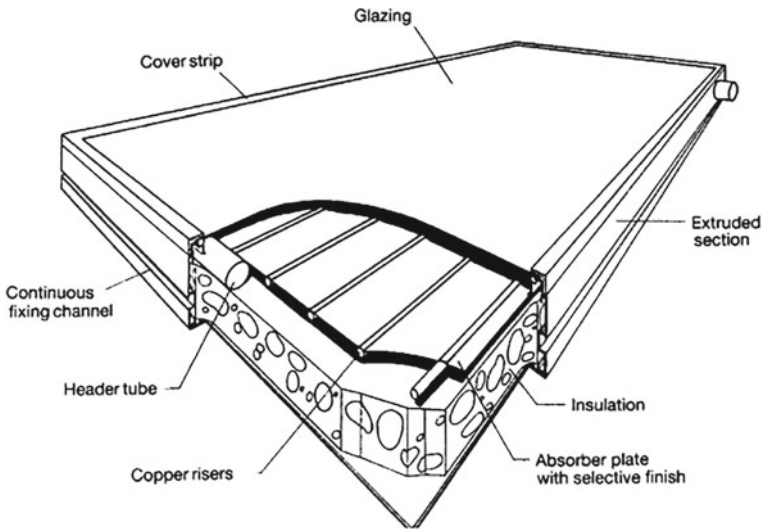
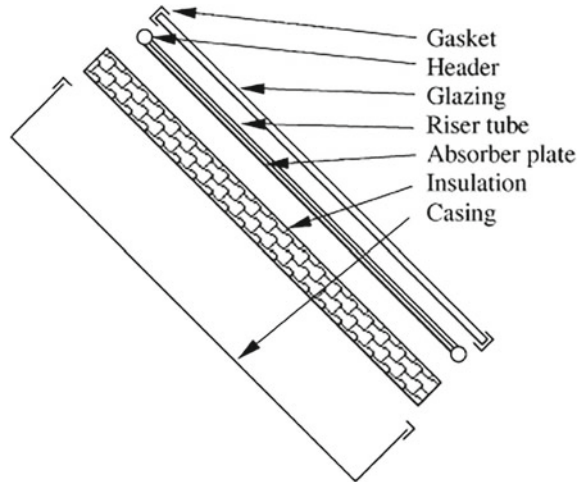


Fig. 1 Schematic view of a flat-plate receiver [15]

Fig. 2 Section view of an FPR with major components [15]



Fluid tunnels for heat dissipation: Heat transfer fluid is carried or directed from the source to the drain via tubing, fins, or channels.

Absorber surface: Absorber surface is a type of surface that is used to absorb water. Coils, fins, or channels are connected to flat, corrugated, or grooved surfaces.

The encoded fixing shown in Fig. 2 is a common attaching technique. A high-absorber and low-emittance coating is commonly applied to the plate.

Pipe Channels: To provide passage for working fluid.

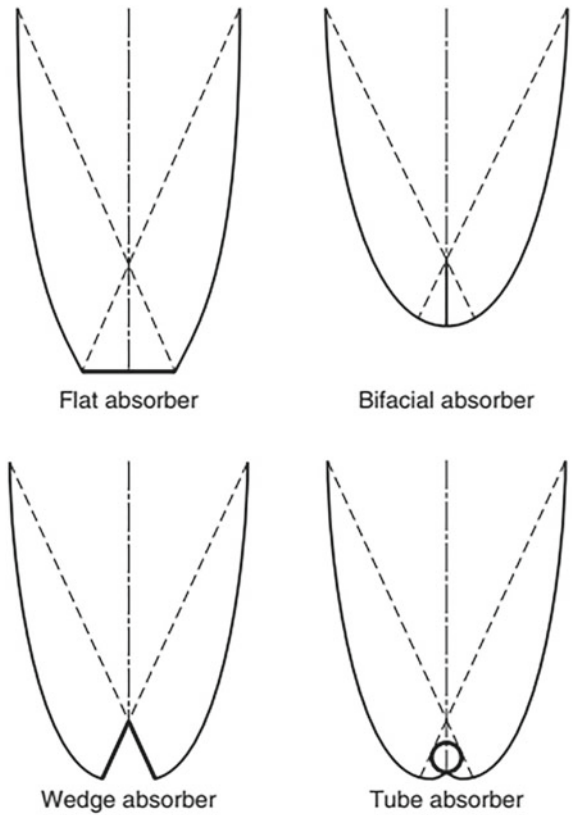
Insulation: To reduce the thermal loss from the bottom and sides of the receivers.

Container: The enclosure covers and defends the foregoing elements from dirt, humidity, and other foreign matter.

3.1.2 Static Compound Parabolic Receivers (SCPR)

Static compound parabolic receivers (SCPRs) are receivers that do not require imaging. These also can reflect all incident radiation to the absorber in certain limits. Winston emphasized their possibilities as solar energy receivers. Using a trough with two parts of a paraboloid approaching each other, shown in Fig. 3 [16], reduces the need to move the concentrator to accept changing solar orientation. Compound parabolic receivers are capable of accepting incident radiation from a broad range of angles. The radiation approaching the aperture inside the receiver acceptance angle makes its way to the absorber tube at the base of the receiver due to various internal reflections [17]. The absorber can be configured in several ways. It can be a linear, cylindrical, rectangular, bifacial, wedge, or flattened. There are two main types of CPR receivers: symmetric and asymmetric.

Fig. 3 Different types of CPR available



3.1.3 Evacuated Tube Receivers (ETR)

General flat-plate receivers (FPR) were originally designed to be used in bright days and in hot climates. When weather conditions are unfavourable, such as colder, cloudy, rainy, and windy days, their advantages are reduced significantly. Also, weathering factors such as precipitation and humidity cause serious materials to deteriorate prematurely, resulting in decreased quality and efficiency and also become the cause of system failure [15].

Solar receivers (pipes) with evacuated heat piping function differently than most other receivers available on the marketplace. As seen in Fig. 4, such solar receivers consist of a heat pipe in a vacuum-sealed container. As shown in Fig. 5, several tubing is linked to the same section in the setup.

The conjunction of a particular surface, as well as an efficient convection silencer in evacuated tube receivers, has demonstrated significant performance at the high-temperature range. The receivers can run at higher temperatures compared to FPRs because the vacuum boundary decreases losses due to convection and conduction heat transfer. These accumulate both beam and diffuse radiation, similar FPRs, as

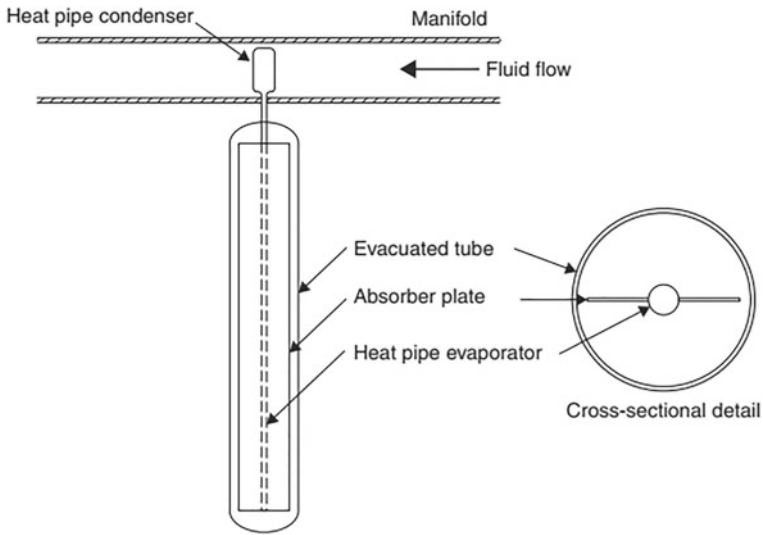


Fig. 4 Schematic diagram of an evacuated tube receiver

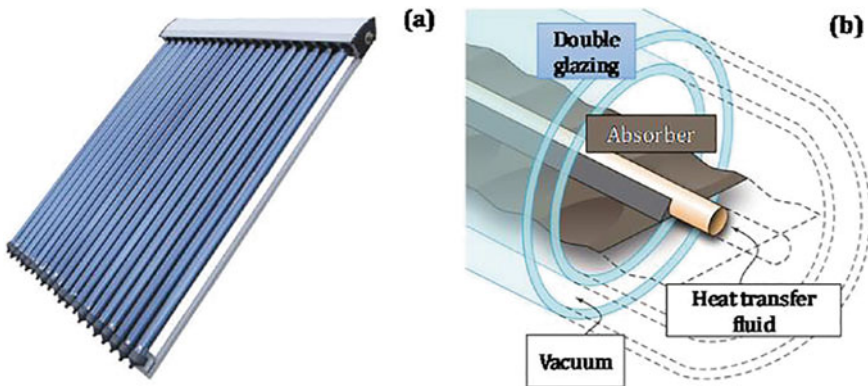


Fig. 5 a Evacuated tube collectors; b representation of a concentric tube [18]

they are more efficient at a low incident angle. This makes ETRs a productivity edge over FPRs over the course of a day.

3.2 Sun-Tracking Concentrating Receivers

The temperature of the energy distribution system can be raised by reducing the area where heat is lost. If a significant amount of solar energy is focussed on a limited

collection area, temperatures far exceeding the achievable by FPRs can be attained. This is accomplished by placing an optical device between both the radiation source and also the energy-absorbing face. Concentrating receivers have a few benefits over traditional flat-plate receivers [19].

For concentrating receivers, a variety of concepts were already proposed. Concentrators may be reflectors or refractors, cylindrical or parabolic, continual or partitioned, and rectangular or curvatures. Convex, smooth, curved, or contoured receivers may be shielded with glass or left exposed. Concentration ratios, or the proportion of aperture to absorption zones, may range from marginally above unity to levels on the scale of 10,000. Higher ratios result in higher temperatures where the energy can be supplied, but this also means that these receivers need more accuracy in optical quality and optical system orientation [15].

Solar energy is optically focussed in focussing receivers before being converted to heat. Solar radiation may be reflected or refracted using mirrors or lenses to achieve concentration. The energy density in the receiving target is increased as the reflected or refracted sunlight is concentrated in a focal zone. Based on whether the picture of the sun is aimed at the receiver, concentrating receivers can be categorized as non-imaging or imaging receiver [20].

The CPR is a receiver that belongs to the very first category, while all other concentrators are imaging receiver.

1. The Parabolic Trough Concentrator (PTC).
2. The Linear Fresnel Reflector (LFR).
3. Parabolic Dish Reflector (PDR).
4. Heliostat Field Receiver (HFR).
5. Fixed Focus Elliptical Scheffler Reflector.
6. The Solar Tower.

3.2.1 The Parabolic Trough Solar Concentrator

Scholars constructed several parabolic troughs concentrators and used tracking mechanisms to monitor the sun. The sun monitor layer (or reflective surface) is used to direct the solar radiation to the central-focus point of the reflector. Scholars used glass, copper, or aluminium solar concentrator trough's focal point to absorb the reflecting solar radiation. The working fluid, primarily water, consumes the latent and sensible heat radiation which allows the fluid to flow through the system [13]. A high-performance solar receiver is needed to deliver high temperatures in high efficiency and maximum reliability. With parabolic through receivers (PTRs), systems with light support frame and moderate technology for process heat operations up to 400 °C could be achieved. PTRs can efficiently generate heat at temperatures ranging from 50 to 400 °C. Sheets of reflective material are bent into a parabolic shape to create PTRs. Along the focal axis of the receiver, a metallic black tube is mounted, which is covered with a glass tube to minimize heat losses Fig. 6.

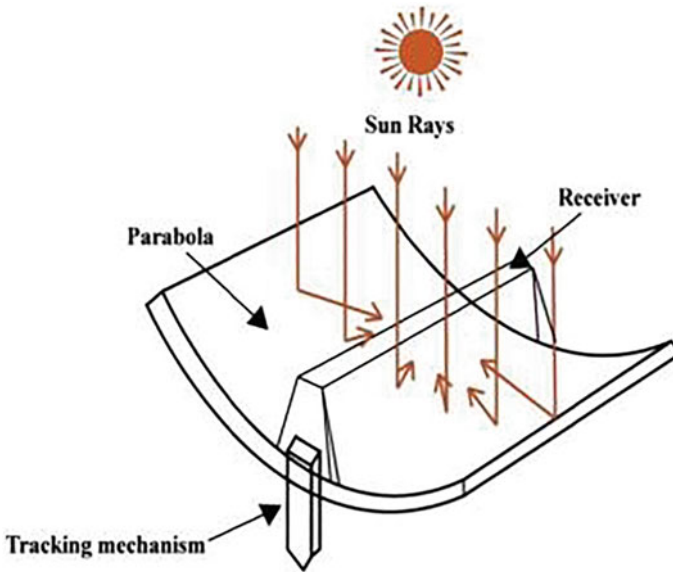


Fig. 6 Parabolic trough concentrator [21]

3.2.2 Fresnel Lens Solar Concentrator

The Fresnel lens receiver (FLR) can be seen in Fig. 8, and the linear Fresnel reflector (LFR) can be seen. The first is made out of plastic and moulded in the manner shown to concentrate suns radiation onto a point receiver, while the latter relies on arrays of linear mirror stripes to reflect sunlight over to a linear receiver. The LFR receiver looks like a broken-up parabolic dish reflector (see Fig. 3); however, unlike parabolic troughs, the individual stripes do not have to be parabolic. The stripes can also be installed on a flat piece of ground (field) to focus light on a linear stationary receiver on a tower (Fig. 7).

Fresnel lens quality characteristics such as limited length, lightweight, mass manufacturing, and cheap cost have made this profitable in the energy department [22]. The Polymethyl methacrylate (PMMA) components (a Fresnel lens modification discovered by some experts in 1928) can construct Fresnel lenses (discovered by Augustine Jean Fresnel) because of their exceptional sunlight resistance and transmissivity [23, 24]. A lens of a Fresnel concentrator comprises a flat optical segment in which it removes heavy materials as its surface comprises many concentric grooves. Because each groove is calculated by a smooth surface that reflects at the position of the regular lens due to curvature, prisms are formed [25].

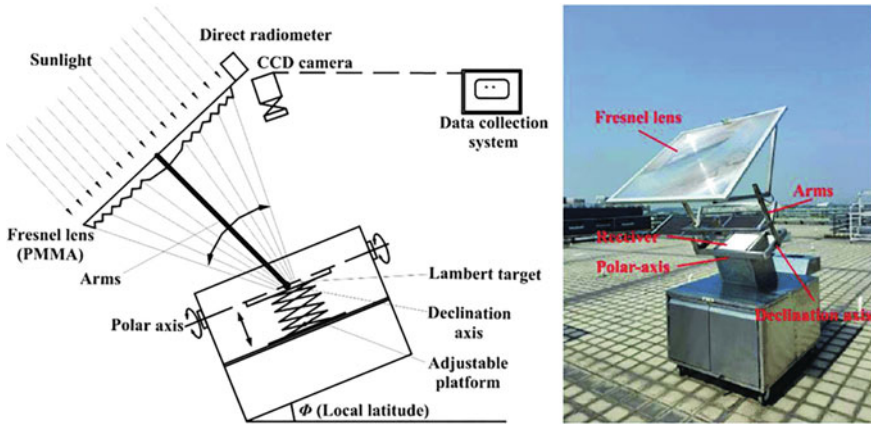


Fig. 7 Experimental setup of Fresnel lens solar concentrator [26]

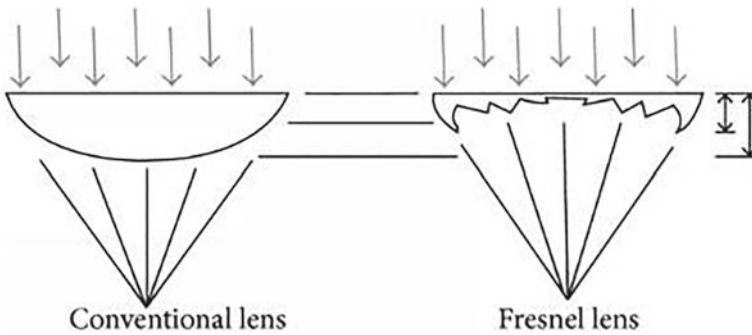


Fig. 8 Fresnel lens and normal lens [20]

3.2.3 The Solar Tower System

A large number of dual-axis tracking mirrors are mounted over a tower of solar thermal turbine power plants. These strongly angled mirrors are sometimes called heliostats; the optimal location for each of these is determined by a computer, and a motor drives them towards the sun. To guarantee the sunlight is much centred on the top of the tower, the device needs to be accurate. The absorber is situated there, and it heats this to temperatures of 1000 °C or higher. Heated air or molten salt then carries the heat energy from the absorber to a gas turbine or steam generator creates super-heated water vapour which operates a turbine and electrical generator [27]. A large number of dual-axis tracking mirrors are mounted over a tower in solar thermal power plants. Often called heliostats are those strongly angled mirrors. A machine determines the optimal location for both of these and drives them towards the sun

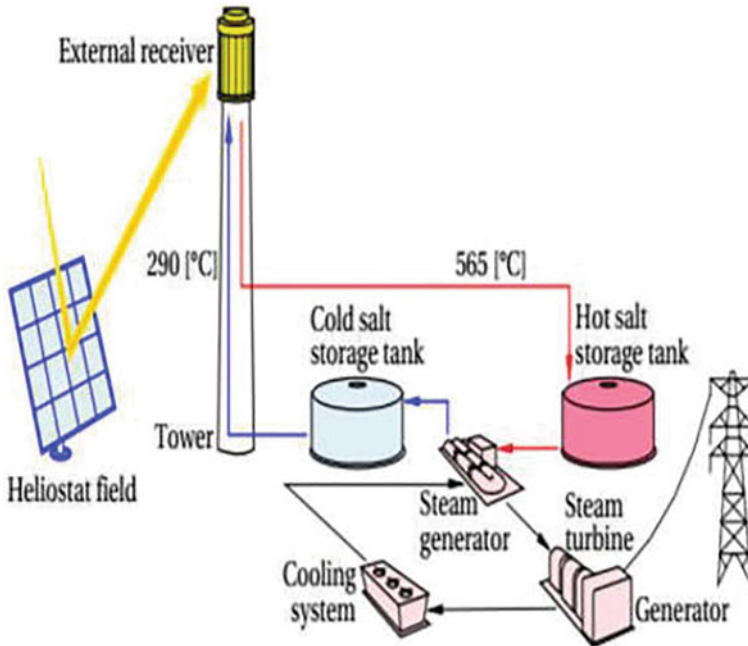


Fig. 9 Solar tower power plant [29]

with a motor drive. To guarantee the sunlight is very centred on the top of the tower, the device needs to be accurate [28] (Fig. 9).

Most of the old towers were using steam as a heat transfer agent but owing to their improved heat transfer and energy conservation capacities, newer buildings use molten salts [30]. Transferring the heat to water transforms into steam. The steam is then transferred to a traditional turbine for the generation of electric energy [31].

3.2.4 Parabolic Dish Based Solar System

A parabolic dish reflector (PDR), as can be seen in Fig. 10, is a central-focus receiver that follows the sun in 2 axes, focussing the sun's radiation onto a receiver only at the dish's point of focus. To reflect the beam into another thermal receiver, the dish system must completely follow the sun. The receiver absorbed solar radiation and converts it into thermal energy in a fluid flowing. The thermal energy can also be converted into electrical energy using a direct-coupled engine power generator or transferred to a centralized power conversion system via pipelines. Temperatures of over 1500 °C can be achieved using parabolic dish arrays. Parabolic dishes are also referred to as distributed receiver systems since these receivers remain distributed across a receiver field, similar to parabolic troughs.

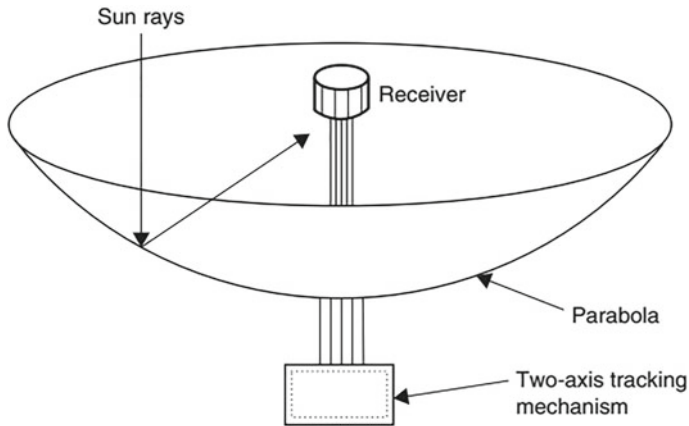


Fig. 10 Schematic diagram of parabolic dish collector

Application in Cooking

In the 1950s, Ghai developed a solar parabolic dish cooker (PDSC) at the National Physical Laboratory located in New Delhi, India [32]. Since then, many researchers have proposed and analyzed various shapes and designs for concentrating solar cookers [33, 34]. A parabolic dish solar cooker consists typically of a parabolic platter-fashioned solar concentrator fitted on a suitable structural base. The cooking vessel is directly placed on a solar cooker and tracked in conjunction with the parabolic platter (Fig. 11).

3.2.5 Fixed Focus Elliptical Scheffler Reflector

A paraboloid reflector dish/mirror is a reflecting plate that is used to collect or focussing on energy such as solar radiation. It takes the shape of a circular paraboloid, a surface formed by a parabola rotating around its axis. The arriving plane light wave moves along the axis, and the parabolic reflector transforms this into a spherical wave which converges itself on focus. Parabolic reflectors gather energy from a remote point and concentrate it into a specific point of focus, eliminating the chromatic aberrations seen in more basic nearly spherical reflectors [36]. Because the reflection laws are reversible, parabolic reflectors can also be used in a parallel light ray to project the light of a source at its focus outward, as seen in car lights and searchlights.

The reflector Scheffler is titled after Wolfgang Scheffler, the developer of the device. As seen in Fig. 12, it is a main concentrating reflector that monitors the sun's motion and focuses the light on a fixed point. Because the focus would move as the dish rotates if the utilized reflector was a rigid paraboloid, the reflector is made more flexible and twists as the platter rotates [37]. The reflector will always be perfectly paraboloid. The light concentrated by the reflector heats a huge vessel that can be

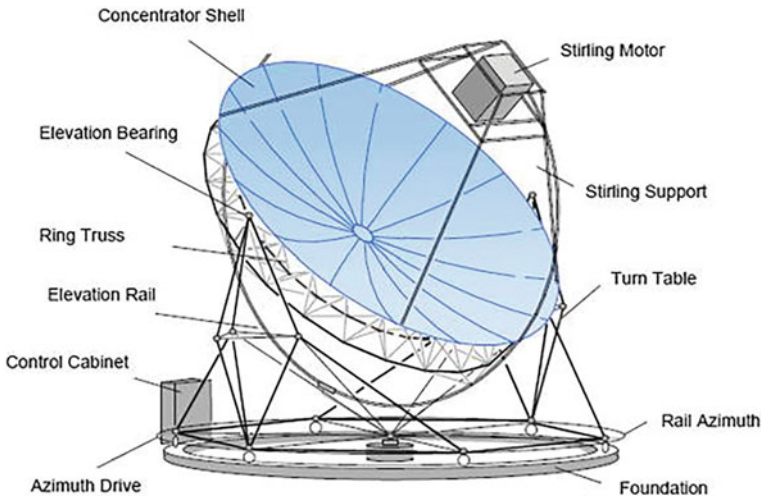


Fig. 11 Layout of a EURODISH parabolic trough system “EURODISH” TM is a Stirling solar dish system with a 10kWe capacity [35]

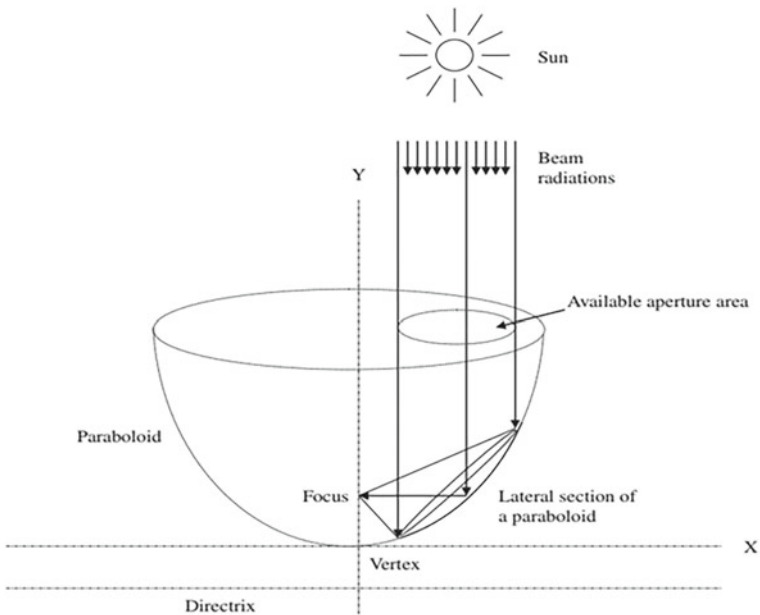


Fig. 12 Scheffler reflector section in a paraboloid shape [36]

applied for heating systems, steam generation, preparing food, including making pieces of bread, and among other things. The Scheffler reflector can be used to heat water in the home [38]. Via the use of sub-uniform solar radiation dispersed on the heated cylindrical absorber surface, Scheffler reflectors can provide efficient water heating. This has a wide spectrum of uses, including solar cooking (in which the sun is concentrated on the cooking vessel), textiles, pharmaceuticals, and so on [39].

4 Conclusion

- This paper discusses a few of the most popular kinds of solar receivers. Flat plate, compound parabolic, evacuated pipe, parabolic trough, Fresnel glass, parabolic dish, solar tower, Scheffler reflector, and parabolic mirrors field collectors are among the different types of collectors mentioned.
- The temperature of the energy delivery system can be raised by reducing the area where heat is lost. If a significant amount of solar energy is focussed on a restricted collection area, temperatures far exceeding the achievable by FPRs can be attained.
- In a concentrator receiver, the working fluid can reach higher temperatures than in an FPR with the same solar energy-collecting surface. As a result, greater thermodynamic performance can be enhanced.
- It is possible to obtain a thermal match between temperature level and tasks using a concentrator receiver. It may be necessary to operate thermionic, thermodynamic, or other high-temperature devices.
- Solar energy receivers can be used for a wide range of systems, can provide substantial economic and environmental advantages, and can be used wherever possible, as the potential applications areas outlined in this paper.
- Reflecting panels use fewer materials and have a simpler structure than FPRs. As a result, the price per unit area of the solar-collecting surfaces for a focussing receiver is lower than for an FPR.
- When compared to FPRs, concentrator systems receive little or no diffuse solar radiation, based on the concentration ratio.

References

1. Behura AK, Padhy A, Vishal B, Verma P, Dwivedi G (2020) Fabrication of parabolic trough hybrid solar PV-T collector using a-Si thin film solar cells in Indian perspective. *Mater Today Proc.* <https://doi.org/10.1016/j.matpr.2020.05.652>
2. Singh AK, Dwivedi G, Srivastava BK, Tiwari BK, Kumar P, Yadav RK, Singh M, Shukla AK, Nandan G (2021) Study of analytical observations on energy matrix for solar stills. *Mater Today: Proc.* <https://doi.org/10.1016/j.matpr.2021.02.109>

3. Mishra S, Dwivedi G, Upadhyay S, Chauhan A (2021) Modelling of standalone solar photovoltaic based electric bike charging. *Mater Today: Proc.* <https://doi.org/10.1016/j.matpr.2021.02.738>
4. Verma S, Dwivedi G, Verma P (2021) Life cycle assessment of electric vehicles in comparison to combustion engine vehicles: a review. *Mater Today: Proc.* <https://doi.org/10.1016/j.matpr.2021.01.666>
5. Verma S, Mohapatra S, Chowdhury S, Dwivedi G (2020) Cooling techniques of the PV module: a review. *Mater Today Proc.* <https://doi.org/10.1016/j.matpr.2020.07.130>
6. Behura AK, Padhy A, Vishal B, Verma P, Dwivedi G (2021) Fabrication of parabolic trough hybrid solar PV-T collector using a-Si thin film solar cells in Indian perspective. *Mater Today Proc.* <https://www.sciencedirect.com/science/article/pii/S2214785320342632>
7. Kumara R, Nandan G, Dwivedi G, Shukla AK, Shrivastava R (2020) Modeling of triangular perforated twisted tape with V-Cuts in double pipe heat exchanger. *Mater Today Proc.* <https://doi.org/10.1016/j.matpr.2020.09.038>
8. Behura AK, Kumar A, Todkari VC, Dwivedi G, Gupta HK (2021) Analysis of thermal efficiency of solar flat plate collector using twisted tape. In: *Advances in air conditioning and refrigeration*, pp 89–97. *Lecture Notes in Mechanical Engineering.* https://link.springer.com/chapter/https://doi.org/10.1007/978-981-15-6360-7_9
9. Suresh AK, Khurana S, Nandan G, Dwivedi G, Kumar S (2018) Role on nanofluids in cooling solar photovoltaic cell to enhance overall efficiency. *Mater Today: Proc* 5(9):20614–20620
10. Approach R et al (1978) Mankind's future source
11. Regin AF, Solanki SC, Saini JS (2008) Heat transfer characteristics of thermal energy storage system using PCM capsules: a review. *Renew Sustain Energy Rev* 12(9):2438–2458. <https://doi.org/10.1016/j.rser.2007.06.009>
12. "Solar Energy Solar PV (for electricity) and Thermal (for hot water) Systems."
13. P. Gorantla, B. Janarthanan, and J. Chandrasekaran, "Solar Concentrators – A Review," pp. 19187–19197, 2016. <https://doi.org/10.15680/IJIRSET.2016.0511088>.
14. Kalogirou SA (2014) *Solar energy engineering processes and systems*, 2nd edn. Elsevier
15. Kalogirou SA (2004) *Solar thermal collectors and applications*, vol 30(3)
16. Winston R (1974) Principles of solar concentrators of a novel design, vol 16(1), pp 89–95
17. Sabahi H, Tofigh AA, Kakhki IM, Bungypoor-Fard H (2016) Design, construction and performance test of an efficient large-scale solar simulator for investigation of solar thermal collectors. *Sustain Energy Technol Assessments* 15:35–41. <https://doi.org/10.1016/j.seta.2016.03.004>
18. Evangelisti L, Vollaro RDL, Asdrubali F (2019) Latest advances on solar thermal collectors: a comprehensive review. *Renew Sustain Energy Rev* 114:109318. <https://doi.org/10.1016/j.rser.2019.109318>
19. Kalogirou SA (2014) *Designing and modeling solar energy systems*
20. Khamooshi M, Salati H, Egelioglu F, Hooshyar Faghiri A, Tarabishi J, Babadi S (2014) A review of solar photovoltaic concentrators. *Int J Photoenergy*, August 2014. <https://doi.org/10.1155/2014/958521>
21. Joardder MUH, Halder PK, Rahim MA, Masud MH (2017) *Solar pyrolysis: converting waste into asset using solar energy*. Elsevier Inc.
22. Xie WT, Dai YJ, Wang RZ, Sumathy K (2011) Concentrated solar energy applications using Fresnel lenses: a review. *Renew Sustain Energy Rev* 15(6):2588–2606. <https://doi.org/10.1016/j.rser.2011.03.031>
23. Akisawa A, Hiramatsu M, Ozaki K (2012) Design of dome-shaped non-imaging Fresnel lenses taking chromatic aberration into account. *Sol Energy* 86(3):877–885. <https://doi.org/10.1016/j.solener.2011.12.017>
24. Nonimaging Fresnel Lens Concentrator|The Prototype Ralf Leutz
25. Sierra C (2005) Photovoltaic materials and phenomena scell-2004 High solar energy concentration with a Fresnel lens, pp 1339–1343 (2005)
26. Wang H, Huang J, Song M, Hu Y, Wang Y, Lu Z (2018) Simulation and experimental study on the optical performance of a fixed-focus Fresnel lens solar concentrator using polar-axis tracking. *Energies* 11(4). <https://doi.org/10.3390/en11040887>

27. Ohkubo T et al (2009) Solar-pumped 80 W laser irradiated by a Fresnel lens. *Opt Lett* 34(2):175. <https://doi.org/10.1364/ol.34.000175>
28. Augsburg G (2013) Thermo-economic optimisation of large solar tower power plants PAR, vol 5648, p 253. <https://doi.org/10.5075/epfl-thesis-5648>
29. Hassan A, Hassan A (2016) Solar tower power plant optimization : a review. no. November, 2016. <https://doi.org/10.13140/RG.2.2.13416.78088>
30. Yabe T et al (2007) High-efficiency and economical solar-energy-pumped laser with Fresnel lens and chromium codoped laser medium. *Appl Phys Lett* 90(26):1–4. <https://doi.org/10.1063/1.2753119>
31. Baharoon DA, Rahman HA, Omar WZW, Fadhl SO (2015) Historical development of concentrating solar power technologies to generate clean electricity efficiently—a review. *Renew Sustain Energy Rev* 41:996–1027. <https://doi.org/10.1016/j.rser.2014.09.008>
32. Tabor H (1966) Conference paper a solar cooker for developing countries al. *Sol Energy* 10(4):1966
33. Nahar NM (2009) Design and development of a large size non-tracking solar cooker. *J Eng Sci Technol* 4(3):264–271
34. Arenas JM (2007) Design, development and testing of a portable parabolic solar kitchen. *Renew Energy* 32(2):257–266. <https://doi.org/10.1016/j.renene.2006.01.013>
35. Hafez AZ, Soliman A, El-Metwally KA, Ismail IM (2016) Solar parabolic dish Stirling engine system design, simulation, and thermal analysis. *Energy Convers Manag* 126:60–75. <https://doi.org/10.1016/j.enconman.2016.07.067>
36. Munir A, Hensel O, Scheffler W (2010) Design principle and calculations of a Scheffler fixed focus concentrator for medium temperature applications. *Sol Energy* 84(8):1490–1502. <https://doi.org/10.1016/j.solener.2010.05.011>
37. Ministry of New and Renewable Energy (2014) Scheffler dish—operation & maintenance manual. Mnre.Gov.in [Online]. Available: http://mnre.gov.in/file-manager/UserFiles/CST-Manuals/SchefflerDish_E.pdf
38. Panchal H, Patel J, Parmar K, Patel M (2018) Different applications of Scheffler reflector for renewable energy: a comprehensive review. *Int J Ambient Energy* 1–13. <https://doi.org/10.1080/01430750.2018.1472655>
39. El-Kassaby MM (1991) New solar cooker of parabolic square dish: Design and simulation. *Renew Energy* 1(1):59–65. [https://doi.org/10.1016/0960-1481\(91\)90104-W](https://doi.org/10.1016/0960-1481(91)90104-W)

Powder Mixed Electric Discharge Drilling of Aluminum Based Metal Matrix Composite



Pabitra Kumar Sahu and Sabindra Kachhap

1 Introduction

A very important, very interesting technical approach in present research is the blending of powder into dielectric fluid in electric discharge drilling (EDD). In EDD, conductive powder is frequently blended into dielectric fluid as it is an efficient solution to increase efficiency and surface strength after machining. There have been several types of powder materials employed, such as Al, W, Si, Cu, WC, SiC, and MoS₂, etc. Powders are mixed into dielectric fluid to improve the material removal rate (MRR) and electrode wear ratio (EWR) surface roughness (SR) in EDD. Micro-hole drilling in different materials has been an important method in the medical, automobiles, and electronics industries for the manufacture of miniature instruments, heat exchangers, micro-fluidic devices, printing equipment, nozzles, etc. PM-EDD is found to be an important method of micro-manufacturing, and it is generally used to create complex shape independent of the hardness of the work piece. Electric sparks are created at the smallest intervals and temperature increases and melts and vaporizes because of this plasma channel. Due to melting and vaporization, material removes from work piece. The molten material is flashed out by the dielectric fluid as the current supply is switched off. A variation of EDM is EDD, and it is used to machine hole of high aspect ratio.

Khanna et al. [1] optimized the input variables of EDD by using the Taguchi method for enhanced tool wear during machining the aluminum 7075 drilling process. Multi-objective optimization of response such as MRR and TWR were done by using the gray relational analysis method (GRA). The results of optimization found that the mixture of maximal on-time pulse and minimal off-time pulse provides maximum MRR. Pulse-on time was the most influential parameter for MRR. Kachhap and Singh [2] studied the effects of input control parameters

P. K. Sahu (✉) · S. Kachhap
Department of Mechanical Engineering, NIT Manipur, Imphal, India

such as discharge current, pulse-on time, pulse-off time, and tool electrode speed on output response such as MRR and tool wear rate TWR during metal matrix composite machining. In contrast with the electric discharge machining process, the rate of material removal in the electric discharge drilling process is maximum. In contrast to the traditional EDM process, the rate of tool wear in the EDD process is still large. Hollow slotted instruments have the highest MRR and TWR of all tool geometries.

Kumar et al. [3] investigated on the micro-EDD (μ -EDD) method for CFRPs. The result indicated that it was possible to drill high aspect ratio micro-holes in CFRPs using EDD by concentrating the energy of the discharge on the carbon layer fiber. Increasing the discharge capacity raised both MRR and TWR. The largest MRR, moderate TWR, and maximum aspect were obtained by a single notch electrode compared with double notch electrode ratio. The most powerful tool speed of 1500 rpm was found in order to improve the MRR. A better surface quality was found during morphological research at lower discharge energy levels. Kachhap et al. [4] studied on a comparison study of EDM and EDD to assess the efficiency measurements for the drilling of blind holes in work piece Al6063/10% of SiC-based MMC. Results have shown that discharge current is the most important factor impacting numerous output characteristics in both EDM and EDD systems. MRR and SR have also been shown to be higher in EDD relative to EDM.

Davis et al. [5] experimented on a comparative analysis in the creation of holes by EDD and PM-EDD of Inconel 718 alloy specimen with copper tool electrode. The finding showed that in powder mixed EDD, MRR went better than EDD, electrode with a rotary copper tool. With an improvement in pulse-on time, rate of material removal raised and deteriorated with an increase in pulse-off time. The MRR only improved to the value of 600 rpm tool speed in both PM-EDD and EDD, although later the same resulted in a negative outcome in both cases when the tool speed went above 600 rpm. Kumar et al. [6] experimented by drilling on Ti-61-7Nb using an electric discharge machine, and the input process parameters were pulse-on time, pulse-off time, electrode material, electrode rotation rate, drilling angles. Drilling rate and electrode wear ratio had been taken as response parameter. The process parameters were optimized for maximum drilling rate and minimum electrode rate by using non-dominated sorting genetic algorithm II (NSGA-II) approach. It was found that increase in drilling rate and EWR with increase in peak current and pulse-on time. The drilling rate raised with rise in pulse-off time but EWR reduced. Jeevamalar et al. [7] experimentally investigated on the efficiency of TWR by machining Inconel 718 super alloy using EDD mixed with tungsten powder. The result showed that with rise in peak current, then the TWR increased, but steadily declined with the rise in pulse-on time.

The experimental characterization of MRR in the dry EDD process was proposed by Govindan and Joshi [8]. It was clear that the rate of material removal was highly affected by the gap voltage, the current discharge, and the rotational velocity of the electrode. Single-spark dry EDM study showed that there was an improvement in MRR as well as crater radius (R_c) in dry EDM relative to liquid dielectric EDM at low input energies. D'Urso et al. [9] investigated on a micro-EDM machine to

conduct an experimental campaign focused on the implementation of micro-holes on stainless steel surface. It was found that higher material removal rate was achieved using brass electrode as compared to tungsten carbide electrode. The MRR increased frequently due to increase both peak values of current and voltage. High electrical conductivity resulted in a quicker drilling process, but the holes were smaller in size as well as geometric accuracy. Munza et al. [10] investigated on electric discharge drilling with the electrode diameter of 1 mm to drill in ZTA-TiC ceramics. The outcomes showed that triangular pulses with 20 A discharge current or smaller were appropriate for EDM ZTA-TiC drilling relative to rectangular pulses. Feed rate as well as drill oversize during machining rely on primarily on the proper flushing state regulated by the volumetric flow rate. Calignano et al. [11] experimental researched using EDD for obtaining holes of 0.4-mm diameter as well as an aspect ratio of 20 in Al_2O_3 -TiC, utilizing copper tool electrodes. The result showed that crater diameter had been observed to increase with increasing power on the eroded surface and demonstrates little dependency on pulse length.

Singh et al. [12] had done comparative study between EDM and EDD during machining MMC. The current work describes the optimized input process parameter such as discharge current, tool speed as well as arc on time for maximum MRR and minimum TWR. It was found that comparison to the EDD system, the MRR for EDM is very small and the TWR for EDD is large compared to the EDM. Islam et al. [13] investigated on elimination of burrs in drilled hole in work piece made of CRPF composite by using dry EDM. In this research, a comparative study had done between dry EDM and oil EDM. In both case, positive polarity of tool provides better material removal rate as compared to negative polarity. With increase in capacitance, gap pressure as well as voltage then MRR raised in both case of EDM. From the above literature review, it concludes that few research have done using powder mixed EDD. In this experiment, the optimization of process parameters has done, and investigation was done to know effect of process parameters on MRR by using powder mixed EDD.

2 Experimental Details

The current study dealing with the aluminum-based MMC using PM-EDD is shown in Fig. 1. The experimental investigation was performed at the Tool Room and Training center (TRTC) in Patna, India, on Electronica Expert 1 CNC EDM machine. After making some improvements in the experimental configuration the traditional electric discharge drilling, a drilling setup was designed as well as integrated into the current EDM configuration, to achieve the EDD system. The EDD configuration was connected to the EDM machine's servo motor. The fixed input control variables selected for the work were the flushing pressure of 20 psi, the voltage difference of 60 V and the straight electrode polarity. In this analysis, the tool electrode was attached to the negative end and the work piece to the positive end of power supply.

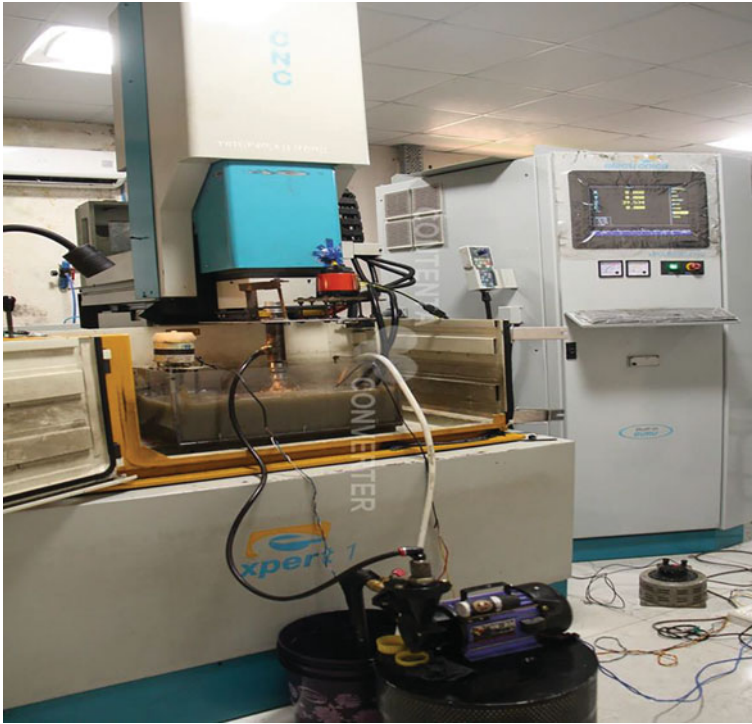


Fig. 1 Powder mixed electric discharge drilling

The 9 mm diameter and 60 mm length of copper tool electrode was used. Commercial EDM oil was taken as dielectric fluid and SiC powder with concentration of 6 gm/l was mixed.

3 Methodology

The research consists of design of experiment including implementation of central composite design approach of response surface method (RSM). In this experimental work, the input control variable such as discharge current, duty factor, tool speed, and pulse-on time were taken. The rate of material removal was taken as response variable, and it was calculated by using below formula.

$$\text{MRR (mm}^3/\text{min)} = \frac{W_i - W_f}{t \times \rho} \times 1000$$

where W_i = Initial weight of work piece (mg), W_f = Final weight of work piece (mg), t = Machining time (Min), and ρ = Density of work piece (kg/m^3).

Table 1 Selected input control parameters and their levels

Symbol	Process parameters	Units	Levels				
			-2	-1	0	+1	+2
A	Discharge current	Amp	3	6	9	12	15
B	Pulse-on time	μs	50	100	150	200	250
C	Duty factor	-	8	12	16	20	24
D	Tool speed	Rpm	400	600	800	1000	1200

The discharge current, pulse-on time, duty factor as well as tool speed were taken as the input process parameters for this experimental investigation. To build the experiment, the central composite design approach of the response surface system was used. The design expert software was utilized to design the experiments. The experiment were designed and analyzed by design expert software. Each input parameter of five level was chosen as shown in Table 1. MRR was taken as output response parameter.

4 Results and Discussion

The response parameter such as MRR obtained by running the experimental test. It has been again tested using ANOVA to find out most effective parameters. Table 2 shows material removal rate of observations. Table 3 shows analysis of variance of material removal rate.

In 95% confidence interval, to be statically significant, the probability should be less than 0.5. But it is considered insignificant if it reaches 0.1. Table 2 shows material removal rate of observations.

The experimenter needs significant models and an insignificant lack of fit. For powder mixed electric discharge drilling, the insignificant of fit values of 0.0552 suggests that the models fit well with the experimental results. The model *F* value of 121.86129 shows that the model is significant. The calculated values of *R*² 0.99128443 reports a good association between the values measured and expected. There is also a sound correlation between the predicted *R*² values (0.95355924) and the adjusted *R*² values (0.9831499). The degree of accuracy is indicated by the coefficient of variance (*CV* = 5.910062381). Discharge current, tool speed as well as pulse-on time have a significant effect on the rate of materials removal. The discharge current was most effective parameter as compared to other parameter.

The normal probability plot for MRR, as shown in Fig. 2, represents a straight line followed by residuals at a closer range and errors along the normal distribution format. Figure 3 indicates a suitable match between the experimental values and the regression model between the real and expected values in the usual probability map.

Figure 4 represents, MRR rises with rise in discharge current to high discharge energy. When pulse-on time increase form 125–175 μs, the MRR raised but pulse-on

Table 2 Results of observations

Std. order	Discharge current A (amp)	Pulse-on time B(μ s)	Duty factor C (-)	Tool speed D (rpm)	MRR (mm^3/min)
1	6	100	12	600	29.41887
2	12	100	12	600	78.25411
3	6	200	12	600	19.96271
4	12	200	12	600	78.74016
5	6	100	20	600	39.48963
6	12	100	20	600	106.1365
7	6	200	20	600	30.39601
8	12	200	20	600	104.1646
9	6	100	12	1000	31.06644
10	12	100	12	1000	75.61275
11	6	200	12	1000	21.72142
12	12	200	12	1000	77.20626
13	6	100	20	1000	40.16335
14	12	100	20	1000	105.2476
15	6	200	20	1000	36.75785
16	12	200	20	1000	103.4905
17	3	150	16	800	12.47437
18	15	150	16	800	112.2852
19	9	50	16	800	56.37965
20	9	250	16	800	49.43973
21	9	150	8	800	40.71007
22	9	150	24	800	75.18336
23	9	150	16	400	63.56827
24	9	150	16	1200	64.43156
25	9	150	16	800	58.99058
26	9	150	16	800	61.52179
27	9	150	16	800	60.64112
28	9	150	16	800	62.22059
29	9	150	16	800	63.79731
30	9	150	16	800	58.66049

time in 175–200 μ s, then MRR decreased. The MRR increases with the discharge current because of the higher discharge energy, and the configuration of the work piece varies rapidly because the heat energy is supposed to be used in a relatively limited part of the geometry due to the higher discharge energy. Figure 5 demonstrates the impact of pulses on time and duty factors on performance parameters. The duty

Table 3 ANOVA for MRR

Source	Sum of squares	Df	Mean square	F value	p-value Prob > F	
Model	21,887.03442	14	1563.359601	121.86129	<0.0001	Significant
A-discharge current	19,238.25825	1	19,238.25825	1499.59034	<0.0001	
B-pulse-on time	91.37325211	1	91.37325211	7.12239355	0.0175	
C-duty factor	2068.517722	1	2068.517722	161.237528	<0.0001	
D-tool speed	1.723084629	1	1.723084629	0.13431159	0.7191	
AB	54.95008567	1	54.95008567	4.2832681	0.0562	
AC	260.7334404	1	260.7334404	20.3237395	0.0004	
AD	16.36127668	1	16.36127668	1.2753344	0.2765	
BC	0.015254103	1	0.015254103	0.00118903	0.9729	
BD	3.170100128	1	3.170100128	0.24710405	0.6263	
CD	2.435214868	1	2.435214868	0.18982096	0.6693	
A ²	11.68987615	1	11.68987615	0.91120647	0.3549	
B ²	80.64527069	1	80.64527069	6.28616518	0.0242	
C ²	5.688984328	1	5.688984328	0.4434469	0.5156	
D ²	30.69485972	1	30.69485972	2.39261344	0.1427	
Residual	192.4351374	15	12.82900916			
Lack of fit	173.2131115	10	17.32131115	4.50558938	0.0552	Not significant
Pure error	19.2220259	5	3.844405181			
Cor total	22,079.46956	29				

factor is ratio of pulse-on time to total time. Total time is sum of pulse-on time and pulse-off time. With rise in duty factor and pulse-on time, the material rate gradually increases.

Figure 6 shows the counter plot of the current discharge and Duty Factor for the rate of material removal. The spark energy increases at higher current values because of the expansion of the plasma channel in the discharge gradient due to the rise in current values. Figure 7 represents that when a higher MRR is achieved with rise in tool speed. The higher rotational speeds of the tool electrode enhance the occurrence of greater centrifugal force magnitude, resulting in more favorable flushing of eroded particles and, thus, greater MRR results.

The scanning electron microscope (SEM) evaluation was carried at the NIT in Durgapur, India, and the images as below have noticeable observations. During EDD with solid tool electrodes, the surface properties shown with the following SEM images were observed. The lower MRR result, where discharge current is 3 amp, pulse-on time 150 μs, duty factor 16 and tool speed 800 rpm, is shown in Fig. 8. In this SEM image, the forming of surface cracks, blow holes and debris globules

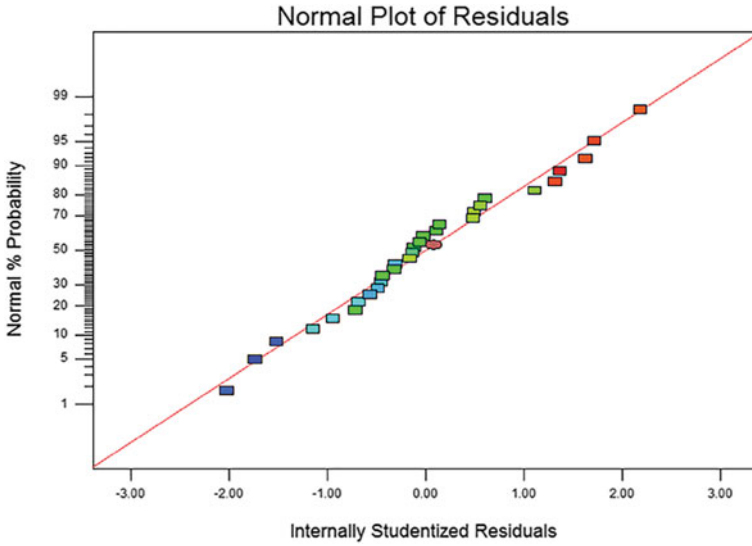


Fig. 2 Normal plot of residuals

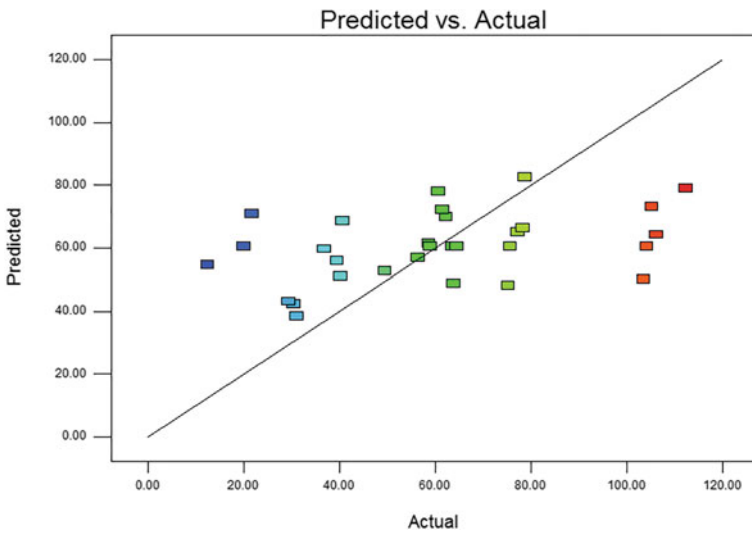


Fig. 3 Predicated versus actual

is detected. This images shows that due to lower discharge current, the small cracks were formed on the work piece surface. The higher MRR result, where discharge current is 15 amps, pulse-on time 150 μ s, duty factor 16 and tool speed 800 rpm, is shown in Fig. 9.

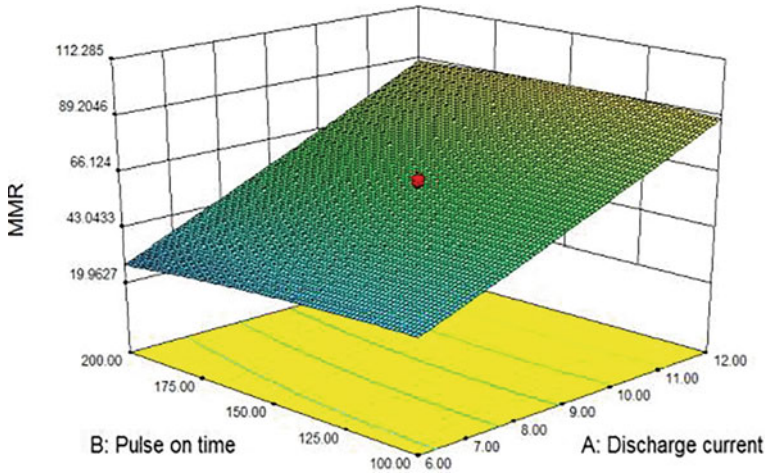


Fig. 4 Discharge current versus pulse-on time

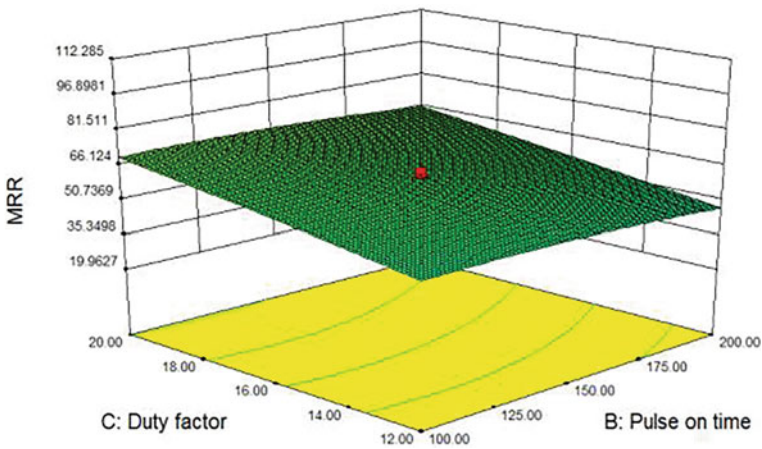


Fig. 5 Pulse-on time versus duty factor

5 Conclusion

The solid tool electrode was effectively utilized to machine aluminum-based MMC work pieces in the latest experimental study. The influence of input control parameters on rate of material removal was found. The findings of the PM-EDD of aluminum-based metal matrix composite make it more usable for making a hole and further research. Tool speed has a lower influence on MRR. Because of current, pulse-on time, as well as duty factor, the performance of material removal rate rises. The influence of input process parameters on process performance was shown by ANOVA.

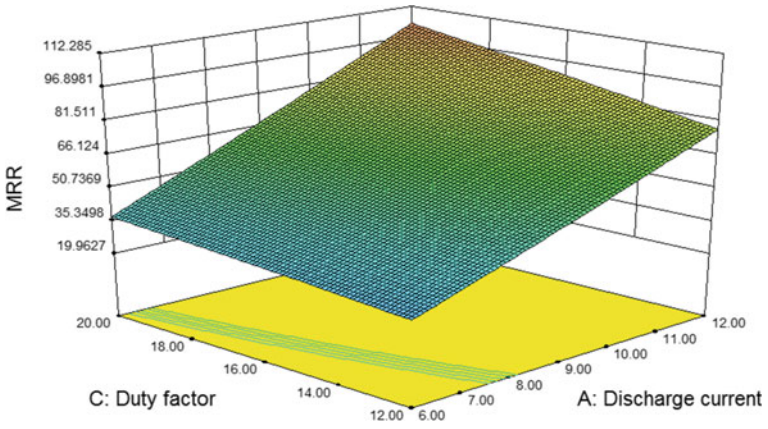


Fig. 6 Discharge current versus duty factor

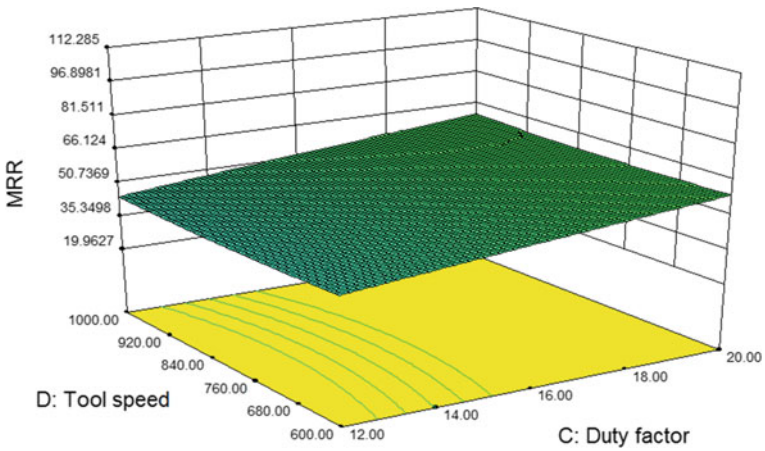


Fig. 7 Duty factor versus tool speed

The important input parameters for the substance removal rate were identified to be the discharge current and duty factor.

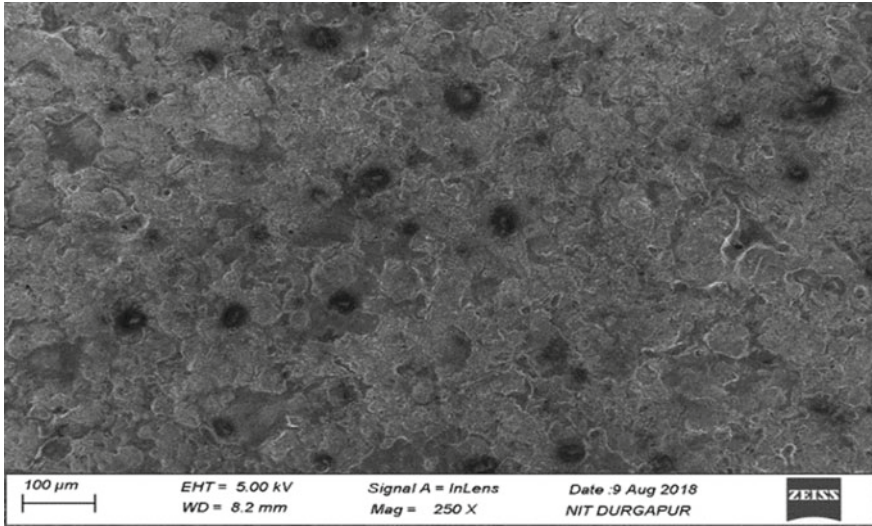


Fig. 8 Surface machined at a discharge current of 3 amp, pulse-on time of 150 μs, duty factor 16 and tool speed of 800 rpm

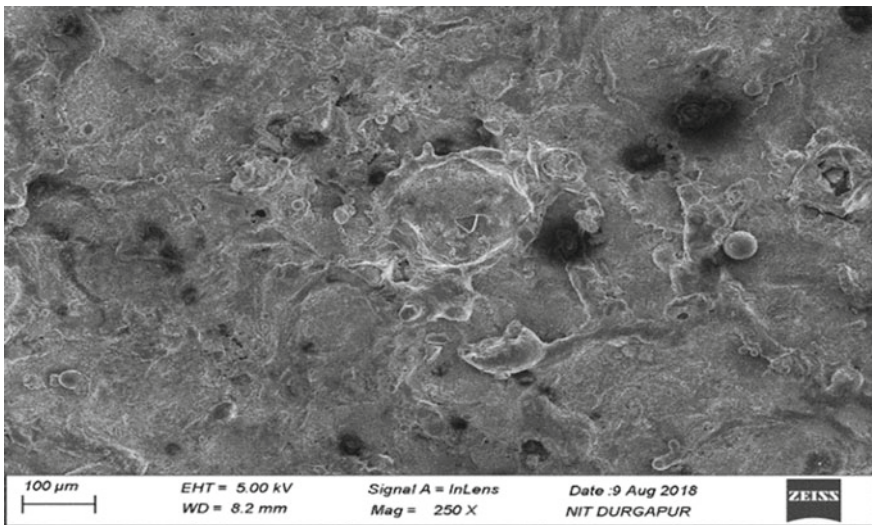


Fig. 9 Surface machined at discharge current is of 15 amp, pulse-on time of 150 μs, duty factor of 16, and tool speed of 800 rpm

References

1. Khanna R, Kumar A, Garg MP, Singh A, Sharma N (2015) Multiple performance characteristics optimization for Al 7075 on electric discharge drilling by Taguchi grey relational theory. *J Ind Eng Int* 11:459–472
2. Kachhap S, Singh A (2019) Performance evaluation of different electrode geometries in electric discharge drilling of MMCs. *Int J Mech Eng Robot Res* 8(4)
3. Kumar R, Kumar A, Singh I (2018) Electric discharge drilling of micro holes in CFRP laminates. *J Mater Process Tech* 259:150–158
4. Kachhapa S, Singha A, Debnath K (2020) Process optimization and comparative analysis of EDM and EDD process in machining Al6063/10% SiC metal matrix composites. *Indian J Eng Mater Sci* 27:750–756
5. Davis R, Singh A, Kachhap S, Nath N (2020) A comparative study of EDD and PM-EDD in producing holes in inconel 718 alloy. *Key Eng Mater* 833:48–53. ISSN: 1662–9795
6. Kumar K, Singh V, Katyal P, Sharma N (2019) EDM μ -drilling in Ti-6Al-7Nb: experimental investigation and optimization using NSGA-II. *Int J Adv Manuf Technol* 104:2727–2738
7. Jeevamalar J, Vimalraj R, Vigneshwaran M, Vignesh G (2020) Tool wear rate on inconel 718 using W-powder mixed electric discharge drilling 9(5). ISSN: 2278–3075
8. Govindan P, Joshi SS (2010) Experimental characterization of material removal in dry electrical discharge drilling. *Int J Mach Tools Manuf* 50:431–443
9. D'Urso G, Maccarini G, Ravasio C (2014) Process performance of micro-EDM drilling of stainless steel. *Int J Adv Manuf Technol* 72:1287–1298
10. Munza M, Ristoa M, Haasa R, Landfriedb R, Kernb F, Gadowb R (2013) Machinability of ZTA-TiC ceramics by electrical discharge drilling. *Procedia CIRP* 6:77–82
11. Calignano F, Denti L, Bassoli E, Gatto A, Iuliano L (2013) Studies on electro discharge drilling of an Al₂O₃-TiC composite. *Int J Adv Manuf Technol* 66:1757–1768
12. Singha A, Kumarb P, Singh I (2013) Process optimization for electro-discharge drilling of metal matrix composites. *Procedia Eng* 64:1157–1165
13. Islam MM, Li CP, Ko TJ (2017) Dry electrical discharge machining for deburring drilled holes in CFRP composite. *Int J Precis Eng Manuf Green Technol* 4(2):149–154

Investigating the Change in Water Characteristics and Scale Formation Under the Varying Turbulent Flow



Amrit Anand Dosar and Vivek Srivastava

Abbreviations

TDS	Total dissolved solids (mg/L)
EC	Electrical conductivity ($\mu\text{s/cm}$)
PVC	Polyvinyl chloride
GI	Galvanized iron
MTD	Magnetic treatment device
MWT	Magnetic water treatment
FESEM	Field emission scanning electron microscope
F_L	Lorentz force (Newton)
q	Quantity of charged species (Coulomb)
v	Velocity of particles (m/s)
B	Magnetic field Tesla (T)
θ	Angle between v and B vectors (Degree)

1 Introduction

Hard water scaling is a major problem in various industries and household installations [1–3]. Scale reduces the heat transfer from pipes in heat exchangers and blocking the water flow in pipes [4]. For scale removal, various conventional methods

A. A. Dosar (✉)
BBD University, Lucknow, India
e-mail: amritdosar@bbdu.ac.in

V. Srivastava
DIT University, Dehradun, India

are generally used like, the application of chemical product, the pre-precipitation of the scale with soda ash or lime and by ion-exchange process. All these conventional methods are very efficient, but they can change the water chemistry and are much costly. So to avoid the chemical use, physical methods were developed, and magnetic treatment device (MTD) methods are the example of such method to prevent scale formation and water treatment. Chemical products used in conventional methods were harmful to the atmosphere as well as human health [5, 6]. Magnetic treatment device helps in reducing the scale formation and deposition on the walls of various domestic and industrial equipments [7]. In water system, MWT has been used for several years as a preventing and controlling tool for scale deposition [8, 9]. Various magnetic devices have been developed to get maximum anti-scale prevention efficiency from last few decades. It changes only the morphology of CaCO_3 scale not its chemical composition [10]. Since 1995 after the first patent of MWT, the use of this method for water treatment has improved [11, 12]. Grimes et al. [13] and Parsons et al. [14] reported about scale reduction by MTD, while Busch et al. [15] found only minor influence on scale reduction.

The deposits of CaCO_3 from magnetically treated water are maybe in the form of calcite and aragonite [10, 16]. Chang et al. [17] analyzed the effect of the magnetic treatment on the growth of aragonite crystals. They observed that under the effect of magnetic field, aragonite crystal grows with faster at low pH and at the high level of supersaturation. Tai et al. [18] analyzed the influence of the static magnetic field on the crystallization of CaCO_3 using a permanent magnet and the calcite crystals growth rate was examined at various levels of supersaturation, pH, and ionic strength. They observed that the magnetic field reduces the growth rates of calcite crystals, and their suppression percentage was higher for the magnetic field of higher intensity. Simonic et al. [19] analyzed using SEM and XRD methods that initially calcite precipitates were formed in water, which converted in to non-adhesive aragonite form after magnetic treatment (0.6 T). That could be removed easily by turbulent flow of water.

The efficiency of MWT depends on the material of pipe, used for water circulation. Alimi et al. [20] investigated the effect of magnetic treatment on different pipe material (PTFE, Tygon, copper, PVC, and stainless steel) by circulating hard water at 0.16 T magnetic field. They found that the increase in total precipitation ratio was obtained when the magnetic field was applied through pipes of non-conductive material.

The rate of flow of water affects the scale formation and water characteristics due to the Lorentz force. Latva et al. [21] examined using a pilot project that MWT gives the best result at 2.3 m/s flow velocity of water and found that the magnetic field reduced calcium scaling by 15% from the pipe.

Magnetic field effects the water characteristics by changing its hardness, alkalinity, pH, TDS, electrical conductivity, etc. Khater et al. [22] analyzed the effect of the magnetic field (18 Gauss) on the physico-chemical characteristics of water, as it decreases conductivity, pH, carbon dioxide and alkalinity in water samples. The magnetic field also decreases the heavy metal concentration like Zinc, Copper, Cobalt, and Aluminum in water. Bali et al. [23] analyzed the scaling effects on treated

water using the magnetic method. The result shows that magnetic treatment increases pH and decreases the resistivity of the solution. Helal et al. [24] analyzed the effect of magnetic treatment at 1500 °C at 6480 Gauss magnetic field. They analyzed that the magnetic field reduces scale formation and changes the electrical conductivity of CaCO₃. The application of a magnetic field decreases the surface tension of water and increases its volume evaporated [25].

On calcium carbonate precipitation by MTD, various experimental works have been done [26, 27]. Othman et al. [28] studied the effect of magnetic water treatment under various conditions. They observed that MWT controls the growth rate of scale; hence improve the life of water pipeline and its performance.

Out of all the above research, very few literatures are available on the effect of the magnetic treatment on scale formation and physico-chemical characteristics of water flow through different pipe materials. The effect of flow rate and circulation time on the percentage change in water characteristics also needed to be explained.

The objective of this research was to experimentally analyze the effect of static magnetic treatment on the formation of aragonite crystal in different materials of pipe and to analyze the change in water characteristics on increasing the flow rate and circulation time. The effect of pipe material on water characteristics also to be examined.

2 Experimental Procedures

The experimental magnetic treatment device (MTD) is shown in Fig. 1. It consists of 3 pairs of permanent magnets with facing each other. The water that has to be treated passed through the pipe arranged between the magnets of opposite polarity, perpendicular to the flow of water. The hard water to be treated was circulated in pipe through the magnetic gap by the centrifugal pump. Three different materials

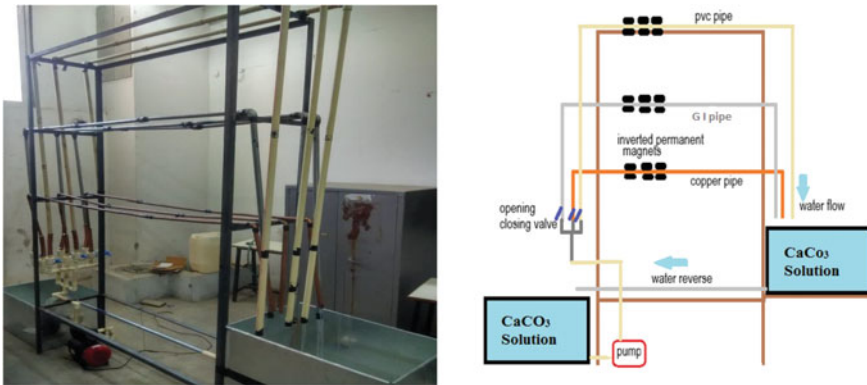


Fig. 1 Experimental setup and its corresponding layout

Table 1 Variables used to conduct the experiment

Variables	Specifications
Number of magnets used	3 pairs
Size of magnet	$40 \times 25 \times 6 \text{ mm}^3$
Intensity of magnets	3800 Gauss
Centrifugal pump power	0.5 hp
Diameter of pipe	0.5 inch
Water circulation time	30 h

of pipes were tested: PVC, G.I., and copper. The water was circulated in pipes at three different flow rates in a turbulent range (3, 5, and 7 L/min). Table 1 shows the different variables like magnets, centrifugal pump, pipe, etc., that is used to conduct experiments.

The series of magnets is used with a static permanent magnetic field. Hardened water was circulated in the different materials of pipe-like copper, GI, and PVC under magnetic and non-magnetic condition (magnetized sample and un-magnetized sample) and different flow rates. Further the analysis was done to obtain the effect of scale formation on different pipe materials. The total dissolved solids, electrical conductivity, hardness, and alkalinity in the water samples were measured for all flow rate conditions.

The field emission scanning electron microscope (FESEM); model Gemini Zeiss Supra 35 VP is used to analyze the morphology of crystal CaCO_3 on pipe walls. The magnifications of this test were at 10,000 X zoom for all materials of pipe and in both magnetic and non-magnetic case.

The TDS, EC, hardness, and alkalinity of water were checked with a 1-L sample of magnetized and non-magnetized water for all flow rates and different materials of pipes.

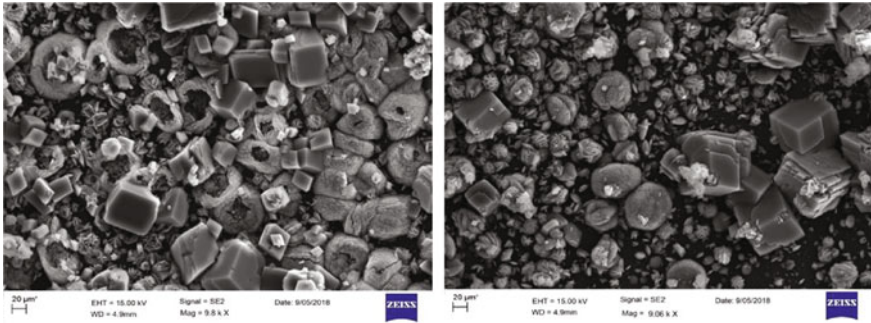
3 Results and Discussions

3.1 *Effect of Magnetic Field on Scale Removal*

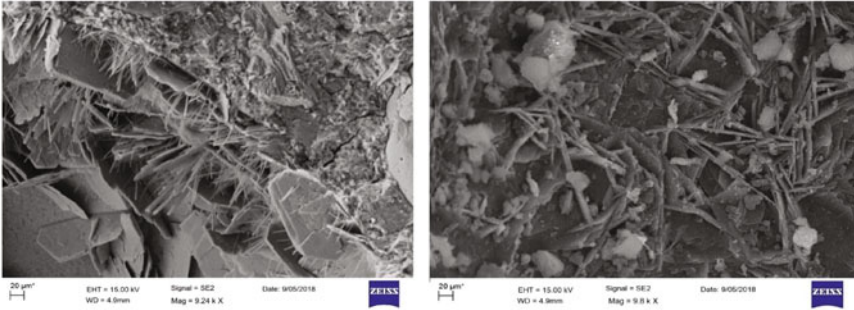
A small number of deposited scales was formed on the inner surface of the pipe walls after magnetized and non-magnetized treatment of water pipes of different materials which was analyzed by FESEM method. Figure 2 shows the size and morphology of the scale. Figure 2a–c shows the magnetized and non-magnetized FESEM images of copper, GI, and PVC pipes, respectively.

All these FESEM images show that the crystal structure on the inner surfaces of pipes of treated water is of orthorhombic or needle crystal, which means after magnetic treatment aragonite crystals are formed which have low-adhesive calcium crystal phase and can easily remove by the turbulent flow of water, while on untreated

(a)



(b)



(c)

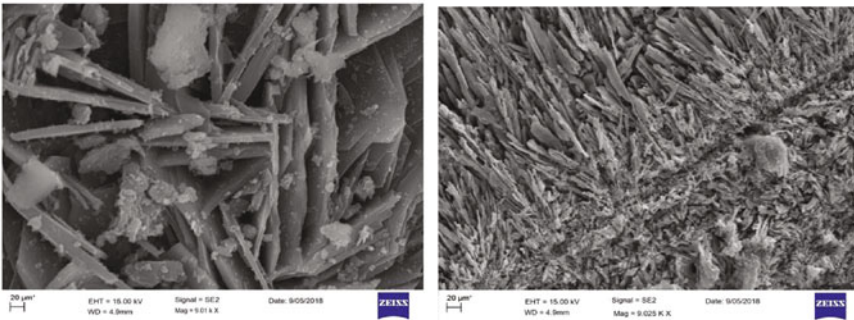


Fig. 2 a FESEM image of untreated and treated copper pipe. **b** FESEM image of untreated and treated GI pipe. **c** FESEM image of untreated and treated PVC pipe

water pipes surface trigonal-rhombohedral-shaped calcite crystals are formed which are usually associated with a hard scale and are difficult to remove.

Figure 3 presents the photos of the plumbing tube of different materials shows that how the scales are formed in treated and untreated water pipes after 30 h circulation of hard water. The scale formed in the pipe is not visible by an unaided eye for this

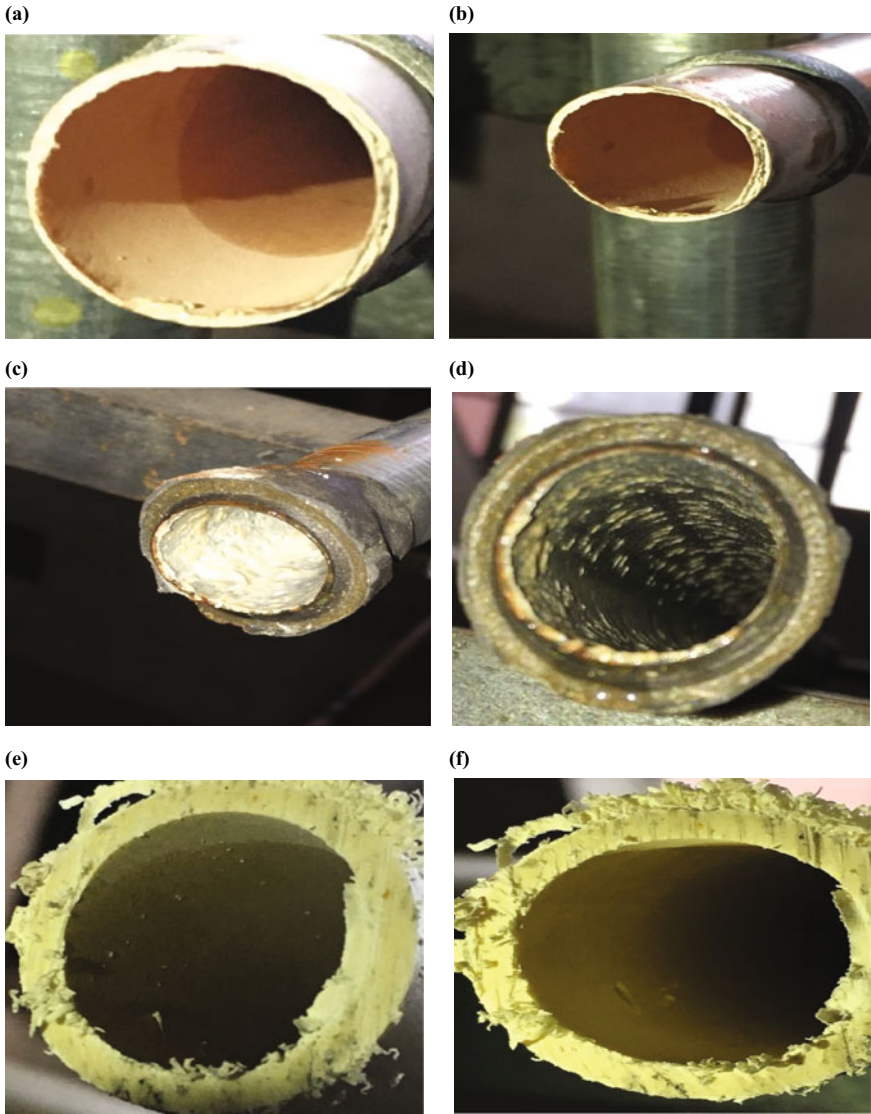


Fig. 3 Photos of water pipes inner section **a** untreated copper pipe, **b** treated copper pipe, **c** untreated GI pipe, **d** treated GI pipe, **e** untreated PVC pipe, **f** treated PVC pipe

interval of time. However, the FESEM images at 10,000 X zoom easily show the scale structure on the inner surface of pipes.

After magnetic treatment, FESEM images show that due to the formation of aragonite crystals the scale removal from pipe increases and less scale formed on the surface of pipes. The results are confirmed with an earlier study in which the

experiment claimed that the aragonite crystals are formed due to the magnetization of the solution [18]. Simonic et al. [19] found by XRD and SEM methods that after magnetic treatment at 0.6 T intensity of magnetic field the calcite crystals of hard water converted into the form of non-adhesive aragonite that could be easily removed by turbulent flow. Chang et al. [17] also analyzed the impact of the magnetic field on aragonite crystals. They observed that under the effect of magnetic field aragonite crystal grows and they grew faster at low pH, high level of supersaturation, and at activity ratio far from unity.

Hence, by the formation of aragonite crystals after magnetic treatment, the scale formation in pipes can be reduced and enhances the life of the pipe.

3.2 Influence of Magnetic Field on the Characteristic of Water

The magnetic field affects the total dissolved solids (TDS), electrical conductivity (EC), hardness, and alkalinity of water under different flow rates in turbulent ranges for PVC pipe. Water circulation time for the study was taken 30 h.

Figure 4a–d shows the effect of flow rate on TDS, EC, total hardness, and alkalinity of water after magnetic treatment. For the above study, PVC pipe material is used in all cases. The graphs are plotted between the characteristics of water and the magnetic circulation time. All the four figures show that on increasing the circulation time the above characteristics of water goes on decreasing due to the magneto-hydrodynamic (MHD) effect. In the magnetic water treatment process, the magneto-hydrodynamic (MHD) mechanism is involved [29, 30].

Hence, the magnetic field reduces the TDS, EC, hardness, and alkalinity of treated water. The results are consistent with an earlier study in which Alkhazan et al. [31] experimentally analyzed the effect of the magnetic field on TDS of water by using magnets of different intensities (130, 260 and 390 μ T) and found that TDS decreases on increasing the magnetic field intensities. Kashef et al. [32] examined the effect of the static magnetic field ($B = 1.45 \text{ T} \pm 0.05$) at open and dead-end flow conditions at a flow rate of 41.93 L/min and 52.16 L/min, respectively. They found that the MF reduces the electrical conductivity and TDS of water. Electrical conductivity analysis was done by Szczes et al. [33] who analyzed the effect of magnetic treatment by exposing water to weak static magnetic field, generated from permanent magnets ($B = 15 \text{ mT}$) at flow condition. They found that the conductivity of water decreases, which is inversely proportional to the flow rate. Khater et al. [22] also examined the effects of the magnetic treatment on water purification. Water was exposed to the weak magnetic field of 18 Gauss. They found that the magnetic field decreases the conductivity and alkalinity of water. Banejad et al. [34] analyzed the influence of the magnetic field on water hardness. For this, the different intensities of magnetic field 0 T, 0.05 T, 0.075 T, and 0.1 T and the different flow rates 4 and 30 L/h was taken.

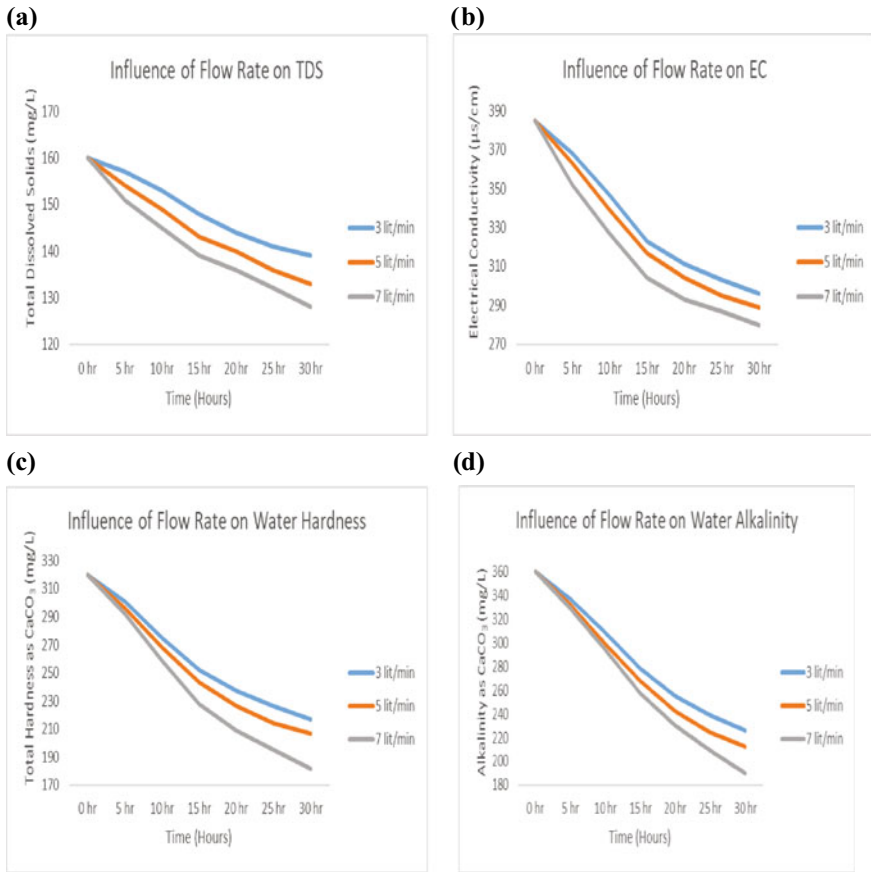


Fig. 4 Influence of flow rate on **a** total dissolved solids (TDS), **b** electrical conductivity (EC), **c** total hardness as CaCO₃, **d** alkalinity as CaCO₃

After analysis, they found that on increasing the intensity of the magnetic field and flow rate the hardness of water reduces.

3.3 Influence of Circulation Time

It is also observed from Fig. 4 that the water characteristics change rate is higher for the first 15 h of the circulation time and comparatively became less for the remaining 15 h. Table 2 shows the percentage reduction of TDS, EC, alkalinity, and hardness of water after 30 h of magnetic water circulation in the PVC pipe.

The reduction in water characteristics is higher for initial hours because of MHD affects. This process is going on as the circulation time increases but most of the

Table 2 Water characteristics change rate for circulation time

Water characteristics	Percentage reduction	
	For the first 15 h	For the last 15 h
TDS	10.41	6.99
EC	18.26	8.36
Alkalinity	24.68	16.29
Total hardness	25.64	21.89

bonds break in the initial interval of time due to MHD effect and maximum physico-chemical properties of the solution changed in that period.

3.4 Influence of Flow Rate

Figure 4a–d is plotted between water characteristics and magnetic circulation time for different flow rates (3, 5 & 7 L/min). The figure shows that the flow rate is inversely proportional to the above water characteristics. The average reduction in TDS, EC, hardness, and alkalinity of water on increasing the flow rates are 16.66%, 25.10%, 36.87%, and 41.85%, respectively, while at 7 L/min flow rate the change in above water characteristics is 20%, 27.27%, 43.12%, and 47.22%, respectively. These changes are occurring due to the Lorentz force. The Lorentz force can be defined as:

$$|F_L| = q|v \times B| = qvB \sin \theta$$

The experiment shows that the flow is perpendicular to the magnetic field and q & B are fixed. So on increasing the velocity of particles, the Lorentz force increases, which increases the magnetic field effect. The above statement can be justified by, Saksono et al. [35] who related the effect of flow rate with Lorentz force. They stated that the increase of Lorentz force directly proportional to the increase in velocity of moving particles. Therefore, on increasing the flow rate, the magnetization effect also increases. Alimi et al. [5] and Fathi et al. [7] also analyzed that the effectiveness of the magnetic field on CaCO_3 precipitation was increased with the flow rates increased.

3.5 Influence of Pipe Material

For analyzing, the effect of pipe material the magnetic water treatment was done on three different materials of pipe-like PVC, GI, and copper pipe. The water was circulated for 30 h, and different water characteristics are analyzed.

Figure 5 shows the influence of pipe material on the TDS of water under the effect of the magnetic field. For the above study, the flow rate was fixed at 7 L/min and the

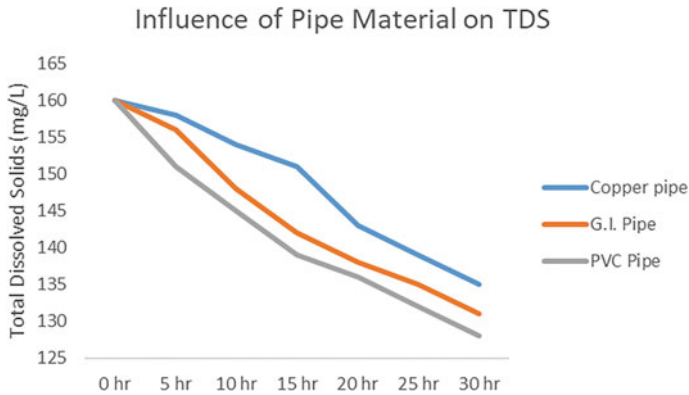


Fig. 5 Influence of pipe material on TDS of water

only TDS of water was measured. The result shows that after magnetic treatment maximum reduction in TDS was observed for PVC pipe 20%, while in GI and copper pipes less reduction was observed 18.12% and 15.62%, respectively. This shows that the efficiency of the magnetic field is different in different materials of pipe and it is maximum non-conductive PVC pipe material. Alimi et al. [20] who experimentally analyzed the effect of MF treatment on various pipe materials also verify the above results. They exposed the water to the static magnetic field (0.16 T) with different flow rates (0.54–0.94 L/min) for 15 min and found that non-conductive pipe materials are much effective than others in respect to the homogeneous and total precipitation ratios. The type of material of pipe plays an important role in the formation of scale also [36, 37].

The rate of TDS reduction is different for different materials of pipe. In PVC and GI pipes, the maximum reduction is obtained in the first 15 h, while for copper pipe maximum reduction is obtained in the last 15 h because magnetic field effectiveness is higher for non-conductive and less conductive material.

4 Conclusions

In the present study, the hard water is circulated in different materials of pipe (PVC, GI, and copper) and at different flow rates (3, 5, and 7 L/min). After 30 h of circulation, it is concluded that:

1. The magnetic treatment enhances the aragonite crystals formation, which is less adhesive than calcite crystals.
2. Magnetic field reduces the TDS, EC, hardness, and alkalinity of the water, and it goes on decreasing on increasing the circulation time of water.

3. The reduction rate of water characteristics like TDS, EC, hardness, and alkalinity is higher for the first 15 h in comparison with the remaining 15 h of circulation time.
4. Flow rate is inversely proportional to the water characteristics (TDS, EC, hardness, and alkalinity), means on increasing the flow rate from 3 to 7 L/min the TDS, EC, hardness, and alkalinity decreases at a faster rate.
5. At 7 L/min the TDS reduction rate in PVC pipe (20%) is much higher than GI (18.12%) and copper (15.62%) pipe.
6. For magnetic treatment, the PVC pipe is much effective than GI and copper pipe.

References

1. Hui F, Lédion J (2002) Evaluation methods for the scaling power of water. *J Eur D Hydrol* 33(1):55–74
2. Legrand L, Leroy P (1990) Prevention of corrosion and scaling in water supply systems. Ellis Horwood Series in Water and Waste Technology, New York
3. Roques H (1990) Fondements theoriques du traitement chimique des edux
4. Gabrielli C, Jaouhari R, Maurin G, Keddam M (2001) Magnetic water treatment for scale prevention. *Water Res* 35(13):3249–3259
5. Alimi F, Tlili M, Amor MB, Gabrielli C, Maurin G (2007) Influence of magnetic field on calcium carbonate precipitation. *Desalination* 206(1–3):163–168
6. Joshy N, Meera V (2020) Scale control on pipe materials: a review. In: *Green buildings and sustainable engineering*, pp 421–429. Springer, Singapore
7. Fathi A, Mohamed T, Claude G, Maurin G, Mohamed BA (2006) Effect of a magnetic water treatment on homogeneous and heterogeneous precipitation of calcium carbonate. *Water Res* 40(10):1941–1950
8. Salman MA, Safar M, Al-Nuwaibit G (2015) The effect of magnetic treatment on retarding scaling deposition. *Turk Online J Sci Technol* 5(3)
9. Sohaili J, Shi HS, Zardari NH, Ahmad N, Muniyandi SK (2016) Removal of scale deposition on pipe walls by using magnetic field treatment and the effects of magnetic strength. *J Clean Prod* 139:1393–1399
10. Coey JMD, Cass S (2000) Magnetic water treatment. *J Magn Magn Mater* 209(1–3):71–74
11. Vermeiren T (1958) Magnetic treatment of liquids for scale and corrosion prevention. *Anti-Corros Methods Mater*
12. Kobe S, Dražić G, Cefalas AC, Sarantopoulou E, Stražičar J (2002) Nucleation and crystallization of CaCO_3 in applied magnetic fields. *Cryst Eng* 5(3–4):243–253
13. Grimes SM (1988) Magnetic field effect on crystals. *Tube Int* 7(2):111–113
14. Parsons SA, Judd SJ, Stephenson T, Udol S, Wang BL (1997) Magnetically augmented water treatment. *Process Saf Environ Prot* 75(2):98–104
15. Busch KW, Busch MA (1997) Laborator studies on magnetic water treatment and their relationship to a possible mechanism for scale reduction. *Desalination* 109(2):131–148
16. Kobe S, Dražić G, McGuinness PJ, Stražičar J (2001) The influence of the magnetic field on the crystallisation form of calcium carbonate and the testing of a magnetic water-treatment device. *J Magn Magn Mater* 236(1–2):71–76
17. Chang MC, Tai CY (2010) Effect of the magnetic field on the growth rate of aragonite and the precipitation of CaCO_3 . *Chem Eng J* 164(1):1–9
18. Tai CY, Chang MC, Shieh RJ, Chen TG (2008) Magnetic effects on crystal growth rate of calcite in a constant-composition environment. *J Cryst Growth* 310(15):3690–3697

19. Simonič M, Urbanč D (2017) Alternating magnetic field influence on scaling in pump diffusers. *J Clean Prod* 156:445–450
20. Alimi F, Tlili MM, Amor MB, Maurin G, Gabrielli C (2009) Effect of magnetic water treatment on calcium carbonate precipitation: influence of the pipe material. *Chem Eng Process* 48(8):1327–1332
21. Latva M, Inkinen J, Rämö J, Kaunisto T, Mäkinen R, Ahonen M, Matilainen J, Pehkonen S (2016) Studies on the magnetic water treatment in new pilot scale drinking water system and in old existing real-life water system. *J Water Process Eng* 9:215–224
22. Khater Z, Ibraheim M (2016) Some ecological studies on the impact of magnetic field on the tap water. *Egypt J Aquat Biol Fish* 20(2):51–60
23. Bali M, Gueddari M (2018) The effect of magnetic treatment on the physico-chemical and microbiological characteristics of hard waters. *Sep Sci Technol* 53(9):1405–1411
24. Al Helal A, Soames A, Gubner R, Iglauer S, Barifcani A (2018) Influence of magnetic fields on calcium carbonate scaling in aqueous solutions at 150° C and 1 bar. *J Colloid Interface Sci* 509:472–484
25. Amor HB, Elaoud A, Salah NB, Elmoueddeb K (2017) Effect of magnetic treatment on surface tension and water evaporation. *Int J Adv Ind Eng* 5:119–124
26. Lipus LC, Dobersek D (2007) Influence of magnetic field on the aragonite precipitation. *Chem Eng Sci* 62(7):2089–2095
27. Parsons SA, Wang BL, Judd SJ, Stephenson T (1997) Magnetic treatment of calcium carbonate scale—effect of pH control. *Water Res* 31(2):339–342
28. Othman A, Sohaili J, Supian NS (2019) A review: methodologies review of magnetic water treatment as green approach of water pipeline system. *Pertanika J Sci Technol* 27(1)
29. Busch KW, Gopalakrishnan S, Busch MA, Tombácz E (1996) Magnetohydrodynamic aggregation of cholesterol and polystyrene latex suspensions. *J Colloid Interface Sci* 183(2):528–538
30. Johan S, Fadil O, Zularisham A (2004) Effect of magnetic fields on suspended particles in sewage. *Malay J Sci* 23:141–148
31. Alkhazan MMK, Saddiq AAN (2010) The effect of magnetic field on the physical, chemical and microbiological properties of the lake water in Saudi Arabia. *J Evol Biol Res* 2(1):7–14
32. El-Kashef E, El-Shamy AM, Abdo A, Gad EA, Gado AA (2019) Effect of magnetic treatment of potable water in looped and dead end water networks. *Egypt J Chem* 62(8):1467–1481
33. Szcześ A, Chibowski E, Hołysz L, Rafalski P (2011) Effects of static magnetic field on water at kinetic condition. *Chem Eng Process* 50(1):124–127
34. Banejad H, Abdosalehi E (2009) The effect of magnetic field on water hardness reducing. In: Thirteenth international water technology conference, IWTC, vol 13, pp 117–128
35. Saksono N, Yuliusman Y, Bismo S, Soemantojo R, Manaf A (2010) Effects of pH on calcium carbonate precipitation under magnetic field. *Makara J Technol* 13(2):79–85
36. MacAdam J, Parsons SA (2004) Calcium carbonate scale formation and control. *Re/Views Environ Sci Bio/Technol* 3(2):159–169
37. Doyle JD, Oldring K, Churchley J, Parsons SA (2002) Struvite formation and the fouling propensity of different materials. *Water Res* 36(16):3971–3978

A Study on Post-harvest Loss Reduction with Solar Dryer



Ajay Vishwakarma, Sunanda Sinha, and Prashant Malik

1 Introduction

Preservation and storage of food are essential and inseparable part of human life. Various techniques have been used to increase the shelf life of food, such as fermenting, dry salting, smoking and sealing all these methods were used for vegetables and fruits [1]. When coming to grains, traditional drying after harvest performed in which grains were spread over the ground and exposed to the sun which is also referred to as open sun drying. Open sun drying has drawbacks like dust contamination, insect infection, etc., which causes spoilage. There is no control over drying rate in open sun drying leads to over drying of grains which causes discoloration, change in nutritional value, and loss of germination power [2]. Because of improper drying or without drying, farmer faces heavy losses of food in the pre- and post-harvest period [3]. In India, cumulative post-harvest loss of fruits and vegetables is estimated to be 5.8–18% which costs 44,000 crores/year [4]. It is important to eradicate this issue by drying agricultural products [5], as it helps to mitigate food scarcity by minimizing the agricultural losses that arise due to the presence of moisture content above the healthy moisture level [6]. Healthy moisture content can be obtained by drying under regulated temperature and humidity conditions, which allows agricultural food products to dry up relatively easily to safe moisture content level and maintain a high quality of the commodity [7]. Mostly in industrial drying processes, controlled drying is practiced. Hot air is commonly produced by the combustion of fossil fuels for industrial drying, and vast amounts of fuels are used for this purpose

A. Vishwakarma · P. Malik

Centre for Energy and Environmental Engineering, National Institute of Technology, Himachal Pradesh, Hamirpur 177005, India

S. Sinha (✉)

Centre for Energy and Environment Malaviya, National Institute of Technology, Jaipur, Rajasthan 302017, India

worldwide. Non-access to grid power is struggling in many rural areas of developed countries; supplies of other non-renewable energy sources are often either inaccessible, inadequate, or too costly for many farmers. The high cost of fossil fuels, the rapid decline of their supplies and the effects of their use on the atmosphere have put significant restrictions on their use. The immense potential of solar energy in the food processing industries is not much exploited scientifically, although drying and thus storing agricultural and horticultural products is one of the oldest applications of solar energy [8]. The use of solar dryers for drying foods is one of the best solutions for the preservation of food as well as a reduction in fossil fuel dependency in the food industry. As a typical solar dryer can easily attain the temperature of up to 60–70 °C more than enough for drying agricultural products [9] and a correctly designed solar dryer can reduce the disadvantages associated with open sun drying, and the consistency of the dried product can be increased [10]. There are many types of solar dryers available based on their working and design for more detail refer to [11]. Performance and advancement in different solar dryers were analyzed by many researchers [12–15]. Bhardwaj [16] used a solar dryer for drying medicinal plants. Djebli et al. [17] used potatoes to analyze drying behaviour in solar dryers. An economic analysis was done by Hage [18]. Mishra [19] reviewed various advancement and parameter impact on the performance of greenhouse dryer. In most of these studies, the emphasis was on the construction and testing of the system, whilst some of them performed drying analysis [20] and simulation analysis [21] but harvest loss due to improper drying was not emphasized. Mohana et al. [22] reviewed solar dryer recently based on concept design and advancement and suggested that there is a need for low cost and energy-efficient dryers for high-quality foods.

In this paper, drying importance of agricultural products has been investigated by pointing out loss associated with improper drying and further, a comparative study of cabinet type solar dryer with open sun drying on chillies and carrot also conducted in Madhya Pradesh to show the effectiveness, benefits of solar dryer in drying applications over open sun drying.

2 Importance of Drying of Agricultural Products: An Indian Context

Open sun drying depends on the weather conditions leads to many problems such as dust, rain, insect infection, etc., which leads to spoilage of yields. India produces 150 million tonnes of food grains per year accounts for 47 million tonnes of wheat, 64 million tonnes of rice from which nearly 70% are stored by local farmers on their own. And due to this storage of food without proper drying causes losses of nearly 6% of total yield. A study conducted by Agricultural Development and Rural Transformation Centre reported that India faces pre- and post-harvest loss which accounts for 25% in rice and maize and 15% in wheat of total production. The projected farm-level post-harvest losses are 3.82 kg/q for rice and 3.28 kg/q

for wheat for 2003–2004 [23]. According to a report published by the Ministry of Agriculture & Farmers Welfare, post-harvest losses account for 9.5 per cent of the output of total pulses.

As shown in Fig. 1a, percentage loss of paddy was highest in Karnataka and West Bengal accounts 16.2% and 15.05% of total yield [24]. Wheat loss due to improper drying and improper storage in Assam and West Bengal was 13.79% and 15.29% of total production, respectively, which shown in Fig. 1b, whereas loss of Tur due to improper drying and storage was maximum in Karnataka nearly half of the yields were spoiled which 43% of the total production of Tur as shown in Fig. 2a, b shows loss of Tur and soybean in different states [25–29], respectively.

This amount of food can feed nearly 10 crores of the population. According to Oxfam’s Food Availability Index [30], India stand 97th and 103rd in the Global Hunger Index which makes these food losses even more critical and makes proper drying of grains and vegetables essential.

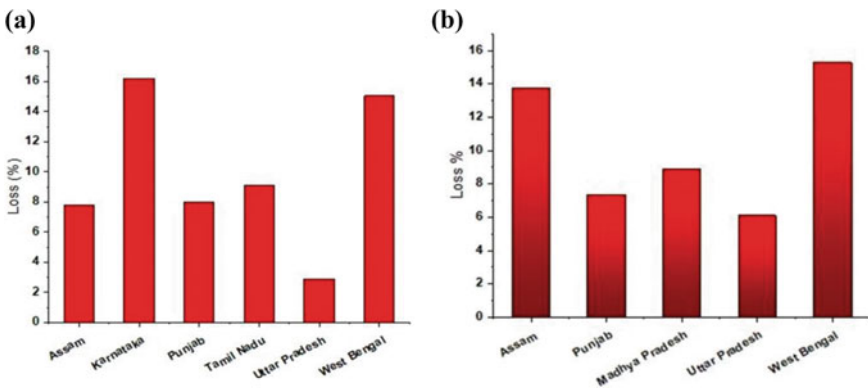


Fig. 1 a Loss percentage of Paddy. b Loss percentage of wheat

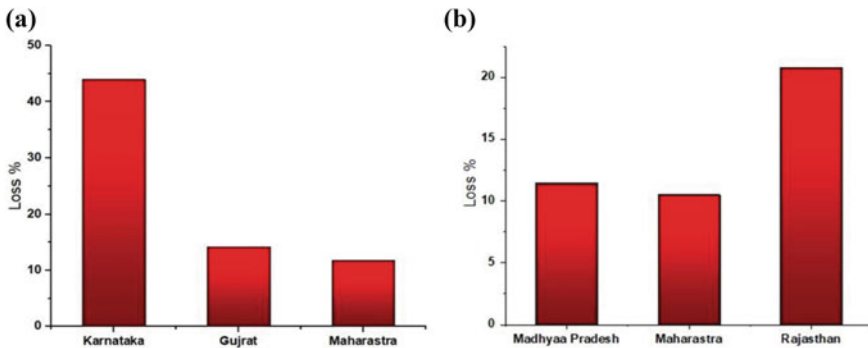


Fig. 2 a Loss percentage of Tur. b Loss percentage in soybean

3 Materials and Methods

In this section, description of the manufactured dryer and followed methodology (Fig. 4) was discussed.

3.1 Description of the Manufactured Dryer

The dryer has a single compartment for fruit drying and solar energy collection. A rectangular section with an area of $100 \times 50 \text{ cm}^2$ was made using plywood. The inner sidewall of the rectangular compartment was attached with thermocol which acts as an insulator avoiding heat loss to the surrounding through conduction. Then, an aluminium foil is laminated over the thermocol to increase the reflectivity of the walls. Figure 3a, b shows the diagram of solar dryer. At the top two 5 mm, thick glass seats having 2 mm separation in between were attached. Two glass with gap provides better trapping of solar radiation and also reduces convective loss from the top. The front height and back height of the dryer were 30 cm and 45 cm, respectively. Ventilation holes of 2-cm diameter are made at the bottom of the cabinet it acts as inlet point of the fresh air, at rear side of the cabinet which acts as the access point inside the cabinet outlet points for warm air is made with the same dimension. A tray is constructed using a wood frame and steel mesh. Steel mesh is used to avoid rusting due to moisture present inside the cabinet. The tray can be accessed and removed from the rear side.

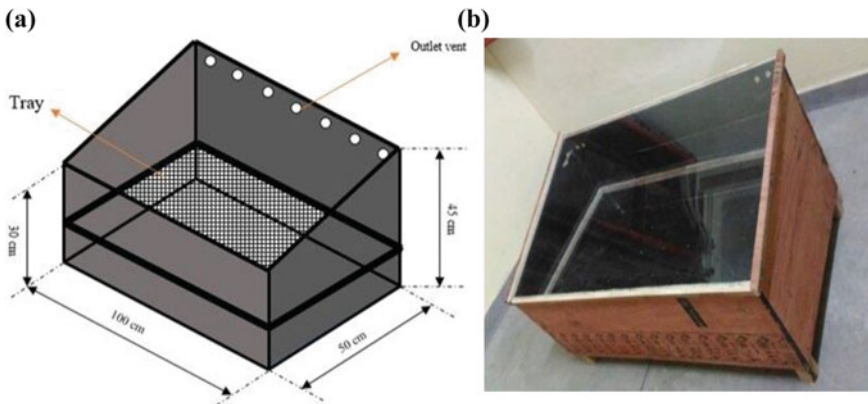


Fig. 3 a 3D model of solar dryer with dimension. b Actual dryer

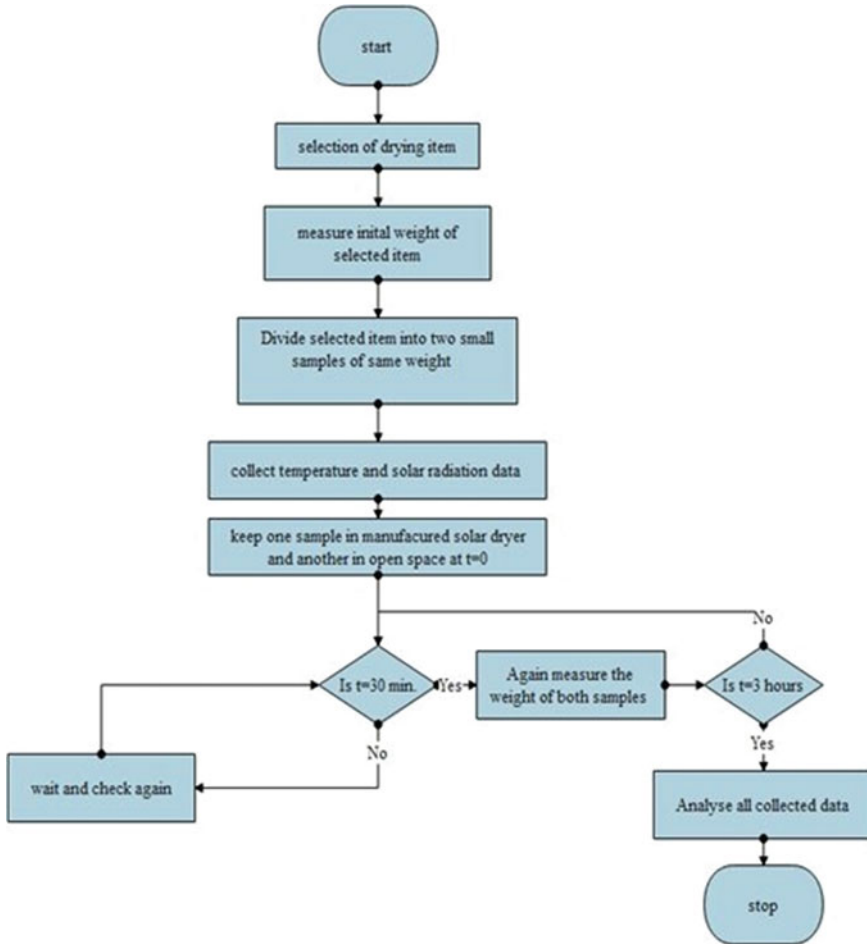


Fig. 4 Followed methodology

3.2 Experimental Details and Methodology

Experiments were conducted in JUET, Guna Madhya Pradesh in the summer season. Two experiments were conducted one using chillies and the other with carrot as shown in the methodology Fig. 4. Experiment begins with weight measurement of two samples of chillies using PCE-BSK 310 balance. Two samples of 50 g each, of chillies were placed, one inside the solar cabinet and the other one is on the floor. Temperature and radiation level were recorded using a digital thermal scanner and pyrometer, respectively. After 30 min, weighing was done of both samples and temperature was noted. This process was repeated after 30 min for 3 h. The weight difference between the initial stage and final stage gives weight reduction. And

consecutive weight difference gives weight reduction rate. Weight reduction with time was plotted for both samples as shown in Fig. 6a.

On the next day, the same process was repeated for carrots from the initial weighing to the final weighing stage. The initial weight was 140.3 g, and its weight reduction curve with time was plotted for both samples as shown in Fig. 6b.

4 Results and Discussion

Figure 5 shows a variation of solar radiation with time and the variation of cabinet temperature in comparison with ambient temperature which is similar to [8, 31]. The maximum temperature achieved by the dryer was 63 °C at 14:00 h which is the ideal temperature for any dryer to remove moisture at a healthy moisture level. Whereas a maximum ambient temperature of 33 °C was recorded this difference increases the drying rate in solar dryer.

Figure 6a shows drying curve of chillies of 50 g. In which, pink line shows weight reduction curve inside the cabinet, and blue line represents weight reduction in open drying. For the same time duration, there was 85.44% of weight reduction in cabinet drying, whereas only 48.64% weight reduction was observed.

Figure 6b shows weight reduction curve for carrot in which black and red lines represent open and cabinet drying, respectively. 140.3 g of carrot shows 83.72% of weight reduction in case of cabinet drying, whereas for open drying it was only 77.4%.

After the experiment, it was observed the quality of the carrot and chillies in the cabinet was superior to the open sun-dried one as shown in Figs. 7a, b and 8a, b.

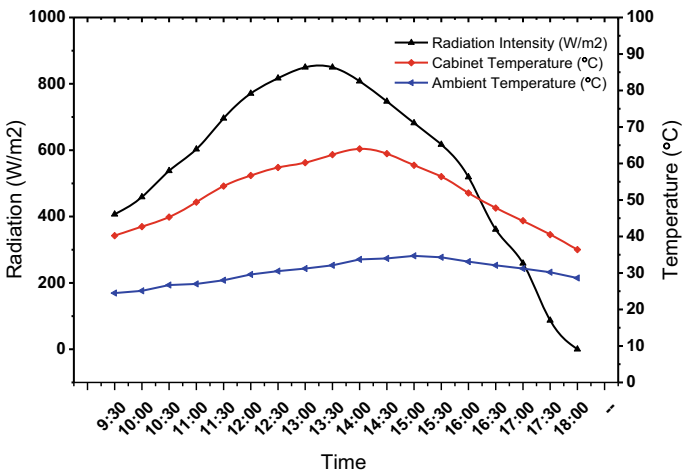


Fig. 5 Variation of solar radiation and the variation of dryer temperature

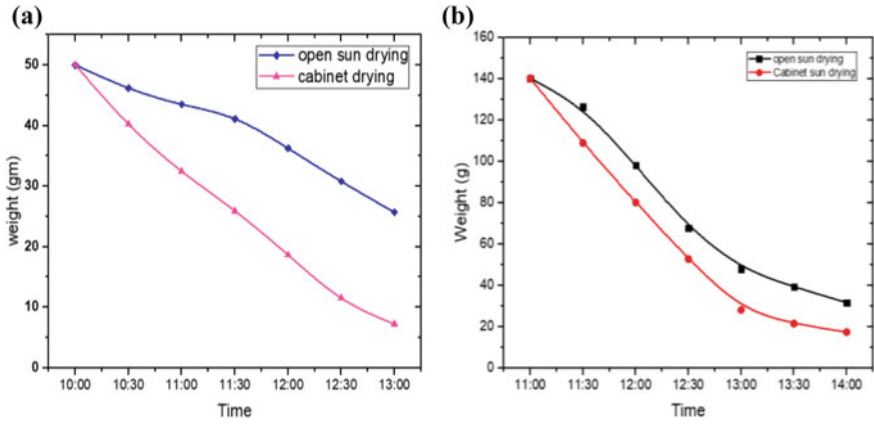


Fig. 6 a Weight reduction curve for chillies. b Weight reduction curve for carrot

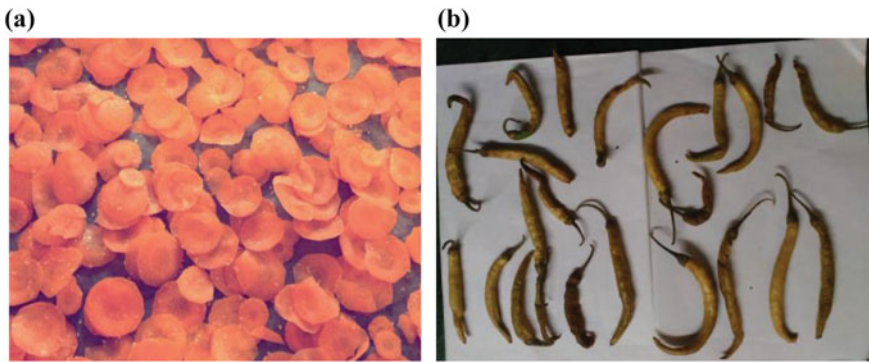


Fig. 7 a Carrot in open drying. b Chillies in open drying



Fig. 8 a Carrot after cabinet drying. b Chillies after cabinet drying

Even though it was a simple solar dryer made with locally available materials, it was able to attain a temperature difference between cabinet and ambient temperature more than 30 °C similar to other studies [8], which is good for a solar dryer for drying vegetables and fruits. Dryer efficiency for chilies and carrots was found to be 9% and 12.53%, respectively, calculated based on the loss of weight in 3 h. which is quite low for a solar dryer with a similar design [32] having drying efficiency of approximately 20%.

5 Conclusion and Recommendations

An economical passive cabinet type solar dryer was constructed to demonstrate the effectiveness of solar dryers using carrots and chillies. A maximum temperature difference of nearly 30 degree was observed between ambient temperature and cabinet temperature. This difference in temperature increases the drying rate in cabinet drying. 85.44 and 83.72% of weight reduction were observed in just 3 h of a short period of solar exposure of solar dryer shows its effectiveness in food drying. Drying of agricultural products is essential as it increases the shelf life of the yield and thus reduces post-harvest losses. In India, farm-level post-harvest losses are 3.82 kg/q for rice and 3.28 kg/q for wheat which is sufficient to feed 10 crores of the population. Post-harvest loss is being neglected in India but sooner or later it will be reflected. This study emphasizes the use of solar dryers for drying agricultural products to reduce post-harvest loss and provides data on loss of agricultural products especially grains in India which need to be taken under consideration.

Following of some suggestions that can help in reducing post-harvest loss.

- Promoting solar dryer-based drying in a rural area by distributing cabinet dryers for drying vegetables at the domestic level can help farmers to understand the concept of the solar dryer.
- The government of India does not have any policies on the promotion of solar dryers. Though the government provides 50–60% subsidy on the purchase of agricultural machinery, which is shared by 60% and 40% of central and state government, respectively, and most of the farmers does not aware of these schemes due to lack of proper information at rural level.
- The modern warehouse does not have enough space to store crops that are produced so there is a need for a secondary greenhouse dryer-based storage unit at panchayat level so that grains can be preserved for a longer duration.

Acknowledgments First author would like to thank Prof. S K Agrawal for kind guidance and also acknowledge the efforts of other student group members of Jaypee University of Engineering and Technology, Guna, M.P. (India).

References

1. Niakousari M, Gahruie HH, Razmjooei M, Roohinejad S, Greiner R (2018) Effects of innovative processing technologies on microbial targets based on food categories: comparing traditional and emerging technologies for food preservation. Elsevier Inc. <https://doi.org/10.1016/B978-0-12-811031-7.00005-4>
2. Ratti C, Mujumdar AS (1997) Solar drying of foods: modeling and numerical simulation. *Sol Energy* 60:151–157. [https://doi.org/10.1016/S0038-092X\(97\)00002-9](https://doi.org/10.1016/S0038-092X(97)00002-9)
3. Bolaji B (2005) Performance evaluation of a simple solar dryer for food preservation, B. In: Proc. 6th Annu. Eng. Technol. Fed. Univ. Technol. Minna, Niger, pp 8–13
4. Bharadwaz K (2020) A review on different solar dryers and drying techniques for preservation of agricultural products abstract. 3:850–859
5. Singh P, Gaur MK (2020) Review on development, recent advancement and applications of various types of solar dryers, *Energy Sources. Part A Recover Util Environ Eff* 00:1–21. <https://doi.org/10.1080/15567036.2020.1806951>
6. Hegde VN, Hosur VS, Rathod SK, Harsoor PA, Narayana KB (2015) Design, fabrication and performance evaluation of solar dryer for banana, *Energy. Sustain Soc* 5. <https://doi.org/10.1186/s13705-015-0052-x>
7. Sharma VK, Colangelo A, Spagna G (1995) Experimental investigation of different solar dryers suitable for fruit and vegetable drying. *Renew Energy* 6:413–424. [https://doi.org/10.1016/0960-1481\(94\)00075-H](https://doi.org/10.1016/0960-1481(94)00075-H)
8. Aliyu B, Kabri HU, Pemi PD (2013) Performance evaluation of a village-level solar dryer for tomato under Savanna climate: Yola, Northeastern Nigeria. *Agric Eng Int CIGR J* 15:181–186
9. Adelaja AO, Babatope BI (2013) Analysis and testing of a natural convection solar dryer for the tropics. *J Energy* 2013:1–8. <https://doi.org/10.1155/2013/479894>
10. Sreekumar A, Manikantan PE, Vijayakumar KP (2008) Performance of indirect solar cabinet dryer. *Energy Convers Manag* 49:1388–1395. <https://doi.org/10.1016/j.enconman.2008.01.005>
11. Udomkun P, Romuli S, Schock S, Mahayothee B, Sartas M, Wossen T, Njukwe E, Vanlauwe B, Müller J (2020) Review of solar dryers for agricultural products in Asia and Africa: an innovation landscape approach. *J Environ Manage* 268:110730. <https://doi.org/10.1016/j.jenvman.2020.110730>
12. Nabnean S, Nimnuan P (2020) Experimental performance of direct forced convection household solar dryer for drying banana. *Case Stud Therm Eng* 22:100787. <https://doi.org/10.1016/j.csite.2020.100787>
13. Lingayat A, Chandramohan VP, Raju VRK (2017) Design, development and performance of indirect type solar dryer for banana drying. *Energy Procedia* 109:409–416. <https://doi.org/10.1016/j.egypro.2017.03.041>
14. Gupta A, Das B, Mondol JD (2020) Experimental and theoretical performance analysis of a hybrid photovoltaic-thermal (PVT) solar air dryer for green chillies. Taylor & Francis. <https://doi.org/10.1080/01430750.2020.1734658>
15. Ssemwanga M, Makule E, Kayondo SI (2020) Performance analysis of an improved solar dryer integrated with multiple metallic solar concentrators for drying fruits. *Sol Energy* 204:419–428. <https://doi.org/10.1016/j.solener.2020.04.065>
16. Bhardwaj AK, Kumar R, Chauhan R (2019) Experimental investigation of the performance of a novel solar dryer for drying medicinal plants in Western Himalayan region. *Sol Energy* 177:395–407. <https://doi.org/10.1016/j.solener.2018.11.007>
17. Djebli A, Hanini S, Badaoui O, Haddad B, Benhamou A (2020) Modeling and comparative analysis of solar drying behavior of potatoes. *Renew Energy* 145:1494–1506. <https://doi.org/10.1016/j.renene.2019.07.083>
18. El Hage H, Herez A, Ramadan M, Bazzi H, Khaled M (2018) An investigation on solar drying: a review with economic and environmental assessment. *Energy* 157:815–829. <https://doi.org/10.1016/j.energy.2018.05.197>

19. Mishra S, Verma S, Chowdhury S, Dwivedi G (2020) Analysis of recent developments in greenhouse dryer on various parameters—a review. *Mater Today Proc.* <https://doi.org/10.1016/j.matpr.2020.07.429>
20. Tiwari S, Tiwari GN, Al-Helal IM (2016) Performance analysis of photovoltaic-thermal (PVT) mixed mode greenhouse solar dryer. *Sol Energy* 133:421–428. <https://doi.org/10.1016/j.solener.2016.04.033>
21. Hatami S, Payganeh G, Mehrpanahi A (2020) Energy and exergy analysis of an indirect solar dryer based on a dynamic model. *J Clean Prod* 244:118809. <https://doi.org/10.1016/j.jclepro.2019.118809>
22. Mohana Y, Mohanapriya R, Anukiruthika T, Yoha KS, Moses JA, Anandharamakrishnan C (2020) Solar dryers for food applications: concepts, designs, and recent advances. *Sol Energy* 208:321–344. <https://doi.org/10.1016/j.solener.2020.07.098>
23. Basavaraja H, Mahajanashetti SB, Udagatti NC (2007) Economic analysis of post-harvest losses in food grains in India: a case study of Karnataka. *Agric Econ Res Rev* 20:117–126
24. Agricultural Statistics at a Glance 2018, 2554. <http://agricoop.gov.in/sites/default/files/agristatglance2018.pdf>
25. Alagh M (2014) Assessment of marketed and marketable surplus of major foodgrains in Gujarat Munish Alagh Centre for Management in Agriculture Indian Institute of Management, Ahmedabad. https://www.iima.ac.in/c/document_library/13Assessment_Marketed_Surplus_Gujarat_Final6a3e.pdf?uuid=7ed1fc64-e12e-48ce-b29b-43f0c3503903&groupId=62390
26. Bordoloi J (2013) Assessment of pre and post harvest losses of paddy and wheat in Assam. [http://www.aercau.org/pages/aerc_report/Assessment of Pre and Post Harvest Losses of Paddy and Wheat in Assam.pdf](http://www.aercau.org/pages/aerc_report/Assessment%20of%20Pre%20and%20Post%20Harvest%20Losses%20of%20Paddy%20and%20Wheat%20in%20Assam.pdf)
27. Grover DK, Singh JM (2012) Assessment of pre and post harvest losses in wheat and paddy crops in Punjab. <https://doi.org/10.13140/RG.2.2.23346.56007>
28. Sarkar D, Datta V, Chattopadhyay KS (2013) Assessment of pre and post harvest losses in rice and wheat in West Bengal. <http://www.visvabharati.ac.in/file/Final-Report-172.pdf>
29. Kannan E, Kumar P, Vishnu K, Abraham H (2013) Assessment of pre and post-harvest losses of rice and red gram in Karnataka. http://www.isec.ac.in/PreandPostHarvestLosses_Karnataka.pdf
30. Dev SM, Sharma AN (2010) Food security in India: Oxfam India working papers series. [https://www.oxfamindia.org/sites/default/files/VII. Food Security in India-Performance, Challenges and Policies.pdf](https://www.oxfamindia.org/sites/default/files/VII.Food%20Security%20in%20India-Performance,%20Challenges%20and%20Policies.pdf)
31. Kamble AK, Pardeshi IL, Singh PL, Ade GS (2013) Drying of chilli using solar cabinet dryer coupled with gravel bed heat storage system. *J Food Res Technol* 1:87–94
32. Sodha MS, Dang A, Bansal PK, Sharman SB (1985) An analytical and experimental study of open sun drying and a cabinet tyre drier. *Energy Convers Manag* 25:263–271. [https://doi.org/10.1016/0196-8904\(85\)90042-1](https://doi.org/10.1016/0196-8904(85)90042-1)

Energetic and Exergetic Comparison of Opaque and Semi-transparent PVT Arrays Under Natural Convection Mode for Building Integration



Amit Sharma, Ravi Kumar, C. S. Rajoria, and Sathans Suhag

Abbreviations

A	Area, m^2
$I(t)$	Solar radiations, W/m^2
P	Electrical energy, W
E	Thermal energy, W
E_x	Overall exergy gain, W
T	Temperature, K
Ψ	Conversion efficiency coefficient

Subscripts

in	Inlet parameter
out	Outlet parameter
m	Maximum condition
PV	Photovoltaic system

A. Sharma · R. Kumar (✉) · C. S. Rajoria
Department of Mechanical Engineering, Government Engineering College Bikaner, Rajasthan
334004, India

S. Suhag
Department of Electrical Engineering, National Institute of Technology, Kurukshetra, Haryana
136119, India

1 Introduction

Solar energy is an inexhaustible, eco-friendly, and freely accessible energy resource on earth. The utilization of solar energy in the civil and industrial sectors is increasing at a rapid pace because it is a lower ecological impression than other conventional ones [1]. Many researchers around the world are worked on the solar base systems. Terrestrial solar radiation comprises 43% infrared rays (IR), 48% visible rays (VR), and remaining are ultraviolet rays (UVR). These radiations are not monochromatic and range of wavelengths between 0.25 and 2.5 μm . These total radiations are not used by photovoltaic system to produce the electricity since it depends on band gap energy of solar cell material and remaining radiation (more than band gap energy) will disseminate as heat in solar cell. This heat is increased the temperature of cell therefore photovoltaic efficiency is decreased [2]. Now photovoltaic cell efficiency varied between 7 and 40%. To improve the performance of photovoltaic system required to maintain lower temperature of solar cell in PV modules, so many research works are carried on heat extraction system.

Yang et al. [3] proposed open loop air-based BIPV/T prototype system and improved thermal efficiency; it adds vertical glazed solar air collector with wire mesh packing. They observed effect of multiple inlets, wind speed, mass flow rate, and wire mesh on thermal efficiency. They developed numerical control volume model and validated with experimental result. They found that 5, 8, and 10% thermal efficiency improved with used of two inlet, vertical glazed, and wire mesh packing. Marginal increment occurs in electrical efficiency. Ozakin et al. [4] had done experimental thermodynamic studies of air-based PVT system with use of different type material fins such as copper, aluminum, and brass. They also used optimization techniques Taguchi and ANOVA to determine best combinations of control parameter like fin material, air velocity, and panel temperature. It used frequent (55 fins) and sparse (27 fins) fins configurations for mono and poly crystal panels. They found that best result occurs in frequent configurations for copper fin material, and it increased electrical efficiency, thermal efficiency, and exergy efficiency 45–48, 61–63, and 107–109% with respect of without fin configurations. Fan et al. [5] developed dynamic model of hybrid photovoltaic thermal collector–solar air heater (PVT-SAH). It is studied to assess the potential of system to provide high temperature outlet air (60–90 °C) with the use of longitudinal fins under dynamic boundary condition. They observed that 35% overestimate thermal gains provided by PVT-SAH under steady-state condition compare with prediction of the dynamic model. Nazri et al. [6] studied on energy economic analysis of photovoltaic thermal thermoelectric air collector. It is described that concept and previous work conducted on thermoelectric and theoretical study performed on PVT-TE air collector. They observed that maximum efficiency is obtained 0.97% at mass flow rate of 0.1 kg/s by use of 90 TE. Annual uniform cost is high for annual overall exergy gain with respect to annual thermal energy gain. Tiwari et al. [7] studied to explore literature on photovoltaic air collector and its integrated greenhouse drying system; they found that forced drying provided better performance in term of controlling drying attributes, and PVT air collector is

better than standalone PV system in term of storage energy. The outcome shown that average thermal, electrical, and overall thermal efficiency are 26.68%, 11.26%, and 56.30%, respectively, for PVT air collector. Amanlou et al. [8] performed numerical and experimental analysis on low concentrated photovoltaic thermal solar collector by use of uniform temperature distribution approach on PV plate. They used eight different geometries diffuser for investigating uniform air flow using CFD method. Results shown that three inner deflectors concave side diffuser improved 20% electrical efficiency. Bambrook et al. [9] done experimental study on unglazed, single pass, open loop PVT air collector. They focused on maximizing the electrical and thermal output by influence of fundamental parameter such air flow rate (0.03–0.05 kg/s m²). It is purposed energy-efficient hydraulic design by using large duct to minimize pressure loss and selection of fan that produce high air flow at low input power. They found that thermal and electrical energy increased with increment of air mass flow rate around 28–55% thermal energy and 10.6–12.2% electrical energy increased. Shamsavar et al. [10] has been experimental and theoretical investigation done on a direct coupled PV/T air collector in which free or forced convection technique used by two four and eight dc fans; therefore, air flow is unsteady and system performance analysis with glass or without glass. They observed that optimum number of fans required for achieving maximum electrical energy and setting glass cover on system lead to improve thermal efficiency and decrease electrical efficiency. Bambrook et al. [11] solved energy balance equation to determine temperature that is functions of distance along collector and calculated thermal energy output under steady state condition. They used RC circuit and capacitor to demonstrate model of PVT air collector. They found that by using of solvable circuit PVT air collector complexity can be easily analyzed. Farshchimonfared et al. [12] determined optimum value of key parameter like channel depth and air mass flow rate for PVT air collector. They varied collector area (10, 15, 25, and 30 m²) and length and width ratio (0.5, 1, 1.5, and 2) to optimize performance of system. They found that for 10° temperature rise and maximum thermal energy output, optimum value of mass/area is constant around 0.021 kg/s m² and optimum depth or air distribution duct are varied 0.09–0.026 m and 0.3–0.5 m, respectively. Fiorentini et al. [13] developed and optimized an innovative solar-assisted HVAC system. This system consisted air-based PVT collector and phase change thermal storage unit integrated with reverse cycle heat pump. This system worked both summer and winter conditions by used day time solar radiation and night time sky radiative cooling, respectively. They presented optimization methodology in operating mode for involving component. Farshchimonfared [14] done optimization and sensitivity analysis of a PVT air collector and linked with residential building. They used optimization methodology for rate of effective thermal output with wide range of air mass flow rate per collector unit areas (0.01–0.2 kg/s m²) and channel depth (0.01–0.09 m). The outcomes show that smaller depth provided good performance, and air mass flow rate is a very sensitive parameter at higher temperature rise opposite this larger depth provide lower temperature rise and less sensitive occurs to variations in air mass flow rate.

By literature survey, it has been observed that limited studies worked on air-based PVT system. This paper represented electrical, thermal, and exergy efficiencies of

air-based PVT system added to two types of PVT arrays such as opaque and semi-transparent arrays. In this study, triangular duct has been used to extract heat and cooling in natural climate condition of Rajasthan. This study shows comparative performance of both type of arrays and follow second law of Thermodynamics.

2 Description of Experiment Setup

The system consists of two type of PVT array which is opaque and semi-transparent PVT array having 7 number of PVT air collectors and each PVT air collector having 1.94 m^2 . In this study, for extract heat from PVT array provided triangular duct. Specifications of both PVT module is shown in Table 1. This parameter is tested under standard conditions at 1000 W/m^2 and $25 \text{ }^\circ\text{C}$. In this study, outlet of one PVT air collector is connected to inlet of second PV module and second PV module outlet is connected to third inlet of PV module and continued up to seven PV module so it is called series connection.

All experiment works done in engineering college Bikaner, Rajasthan, at September month. The main section of air-cooling duct is shown in Fig. 1 in which single inlet and outlet has been provided in circular section.

To ensure thermal insulation, the bottom and sides has been covered by wooden ply (6 mm), polyvinylchloride sheet (6 mm) and polystyrene (25.4 mm). Natural air has been circulated through the duct, and air velocity has measured by anemometer with hot wire. The inlet and outlet air temperature has been measured by K type thermocouples. All measuring devices have been calibrated and adjusted according

Table 1 Specification PVT module

Array type	$P_{\max} (W_p)$	$V_{oc} (V)$	$I_{sc} (A)$	$I_m (A)$	$V_m (V)$
Semi-transparent	270	37.80	9.10	8.66	31.20
Opaque	270	38.16	8.96	8.48	32.46



Fig. 1 Front and side cross section view

to requirement range. Daily climate data have been recorded by weather condition station in data logger.

3 Research Methodology

In this study, electrical, thermal, and exergy have been evaluated by considering natural climate of Rajasthan for September month. For calculating hourly performance of both system, averaging data methodology [15] has been used to carryout performance parameter.

3.1 Electrical Efficiency

Electrical efficiency of opaque and semi-transparent photovoltaic system has been calculated follows:

$$P_{out} = FF * V_{oc} * I_{sc} \text{ (kW)} \quad (1)$$

$$\text{Here Fill Factor(FF)} = \frac{V_m \times I_m}{V_{oc} \times I_{sc}}$$

$$P_{in} = I(t) * A_{pv} \text{ (kW)} \quad (2)$$

where P_{out} is electrical energy output, FF is fill factor, V_{oc} is hourly average open circuit voltage, I_{sc} is hourly average short circuit current, $I(t)$ is hourly average solar radiation, and V_m and I_m are maximum voltage and current. Then electrical efficiency (η)

$$\text{Electrical efficiency } (\eta) = \frac{P_{out}}{P_{in}} \quad (3)$$

3.2 Thermal Efficiency

$$E_{out} = P_{out} + \dot{m}c_p(T_{out} - T_{in}) \text{ (kW)} \quad (4)$$

where E_{out} is output energy of PVT system, \dot{m} is air flow rate (kg/s), c_p is specific heat capacity of air (kJ/kg K), T_{in} and T_{out} are inlet and outlet temperature of air ($^{\circ}$ C). E_{in} input energy of PVT system is as

$$E_{in} = I(t) * A_{pv} \text{ (kW)} \quad (5)$$

Then thermal efficiency (η_t)

$$\text{Thermal efficiency}(\eta_t) = \frac{E_{\text{out}}}{E_{\text{in}}} \quad (6)$$

3.3 Overall Exergy Gain

Maximum useful work that can be obtained by any energy conversion process is known as exergy.

$$\Psi = \left[1 - \frac{4}{3} \frac{T_a}{T_s} + \frac{1}{3} \left(\frac{T_a}{T_s} \right)^4 \right] \quad (7)$$

where Ψ is a conversion efficiency coefficient proposed by Petela, T_a is ambient temperature (K), and T_s is sun temperature which is taken as 5777 K.

$$Ex_{\text{out}} = \sum P_{\text{out}} + \sum \dot{m}c_p(T_{\text{out}} - T_{\text{in}})(\text{kW}) \quad (8)$$

Here, thermal energy is converted into electrical energy by utilization of Carnot cycle, and Ex_{out} is output exergy, and Ex_{in} is input exergy as follow

$$E_{\text{in}} = \Psi * I(t) * A_{\text{pv}}(\text{kW}) \quad (9)$$

Exergy efficiency of PVT system has been calculated by

$$\Psi_{\text{PVT}} = \frac{Ex_{\text{out}}}{Ex_{\text{in}}} \quad (10)$$

4 Experiment Result

The performance of the air-based PVT system for opaque and semi-transparent has been determined by electrical and thermal properties. Experimental work has been performed in Engineering College Bikaner, Rajasthan, under natural climate condition. Experimental work and calculations have been performed with average values obtained from the weather monitoring station installed on the roof top of mechanical engineering department. Hourly variation of solar radiation and ambient temperature is shown in Fig. 2. It has been recognized that maximum solar radiation and ambient temperature are obtained between 12:00 a.m. and 03:00 p.m.

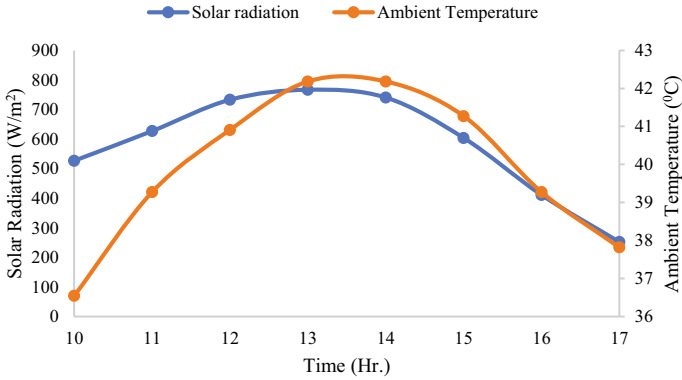


Fig. 2 Hourly variation of solar radiation and ambient temperature

Electrical current and voltage are depended on solar radiation; therefore, electrical current and voltage are fluctuated during the day. Hourly fluctuation in open-circuit voltage and short-circuit current for opaque and semi-transparent PVT array are shown in Fig. 3.

Electrical performance parameter of opaque and semi-transparent has been shown in Table 2. Result of electrical performance depicts that opaque PVT system performs better as compared to semi-transparent PVT system. As seen in Fig. 4, the average electrical efficiency of opaque PVT system is 8.08% higher with respect to semi-transparent PVT system. It can also be observed that the electrical gain reaches a maximum at 5 pm due to less temperature of the modules which can be attributed to the dependence of electrical efficiency on temperature.

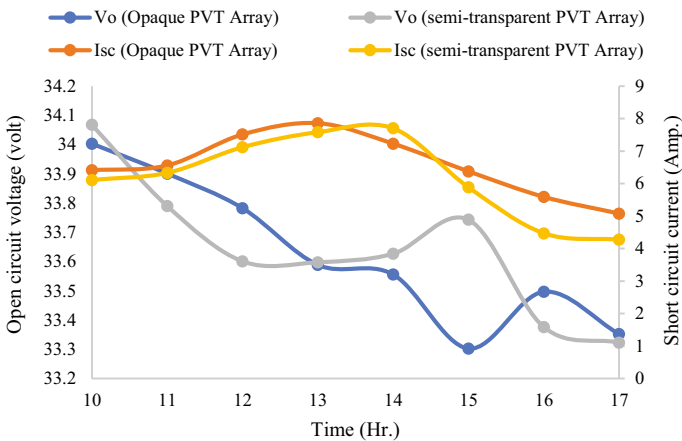


Fig. 3 Hourly fluctuation in open-circuit voltage and short-circuit current

Table 2 Parameters of electrical performance

Time (h)	Solar radiation (W/m ²)	Opaque PVT system			Semi-transparent PVT system		
		P_{in} (kWh)	P_{out} (kWh)	η (%)	P_{in} (kW)	P_{out} (kW)	η (%)
10	526.85	7.15	1.22	17.06	7.15	1.17	16.30
11	627.32	8.52	1.24	14.61	8.52	1.20	14.06
12	733.33	9.96	1.42	14.27	9.96	1.34	13.46
13	767.13	10.42	1.48	14.19	10.42	1.43	13.70
14	740.74	10.06	1.36	13.50	10.06	1.45	14.42
15	604.17	8.20	1.19	14.49	8.20	1.11	13.55
16	411.11	5.58	1.05	18.79	5.58	0.84	14.96
17	251.85	3.42	0.95	27.73	3.42	0.80	23.31

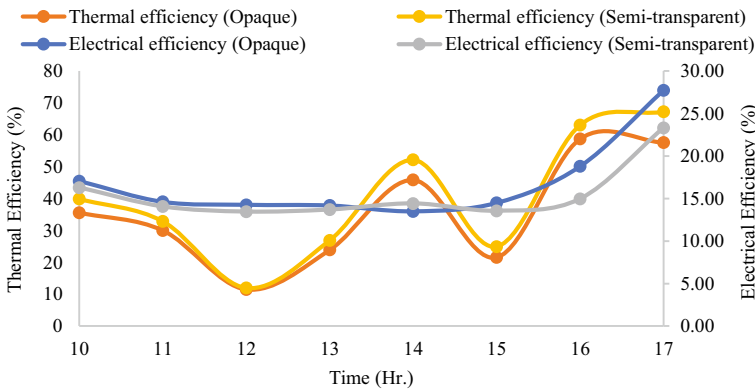


Fig. 4 Hourly variation in thermal and electrical efficiency for Bikaner location

The average thermal efficiency values of the air-based PVT system with changes in the mass flow rate values from 0.03 to 0.10 kg/s for the opaque and semi-transparent were compared. The study shows that the thermal efficiency of the air-based PVT system greatly depends on solar radiation and mass flow rate. All parameters have been shown in Table 3.

The hourly variation of thermal efficiency of opaque and semi-transparent PVT array for Bikaner region has been shown in Fig. 4. The results show that thermal efficiency of system increased with increase of air mass flow rate and solar radiation. Maximum thermal efficiency occurs between 2 and 5 p.m. under natural convection.

It has been observed that under natural convection, the heat extraction greatly depends on the velocity inside the duct, and in the month of September, the velocity was observed to be higher during 4–5 p.m. which has resulted in higher thermal efficiency of both the arrays. The average thermal efficiency of semi-transparent PVT system is increased 10.71% with respect of opaque PVT system due to heat

Table 3 Parameters of thermal performance

Time (h)	Air mass flow rate (kg/s)	Opaque PVT system			Semi-transparent PVT system		
		T_{in} (K)	T_{out} (K)	η_t (%)	T_{in} (K)	T_{out} (K)	η_t (%)
10	0.09	311	340	35.58	310	343	39.86
11	0.07	314	350	30.01	312	351	32.84
12	0.03	316	356	11.53	314	355	11.95
13	0.06	318	361	23.90	315	364	26.88
14	0.10	319	365	45.83	315	367	52.14
15	0.04	317	358	21.57	314	361	24.94
16	0.09	313	351	58.68	312	353	63.05
17	0.06	312	346	57.58	311	351	67.22

dissipation rate of semi-transparent PVT system is higher as compared with opaque PVT array.

The hourly variation of overall exergy gain and overall exergy efficiency of opaque and semi-transparent PVT array for Bikaner region has been shown in Table 4. The result depicts that the overall exergy is higher in opaque PVT system as compared to semi-transparent PVT array, but at 02:00 p.m. the performance of semi-transparent PVT array is higher because of marginal difference in the temperature of both the arrays; therefore, the heat extraction of semi-transparent array is increased as compared to opaque PVT array and thereby increasing the efficiency of the former.

Figure 5 shows that the average overall exergy gain and exergy efficiency of opaque system is higher 1.3%, 2.4%, respectively, as compared to semi-transparent system, but at 02:00 p.m., the overall exergy efficiency of semi-transparent system is increased 9.94% with respect to opaque PVT system. The overall performance of opaque PVT system and semi-transparent PVT array are shown in Fig. 6.

For the September month, energy gain distribution is shown in Fig. 7. The electrical and exergy gain of opaque PVT array is higher by 5.8% and 1.3%, respectively, as compared to semi-transparent, but thermal gain for semi-transparent PVT array is 10.47% higher due to maximum solar energy intensity absorbed by packing area of semi-transparent PVT array and remaining energy is transferred to duct section by non-packing area.

5 Conclusion

In the present study, a comparative performance analysis of opaque and semi-transparent PVT system has been conducted. This analysis was to investigate electrical efficiency, thermal efficiency, and overall exergy gain for both PVT systems. Triangular heat exaction system was fabricated for air flow configuration. All experimental work was conducted in the month of September, and performance evaluation

Table 4 Parameters of overall energy gain

Time (h)	Ambient temperature (K)	Energy conversion factor (Ψ)	Opaque PVT system			Semi-transparent PVT system		
			Ex _{in} (kWh)	Ex _{out} (kWh)	Ψ_{PVT} (%)	Ex _{in} (kWh)	Ex _{out} (kWh)	Ψ_{PVT} (%)
10	310	0.92	6.64	1.45	21.85	6.6	1.44	21.84
11	312	0.92	7.9	1.52	19.19	7.8	1.51	19.15
12	314	0.92	9.2	1.56	16.85	9.1	1.48	16.09
13	315	0.92	9.6	1.80	18.58	9.6	1.80	18.73
14	315	0.92	9.3	1.98	21.27	9.2	2.19	23.62
15	314	0.92	7.6	1.40	18.46	7.5	1.38	18.21
16	312	0.92	5.1	1.41	27.20	5.15	1.24	24.04
17	311	0.92	3.17	1.15	36.20	3.15	1.06	33.57

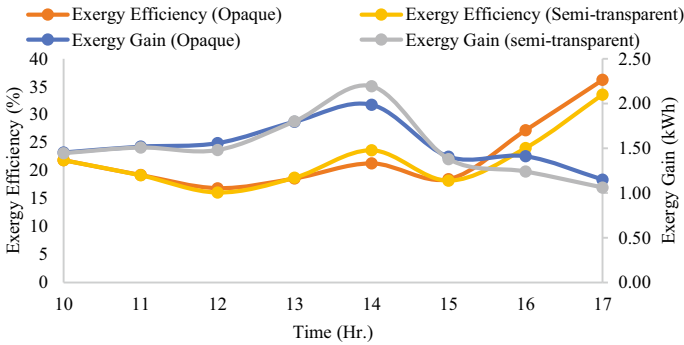


Fig. 5 Hourly variation of overall exergy gain and overall exergy efficiency of opaque and semi-transparent PVT array for Bikaner region

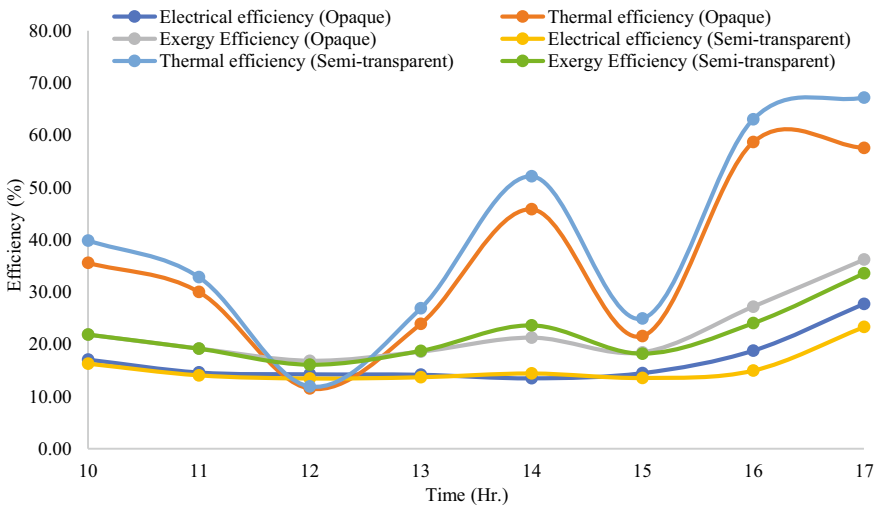


Fig. 6 Overall performance of opaque PVT system and semi-transparent PVT array

has been carried out during 10:00 a.m. to 05:00 p.m. for both PVT systems. The average electrical efficiency of opaque PVT array in the month of September is 8.08% higher with respect to semi-transparent PVT array and the highest being 15.9% at 05:00 p.m. The average thermal efficiency of semi-transparent PVT array is 10.7% higher with respect to opaque PVT array and the highest value obtained 12.09% at 02:00 p.m. The average overall exergy gain of opaque PVT system is 1.3% higher with respect to semi-transparent PVT system, and maximum gain is 7.2% at 05:00 p.m. At 02:00 p.m., the overall exergy gain performance of semi-transparent PVT system is 9.94% higher with respect to opaque PVT system. This investigation can provide a guideline for the analysis of the performance of PVT air collectors

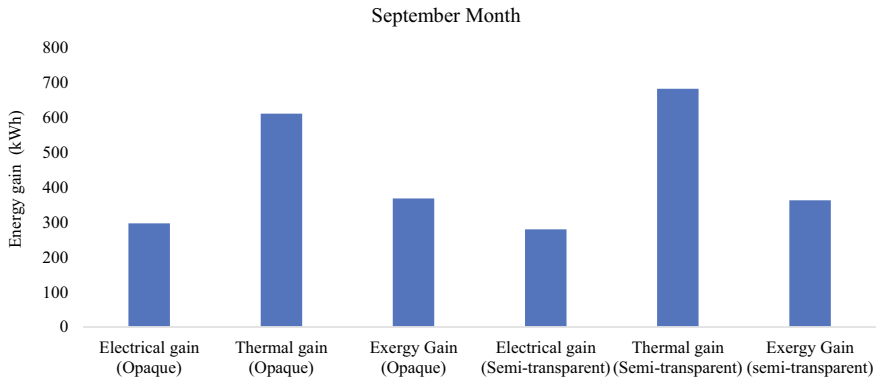


Fig. 7 Distribution of energy gain of opaque and semi-transparent PVT array for Bikaner location

with different type of module. Our goal in future is to control affecting parameters and evaluate optimum condition for our system.

Acknowledgements The authors greatly acknowledge the financial support from the collaborative research scheme (CRS) Project ID 1-5763884671 from NPIU under TEQIP-III phase.

References

1. Kumar R, Rajoria CS, Sharma A, Suhag S (2020) Design and simulation of standalone solar PV system using PVsyst Software: a case study. *Mater Today: Proc.* <https://doi.org/10.1016/j.matpr.2020.08.785>
2. Rajoria CS, Kumar R, Sharma A, Singh D, Suhag S (2020) Development of flat-plate building integrated photovoltaic/thermal (BIPV/T) system: a review. *Mater Today: Proc.* <https://doi.org/10.1016/j.matpr.2020.08.790>
3. Yang T, Athienitis AK (2014) A study of design option for a building integrated photovoltaic/thermal (BIPV/T) system with glazed air collector and multiple inlets. *Solar Energy* 104:82–92
4. Ozakm AN, Kaya F (2020) Experimental thermodynamic analysis of air-based PVT system using fins in different materials: optimization of control parameters by Taguchi method and ANOVA. *Solar Energy* 197:199–211
5. Fan W, Kokogiannakis G, Ma Z, Cooper P (2017) Development of a dynamic model for a hybrid photovoltaic thermal collector-solar air heater with fins. *Renew Energy* 101:816–834
6. Nazri NS, Fudholi A, Bakhtyar B, Yen CH, Ibrahim A, Ruslan MH, Mat S, Sopian K (2018) Energy economic analysis of photovoltaic thermal thermoelectric (PVT-TE) air collectors. *Renew Sustain Energy Rev* 92:187–197
7. Tiwari S, Agrawal S, Tiwari GN (2018) PVT air collector integrated greenhouse dryers. *Renew Sustain Energy Rev* 90:142–159
8. Amanlou Y, Hashjin TT, Ghabadian B, Najafi G (2018) Air cooling low concentrated photovoltaic/thermal (LCPV/T) solar collector to approach uniform temperature distribution on PV plate. *Appl Thermal Eng* 143:413–421
9. Bambrook SM, Sproul AB (2012) Maximising the energy output of a PVT air system. *Solar Energy* 86:1857–1871

10. Shahsavari A, Ameri M (2010) Experimental investigation and modeling of a direct-coupled PV/T air collector. *Solar Energy* 84:1938–1958
11. Bambrók SM, Sproul AB (2016) A solvable thermal circuit for modelling PVT air collectors. *Solar Energy* 138:77–87
12. Farshchimofared M, Bilbao JI, Sproul AB (2015) Channel depth, air mass flow rate and air distribution duct diameter optimization of photovoltaic thermal (PV/T) air collectors linked to residential buildings
13. Fiorentini M, Cooper P, Ma Z (2015) Development and optimization of an innovative HVAC system with integrated PVT and PCM thermal storage for a net-Zero energy retrofitted house. *Energy Build.* <https://doi.org/10.1016/j.enbuild.2015.02.018>
14. Farshchimofared M, Bilbao JI, Sproul AB (2016) Full optimization and sensitivity analysis of a photovoltaic-thermal (PV/T) air system linked to a typical residential building. *Solar Energy* 136:15–22
15. Rajoria CS, Agrawal S, Tiwari GN (2012) Overall thermal energy and exergy analysis of hybrid photovoltaic thermal array. *Solar Energy* 86:1531–1538

Fabrication of IoT System for Structural Health Monitoring Considering Maintenance 4.0



Priyank Srivastava, Anoop Kumar Shukla, Krishna Mohan Agarwal, Sanjeev Kumar Sharma, and Shubham Sharma

Abbreviations

IOT	Internet of Things
PIC16F877	Microcontroller
NodeMCU	Microcontroller
ADC	Analog to Digital converter
DGA	Dissolved Gas Analysis
Tan Delta	Dielectric Dissipation

1 Introduction

There are different types of systems used in monitoring the condition of distribution transform. Traditionally, the monitoring of distribution network is more focused on primary distribution stations, which are located near the power grids because of their high value compared to the distribution transformers placed in a subdivisions such as (locality, industry, villages, etc.) [1]. Distribution transformer is a very useful component as it is a main connection link between utility and customer. Because of this, there can be a tremendous effect on reliability of distribution network due to the failure of distribution transformer. In present, there are smart systems that can be used to monitor the load on a transformer which can monitor the condition of transformer and internal or external electrical failure [2]. Monitoring of a distribution transformer enables the possibilities of avoiding premature aging, fast detection of the fault in a transformer, proactive communication with authority for an appropriate action, etc. There can be an economical constraint in considering the implementation of a smart

P. Srivastava · A. K. Shukla (✉) · K. M. Agarwal · S. K. Sharma · S. Sharma
Amity University Uttar Pradesh, Noida 201313, India

© The Author(s), under exclusive license to Springer Nature Singapore Pte Ltd. 2022
P. Verma et al. (eds.), *Advancement in Materials, Manufacturing and Energy Engineering*,
Vol. II, Lecture Notes in Mechanical Engineering,
https://doi.org/10.1007/978-981-16-8341-1_30

375

system in a large scale as there is a huge amount of distribution transformer in a small region compared to power transformer. The economical comparison between the implementation of these systems and the cost of maintenance once distribution transformer is damaged will be very heterogeneous as we will be able to observe the clear difference between the costs. This system can reduce the economic losses due to breakdown of the distribution transformer by providing the real-time data and the analysis done over it. This system will not be involving any disruption to the working of the distribution transformer to analyze the condition of the system. Economic aspects of a condition monitoring of a distributive transformer and online condition monitoring system for distribution transformer is discussed in [3, 4], respectively. There can be many reasons of the failure of distribution transformer such as dielectric stresses, electrical stresses, electromagnetic stresses, and chemical stresses. The main reason for failure is difficult to deduce as there are so many process parameters. The measurement of the temperature, oil level, sound level, etc., are just a way of finding some of the issues in a transformer rather than finding an exact cause of the fault [5]. There are different type of failures and all of them are shown in a Table 1 given in [5].

There will be no cause to the body of the proposed system as the system will be mounted over the body of the distribution transformer. This will also not interfere with the working of it. This system will be easy to install over the distribution transformer and can be operational as soon as it is installed and connected to the internet for data transfer. This quick and easy installation will make the system easy to use and can be handled by anyone with basic technical knowledge. System is also using some common components which can be easily available in a market in a case of damage by any means. One can modify the system as per their requirement for Maintenance 4.0, where it is a subsystem of Industry 4.0 [6, 7].

Table 1 Causes of distribution transformer failure

Causes	% of failures
Insulation failure	26
Loose connection	7
Over loading	24
Manufacturing Problem	5
Improper Maintenance	16
Oil contamination	4
Line Surges	4
Fire/Explosions	3
Lightning	3
Floods	2
Moisture	1
Unknown	5

2 Literature Review

There are many research papers describing the system for condition of distribution transformer and using some Web Services and these are discussed in a paragraph. Mohamadi and Akbari proposed an on-line monitoring system having GSM modem with a single chip microcontroller and sensors. One will be getting an SMS and data in computer server by using a software [8].

Thiyagarajan and Palanivel had a design which was used to monitor and control different parameters such as oil level, temperature, voltage, and power [9].

Nelson et al. [10] used a system in which multiple sensors are connected to a single chip PIC16F877, a microcontroller, and an application is used made on VisualStudio.NET and MATLAB.

Nelson et al. [3] describe the economical aspect of all the distribution transformer which are having remote condition monitoring systems. These systems are used to provide essential information regarding the status and operation of the distributive transformer. They have compared and analyzed the DT with and without the system in terms of consumer and economic life, revenue loss to utility as well.

Pawar and Deosarkar [11] proposed the development of a mobile-embedded system which will be used to monitor the different parameters of the distribution transformer using multiple sensors and an 8-channel analog to digital converter (ADC) in an embedded system with system memory. They also designed a system to send an alert to mobile phones and monitoring units. They have used PIC18F4550 microcontroller connected with GSM module and a self-made software for the processing of the data collected from the sensors.

Jamal et al. [12] developed an efficient and reliable IoT-based system which is developed for thermal monitoring and protection system. They have developed different units such as current sensing unit, humidity, and temperature measuring units which will be sensing the data and sending it to microcontroller and then to network space called ThingSpeak. This will be used to update data in real time for monitoring purpose, and then alert can be sent to the recipient using it. This system will also trigger the coming fan in a transformer as the system is developed for thermal monitoring and protection.

Jaiswal et al. [4] had a proposal of an economical approach to calculate and determine the status of health by processing an online available data by intelligent condition monitoring system. These online data can be either measured by self-using multiple sensors connected to it or by the online data available.

Faria et al. [13] presented a solution for the condition monitoring and diagnosis for the distribution transformer. They proposed a system with lots of different sensors and components in such a way that they have used three PCB to mount them in a U-shape. This will enable the study of all the elements which are being observed and will improve the quality of the services such as preventive and predictive maintenance.

By going through all the literature and reviewing them well, it was concluded that everyone has their own system to monitor the condition of the distribution transformer and each system is developed to reduce the cost and improve the efficiency and quality

of data and analysis. But by proposed microcontroller NodeMCU and Amazon Web Service (AWS), we can enhance it more and can move one step ahead by using cloud applications from AWS for IoT.

3 System Design and Fabrication

As we have already discussed the literature for the system development and analysis of the data by them, but in this paper, we have proposed the system fabrication as a primary objective to collect the data from the distributive transformer. This system will collect the essential data from the distribution transformer and send those data to the AWS IoT apps. To collect data, one should know the parameters to be monitored, and for that, we will be measuring temperature, current, oil level, humidity, and sound level (humming noise). These are not the only parameters to be considered for the condition monitoring of the distribution transformer; there are other parameters too such as DGA, TAN, and DELTA measurement of bushiest, etc., which are not considered due to the economical concern as we are working on making an economical system for the distribution transformer monitoring [14].

3.1 Components

The system contains the various components which will be using to measure the parameters we have mentioned earlier in this paper.

The component used to measure the temperature and humidity will be DHT 22 (temperature and humidity) sensor. This sensor is used due to its configuration such as measuring temperature ranging from -40°C to $+125^{\circ}\text{C}$ with $\pm 0.5^{\circ}\text{C}$ accuracy. Talking about humidity measuring range from 0 to 100% with 2–5% accuracy.

Next, we will be measuring the current, so we will be using ACS712ELCTR-30A-T because it can measure 30 to -30 A current, and if there is 66 mV change in output, voltage from initial state represents 1-A change in input current. We will be using 3 ACS712ELCTR-30A-T sensors tech for the three different phases.

Next, we will be measuring the sound and the oil level. To measure the sound, we are using SparkFun Sound detector which will be giving us analog and digital output with. Analog output will be in.wav format because it is small in size [14]. Potentiometer will be coupled with the magnetic oil gage (MOG) which is coupled with an analog needle which represents the level of the oil in an oil level meter of the overhead oil reservoir of the distributive transformer. As the needle rotates due to the magnetic couple, the potentiometer note will also rotate as it will be coupled to the needle of the gage and give an analog output which will be converted into the level of oil by programming.

To connect these all components together and process a data and upload it, we will be using a brain called NodeMCU which is best suited for the development of

any IoT project as it is low in cost with WiFi module using ESP8266 chip. This is a compact microcontroller which is economical and can be used anywhere with low voltage. The only disadvantage of this microcontroller is that it is having one analog port (A0) and rest of the ports are digital. This makes us to connect an external component so that we can connect the sensors with analog output to the NodeMCU.

By using 74HC4051 Multiplexer/Demultiplexer chip which is a digitally controlled analog switch. It is a single 8 channel multiplexer having binary control input A, B, and C also having an inhibit input. These three binaries collectively decide to select 1–8 channels to be turned on and connect one of the 8 different inputs to the output. So, 8 different analog output sensors to one NodeMCU can be connected for high performance and less cost.

3.2 Overall Structure of System

From Fig. 1, one can understand the basic working principle of the proposed system. As there will be different sensors mounted over the surface of the distribution transformer, and these sensors will be connected to the brain of the system called NodeMCU. These connections will be made either directly if they are having digital output or indirectly by using 74HC4051 Multiplexer/Demultiplexer chip if the output of the sensors is analog. DHT 22 and SparkFun sound detector (one of its PIN) will be having digital output and ACS712ELCTR-30A-T, Potentiometer & SparkFun Sound Detector will be having analog output. (It is recommended to use all the sensors with the voltage of 5 V as that can help to collect the data for the sensor by using a long wire cord too) (Fig. 2).

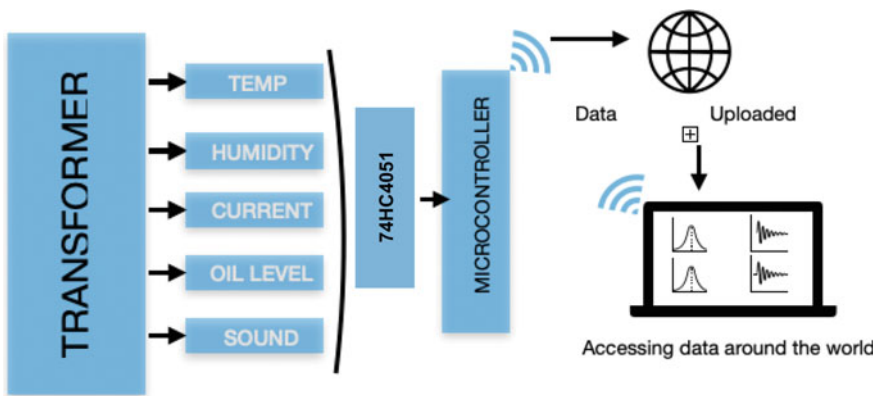


Fig. 1 System diagram representing working structure for monitoring

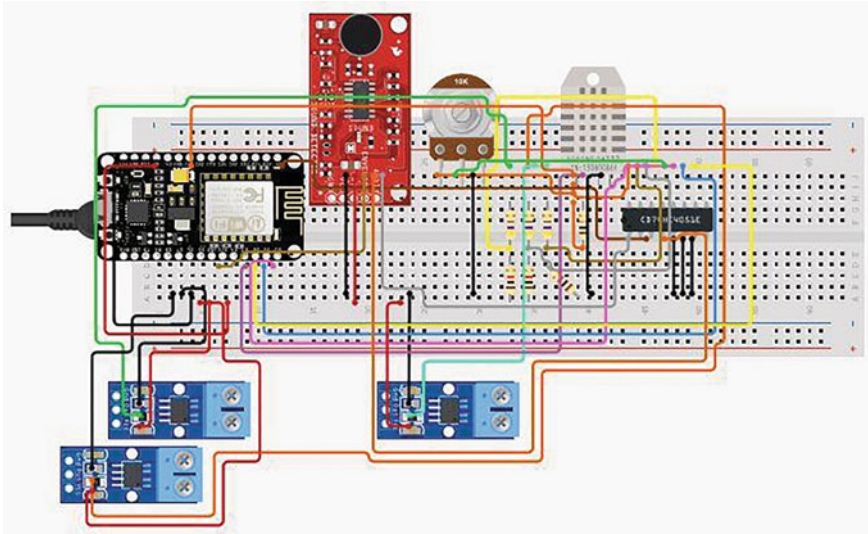


Fig. 2 Connection of all the components to develop a proposed system

3.3 Wireless Monitoring

By using NodeMCU-ESP8266 as a microcontroller for the system, it can be connected to the Internet by any nearby network using WiFi so that connection between cloud and sensor data can be established and used for research purpose for anyone (open source) or to trigger the alert if any of the parameter is out of its desired level. Amazon Web Service (AWS) will be used for this. AWS is having a dedicated section for IoT applications [15]. The connection of the AWS and the system can be established and different apps can be used to analyze data and use it to send a mail, SMS, control the components, etc.

4 Conclusion

Prototype of the proposed system is developed and the connection is well established between the AWS and the hardware. This system is collecting the data well, and its working is encouraging for now. There are different types of applications used from AWS IoT to explore the possibilities and capability of the system to monitor the distribution transformer. In further work and publication, the results will be evaluated and different applications use will be discussed and published.

5 Future Work

In future work, one can work on placing the proposed system on distribution transformer and collect the sensors data periodically in a cloud database. Then the different type of applications can be used on the data stored by the system by using the application provided by AWS IoT such as: AWS IoT Core, FreeRTOS, AWS IoT Greengrass, AWS IoT 1-Click, AWS IoT Analytics, AWS IoT Button, and AWS IoT Device Defender. The data collected will be in an open platform from where any researcher or engineer can use the data for their study and research purpose. The analysis of data can be used to prevent and predict the faults and failures in distributive transformer; note that the first paragraph of a section or subsection is not indented.

References

1. Alves JM, Carreira P, Ferreira H, Pereira H, Oliveira J, Cardoso F (2013) Smart grids: asset management in primary distribution substations, with smart sensor networks
2. Wang MVAJ, Vandermaar AJ, Srivastava KD (2002) Review of condition assessment of power transformers in service. *IEEE Electr Insul Mag* 18(6):12–25
3. Nelson AA, Jaiswal GC, Ballal S (2014, October) Economical aspects of remote condition monitoring system for distribution transformer. In: 2014 international conference on power, automation and communication (INPAC), pp 45–49. IEEE
4. Jaiswal GC, Ballal MS, Tutakne DR, Vishnu P (2018, January) Intelligent condition monitoring system for distribution transformer and health status diagnosis. In: 2018 international conference on power, instrumentation, control and computing (PICC), pp 1–6. IEEE
5. Srivastava P, Shukla RK, Sharma S, Khanduja D, Gupta R, Alrasheedi M, Singh G (2020, January) Fuzzy methodology approach for prioritizing maintenance 4.0 attributes. In: 2020 international conference on computation, automation and knowledge management (ICCAKM), pp 308–311). IEEE
6. Srivastava P, Mustafa A, Khanduja D, Chowdhary SK, Kumar N, Shukla RK (2020) Prioritizing autonomous maintenance system attributes using fuzzy EDAS approach. *Procedia Comput Sci* 167:1941–1949
7. Mohamadi SH, Akbari A (2012) A new method for monitoring of distribution transformers. Retrieved June 1, 2020, from <https://doi.org/10.1109/eeeic.2012.6221453>
8. Thiyagarajan V, Palanivel TG (2010) An efficient monitoring of substations using microcontroller-based monitoring system. *Int J Res Rev Appl Sci* 4(1):63–68
9. Siddique MAA, Mehruz S (2015, December) Artificial neural networks based incipient fault diagnosis for power transformers. In: 2015 annual IEEE India conference (INDICON), pp 1–6. IEEE
10. Nelson AA, Jaiswal GC, Ballal MS, Tutakne DR (2014) Remote condition monitoring system for distribution transformer. Retrieved June 1, 2020, from <https://doi.org/10.1109/npsc.2014.7103848>
11. Pawar RR, Deosarkar SB (2017, July) Health condition monitoring system for distribution transformer using Internet of Things (IoT). In: 2017 international conference on computing methodologies and communication (ICCMC), pp 117–122. IEEE
12. Jamal H, Khan MFN, Anjum A, Janjua MK (2018, December) Thermal monitoring and protection for distribution transformer under residential loading using internet of things. In: 2018 IEEE global conference on internet of things (GCIoT), pp 1–6. IEEE
13. Faria JR, Lima DM, Cardoso FJ (2018, October) A smart multi-sensor for the diagnosis of distribution transformers. In: 2018 IEEE SENSORS, pp 1–4. IEEE

14. Nelson AA, Jaiswal GC, Ballal MS, Tutakne DR (2014, December) Remote condition monitoring system for distribution transformer. In: 2014 eighteenth national power systems conference (NPSC), pp 1–5. IEEE
15. Internet of Things (IoT)—Overview of Amazon Web Services, from <https://docs.aws.amazon.com/whitepapers/latest/aws-overview/internet-of-things-services.html>

Effect of Biodiesel on Engine Performance and Emissions



Anna Raj Singh, Sudhir Kumar Singh, and Siddharth Jain

1 Introduction

The overusage of natural resources is at its highest peak due to which the cost in the synthesis of natural petrol resource is increasing and cannot be recycled. Biofuels work as a substitution for natural resources, and these resources can be in different varieties as liquid or gas synthesized from the source of biomass. Biofuels can be operated separately in diesel engines or combined with petrol. Biofuels are categorized into three varieties of biodiesel [1]. In the first generation, biofuel is ethanol which is developed from sugar. Wheat, corn, and barley come under the same category. The second-generation biofuel is synthesized from lignocellulosic biomass such as grass, straw, and wood. The algae oil comes under the third generation which has been produced from varieties of feedstock materials from algal biomass. The researchers have been focused on renewable sources of biofuel; as incoming generations, the non-renewable resources will be in a limited range. Global warming is the reason due to increase in the amount of carbon dioxide from fossil fuels [2]. The algae are the best choice in the production of biodiesel as it has less range of pollutants like carbon, hydrocarbon, and nitrogen oxide which make it environmentally friendly and can be reused again. The production of algae can be easily done in any environmental conditions in aquatic or salty areas. With the use of the third generation of biodiesels, the demand for crude oil can be reduced as such type of biodiesel can be reused and recycled very easily and is cheaper than diesel fuel [3, 4]. The biodiesel in the diesel engines leads to the elevation of nitrogen oxide particulates and reduction in hydrocarbon with carbon dioxide. Blends of biodiesel have been

A. R. Singh · S. K. Singh
School of Mechanical Engineering, Galgotias University Greater Noida, Noida, Uttar Pradesh
203201, India

S. Jain (✉)
Department of Mechanical Engineering, College of Engineering Roorkee, Roorkee 247667, India

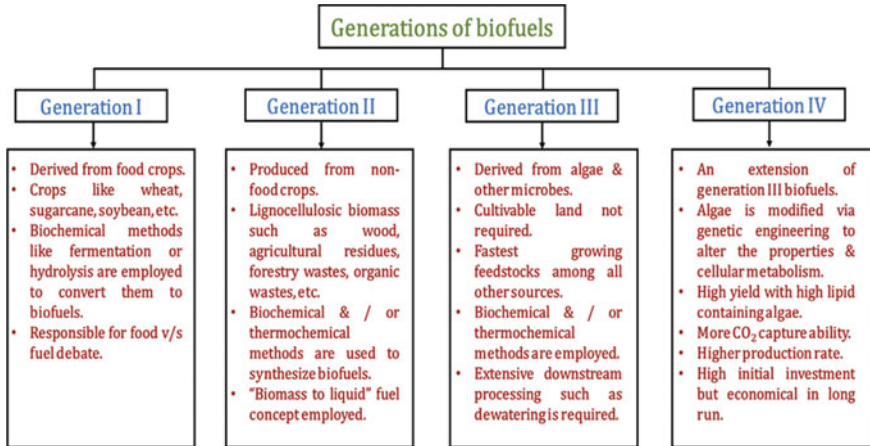


Fig. 1 Generation of biofuel [13]

used by researchers in which B 30 biofuel has been more effective as compared with diesel fuel [5–7]. The use of response surface methods in the synthesis as well as in the enhancement of varieties of blends seems to be efficient jatropha curcas oil and has been considered as a favorable feedstock in the yielding of natural fuel. The pure configuration of such oil is not suited until the addition of some metal adulterants [8–12] (Fig. 1).

2 Comparison of Properties of Biodiesel with Petroleum Diesel Fuel

The molecular size in both fuels remains accurate but there is variation in the chemical structure. Chemical like FAME is present in the biodiesel as compared to petroleum diesel with 95% hydrocarbon along with 5% fragrant compounds. The biodiesel has better lubricating properties and can result in a reduction of friction in moving parts of the engine. The contents of sulfur pollutants are lower than petroleum diesel which reduces the pollution in the environment. The oxygen contents are excessive in biodiesel which results in minimization of power in the engine as compared to petroleum diesel fuel. In low-range temperature, the biodiesel gets stiffened than petroleum diesel fuel. The chemical activity in the form of solution is due to which it can easily react with some substance which is invulnerable with diesel fuel. Few properties present in biodiesel are not suitable for the performance of the engine. The use of additives makes them idle for operating diesel engines. The use of additives makes them stable in low temperatures up to 5 °C. The additives keep the fuel in stable condition and bring down the chances of decomposition of biofuel. They also

avoid the formation of corrosion in the engine parts by developing a shield of a layer to reduce the wear and tear of engine parts due to corrosion [14–20].

3 Methods of Biodiesel Production

Figure 2 shows different biodiesel preparation/oil modification methods.

3.1 Pyrolysis

It is the conversion of a natural substance into solid, liquid, and gaseous forms at peak temperatures of 500–800 °C with the help of decomposition in the lack of air. The pyrolysis at the same time faces variation in chemical distribution and the physical properties. This method is irreversible and endothermic. The products of the pyrolytic are fuels, biochar, and gases like methane, carbon dioxide, carbon monoxide, and hydrogen gases. The materials used are coal, paper, biomass, and waste products of food and animals. There are two types of pyrolysis which are named slow and fast pyrolysis. The slow pyrolysis method is less favorable as it is very time-consuming. The temperature for slow pyrolysis is set at 300–700 °C and the product is biochar. The fast pyrolysis works in a range of 400–800 °C. This method is quicker than that of slow pyrolysis and provides residence time which is lower than one second. The synthesis of bio-oil is estimated to be 60% with a calorific rate of 3500 kcal. In areas where there is a lack of petrol this methodology been preferred for decades [22] (Fig. 3).

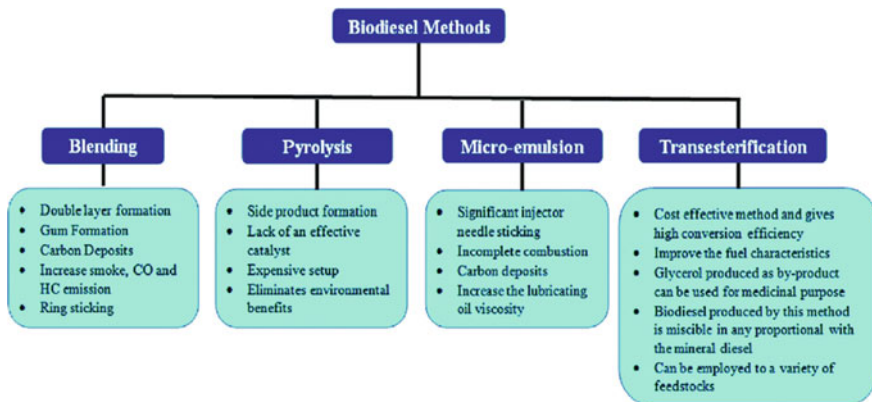


Fig. 2 Methods of biodiesel production [21]

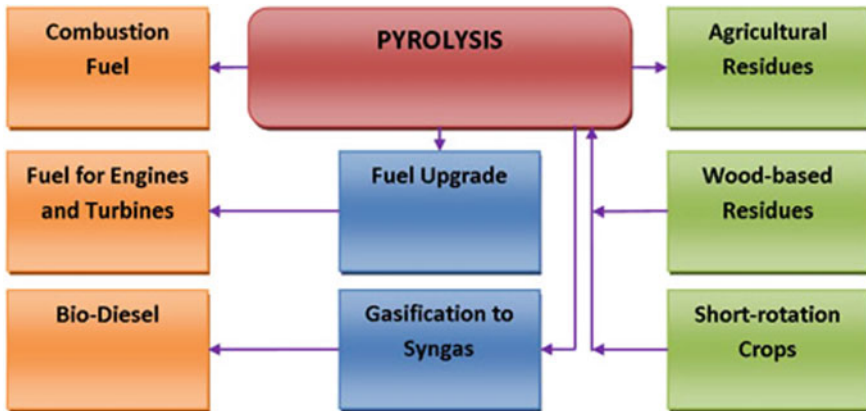


Fig. 3 Pyrolysis method [22]

3.2 Blending

Different blends of biodiesel are been performed by researchers for the usage of biofuel in diesel engines. The various categories are B5, B20, and B100. B20 is cheaper, ecofriendly to the natural surroundings, suitable with the material and operative in cold climate reigns. Such type of biofuel blends can be easily used in any type of engine model without making any adjustment in the design of the engine. The performance of the diesel engines on diesel fuel is similar to the application of B20 biofuel blends. The pollution of harmful gases from 10 years older car engines has been reduced with the use of biofuel blends. The engines installed with catalytic converter devices also resulted in less formation of harmful pollutants with the usage of both biofuel and diesel fuel. These are the best alternatives to reduce the greenhouse gases which result in global warming.

The B100 shows different properties as compared to B10 biofuel blends. B100 biofuel blends result in less power as compared to petroleum diesel fuel. The purest form of biodiesel is B100 which indicates higher the purity of biodiesel less power it will provide to the engine. The B100 may damage the sealing in diesel engines. It is not suitable in cold climatic reigns as compared to B10. In some engines, issue of excessive viscosity is resolved with the process of transesterification [23, 24].

3.3 Transesterification Process

It is a method through which the biodiesel is produced in which the present ester gets modified to a new variety of ester. The by-product that remained in the process of transesterification is glycerol which gets settle down and the biodiesel which is

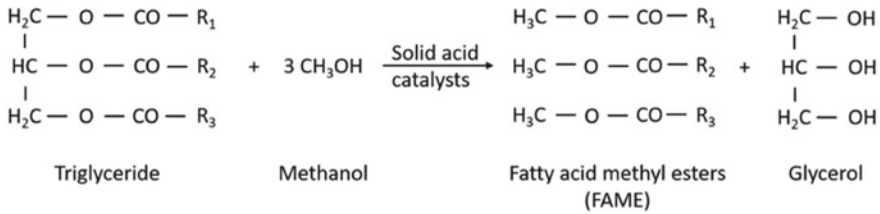


Fig. 4 Acid-catalyzed transesterification [25]

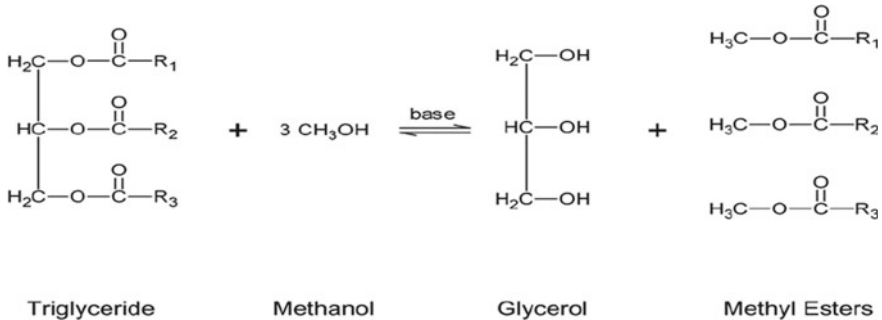


Fig. 5 Base-catalyzed transesterification [26]

lighter in weight gets collected at the top. There are three reversible stages. The transformation of triglycerides in the form of diglycerides, in the second stage of diglycerides gets converted into monoglycerides and in the third stage, monoglycerides get converted into glycerol. In the transesterification process, there are three varieties of catalyzed type transesterification. The researchers mostly prefer the acid-based transesterification method to synthesize the biofuel. If the quantity of free fatty acids is larger, it will result in the formation of soap in the transesterification process. The enzyme-catalyzed transesterification process is very less preferable as it is expensive to operate but an issue of catalyst separation is easier in this method (Figs. 4, 5, and 6).

4 Effect of Biodiesel on Engine Performance

In this, the review toward the variation of engine parameters like consumption of fuel and output power of engine along with its efficiency has been analyzed by various researchers.

Cherng et al. [28] analyzed the performance of the engine by using fish oil which has been produced by waste organs of fish. It has been observed that with the rise in the speed of diesel engines the overall efficiency of the brake fuel alteration has

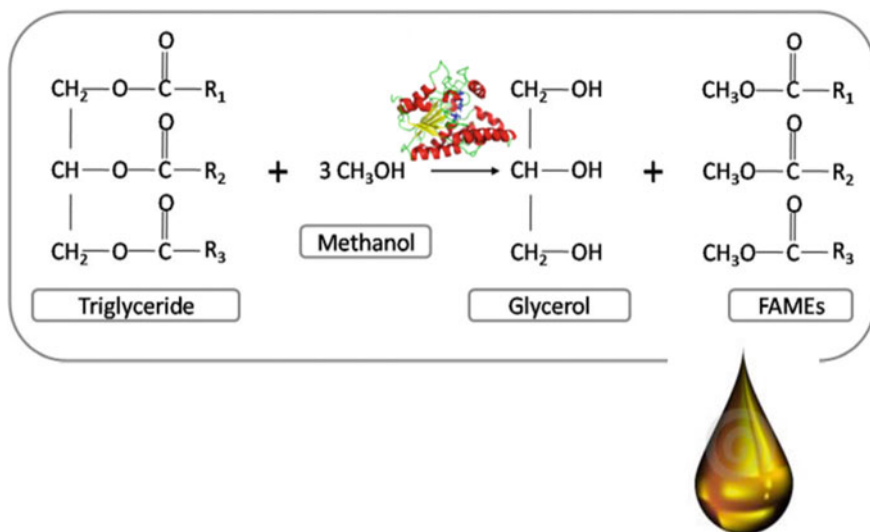


Fig. 6 Enzyme-catalyzed transesterification [27]

improved. The diesel engine seems suitable to operate and is eco-friendly with the environment.

Godiganur et al. [29] measured the variation in the engine performances by purposing methyl esters of a fish oil operated on Kirloskar H4394 diesel engine. It has been observed that biofuel seems a better substitute for diesel-based fuel from natural resources. It is concluded that the specific brake consumption of fuel for the B100 result seems to be favorable. The range of thermal efficiency was noted to be 31.74% which is more preferable as compared to diesel fuel.

Murugesan et al. [30] discussed that the B100 biodiesel in the form of methyl ester can be operated without changing the design of the engine model. The B100 biodiesel resulted in slighter enhancement with low brake specific energy as compared to diesel fuel.

Lujan et al. [31] concluded that the varieties of biodiesel blends can be easily operated in diesel engines in varied proportions combined with the diesel-based fuel. The efficiency of the diesel engine remains compatible for operating which has been recorded same from diesel fuel separately.

Utlu and Kocak [32] used the waste frying oil to produce methyl ester which is examined to inspect the performance of diesel engines which consist of a direct injection system. The waste frying oil can be recycled and reused again which is not possible in the case of diesel fuel. The properties present in the waste frying oil either in chemical or physical form are quite comparable with the diesel-based fuel. Biofuel is cheaper for application purposes and serves better economy as well as efficient performance in diesel engines.

Xue et al. [33] stated that many methodologies were adopted by various researchers in the production as well as in the study of biodiesel on engine parameters. There was no closure for the case of power restoration in some case study of biofuel.

Chhetri and Watts [34] concluded that the chances of reduction in the engine performance are due to the cause of deficient atomization inside the engine cylinder as the biodiesel consists of intensified tension in its surface.

Carraretto et al. [35] cleared that the increase in the proportion of biodiesel in form of blends will reduce the power and the performance of the diesel engine. They used different varieties of biofuel blends from B20 to B100 and operated them on diesel engines which resulted in a reduction in the efficiency of the engine.

5 Review Based Observation From Various Journals

With the use of biodiesel in the engine, it is very common to face power loss. The loss of this power is resolved by using a low proportion of biofuel blends, and also if the load on a vehicle is less, the engine efficiency as well as its performance will be accurately similar to a diesel-based fuel with less pollution. The heating range of biodiesel is lower as compared to diesel fuel which has been accepted by various researchers. The role of feedstock toward the reduction in the engine power seems to be less concerned.

Proper knowledge of the functioning of the injection system in the cylinder head along with the suitable range of pressure used for spraying inside the engine must be researched widely to get the best favorable design for using the biodiesel. The use of additives helps in the reduction of incomplete combustion by improving the timings of ignition in the cylinder [36]. The overconsumption of biodiesel is due to the reduced value of the biofuel heating and also the density along with the viscosity are at peak level. The researchers experimentally perform different categories of feedstock in the biodiesel which have variations in its heating value and the design structure of the carbon chain, and all these parameters affect the performance or economy in the engine.

The use of additives is a better way to improve the economy as well as the operating parameters. Various types of oils have been performed at a reduced temperature range with biofuel blend which resulted in a fair yield which is up to 81.98%. The use of various heterogeneous catalysts enhanced the transesterification process as compared to homogenous catalysts. The issue related to the oxidation has been sorted by the addition of petroleum-based biodiesel at a low ratio without antioxidants in it. The waste products have also been utilized in the synthesis of bioenergy as well as biofuels. Less amount of modification inside the engine cylinder is needed for the low proportion of biofuel blend like B20 [37–45]. The use of soybean blends provides the same results when compared to petroleum diesel in comparison with torque and performance in its engine speed in Fig. 7.

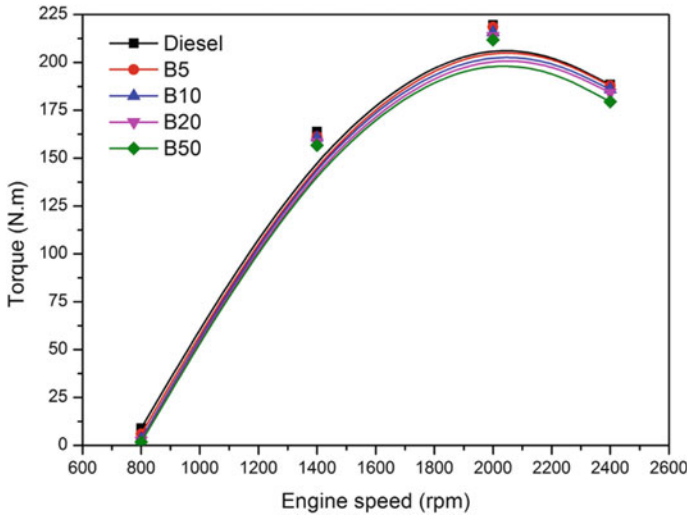


Fig. 7 Engine performance with use of soybean biodiesel blends [46]

6 Effect of Biodiesel on Engine Emission

In this, the review of the emissions of gases like nitrogen dioxide, carbon dioxide, carbon monoxide along with hydrocarbon has been evaluated by researchers.

Karthikeyan et al. [47] performed the experimental analysis by using *Botryococcus braunii* algae as feedstock along with nanoadditives of CuO_2 . To examine the characteristics of the emission, the engine is operated at a fixed rpm of 1500. The nanoadditives used in the diesel engine yield a reduced amount of hydrocarbon, carbon monoxide, and smoke pollutants. A slight rise in the level of nitrogen oxide pollutants has been observed. The ratio of surface to volume along with the rise of the mixture of air and fuel has considered the reason for increase in nitrogen dioxide.

Mahendran et al. [48] analyzed emission gases by using blends of biofuel which are named B5, B15, and B25 and have inspected, and their performance is correlated with the diesel fuel. It is been observed that the amount of carbon monoxide gas released is larger as compared to diesel fuel. It is due to incomplete atomization which results in improper combustion leading to a rise in the gases of hydrocarbon which is not burned properly inside the cylinder. The smoke formation is larger as compared with the clean diesel fuel. It seems a fairer biofuel that can be operated at a cheaper cost.

Saravanan et al. [49] worked toward the reduction of the particulates of carbon dioxide by the use of antioxidant named butylated hydroxytoluene with B20 biofuel blend. The timings in the injection system are to be analyzed at the leading stage and backward stage in the diesel engine. When the timing in the injection is lowered and raised, the particulates of nitrogen oxide gas are reduced; similarly, when injection

timings have been raised and lowered, the particulates of gases like carbon monoxide and unburnt hydrocarbon gas are enriched.

Sayed et al. [50] performed the experimental analysis by running dissimilar products of biofuel and biofuel blends. The variation in loads of engine has been done to analyze the engine emissions at a fixed momentum of 1500 rpm. It has been remarked that the gases like carbon monoxide, hydrocarbon, and the particles of smoke showed less emission for the biodiesel varieties like palm, jatropha, and biofuel blends. The waste cooking oil resulted in a large quantity of carbon dioxide gas which has been used in the form of blends. Rise in the particulates of nitrogen dioxide from the mixtures of biodiesel is in the form of B20 and B10.

7 Conclusions

Biodiesel got a large amount of experimental analysis in the research field as it is the best source of eco-friendly biofuel which can be yielded at a cheaper cost. Biodiesel developed from a variety of feedstock as well as in the form of blends resulted in similar properties which are suitable with natural diesel. Due to the enlargement of its requirement in the global areas of the transportation sector, researchers are now studying possible new methodologies to develop cleaner and efficient biodiesel with less harmful gases while using it for the industrial and automobile sector. The use of heterogeneous catalyst is to be given more attention in transesterification as these types of catalyst have a good surface area and can be reused again and will lead to the enhancement of engine performance as well as low emissions. Based on the following reviews, it has been concluded that the synthesis of biodiesel by the implementation of various blends or from various starting material of biofuel seems a better processing technique to develop eco-friendly biofuel and will make the environment cleaner and will diminish toxic pollutants.

References

1. Rasool U, Hemalatha S (2016) A review on bioenergy and biofuels: sources and their production. *Braz J Biol Sci* 3(5):3–22
2. Dwivedi G, Jain S, Sharma MP (2011) Impact analysis of biodiesel on engine performance—a review. *Renew Sustain Energy Rev* 15(9):4633–4641
3. Ahmad F, Khan AU, Yasar A (2013) *Afr J Environ Sci Technol* 7:358–364
4. Bhatia S (2014) *Advanced renewable energy systems (Part 1 and 2)*, WPI, Publishing, pp 1–31
5. Khalid A, Osman SA, Jaat NM, Mustaffa N, Basharie SM, Manshoor, B (2012) Performance and emissions characteristics of diesel engine fueled by biodiesel derived from palm oil. In: *International conference on mechanical and manufacturing engineering*, vol 3, No. 150
6. Srinivasa RP, Gopalakrishnan KV (1991) Vegetable oils and their methyl esters as fuels for diesel engines. *Indian J Technol* 29:292–297

7. Piloto-Rodríguez R, Sánchez-Borroto Y, Melo-Espinosa EA, Verhelst S (2017) Assessment of diesel engine performance when fueled with biodiesel from algae and microalgae: an overview. *Renew Sustain Energy Rev* 69:833–842
8. Chamola R, Khan MF, Raj A, Verma M, Jain S (2019) Response surface methodology based optimization of in situ transesterification of dry algae with methanol, H₂SO₄ and NaOH. *Fuel* 239:511–520
9. Kumar S, Jain S, Kumar H (2017) Process parameter assessment of biodiesel production from a Jatropha–algae oil blend by response surface methodology and artificial neural network. *Energy Sources Part A: Recovery Util Environ Eff* 39(22):2119–2125
10. Goyal P, Sharma M, Jain S (2013) Optimization of transesterification of Jatropha curcas oil to biodiesel using response surface methodology and its adulteration with kerosene. *J Mater Environ Sci* 4:277–284
11. Jain S, Sharma MP (2012) Oxidation, thermal, and storage stability studies of Jatropha curcas biodiesel. *Int Sch Res Not* 2012. Article ID 861293, 15 pages
12. Jain S, Sharma M (2011) Oxidation and thermal behavior of Jatropha curcas biodiesel influenced by antioxidants and metal contaminants. *Int J Eng Sci Technol* 3:65–75. <https://doi.org/10.4314/ijest.v3i4.68542>
13. Sikarwar V, Zhao M, Fennell P, Shah N, Anthony E (2017) Progress in biofuel production from gasification. *Prog Energy Combust Sci* 61:189–248. <https://doi.org/10.1016/j.pecs.2017.04.001>
14. Agarwal AK, Bijwe J, Das L (2003) Wear assessment in a biodiesel-fueled compression ignition engine. *J Eng Gas Turbines Power* 125:820–826
15. Bhale P, Deshpande N, Thombre S (2008) Improving the low temperature properties of biodiesel fuel. *Renew Energy* 1–7
16. Cetinkaya M, Ulusoy Y, Tekin Y, Karaosmanoglu F (2005) Engine and winter road test performances of used cooking oil originated biodiesel. *Energy Convers Manage* 46:1279–1291
17. Hancsok J, Bubalik M, Beck A, Baladincz J (2008) Development of multifunctional additives based on vegetable oils for high-quality diesel and biodiesel. *Chem Eng Res Des* 86:793–799
18. Knothe G (2005) Dependence of biodiesel fuel properties on the structure of fatty acid alkyl esters. *Fuel Process Technol* 86:1059–1070
19. Lapuerta M, Armas O, Rodríguez-Fernández J (2008) Effect of biodiesel fuels on diesel engine emissions. *Prog Energy Combust Sci* 34:198–223
20. Zheng M, Mulenga M, Reader G, Wang M, Ting D, Tjong J (2008) Biodiesel engine performance and emissions in low temperature combustion. *Fuel* 87:714–722
21. Ramli A, Farooq M, Naeem A, Khan S, Hummayun M, Iqbal A, Ahmed S, Shah LA (2017) Bifunctional heterogeneous catalysts for biodiesel production using low cost feedstocks: a future perspective. <https://doi.org/10.5772/65553>
22. Srinivasa Rao P, Gopalakrishnan KV (2004) Esterified oils as fuel in diesel engines. In: 11th National conference on I.C. Engines, I.I.T. Madras, India, 1983. 740. Ramadhas AS et al (2004) *Renew Energy* 29:727–742
23. Narayan CM (2002) Vegetable oil as engine fuels—prospect and retrospect. In: *Proceedings on recent trends in automotive fuels*, Nagpur, India
24. Azad K, Uddin S, Alam M (2012) Mustard oil, an alternative fuel: an experimental investigation of Bio-diesel properties with and without Trans-esterification reaction. *Glob Adv Res J Eng Technol Innov* 1:75–84
25. Vasić K, Hojnik Podrepšek G, Knez Ž, Leitgeb M (2020) Biodiesel production using solid acid catalysts based on metal oxides. *Catalysts* 10:237
26. Babcock R, Clausen P, Michael P, Schulte I (2020) Yield characteristics of biodiesel produced from chicken fat-tall oil blended feedstocks
27. Cesarini S, Pastor FIJ, Nielsen PM, Diaz P (2015) Moving towards a competitive fully enzymatic biodiesel process. *Sustainability* 7(6):7884–7903
28. Cherg YL, Rong JL (2009) Engine performance and emission characteristics of marine fish-oilbiodiesel produced from the discarded parts of marine fish. *Fuel Process Technol* 90:883–888

29. Godiganur S, Murthy S, Reddy RP (2010) Performance and emission characteristics of a Kirloskar HA394 diesel engine operated on fish oil methyl esters. *Renew Energy* 35:355–359
30. Murugesan A, Umarani C, Subramanian R, Nedunchezhian N (2009) Bio-diesel as an alternative fuel for diesel engine a review. *Renew Sustain Energy Rev* 13:653–662
31. Lujan JM, Bermudez V, Tormos B, Pla B (2009) Comparative analysis of a DI diesel engine fueled with biodiesel blends during the European MVEG-A cycle: performance and emissions (II). *Biomass Bioenergy* 33:948–956
32. Utlu Z, Kocak MS (2008) The effect of biodiesel fuel obtained from waste frying oil on direct injection diesel engine performance and exhaust emissions. *Renew Energy* 33:1936–1941
33. Xue J, Grift E, Hansen AC (2001) Effect of biodiesel on engine performances and emissions. *Renew Sustain Energy Rev* 15(2):1098e116
34. Chhetri AB, Watts KC (2013) Surface tensions of petro-diesel, canola, jatropha and soapnut biodiesel fuels at elevated temperatures and pressures. *Fuel* 104(0):704e10
35. Carraretto C, Macor A, Mirandola A, Stoppato A, Tonon S (2004) Biodiesel as alternative fuel: experimental analysis and energetic evaluations. *Energy* 29:2195–2211
36. Xue J, Grift TE, Hansen AC (2011) Effect of biodiesel on engine performances and emissions. *Renew Sustain Energy Rev* 15(2):1098–1116
37. Narula V, Thakur A, Uniyal A, Kalra S, Jain S (2017) Process parameter optimization of low temperature transesterification of algae-Jatropha Curcas oil blend. *Energy* 119:983–988
38. Dwivedi G, Sharma MP, Jain S (2013) Performance evaluation of diesel engine using biodiesel from pongamia oil. *Int J Renew Energy Res* 3(2):325–330
39. Jain S, Sharma MP (2013) Engine performance and emission analysis using oxidatively stabilized Jatropha curcas biodiesel. *Fuel* 106:152–156
40. Jain S, Sharma MP (2012) Correlation development between the oxidation and thermal stability of biodiesel. *Fuel* 102:354–358
41. Jain S, Sharma M (2011) Study of oxidation stability of Jatropha curcas biodiesel/diesel blends. *Int J Energy Environ* 2:533–542
42. Jain S, Sharma MP (2011) Power generation from MSW of Haridwar city: a feasibility study. *Renew Sustain Energy Rev* 15(1):69–90
43. Dwivedi G, Jain S, Sharma M (2011) Impact of biodiesel and its blends with diesel and methanol on engine performance. *Int J Energy Sci* 1:105–109
44. Dwivedi G, Sharma MP (2015) Application of Box-Behnken design in optimization of biodiesel yield from Pongamia oil and its stability analysis. *Fuel* 145:256–262
45. Chhabra M, Saini BS, Dwivedi G (2019) Impact assessment of biofuel from waste neem oil. *Energy Sources Part A Recover Util Environ Eff* 0(0):1–12
46. Azad AK, Rasul MG, Giannangelo B, Ahmed SF (2018) Diesel engine performance and emission study using soybean biodiesel blends with fossil diesel. In: Aloui F, Dincer I (eds) *Exergy for a better environment and improved sustainability 2*. Green energy and technology. Springer, Cham
47. Dharmaprabakaran T, Karthikeyan S, Periyasamy M, Mahendran G (2020) Emission analysis of CuO₂ nanoparticle addition with blend of Botryococcus braunii algae biodiesel on CI engine. *Mater Today: Proc*
48. Mahendran J, Saravanan K, Ragulnath D (2019) Performance and emission characteristics of algae derived biodiesel processes. *Mater Today: Proc*
49. Saravanan S, Krishnamoorthy N (2020) Investigation on reduction in consequences of adding antioxidants into the algae biodiesel blend as a CI engine fuel. *Fuel* 276:117993
50. Abed KA, Gad MS, El Morsi AK, Sayed MM, Abu Elyazeed S (2019) Effect of biodiesel fuels on diesel engine emissions. *Egypt J Petrol* 28(2):183–188

Jatropha: A Sustainable Source of Transportation Fuel in India



Rahul Chamola, Nitin Kumar, and Siddharth Jain

1 Introduction

In the past few years, science and technology have progressed very swiftly due to modernization, industrial advancement, and economic growth [1]. Technology has great impact to improve living standards of people. For example, transportation has extended for human comfort, and scientific research in various sectors and expansion in communication engineering has reduced human fatigue and effective time. However, technical growth is also associated with many problems such as energy demand, climate change, air pollution, and hazardous human risk. As per the report of world energy scenario 2014, world coal energy consumption was 40.8% and fossil fuels will be primary sources of energy by the end of 2040 (world energy 2015 report). The largest share of energy is consumed by transportation sector, and it accounts 98% of CO₂ emission [2]. Fossil fuels are conventional fuels usually related with environmental concerns like acid precipitation, global warming, air and ground water pollution, toxic emission of exhaust gases such as oxides of nitrogen (NO_x), carbon monoxide (CO), unburned hydrocarbons, carbon dioxide (CO₂), and particulate matter. Hence, these limitations of conventional fuel draw the attention of researchers, and there was an urgent need for clean and sustainable alternative fuels in order to fulfill the demand of energy by eco-friendly resources [3]. In the last few decades, renewable energy is found one of the most promising and alternate future fuels. Renewable energy sources are environment-friendly, clean, and most reliable sources till date. Many scholars and researchers are now focusing on biofuels. It includes both edible (soybean, sunflower, coffee, and palm oil) and non-edible (jatropha curcas, mahua, micro-, and macroalgae) biofuels.

R. Chamola · N. Kumar · S. Jain (✉)

Department of Mechanical Engineering, College of Engineering Roorkee, Roorkee, Uttarakhand 247667, India

Numerous works have been conducted in the field of unconventional energy yet it contributes only 13.5–17.9% of total world energy consumption [4]. Traditional renewable energy resources are organic matter taken from or produced by plants and animals. It comprises mainly wood, agricultural crops and products, aquatic plants, forestry products, wastes and residues, and animal wastes. In its most general meaning, biofuels are all types of solid, gaseous, and liquid fuels that can be derived from biomass. Traditional renewable energy sources cause air pollution and respiratory infections when burn directly in open atmosphere [5–7]. Moreover, plant residual, cow dung, and charcoal are excessively used for the domestic energy production in various part of India till date, as a result of which deforestation, poor soil fertility, and heart-based diseases are very common in several part of the country [8, 9]. Hence, traditional resources can be converted in useful biofuels by direct combustion practices.

Biodiesel refers to long fatty acid alkyl esters (FAAE) with biodegradability, low sulfur content, and thus reducing emissions [10]. To use biodiesel as a fuel, it should be mixed with petroleum diesel fuel to create a biodiesel-blended fuel. Biodiesel refers to the pure fuel before blending. Almost 95% of biofuel is produced from edible biodiesel resources like soybean, sunflower, palm oil, maize, etc., but these energy sources are responsible for deforestation, land issues, and loss of biodiversity [11–13]. Hence, non-edible energy sources such as *Jatropha curcas*, *Madhuca indica*, sea mango, algae, waste cooking oils, and animal fats are being used for sustainable biodiesel production. Commercially, biodiesel is produced by transesterification of triglycerides which are the main ingredients of biological origin oils in the presence of an alcohol (e.g., methanol and ethanol) and a catalyst (e.g., alkali, acid, and enzyme) with glycerin as a major by-product Dube et al. [14]. After the reaction, the glycerin is separated by settling or centrifuging and the layer obtained is purified prior to using it for its traditional applications (pharmaceutical, cosmetics, and food industries) or for the recently developed applications (animal feed, carbon feedstock in fermentations, polymers, surfactants, intermediates, and lubricants) by Vicente et al. [15].

India has a vast potential of renewable energy resources. Ministry of New & Renewable Energy (MNRE) supports the implementation of new and renewable energies. Exploitation of hydrogen energy, geothermal energy, tidal energy, and biofuels for power generation and automotive applications has also planned by the ministry. With high economic growth rates and over 15% of the world's population, India is a significant consumer of energy resources. Recent IBEF analysis 2020 shows that Indian renewable energy capacity will be 175 GW by 2022. Government is looking forward to achieve 227 GW of renewable capacity including 114 GW solar and 67 GW of wind energy by 2022. Power generation from renewable sources accounts 127.01 billion units in FY20.

2 Challenges in Jatropha Cultivation

Jatropha is one of the most widely used feedstock for biodiesel production that requires lower processing time than that of another feedstock. Plant that has high percentage of fatty acids makes it most suitable for biodiesel production. The plant can grow in desert or semi-arid regions. Jatropha has high seed oil content. It can be planted anywhere where land is marginal [16, 17]. Jatropha curcas is successfully employed for biofuel production that can be used in diesel engine without major modification. Despite huge benefits of jatropha plant, many jatropha-based biodiesel producer companies across the globe wrapped out their investments. The success of jatropha biodiesel hampered since production cost increases 70–80%. Some of the factors like environmental, ecological, social, and economic are responsible for the failure of jatropha production around the world. Various studies have been conducted by scholars and researchers to look into the sole effect of failure. The inter-corelated factors like low-income, low-yield, and cultivation issues are examined by scholars. In this review, we deal with all-inclusive and crucial factors effecting the sustainable biodiesel production from jatropha. Thus, large-scale production of biodiesel from jatropha can be improved by comparing the performance of biodiesel fuel characteristics and combustion quality with various relevant information available. This study could be used as policy directive for sustainable growth of biodiesel production from jatropha.

Jatropha belongs to euphorbiaceane family, fast-growing tree with height ranges from 3 to 7 m. The plant is widely available in Mexico, America, Asia, and Africa [18–21]. Some of the author considers the plant as magical crop [22] because of its huge biodiesel potential and ability to grow even in dry and semi-arid regions. The deep roots [23] of the plant help to uphold soil against land erosions. Plant species are also called green gold because of its economic benefits for small and developing countries which are facing environmental issues and pollution. Jatropha-based biodiesel can fulfill the requirements of a country by prevailing climatic and energy security issues [24, 25]. Therefore, jatropha is one of the most reliable and eco-friendly sources of future fuel due to its multiple advantages and availability. Jatropha plant can survive for over 49 [26] years and capable of producing seed for 30–40 years [16, 27]. Jatropha plant can be propagated by seed sowing and stem cutting. First flowering since plantation in 12 months and seeds appears within 90 days [28] after flowering. Jatropha plant needs very less agronomic practices like pesticides water and pest/diseases control than that of other feedstock make it most suitable for sustainable future fuel. Jatropha plant requires certain atmospheric conditions such as temperature from 18 to 40 °C, rainfall (1250–3000 mm), [16, 17, 29] soil nutrients like nitrogen phosphorous and potassium, soil depth that should be greater than 50 cm, and altitude(500–2150 m.a.s.l) to grow. Usually, plant has pest and diseases resistance properties [29] but some of the studies claimed that jatropha is highly vulnerable to pest attack [30–32]. The optimum yield of 2.236 L oil/tree can be generated through jatropha which is third highest after palm and coconut in

terms of oil yield [33]. The plant oil is non-edible, toxic, and contains fatty acid alkyl ester for biodiesel production.

The cost of jatropha seed is inferior to other feed stocks, although it accounts 70–80% [34] of total operating cost. Need of farm equipment and agronomic practices are also justifiable than that of anticipated. Plant can grow in marginal land [35] without any conflict with other food crops. All these virtues make it a valuable feedstock for biodiesel application. Even with all such great qualities, there is no mass scale production from jatropha. Numerous companies invested in jatropha cultivation leading toward disinvestment due to lower biodiesel yield than the anticipated production contributed. On the other hand, agricultural properties of jatropha are underestimated somewhere due to poor soil quality. A study [36] conducted in Ethiopia on large-scale jatropha plantation revealed that inferior soil properties and poor agronomy of the area influence Jatropha production. 5-ton/ha/year [27] can produce with moderate rainfall ranging from 900 to 1200 ml, which is higher than the rainfall of 750 mm per year. The soil type and quality played vital role. Most of the study reported well-drained soil is suitable for production. In contrast waterlogged soil or clay-rich soil reported lower production capabilities. Despite all the challenges, various methods are introduced to convert jatropha into biodiesel in laboratories [37]. The primary stage includes the collection of seeds and processing for oil extraction. The initial stage is labor-centric and that is why consumes maximum production expensive. This is one of the reasons of jatropha project's declination and termination [38].

2.1 Factors Affecting Jatropha Seed Yield and Its Oil Content

The main criteria for selecting of any feedstock for sustainable biodiesel should have sufficient oil content for biodiesel production. This review mentioned all the parameters that are assumed to be essential for optimum yield and oil extraction process [39]. Near-infrared spectroscopy conducted on jatropha seeds by Vaknin et al. [17] to examine the influence of various geographical locations on oil content. Study reported that Ethiopian jatropha seed has low oil content than that of Ghana. Dry climatic conditions are favorable for high oil content than that of wet climates. Signification variation in Jatropha oil content in Brazil, Nigeria, China, and Congo-Brazzaville has been reported [40–43]. Jingura et al. [29] examined the impact of land use and different agronomical conditions on oil percentage. Biotic factors such as pest, human intervention, diseases, and genotype and abiotic factors like soil properties temperature rain, thinning, and agronomical conditions play significant role in oil yield of jatropha [5, 31, 44]. Jatropha is very sensitive toward the temperature. It grows better at a higher temperature but enable to sustain at very low temperature below 0 °C [45]. Some of the studies revealed that lower seed yield of jatropha in temperature ranges between 15 and 17 °C; the ideal condition for growing jatropha in temperature ranges of 15–30 °C; rainfall is of 250–3000 mm/year [23, 28]; and elevation bellow is 500 m above sea level. Although jatropha is highly resistant to pest

attack, many reports also claimed that stem, root, fruit, and bark could be affected due to some dominating pests like *Pempelia morosalis*, *Stomphastis thraustica*, *Pachycoris klugii*, and *Agonosoma trilineatum* [32]. Apart from pest and diseases, jatropha oil yield is also affected by different genotypes and maturity level of plant [46]. Usually, yellow brown colored fruit contributes higher seed content; however, it is also identified that oil extraction method could affect oil yield. Farahani et al. [47] reported higher oil yield of 10.38–59.38% with suitable process parameters like time temperature and solvent-to-solid ratio. The optimum yields were received through supercritical and ultrasound extraction methods whereas comparatively lower yield is achieved by mechanical extraction technique.

3 Methods for Jatropha Oil Extraction

Jatropha biodiesel requires many preprocessing which includes shelling, drying, crushing, and grinding. Different oil extraction processes are famous among scholars such as mechanical processing, thermal cracking (pyrolysis), enzymatic extraction, supercritical extraction, and solvent extraction [48]. The pros and cons of each process are critically examined in this review.

3.1 Mechanical Oil Extractions

Mechanical oil extraction is closed to traditional methods, and the role of this method has been obsolete now. In this process, boiling water is used as solvent and completely dried crushed seeds are dipped into boiled water. Further, the moisture is processed under mechanical stirring for a certain time limits. The paste is filtered at last using different filtration techniques. Although the operation carrying cost is not so much than that of other techniques, the oil yield from this method is lower. Aboubakar et al. [1] reported 75% seed yield from mechanical extraction technique [49]. This technique is adopted for commercial oil production; however, yield is lower as compared to supercritical and solvent technique. Mechanical oil extraction depends upon various process parameters, viz. processing time, reaction temperature, moisture content, and mechanical equipment used and stirring speed. According to Evon et al. [50], twin screw extruder with rotational speed of 153 rpm, 80 °C temperature, and 4% moisture content can be used in place of mechanical screw press for high yield approx. to 70.6%.

3.2 Solvent Extraction Methods

Kernel powder is most adopted solvent widely applied in laboratories for high oil content. It recovers almost 98% of available oil. As per a study conducted in India, kernel solvent is more effective (55.2%) than that of seed with coat intact (25.5%) [51]. No doubt solvent technique has clear advantages over traditional and mechanical method but the results of this method are vulnerable to reaction time, temperature, moisture content and grain size of seeds and solvent-to-seed ratio [42, 52]. Sepidar et al. [53] conducted research on jatropha with 68 °C temperature, 8 h of reaction time, grain size of 0.5–0.75 mm and hexane as a solvent for maximum yield. N-hexane is widely used by scholars for optimum output. Other solvents like petroleum ether, ethyl ether, pentane, isopropane, ethyl acetate, acetone, chloroform, ethanol, and methanol are also including in biodiesel extraction [54].

3.3 Supercritical Oil Extraction

Supercritical oil extraction is recent in method for extracting oil from jatropha seed. The process is carried out with controlled flow rate of CO₂. Supercritical fluid with the pressure and temperature higher than critical point is used as a solvent [39]. The process needs critical pressure 350 bar and critical temperature 220 °C. Higher oil yield of around 40.28% was obtained by supercritical extraction in comparison with subcritical extraction and ultrasonic extraction at a temperature and pressure 90 °C and 5 bar, respectively. Chen et al. [55] found that optimum oil yield of 45.51% as compared to other methods using 60 °C, temperature, 350 bar pressure, and 125:1 solvent-to-solid ratio. Method is environment-friendly due to need of minimum purification and no use of solvent. Supercritical methods take almost 50 min process time whereas other methods take several hours [56]. High operation cost and high temperature resisting equipment control the uses of this method for large-scale production of yield.

3.4 Ultrasound-Based Solvent Extraction

Ultrasound solvent extraction is based on the application of high-intensity and high-frequency sound waves that interacts with the materials so that seed yield can be improved [57]. Sound waves accelerate the heat and mass transfer to boost the oil output with no use of solvent [47]. Farahani et al. [47] examined that ethanol-assisted ultrasonic solvent extraction method is efficient as compared to other solvents, viz. n-hexane, chloroform, and acetone. They obtained yield of 59.38% at 35 °C temperature and 30 min of reaction time. Recently an in situ transesterification method is being used by many scholars for jatropha oil extraction to reduce processing time

and solvent requirements. Kumar [58] worked on ultrasonic-based reactive transesterification on jatropha oilseed with methanol, catalyst (KOH), seed grain size of 1–2 mm and for reaction time of 0.3 s cycle to get 92% yield.

3.5 Enzymatic Extractions

This technique uses water as a solvent which is safe, inexpensive, and widely available. It is also called aqueous enzymatic extraction by some researchers [51]. The oil yield concentration is relatively lower than that of solvent extraction. The other demerits are long processing time and energy. The cost of enzyme is also higher compared to anticipated methods. Aqueous enzymatic method is mostly influenced by enzyme, water, particle size, temperature, and process speed.

4 Techniques for Converting Jatropha Oil as Engine Fuel

Jatropha is non-edible oil which is being used as a fuel in combustion engine without any major modifications in diesel engines. Different methods such as microemulsification, thermal cracking, blending, and transesterification are employed to utilize jatropha as a biofuel [16, 59, 60]. The main objectives of these methods are to reduce process time, obtain high oil yield, and to minimize the cost associated with production of fuel. Thus, some of the techniques used to convert jatropha oilseeds into fuel are examined in this section.

4.1 Direct Use and Blending of Jatropha Oil with Diesel

Numerous studies have conducted for the direct use of jatropha oil in place of diesel and petrol without any mixing. However, direct use of biodiesel was not satisfactory due to high viscosity lower calorific value and lower volatility [61, 62]. That is why biofuel is used as blends. It means that jatropha biofuel mixes with regular diesel for use to limit its drawbacks. Ong et al. [16] examined high viscosity is one of main drawbacks of biofuel, leads ignition delay and knocking. According to Wang [63], high viscosity of jatropha promotes flue gases and thus reduces engine efficiency. Jatropha oil is mixed with diesel in concentration of 40–50%. Tainaka et al. [60] conducted a research on jatropha blend biodiesel for soot formation characteristics (SFC) in a 550 kW class furnace using an optical measurement system. They conclude that SFC reduced with heavy petrol oil, while Hashimoto et al. reported that radiation intensity was declined when jatropha oil was mixed with heavy oil. Therefore, blend of jatropha oil and diesel is used nowadays in various parts of the globe [43, 46, 52, 60–85].

4.2 *Microemulsification Process*

Higher viscosity issues of jatropha oil can be resolved by emulsification with alcohol. The process is non-polluting and energy efficient [59]. Surfactant employs as an emulsifier to provide stability to the fuel. The most commonly used surfactants [64] are ethanol and butanol. The kinematic viscosity and calorific value are improved by the application of this method which result in lower carbon emission than conventional liquid fuels.

4.3 *Pyrolysis*

Pyrolysis refers to chemical change caused by application of thermal energy to crack complex hydrocarbon of triglyceride. The process needs relatively high temperature compared to the conventional processes and pressure and catalyst (if required). Catalyst like KOH, ZnO, ZrO₂, Na₂CO₃, and zeolite increases the rate of reaction at minimum possible temperature [65, 66]. Pyrolysis is carried out in batch reactor. Thermal cracking refines oil quality and octane number. Zheng et al. [67] worked on jatropha oil and analyzed that utmost biodiesel yield and lower reaction time were obtained at high catalyst volume. The biofuel production through pyrolysis is affected by excessive equipment cost [13].

4.4 *Transesterification*

Transesterification is a process that eliminates certain stages like extraction to biofuel production that makes it most effective and efficient process for biodiesel extraction [81–101]. Transesterification is carried out with catalyst, solvent, and an alcohol for biodiesel production [3, 68]. It helps to reduce experimental installation and energy cost. Ong et al. [16] worked on two-step transesterification process on jatropha seed with both acid and base catalyst. Dubey et al. [69] stated that viscosity of jatropha oil can be minimized by the use of transesterification by 74.8% than that of unprocessed oil.

Transesterification process depends upon methanol-to-seed ratio, temperature, reaction time, catalyst concentration, and solvent [70]. Homogenous (acid and base) and heterogeneous catalysts (alkaline and acids) are used in this process. Most commonly used homogenous catalyst is NaOH and KOH. Studies showed that low free fatty acid (FFA) is one of the drawbacks of homogenous catalyst. Homogenous catalyst is prohibited for large-scale production which can be compensated by homogenous acid catalyst namely H₂SO₄, HCl, and H₃PO₄. Homogenous acid catalyst increases the FFA. However, reaction time is much slower as compared to base [12, 13]. Heterogeneous catalysts are also in demand due to green and economical

properties. Heterogeneous catalyst gives relatively higher biodiesel with minimal side saponification process than that of homogenous catalyst. However, cost along with temperature and processing time affects the application of heterogeneous catalysts [71]. Recently, desire of ultrasonic-based transesterification has been increased in order to lessen reaction time and energy demand. Some scholars are also working with enzymatic transesterification [13] due to their green characteristics. However, high cost of enzymes prevents its application for large scale application [72].

5 Physicochemical and Fuel Properties

Below are the physicochemical and fuel properties of biodiesel which need to be focussed while using the same in the engine:

- Viscosity
- Density
- Flash point
- Fire point
- Free fatty acid content
- Water content and sedimentation
- Flashpoint
- Calorific value
- Cetane number
- Cloud and pour point properties
- Oxidation stability

6 Conclusions and Future Directions

The greatest expense and serious rivalry with food and feed creation because of biodiesel making from consumable oils have examined analysts, governments, ventures, and policymakers to discover new stumpy cost and non-eatable energy oil crops. Jatropha is recognized as a likely raw material for reasonable biodiesel making because of its appropriate physicochemical structure, higher seed and oil yields, and lower rivalry with food crops. Though getting practical and adequate measures of Jatropha oil for huge scope biodiesel making is not accomplished at this point, the usage of fresh jatropha tasks has been dropped, and a few continuous activity tasks have been ended. The development of jatropha for supportable biodiesel making is essentially influenced by different aspects, which could be deliberated as natural, financial, social, institutional, and mechanical boundaries. Lacking business sector opportunity, little motivators from the public authority, non-attendance of clear strategies and authoritative, possession issue, deficiency of land, restricted innovation in seed assortment and preparing, and inferior agronomic performance Jatropha seed

were the fundamental imperatives influencing the development of jatropha for reasonable biodiesel making. Taking everything into account, the capability of jatropha for feasible biodiesel making ought to be assessed as far as its monetary, social, ecological, and specialized points of interest for the separate rising area prior to setting up an enormous scope biodiesel production.

References

1. Aboubakar X, Goudoum A, B  b   Y, Mbofung CMF (2017) Optimization of *Jatropha curcas* pure vegetable oil production parameters for cooking energy. *S Afr J Chem Eng* 24:196–212
2. Sharma KD, Jain S (2019) Overview of municipal solid waste generation, composition, and management in India. *Environ Eng* 3:1–45
3. Aghbashlo M, Tabatabaei M, Amid S, Hosseinzadeh-Bandbafha H, Khoshnevisan B, Kianian G (2020) Life cycle assessment analysis of an ultrasound assisted system converting waste cooking oil into biodiesel. *Renew Energy*
4. Chamola R, Khan MF, Raj A, Verma M, Jain S (2019) Response surface methodology based optimization of in situ transesterification of dry algae with methanol, H₂SO₄ and NaOH. *Fuel* 239:511–520
5. Kumar S, Jain S, Kumar H (2017) Process parameter assessment of biodiesel production from a *Jatropha*–algae oil blend by response surface methodology and artificial neural network. *Energy Resour* 39:2119–2125
6. Gabisa EW, Gheewala SH (2019) Potential, environmental, and socio-economic assessment of biogas production in Ethiopia: the case of Amhara regional state. *Biomass Bioenergy* 122:446–456
7. Goyal P, Sharma MP, Jain S (2013) Optimization of transesterification of *Jatropha curcas* oil to biodiesel using response surface methodology and its adulteration with kerosene. *Material Environ Sci* 4:277–284
8. Abadi N, Gebrehiwot K, Techane A, Nerea H (2017) Links between biogas technology adoption and health status of households in rural Tigray, Northern Ethiopia. *Energy Pol* 101:284–292
9. Negash D (2017) Household energy and recycling of nutrients and carbon to the soil in integrated crop-livestock farming systems: a case study in kumbursa village, vol. 9. *Central Highlands of Ethiopia Wiley & Sons Ltd.*, pp 1588–1601
10. Jain S, Sharma MP (2012) Oxidation thermal and storage stability studies of *Jatropha Curcas* biodiesel. *Int Sch Res Not*
11. Jain S, Sharma MP (2011) Oxidation and thermal behavior of *Jatropha curcas* biodiesel influenced by antioxidants and metal contaminants. *Int J Eng Sci Technol*
12. Aderibigbe FA, Mustapha SI, Adewoye TL, Mohammed IA, Gbadegesin AB, Niyi FE et al (2020) Qualitative role of heterogeneous catalysts in biodiesel production from *Jatropha curcas* oil. *Biofuel Res J* 7:1159–1169
13. Narula V, Thankur A, Uniyal A, Kalra S, Jain S (2016) Process parameter optimization of low temperature transesterification of algae-*Jatropha Curcas* oil blend. *Energy* 119:983–988
14. Mazumdar P, Borugadda VB, Goud VV, Sahoo L (2012) Physico-chemical characteristics of *Jatropha curcas* L. of North East India for exploration of biodiesel. *Biomass Bioenergy* 46:546–554
15. Atabani AE, Silitonga AS, Badruddin IA, Mahlia TMI, Masjuki HH, Mekhilef S (2012) A comprehensive review on biodiesel as an alternative energy resource and its characteristics. *Renew Sustain Energy Rev* 16:2070–2093
16. Ong HC, Silitonga AS, Masjuki HH, Mahlia TMI, Chong WT, Boosroh MH (2013) Production and comparative fuel properties of biodiesel from non-edible oils: *jatropha curcas*, *Sterculia foetida* and *Ceiba pentandra*. *Energy Convers Manag* 73:245–255

17. Vaknin Y, Ghanim M, Samra S, Dvash L, Hendelsman E, Eisikowitch D et al (2011) Predicting *Jatropha curcas* seed-oil content, oil composition and protein content using near-infrared spectroscopy—a quick and non-destructive method. *Ind Crop Prod* 34:1029–1034
18. Agyemang DNS, Daniel S, Antwi OK (2014) Variations in oil content and biodiesel yield of *Jatropha curcas* from different agro-ecological zones of Ghana. *Int J Renew Sustain Energy* 3(4):76–81
19. Chandra R, Vijay VK, Subbarao PMV, Khura TK (2012) Production of methane from anaerobic digestion of *jatropha* and *pongamia* oil cakes. *Appl Energy* 93:148–159
20. Narula V, Khan MF, Negi A, Thankur A, Kalra S, Jain S (2017) Low temperature optimization of biodiesel production from algal oil using CaO and CaO/Al₂O₃ as catalyst by the application of response surface methodology. *Energy* 140:9879–9884
21. Jain S, Sharma MP (2013) Engine performance and emission analysis using oxidatively stabilized *Jatropha curcas* biodiesel. *Fuel* 106:152–156
22. Jain S, Sharma MP (2012) Correlation development between the oxidation and thermal stability of biodiesel. *Fuel* 102:354–358
23. Achten WMJ, Verchot L, Franken YJ, Mathijs E, Singh VP, Aerts R et al (2008) *Jatropha* bio-diesel production and use: review. *Biomass Bioenergy* 32:1063–1084
24. Jain S, Sharma MP (2011) Study of oxidation stability of *Jatropha curcas* biodiesel/ diesel blends. *Energy Environ* 2:533
25. Wendimu MA (2016) *Jatropha* potential on marginal land in Ethiopia: reality or myth? *Energy Sustain Dev* 30:14–20
26. Ntaribi T, Paul DI (2018) Status of *Jatropha* plants farming for biodiesel production in Rwanda. *Energy Sustain Dev* 47:133–142
27. Jain S, Sharma MP (2011) Power generation from MSW of Haridwar city: a feasibility study. *Renew Sustain Energy Rev* 15:69–90
28. Ntaribi T, Paul DI (2019) The economic feasibility of *Jatropha* cultivation for biodiesel production in Rwanda: a case study of Kirehe district. *Energy Sustain Dev* 50:27–37
29. Jingura RM, Matengaifa R, Musademba D, Musiyiwa K (2011) Characterisation of land types and agro-ecological conditions for production of *Jatropha* as a feedstock for biofuels in Zimbabwe. *Biomass Bioenergy* 35:2080–2086
30. Singh B, Singh K, Rejeshwar Rao G, Chikara J, Kumar D, Mishra DK et al (2013) Agrotechnology of *Jatropha curcas* for diverse environmental conditions in India. *Biomass Bioenergy* 48:191–202
31. Soto I, Ellison C, Kenis M, Diaz B, Muys B, Mathijs E (2018) Why do farmers abandon *jatropha* cultivation? The case of Chiapas, Mexico. *Energy Sustain Dev* 42:77–86
32. Chitra S, Dhyani S (2006) Insect pests of *Jatropha curcas* L. and the potential for their management. *Curr Sci* 91:162–163
33. Riera O, Swinnen J (2016) Household level spillover effects from biofuels: evidence from castor in Ethiopia. *Food Pol* 59:55–65
34. Gonzales C, Fabiola N (2016) International experiences with the cultivation of *Jatropha curcas* for biodiesel production. *Energy* 112:1245–1258
35. Nygaard I, Bolwig S (2018) The rise and fall of foreign private investment in the *jatropha* biofuel value chain in Ghana. *Environ Sci Pol* 84:224–234
36. Lakew H, Shiferaw Y (2008) Rapid assessment of biofuels development status in Ethiopia. In: Anderson T, Belay M, editors. *Rapid assessment of biofuels development status in Ethiopia and proceedings of the national workshop on environmental impact assessment and biofuels*. Addis ababa, Ethiopia. MELCA Mahiber
37. Islam A, Yaakob Z, Anuar N, Primandari S, Osman M (2012) Physiochemical properties of *jatropha curcas* seed oil from different origins and candidate plus plants (CPPs). *J Am Oil Chemist's Soc* 89
38. Ahmad T, Danish M, Kale P, Geremew B, Adejolu SB, Nizami M et al (2019) Optimization of process variables for biodiesel production by transesterification of flaxseed oil and produced biodiesel characterizations. *Renew Energy* 139:1272–1280

39. Karmakar B, Halder G (2019) Progress and future of biodiesel synthesis: advancements in oil extraction and conversion technologies. *Energy Convers Manag* 182:307–339
40. Akintayo ET (2004) Characteristics and composition of *Parkia biglobbossa* and *Jatropha curcas* oils and cakes. *Bioresour Technol* 92:307–310
41. de Oliveira JS, Leite PM, de Souza LB, Mello VM, Silva EC, Rubim JC et al (2009) Characteristics and composition of *Jatropha gossypifolia* and *Jatropha curcas* L. oils and application for biodiesel production. *Biomass Bioenergy* 33: 449–453
42. Nzikou JM, Matos L, Kimbonguila A, Mbemba F, Silou T, Ndangui CB et al (2009) Characteristics and composition of *jatropha curcas* oils, variety Congobrazzaville. *Res J Appl Sci Eng Technol* 1(3):154–159
43. Wang R, Hanna MA, Zhou WW, Bhadury PS, Chen Q, Song BA et al (2011) Production and selected fuel properties of biodiesel from promising non-edible oils: *Euphorbia lathyris* L., *Sapium sebiferum* L. and *Jatropha curcas* L. *Bioresour Technol* 102:1194–1199
44. Keith O (2000) A review of *Jatropha curcas*: an oil plant of unfulfilled promise. *Biomass Bioenergy* 19:1–15
45. Nallathambi GV (2009) Biomass estimates, characteristics, biochemical methane potential, kinetics and energy flow from *Jatropha curcas* on dry lands. *Biomass Bioenergy* 33:589–596
46. Sinha P, Islam MA, Negi MS, Tripathi SB (2015) Changes in oil content and fatty acid composition in *Jatropha curcas* during seed development. *Ind Crop Prod* 77:508–510
47. Farahani GT, Azari PY (2016) Improving the oil yield of Iranian *Jatropha curcas* seeds by optimising ultrasound-assisted ethanolic extraction process: a response surface method. *Qual Assur Saf Crop Foods* 8:95–104
48. Mouahid A, Bouanga H, Crampon C, Badens E (2018) Supercritical CO₂ extraction of oil from *Jatropha curcas*: an experimental and modelling study. *J Supercrit Fluids* 141:2–11
49. Henning R (2000) The *Jatropha* booklet—a guide to the *Jatropha* system and its dissemination in Zambia. Weissenberg: Bagani GbR
50. Evon P, Amalia Kartika I, Cerny M, Rigal L (2013) Extraction of oil from *jatropha* seeds using a twin-screw extruder: feasibility study. *Ind Crop Prod* 47:33–42
51. Mat Yusoff M, Gordon MH, Ezeh O, Niranjan K (2016) Aqueous enzymatic extraction of *Moringa oleifera* oil. *Food Chem* 211:400–408
52. Keneni GY, Jorge MM (2017) Oil extraction from plant seeds for biodiesel production. *AIMS Energy* 5:316–340
53. Sepidar S, Zainal AZ, Robiah Y, Azhari M (2009) Extraction of oil from *jatropha* seeds optimization and kinetics. *Am J Appl Sci* 6:1390–1395
54. Mohadesi M, Moradi G, Ghanbari M, Moradi MJ (2019) Investigating the effect of nhexane as solvent on waste cooking oil conversion to biodiesel using CaO on a new support as catalyst. *Measurement* 135:606–612
55. Chen W-H, Chen C-H, Chang C-MJ, Chiu Y-H, Hsiang D (2009) Supercritical carbon dioxide extraction of triglycerides from *Jatropha curcas* L. seeds. *J Supercrit Fluids* 51:174–180
56. Hawthorne SB (1990) Analytical-scale supercritical fluid extraction. *Anal Chem* 62:633A-A642
57. Li H, Pordesimo L, Weiss J (2004) High intensity ultrasound-assisted extraction of oil from soybeans. *Food Res Int* 37:731–738
58. Kumar G (2017) Ultrasonic-assisted reactive-extraction is a fast and easy method for biodiesel production from *Jatropha curcas* oilseeds. *Ultrason Sonochem* 37:634–639
59. Demirbas A, Karslioglu S (2007) Biodiesel production facilities from vegetable oils and animal fats. *Energy Sources Part A* 29:133–141
60. Tainaka K, Fan Y, Hashimoto N, Nishida H (2019) Effects of blending crude *Jatropha* oil and heavy fuel oil on the soot behavior of a steam atomizing burner. *Renew Energy* 136:358–364
61. Abbaszaadeh A, Ghobadian B, Omidkhan MR, Najafi G (2012) Current biodiesel production technologies: a comparative review. *Energy Convers Manag* 63:138–148
62. Nabi MN, Rahman MM, Akhter MS (2009) Biodiesel from cotton seed oil and its effect on engine performance and exhaust emissions. *Appl Therm Eng* 29:2265–2270

63. Wang Z (2012) Producing jatropha biodiesel in China: policies, performance and challenges. *Jatropha*, challenges for a new energy crop, pp 95–121
64. Sankumgon A, Assawadithalerd M, Phasukarratchai N, Chollacoop N, Tongcumpou C (2018) Properties and performance of microemulsion fuel: blending of jatropha oil, diesel, and ethanol-surfactant. *Renew Energy Focus* 24:28–32
65. Ong YK, Bhatia S (2010) The current status and perspectives of biofuel production via catalytic cracking of edible and non-edible oils. *Energy* 35:111–119
66. Mancio AA, da Costa KMB, Ferreira CC, Santos MC, Lhamas DEL, da Mota SAP et al (2016) Thermal catalytic cracking of crude palm oil at pilot scale: effect of the percentage of Na₂CO₃ on the quality of biofuels. *Ind Crop Prod* 91:32–43
67. Zheng Q, Huo L, Li H, Mi S, Li X, Zhu X et al (2017) Exploring structural features of USY zeolite in the catalytic cracking of *Jatropha Curcas* L. seed oil towards higher gasoline/diesel yield and lower CO₂ emission. *Fuel* 202:563–571
68. Quah RV, Tan YH, Mubarak NM, Khalid M, Abdullah EC, Nolasco-Hipolito C (2019) An overview of biodiesel production using recyclable biomass and non-biomass derived magnetic catalysts. *J Environ Chem Eng* 7
69. Dubey AK, Sariv RM, Rehman A (2011) Characterization of processed jatropha oil for use as engine fuel. *Curr World Environ* 6
70. Noriega MA, Narvaez PC, Heinz C (2014) Kinetics of *Jatropha* oil methanolysis. *Fuel* 134:244–249
71. Aghbashlo M, Hosseinpour S, Tabatabaei M, Mojarab SM (2019) Multi-objective exergetic and technical optimization of a piezoelectric ultrasonic reactor applied to synthesize biodiesel from waste cooking oil (WCO) using soft computing techniques. *Fuel* 235:100–112
72. Thapa S, Indrawan N, Bhoi PR (2018) An overview on fuel properties and prospects of *Jatropha* biodiesel as fuel for engines. *Environ Technol Innov* 9:210–219
73. Canakci M, Sanli H (2008) Biodiesel production from various feedstocks and their effects on the fuel properties. *J Ind Microbiol Biotechnol* 35:431–441
74. Kumar U, Paul SJ, Jain S (in Press) Biocar: a source of nanocatalyst in transesterification process. *Mater Today: Proc* (7 July 2020)
75. Lee HV, Yunus R, Juan JC, Taufiq-Yap YH (2011) Process optimization design for jatropha-based biodiesel production using response surface methodology. *Fuel Process Technol* 92:2420–2428
76. Nigatu GS, Mario MJ (2017) Biodiesel production technologies: review. *AIMS. Energy* 5:425–457
77. J.V. G Knothe G, Krahl J (2010) *Biodiesel handbook*, 2nd edn. Urbana, Illinois: United States of America
78. Aransiola EF, Ojumu TV, Oyekola OO, Madzimbamuto TF, Ikhu-Omoregbe DIO (2014) A review of current technology for biodiesel production: state of the art. *Biomass Bioenergy* 61:276–297
79. (IEA) (2013) IEA. *International energy outlook 2013 with projections to 2040*. Washington, DC: U.S. Energy Information Administration Office of Energy Analysis, U.S. Department of Energy, 20585
80. Paterson RR, Lima N (2018) Climate change affecting oil palm agronomy, and oil palm cultivation increasing climate change, require amelioration. *Ecol Evol* 8:452–461
81. Osawa CC, Gonçalves LAG, Ragazzi S (2007) Correlation between free fatty acids of vegetable oils evaluated by rapid tests and by the official method. *J Food Compos Anal* 20:523–528
82. Pramanik K (2003) Properties and use of jatropha curcas oil and diesel fuel blends in compression ignition engine. *Renew Energy* 28:239–248
83. Koh MY, Mohd Ghazi TI (2011) A review of biodiesel production from *Jatropha curcas* L. oil. *Renew Sustain Energy Rev* 15:2240–2251
84. Gerpen JV (2005) Biodiesel processing and production. *Fuel Process Technol* 86:1097–1107
85. Asmare M (2014) Synthesis and characterization of biodiesel from Castor bean as alternative fuel for diesel engine. *Am J Energy Eng* 2

86. Berchmans HJ, Hirata S (2008) Biodiesel production from crude *Jatropha curcas* L. seed oil with a high content of free fatty acids. *Bioresour Technol* 99:1716–1721
87. Holliger C, Alves M, Andrade D, Angelidaki I et al (2016) Towards a standardization of biomethane potential tests. *Water Sci Technol* 74:2515–2522
88. Vicente G, Martinez M, Aracil J (2004) Integrated biodiesel production: a comparison of different homogeneous catalysts systems. *Bioresour Technol* 92:297–305
89. Eevera T, Rajendran K, Saradha S (2009) Biodiesel production process optimization and characterization to assess the suitability of the product for varied environmental conditions. *Renew Energy* 34:762–765
90. Parawira W (2010) Biodiesel production from *Jatropha curcas*. *A Rev Sci Res Essays* 5:1796–1808
91. Tambunan AH, Situmorang JP, Silip JJ, Joelianingsih A, Araki T (2012) Yield and physico-chemical properties of mechanically extracted crude *Jatropha curcas* L oil. *Biomass Bioenergy* 43:12–17
92. Sharma Dugala N, Singh Goindi G, Sharma A (in Press) Evaluation of physicochemical characteristics of Mahua (*Madhuca indica*) and *Jatropha* (*Jatropha curcas*) dual biodiesel blends with diesel. *J King Saud Univ Eng Sci* 1–13
93. Keera ST, El Sabagh SM, Taman AR (2018) Castor oil biodiesel production and optimization. *Egypt J Pet* 27:979–984
94. Kumar R, Dixit AK (2014) Combustion and emission characteristics of variable compression ignition engine fueled with *Jatropha curcas* ethyl ester blends at different compression ratio. *J Renew Energy*
95. Avhad MR, Sánchez M, Bouaid A, Martínez M, Aracil J, Marchetti JM (2016) Modeling chemical kinetics of avocado oil ethanolysis catalyzed by solid glycerol-enriched calcium oxide. *Energy Convers Manag* 126:1168–1177
96. Singh RK, Padhi SK (2009) Characterization of *jatropha* oil for the preparation of biodiesel. *Nat Product Radianance* 2009(8):127–132
97. Bello EI, Mogaji TS, Agge M (2011) The effects of transesterification on selected fuel properties of three vegetable oils. *J Mech Eng Res* 3:218–225
98. Kartika IA (2010) Moisture sorption behavior of *Jatropha* seeds at 20 °c as a source of vegetable oil for biodiesel production. *J Tek Ind Pert* 3:123–129
99. Rizwanul Fattah IM, Masjuki HH, Kalam MA, Wakil MA, Rashedul HK, Abedin MJ (2014) Performance and emission characteristics of a CI engine fueled with *Cocos nucifera* and *Jatropha curcas* B20 blends accompanying antioxidants. *Ind Crop Prod* 57:132–140
100. Kumar K, Sharma MP (2016) Performance and emission characteristics of a diesel engine fuelled with biodiesel blends. *Int J Renew Energy Resour* 6:658–662
101. Sarin R, Sharma M, Sinharay S, Malhotra RK (2007) *Jatropha*-Palm biodiesel blends: an optimum mix for Asia. *Fuel* 86:1365–1371

Morphological and Nanostructural Characteristics of Diesel Exhaust Soot Particles at Different Engine Operating Conditions



Priyanka Arora, Puneet Verma, Faisal Lodi, Mohammad Jafari, Ali Zare, Svetlana Stevanovic, Timothy A. Bodisco, Richard J. Brown, and Zoran Ristovski

1 Introduction

Diesel engines are the primary source of transport from light ground vehicles to heavy-duty trucks [1]. Diesel engine exhaust emissions consist of a high amount of nitrogen oxides (NO_x) and particulate emissions. Reducing these exhaust emissions and meeting the standard of strict emissions legislation is a challenge. Particulate matter (PM) is primarily composed of black carbon/soot formed due to the incomplete combustion of fuel [2] and have an adverse effect on both human health [3] and the environment [4]. Thus, it is extremely important to reduce the negative effects of PM by evaluating the physiochemical properties of diesel soot. Various techniques have been implemented to reduce gaseous emissions and PM. Selective catalytic reduction (SCR) [5] and lean NO_x trap (LNT) [5] are used to reduce NO_x emissions. Diesel oxidation catalyst (DOC) [6] is a modern after-treatment system to reduce carbon monoxides (CO), hydrocarbons (HC), and NO_x by the process of oxidation. Diesel particulate filters (DPF) are used to trap particulate matter, and after a certain period of time, the trapped PM may cause high-back pressure and an increase in engine fuel economy, hence needs to be regenerated [7, 8]. The regeneration of DPFs depends on the oxidation of soot which consequently depends upon the structural characteristics of the soot particle deposited on the filter surface [9]. The variability of geometrical characteristics of soot agglomerates can be computed by the size distribution and fractal dimension, whereas the oxidation reactivity of

P. Arora (✉) · P. Verma · R. J. Brown · Z. Ristovski
International Laboratory for Air Quality and Health, QUT, Brisbane, QLD 4000, Australia
e-mail: p2.arora@hdr.qut.edu.au

P. Arora · M. Jafari · R. J. Brown · Z. Ristovski
Biofuel Engine Research Facility, QUT, Brisbane, QLD 4000, Australia

F. Lodi · A. Zare · S. Stevanovic · T. A. Bodisco
School of Engineering, Deakin University, 75 Pigdons Rd, Geelong, VIC 3216, Australia

© The Author(s), under exclusive license to Springer Nature Singapore Pte Ltd. 2022
P. Verma et al. (eds.), *Advancement in Materials, Manufacturing and Energy Engineering*,
Vol. II, Lecture Notes in Mechanical Engineering,
https://doi.org/10.1007/978-981-16-8341-1_33

soot particles can be quantified by nanostructural analysis of soot particles [10]. It has been reported in the literature that the morphological and nanostructural characteristics of PM have been analyzed by transmission electron microscope (TEM) [9, 11–13]. However, authors have implemented various analytical techniques such as Fourier transform infrared spectroscopy (FTIR), X-ray photoelectron spectroscopy (XPS) to study the functional groups present on soot surface, thermogravimetric analysis (TGA) and differential scanning calorimetry (DSC) for the analysis of soot reactivity by identifying the temperature and time, respectively, required by the soot to be oxidized.

Several studies have been conducted to investigate the impact of the combustion process on exhaust emissions. It has been well documented that the type of engine used, air–fuel ratio and engine operating conditions affect the exhaust emissions and the size distributions of diesel particulate matter [14]. Engine operating conditions and fuel injection timing effects on soot emissions have been observed by Chan et al. [15]. He reported that delaying fuel injection timing increases the soot concentration significantly, whereas it decreases NO. There have been mixed observations in the literature on the morphology and nanostructure characteristics of soot particles. Savic et al. [2] observed an increase in the fractal dimension of diesel exhaust compared to different oxygenated fuels, whereas Agudelo et al. [16] observed opposite trends. Some researchers have observed an increase in primary particle diameter and aggregate size with an increase in engine load and temperature. Therefore, a deeper understanding of physiochemical characteristics of soot particles is required for the reliability of the DPF and the overall performance of the engine. The main objective of this analysis is to examine the effect of engine operating conditions on the characteristics of soot particles (morphology and nanostructure).

2 Experimental Methods

For this experimental study, a common rail compression ignition, turbocharged, after-cooled, six-cylinder diesel engine were used. To control the engine load, the engine was coupled to a water brake dynamometer which was electronically controlled. The specifications details of the engine can be found in references [17]. Experimental details are shown in Fig. 1. Different operating modes for engine run were selected based on maximum power (at 2000 rpm, 162 kW) and maximum torque (at 1500 rpm, 820 Nm) of the engine. Steady states test was performed at different loads (25, 50, 75, and 100%) for two speeds (1500 and 2000 rpm) using ultra low-sulfur diesel fuel.

Nanometre aerosol sampler (NAS) (TSI 3089) was used to collect soot samples on 300-carbon mesh copper-coated TEM grids. For nanostructure and morphology analysis, the sampling time was adjusted approximately five minutes for enough collection of soot particles. A transmission electron microscope (TEM) (JEOL 2100) with LaB₆ filament equipped with TVIPS 4K F416 CCD camera was used to capture TEM imaging. Low-resolution images at 120K magnification with a resolution of the order

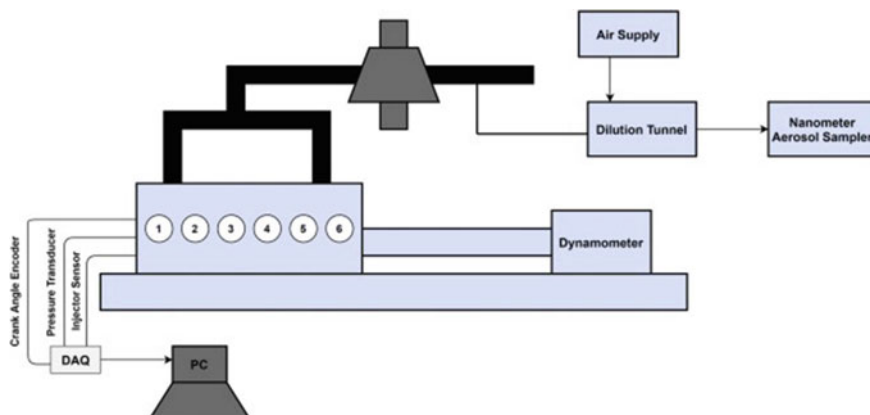


Fig. 1 Engine schematic

of 100–200 nm were captured for determining the morphology of soot agglomerates. Approximately, 50 images were captured by placing the sample in different positions. High-resolution images at 500k times magnification with a resolution of the order of 20 nm were captured for nanostructural analysis of soot particles. To analyze the TEM images and study the nanostructural and morphological characteristics of soot particles, a MATLAB code is used mentioned in literature [18].

3 Results and Discussions

3.1 Morphology Characteristics of Soot Particles

Primary particle diameter and fractal dimension are the two main essential parameters considered to study the morphology of soot agglomerates. TEM images of soot aggregates captured at low magnification for diesel fuels at different loads and speeds are shown in Fig. 2. It can be seen that soot aggregate has irregular clusters, and the shape of soot particle becomes more compact with an increase in engine load. The size of the soot particle is directly related to the oxidation of soot and surface growth. The dominance of each process varies at different stages of the oxidation process [19]. Thus, it is important to study the role of engine operating conditions on the primary particle diameter and fractal dimension. The size of the primary particle has been observed to increase with an increase in engine load, while the particle size decreases with an increase in engine speed, as shown in Fig. 3a.

Lower engine load would result in fuel-lean mixture; therefore, the oxidation of primary particle is enhanced by the presence of excess air resulting in smaller size of soot particle. Higher engine load results in a fuel-rich mixture, hence burning more fuel in the combustion chamber. A decrease in air–fuel ratio results in less oxygen

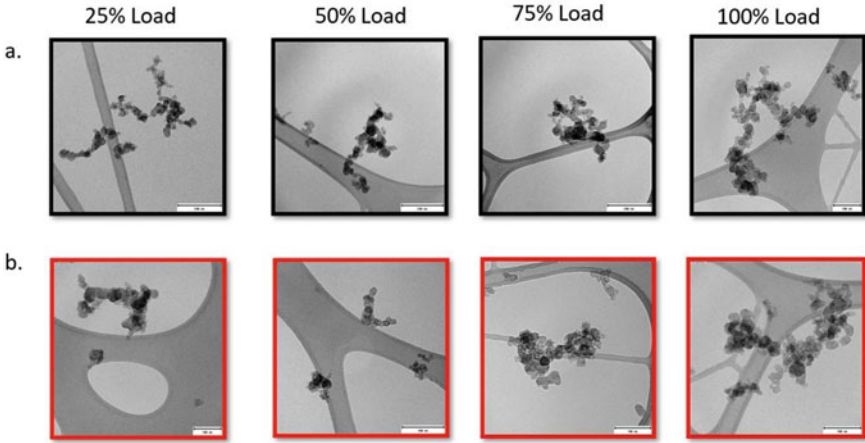


Fig. 2 TEM low-resolution images for different loads a 1500, b 2000 rpm

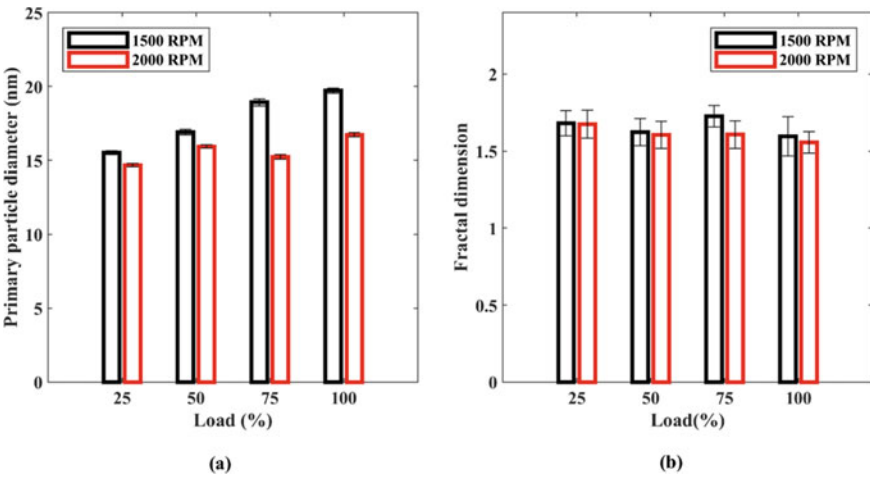


Fig. 3 a Primary particle diameter. b Fractal dimension for diesel at different speeds and loads (error bars show standard error)

availability which results in dominance of surface growth over soot oxidation leading to large size of soot particle. The formation of soot nuclei and surface growth is time-dependent processes [12]. Therefore, lower engine speeds allow more time to the soot particles for surface growth than higher engine speeds resulting in smaller size particles with an increase in engine speed.

Soot aggregates have fractal-like morphology and consist of a number of spherule primary particles clustered irregularly. The fractal dimension helps us to understand the degree of aggregation and the growth process of soot structure [20]. Figure 3b

represents the variation in fractal dimension (D_f) for different operating modes of the engine. Fractal dimension value varies from 1 to 3, where value 1 a chain-like structure and value 3 means a spherical structure. Across all engine operating conditions, the value for fractal dimension varies from 1.55 to 1.78. Similar observations were reported by researchers [13, 21]. The maximum value for fractal dimension was observed at 75% load and 1500 rpm.

3.2 Nanostructural Characterization of Soot Particles

High-resolution TEM images were used to obtain the information for nanostructure analysis. Figure 4 represents the high-resolution TEM images of soot aggregates for diesel at different loads and speeds. Fringe length, fringe tortuosity, and fringe separation distance are the three important parameters considered for the study of nanostructural characteristics of soot particles. Fringe length can be described as the atomic distance of the carbon layer. It has been reported that the soot particles with shorter fringes and higher curvature have a lower degree of graphitization. Alternatively, long and straight fringes tend to have a high degree of graphitization [10, 22, 23].

Figure 5a represents the change in fringe length with respect to load and speed. Similar observations were reported in the literature [2, 13]. It has been observed that the value of fringe length increases with an increase in load. A more ordered graphitic structure is observed for higher engine loads. Researchers reported that the longer fringe length could be related to the combustion cylinder's temperature [24]. Higher in-cylinder temperature promotes the formation of nuclei which enables the formation of orderly graphitic structure. Longer fringe length could also be related

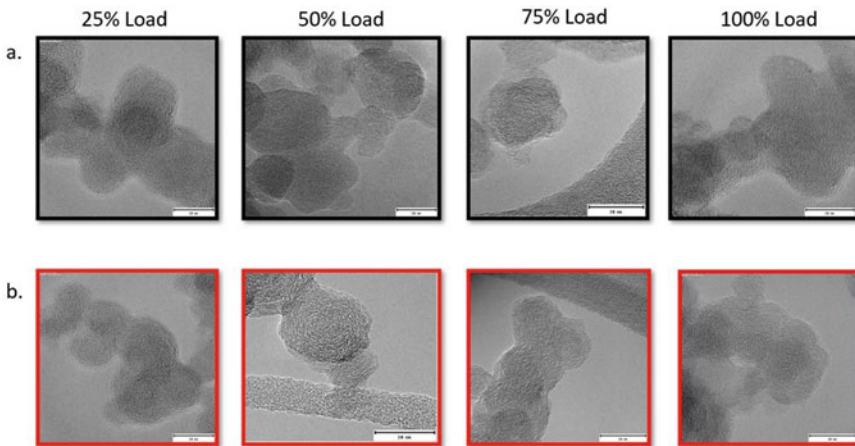


Fig. 4 TEM high-resolution images for different loads **a** 1500, **b** 2000 rpm

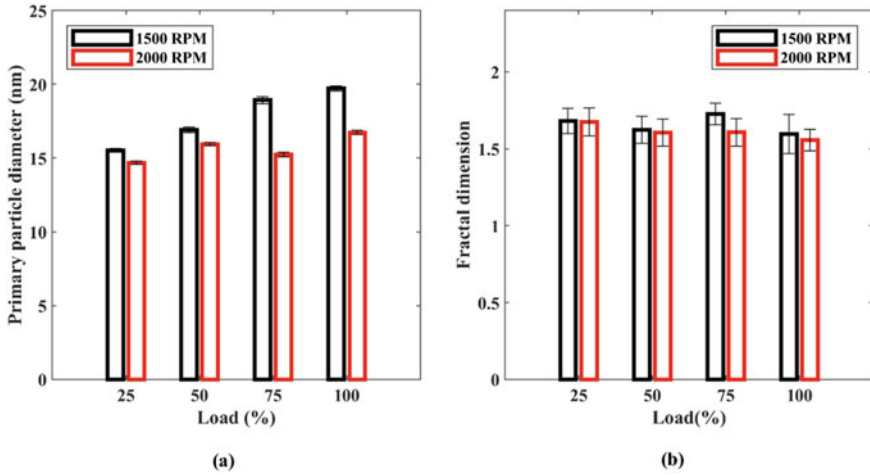


Fig. 5 **a** Fringe length, **b** fringe tortuosity at different loads and speeds (error bars represent standard error)

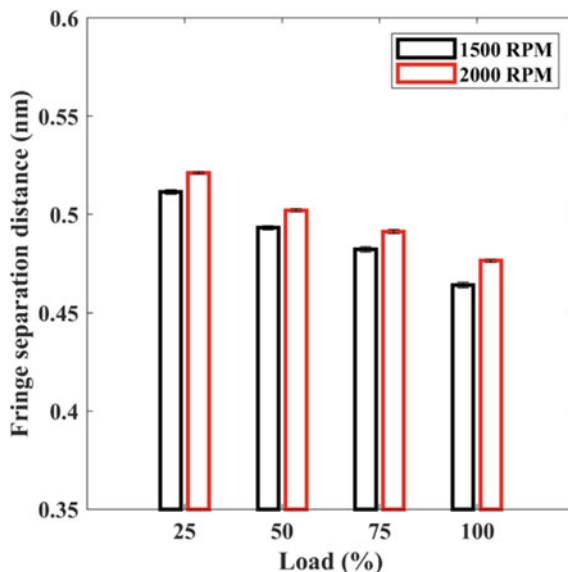
to the residence time of soot in the combustion chamber. As discussed before, longer residence time promotes surface growth, and this could also be a potential reason for ordered graphitic structure. As engine speed increases, a decrease in fringe length has been observed. Less residence time at higher engine speeds results in shorter fringes.

Fringe tortuosity is an important parameter that helps in determining the structural disorder within the carbon layer. Fringe tortuosity is a dimensionless parameter and is expressed as the ratio of actual fringe length to the endpoints distance of a fringe. Increase in fringe tortuosity results in an increase in the gap between the adjacent fringes. The change in fringe tortuosity with respect to loads and speeds is presented in Fig. 5b. Results show that as engine load increases, fringe tortuosity increases, and as engine speed increases, fringe tortuosity decreases. Researchers have observed contrary results for the mean fringe tortuosity.

The distance between two adjacent fringes in a carbon layer is defined as fringe separation distance. As shown in Fig. 6, the fringe separation distance increases with an increase in engine speed and decreases with an increase in the engine load. The results for the fringe separation distance correlate well with the literature [2, 10, 13, 25].

The internal arrangement of the soot particle is highly dependent on the in-cylinder temperature. The higher temperature in the combustion chamber results in a more ordered graphitic structure of soot [26]. Verma et al. [10] concluded that as the temperature inside the combustion chamber increases with engine load, polyaromatic hydrocarbon (PAHs) experiences growth due to the presence of sufficient soot precursors, which in turn results in an increase in the carbon layers and hence, lower the oxidation reactivity of soot.

Fig. 6 Fringe separation distance at different loads and speeds (error bars represent standard error)



4 Conclusion

The impact of engine operating conditions on the morphology and nanostructure of diesel soot particles has been investigated. The main parameters investigated for this study were: the size of primary particle, fractal dimension, fringe separation distance, fringe tortuosity, and fringe length. The summary of the outcomes from the study is as follows:

1. Results show that increasing the engine load results in an increase in the primary particle size. Fuel-rich mixture at higher engine loads decreases the oxidation of soot particles resulting in surface growth being the dominant factor in the process. Soot agglomerate from diesel has compact structure resulting in higher fractal dimension. Shorter fringes at low loads and speeds were observed. Fuel-rich mixture at high loads could be the reason for longer fringes resulting in an ordered arrangement of soot internal structure. Temperature inside the combustion chamber could possibly be the reason for ordered structure of soot particles. Increasing the load on the engine results in a decrease in mean fringe tortuosity. Also, as engine load increases, fringe separation distance decreases.
2. An increase in the size of the primary particle was observed due to an increase in engine speed. Less residence time at high-engine speeds results in a decrease in the size of primary particle as surface growth is a time-dependent process. Longer fringes with high tortuosity were found for higher speeds. Higher tortuosity results in a disordered structure, hence a higher oxidation reactivity of the soot particles. As engine speed increases fringe separation distance increases.

Higher fringe spacing distance results in the higher oxidation reactivity of the soot structure.

Acknowledgements Author (P.A) wish to thank QUT for facilitating as well as assisting financially in the form of a postgraduate research scholarship. The author would like to thank Amir Moghaddam, a laboratory assistant at biofuel Engine Facility Research. The author would like to thank Caltex Ltd. for providing diesel fuel to carry out the experiments. The authors would also like to express thanks to Central Analytical Research Facility (CARF) at QUT for providing all the support regarding TEM training during the process.

References

1. Rajesh Kumar B, Saravanan S (2016) Use of higher alcohol biofuels in diesel engines: a review. *Renew Sustain Energy Rev* 60:84–115. <https://linkinghub.elsevier.com/retrieve/pii/S1364032116001155>
2. Savic N, Saathoff H, Motta N, Leisner T, Gupta B, Rahman MM, Ristovski ZD, Riches J, Miljevic B, Naumann KH (2016) Influence of biodiesel fuel composition on the morphology and microstructure of particles emitted from diesel engines. *Carbon* 104:179–189. <https://doi.org/10.1016/j.carbon.2016.03.061>
3. Ristovski ZD, Miljevic B, Surawski NC, Morawska L, Fong KM, Goh F, Yang IA (2012) Respiratory health effects of diesel particulate matter. *Respirology* 17:201–212
4. Goyal P, Jaiswal N, Kumar A, Dadoo JK, Dwarakanath M (2010) Air quality impact assessment of NOx and PM due to diesel vehicles in Delhi. *Transp Res Part D: Transp Environ* 15:298–303
5. Forzatti P, Lietti L, Nova I, Tronconi E (2010) Diesel NOx aftertreatment catalytic technologies: analogies in LNT and SCR catalytic chemistry. *Catal Today* 151:202–211
6. Caliskan H, Mori K (2017) Environmental, enviroeconomic and enhanced thermodynamic analyses of a diesel engine with diesel oxidation catalyst (DOC) and diesel particulate filter (DPF) after treatment systems. *Energy* 128:128–144. <https://doi.org/10.1016/j.energy.2017.04.014>
7. Galvez ME, Zhang H, Legros G, Chen Y, Da Costa P, Iojoie EE, Pereira O (2018) Structure-reactivity study of model and Biodiesel soot in model DPF regeneration conditions. *Fuel* 239:373–386. <https://doi.org/10.1016/j.fuel.2018.11.050>
8. Guo Y, Stevanovic S, Verma P, Jafari M, Jabbour N, Brown R, Cravigan L, Alroe J, Osuagwu CG, Brown R, D'Anna B, Ristovski Z (2019) An experimental study of the role of biodiesel on the performance of diesel particulate filters. *Fuel* 247:67–76. <https://doi.org/10.1016/j.fuel.2019.03.042>
9. Lapuerta M, Oliva F, Agudelo JR, Boehman AL (2012) Effect of fuel on the soot nanostructure and consequences on loading and regeneration of diesel particulate filters. *Combust Flame* 159:844–853
10. Verma P, Jafari M, Guo Y, Pickering E, Stevanovic S, Bodisco TA, Fernando JFS, Golberg D, Brooks P, Brown R, Ristovski Z (2019) Experimental analysis of the morphology and nanostructure of soot particles for butanol/diesel blends at different engine operating modes. *Energy Fuels* 33:5632–5646
11. Vander Wal RL, Tomasek AJ (2004) Soot nanostructure: Dependence upon synthesis conditions. *Combust Flame* 136:129–140
12. Li Z, Song C, Song J, Lv G, Dong S, Zhao Z (2011) Evolution of the nanostructure, fractal dimension and size of in-cylinder soot during diesel combustion process. *Combust Flame* 158:1624–1630. <https://doi.org/10.1016/j.combustflame.2010.12.006>

13. Verma P, Pickering E, Jafari M, Guo Y, Stevanovic S, Fernando JFS, Golberg D, Brooks P, Brown R, Ristovski Z (2019) Influence of fuel-oxygen content on morphology and nanostructure of soot particles. *Combust Flame* 205:206–219. <https://linkinghub.elsevier.com/retrieve/pii/S0010218019301543>
14. Yehliu K, Armas O, Vander Wal RL, Boehman AL (2013) Impact of engine operating modes and combustion phasing on the reactivity of diesel soot. *Combust Flame* 160:682–691. <https://doi.org/10.1016/j.combustflame.2012.11.003>
15. Chan TL, Cheng XB (2007) Numerical modeling and experimental study of combustion and soot formation in a direct injection diesel engine. *Energy Fuels* 21:1483–1492
16. Agudelo JR, Álvarez A, Armas O (2014) Impact of crude vegetable oils on the oxidation reactivity and nanostructure of diesel particulate matter. *Combust Flame* 161:2904–2915. <https://doi.org/10.1016/j.combustflame.2014.05.013>
17. Rahman MM, Pourkhesalian AM, Jahiril MI, Stevanovic S, Pham PX, Wang H, Masri AR, Brown RJ, Ristovski ZD (2014) Particle emissions from biodiesels with different physical properties and chemical composition. *Fuel* 134:201–208. <https://doi.org/10.1016/j.fuel.2014.05.053>
18. Verma P, Pickering E, Savic N, Zare A, Brown R, Ristovski Z (2019) Comparison of manual and automatic approaches for characterisation of morphology and nanostructure of soot particles. *J Aerosol Sci* 136:91–105. <https://doi.org/10.1016/j.jaerosci.2019.07.001>
19. Tree DR, Svensson KI (2007) Soot processes in compression ignition engines. *Prog Energy Combust Sci* 33:272–309
20. Köylü ÜÖ, Faeth GM, Farias TL, Carvalho MG (1995) Fractal and projected structure properties of soot aggregates. *Combust Flame* 100:621–633
21. Wu Z, Song C, Lv G, Pan S, Li H (2016) Morphology, fractal dimension, size and nanostructure of exhaust particles from a spark-ignition direct-injection engine operating at different air–fuel ratios. *Fuel* 185:709–717
22. Ess MN, Bladt H, Mühlbauer W, Seher SI, Zöllner C, Lorenz S, Brüggemann D, Nieken U, Ivleva NP, Niessner R (2016) Reactivity and structure of soot generated at varying biofuel content and engine operating parameters. *Combust Flame* 163:157–169
23. Pfau SA, La Rocca A, Haffner-Staton E, Rance GA, Fay MW, Brough RJ, Malizia S (2018) Comparative nanostructure analysis of gasoline turbocharged direct injection and diesel soot-in-oil with carbon black. *Carbon* 139:342–352. <https://doi.org/10.1016/j.carbon.2018.06.050>
24. Vander Wal RL, Tomasek AJ (2003) Soot oxidation: dependence upon initial nanostructure. *Combust Flame* 134:1–9
25. Soewono A, Rogak S (2011) Morphology and Raman spectra of engine-emitted particulates. *Aerosol Sci Technol* 45:1206–1216
26. Li X, Xu Z, Guan C, Huang Z (2014) Impact of exhaust gas recirculation (EGR) on soot reactivity from a diesel engine operating at high load. *Appl Therm Eng* 68:100–106

Design and Simulation Study of a Piezoelectric Microcantilever-Based Energy Harvester for Ambient Vibrations



Vinod Belwanshi, Vishnuram Abhinav, and Vibhor Kumar

1 Introduction

The inherent properties associated with the piezoelectric materials have been enabled it as an attractive material for small magnitude energy harvesting from the environmental and other vibration sources. The increasing demands of the microsystem with energy harvesting technology make it a very prominent candidate to replace the conventional chemical batteries or external power supply. Hence, the piezoelectric-based micro energy harvesters can eliminate battery constrain and complicated wirings in low-power microsystems and sensor arrays, which are generally used for IoT (Internet of Things) applications. Therefore, it becomes a solution for the wireless microsensors network that is deployed in a remote location [1]. The various designs of the energy harvester are proposed in the literature [2]. Piezoelectric, electrostatic and electromagnetic transduction mechanisms are mainly adopted for the energy harvester in MEMS technology. The transduction mechanism is accountable for converting mechanical domain physical inputs into electrical domain output. In the case of the piezoelectric technique, the input mechanical displacement/vibration generates stress/strain that is responsible for the generation of the charge in the piezoelectric material, hence output voltage. Piezoelectric-based energy harvesters are commonly used in the microsystems due to their ease of implementation and comparatively higher electrical output. The frequency for human body motion (i.e.

V. Belwanshi (✉)

School of Physics and Astronomy, University of Glasgow, Glasgow G12 8QQ, UK

e-mail: vinod.belwanshi@glasgow.ac.uk

V. Abhinav

Dept. of Electrical Engineering, Indian Institute of Technology, Mumbai 400076, India

V. Kumar

Department of Electrical Engineering, Northern Illinois University, Dekalb 60115, USA

≤ 10 Hz) and machine induced vibration (i.e. ≥ 50 Hz) lies in the lower end of the spectrum. Therefore, it is a prime concern to design and simulate a piezoelectric energy harvester that can generate micropower using ambient vibration. It has the potential application to power a few microsensors used in IoT applications. In this paper, a multilayered microcantilever design is presented for the micro energy harvester. The design was carried out based on the piezoMUMPs process. The response of microcantilever is analyzed in terms of displacement, generated charge, power and energy output. The paper is divided as follows: Section 2 introduces the theory and mathematical model used, Sect. 3 describes methodology and material, Sect. 4 deals with the results and discussions, and Sect. 5 presents the conclusions.

2 Mathematical Modelling

A piezoelectric crystal exhibits the property to generate electrical charges under the applied mechanical force and vice versa. The charges are generated due to the deformation and induce stresses in piezoelectric materials on top of the microcantilever. An applied mechanical force gives rise to the charge separation; hence, voltage is induced. The piezoelectric effect is reversible. Therefore, by means of applied mechanical input, it resulted in the output voltage and by applying the electrical voltage it will give vibration as mechanical output.

2.1 Electrical Modelling

The equivalent circuit of the piezoelectric crystal is depicted in Fig. 1. Based on the applied input to the piezoelectric crystal, there are two categories of constant which are used to describe the piezoelectric effect: (1) g constant; when voltage is applied to the crystal as input and mechanical vibration become the response (output), and (2) d constant; when mechanical input is applied to the crystal and voltage induced is a response (output). These are written as g_{ij} and d_{ij} ; i is the direction of the electric effect, j is the direction of a force.

(i) g constant is defined as:

$$g_{33} = \frac{V/c}{F/ab}; \text{ field produced in direction 3 and stress applied in direction 3.}$$

(ii) d constant is defined as: $d_{33} = \frac{q}{F}$; charge generated in direction 3 and force applied in direction 3

$$C_{eq} = C_s + C_c + C_a \quad (1)$$

$$R_{eq} = R_s || R_a \quad (2)$$

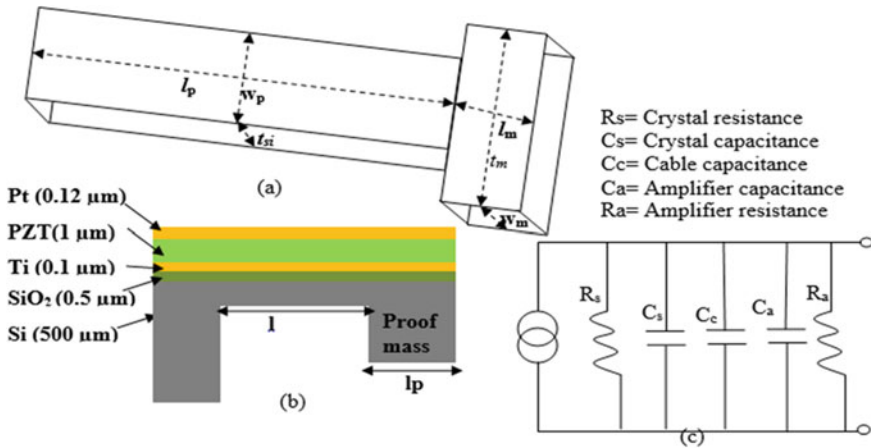


Fig. 1 Schematic of microcantilever beam **a** Geometrical dimensions. **b** Multilayer view of microcantilever. **c** Electrical equivalent of a piezoelectric crystal

$$\frac{dq}{dt} - C_{eq} \frac{dV}{dt} = i \tag{3}$$

$$V_o = i R_{eq} = \left(\frac{dq}{dt} - C_{eq} \frac{dV}{dt} \right) R_{eq} \tag{4}$$

$$R_{eq} C_{eq} \frac{dV}{dt} + V_o = R_{eq} \frac{dq}{dt} \tag{5}$$

By the Laplace transform,

$$\frac{V_o(S)}{q(S)} = \frac{R_{eq} S}{R_{eq} C_{eq} S + 1} \tag{6}$$

2.2 Mechanical Modelling

The charge is being generated based on the applied force. At this juncture, the microcantilever beam is utilized to convert the force in the induced stress, and hence, the charge is developed in the piezoelectric material. To get the maximum output power density one has to tune a resonant frequency of microcantilever equal to the frequency of the environmental vibration. The maximum output is not attained if the resonant frequency fails to match with the vibration frequency [3]. An acceleration of vibration source is an important parameter in which the device can withstand.

The commonly available vibrating source lies in the moderate acceleration amplitude (<1 g) and low-frequency range (60–200 Hz) [4]. Current work is projected to design an energy harvester for natural vibration and low magnitude of acceleration using a multilayered microcantilever based on MEMS technology. A multilayer microcantilever comprises of Pt/PZT/Pt/Si/SiO₂ multilayers that are deposited in the silicon substrate. The PZT layer is sandwiched between two electrodes of platinum. Silicon is the main structural material for the microcantilever. The proof mass on the tip of the microcantilever is created to decrease its resonant frequency that leads to better sensing for natural vibration to convert in energy.

The resonant frequency of a cantilever (without a proof mass) as a first-order mass-spring system is expressed as;

$$f_n = \frac{1}{2\pi} \sqrt{\frac{k_{\text{eff}}}{m_{\text{eff}}}} \quad (7)$$

The effective mass of a cantilever beam with the proof mass is modelled a point load at the tip is defined as;

The total effective mass is

$$m_{\text{eff}} = 0.236\rho Al + m_{\text{proof}} \quad (8)$$

Similarly, the effective stiffness of the rectangular cantilever beam (without proof mass) is;

$$k_{\text{eff}} = \frac{3EI}{l^3}; \quad (9)$$

Analytically, modal frequency of the cantilever is calculated by [5];

$$f_n = \frac{v_n^2}{2\pi} \frac{1}{l^2} \sqrt{\frac{EI}{m'}}; \quad (10)$$

where, $v_n = 1.875, 4.694, 7.885, \dots$ is n th eigen value, which shows the modes of the natural frequency. f_n is the natural frequency of cantilever, l is the length of the cantilever, EI is the flexural rigidity, and $D_p = EI/w$ is the bending modulus per unit width. m' is the mass per unit length of the cantilever beam, I is the area moment of inertia about the neutral axis.

$$f_n = \frac{v_n^2}{2\pi} \frac{1}{l^2} \sqrt{\frac{D_p}{m}}; \quad (11)$$

where, D_p is the dependent on the young's modulus of silicon (E_{si}) and piezoelectric material (E_p) and their thickness t_{si} (silicon) and t_p (piezoelectric material), respectively, for unimorph composite cantilever.

$$D_p = [E_p^2 t_p^4 + E_{si}^2 t_{si}^4 + 2E_p E_{si} t_p t_{si} (2t_p^2 + 2t_{si}^2 + 3t_p t_{si})] \times [12(E_p t_p + E_{si} t_{si})]^{-1}$$

and mass per unit area m is calculated from the thicknesses and densities.

$$m = \rho_p t_p + \rho_{si} t_{si} \quad (12)$$

The resonant frequency of a cantilever with a point proof mass placed at free end tip can be approximated as,

$$f'_n = \frac{v_n'^2}{2\pi} \frac{1}{l^2} \sqrt{\frac{k_{\text{eff}}}{m_{\text{canti}} + m_{\text{proof}}}} \quad (13)$$

where $v_n'^2 = v_n^2 \sqrt{0.236/3}$ and effective mass at the cantilever tip $m_{\text{canti}} = 0.236 mwl$ and $m = \rho_p t_p + \rho_{si} t_{si}$ m_{proof} is added at the free tip of the cantilever.

$$k_{\text{eff}} = \frac{3D_p w}{l^3} \quad (14)$$

For a distributed mass at the free end of the cantilever, centre of mass will be the centre of the proof mass at $l_{\text{proof}}/2$., therefore effective spring constant in this location is given by [6]

$$k' = k \left(\frac{l}{l - \frac{l_{\text{proof}}}{2}} \right)^3 \quad (15)$$

Substituting these values.

$$f'_n = \frac{v_n'^2}{2\pi} \sqrt{\frac{0.236 D_p w}{\left(l - \frac{l_{\text{proof}}}{2}\right)^3 (0.236 mwl + m_{\text{proof}})}} \quad (16)$$

The targeted resonant frequency has been reached by modification in the lengths and widths of the cantilever beam and dimensions of the proof mass.

3 Methodology and Materials

The MEMS technology-based energy harvesters are becoming a very prominent candidate for low-power devices. The piezoelectric material-based energy harvester with a microcantilever is commonly used to detect natural vibration and produce the corresponding electrical output. A microcantilever with multilayered films of SiO₂/Pt/PZT/Pt-Ti deposited on the structural cantilever of silicon material. The

Table 1 Material properties dimension of multilayered cantilever [7]

Properties	Si	SiO ₂	Pt	Pt-Ti	PZT
Density (kg/μm ³)	2.3×10^{-15}	2.2×10^{-15}	2.1×10^{-14}	2.1×10^{-14}	7.8×10^{-15}
Young's modulus (MPa)	1.65×10^5	7.0×10^4	1.68×10^5	1.68×10^5	26.2×10^4
Thickness (μm)	465	0.5	0.1	0.12	1

silicon as proof mass is used at the end of the cantilever beam to enhance its sensitivity towards the natural vibration and decreased in natural frequency. To create the solid structure of the multilayered microcantilever the material properties, process steps of fabrication and layout are defined in advanced. The major material properties are listed in Table 1. Moreover, the predefined fabrication process sequence is used. The geometrical dimension of the cantilever is optimized for the desired frequency. The geometrical dimension is selected for the microcantilever with proof mass is (2260 μm × 400 μm × 12 μm) and (940 μm × 1560 μm × 465 μm), respectively.

Process steps for fabrication of microcantilever for energy harvester used as PiezoMUMPs process:

- (i) Substrate selection
- (ii) oxide growth
- (iii) oxide etching
- (iv) sputtering of the bottom electrode
- (v) PZT chemical solution deposition
- (vi) Metal deposition for the top electrode
- (vii) patterning of the top electrode
- (viii) patterning of PZT
- (ix) patterning of the bottom electrode.

The required initial inputs (i.e. material properties, fabrication process and layout for microstructure and microelectronics components) are given to the software. The final 3D model is created based on the input. The analysis of the solid model is performed after meshing the model. Mechanical analysis has been performed to get the modal frequency of the microstructure, followed by the piezoelectric analysis. The results are presented in the subsequence section.

4 Results and Discussion

The designed microcantilever is analyzed to predict its performance as an energy harvester using the commercially available MEMS tool. Investigation of microcantilever-based energy harvester is presented in this section. The desired modes, generated output voltage and output charge and resulting current are presented for the microcantilever energy harvester.

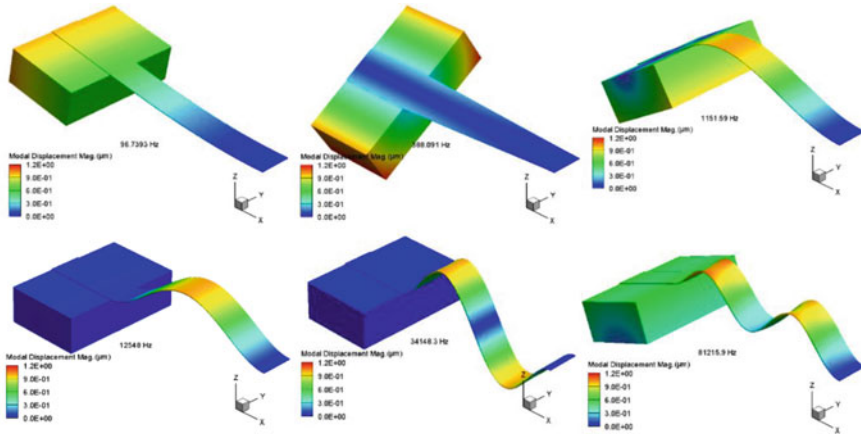


Fig. 2 Six modes of the vibration in which the first mode is desirable

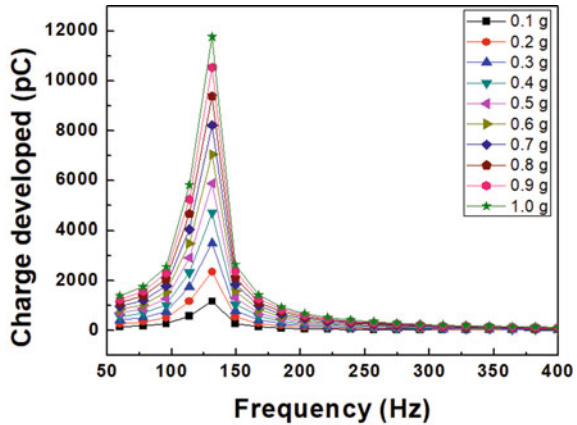
4.1 Modal Analysis

Modal analysis is used to calculate the resonant frequency of the microcantilever. The first mode is a desired mode of operation for the microcantilever. The vibration modes are analyzed and presented in this section. The desired operating frequency is obtained by modifying the geometrical parameter of the cantilever. Results with six modes are presented in Fig. 2.

4.2 Harmonic Piezoelectric Analysis

The harmonic analysis is carried out in order to find the frequency response of the microcantilever, and a piezoelectric analysis provides the generated output charge and voltage when it is subjected to an oscillating load in a certain mode of vibration. The output charge and voltage around the natural frequency are plotted for the microcantilever with varying frequency. The analysis for the response of the micro energy harvester is presented with varying frequency and amplitude of the vibration (0.1–1 g). The piezo analysis is performed to get an output charge or output voltage which corresponds to the close circuit and open circuit analysis, respectively. In close circuit analysis ($R_{load} = 0$), the piezoelectric layer generates only charge (no voltage) across the electrode. However, in open circuit analysis, output voltage is generated. Simulation for charge calculation: Both electrode potential is set to zero to get the charge output. However, the simulation for voltage calculation is carried out with top electrode as Tiepotential is set to zero, and also, the bottom electrode potential is set to zero. The displacement magnitude of the microcantilever is observed maximum at the resonant frequency (~126 Hz) of the structure shown in Fig. 3.

Fig. 3 Harmonic displacement magnitude of microcantilever for a varying magnitude of applied acceleration



The magnitude of displacement of microcantilever is increasing linearly with an increase in the acceleration magnitude of vibration from 0.1 to 1 g. Displacement of microcantilever is responsible for the generation of stress on the micro-cantilever. Hence, PZT material layer experienced the same stress and result in the charge separation on its top and bottom layer shown in Fig. 4. Based on the harmonic analysis, the charges are induced in the piezoelectric material. The induced charge is due to applied stress in the material. It is also observed that the maximum charge was generated at the resonant frequency. It is also seen that generated charge is increasing with an increase in the acceleration (Fig. 4).

Similarly, the induced voltage analysis using an open circuit configuration was carried out. It was observed that the maximum voltage at the resonance frequency of the microcantilever. It is also seen that the maximum generated voltage was increasing with the applied acceleration shown in Fig. 5. It is observed that maximum charge induced at the resonant frequency of the microcantilever, and it leads to the

Fig. 4 Generated charge versus frequency under varying magnitude of acceleration (0.1–1 g) at resistive load of 1 MΩ

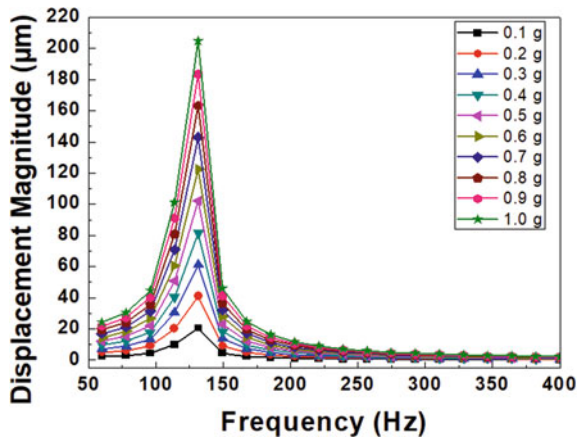
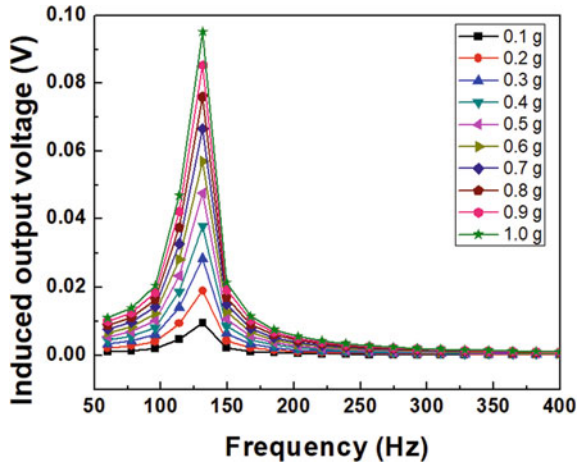


Fig. 5 Induced voltage as a function of frequency with a varying magnitude of acceleration (0.1–1 g) at 1 MΩ load



maximum output voltage and current as shown in Figs. 5 and 6, respectively. It is because of matching the input frequency of vibration with a resonant frequency of microstructure.

Moreover, the maximum power is achieved at the resonant frequency of the cantilever due to maximum current and voltage. Maximum power is transferred when the load resistance is equal to an internal resistance of the equivalent circuit. Hence, load optimization analysis is done around the resonance frequency of the microcantilever as shown in Fig. 7. The maximum power transfer depends on the internal impedance of the PZT layer; therefore, varying load analysis has been carried out to find out the internal resistance, and hence, maximum power and energy dissipation were depicted in Figs. 7 and 8, respectively.

Fig. 6 Generated current versus frequency with a varying magnitude of acceleration (0.1–1 g) at 1 MΩ load

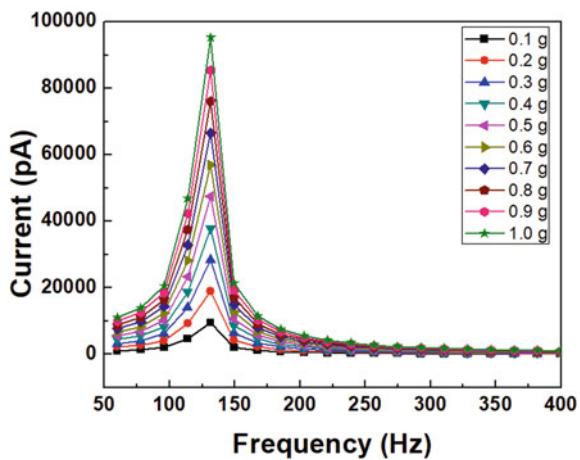


Fig. 7 Power dissipation versus load around the resonance frequency of the microcantilever at 1 g acceleration

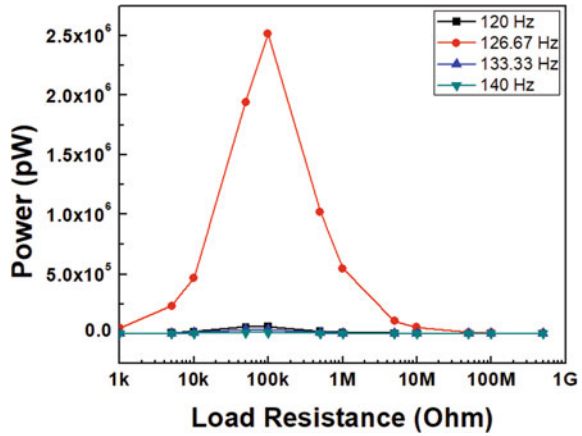
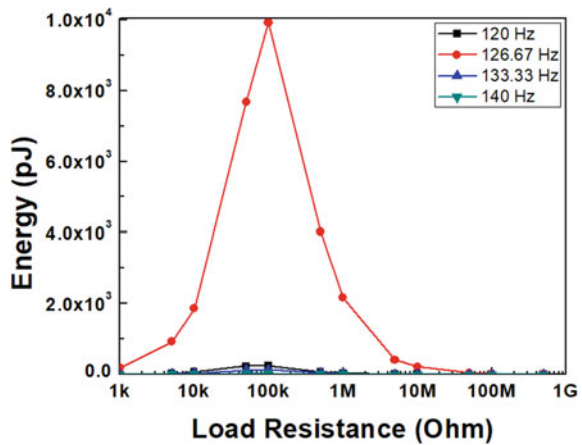


Fig. 8 Energy dissipation versus load at 1 g acceleration



5 Conclusions

The design and simulation of a multilayered microcantilever-based piezoelectric energy harvester are presented. The micro energy harvester is modelled based on the piezoMUMPs process. The micro energy harvester can be used to drive low-power microsensors. The results are presented in terms of displacement magnitude, total charge induced, generated output voltage and output current of the PZT based micro-cantilever. It is observed that maximum power is generated at the resonant frequency of the cantilever. The finalized design gives a significant energy to drive a microsensor in a remote location. The internal impedance of 100 kΩ is obtained with a maximum power transfer of 2.5 μW for the piezoelectric energy harvester.

References

1. Kim S-G, Priya S, Kanno I (2012) Piezoelectric MEMS for energy harvesting. *MRS Bull* 37(11):1039–1050
2. Saadon S, Sidek O (2011) A review of vibration-based MEMS piezoelectric energy harvesters. *Energy Convers Manag* 52(1):500–504
3. Roundy S, Leland ES, Baker J, Carleton E, Reilly E, Lai E, Otis B, Rabaey JM, Wright PK, Sundararajan V (2005) Improving power output for vibration-based energy scavengers. *IEEE Pervasive Comput* 4(1):28–36
4. Roundy S, Wright PK (2004) A study of low level vibrations as a power source for wireless sensor nodes. *Comput Commun* 26:1131–1144
5. Yi JW, Shih WY, Shih WH (2002) Effect of length, width, and mode on the mass detection sensitivity of piezoelectric unimorph cantilevers. *J Appl Phys* 91(3):1680–1686
6. Sader JE, Chon JWM, Mulvaney P (1999) Calibration of rectangular atomic force microscope cantilevers. *Rev Sci Instrum* 70(10):3967–3969
7. Shen D, Park JH, Noh JH, Choe SY, Kim SH, Wickle HC, Kim DJ (2009) Micromachined PZT cantilever based on SOI structure for low frequency vibration energy harvesting. *Sens Actuators A Phys* 154(1):103–108

Utilization of Local Riverbed Sand in Green Sand Mould Casting—A Study



Jatin Sadarang, Ramesh Kumar Nayak , and Isham Panigrahi

1 Introduction

Foundry industries use high silica content sand in mould making. The silica sand has high refractoriness and is readily available; therefore, it is used in foundry applications [1]. The foundry industries used around 85% silica sand to prepare a sand mould [2]. Silica sand is the basic raw material of foundry industries. Nowadays, foundry industries are facing challenges due to shortage and rise in price of silica sand. Silica sand is also used in various industrial applications like glass making, ceramics, refractory lines, construction, etc., which increases its consumption and cost. Therefore, foundry engineers, researchers and scientists are trying different sands in sand mould casting.

Aweda and Jimoh [3] evaluated compactibility, shatter index, permeability, dry and green compressive strength of Ilesha and Ilorin (river sand) sand mould. They observed that both moulding sands had desired mould properties for non-ferrous casting.

The refractoriness of river Gurara located in Nigeria is 1500 °C and has desired mould properties for non-ferrous, light grey iron and some grade of steel castings [4]. The use of chill in sand mould increases the cooling rate of casting [5, 6]. Permeability of moulding sand affected by particle size distribution [7]. The sand having an 80:20 ratio of coarse and fine particles provides good surface morphology for aluminium alloy casting [8]. Oyun river sand contains 84.49–84.58% silica and has desired mould properties for non-ferrous casting [9]. Niger river sand has a 1575 °C melting point and contains 94% silica. Therefore, it is used in green sand mould for ferrous and non-ferrous casting [10]. The river Niger sand mould has 420 permeability with 4%

J. Sadarang (✉) · I. Panigrahi

School of Mechanical Engineering, KIIT Deemed To Be University, Bhubaneswar 754024, India

R. K. Nayak

Department of Materials and Metallurgical Engineering, MANIT, Bhopal 462003, India

moisture content. The shearing of Niger sand mould increases as the concentration of moisture increases [11]. The green and dry shear strength of Igbokoda silica sand increase with increase in clay concentration [12]. Enugu silica sand has desired mould properties for steel casting with 3% moisture and 8% binder in moulding sand [13]. The fine mould aggregates reduce mould compactability; therefore, increase in bentonite percentage in river sand mould compactability decreases [14]. Many researchers used different sands in mould and evaluated mould properties for the feasibility of the casting process. Hence, in the present investigation, local river sand is used in sand mould and evaluated shear strength and compactability at different percentage of moisture and bentonite content.

2 Materials and Methods

2.1 Materials

The materials required to make the sand mould is basically silica sand, bentonite, coal dust and moisture. In this investigation, instated of silica sand, we have used local riverbed sand for the analysis. The local riverbed sand was collected from Cuttack, Odisha. Figure 1a–d shows the physical appearance of all materials.

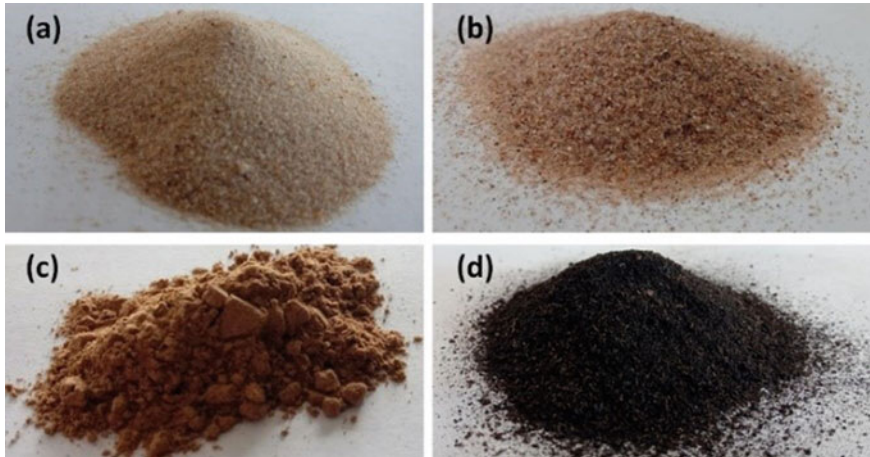


Fig. 1 Physical appearance of **a** silica sand, **b** riverbed sand, **c** bentonite clay and **d** coal dust

Table 1 Particle size distribution of river sand

Sieve size (μm)	Retained %
	River sand
4750	0
4000	0
2360	0
600	0
212	84.5
150	12.7
106	0.8
75	0.8
Pan	0.2
AFS number	54

2.2 Sieve Analysis

The particle size distribution of mould ingredients effect mould properties. Therefore, in the present investigation, sieve analysis was carried out to determine particle size distribution of river sand. The river sand sample of 100 g was put in top sieve and vibrated in sieve vibrator for 15 min. The sand sample retained in each sieve was measured with weighing machine and reported in Table 1. It is observed that the sand sample contains 90% of sand particles of size between 600 and 212 μm. The grain fineness number (GFN) of river sand was evaluated as per Eq. 1. The GFN of river sand is 54.

$$\text{AFS Grain Fineness Number} = \frac{\text{Sum of multiplication product}}{\text{total \% of retained grains}} \quad (1)$$

2.3 Sample Preparation

The systematic flow diagram of testing of river sand mould is shown in Fig. 2. The mould ingredients (river sand, bentonite clay, coal dust and water) were mixed in sand muller for uniform mixing. Mould shear strength and compactibility were determined with different compositions of mould, as reported in Table 2. The moisture content in moulding sand was determined by moisture teller equipment as shown in Fig. 3a. River sand mould sample and calcium carbide powder of 6 and 12 g, respectively, were mixed in moisture teller. Moisture reacts with calcium carbide powder and generates acetylene gas. The gas raises pressure in moisture teller. The calibrated pressure gauge of moisture teller shows percentage of moisture in moulding sand.

Fig. 2 Systematic flow diagram of river sand mould testing

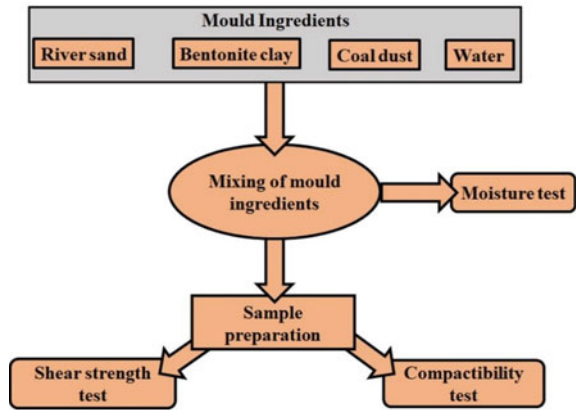


Table 2 River sand mould composition

Specimen	Moisture (%)	River sand (%)	Bentonite clay (%)	Coal dust (%)
RS-1	3	85	10	5
RS-2	3	83	12	5
RS-3	3	81	14	5
RS-4	4	85	10	5
RS-5	4	83	12	5
RS-6	4	81	14	5
RS-7	5	85	10	5
RS-8	5	83	12	5
RS-9	5	81	14	5
RS-10	7	85	10	5
RS-11	7	83	12	5
RS-12	7	81	14	5

American foundry society (AFS) standard sample was used to determine shear strength of mould. The cylindrical sample was prepared with sand rammer having 6.35 kg ramming mass and 50 mm falling height, as shown in Fig. 3b. The sample tube was filled with 140–145 g river mould sample, and three ramming strokes were applied. The cylindrical sample was formed having 50 mm diameter and height.

2.4 Shear Strength

Universal strength machine (USM) was used to determine the green shearing strength of river sand mould. The AFS cylindrical sample was placed between shearing heads,

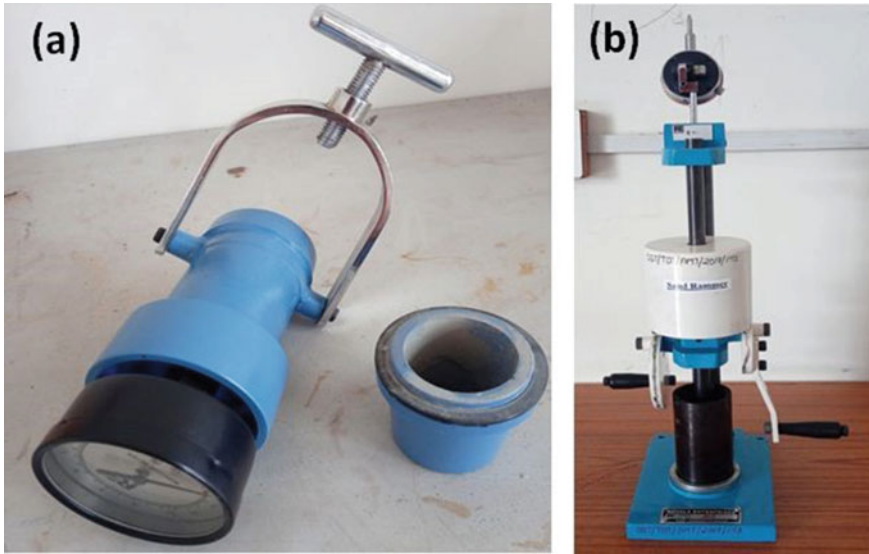


Fig. 3 a Moisture teller and b sand rammer

and shear force was applied. The green shear strength of river sand was recorded from an attached computer.

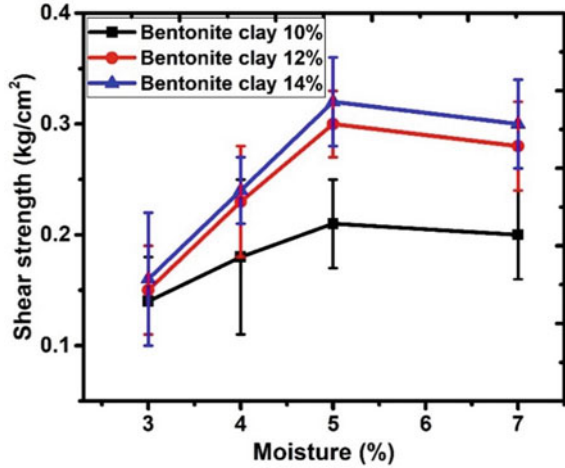
2.5 Compactibility

Compactibility of moulding sand is defined as reduction in volume percentage of loose moulding sand under standard compressive load. The compactibility tube was filled with loose riverbed sand mould mixture. Then, three ramming strokes were applied before testing. The reduction in volume was evaluated with compactibility measuring scale.

3 Results and Discussions

The shear strength of green sand mould casting is very important to understand the mould's load-bearing capacity during casting. Figure 4 shows the shear strength versus moisture content in the sand mould mixture. It is observed that with the increase in moisture content, shear strength increases up to 5 wt% and decreases with further increase in moisture content. However, the shear strength increases with increase in bentonite content and maximum as 5 wt% of moisture. This is because bentonite acts as binder in the presence of moisture [15]. Therefore, as concentration

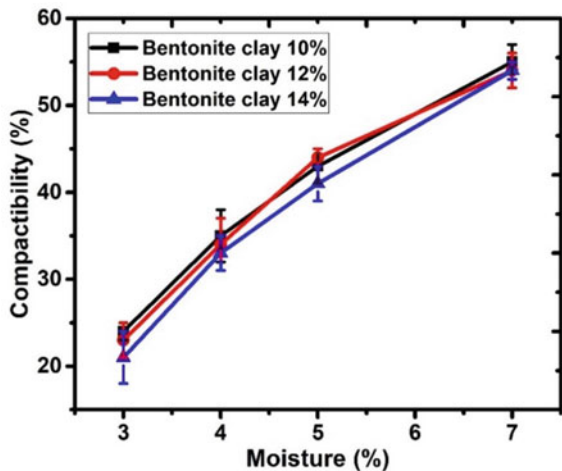
Fig. 4 Shear strength versus moisture content of riverbed sand mould



of moisture increases, the shear strength of the mould increases. However, excess moisture content creates a thin layer on sand mould ingredients which reduces green mould strength. Therefore, the shear strength decreases with addition of moisture above 5% in moulding sand.

Compactibility of sand mould gives an idea about its porosity or permeability level of sand mould. If the compactibility increases, sand mould's permeability decreases and leads to gas-related defects in casting products. Therefore, in this investigation, the effect of moisture content on compactibility has been studied and shown in Fig. 5. It is observed that with the increase in moisture content, the compactibility increases irrespective of binder content in the mould. This is because with the increase in moisture content the lubricating properties increases and hence increase

Fig. 5 Compactibility versus moisture content of riverbed sand mould



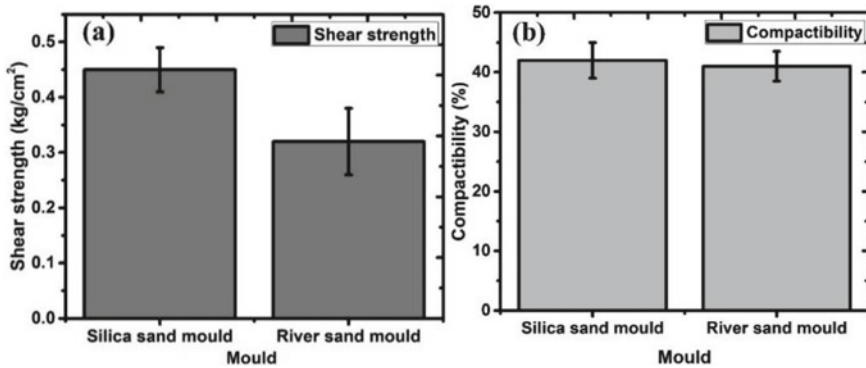


Fig. 6 Comparison between silica sand and local riverbed sand **a** shear strength and **b** compactibility

the compactibility. The compactibility of the mould has related to the density of the mould [16]. It is observed that the compactibility is 41 at 5 wt% of moisture and 10% binder, which is suitable for sand casting process.

The newly developed riverbed sand mould properties are compared with commercial silica sand mould in Fig. 6a, b. It is observed that the shear strength of riverbed sand mould is lower than silica sand mould at same amount of moisture and bentonite content. This is due to smaller particle size of commercial silica sand as compared to local riverbed sand. Nevertheless, the shear strength of local river sand is as per the sand casting process requirement [15]. However, the compactibility of both silica sand moulds is similar.

4 Conclusions

The demand for high purity silica sand is increasing day by day. The authors have tried to investigate the suitability of local riverbed sand for sand mould casting. In this investigation, some of the sand mould properties were evaluated and compared with high purity silica sand mould. The following conclusions are made.

- The shear strength of local riverbed sand mould has lower value than commercial high purity silica sand mould at same wt% of moisture and bentonite content. However, the shear strength of local riverbed sand may be suitable for non-ferrous and small size casting.
- There is no significant difference in compactibility in silica sand and river sand mould having moisture (5%), coal dust (5%) and bentonite (14%) content.
- The local riverbed sand may be used for non-ferrous casting process, where the surface finish is not so critical. The detail analysis on the effect of mold constituents and casting quality need to be investigated before use in Industries.

Funding The authors would like to express their sincere thanks to the Advanced Manufacturing Technology program of the Department of Science & Technology, Govt. of India, for the financial support to carry out this work (Grant no. DST/TDT/AMT/2017/173). Special thanks to RSB Metal-tech, Pvt. Ltd, Cuttack, India, for their support as an industrial partner to develop alternate source to commercial-grade silica sand for Indian foundry industries.

References

1. Murthy IN, Rao JB (2016) Investigations on physical and chemical properties of high silica sand, Fe-Cr slag and blast furnace slag for foundry applications. *Procedia Environ Sci* 35:583–596
2. Guney Y, Sari YD, Yalcin M, Tuncan A, Donmez S (2010) Re-usage of waste foundry sand in high-strength concrete. *Waste Manage* 30:1705–1713. <https://doi.org/10.1016/j.wasman.2010.02.018>
3. Aweda J, Jimoh Y (2009) Assessment of properties of natural moulding sands in Ilorin and Ilesha, Nigeria. *USEP: J Res Inf Civil Eng* 6:68–77
4. Ademoh NA, Ibrahim AO (2019) Determination of the suitability of River Gurara bed sand bonded with clay for foundry casting moulds. *Ind Eng Lett* 9:43–51
5. Nayak RK, Sundarraj S (2009) Sensitivity study of IHTC on solidification simulation for automotive casting. *Int J Cast Met Res* 22:294–297. <https://doi.org/10.1179/136404609X367812>
6. Nayak RK, Sundarraj S (2010) Selection of initial mold-metal interface heat transfer coefficient values in casting simulations—a sensitivity analysis. *Metall Materi Trans B* 41:151–160. <https://doi.org/10.1007/s11663-009-9317-0>
7. Adegbuyi PAO, Uhomoihi JO (2007) Foundry properties of backing sand: some engineering studies and improvements. 6
8. Ajibola O, Oloruntoba D, Adewuyi B (2015) Effects of moulding sand permeability and pouring temperatures on properties of cast 6061 aluminium alloy. *Int J Metals* 13 pages. <https://doi.org/10.1155/2015/632021>
9. Shuaib-Babata Y, Kabiru Suleiman A, Ambali I, Bello M (2019) Evaluation of the foundry properties of Oyun River (Ilorin) moulding sand. *Adeleke Univ J Eng Technol* 2:12–24
10. Sheidi HM, Ajuwa CI (2008) Investigation on properties of river sand for sand casting, River Niger, Bacita, Nigeria. *J Eng Appl Sci* 3:214–216
11. Abolarin MS, Lawal SA, Salawu AA (2010) Effect of moisture content on the moulding properties of River Niger sand using Tudun-Wada clay as a binder. Technical report, 5
12. Olasupo OA, Omotoyinbo JA (2009) Moulding properties of a Nigerian silica–clay mixture for foundry use. *Appl Clay Sci* 45:244–247. <https://doi.org/10.1016/j.clay.2009.05.001>
13. Orumwense FFO (2002) Moulding properties of synthetic sand mixtures. A comparative study. *Scandinavian J Metall* 31:100–106. <https://doi.org/10.1034/j.1600-0692.2002.310203.x>
14. Sadarang J, Nayak RK, Panigrahi I (2020) Effect of binder and moisture content on compactibility and shear strength of river bed green sand mould. *Mater Today: Proc.* <https://doi.org/10.1016/j.matpr.2020.08.640>
15. Heine RW, Loper CR, Rosenthal PC (1967) *Principles of metal casting*. Tata McGraw-Hill Education
16. Chakrabarti AK (2005) *Casting technology and cast alloys*. PHI Learning Pvt. Ltd.

Ferrochrome Slag as an Alternative Mould Material for Green Sand Mould Casting—A Study



Jatin Sadarang, Ramesh Kumar Nayak , and Isham Panigrahi

1 Introduction

Natural materials like sand are readily available in the earth crust. Foundry industries are continuously using high silica content sand in green sand mould casting. High silica content sand is used as raw materials in various industrial applications. Consumption and cost of silica sand increases due to increased requirements in industries. Therefore, foundry engineers, researchers and scientists find different materials and additives to replace silica sand and improve mould properties. Sahoo et al. [1] used 1% camphor powder and 2% coconut shell ash in mould to increase mould permeability. They observed that moulding sand containing 1% camphor powder has high mould permeability [2]. The green and dry compressive strength increase with the use of 2.25% molasses and 15% fly ash in moulding sand [3]. Zirconium alcohol coating reduces mould permeability. However, it gives a better surface finish [4]. The mould compressive strength increases as percentage of binder increases; however, mould permeability decreases [5]. Mould dry strength increases as moisture content increases [6]. The compactibility and shear strength of river sand mould increases as the percentage of moisture increases [7]. The thermal conductivity of green sand mould increase with the use of chill [8, 9].

Slag is waste material generated during the production of pig iron, steel, and ferroalloys plant. Slags are the impurities that float on molten material during smelting process. Worldwide around 11.8 million tons of blast furnace slag is generated [10]. A large area of land is required to dispose of slags. Therefore, researchers and scientists used slags in different applications. The use of blast furnace slag in cement

J. Sadarang (✉) · I. Panigrahi

School of Mechanical Engineering, KIIT Deemed To Be University, Bhubaneswar 754024, India

R. K. Nayak

Department of Materials and Metallurgical Engineering, MANIT, Bhopal 462003, India

increases the mechanical property and reduces construction costs [11]. Compressive strength increases by adding around 70 wt% of blast furnace slag with cement [12]. Water-quenched slag is used for the manufacturing of cement [13]. Bricks with blast furnace slag have shown good properties compared to conventional sand bricks, thereby increasing structure life and decreasing manufacturing cost [14]. Blast furnace slag is a good industrial waste product for the manufacturing of the glass–ceramic [15]. Ferrochrome slag used in CO₂ mould has similar surface finish to silica sand mould [16, 17]. Mould hardness increases with the use of blast furnace slag in CO₂ mould [18]. Therefore, in the present investigation, ferrochrome slag is used in green sand mould. The effect of bentonite clay and moisture on mould shear strength and compactibility is also evaluated.

2 Materials and Methods

2.1 Materials

In the present investigation, crushed slag, silica sand, bentonite clay and coal dust were used, as shown in Fig. 1a, b, c, and d. The slag was collected from a ferrous steel plant, Jajpur, Odisha, India. Silica sand, bentonite clay, and coal dust are procured from different industries in India.

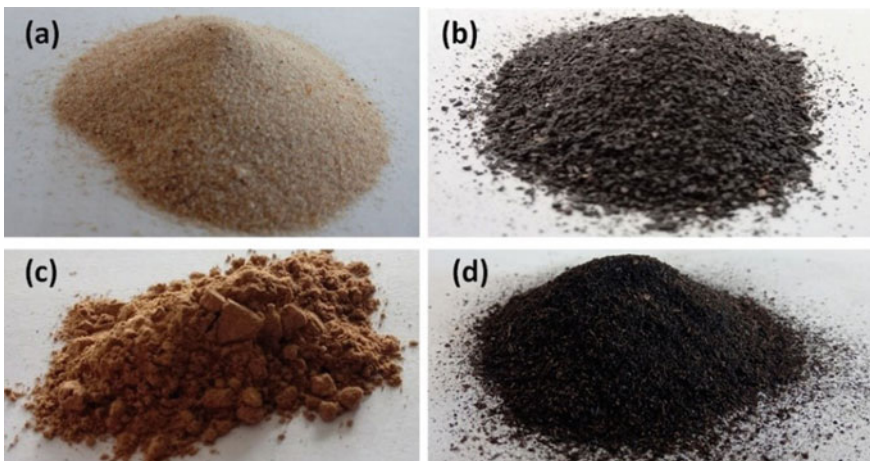


Fig. 1 Mould ingredients **a** silica sand, **b** slag, **c** bentonite clay and **d** coal dust

Table 1 Sieve analysis of slag

Sieve size(μm)	Retained % slag
4750	0
4000	0
2360	0
600	0.7
212	78.9
150	9.7
106	2.6
75	6.6
Pan	1.5
AFS number	63

2.2 Sieve Analysis

Sieve analysis was carried out to determine particle size distribution and grain fineness number (GFN) of slag. The sample of 100 g was placed on the top sieve and vibrated for 15 min in sieve vibrating equipment. The leftover sample weight in each was weighted in a digital weighing machine. Equation 1 was used to determine the American foundry society (AFS) GFN of slag. Table 1 shows the particle size distribution of slag. It is observed that the GFN of slag is 63. The slag contains 78.9% particle having a particle size between 600 and 212 μm .

$$\text{AFS Grain Fineness Number} = \frac{\text{Sum of multiplication product}}{\text{Total \% of retained grains}} \quad (1)$$

2.3 Sample Preparation

The AFS sample was prepared with different percentages of bentonite and moisture in moulding sand, as reported in Table 2. Figure 2 shows the flow chart to evaluate shear strength and compactibility of slag mould. The mould ingredients were uniformly mixed with the use of sand muller. Rapid moisture teller was used to ensuring the desired quantity of moisture in moulding sand. Figure 3a shows the moisture teller equipment. Moulding sample of 6 g was vigorously mixed with 12 g calcium carbide powder in rapid moisture teller equipment. The moisture present in sample reacts with calcium carbide and forms acetylene gas inside moisture teller chamber. A calibrated pressure gauge mounted on moisture teller shows the moisture percentage in moulding sand.

Sand rammer was used to prepare AFS standard cylindrical sample. The sample tube was filled with 150–155 g moulding sand. The moulding sand was compacted

Table 2 Composition of slag mould

Specimen	Slag (%)	Bentonite clay (%)	Coal dust (%)	Moisture (%)
SM-1	81	14	5	3
SM-2	81	14	5	4
SM-3	81	14	5	5
SM-4	81	14	5	7
SM-5	83	12	5	3
SM-6	83	12	5	4
SM-7	83	12	5	5
SM-8	83	12	5	7
SM-9	85	10	5	3
SM-10	85	10	5	4
SM-11	85	10	5	5
SM-12	85	10	5	7

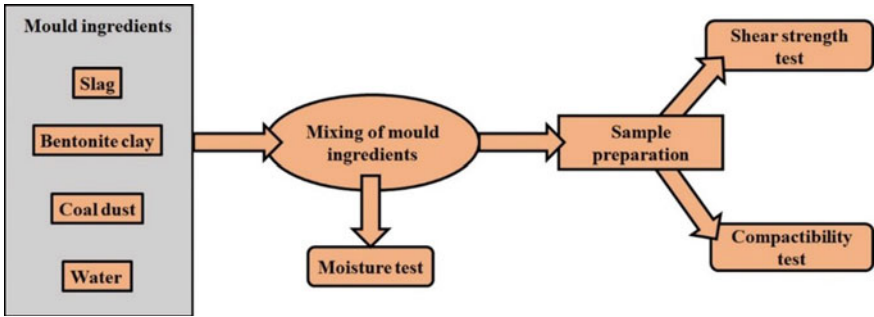


Fig. 2 Flow chart to evaluate shear strength and compactibility of slag mould

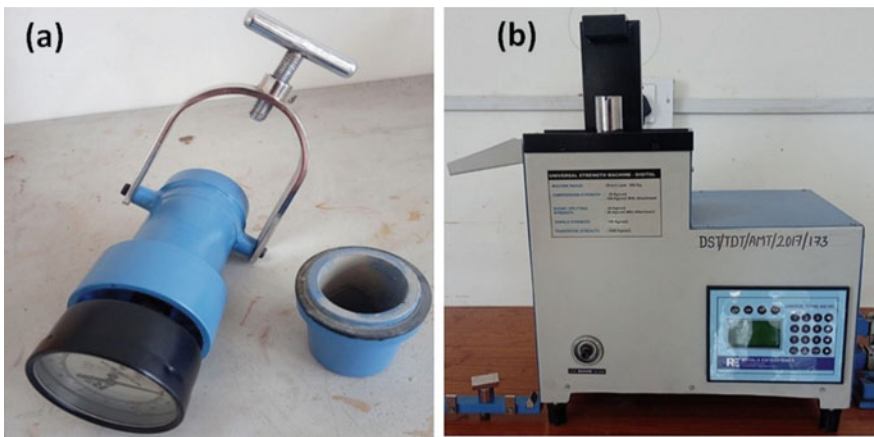


Fig. 3 a Moisture teller, b USM

with three rammed strokes having 6.35 kg and falling height 50 mm. The AFS test samples were produced by sand rammer having 50 mm height and 50 mm diameter. The AFS sample was used to determine shear strength.

2.4 Shear Strength

The universal strength machine (USM) was used to determine shear strength of slag mould samples. Figure 3b shows USM. The AFS sample was placed in between the shear strength gripper of USM. The shear force was applied to the sample, and shear strength of the sample were noted down from the attached computer.

2.5 Compactibility

The reduction in volume of loose moulding sand under the standard compacting load is known as compactibility. The compactibility tube was filled with loose moulding sand, and three ramming strokes were applied through sand rammer. The compactibility measuring scale was used to determine the compactibility % of moulding sand.

3 Results and Discussions

The shear strength of slag mould under different moisture and bentonite content is shown in Fig. 4. It is observed that as the concentration of bentonite clay and moisture increases, the shearing strength of slag mould increases. The bentonite clay creates a bond with mould ingredients in the presence of moisture or water [19]. Therefore, as moisture and bentonite clay concentration increases, the shear strength of slag mould increases. The moulding mixture contains 7% moisture, and 14% bentonite clay has 0.47 kg/cm² shear strength.

The effect of moisture and bentonite content on slag mould compactibility is shown in Fig. 5. It is observed that as the percentage of bentonite clay increases in moulding sand the compactibility decreases. The compactibility of moulding sand is inversely proportional to bulk density [20]. As the concentration of fine aggregates increases in moulding sand, the bulk density increases. Therefore, compactibility of slag mould decreases as increase in bentonite percentage. The moisture increases the lubricant property of moulding sand. Hence, as the concentration of moisture increases, slag mould compactibility increases. The moulding sand containing 14% bentonite and 7% moisture has 51% compactibility.

The slag mould containing 14% bentonite and 7% moisture has high shear strength. Therefore, shear strength and compactibility of silica sand mould containing

Fig. 4 Effect of bentonite clay and moisture on shear strength

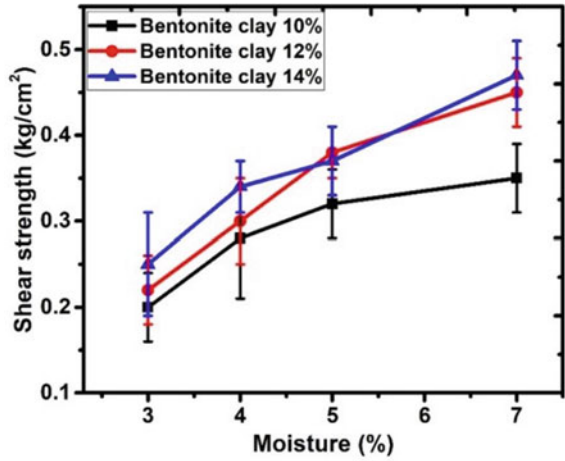
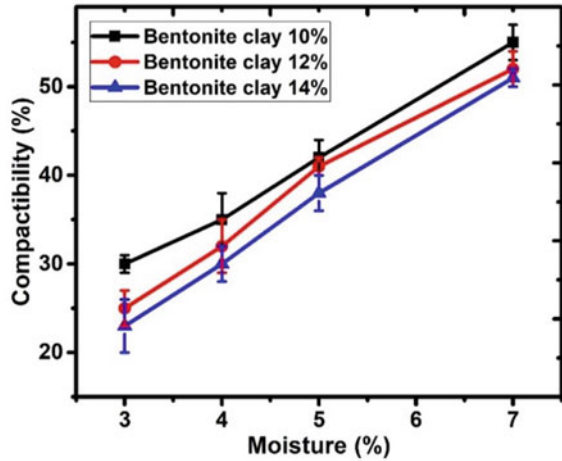


Fig. 5 Effect of bentonite clay and moisture on mould compactibility



14% bentonite clay and 7% moisture are evaluated and compared with slag mould. Figure 6 shows comparative study between silica sand and slag mould (a) shear strength and (b) compactibility. It is observed that the compactibility of both moulds is similar. The slag mould contains less shear strength than silica sand mould with the same moisture and bentonite content. The shear strength of slag is lower than silica sand but in the accepted range [19]. In future, mould property like compressive strength, permeability, and hardness can be evaluated to determine the feasibility of slag mould for ferrous or non-ferrous castings.

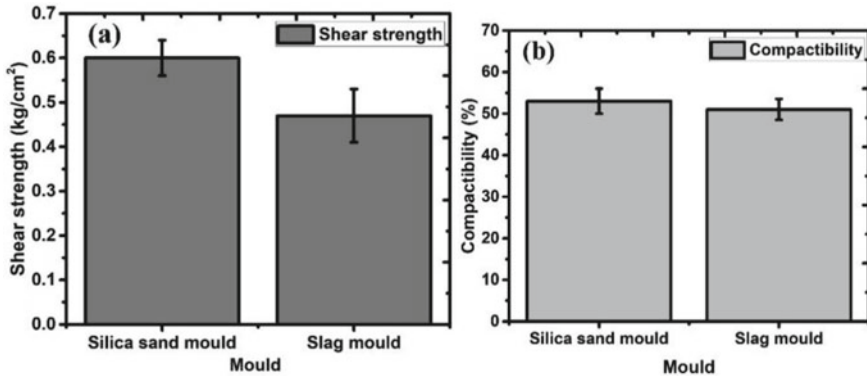


Fig. 6 Compression between silica sand mould and slag mould **a** shear strength and **b** compactibility

4 Conclusions

The slag mould samples were prepared with different moisture, and bentonite percentage and shear strength and compactibility were evaluated. The following conclusions are drawn from this study.

- The shear strength of slag mould increases as percentage of moisture and bentonite increases.
- The slag mould containing 14% bentonite and 7% moisture has 0.47 kg/cm² shear strength. However, ferrochrome slag mould has less shear strength than silica sand mould at similar bentonite and moisture content.
- Mould compactibility of slag mould increases as the percentage of moisture increases. Fine particles of mould aggregates reduce compactibility of moulding sand. Hence, as percentage of bentonite increases, the compactibility decreases.
- Further investigation on other mould properties is required to confirm the suitability of ferrochrome slag as alternative materials for sand mould casting.

Acknowledgements The authors would like to express their sincere thanks to the Advanced Manufacturing Technology program of the Department of Science & Technology, Govt. of India, for the financial support to carry out this work (Grant no. DST/TDT/AMT/2017/173). Special thanks to RSB Metaltech, Pvt. Ltd, Cuttack, India, for their support as an industrial partner to develop alternate source to commercial-grade silica sand for Indian foundry industries.

References

1. Sahoo PK, Pattnaik S, Sutar MK (2020) Investigation on the influence of different additives on properties of green sand mould. *Mater Sci Forum*. <https://doi.org/10.4028/www.scientific.net/MSF.978.29>
2. Sahoo PK, Pattnaik S, Sutar MK (2020) Parametric optimization of permeability of green sand mould using ANN and ANFIS methods. In: Li L, Pratihari DK, Chakrabarty S, Mishra PC (eds) *Advances in materials and manufacturing engineering*. Springer, Singapore, pp 495–501. https://doi.org/10.1007/978-981-15-1307-7_56
3. Srinivasa Rao P, Birru AK (2017) Effect of mechanical properties with addition of molasses and flyash in green sandmoulding. *Mater Today Proc* 4:1186–1192. <https://doi.org/10.1016/j.matpr.2017.01.136>
4. Jamrozowicz Ł, Siatko A (2020) The assessment of the permeability of selected protective coatings used for sand moulds and cores. *Arch Foundry Eng* 20(1)
5. Aramide F, Aribo S, Folorunso D (2011) Optimizing the moulding properties of recycled Ilaro silica sand. *Leonardo J Sci* 10
6. Ihom PA, Agunsoye J, Anbua EE, Ogbodo J (2011) Effects of moisture content on the foundry properties of yola natural sand, vol 12
7. Sadarang J, Nayak RK, Panigrahi I (2020) Effect of binder and moisture content on compactibility and shear strength of river bed green sand mould. *Mater Today Proc*. <https://doi.org/10.1016/j.matpr.2020.08.640>
8. Nayak RK, Sundarraj S (2009) Sensitivity study of IHTC on solidification simulation for automotive casting. *Int J Cast Met Res* 22:294–297. <https://doi.org/10.1179/136404609X367812>
9. Nayak RK, Sundarraj S (2010) Selection of initial mold-metal interface heat transfer coefficient values in casting simulations—a sensitivity analysis. *Metall Mater Trans B* 41:151–160. <https://doi.org/10.1007/s11663-009-9317-0>
10. Al-Jabri K, Shoukry H, Khalil IS, Nasir S, Hassan HF (2018) Reuse of waste ferrochrome slag in the production of mortar with improved thermal and mechanical performance. *J Mater Civil Eng* 30:04018152. [https://doi.org/10.1061/\(ASCE\)MT.1943-5533.0002345](https://doi.org/10.1061/(ASCE)MT.1943-5533.0002345)
11. Das B, Prakash S, Reddy PSR, Misra VN (2007) An overview of utilization of slag and sludge from steel industries. *Resour Conserv Recycl* 50:40–57. <https://doi.org/10.1016/j.resconrec.2006.05.008>
12. Kumar S, Kumar R, Bandopadhyay A, Alex TC, Kumar BR, Das SK, Mehrotra SP (2008) Mechanical activation of granulated blast furnace slag and its effect on the properties and structure of portland slag cement. *Cem Concr Compos* 30:679–685
13. Mostafa NY, El-Hemaly SAS, Al-Wakeel EI, El-Korashy SA, Brown PW (2001) Characterization and evaluation of the hydraulic activity of water-cooled slag and air-cooled slag. *Cem Concr Res* 31:899–904. [https://doi.org/10.1016/S0008-8846\(01\)00497-5](https://doi.org/10.1016/S0008-8846(01)00497-5)
14. Sadek DM (2014) Effect of cooling technique of blast furnace slag on the thermal behavior of solid cement bricks. *J Clean Prod* 79:134–141. <https://doi.org/10.1016/j.jclepro.2014.05.033>
15. Fredericci C, Zanutto ED, Ziemath EC (2000) Crystallization mechanism and properties of a blast furnace slag glass. *J Non-Cryst Solids* 273:64–75. [https://doi.org/10.1016/S0022-3093\(00\)00145-9](https://doi.org/10.1016/S0022-3093(00)00145-9)
16. Inampudi NM, Jinugu BR (2016) Ferro chrome slag: an alternative mould material in ferrous and non-ferrous foundries. *Int J Metalcast* 11. <https://doi.org/10.1007/s40962-016-0103-x>
17. Murthy IN, Babu NA, Rao JB (2016) High Carbon ferro chrome slag—alternative mould material for foundry industry. *Procedia Environ Sci* 35:597–609. <https://doi.org/10.1016/j.proenv.2016.07.046>

18. Rao KT, Babu PS (2015) Usage of blast furnace slag in moulding sand to produce Al-Mg alloy castings, vol 7
19. Heine RW, Loper CR, Rosenthal PC (1967) Principles of metal casting. Tata McGraw-Hill Education
20. Chakrabarti AK (2005) Casting technology and cast alloys. PHI Learning Pvt. Ltd.

Evaluation of Compactibility and Shear Strength of Sand-Less Casting Mould for Sand Casting Process



Jatin Sadarang, Ramesh Kumar Nayak , and Isham Panigrahi

1 Introduction

Sand casting process is the oldest and mostly used to cast ferrous and non-ferrous castings [1]. Silica sand is the main mould ingredient of sand mould. The silica sand is obtained from riverbed by river sand mining. The river sand mining causes water pollution and also affects biodiversity in the nearby area [2]. Therefore, many researchers and scientists used different additives in sand mould to replace silica sand and improve sand mould properties. The mould permeability increases with the use of 1% camphor powder in moulding sand [3]. Saw dust additives improve mould compaction properties which improve mould compressive strength [4]. Nayak et al. [5, 6] found that the sand mould and casting interface heat transfer coefficient is sensitive to the solidification process of sand casting process. Mould permeability depends on the size of mould aggregates, and also the blow holes and pin holes are formed in casting due to low mould permeability [7]. Fine aggregates like bentonite clay and coal dust decreases mould permeability [8]. Binder percentage increase in sand mould decreases mould permeability; however, mould compressive strength increases [9]. The mould compactibility decreases as increase bentonite percentage in river sand mould [10].

The crushed stone powder is a waste material produced during production of various sized stones in stone crushing plant. The crushed stone powder contains fine aggregates, flowing in air and creating air pollution [11]. The fine aggregate of crushed stone powder affects soil fertility [11] and causes respiratory and skin problems in nearby human beings [12]. The waste crushed stone powder is used in construction industries as a raw material. The use of 35% crushed stone powdered

J. Sadarang (✉) · I. Panigrahi

School of Mechanical Engineering, KIIT Deemed To Be University, Bhubaneswar 754024, India

R. K. Nayak

Department of Materials and Metallurgical Engineering, MANIT, Bhopal 462003, India

powder in concrete gives better mechanical property [13]. The compressive strength of mortar is increased by 85% with the use of crushed stone powder in place of river sand [14]. The replacement of 50% fine aggregate with crushed stone powder gives better flexural, split, and compressive strength to concrete [15]. The crushed stone powder used as a filler material in bituminous concrete decreases indirect tensile strength at elevated temperature [16]. The construction industries use crushed stone powder as a raw material in concrete and cement. A large quantity of crushed stone powder is not utilized. Therefore, in the present investigation, an approach was made to utilize crushed stone powder in mould to decrease casting costs and develop alternative materials for green sand casting process.

2 Materials and Methods

2.1 Materials

The materials used in present investigation were crushed stone powder, commercially available silica sand, bentonite clay, and coal dust. The physical appearance of mould ingredients is shown in Fig. 1a, b, c, and d. The crushed stone powder was collected from nearest crushed stone powder plant in Bhopal, India. The commercially available silica sand, bentonite clay, and coal dust were procured.

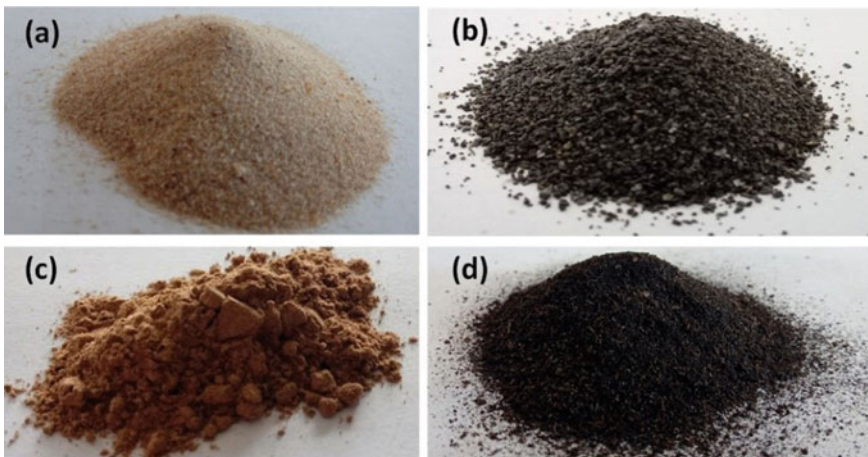


Fig. 1 Physical appearance of **a** silica sand, **b** crushed stone powder, **c** bentonite clay and **d** coal dust

Table 1 Particle size distribution of crushed stone powder

Sieve size(μm)	Retained % crushed stone powder
4750	0
4000	0
2360	0
600	1.1
212	87.9
150	6.9
106	0.4
75	1.4
Pan	2.1
AFS Number	58

2.2 Sieve Analysis

Compactibility and strength of mould depend on particle size distribution of sand mould aggregates. Therefore, in the present investigation, particle size distribution of crushed stone powder was determined using the sieve analysis method. The crushed stone powder sample of 100 g is sieved through a set of sieve and vibrates in sieve vibrator for 15 min. The leftover weight of crushed stone powder in each sieve was weighed and reported in Table 1. It is observed that 87.9% of crushed stone powder has particle size between 600 and 212 micron. The American Foundry Society (AFS) Grain fineness number was obtained as per Eq. 1. The AFS number of crushed stone powder used in the present investigation was 58.

$$\text{AFS Grain Fineness Number} = \frac{\text{Sum of multiplication product}}{\text{Total \% of retained grains}} \tag{1}$$

2.3 Sample Preparation

The uniform sand mould properties were obtained by proper mixing of sand aggregates. Therefore, in the present investigation, a sand muller was used to properly mix sand mould aggregates. The different sand mould composition was used to determine the effect of moisture and bentonite on mould compactibility and shear strength as reported in Table 2. The systematic diagram of the testing procedure is shown in Fig. 2. The bentonite clay and moisture content vary from 10 to 14 and 3 to 7%, respectively. Moisture teller equipment was used to ensure the moisture content in mould mixture. The moulding sand of 6 g was properly mixed with 12 g calcium carbide powder in moisture teller pressure chamber. The calibrated pressure gauge shows moisture percentage in sand mould mixture.

Table 2 Composition of crushed stone powder mould mixture

Specimen	Bentonite clay (%)	Moisture (%)	Coal dust (%)	Crushed stone powder (%)
S-1	10	3	5	85
S-2	10	4	5	85
S-3	10	5	5	85
S-4	10	7	5	85
S-5	12	3	5	83
S-6	12	4	5	83
S-7	12	5	5	83
S-8	12	7	5	83
S-9	14	3	5	81
S-10	14	4	5	81
S-11	14	5	5	81
S-12	14	7	5	81

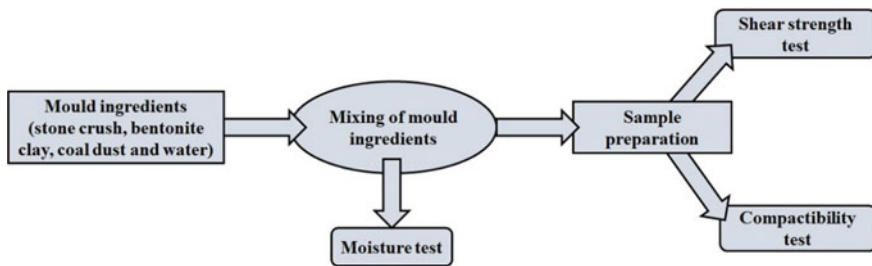


Fig. 2 Systematic flow diagram for crushed stone powder mould properties

The AFS standard sample 50 mm diameter and 50 mm height was prepared with sand rammer, as shown in Fig. 3a. The rammer has a 6.35 kg ramming weight and 50 mm falling height. The sample tube of sand rammer was filled with 145–150 g of moulding sand. The sample tube was placed at the sand rammer, and three ramming strokes were applied to prepare AFS cylindrical sample. The prepared samples were used to determine mould shear strength.

2.4 Mould Compactibility

Reduction in the volume of loose moulding sand under standard load is known as mould compactibility. Figure 3b shows compactibility tube and scale. The compactibility tube of 50 mm diameter and 100 mm height are filled with loose moulding sand. The compactibility tube was placed at the sand rammer, and three ramming strokes was applied. The reduction in volume was measured with

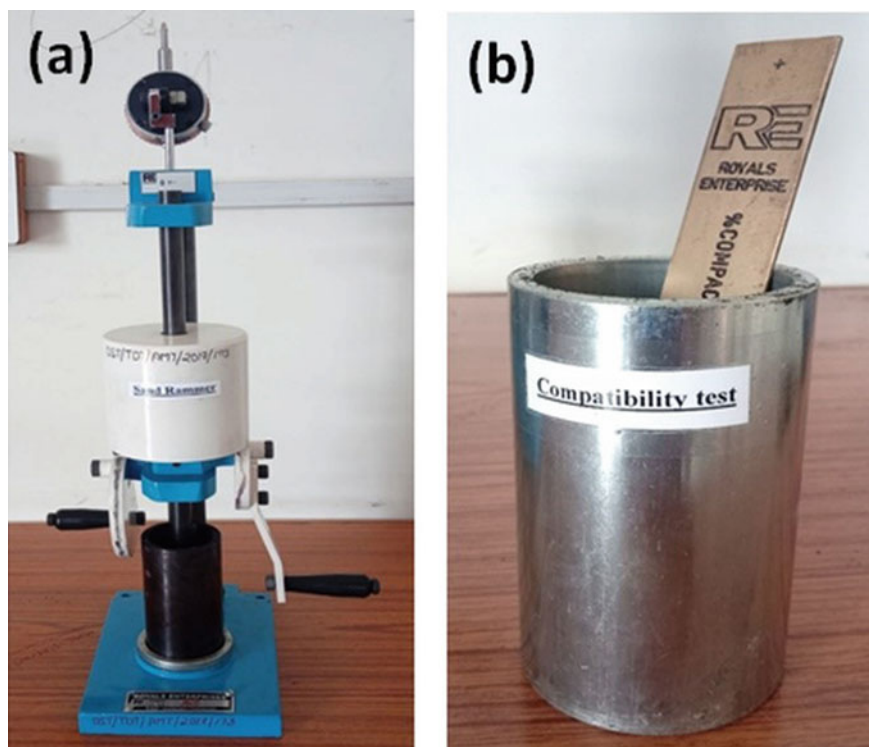


Fig. 3 a Sand rammer and b compactibility tube and scale

compactibility scale. The scale reading shows the compactibility percentage of moulding sand.

2.5 *Shear Strength*

Universal strength machine (USM) was used to determine shear strength of crushed stone powder mould. The AFS test sample placed in between the shearing gripper of USM and shearing force was applied. The USM connected to the computer having USM software shows the shear strength of the crushed stone powder mould.

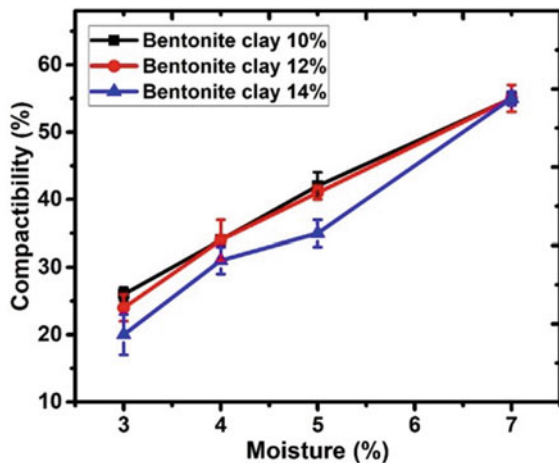
3 Results and Discussion

Mould compactibility depends on the moisture and bentonite content in moulding sand. Figure 4 shows the effect of moisture and bentonite content on stone dust mould compactibility. It is observed that as the concentration of bentonite in moulding sand increases the compactibility decreases. The small size bentonite clay particle increases bulk density due to which compactibility of moulding sand decreases [17]. The compactibility of moulding sand was higher at 7% moisture content. The excess amount of water in mould increases mould lubricating property; therefore, as the concentration of moisture increases, the compactibility of moulding sand also increases. Hence, crushed stone powder mould contains 7% moisture and 10% bentonite content and has high compactibility (55%).

The effect of moisture and bentonite clay on shear strength of crushed stone powder mould (sand-less) is shown in Fig. 5. It is observed that as the concentration of moisture and bentonite clay increases the strength of crushed stone powder mould increases. Bentonite clay is used in moulding sand to bind mould ingredients. The binding action of bentonite develops in the presence of moisture [18]. Hence, as the concentration of moisture and bentonite increases, the shear strength of crushed stone powder mould increases. The crushed stone powder mould contains 14% bentonite clay and 7% moisture and has high shearing strength (0.52 kg/cm^2).

The high shear strength of crushed stone powder mould was obtained at 7% moisture and 14% bentonite clay content. Therefore, compactibility and shear strength of silica sand mould containing 7% moisture and 14% bentonite clay were determined and compared with 7% moisture and 14% bentonite clay containing crushed stone powder mould. Figure 6 shows comparative study between silica sand and crushed stone powder mould (a) compactibility and (b) shear strength. It is observed that compactibility of both the moulding sand is equal; however; shearing strength of crushed stone powder mould is slightly lesser than silica sand mould.

Fig. 4 Effect of moisture and bentonite on mould compactibility of crushed stone powder mould



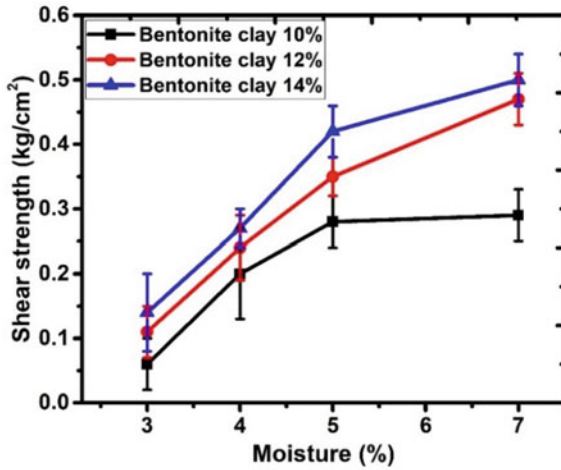


Fig. 5 Effect of moisture and bentonite on shearing strength of crushed stone powder mould

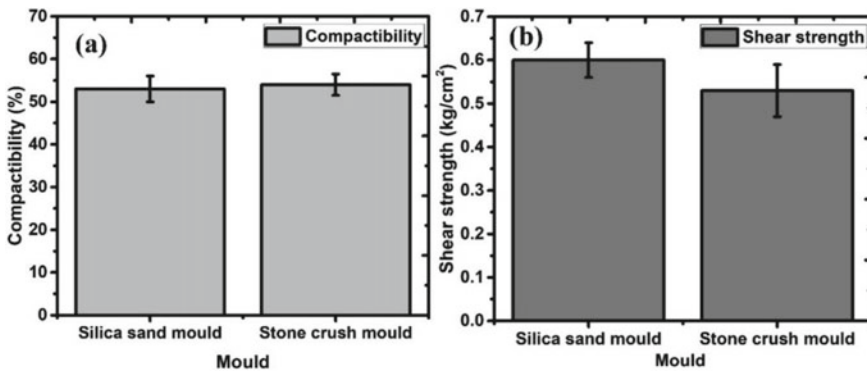


Fig. 6 Comparative study between silica sand and crushed stone powder mould a compactibility and b shear strength

4 Conclusions

The effect of moisture and bentonite content on compactibility and shear strength of crushed stone powder mould (sand-less mould) has been evaluated and compared with commercially available silica sand mould. The following conclusions are drawn from the present study.

- The crushed stone powder mould (sand-less) compactibility increases with increase in moisture content and decreases with increase in bentonite content.
- The maximum compactibility (55%) of crushed stone powder mould was obtained at 7% moisture content.

- Shear strength of crushed stone powder mould increases as the concentration of moisture and bentonite increases.
- The high shear strength (0.52 kg/cm²) of crushed stone powder mould was obtained at 7% moisture and 14% bentonite clay content.
- The compactibility and shear strength of crushed stone powder and silica sand mould is similar and may be used as alternative material for green sand mould casting. However, other sand mould properties such as porosity, compressive strength, flowability, collapsibility, and fusion point of crushed stone powder need to be evaluated to understand the full potential of the material to be used as alternative material for green sand mould casting process.

Acknowledgements The authors would like to express their sincere thanks to the Advanced Manufacturing Technology program of the Department of Science & Technology, Govt. of India, for the financial support to carry out this work (Grant no. DST/TDT/AMT/2017/173). Special thanks to RSB Metaltech, Pvt. Ltd, Cuttack, India, for their support as an industrial partner to develop alternate source to commercial-grade silica sand for Indian foundry industries.

References

1. Alonso-Santurde R, Coz A, Viguri JR, Andrés A (2012) Recycling of foundry by-products in the ceramic industry: green and core sand in clay bricks. *Constr Build Mater* 27:97–106. <https://doi.org/10.1016/j.conbuildmat.2011.08.022>
2. Padmalal D, Maya K (2014) Sand mining: the world scenario. In: Padmalal D, Maya K (eds) *Sand mining: environmental impacts and selected case studies*. Springer Netherlands, Dordrecht, pp 57–80. https://doi.org/10.1007/978-94-017-9144-1_5
3. Sahoo PK, Pattnaik S, Sutar MK (2020) Investigation on the influence of different additives on properties of green sand mould. *Mater Sci Forum*. <https://doi.org/10.4028/www.scientific.net/MSF.978.29>
4. Seidu SO, Kutelu BJ (2014) Effects of additives on some selected properties of base sand. *J Miner Mater Charact Eng* 02:507. <https://doi.org/10.4236/jmmce.2014.25051>
5. Nayak RK, Sundarraj S (2009) Sensitivity study of IHTC on solidification simulation for automotive casting. *Int J Cast Met Res* 22:294–297. <https://doi.org/10.1179/136404609X367812>
6. Nayak RK, Sundarraj S (2010) Selection of initial mold-metal interface heat transfer coefficient values in casting simulations—a sensitivity analysis. *Metall Mater Trans B* 41:151–160. <https://doi.org/10.1007/s11663-009-9317-0>
7. Parappagoudar MB, Pratihari DK, Datta GL (2007) Non-linear modelling using central composite design to predict green sand mould properties. *Proc Inst Mech Eng Part B J Eng Manuf* 221:881–895. <https://doi.org/10.1243/09544054JEM696>
8. Ohdar RK, Pushp PT (2007) Application of intelligent techniques for controlling the green sand properties application of intelligent techniques for controlling the green sand properties. Presented at the 55th Indian Foundry Congress, pp 177–186
9. Aramide F, Aribo S, Folorunso D (2011) Optimizing the moulding properties of recycled Ilaro silica sand. *Leonardo J Sci* 10
10. Sadarang J, Nayak RK, Panigrahi I (2020) Effect of binder and moisture content on compactibility and shear strength of river bed green sand mould. *Mater Today Proc*. <https://doi.org/10.1016/j.matpr.2020.08.640>

11. Marichamy V, Ganesan S, Kalirajan R (2020) Influence of stone crusher units' dust pollution on agriculture in Virudhunagar district of Tamil Nadu. *Shanlax Int J Econ* 8:41–48
12. Sheikh A, Rana SVS, Pal A (2011) Environmental health assessment of stone crushers in and around Jhansi, U. P., India. *J Ecophysiol Occup Health* 11:107–115. <https://doi.org/10.18311/jeoh/2011/2255>
13. Muhit IB, Raihan MT, Nuruzzaman M (2014) Determination of mortar strength using stone dust as a partially replaced material for cement and sand. *Adv Concr Constr* 1(2):249–559
14. Rajput SPS, Chauhan MS (2014) Suitability of crushed stone dust as fine aggregate in mortars, vol 4, issue 3
15. Verma SK (2018) Study the effect of stone dust as partial replacement of sand adding steel fibre, vol 3, issue 5
16. Gupta L, Suresh G (2018) Determination of indirect tensile strength of bituminous concrete mix prepared using stone dust and cement as filler materials. In: Struble L, Tebaldi G (eds) *Materials for sustainable infrastructure*. Springer International Publishing, Cham, pp 249–261. https://doi.org/10.1007/978-3-319-61633-9_16
17. Chakrabarti AK (2005) *Casting technology and cast alloys*. PHI Learning Pvt. Ltd.
18. Heine RW, Loper CR, Rosenthal PC (1967) *Principles of metal casting*. Tata McGraw-Hill Education

A Study on the Design and Fabrication of Dry Cell Electrolysis Setup for Hydrogen Generation



Kamaraj Nithyanandhan, S. Ranjithkumar, Gaurav Dwivedi,
and Somasundaram Periasamy

Abbreviations

KOH	Potassium Hydroxide
H ₂	Hydrogen
O ₂	Oxygen NO _x : Oxides of Nitrogen
CO	Carbon-monoxide
CO ₂	Carbon-dioxide
CNG	Compressed Natural Gas
LPG	Liquefied Petroleum Gas
DC	Direct Current
PWM	Pulse Width Module

1 Introduction

Many environmental concerns were caused by air contaminants such as CO and NO_x and international concern for its regulation, and restriction was raised. Alternative fuel is the only way to reduce emissions from IC engines. Many alternative fuels are there in the World. Some of the alternative fuels are Compressed Natural Gas (CNG), Liquefied Petroleum Gas (LPG), Dimethyl Ether (DME), Gas to Liquid (GTL), and hydrogen [1–3]. From that, hydrogen fuel is used to reduce the emission. Hydrogen fuel can be generated by using various methods like steam method, electrolytic method, biological process. For our project, an electrolytic method is used

K. Nithyanandhan · S. Ranjithkumar · S. Periasamy
Department of Automobile Engineering, Kongu Engineering College, Erode 638060, India

G. Dwivedi (✉)
Energy Centre, Maulana Azad National Institute of Technology, Bhopal 462003, India

© The Author(s), under exclusive license to Springer Nature Singapore Pte Ltd. 2022
P. Verma et al. (eds.), *Advancement in Materials, Manufacturing and Energy Engineering*,
Vol. II, Lecture Notes in Mechanical Engineering,
https://doi.org/10.1007/978-981-16-8341-1_38

because an electrolytic method is the easiest and cost-effective method of hydrogen generation. Wet cell electrolysis and dry cell electrolysis are two distinct kinds of electrolytic techniques. The dry cell electrolysis method is used in our project because the rate of hydrogen generation is more than the wet cell electrolysis method [4, 5]. Many catalysts are used for electrolysis methods like sodium hydroxide, sodium bicarbonate. It uses Potassium Hydroxide (KOH) as a catalyst. Catalyst is used to speed up the reaction process for hydrogen generation. This process can be done by using distilled water. Many electrodes are used for dry cell electrolysis processes like stainless steel, platinum, nickel. If using the stainless steel plates, hexavalent chromium was formed at the surfaces after 2–3 months duration [6, 7]. Hexavalent chromium can irritate the nose, throat, and lungs. Also, the HHO gas generation is less. So, nickel-coated stainless steel plates are used. By using this plate, generate hydrogen effectively [8].

2 Design and Fabrication

2.1 Design Layout

The battery is used to supply the DC power supply to the PWM circuit. The PWM circuit is used to supply the constant power flow into modulated pulse flow to the dry cell electrolyzer. The stainless steel plates are coated with nickel and are used as anode and cathode. Hydrogen and oxygen are split from the electrolyte by electron decomposition between electrodes. The bubbler tank which has two purpose—as electrolyte holder and moisture separation from the HHO gas [9–11]. Pyrogallol tank is used to absorb the oxygen from the gas. The flame arrestor is used to stop the backfire, when hydrogen burns on outside the setup, and the schematic layout is shown in Fig. 1.

2.2 Battery

Chemical energy is transformed by batteries into electricity is shown in Fig. 2. A battery consists of two electrodes, a positive cathode and a negative anode, divided by an electrolyte called a liquid chemical, which is capable of carrying charged particles. The DC power load is given from the battery to dry cell for generating the HHO gas. It is recharged by the engine alternator. In this project, a lead-acid battery (12 V) is used.

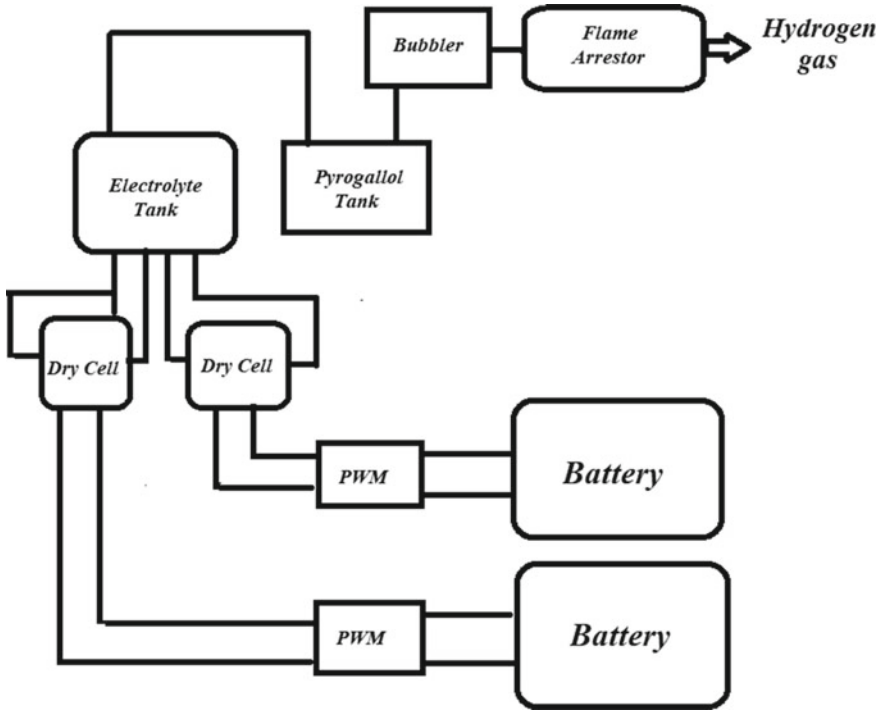


Fig. 1 Schematic representation of experiment layout

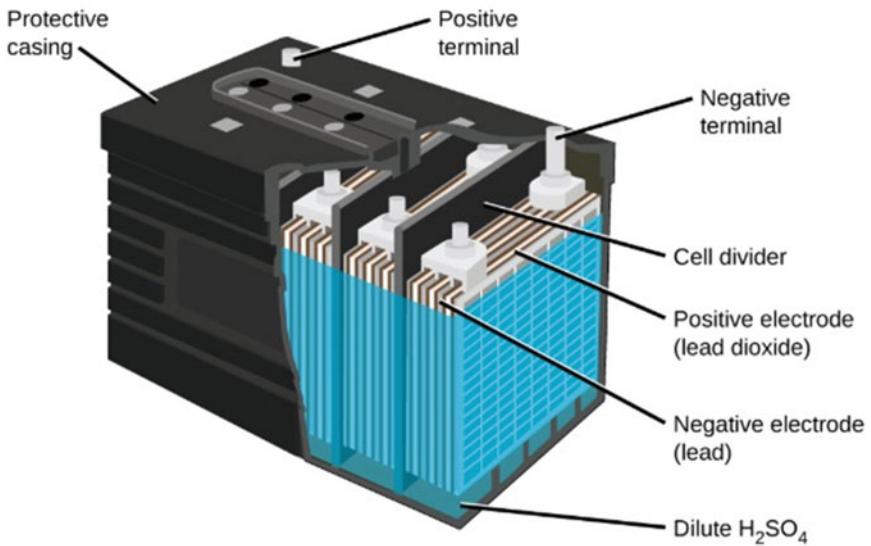
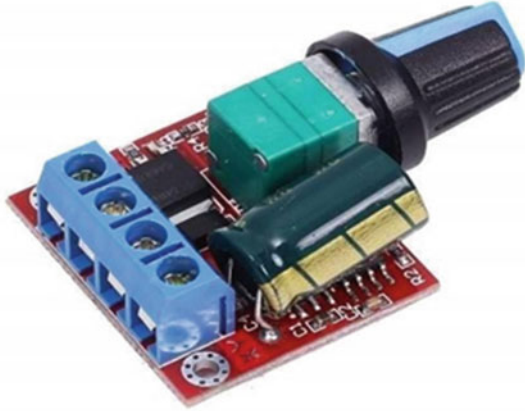


Fig. 2 Schematic representation of battery

Fig. 3 Schematic representation of PWM



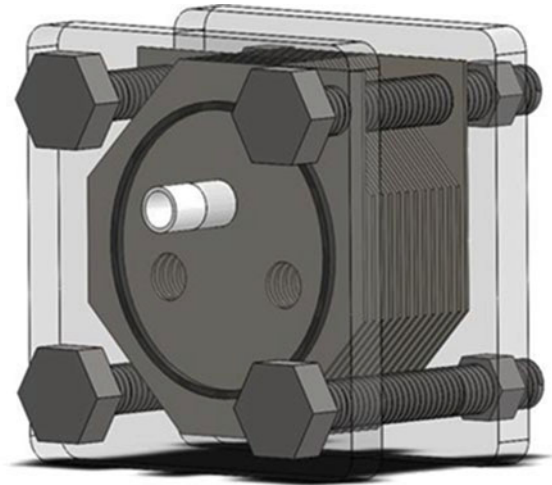
2.3 PWM

The PWM allows you to use more electrolytes, but the HHO generator's output is still regulated, and its schematic representation is shown in Fig. 3. Pulse width modulation (PWM) is a technique for producing high-frequency pulses with low-frequency output signals. Depending on the load and application, the rate (or frequency) at which the power supply must be switched can vary greatly. Several methods of producing modulated pulse width signals, including analog techniques, modulation of sigma-delta, and direct digital synthesis. Comparing two control signals, a carrier signal and a modulation signal, is one of the easiest methods of producing a PWM signal. This is referred to as PWM carrier-based. The PWM is intended to pulse the voltage of DC to the cell. To reduce the heat generated by continuous current flow, pulsing the voltage turns the current off on-off. Furthermore, the PWM allows the amperage to be regulated (current).

2.4 Dry Cell Generator

HHO gas generator is where the electrode is not partially immersed in electrolytes and electrolytes fill only the gaps between the electrodes themselves, as shown in Fig. 4. Dry cell types HHO gas generator is the first less electrolyzed water, i.e., the only water trapped between the cell plates. The electrolyte is contained in a dry cell generator in an electrolytic tank that also serves as a bubbler, and the electrolyte enters the cell under gravity. Compared to wet cells, less current is needed. Potassium Hydroxide is a catalyst that is used to speed up the reaction process. The generator consists of one inlet and outlet for circulation of electrolyte [12–14]. The cells were found to be in a uniform structure. Each plate was provided with gaskets to prevent

Fig. 4 CAD model of the dry cell generator



the leakages and to make it free from the atmosphere. The generator consists of one negative electrode and two positive electrodes.

2.5 Electrolyte Tank

An electrolyte tank is used to store the distilled water and acting as a safety barrier. In an electrolyte tank, distilled water is mixed with Potassium Hydroxide which is used to speed up the reaction process of hydrogen generation as shown in Fig. 5. When HHO gas is emitted from a dry cell, there is also some water vapor produced. This water vapor can hold tiny electrolyte particles that can cause harmful corrosions.

2.6 Flame Arrestor

The fire arrester is also a device that allows gas to pass through it but stops a flame to prevent a larger fire or explosion, and its schematic representation is shown in Fig. 6. It is only in the gas group that flame arresters should be used. There is a huge range of circumstances in which flame arresters are used. For our project, a flame arrester is used to stop the fire, when the backfire occurs.

Fig. 5 CAD model of the electrolyte tank



Fig. 6 Schematic representation of flame arrestor



3 Design Calculation

3.1 *Electrode Plate*

See Fig. 7.

Length	=	120 mm
Breadth	=	120 mm
Diameter of bolt hole	=	16 mm

(continued)

(continued)

Diameter of vent hole	=	15 mm
Thickness of plate	=	1.20 mm

3.2 Gasket

See Fig. 8.

Internal Diameter	=	90 mm
Outer Diameter	=	95 mm
Thickness	=	5 mm

3.3 Pyrogallol Tank

See Fig. 9.

Outer Diameter	=	63.5 mm
Inner Diameter	=	55 mm
Length	=	190 mm
Volume of the tank	=	$(\pi/4) * d^2 * L$
	=	$(\pi/4) * 0.055 * 0.055 * 0.190$
	=	$4.514 * 10^{-4} \text{ m}^3$

3.4 Experimental Setup

In electrolysis, some individuals have attempted to develop a hydrogen generator in various ways to increase gas output, while reducing current input. Some models are more successful than other models. Some of them developed a generator called a “wet system” consisting of plates or tubes immersed in water to enhance the conventional way, while others developed a design called “dry cell” where the water is constantly running through the plates [7–10, 15–19]. The dry cell electrolysis in which rate of hydrogen generated is more when compared to wet cell method. So, dry cell electrolysis method is used. In this setup, nickel-coated stainless steel plates are used plates, and its dimensions in shown in Fig. 7, because if using stainless steel

Fig. 7 CAD model of electrode plate

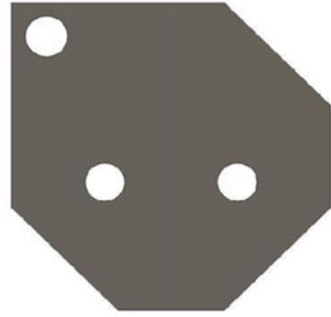


Fig. 8 Schematic representation of gasket

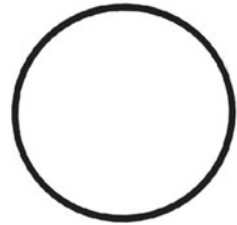


Fig. 9 CAD model of progallol tank



plates, hexavalent chromium was formed at the surfaces after 2–3-month duration. Hexavalent chromium can irritate the nose, throat, and lungs. In addition to that the HHO gas generation also low. A rubber gasket is used for splitting the cell. The rubber gasket is used to prevent the leakages and to make it free from the atmosphere is shown in Fig. 8. The generator consists of one negative electrode and two positive electrodes. The DC power is given from the battery to the PWM (pulse with modulator) circuit. The power from the source is received by the PWM circuit and transferred to the dry cell generator. The PWM circuit supplies the power in the form of an electrical pulse. The cathode separates oxygen from the electrolyte, and the anode splits hydrogen from the electrolyte [20–23]. Then, the separated H_2 and O_2 generated HHO generator is given to the electrolyte tank. Two generators are used in this project. There are 13 electrodes in each generator with a length of 120 mm, a width of 120 mm, a thickness of 1.2 mm, where (+) represents the positive electrode, (N) is neutral, and (–) is the negative electrode, and its schematic representation of the CAD model is shown in Figs. 9 and 10.

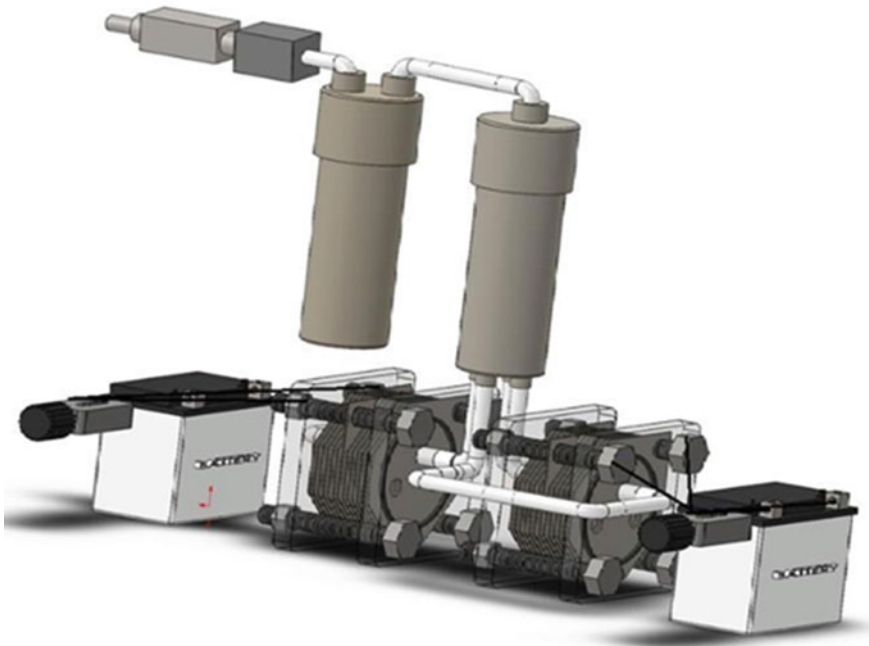


Fig. 10 CAD model of the dry cell electrolyzer setup

4 Result and Discussion

One of the most simple and cost-effective methods is the generation of hydrogen using the dry cell electrolysis method. By using nickel-coated stainless steel plate instead of stainless steel, the rate of hydrogen generation is more and to avoid the hexavalent chromium formation on the gas. The rate of hydrogen generation is higher in dry cell electrolysis compared to wet cell electrolysis. The amount of power required for dry cell electrolysis also lower compared to wet cell electrolysis [24]. According to the result, the amount of hydrogen generation increases with an increased amount of power supply to the dry cell. Also, it is observed that maintaining the cell temperature to a certain range also leads to an increase in the production of hydrogen. PWM is used to control the electricity passed to the generator. From that, the temperature of the dry cell was also maintained. The catalyst used for dry cell generator is Potassium Hydroxide. It is used to increase the rate of hydrogen generation and also speed up the electrolysis reaction [25]. Pyrogallol is used to absorb the oxygen from the generated hydrogen gas. To build an efficient hydrogen generator, the distance between the plates, the catalyst used for the generation of hydrogen, the material used for the cell, the number of plates, and the electrodes used should be considered thoroughly. The amount of current flows through the generator increases or decreases about the generator's temperature in the proposed approach.

5 Conclusion

A more convenient and effective way to build a hydrogen generator is the dry cell electrolysis technique. With an increased power supply to the dry cell, the amount of hydrogen production increases. Maintaining the cell temperature to a certain range also leads to an increase the production of hydrogen. The amount of current flows through the generator increases or decreases about the generator's temperature in the proposed approach. For such, a large-scale hydrogen generation a feasible, harmless, and cheapest catalyst like Potassium Hydroxide can be used. The dry cell electrolysis process is more efficient than wet cell electrolysis because the rate of hydrogen generation will be more. Dry cell electrolysis is a less initial investment cost, and it is an effective method to generate HHO gas. The flame arrestor is one of the main components in this setup which is used to arrest the backfire when the explosion occurs outside the setup. As a development of this project, it is going to calculate the flow rate of hydrogen for different input voltages and mixed catalysts like methanol sodium hydroxide. We have a plan to try different catalysts for electrolytes with various concentrations.

6 Future Scope

To obtain an optimal hydrogen production rate, future research will concentrate on restricting the current flow through the generator. As an important energy carrier, hydrogen will be incorporated into electricity as it can be produced safely from renewable energy sources and is virtually non-polluting. It is used to heat homes and offices, generate electricity, and fuel aircraft as fuel for “zero-emissions” vehicles. The use of hydrogen fuel cells, mainly in transportation, will improve the efficiency of hydrogen as a fuel source. A fuel cell of hydrogen has an efficiency of 60%. That is three times as much as the efficiency of a car powered by fossil fuel with about 20% efficiency, which loses the surrounding environment a lot of energy as heat. With new regulations of emissions aiming to reduce the NO_x levels for the SI Engine, electrolyzer invention could have a substantial influence in various industrial applications. Countries like India, France, the UK, the USA, Russia, Finland, Japan, Korea, and most of the countries in Europe have severe attention toward reducing vehicular emissions. Also, to utilize hydrogen as a primary fuel in the SI engine, the engine should be modified to withstand high temperature, transmit heavy torque, better combustion of fuel. The next step of this project is to link the hydrogen generator to an internal combustion engine, i.e., a spark-ignition engine, to measure fuel efficiency in the car, and to measure air pollutant emission reductions such as CO, CO₂, etc.

References

1. Puniyani K, Malik R, Kumar H, Dwivedi G (2019) Optimization of fuel properties of cottonseed biodiesel and its impact on engine performance and emission. *SN Appl Sci* 1:1316. <https://doi.org/10.1007/s42452-019-1348-9>
2. Chhabra M, Saini BS, Dwivedi G, Behura AK, Kumar A, Jain S, Sarin A, Verma P (2021) Investigation of the shelf life of the optimized Neem biodiesel and its execution and excretion characteristics on automotive diesel engine. *Energy sources, part A: recovery, utilization, and environmental effects*, pp 1–24
3. Jain S, Chhabra M, Dwivedi G, Baredar P, Shukla AK, Garg A (2021) Production & optimization of biodiesel from rubber oil using BBD technique. <https://doi.org/10.1016/j.matpr.2020.05.791>
4. Sudarmanta B, Darsopuspito S, Sungkono D (2016) Application of dry cell HHO gas generator with pulse width modulation on sinjai spark ignition engine performance. *Int J Res Eng Technol* 5:105–112
5. De Silva TS, Senevirathne L, Warnasooriya TD (2015) HHO generator—an approach to increase fuel efficiency in spark ignition engines. *Eur J Adv Eng Technol* 2:1–7
6. Salek F, Zamen M, Hosseini SV (2019) Experimental study, energy assessment and improvement of hydroxy generator coupled with a gasoline engine. *Energy Rep* 6:146–156 (Nov 2020)
7. Gambhir A, Hawkes A, Nelson J, Schmidt O, Staffell I (2017) Future cost and performance of water electrolysis. *Int J Hydrogen Energy* 42:30470–30492
8. Hagen G, Rasten E, Tunold R (2003) Electrocatalysis in water electrolysis with solid polymer electrolyte. *Electrochim Acta* 48:3945–3952

9. Luo H, Jenkins PE, Ren Z (2010) Concurrent desalination and hydrogen generation using microbial electrolysis and desalination cells. *Environ Sci Technol* 45:340–344
10. Hendrik Elvian Gayuh Prasetya, Joke Pratilastiarso, Arrad Ghani Safitra, Rif'ah Amalia, and Hakimatul Ubudiyah, "The experimental study of wet cell HHO generator type with Ba (OH)₂ catalyst on performance and exhaust gaseous emissions of 4 stroke engine 120 cc" *A Journal of chemical physics*, Vol. 1977, PP. 060014–1–060014–7, June 2018.
11. Staffell I, Scamman D, Abad AV, Balcombe P, Dodds PE, Ekins P, Shah N, Ward KR (2019) The role of hydrogen and fuel cells in the global energy system. *Energy Environ Sci* 12:463–491
12. Fadul IMAI (2006) Using HHO gas to reduce fuel consumption and emissions in internal combustion engines. University of Khartoum, Jan 2010
13. Harrison KW, Remick R, Martin GD (2010) Hydrogen production: fundamentals and case study summaries. National Renewable Energy Laboratory, May 2010
14. Manua PV, Sunil A, Jayaraj S (2015) Experimental investigation using an on-board dry cell electrolyzer in a CI engine working on dual fuel mode. *J Mech Eng Vocat Educ* 1:1–8 (2018)
15. Shimizu N, Hotta S, Sekiya T, Oda O (2005) A novel method of hydrogen generation by water electrolysis using an ultra-short-pulse power supply. *J Appl Electro Chem* 36:419–423
16. Patil NN, Chavan CB, More AS, Baskar P (2017) Generation of oxy-hydrogen gas and its effect on performance of spark ignition engine. *Mater Sci Eng* 263:1–14
17. Kumar PP, Prabha KA, Priyadarsini C, Swetha S (2019) Development and applications of HHO water based flame torch. *Int J Recent Technol Eng* 7:515–517
18. Rozendal RA, Hamelers HVM, Euverink GJW, Metz SJ, Buisman CJN (2006) Principle and perspectives of hydrogen production through biocatalyzed electrolysis. *Int J Hydrogen Energy* 31:1632–1640
19. Nag R, Shrivastava S (2016) Oxy-hydrogen fuel as supplement for gasoline vehicles using Dry cell Generator. *Int J Sci Eng Res* 7:1139–1143
20. Essuman SPK, Nyamful A, Yao V, Agbodemegbe SKD (2018) Design and development of an oxyhydrogen generator for production of brown's (HHO) gas as a renewable source of fuel for the automobile industry. *Int J Eng Sci Invention* 8:1–7
21. Shashikant J, Gabhane D, Deshmukh SS (2016) Investigating the effect of OxyHydrogen (HHO) gas and gasoline blend addition on the performance of constant speed internal combustion engines. *Int Eng Res J* 26–31 (Nov 2015)
22. Tamer Nabil (2019) Efficient use of Oxy-hydrogen Gas (HHO) in vehicle engines. *J Eur des Syst Autom* 52:87–96
23. Brayek M, Jemni MA, Kantchev G, Abid MS (2016) Improving Tahe performance of a gasoline engine with the addition of oxygen-hydrogen mixtures. *Arab J Sci Eng* 41:4635–4642
24. Kamaraj N, Arun kumar S, Ragul kumar M, Sivakumar R (2020) A review of hydrogen generation by dry cell electrolysis method to improve fuel economy and emission reduction in SI engine by cleaner combustion. *Int J Sci Technol Res* 9:555–561
25. Kamaraj N, Subburaj AK, Mohanraj RK, Rasu S (2020) Experimental investigation on performance, combustion and emission characteristics of CI engine with on-site hydrogen generation. *Mater Today Proc* (7 September 2020)

A Short Review on Biped Robots Motion Planning and Trajectory Design



Kunchala Balakrishana Reddy, Gamini Suresh, Ravi Kumar Mandava,
and T. Ch. Anil Kumar

1 Introduction

Biped robots have emerged into various domains ranging from scientific exploration to specific applications utilized in emergencies like treating coronavirus affected patients with utmost care. To tackle this kind of conditions, it should be programmed and planned in a sophisticated manner. To be able to move in complex environments, a biped bot should have an anthropomorphic gait cycle. From the studies of biomechanics, it is observed that the human body balance is influenced by the altitude of the hip movement in lateral and sagittal planes as well. Most of the research work is carried out with an assumption that hip height is a fixed constraint, and the torso is perpendicular to the transverse plane. The studies on the biped bots had started in the 1960s with the. Further many researchers realized the bipeds for the specific applications. The concept of ZMP is coined by the renowned scientist Vukobratovic in 1969. From the studies of biomechanics, it is observed that the human body balance is influenced by the altitude of the hip movement in lateral and sagittal planes as well. Most of the research work is carried out with an assumption that hip height is a fixed constraint, and the torso is perpendicular to the transverse plane. Numerous researchers have initiated legged robots like bipeds, quadrupeds, snake-like, cockroach structured walking robots for their specific applications.

K. Balakrishana Reddy (✉) · G. Suresh · T. Ch. Anil Kumar
Department of Mechanical Engineering, VFSTR, Guntur, Andra Pradesh, India

R. K. Mandava
Department of Mechanical Engineering, MANIT, Bhopal, India

1.1 Analogy of Natural Gait and Biped Gait

The imitation [1] of the gait of biped and quadrupeds along with human beings [2] is a complex mechanism. As shown in Fig. 1, human gait cycle consists of sixty per cent of the stance phase, forty per cent is single contact and ten per cent double contact with the ground. The features of terrain adaptive, optimal motion in the path and continues trajectory control approach complies with adaptive trajectory generator and the tracking of the system with PD controllers. The researcher used a methodology in which the number of servo systems is equal to the DOF in a multivariable system, to complain of the normal gait. The motion [3] of the biped robot with the mathematical model that comprises complicated dynamics, stability, and feedback control. In literature, the researcher treats biped locomotion dynamics concerning planner motion, with the following assumptions. Sixth order nonlinear differential equation with the considerations that hypothetical biped posses 3-DOF by one rotational and two translational. Furthermore, it is proposed that 3-DOF biped follows singular gait, i.e. only SSP at any instant of time, with no theoretical slippage. However, with the large initial disturbances, a stable gait is attained. An autonomous biped [4] with anthropomorphic data is realized, to attain the dynamically stable motion with high power to weight ratio on the precise selection of mechatronics elements [5]. As shown in Fig. 2, few of biped robot laboratory models are evaluated on the specific terrians, till now no such all terrain biped is made due to complexity in design control process.

Considering the variety of foot motion parameters, various modes of foot motion is adapted concerning the terrain conditions, to maintain the stability margin of the biped [6, 7]. With the advent of the 3-D linear inverted pendulum model [7], real-time gait generation is tested using the 12 degrees of freedom biped robot which is realized in the part of humanoid robotics project-2 (HRP-2), under METI of Japan.

For footstep planning, the planner depends on the input parameters such as stable trajectories, with heuristics functions. As shown in Fig. 3, a target-oriented footstep planning algorithm [8] is developed to that navigate through obstacles on the path and a heuristic metrics data with relative safety to bypass the obstacles on the path [9]. A cart-table model-based ZMP controller is designed to review the generated

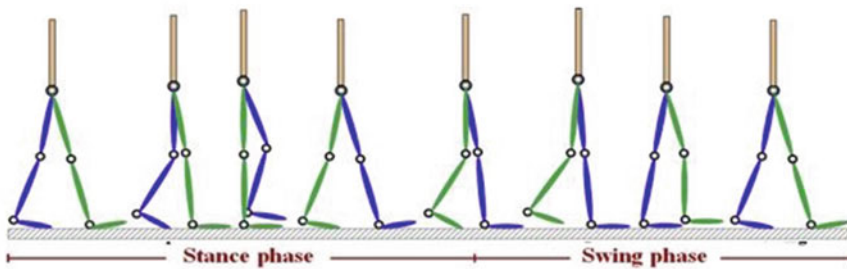


Fig. 1 Human gait cycle

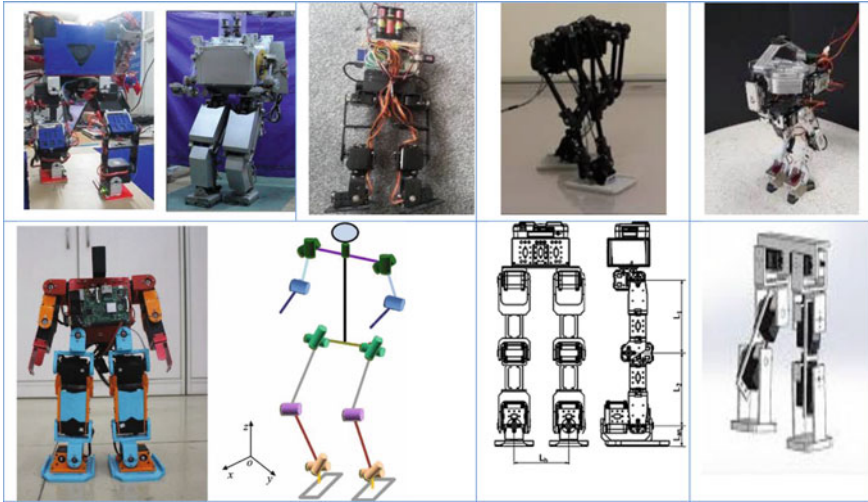


Fig. 2 Laboratory biped robot models and schematic of biped robot

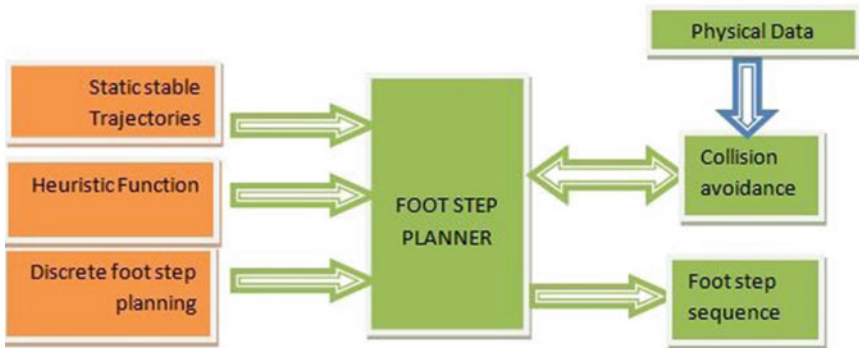


Fig. 3 Block diagram of the footstep planning

walking patterns [9]. The ZMP error is suppressed by a preview controller [10]. To avoid an obstacle in the path of the robot, the foot movement to the fixed shank will be in a set of transitions [11]. A set of 8 transitions, 16 transitions, 24 transitions, and 40 transitions is used to avoid the obstacle.

2 ZMP Criterion

Zero moment point is a point the horizontal component of inertia along with gravity is zero, which means that the point of contact of feet is under sufficient friction without sliding. Asymptotically, stable walking is proved in bipeds with an assumption of rigid contact and instantaneous DSP [12]. The presence of ZMP location is discussed including some fictitious cases where it lies beyond the foot support area [13], and energetically, optimal gait [14] speeds are addressed. An activity-based, dynamically balanced [15], 7 DOF biped robot gait generation presented, in which ZMP is within the foot support polygon. Biped will be more dynamically balanced with reduced trunk and legs mass and an inverse relation with the power consumption [16]. Focused on the foot of the biped robot, which is normally rigid and replaces with a soft sole, a layer of rubber sole which behaves as the shock absorber. The author proposed four states of the walk with the deformation correction factor. Each of the joint angles of the 8-DOF biped robot uses a cubic spline trajectory which is continuous and localized control points or via points or knot points [17]. The ZMP reference trajectories of a biped robot of 12 DOF, i.e. 6 DOF at each leg. This article utilized the concepts of ZMP and inverted pendulum, and he found that ZMP in natural human walking does not stay fixed in the feet touching the ground. He adopted the trajectory reference generation technique based on the fore mentioned concepts. With the advent of fourier series approximation, solutions are obtained for the linear inverted pendulum dynamics. Moreover, with smoothing techniques DSP, ZMP is obtained [18]. A 7-DOF biped robot that generates dynamically balanced gait for ditch crossing activity is presented with three modes of comparison namely, analytical, neural network (NN) based and fuzzy logic (FL) based out of which FL based modes are more adaptive to the conditions and results in more dynamically balanced margin (DBM) and are energy cost-effective compared to former mode. With the feeding of cubic polynomial [19], as the trajectory offers more smoothness with lesser calculation as well as the high-computation speed. The torque at the joint of supporting leg knee is relatively high compared to the rest of joint torques, followed by hip and ankle joints [20]. The author makes the analogy imitation with humans to that of a biped robot proposed in the paper. He mentioned the common interest of the biped robot researchers to coexist with the human beings, specifically the author pointed out the functionality of knee bending forward in biped bots and make an attempt to coexist functions as humans. The main contribution of the researcher is trajectory design using the kinematic model of the linear inverted pendulum (LIPM) with an assumption that hip level is constraint is not utilized. Because of the group researchers, an optimized trajectory possess high stability, whereas the author optimized the energy consumption of the actuators to 28% lesser than conventional systems. The researcher realized and fed the separate independent trajectories for the upper body and lower body with the help of roll motion constraint [21]. Three different modes of active walking which are underactuated without toe and heel actuation are studied with the alteration of existing barefoot with ankle rocker function. Increased heel strike angles and toe results in increased low-speed gait and a nominal decrease in energy efficiency [22].

An anthropomorphic 11-DOF human-sized Russian robot AR-601 M is simulated to coexist the human walking using sim mechanics tool [23]. The phase of DSP of a 7-DOF biped robot with the multi-objective optimization on the parameters power consumption and DBM with the stairs ascending and descending activity using the concept of ZMP is simulated which results in a smoother transition of SSP to DSP, and energy consumption of underactuated bipeds with the stability criteria and control strategies [24] is studied [25]. The evolution of bipeds along with motion planning, dynamic stability control is analyzed. Their intended purposive service in the field of gait rehabilitation and in the cutting edge of biomechanics, human lower limb prosthetics ranging from active to passive wearable exoskeletons along with control strategies is presented (Table 1).

3 Variation of COM Trajectories

The variation of CoM (Centre of Mass) in the friction cone [26] is analyzed with the ditch crossing activity to trace the joint trajectories in consideration of friction, impact, ZMP and power consumption, in both the phases (SSP and DSP) of gait with the biped customized assumptions along with uncertainties [27, 28]. The stance phase takes 64% of the gait cycle, and the forces acting during the different activities of human daily life are help full to realize a biped with better gait capability without slippage [29]. The biped gait planning using cubic spline and obtained a smooth trajectory. In this paper, author focused on hip height and altitude compensation.

4 Energy-Efficient Gait

An energy-efficient 12-DOF biped [30] that can walk on uneven terrain with the trajectories generation and step planning with obstacles separately. Unlike the conventional flat surface for gait study, the author proposed an uneven terrain with the obstacles on the path statically and dynamically. A trajectory is generated using the gait variables database, whereas the step plan is done using an A* planner [5]. An 18-DOF two-legged robot, focusing on path generation for the static as well as dynamic cases of simulation versus real-time conditions by developing or prototyping the 18-DOF legged biped. In this research work, with the help of biped robot prototyped, the author experimentally validated the simulation results. The author initially developed the trajectory path using static conditions to be, followed by the biped, with the author proposed (FMM) fast marching method. After the generation of the path, the author shifted to dynamic conditions by creating timely variant obstacles in the path of the biped, and this obstacles can be found by hybridized regression search (HRS), on a whole it FMMHRS [31] to reach in a continuous or discontinuous terrain or path, where the wheeled robots can only navigate on continuous terrain by specifying poor stability and mobility of the legged robot [32].

Table 1 The evolution of Bipeds [21]

Time	Biped Name	Place	Founder
1969	ZMP stability criteria	Yugoslavia	M. Vukobratovic
1969	WAP-1	Japan	Kato Ichiro, Japan
1970	“Witt” type robot	UK	Witt
1984	WL-10RD	Japan	Kato Ichiro
1986	E0	Japan	Honda
1988	KDW-I	China	National University of Defence Technology
1989	Passive Dynamic Walking	USA	Moger, United States
1990	Neural networks, SD-1	USA	Y. F. Zheng et al., United States
1997	P-3	Japan	Honda
1997	Virtual model control	USA	J. E. Pratt and G. A. Pratt
1999	COG	USA	MIT
2000	ASIMO	Japan	Honda
2000	SDR-3X	Japan	Sony
2002	BHR	China	Beijing Institute of Technology
2004	HUBO	South Korea	South Korea
2004	iCUB	Italy	RobotCub Consortium
2005	Rabbit	USA	University of Florida
2005	Domo	America	MIT
2007	NAO	France	Aldebaran Robotics
2008	Surena I	Iran	University of Tehran
2009	LOLA	German	Technical University of Munich
2009	Romeo	France	Aldebaran Robotics
2010	HRP-4C	Japan	AIST
2012	SAFFiR	USA	NRL
2013	TORO	German	Institute of Robotics and Mechatronics
2013	PETMAN	USA	Boston Dynamics
2015	Surena III	Iran	University of Tehran
2016	Atlas	USA	Boston Dynamics
2018	18-DOF Biped	India	IIT BBSR
2019	Ditch Crossing Biped	India	IIT Hyderabad

The researcher realized an 8-DOF biped robot that moves on inclined terrain, and compared the different types of link shapes likely V, S, U and constrained versions on a flat surface, and out of those designs author chosen by analysis, the U shaped link as the shank design and performed simulations and performed experimental activities to validate the design as well the model with better results than those were done

earlier. The researcher realized an 18-DOF biped [33] robot that generates dynamically balanced gait, negotiating single- and double-support phases of walking. The author sequentially carried out the work in which trajectories of the biped bot are designed researcher adopted the concept of ZMP (Zero moment point) over the inverted pendulum by which the author finds the dynamic stability through the calculation of DBM (Dynamic balance margin). An analytical strategy is coined to obtain dynamically balance gaits. Suitable trajectories are considered for swing leg and hip, later with the case of inverse kinematics, the motion of the rest of the limbs are generated, in lateral and frontal planes. ZMP influences dynamic stability. Later researcher, calculated the power requirements by the product of torque and angular velocity for the real-time environment. The simulation is carried out for the four steps forward, with the physical parameters consideration. The researcher recommends the cubic polynomial trajectory on a whole contrast with the quadratic and fifth order. He also mentioned the work that can extend with the activities of walking on the staircase, sloping surface, and ditch crossing along with the torque based controller [34]. The researcher differentiates the locomotion by the centre of gravity and the concept of dynamic stability in which ZMP lies inside the foot support polygon. Unlike earlier researchers, the author proposed and realized an 18-DOF biped bot for validation. In this work, the author designed a torque based PID controller for the activities mentioned in previous work with the optimization algorithms like MICWO and PSO are used to solve the problem and obtain the gains of the controller [35]. The author compared the impact of the hip trajectory on the balance of the biped bot by negotiating the straight-line trajectory and cubic polynomial trajectory with the hip joint of the bot. In this research work, author optimized the hip trajectory with (PSO) particle swarm optimization using cubic polynomial accordingly, and the performance of developed algorithms is validated with the dynamically balanced gaits. The author concluded that the straight-line trajectory case of the work results in a higher dynamically balance gait, and he also compared the work effectively with natural human walking with hip heights results in tardy walking.

5 Application of Trajectory Design

Problems faced by the users of knee-ankle-foot-orthosis [36] are the guidelines for the researchers to design and realize the lower limb orthosis device in a more sophisticated way which will eliminate the addressed issues like, avoiding slip with direct contact of orthosis and tiled floor example temples, lightweight, flexibility [37]. To fit with the human walking gait trajectory, sliding mode controller (SMC) [36] is designed, by establishing the human-machine coordination in a co-simulation platform of ADAMS and MATLAB. On a contrary, with PID controller SMC is aggressive in performance (Table 2).

To recover the normal functionality of the disabled content using customized gait generation [39], and hybrid structure design gait rehabilitation devices are analyzed [40]. The influence of ankle joint stiffness [41] on the dynamical balance gait, energy

Table 2 Utilization of robots in the field of health care [38]

ROBOT NAME	USAGE
ARMAR-II	For domestic applications
CARE-O-BOT-3	For domestic applications
CODY	Hospital hygiene maintenance
RIBA	High load transfer and lift applications
PR2	House hold applications
RNAHWR	Serving patients
ASIMO	Human-like activities
ROSE	Tele-operated house hold applications

efficiency is analyzed. A time-variant mathematical model and multivariable, time-independent structure of a robot with 17 DOF, for representing the impact parameters are analyzed with a nonlinear feedback controller design [42]. Lyapunov function and time delay estimation technique [43] are used to study the influences of the uncertainties and external disturbances on the dynamic balance of biped robots. To minimize the errors, the generated control gains an adaptive controller is designed. The dynamic characteristics of lower extremity prostheses [44] and the stability of the system were analyzed to be feasible and effective by phase trajectories. A special ADAMS simulation platform was built to simulate the walking process. The feasibility of the gait planning and COM trajectory is optimized based on the minimum energy criterion.

6 Conclusion

Even though biped robots attained high altitudes in the service sector, there are particular limitations because of stability; man-machine interface coordination is yet to more studied. The emerging of service robots in the domestic lifestyle of human beings on a large scale is more inevitable with an overcome of the limitations. The usage of biped robots in assistance and rehabilitation of the elderly and patients requires more structural stability, controlled interaction. Integration of biomechanics with the mechatronics approach will serve the need of the rehabilitation process as well as the emerging field service robots. In the coming days, these service robots are featured with artificial intelligence and can take decisions rationally as similar to that of an intelligent human being and delivers their enriched service to the world. Human-like movement adaptive to the terrain requires a lot of control strategies and much sensory feedback signal processing. This continuous control may have integration of certain elements such as comparators, amplifiers, and artificial muscles which again be the complexity of trajectory design and motion planning. Precise selection and controlled methods are crucial to serving the dedicated intend purpose.

References

1. I Transactions and O N B Engineering, “to the,” no 1, pp 2–7, 1969
2. Chen B, Zi B, Qin L, Pan Q (2020) State-of-the-art research in robotic hip exoskeletons: a general review. *J Orthop Transl* 20:pp 4–13
3. Gubina F (1974) The dynamic stability, no 2, pp 102–108
4. Gienger M, Loffler K, Pfeiffer F (2001) Towards the design of a biped jogging robot
5. Mrudul K, Kumar R, Vundavilli PR (2018) ScienceDirect sciencedirect an efficient path planning algorithm for biped robot using fast marching method. *Procedia Comput Sci* 133:116–123
6. Huang Q, Yokoi K, Kajita S, Kaneko K (2001) Planning walking patterns for a biped robot, vol 17, no 3, pp 280–289
7. Kajita S, Kanehiro F, Kaneko K, Yokoi K, Hirukawa H, Science AI (2002) Real-time pattern generator for biped walking, no May, pp 31–37
8. Kuffner JJ (2001) Footstep planning among obstacles for biped robots, pp 500–505
9. Chestnutt J, Kuffner J, Nishiwaki K, Kagami S (2003) Planning Biped navigation strategies in complex environments, no. Humanoids
10. Kajita S, Kanehiro F, Kaneko K, Fujiwara K (2003) Biped walking pattern generation by using preview control of zero-moment point, pp 1620–1626
11. Suresh G, Reddy KB, Nagarjuna M (2020) Simulation of shank-foot 2-DOF manipulator with computed torque control for, pp 416–425
12. Plestan F, Member A, Grizzle JW, Westervelt ER, Member S, Abba G (2003) Stable walking of a 7-DOF biped robot, vol 19, no 4, pp 653–668
13. Borovac B (2004) Zero-moment point—thirty five years of its life, vol 1, no 1, pp 157–173
14. Srinivasan M, Ruina A (2006) Computer optimization of a minimal biped model discovers walking and running, vol 439, no January
15. Vundavilli PR, Sahu SK, Pratihari DK (2007) Dynamically balanced ascending and descending gaits of a two-legged robot, vol 4, no 4, pp 717–751
16. Shrivastava M, Dutta A, Saxena A (2007) Trajectory generation using GA for an 8 DOF biped robot with deformation at the sole of the foot, pp 67–84
17. Erbaturo K, Kurt O (2009) Natural ZMP trajectories for biped robot reference generation. *IEEE Trans Ind Electron* 56(3):835–845
18. Vundavilli PR, Pratihari DK (2010) Dynamically balanced optimal gaits of a ditch-crossing biped robot. *Rob Auton Syst* 58(4):349–361
19. Ramirez M (2010) Polynomial trajectory algorithm for a biped robot, vol 25, no 4, pp 294–303
20. Park JH, Chung S (2011) Optimal locomotion trajectory for biped robot ‘D 2’ with knees stretched, heel-contact landings, and toe-off liftoffs †, vol 25, no 12, pp 3231–3241
21. Kumar RP, Özer A, Kim G, Yoon J, Yoon J (2014) A novel dynamic walker with heel, ankle, and toe rocker motions †, Gabsoon Kim ‡ R. Prasanth Kumar †, Abdullah Ozer,” no March 2011, pp 883–893
22. Khusainov R, Shimchik I, Afanasyev I, Magid E (2014) Toward a human-like locomotion : modelling dynamically stable locomotion of an anthropomorphic robot in simulink environment. In: 2015 12th International Conference on Informatics Control, Automation and Robotics, vol 02, pp 141–148
23. Rajendra R, Pratihari DK (2014) Analysis of double support phase of biped robot and multi-objective optimization using genetic algorithm and particle swarm optimization algorithm
24. Gupta S, Kumar A (2017) A brief review of dynamics and control of underactuated biped robots. *Adv Robot* 1864(April):1–17
25. Yang X, She H, Lu H, Fukuda T, Shen Y (2017) Applied sciences State of the Art: bipedal robots for lower limb rehabilitation, pp 1–18
26. Janardhan V, Kumar RP (2017) Online trajectory generation for wide ditch crossing of biped robots using control constraints. *Rob Auton Syst*
27. Janardhan V, Kumar RP (2018) Generating real-time trajectories for a planar biped robot crossing a wide ditch with landing uncertainties

28. Nandikolla VK, Bochen R, Meza S, Garcia A (2017) Experimental gait analysis to study stress distribution of the human foot, vol 2017
29. Li P, Li K (2017) The research on the method of gait planning, pp 39–50
30. Gupta G, Dutta A (2018) Trajectory generation and step planning of a 12 DoF biped robot on uneven surface
31. Mandava RK, Mrudul K, Vundavilli PR (2019) Dynamic motion planning algorithm for a biped robot using fast marching method hybridized with regression search, vol 16, no 1, pp 189–208
32. Sarkar A, Dutta A (2018) Optimal trajectory generation and design of an 8-DoF compliant biped robot for walk on inclined ground
33. Modelling J, Sciences M, Bhubaneswar IIT (2018) Whole body motion generation of 18-DOF biped robot on flat surface during SSP & DSP Ravi Kumar Mandava * and Pandu Ranga Vundavilli, vol 29, no 3, pp 266–277
34. Kumar R, Pandu M, Vundavilli R (2018) Near optimal PID controllers for the biped robot while walking on uneven terrains, vol 15, no December, pp 689–706
35. Mandava RK, Vundavilli PR (2017) Study on influence of hip trajectory on the balance of a biped robot, pp 265–272
36. Bapat GM, Sujatha S (2017) Disability and rehabilitation : assistive technology identification and analysis of knee–ankle–foot orthosis design requirements based on a feedback survey of orthosis users in India. *Disabil Rehabil Assist Technol* 0(0):1–9
37. Wu H, Jia T, Li N, Wu J, Yan L (2017) 2510 . Study on the control algorithm for lower limb exoskeleton based on ADAMS/Simulink co-simulation, pp 2976–2986
38. Joseph A, Christian B, Abiodun AA, Oyawale F (2018) A review on humanoid robotics in healthcare, vol 02004, pp 1–5
39. Shi D, Zhang W, Zhang W, Ding X (2019) A review on lower limb rehabilitation exoskeleton robots. *Chin J Mech Eng*
40. Bi Q et al (2019) Walking of biped robot with variable stiffness at the ankle joint *, no. December, pp 1899–1903
41. Khan UI, Chen Z (2019) Natural oscillation gait in humanoid biped locomotion. In: *IEEE Transaction on Control System Technology*, pp 1–13
42. Sherif S (2019) Identification of humanoid biped robot during walking with linear regression models. In: *2019 22nd International Conference on Process Control*, pp 197–202
43. Pi M, Kang Y, Xu C, Li G, Li Z (2020) Adaptive Time-delay balance control of biped robots. *IEEE Trans Ind Electron* 67(4):2936–2944
44. Xie H, Zhao X, Sun Q, Yang K, Li F (2020) A new virtual-real gravity compensated inverted pendulum model and ADAMS simulation for biped robot with heterogeneous legs, vol 34, no 1, pp 401–412

Optimization of Machining Process Parameters Using Grey Fuzzy Method



Vajrala Venkata Reddy, Ravi Kumar Mandava, and K. Srunivasulu Reddy

1 Introduction

Turning operation is one of the most common machining operations in which rotational parts are being produced by removing material, thereby obtaining reduced size of required diameter. The turning operation can be performed generally in lathe machine with the use of single-point cutting tool. For turning the workpiece in lathe, it is required to fix the cutting tool in the fixture and the workpiece made to be rotated continuously. In various kinds of industries, the turning is the most widely used machining operation to produce required shape of different components [1, 2]. According to the wide research conducted in the area of MMC cutting process by the researchers around the globe, it has been found that the main aspects affecting MMC turning operation predominantly depend on the type of material being used [3, 4]. Usually, according to the guidelines set by standard handbooks, the experience of operators and the knowledge, the machining parameters are selected. However, if the chosen machining parameters are not optimum, then it may eventually increase the cost of the product [5]. By choosing the best machining parameters, one can achieve high machining performance [6]. In the process of choosing the best combination of best machining parameters, the researcher makes use of the optimization techniques [7]. With improved properties, metal matrix composites (MMCs) render a wide range of excellent options in designing new products. MMCs have increased strength and

V. V. Reddy (✉)

School of Mechanical and Industrial Engineering, Diredawa University, Dire dawa, Ethiopia

R. K. Mandava

Department of Mechanical Engineering, MANIT Bhopal, Bhopal 462003, India

K. Srunivasulu Reddy

Department of Mechanical Engineering, Sreenidhi Institute of Science and Technology, Hyderabad, India

enhanced stiffness, wear resistance, dimensional stability even at highest temperatures and low coefficient of thermal expansion. When it comes to aluminium metal matrix composites (AMCs), aluminium alloy remains the matrix material, whereas the other phases comprise of B_4C , SiC, Gr, Al_2O_3 , etc. The composite's mechanical strength and its wear resistance increase when the ceramic particles are incorporated in aluminium alloys [8–10]. Suhasini G [11], reported that the significant impact-creating factor is the feed rate followed by depth of cut and cutting speed for quality characteristics like surface roughness (Ra) and material removal rate (MRR) when turning A356/5 wt. % SiCp. According to Ciftci [12], the surface roughness values produced by uncoated carbide tools are quite better than the coated carbide tools, during turning of Al 2014/SiC MMCs in dry machining condition. With the help of sensitivity, a multiple criteria optimization approach was proposed by Isik and Kentli [13], and the study considered two objectives such as the lessening of cutting forces and increased removal of material, when the unidirectional glass fibres are turned, in order to minimize the specific cutting pressure, surface roughness and tool wear and further to maximize the material removal, a research was conducted by Palanikumar [14] which made use of grey relational grade and Taguchi method. In that study, the GFRP/epoxy composites were turned on with the help of carbide (K10) tool. Further, in the study conducted by Krishnamoorthy [15], grey fuzzy logic was applied to optimize the parameters involved in the drilling process of plastic composite plates that are reinforced with carbon fibre. In order to optimize the machining parameters followed when drilling hybrid aluminium metal matrix composites, Rajmohan [16] utilized grey fuzzy algorithm.

In case of unclear and indecisive environment, fuzzy logic-based applications are primarily used. In today's research trends, the optimization of various manufacturing processes is primarily executed by fuzzy logic-based, multicriteria decision-making techniques. Deng [17] introduced the grey system which is an influential tool that can make use of poor, incomplete and vague data [18, 19] too. Grey relational technique is the hot research topic among today's researchers who effectively used it to trace the intricate relationships among different objectives in a wide range of manufacturing fields [20–23]. Grey relational grade (GRG) is determined by averaging the GRC of every response for converting the optimization of multi-objective performance characteristics into optimization of a single GRG [21]. In their study [23], Lin and Lin utilized grey fuzzy logic method to optimize the EDM process of SKD11 alloy steel with a number of process responses. Present investigation is focused on turning performance of A7075/fly ash/SiC AMMC in terms of Ra and MRR under dry machining condition with uncoated carbide-tipped tool inserts.

2 Experimentation

The weight of AMMCs having 10% of SiC and fly ash particles of size $53 \mu\text{m}$ were fabricated by stir casting route taken as reference for machining as at this percentage, better mechanical properties were analysed by Venkata Reddy [10].

Stir casting route was followed to prepare the composites. Melting of A7075 ingots was performed in an electric furnace with graphite crucible. At 770 °C, molten metal pool was stirred at the centre of the crucible with the help of a mechanical stirrer that rotates at 500 rpm. SiC and fly ash particulates were preheated and dropped in a uniform fashion into the melt. With the purpose of avoiding agglomeration at the time of stirring, the particles were ensured to have a smooth and continuous flow. Since the cast gets exposed to the atmosphere while stirring, argon inert gas-based shielding was maintained throughout for 2–3 min to avoid oxidation. Then, molten metal is poured into cast iron moulds which is preheated to 200 °C. The fabricated ingots were kept in a muffle furnace at 110 °C for 24 h to remove any residual stresses induced in the castings and to reduce the chemical inhomogeneity [10].

Uncoated tungsten carbide inserts are used as a cutting tool. Rough turning on fabricated ingots is first performed on lathe machine to make specimens of uniform diameter as shown in Fig. 1. Initially, based on the available feeds and speeds on the lathe, pilot experiments were conducted to find the range of feeds and speeds for material removal rate as well as good surface finish. Once the levels were identified for depth of cut, cutting speed and feed, the Taguchi’s L16 orthogonal array was opted to develop the experimental design. Table 1 lists all the factors and their selected levels.

Mitutoyo’s surf test SJ-210, an instrument which is generally used to measure the surface roughness, was used in this experiment to calculate the average surface



Fig. 1 Specimens of A7075 reinforced with fly ash and SiC

Table 1 Factors and levels selected

S. No.	Factor	Unit	Levels of factors			
			Level 1	Level 2	Level 3	Level 4
1	Cutting speed	rpm	400	800	1200	1600
2	Feed	mm/rev	0.05	0.10	0.16	0.20
3	Depth of cut	mm	0.2	0.4	0.6	0.8

roughness (Ra) of 16 specimens by measuring the surface roughness at three various locations.

Either using Eqs. (1) or (2), the material removal rate was calculated so as to deduce the productivity evaluation.

$$\text{MRR} = 1000 vfd \text{ mm}^3/\text{min} \tag{1}$$

$$\text{(or) MRR} = \pi DNfd. \tag{2}$$

In the equations above, N denotes spindle speed (rpm), whereas the cutting speed is denoted by v (m/min). Here, D denotes the workpiece diameter and f denotes the feed (mm/rev), while d is the depth of cut (mm).

3 Methodology, Results and Discussion

3.1 Grey Relational Analysis (GRA)

Grey relational analysis (GRA) converts the optimization of multiple response characteristics into single grey relational grade. The procedure involves (i) conversion of experimental data into normalized values, (ii) evaluation of GRCs and (iii) generating GRG. In this work, it is decided to optimize simultaneously Ra and MRR. Experimental data sets based on L16 orthogonal array were used.

The response values are normalized to Z_{ij} (i.e. $0 < Z_{ij} < 1$) utilizing the third equation (Eq. 3) for smaller better type, whereas for larger better type, Eq. (4) is used.

$$Z_{ij} = \frac{\max(y_{ij}, i = 1, 2, \dots, n) - y_{ij}}{\max(y_{ij}, i = 1, 2, \dots, n) - \min(y_{ij}, i = 1, 2, \dots, n)} \tag{3}$$

In the equation above, n denotes the number of replications while y_{ij} denotes the observed response value with $i = 1, 2, \dots, n$ and $j = 1, 2, \dots, k$.

$$Z_{ij} = \frac{y_{ij} - \max(y_{ij}, i = 1, 2, \dots, n)}{\max(y_{ij}, i = 1, 2, \dots, n) - \min(y_{ij}, i = 1, 2, \dots, n)} \tag{4}$$

Equation (5) is nothing but the grey relational coefficient (ζ) which can be exhibited as the relation that exists among the ideal best and actual normalized experimental values

$$\zeta(k) = \frac{\Delta_{\min} + \zeta \Delta_{\max}}{\Delta_{oi k} + \zeta \Delta_{\max}} \tag{5}$$

where $i = 1, 2, \dots n; k = 1, 2, \dots n; \Delta_{\min} = \min_i \min_j \|x_0(k) - x_i(k)\|; \Delta_{\max} = \max_i \max_j \|x_0(k) - x_i(k)\|$. When taking an average of grey relational coefficients of every performance characteristic, then it results in grey relational grade (α_i) and Eq. (6) denotes the same.

$$\alpha_i = \frac{1}{n} \sum_{k=1}^n \zeta(k) \tag{6}$$

where α_i denotes the GRG for i th experiment, whereas k denotes the number of output responses.

3.2 Fuzzy Inference System

There are four models present in the fuzzy inference system such as defuzzification interface, fuzzification interface, rule base and database followed by decision-making unit finally [24]. The database defines the fuzzy sets' membership functions and is followed by fuzzy rules, while the decision-making component executes the implication operations based on the framed rules. The fuzzification line converts the inputs into degrees of matching with linguistic values, whereas the fuzzy rules of the implication are converted into output by defuzzification interface [25]. In fuzzy rule base, there are two inputs and one output present which are driven by if-then control rules. In Fig. 2, the fuzzy interface system is illustrated on the basis of which further prediction is executed.

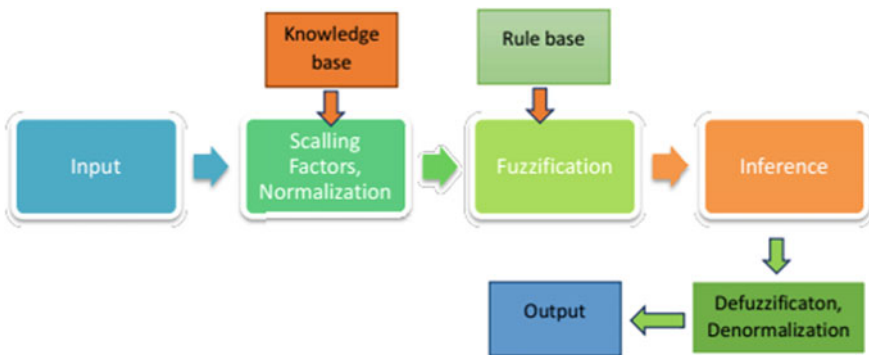


Fig. 2 Fuzzy interface system

3.3 Steps for the Grey Fuzzy Logic Method

Figure 3 shows the process that was followed to determine the best possible machining parameters for multi-response optimization. In this methodology, there are totally six steps followed which are described herewith.

- Step 1 The turning parameters and their levels are all pre-authorized so that the experiments are executed with the help of L16 orthogonal array.
- Step 2 Based on Eqs. (3) and (4), the face values of all the data pre-processing responses are obtained. Using Eq. (5), the grey relational coefficient $\zeta_i(k)$ is calculated for every response following which the same equation is utilized to produce the overall GRG α too.
- Step 3 Using membership function, the fuzzification of the grey relational coefficient is acquired from all the responses in addition to the fuzzification of the overall GRG. The fuzzy rules being established in linguistic form relating GRC as well as overall GRG seem to be satisfactory.
- Step 4 The fuzzy multi-response output is determined with the help of max–min interface operation, after which the centroid defuzzification is deployed so as to determine the grey fuzzy reasoning grade using MATLAB tool box.
- Step 5 Based on response table and response graph, the best combination of parameters is chosen. Further it is anticipated to identify the contribution from every single factor and its interactions on multi-response output with the help of ANOVA.
- Step 6 The confirmation tests are carried out in order to verify the outcome.

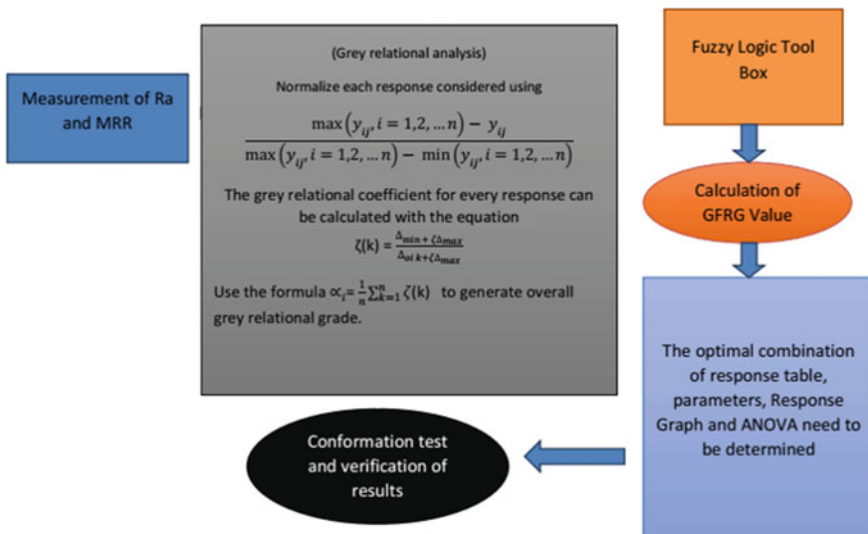


Fig. 3 Steps for the grey fuzzy logic method

3.4 Analysis of Variance

Analysis of variance (ANOVA) was conducted in order to measure the difference per cent among the available set of sources. It is generally applied in order to calculate the contribution made by the input parameters chosen for the study than the output response. The results and the inferences made from the ANOVA can be utilized to find out the parameters that can be held accountable for the performance of the particular process, and it can regulate the parameters for better performance.

4 Results and Discussions

4.1 Calculating the Grey Relational Coefficients

The current research work makes use of two inputs and one output (GFRG) fuzzy logic system. Mamdani fuzzy inference system, i.e. the inference engine, was made to perform fuzzy reasoning on the basis of fuzzy rules so as to generate a fuzzy value. The fuzzy rules mentioned above are designed in the form of if-then control rule. The fuzzy logic system has Ra and MRR grey relational coefficients as inputs. The linguistic membership functions, for example, very low, low, medium and high, were utilized to denote the GRC of Ra and MRR input variables. In a similar manner, the output GRG was denoted through the membership functions, for instance, very low (VL), low (VL), medium (M), low, high (H) and very high (VH). Figures 4 and 5 show the triangular-shaped membership functions which were utilized for this work. The current research work put forth 16 fuzzy rules which were developed

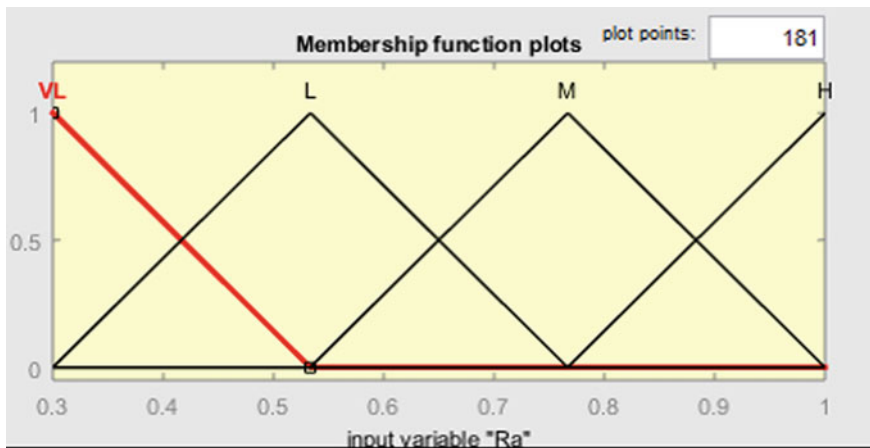


Fig. 4 Membership functions for surface roughness and MRR

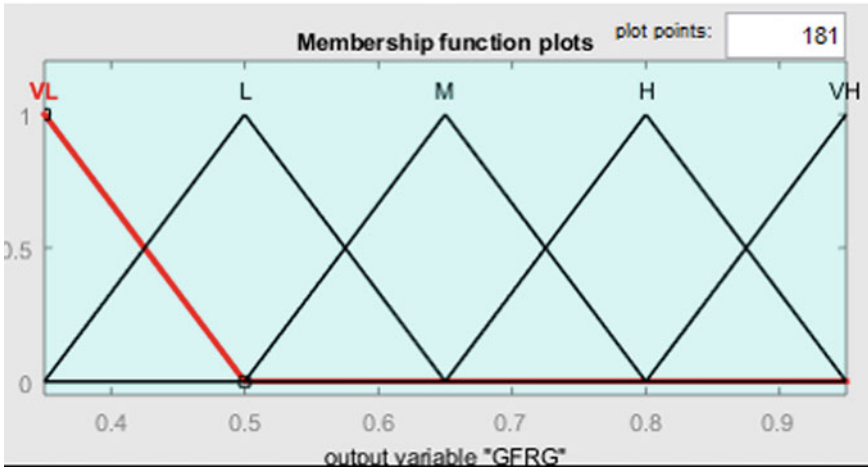


Fig. 5 Membership function for multi-response output

by projecting the relationships that exist between GRC and GFRG values. Figure 6 shows the rule-based fuzzy logic reasoning. The fuzzy output can be achieved through maximum–minimum compositional operation via tracking of the fuzzy reasoning. With the help of MATLAB (R2018b) fuzzy logic toolbox, the defuzzifier changes the fuzzy predicted values into GRFG, and these values are listed in Table 2.

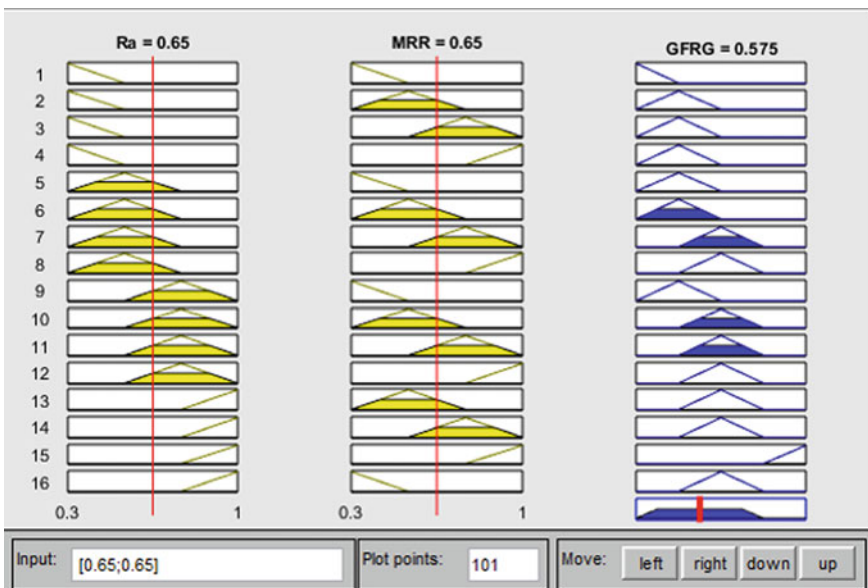


Fig. 6 Fuzzy logic rules viewer

Table 2 Data pre-processing, GRC and GRG

Exp. No	Normalized Data		Ideal Sequence	1	Grey Relational Coefficient		GFRG
	MRR	Ra	Delta MRR	Delta (Ra)	MRR	Ra	
1	0.0000	0.7574	1.0000	0.2426	0.3333	0.6733	0.531
2	0.1102	0.6036	0.8898	0.3964	0.3598	0.5578	0.522
3	0.3043	0.1893	0.6957	0.8107	0.4182	0.3815	0.481
4	0.6117	0.0000	0.3883	1.0000	0.5629	0.3333	0.525
5	0.1223	0.6982	0.8777	0.3018	0.3629	0.6236	0.549
6	0.1264	0.8284	0.8736	0.1716	0.3640	0.7445	0.547
7	0.9741	0.3669	0.0259	0.6331	0.9508	0.4413	0.588
8	0.9110	0.3432	0.0890	0.6568	0.8489	0.4322	0.583
9	0.3104	0.9112	0.6896	0.0888	0.4203	0.8492	0.577
10	0.8382	0.8402	0.1618	0.1598	0.7555	0.7578	0.642
11	0.3529	0.4497	0.6471	0.5503	0.4359	0.4761	0.494
12	0.8868	0.3905	0.1132	0.6095	0.8153	0.4507	0.593
13	0.5632	1.0000	0.4368	0.0000	0.5337	1.0000	0.65
14	0.9353	0.9527	0.0647	0.0473	0.8854	0.9135	0.734
15	1.0000	0.7633	0.0000	0.2367	1.0000	0.6787	0.65
16	0.6117	0.5917	0.3883	0.4083	0.5629	0.5505	0.525

When the GFRG values are higher, it denotes its optimal multidimensional performance characteristics. The mean value was analysed for GFRG. Table 3 lists the rank of parameters on the basis of Δ (delta) statistics that can be derived from the difference between highest and least average of GFRG of every factor. This rank of parameters impacts multiple performance response. Figure 7 plots these rank values like the response graph in case of machining parameters. When the response graph is greatly inclined, then the impact of the process parameters upon multiple performance response would also be higher.

Figure 5 shows all the three inputs' fuzzification. For example, Ra takes up its GRC value. The triangular membership function graph is exhibited in such a way that defines the way of mapping input and output values ($Y = \text{GFRG}$) between 0 and 1. Figure 6 shows the triangular-shaped membership function which is utilized in the current research work.

Table 3 Response table for GFRG

Machining parameters	Level 1	Level 2	Level 3	Level 4	Delta	Rank
Cutting speed (A)	0.5147	0.5668	0.5765	0.6397	0.125	1
Feed rate (B)	0.5767	0.6112	0.5533	0.5565	0.058	3
Depth of cut (C)	0.5242	0.5785	0.5938	0.6012	0.077	2

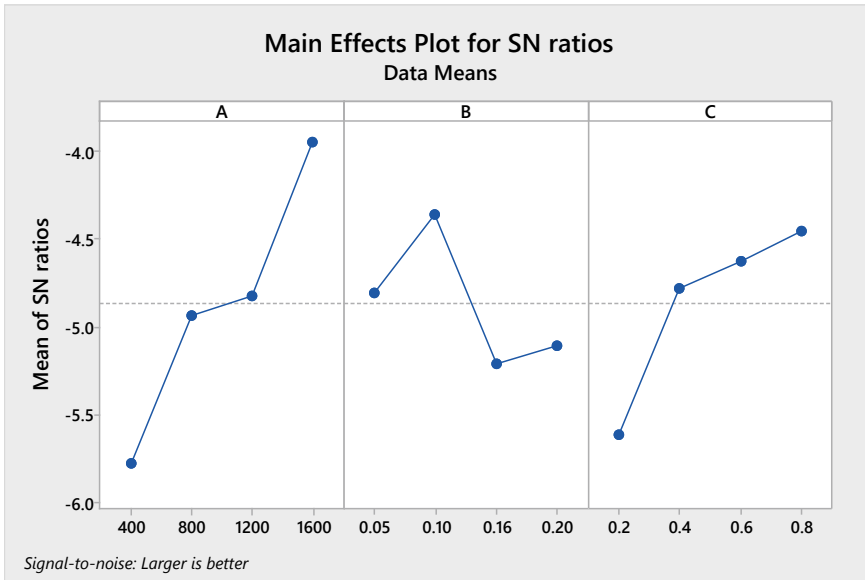


Fig. 7 Response graph for every level of machining parameters

On the basis of Table 3 and Fig. 7, the optimum values in case of machining process parameters are listed as follows: depth of cut at level four (0.80 mm) (C4); feed rate at level two (0.10 mm/min) (B2); cutting speed at level four (1200 rpm) (A4). Simultaneously, when these conditions are used, it diminishes Ra and enhances MRR along machining with all the investigated factors. Equation (7) shows the response equation of GFRG. The maximum value (rank 1) of cutting speed (A) highly influenced its multi-performance which can also be understood from Fig. 7.

$$\begin{aligned}
 GFRG = & 0.6313 - 0.000068A - 0.957B - 0.316C \\
 & + 0.000000A * A - 3.49B * B - 0.292C * C \\
 & + 0.000346A * B + 0.000328A * C + 3.414B * C \quad (7)
 \end{aligned}$$

ANOVA, having executed at 95% confidence level, was done so in order to assess the role played by every factor in multiple performance characteristics. Large F-value inferred that the change in process parameters severely impacted the performance characteristic. Table 4 shows the ANOVA results. The % contribution of cutting speed was determined as 43.43 as mentioned in ANOVA table of GFRG which infers that a prominent role was played by cutting speed in the determination of GFRG. Once the best level parameters for machining were decided from S/N ratio graph, the tests for confirmation were conducted in order to ensure the improvement in the multi-response feature of turning as shown in Table 5. Using optimal level of turning parameters and using Eq. (8), the forecasted response value ($\gamma_{\text{predicted}}$) can be

Table 4 ANOVA for GFRG

Source	DF	Seq SS	Adj MS	F-value	P-value	Contribution (%)
A	1	0.029607	0.005077	0.56	0.484	43.43
B	1	0.003095	0.008170	1.83	0.225	4.54
C	1	0.012128	0.010458	3.02	0.133	17.79
A*A	1	0.000127	0.002432	0.31	0.596	0.19
B*B	1	0.001526	0.041243	2.67	0.154	2.24
C*C	1	0.002186	0.000041	5.4	0.059	3.21
A*B	1	0.001132	0.041960	1.03	0.350	1.66
A*C	1	0.005806	0.050393	14.34	0.009	8.52
B*C	1	0.010144	0.001110	25.06	0.002	14.88
Error	6	0.002428	0.000405			3.56
Total	15	0.068178				100.00

Table 5 Conformation experiments

Index	Optimal settings	Predicted values	Experimental value
GFRG	N = 1600 rpm, f = 0.10 mm/rev, d = 0.8 mm	0.7033	0.6923

calculated.

$$\gamma_{\text{predicted}} = \gamma_m + \sum_{j=1}^n (\gamma_0 - \gamma_m) \tag{8}$$

in which, the γ_m denotes the overall mean multi-response value and γ_0 denotes the mean multi-response value at the optimum level of factors. In the equation, n denotes the number of input process parameters. From the outcomes, it can be inferred that the GFRG value of the optimal parameter condition ($A_4B_2C_4$) seems to be high when compared with the initial setting parameter condition. In addition to that, the forecasted response value also seems to be closer to the experimental value.

5 Conclusion

The current study utilized the hybrid approach of grey fuzzy method in addition to orthogonal array so as to best enhance the process parameters in the turning process of Al7075/FA/SiC hybrid MMC for multi-response features. The researcher identified a best combination of turning parameters along with their levels when it comes to achieving the least surface roughness (Ra) value and a better material removal rate (MRR). Based on the response noted from GFRG values, the researcher found out the

optimum combination levels of input process parameters: cutting speed 1600 rpm, feed 0.1 mm/rev. and depth of cut 0.8 mm as shown in Fig. 7. Further, the study concluded with the proposed method showing efficiency in finding a solution for turning multi-response problems when compared to the methods used earlier.

References

1. Kanta DD, Mishra PC, Singh S, Thakur RK (2015) Tool wear in turning ceramic reinforced aluminum matrix composites—A review. *J Compos Mater* 49(24):2949–2961
2. Muthukrishnan N, Murugan M, Rao KP (2008) Machinability issues in turning of Al-SiC (10p) metal matrix composites. *Int J Adv Manuf Technol* 39(3–4):211–218
3. Niknam SA, Kamalizadeh S, Asgari A, Balazinski M (2018) Turning titanium metal matrix composites (Ti-MMCs) with carbide and CBN inserts. *Int J Adv Manuf Technol* 97(1–4):253–265
4. Dandekar CR, Shin YC (2012) Modeling of machining of composite materials: a review. *Int J Mach Tools Manuf* 57:102–121
5. Thakur D, Ramamoorthy B, Vijayaraghavan L (2009) Optimization of high speed turning parameters of superalloy Inconel 718 material using Taguchi technique
6. Yang WP, Tarng YS (1998) Design optimization of cutting parameters for turning operations based on the Taguchi method. *J Mater Process Technol* 84(1–3):122–129
7. Zuperl U, Cus F, Milfelner M (2005) Fuzzy control strategy for an adaptive force control in end-milling. *J Mater Process Technol* 164:1472–1478
8. Surappa MK (2003) Aluminium matrix composites: Challenges and opportunities. *Sadhana* 28(1–2):319–334
9. Gopalakrishnan S, Murugan N (2012) Production and wear characterization of AA 6061 matrix titanium carbide particulate reinforced composite by enhanced stir casting method. *Compos B* 43:302–308
10. Venkata Reddy V et al (2018) Studies on microstructure and mechanical behavior of A7075 -Flyash/SiC hybrid metal matrix composite. *IOP Conf Ser Mater Sci Eng* 310:012047
11. Suhasini G et al (2013) Machining of MMCs: a review. *Mach Sci Technol Int J* 17(1):41–73
12. Andrews C et al (2000) Machining of Aluminium/SiC composite using diamond inserts. *J Mater Process Technol* 102:25–29
13. Işık B, Kentli A (2009) Multicriteria optimization of cutting parameters in turning of UD-GFRP materials considering sensitivity. *Int J Adv Manuf Technol* 44:1144–1153
14. Palanikumar K, Karunamoorthy L, Karthikeyan R (2007) Multiple performance optimization of machining parameters on the machining of GFRP composites using carbide (K10) tool. *Mater Manuf Process* 21(8):846–852
15. Krishnamoorthy A, Boopathy RS, Palanikumar K, Davim PJ (2012) Application of grey fuzzy logic for the optimization of drilling parameters for CFRP composites with multiple performance characteristics. *Measurement* 45:1286–1296
16. Rajmohan T, Palanikumar K, Prakash S (2013) Grey-fuzzy algorithm to optimise machining parameters in drilling of hybrid metal matrix composites. *Compos Part B* 50:297–308
17. Deng J (1989) Introduction to grey system. *J Grey Syst* 1(1):1–24
18. Pattnaik S, Karunakar DB, Jha PK (2013) Multi-characteristic optimization of wax patterns in the investment casting process using grey-fuzzy logic. *Int J Adv Manuf Tech* 67(5–8):1577–1587
19. Liu NM, Horng JT, Chiang KT (2009) The method of grey fuzzy logic for optimizing multi-response problems during the manufacturing process: a case study of the light guide plate printing process. *Int J Adv Manuf Tech* 41:200–210
20. Ahilan C, Kumanan S, Shivakamran N (2009) Multi objective optimization of CNC turning process using grey based fuzzy logic. *Int J Mach Mach Mater* 5:434–451

21. Hsiao YF, Tarng YS, Huang WJ (2008) Optimization of plasma arc welding parameters by using the Taguchi method with the grey relational analysis. *Mater Manuf Process* 23:51–58
22. Chiang KT, Chang FP (2006) Application of grey-fuzzy logic on the optimal process design of an injection-molded part with a thin shell features. *Int Commun Heat Mass Transfer* 33:94–101
23. Lin JL, Lin CL (2005) The use of grey-fuzzy for the optimization of the manufacturing process. *J Mater Process Technol* 160:9–14
24. Klir GN, Yuan B (1995) *Fuzzy sets and fuzzy logic: theory and applications*. Prentice-Hall, USA
25. Ross TJ (2004) *Fuzzy logic with engineering applications*. John Wiley & Sons, UK

Energy Analysis of R1234yf/R134a as Replacement of R134a in a Domestic Refrigerator



P. Saji Raveendran, P. C. Murugan, T. Darwin, Godwin Glivin,
and Gaurav Dwivedi

1 Introduction

India, like other developing countries, has experienced dramatic growth in the use of domestic refrigerator. More than 1 billion domestic refrigerators are currently in operation worldwide. HFC refrigerants have a high global warming potential and have an effect on the environment [1]. In compliance with the Kyoto Protocol, HFC refrigerants release additional greenhouse gases, thereby reducing the use of HFC coolants. Especially, the existing refrigerants R134a have a high GWP (1430), and it is to generate TFA and to bring about the new environmental issue [2]. Based on the environmental safety, it will soon be phased out. By 2012, the European Union took steps to control the emissions of F-gases by two-thirds of its existing 2030 rate and specified that it would be under 150 GWP for the new refrigerant. This gives the research potential to select on alternate refrigerants.

The hydrocarbons as an environmental-friendly refrigerant have a good performance in refrigeration as well as air-conditioning system. Nevertheless, some accidents were observed during manufacture or retrofitting of hydrocarbon equipment [3] because it is denser than air and spreads close to the floor in case of a leakage, thus increasing the risk of inflammation. This reason, the manufacturers fear for, used hydrocarbons in domestic refrigerators. R1234yf is a good environmentally

P. Saji Raveendran · P. C. Murugan · T. Darwin
Department of Mechanical Engineering, Kongu Engineering College, Erode, Tamil Nadu 638060,
India

G. Glivin
Department of Energy and Environment, National Institute of Technology, Tiruchirappalli, Tamil
Nadu 620015, India

G. Dwivedi (✉)
Energy Centre, Maulana Azad National Institute of Technology, Bhopal, India

friendly refrigerant [4]. It is best suitable alternate for R134a, and its thermo-physical properties are almost nearer than R134a.

Compared to R134a [5], it has GWP-4 and good climate cycle performance and does not increase significantly in the concentration of rainwater in TFA [6]. Regarding safety features, R1234yf has low toxicity, comparable to R134a [7]. The performance assessment has been reported for R1234yf refrigerant for mobile air conditioners, air-conditioning rooms or beverage coolers as a replacement for R134a. There is no proof of breakdown or reaction based on ASHRAE/ANSI standard 97 assessment of R1234yf with copper, steel, aluminium and POE oils [8]. Further testing with polymers and lubricants reveals that R1234yf is close to R134a to material consistency. The beverage cooler optimized experimentally for R1234yf had a very similar energy efficiency to R134a and a decreased environment performance of the overall life cycle [4].

Some research has been performed on R1234yf substitutes for R134a in the domestic refrigeration application. As such, when comparing R134a in domestic refrigeration system, R1234yf has achieved the required requirements in terms of security, reliability and compatibility. R1234yf's thermo-physical properties were compared to R134a in refrigeration cycles. It was shown that the capacity was 2.9% lower and COP was 2–7% less than R134a [8]. The theoretical model was developed and validated by experimental data from R134a. Their model indicated that R1234Yf was 9% less COP and 6% less capacity than R134a [9].

The mild flammability is a major problem for R1234yf. Recently, one of Europe's major auto companies has refused to adopt R1234yf because of its inflammability, with its low flammability limit of 6.2%. For the replacement of R134a in chillers, an azeotropic blend consisting primarily of the R1234yf was recommended [10]. For different applications like MACs and bottle coolers, an azeotropic blend of R1234yf/R134a is proposed for substitution. When the R134a mixture is added to the R1234yf by 10–11%, with GWP under 150 and COP, it is non-flammable and the discharge capacity temperature is similar to that of the R134a [11].

In this work, a mathematical simulation studied to check the performance of an R1234yf/R134a mixture in a household refrigerator. The result shows that R134a can be added up to 10% to keep the GWP of the mixture below 150. The simulation also shows that the variation in COP is not significant, when the mixture is used instead of pure refrigerant. In the simulation process, the software tool 'MATLAB' was used for the simulation, and the 'REFPROP' refrigerant property database was used to integrate difference in thermal physical properties of refrigerants in the simulation [12].

1.1 Refrigerant Selection

The choice of refrigerant is one of the most important functions to choose the appropriate refrigerant based on its thermo-physical properties. The properties of refrigerants obtained from REFPROP are plotted for the operating temperatures -23 – 47 °C

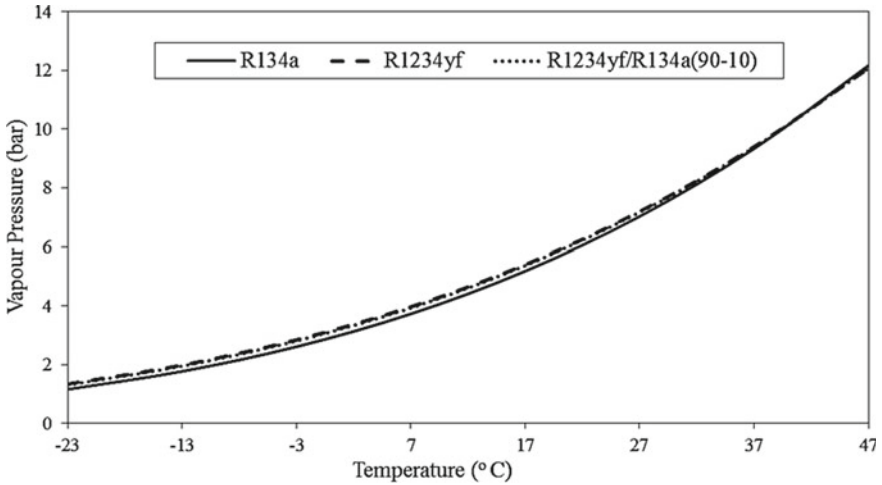


Fig. 1 Variation of vapour pressure with respect to temperature

(Fig. 1). It indicates the vapour pressure of refrigerants. When the vapour pressure is low, the compressor needs less amount of work and gives better performance to the system. However, the vapour pressure of R1234yf and R1234yf mixture is slightly higher than the R134a by about of 7% (Fig. 2) indicating latent heat of refrigerants. The latent heat of refrigerant plays an important role to deciding the refrigeration capacity. The R1234yf and R1234yf blends have an 18% lower latent heat than

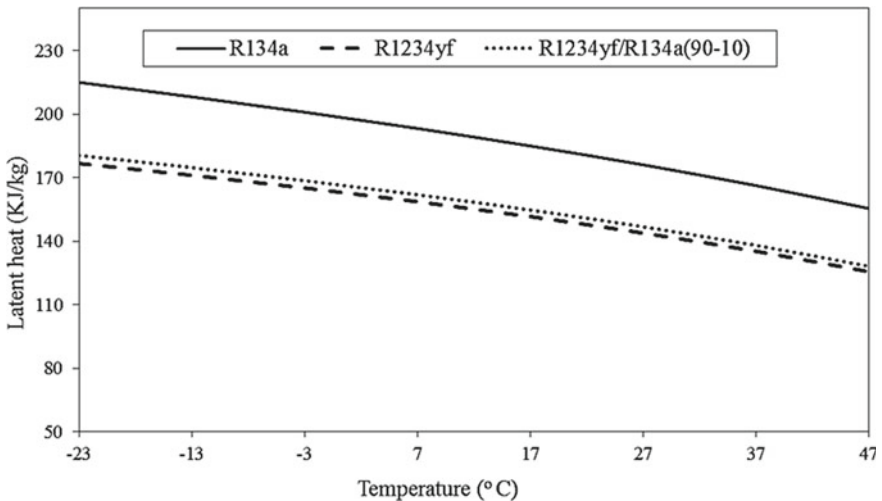


Fig. 2 Variation of latent heat with respect to temperature

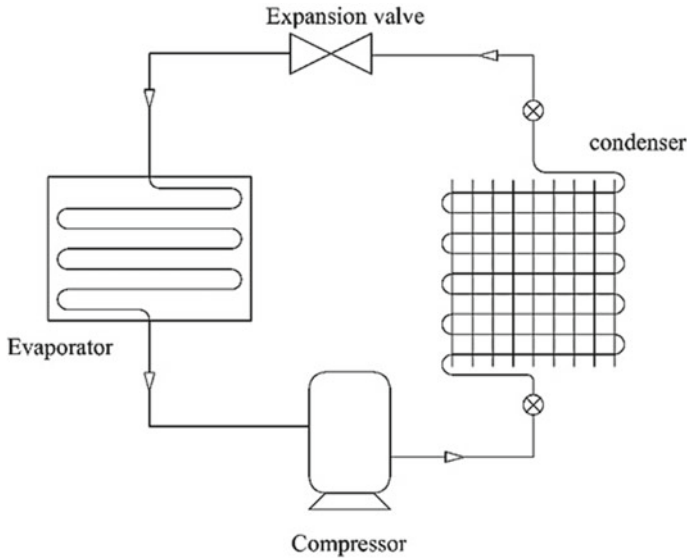


Fig. 3 Schematic diagram of domestic refrigerator

R134a. Based on the observation, the suggested refrigerants properties are almost near than the conventional refrigerant.

2 Analytical Study

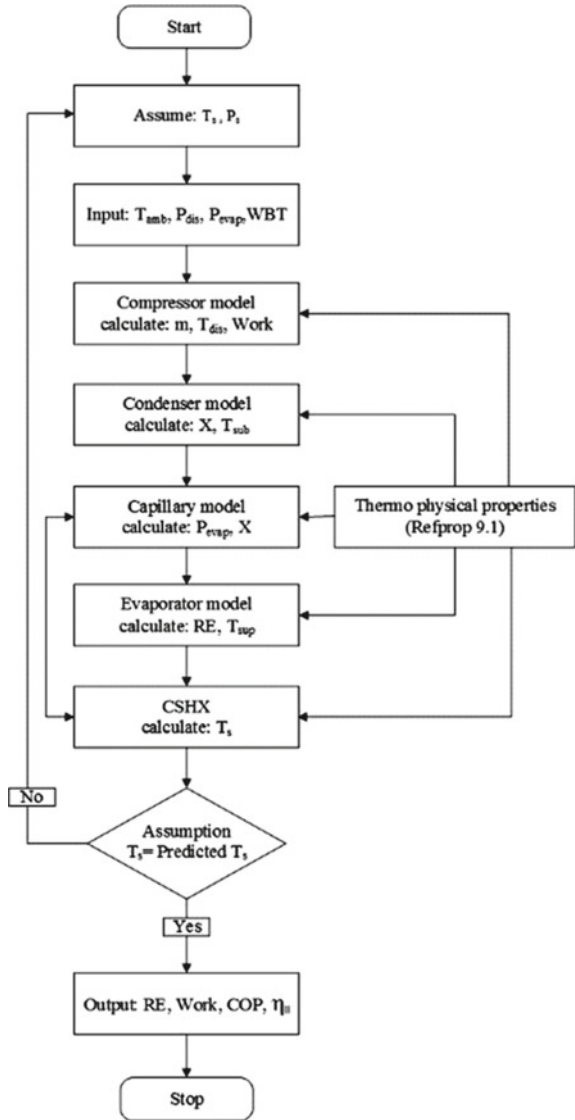
The schematic diagram considered in the analysis is illustrated in Fig. 3. It consists of hermetically sealed reciprocating compressor, air-cooled condenser, capillary tube and evaporator. For the simulation of the above components, MATLAB software was used.

In previous studies [13–18], the compressor, condenser, capillary and evaporator are modelled. The different steps used for the simulation are shown in the flow chart (Fig. 4).

3 Result and Discussion

The variation of refrigeration effect with ambient temperature using with both refrigerants such as R1234yf and R1234yf mixture has been calculated and plotted in Fig. 5. Here, the cooling effect decreases as the ambient temperature increases. It is observed that the R1234yf mixture is about 8% and 2% lower than R134a and 2% higher than R1234yf.

Fig. 4 Flow chart for simulation model of the domestic refrigerator



The compressor work variations with ambient temperature using both the R1234yf and R1234yf blend have been calculated and recorded in Fig. 6. Here the compressor work increases as the ambient temperature increases. It is observed that R1234yf blend is higher than the R134a and lower than R1234yf by about of 6% and 1%, respectively.

The variation of COP with ambient temperature using both refrigerants such as R1234yf and R1234yf mixture has been calculated and plotted in Fig. 7. Here the COP decreases with increase in ambient temperature. It is observed that R1234yf

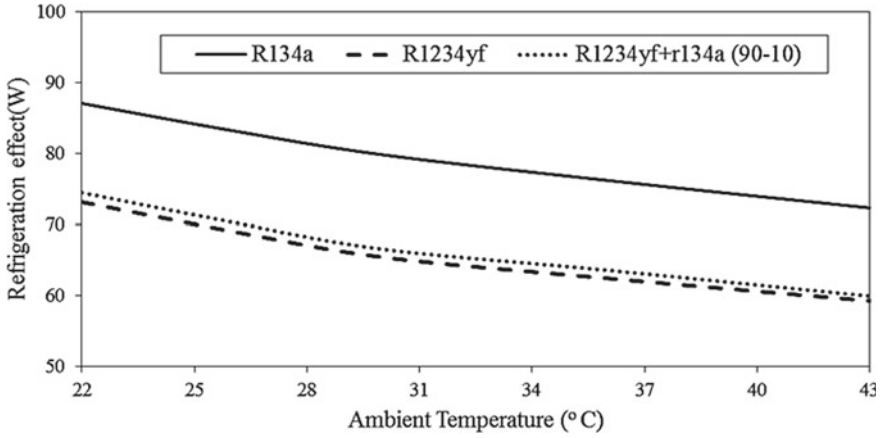


Fig. 5 Variation of refrigeration effect with various ambient temperature

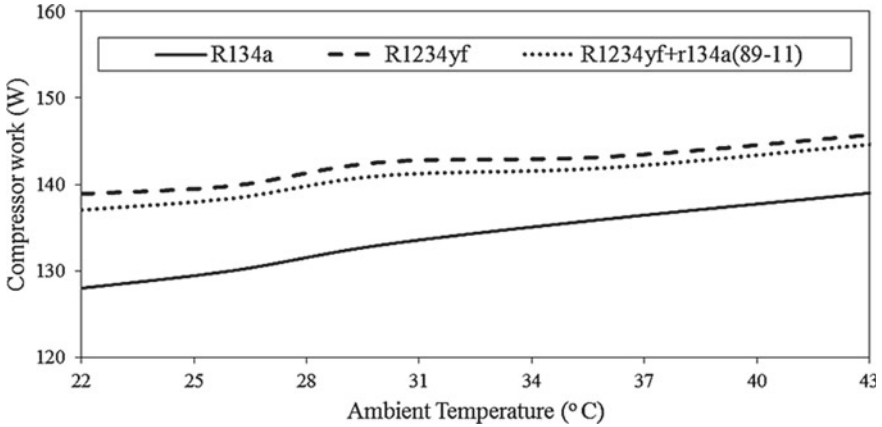


Fig. 6 Variation of compressor work with various ambient temperatures

blend is lower than the R134a and higher than R1234yf by about of 8% and 3%, respectively.

4 Conclusion

The performance analysis of domestic refrigeration systems with environmentally friendly refrigerants, such as R1234yf and R1234yf blends rather than conventional refrigerants, was studied in order to assess the potential for energy conservation, and the following conclusions are drawn from the theoretical study using MATLAB:

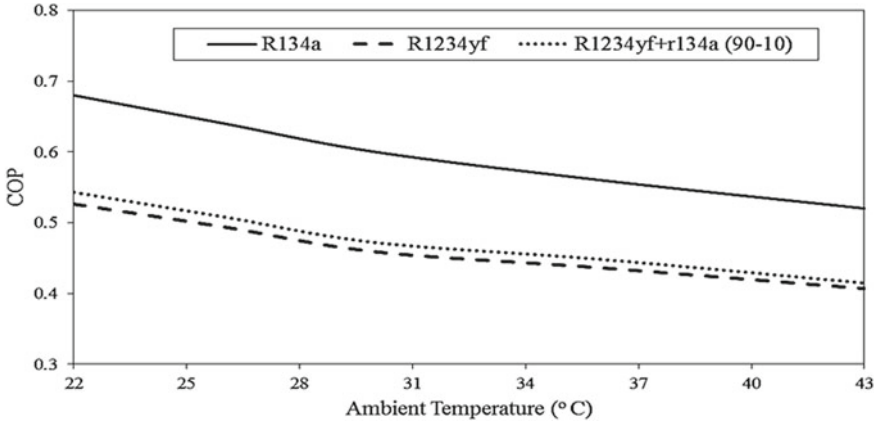


Fig. 7 Variation of COP with various ambient temperatures

1. The refrigeration effect R1234yf blend is lower than the R134a and higher than R1234yf by about of 8% and 2%, respectively.
2. The compressor work R1234yf blend is higher than the R134a and lower than R1234yf by about of 6% and 1%, respectively.
3. The COP of R1234yf blend is lower than the R134a and higher than R1234yf by about of 8% and 3%, respectively.
4. The performance of R1234yf blend is slightly lower than the R134a. Based on the environment, it is a suitable alternate for R134a.
5. The R1234yf/R134a has considerable environmental advantages and requires limited technical developments, and the gas is mild flammable. As a result, additional protections in handling, storage, implementation and servicing are needed by the manufacturing industry.

References

1. Mohanraj M, Jayaraj S, Muraleedharan C (2008) Comparative assessment of environment-friendly alternatives to R134a in domestic refrigerators. *Energy Efficiency* 1(3):189–198
2. He MG, Li TC, Liu ZG, Zhang Y (2005) Testing of the mixing refrigerants HFC152a/HFC125 in domestic refrigerator. *Appl Therm Eng* 25(8–9):1169–1181
3. Colbourne D, Suen KO (2004) Appraising the flammability hazards of hydrocarbon refrigerants using quantitative risk assessment model Part I: modelling approach. *Int J Refrig* 27(7):774–783
4. Minor BH, Montoya C, Kasa FS (2010) HFO-1234yf performance in a beverage cooler. In: International refrigeration and air conditioning conference at Purdue, West Lafayette, USA, paper no 2422
5. Nielsen OJ, Javadi MS, Andersen MS, Hurley MD, Wallington TJ, Singh R (2007) Atmospheric chemistry of CF₃CFCH₂: Kinetics and mechanisms of gas-phase reactions with Cl atoms, OH radicals, and O₃. *Chem Phys Lett* 439(1–3):18–22

6. Henne S, Shallcross DE, Reimann S, Xiao P, Brunner D, O'Doherty S, Buchmann B (2012) Future emissions and atmospheric fate of HFC-1234yf from mobile air conditioners in Europe. *Environ Sci Technol* 46(3):1650–1658
7. Koban M (2009) HFO-1234yf low GWP refrigerant LCCP analysis. SAE technical paper (no. 2009-01-0179)
8. Leck TJ (2010) New high performance, low GWP refrigerants for stationary AC and refrigeration. In: International refrigeration and air conditioning conference at Purdue, West Lafayette, USA, paper no 1032
9. Leighton D, Hwang Y, Radermacher R (2012) Modeling of household refrigerator performance with low global warming potential alternative refrigerants. *ASHRAE Trans* 118(1)
10. Kontomaris K, Leck TJ, Hughes J (2010) A non-flammable, reduced GWP, HFC-134a replacement in centrifugal chillers: DR-11 In: International refrigeration and air conditioning conference at Purdue, West Lafayette, USA, paper no 2142
11. Lee Y, Kang DG, Jung D (2013) Performance of virtually non-flammable azeotropic HFO1234yf/HFC134a mixture for HFC134a applications. *Int J Refrig* 36(4):1203–1207
12. Lemmon EW, Huber ML, McLinden MO (2002) NIST reference fluid thermodynamic and transport properties—REFPROP. NIST standard reference database, 23, v7
13. Cooper MG (1984) Heat flow rates in saturated nucleate pool boiling—a wide-ranging examination using reduced properties. *Adv Heat Transf* 16:157–239
14. Sami SM, Tribes C (1998) Numerical prediction of capillary tube behaviour with pure and binary alternative refrigerants. *Appl Therm Eng* 18(6):491–502
15. Li RY, Lin S, Chen ZY, Chen ZH (1990) Metastable flow of R12 through capillary tubes. *Int J Refrig* 13(3):181–186
16. Jia X, Tso CP, Chia PK, Jolly P (1995) A distributed model for prediction of the transient response of an evaporator. *Int J Refrig* 18(5):336–342
17. Jung D, Radermacher R (1993) Prediction of evaporation heat transfer coefficient and pressure drop of refrigerant mixtures in horizontal tubes. *Int J Refrig* 16(3):201–209
18. Raveendran PS, Sekhar SJ (2017) Performance studies on a domestic refrigerators retrofitted with building-integrated water-cooled condenser. *Energy Build* 134:1–10

Effect of Na₂O Content on Ground Granulated Blast Furnace Slag Incorporated Fly Ash-Based Geopolymer Pastes



Rohit Kumar and Mayengbam Sunil Singh

1 Introduction

The growing appeal of infrastructural improvement within growing international locations contributes to more concrete consumption. A hefty quantity of standard Portland Cement (OPC) is used as the main binder cloth to meet the insistence for the manufacture of concrete. But the processing of OPC calls for a large quantity of herbal sources, as well as a large system of energy, and additionally releases more quantity of carbon dioxide within the surroundings.

As a result, environmental degradation and the protection of natural resources have become critical issues that need to be sorted out in order to promote sustainability within the construction industry. Therefore, the use of additional building materials in concrete has an excellent momentum to protect the environment. GGBS is used as an auxiliary for cement, and the replacement share may be up to 85 percent depending upon the applications. Usually, 50% is employed in most applications. Geopolymers mainly comprise of aluminosilicate source materials like FA, blast furnace slag, etc., hardened by activating solution. Mixture of X-hydroxide and X-silicate (where X-sodium, potassium, barium, etc.) is treated as activating solution. Several researches have been conducted on various source materials and activating solution. The mechanism for geopolymers may be a chemical action that involves a chemical change of alumina-silicate materials within the presence of alkaline medium, which ends to the formation of three-dimensional compound chain [1–5]. The results reveal that geopolymers are resistant to acids, sulfate, and elevated temperatures [6, 7]. Nath and Sarkar investigated the effect of incorporation of different percentage of GGBS (0%, 10%, and 20%) on workability and mechanical potency of FA-based geopolymer

R. Kumar (✉)

Madan Mohan Malaviya University of Technology, Gorakhpur, India

M. S. Singh

National Institute of Technology, Manipur, India

concrete. They concluded that strength is increased significantly but the workability was decreased with higher percentage of GGBS [8]. He et al. compared the strength parameter of metakaolin and red mud-based geopolymers. The results indicate the superiority of metakaolin over red mud [9]. Nath and Kumar studied about FA, GGBS, and granulated corex slag geopolymer of 6M sodium hydroxide solution. They quoted that performance wise, granulated corex slag has an edge over granulated furnace slag [10]. Salih et al. reported that higher degree of geopolymerization takes place when blast furnace slag with higher percentage of calcium and aluminum is added to geopolymer [11]. Mehta and Siddique presented their experimental results on performance of partially replaced FA by ordinary Portland cement (0%, 10%, 20%, and 30%) as source material in geopolymer concrete. The results denote increase in compressive strength and decrease in porosity, sorptivity, and chloride permeability [12]. Aiken et al. compared the performance of Portland cement and geopolymer system to silage effluent attack and concluded that geopolymer has better resistance [13]. Tamburini et al. provide thorough data of chemical and physical characterization of geopolymer which shows the stable nature of geopolymers toward leaching, freeze-thaw effect, and elevated temperature treatments [14]. Rashad et al. investigated the performance of GGBS activated by two concentrations (1% and 3% by weight) by sodium sulfate. The early strength examination was done on 3 days and 7 days along with 28 days. The specimens were also exposed to high temperatures ranging from 200 to 800 °C. The results indicate that sodium sulfate is an efficient activator and shows better chemical stability at elevated temperatures [15]. Soustos et al. studied the curing temperature, alkaline activators dosage, properties (physical and chemical) of FA, and amount of GGBS incorporation on FA reactivity as a source material in geopolymer concrete. The results indicate that curing temperature, alkaline activators dosage, amount of GGBS incorporated play a very important role in strength development of geopolymer [16]. Mehta and Siddique studied about various industrial waste (bottom ash, FA, metakaolin, blast furnace slag, etc.) and concise their review that geopolymers can be synthesized by these industrial waste [17]. Kumar and Singh studied the behavior of potassium feldspar mixed FA-based geopolymer paste at preminent temperature [18].

From the study of literature, it is concluded that synthesis of geopolymers is done by source materials which mainly comprises of aluminosilicate source materials and alkaline activating solution. The strength of geopolymer is imparted due to the concentration of alkali solution which depends on molarity of sodium hydroxide. As the molarity increase, the compressive strength and durability increase. Higher molarity corresponds to higher Na₂O content in the solution, but the amount of Na₂O present in sodium silicate is not taken in the consideration. As sodium hydroxide contains Na₂O in some percentage, sodium silicate also contains Na₂O in some percentage. Therefore, the current research and experiments were carried out to estimate the consequence of Na₂O content on the incorporation of five different percentages (10%, 20%, 30%, 40%, and 50% by weight) of blast furnace slag in alkali-activated FA-based geopolymer paste. From the best of researcher's knowledge from previous literature reviews, it can be concluded that there is lack of work on

the effect of Na₂O content. Therefore, the enactment of specimens was assessed in terms of compressive strength after incorporation of GGBS in FA geopolymers paste.

2 Experimental Procedure

2.1 Source Materials

In the current experimental program, fly ash (FA) was supplied by Marshall Corporation, Kolkata, India, and GGBS was purchased from Owndust India. The chemical composition of ash and blast furnace slag is shown in Table 1. Figure 1 shows the mineralogical composition of GGBS and FA, respectively. More than 75% of particles were finer than 45 microns of FA.

Table 1 Chemical composition of fly ash and ground granulated blast furnace slag

Chemical composition	SiO ₂	Al ₂ O ₃	Fe ₂ O ₃	CaO	Na ₂ O	K ₂ O	TiO ₂	MgO	P ₂ O ₅	MnO	SiO ₂
Fly ash	41.72	27.34	5.111	1.145	0.07	1.418	1.989	0.567	0.722	0.046	41.72
Blast furnace slag	63.22	15.15	0.134	0.197	3.0	10.86	0.017	0.299	0.016	0.003	63.22

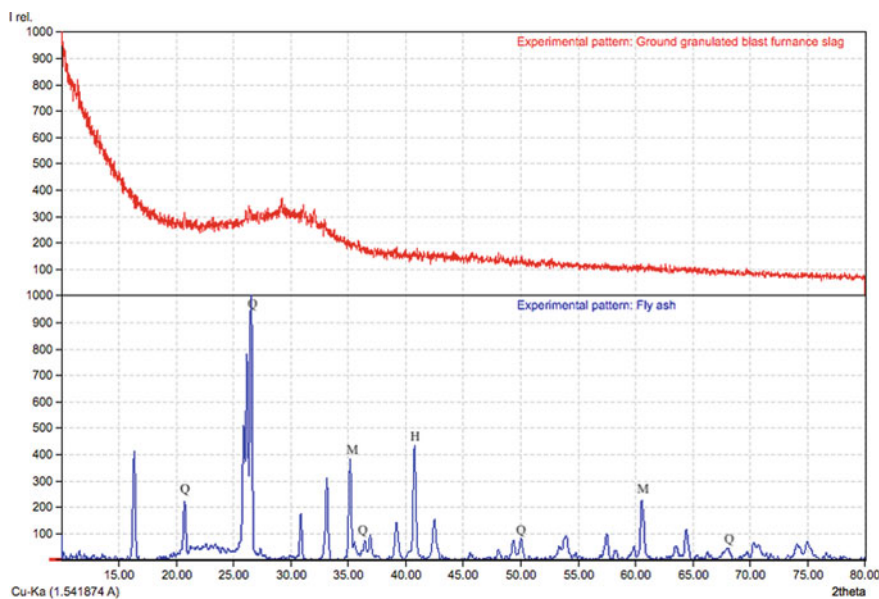


Fig. 1 Mineralogical composition of ground granulated blast furnace slag and fly ash (XRD)

2.2 Alkaline Solution

Sodium silicate solution ($\text{SiO}_2 = 26.5\%$, $\text{Na}_2\text{O} = 8\%$, and 65.5% water) with bulk density of 1410 kg/m^3 and silicate modulus of 3.30 (approx.) and sodium hydroxide pellets (98% purity) of laboratory grade were acquired from Sharma Bros, Imphal, India. The percentage of $\text{Na}_2\text{O} = 7\%$, 8% , and 9% along with $\text{SiO}_2 = 8\%$ by weight of source material was fixed in activating solution, prepared one day before the fabrication of geopolymer paste. Water from a pond nearby the NIT campus was used in the study [18]. Figure 1 presents X-ray diffractogram (XRD) for mineralogical composition of fly ash and GGBS. In the FA, the existence of quartz (Q), mullite (M), and hematite (H) is detected while in GGBS shows its amorphous nature.

2.3 Preparation of Specimens

The calculated measure of sodium hydroxide pellets was mixed directly with sodium silicate solution to produce a homogeneous geopolymer paste. So, we got three alkaline solutions with 7, 8 and 8% Na_2O content, keeping 8% SiO_2 constant. The water-to-source material ratio was 0.33. The mixture of sodium hydroxide and sodium silicate is an exothermic reaction; therefore, the alkaline solution obtained was kept overnight at room temperature to produce geopolymeric paste. Aluminosilicate source material and alkaline activator solution have been mixed in the Hobart mixer for 5 min. The paste was of gray color, sticky in nature and of normal workability. The mixture was poured into cube molds of $50 \times 50 \times 50 \text{ mm}$ and vibrated on a vibration table for 10 minutes to expel the air. The specimens were demolded after 24 hours of casting and kept at room temperature till the predetermined time for testing.

2.4 Compressive Strength

The compressive strength testing was done on UTM at 7 days, 28 days, and 56 days. Specimens were casted in cube molds of dimensions $50 \times 50 \times 50 \text{ mm}$. Cubes were demolded after 24 hours of casting and kept at room temperature for testing till 7 days, 28 days, and 56 days. Compressive strength test was performed as per guidelines of IS-4031 (part6)-1988.

3 Results and Discussion

3.1 Residual Compressive Strength

Figures 2, 3, and 4 represent the effect of Na₂O content on the initial compressive strength of FA geopolymer paste specimens with 10%, 20%, 30%, 40%, and 50% GGBS replacement at time intervals of 7 days, 28 days, and 56 days. Samples GPC6, GPC7, and GPC8 represent geopolymer paste having 6, 7, and 8% Na₂O, respectively, with SiO₂ percentage fixed at 7%. All the geopolymer specimens were cured at ambient temperature. The experimental data shows that majority of strength is achieved in early days after casting the geopolymer paste specimens. The data of experiments reveal that both Na₂O content and incorporation of GGBS affect the compressive strength of geopolymer paste. The geopolymer specimen's strength increases in due course of time which exhibits that continuity of geopolymerization reaction. However, previous studies show that without heat curing fly FA of heat curing GGBS is added and it is observed that the setting time is significantly reduced along with the increase in compressive strength. Mainly two factors are responsible for crediting compressive strength to FA geopolymer paste, which is (a) Na₂O content and (b) GGBS.

Na₂O content facilitates the formation of sodium aluminate silicate hydrate gel (N-A-S-H) which leads to polycondensation to form a 3D network of aluminosilicate

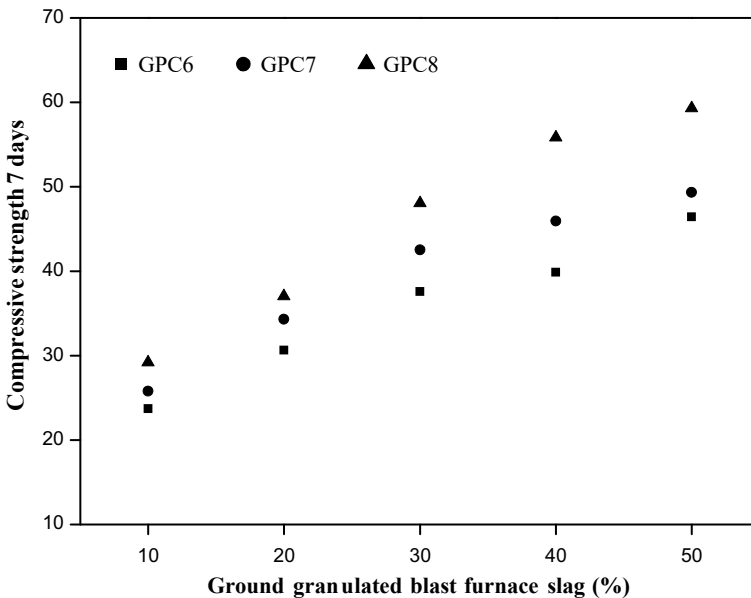


Fig. 2 Compressive strength (7 days) with different % of ground granulated blast furnace slag and Na₂O content

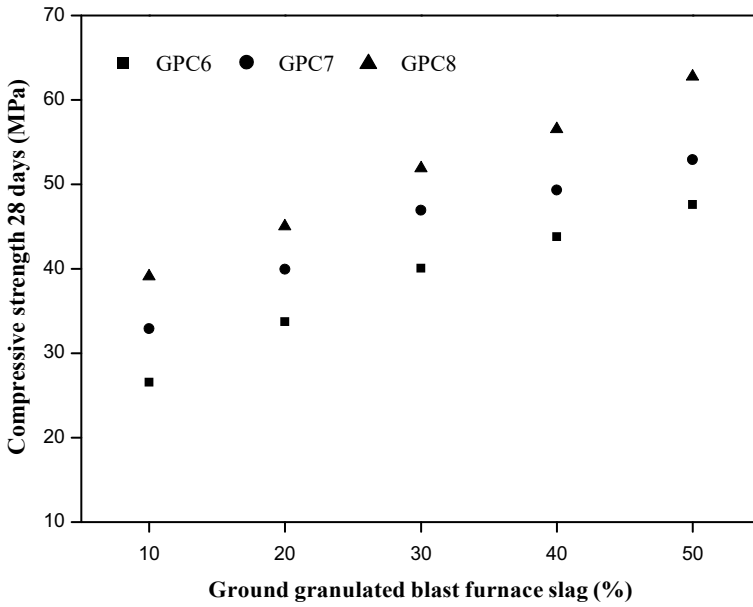


Fig. 3 Compressive strength (28 days) with different % of ground granulated blast furnace slag and Na₂O content

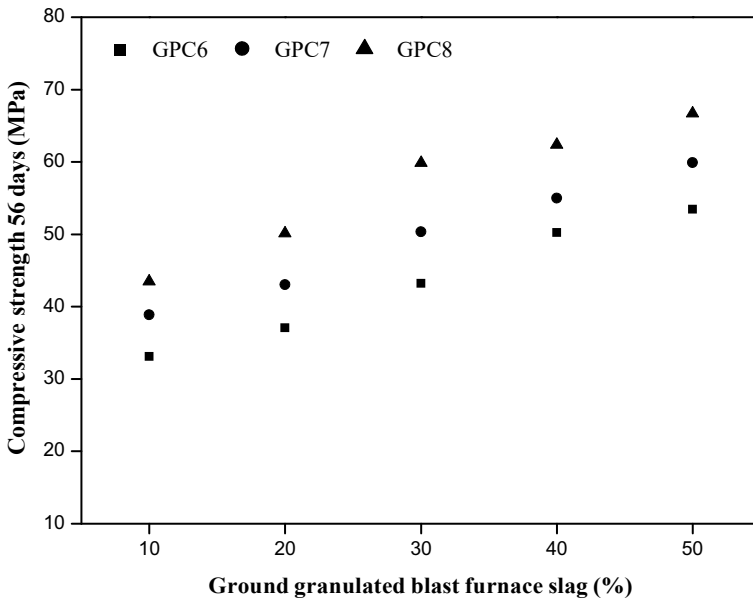


Fig. 4 Compressive strength (56 days) with different % of ground granulated blast furnace slag and Na₂O content

structure. Higher the Na₂O content, higher dissolution of Si and Al ions takes place. It forms a dense network and reduces pore volume [19]. A stable network imparts greater strength to geopolymer.

Addition of GGBS plays two roles in the mechanism. Primarily, it reduces the need for heat curing required for geopolymerization reaction and helps in its casting at ambient temperature. Secondly, it imparts the strength. From the experiments, replacement of FA with ground GGBS increases the compressive strength of geopolymer. The same phenomenon was also observed in previous literature. The reason for proving the strength to geopolymer can be due to two reasons: firstly, due to the higher content of calcium which results in formation of C-S-H gel; secondly, the requirement of water to C-S-H gel which causes the deficiency of water, resulting in the rise in alkalinity of the medium. Higher alkalinity results in higher dissolution of Si and Al ions from source materials and forms a dense network which imparts the strength [10, 19, 21, 22].

3.2 XRD

Figure 5 shows the diffraction spectra of geopolymer specimens having 40% GGBS and 60% FA. Diffraction pattern in a, b, c shows the specimens of 6%, 7%, and 8% of Na₂O, respectively, with SiO₂ 7% at 56 days. Comparing Figs. 1 and 5, we observe

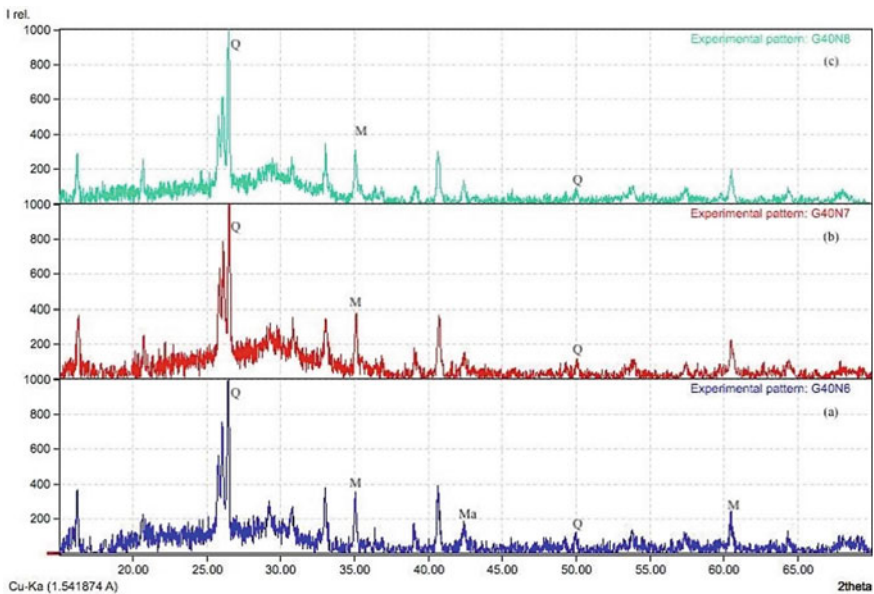


Fig. 5 A diffraction pattern in a, b, c shows the specimens of 6%, 7%, and 8% of Na₂O, respectively, with SiO₂ 7% at 56 days with 40% GGBS and 60% FA

a change hump shape which refers to the formation of new amorphous materials when geopolymerization takes place. Within Fig 2a, b, c, it is seen that due to alkali activation of source materials, the intensity of SiO₂ (quartz) varies. As the percentage of Na₂O increases, more dissolution of ions takes place which leads to strength in specimens. Due to this, SiO₂ peaks show a lower level of intensity with increase in Na₂O content. The same results were detected in previous studies [23, 24]. This may demonstrate the arrangement of a higher measure of geopolymerized gel with a higher level of crystallinity as the dose of GGBS in the fastener expanded. It might well explain the expanding pattern in compressive quality outcomes saw at 10% to half GGBS substitution [25].

4 Conclusion

This paper shows the effect of Na₂O content on compressive strength of specimens casted with incorporation of different percentages of GGBS in FA geopolymer paste.

- It reveals that both Na₂O and GGBS promote the performance of geopolymers. Increase in Na₂O content favors the geopolymerization, and GGBS reduces the need of heat curing required for geopolymerization reaction.

References

1. Author F, Hardjito D, Wallah SE, Sumajouw DMJ, Rangan BV (2004) Brief review of development of geopolymer concrete. Invited Paper, George Hoff symposium, American Concrete Institute
2. Van Deventer JSJ, Provis JL, Duxson P (2012) Technical and commercial progress in the adoption of geopolymer cement. *Miner Eng* 29:89–104
3. Duxson JL, Fernández-Jiménez P, Provis A et al (2007) Geopolymer technology: the current state of the art. *J Mater Sci* 42:2917–2933. <https://doi.org/10.1007/s10853-006-0637-z>
4. Hardjito D, Wallah SE, Sumajouw DMJ, Rangan BV (2004) On the development of fly ash-based geopolymer concrete. *ACI Mater J* 101:467–472. <https://doi.org/10.14359/13485>
5. Bakharev T (2005) Durability of geopolymer materials in sodium and magnesium sulfate solutions. *Cem Concr Res* 35:1233–1246. <https://doi.org/10.1016/j.cemconres.2004.09.002>
6. Tempest B, Sanusi O, Gergely J, Ogunro V, Weggel D (2009) In world of coal ash (WOCA) conference, pp 1–17. <http://www.flyash.info/2009/045-tempest2009.pdf>
7. Assi LN, (Eddie) Deaver E, ElBatanouny MK, Ziehd P (2016) Investigation of early compressive strength of fly ash-based geopolymer concrete. *Constr Build Mater* 112:807–815. <https://doi.org/10.1016/j.conbuildmat.2016.03.008>
8. Nath P, Sarker PK (2014) Effect of GGBFS on setting, workability and early strength properties of fly ash geopolymer concrete cured in ambient condition. *Constr Build Mater* 66:163–171. <https://doi.org/10.1016/j.conbuildmat.2014.05.080>
9. He J, Zhang J, Yu Y, Zhang G (2012) The strength and microstructure of two geopolymers derived from metakaolin and red mud-fly ash admixture: A comparative study. *Constr Build Mater* 30:80–91. <https://doi.org/10.1016/j.conbuildmat.2011.12.011>

10. Nath SK, Kumar S (2013) Influence of iron making slags on strength and microstructure of fly ash geopolymer. *Constr Build Mater* 38:924–930. <https://doi.org/10.1016/j.conbuildmat.2012.09.070>
11. Salih MA, Farzadnia N, Abang Ali AA, Demirboga R (2015) Development of high strength alkali activated binder using palm oil fuel ash and GGBS at ambient temperature. *Constr Build Mater* 93:289–300
12. Mehta A, Siddique R (2017) Properties of low-calcium fly ash based geopolymer concrete incorporating OPC as partial replacement of fly ash. *Constr Build Mater* 150:792–807. <https://doi.org/10.1016/j.conbuildmat.2017.06.067>
13. Aiken TA, Sha W, Kwasny J, Soutsos MN (2017) Resistance of geopolymer and Portland cement based systems to silage effluent attack. *Cem Concr Res* 92:56–65. <https://doi.org/10.1016/j.cemconres.2016.11.015>
14. Tamburini S et al (2017) Geopolymer matrix for fibre reinforced composites aimed at strengthening masonry structures. *Constr Build Mater* 141:542–552. <https://doi.org/10.1016/j.conbuildmat.2017.03.017>
15. Rashad AM, Bai Y, Basheer PAM, Collier NC, Milestone NB (2012) Chemical and mechanical stability of sodium sulfate activated slag after exposure to elevated temperature. *Cem Concr Res* 42:333–343. <https://doi.org/10.1016/j.cemconres.2011.10.007>
16. Soutsos M, Boyle AP, Vinai R, Hadjierakleous A, Barnett SJ (2016) Factors influencing the compressive strength of fly ash based geopolymers. *Constr Build Mater* 110:355–368. <https://doi.org/10.1016/j.conbuildmat.2015.11.045>
17. Mehta A, Siddique R (2016) An overview of geopolymers derived from industrial byproducts. *Constr Build Mater* 127:183–198. <https://doi.org/10.1016/j.conbuildmat.2016.09.136>
18. Kumar R, Mayengbam SS (2021) Enhancement of the thermal durability of fly ash-based geopolymer paste by incorporating potassium feldspar. *J Inst Eng India Ser A*. <https://doi.org/10.1007/s40030-020-00498-6>
19. Li Z, Liu S (2007) Influence of Slag as Additive on Compressive Strength of Fly Ash-Based Geopolymer. *J Mater Civ Eng* 19:470–474
20. Puligilla S, Mondal P (2013) Role of slag in microstructural development and hardening of fly ash-slag geopolymer. *Cem Concr Res* 43:70–80. <https://doi.org/10.1016/j.cemconres.2012.10.004>
21. Kumar S, Kumar R, Mehrotra SP (2010) Influence of granulated blast furnace slag on the reaction, structure and properties of fly ash based geopolymer. *J Mater Sci* 45:607–615. <https://doi.org/10.1007/s10853-009-3934-5>
22. Khater HM (2012) Effect of Calcium on Geopolymerization of Aluminosilicate wastes. *J Mater Civil Eng* 24:92–101. [https://doi.org/10.1061/\(ASCE\)MT.1943-5533.0000352](https://doi.org/10.1061/(ASCE)MT.1943-5533.0000352)
23. Zhang L, Ahmari S, Zhang J (2011) Synthesis and characterization of fly ash modified mine tailings-based geopolymers. *Constr Build Mater* 25:3773–3781. <https://doi.org/10.1016/j.conbuildmat.2011.04.005>
24. Boonserm K, Sata V, Pimraksa K, Chindaprasit P (2012) Improved geopolymerization of bottom ash by incorporating fly ash and using waste gypsum as additive. *Cem Concr Compos* 34:819–824. <https://doi.org/10.1016/j.cemconcomp.2012.04.001>
25. Salih MA, Farzadnia N, Abang Ali AA, Demirboga R (2015) Development of high strength alkali activated binder using palm oil fuel ash and GGBS at ambient temperature. *Constr Build Mater* 93:289–300. <https://doi.org/10.1016/j.conbuildmat.2015.05.119>

Performance and Emissions Characteristics of Diesel Engine Run on Citrullus Colocynthis Biodiesel with Zinc Oxide Additive



K. Logesh, M. Karthick, S. Baskar, and Abhishek Sharma

1 Introduction

In the past, wood was the primary source of energy due to the frequent deforestation; however, wood as fuel was deeply concerned about its durability. An alternative to timber, namely coal, was then discovered. Later oil goods, such as petrol and diesel, were established [1]. It appears that the energy dilemma was completely solved in the initial process. However, global energy demand is intensified by population growth and shifts in lifestyle [2]. It became evident later that the opportunities for fossil fuels were also minimal. One of the biggest energy users in the automotive industry, because 600 million vehicles are used globally and are mainly used in diesel engines [3]. The second approach appears to be easier because a vast number of existing engines already exist. The cost of shipping and pollution for biofuels are also lowered.

Biodiesel is one of the most sustainable and environmentally friendly renewable fuels for CI engines. Biodiesel is capable of replacing diesel, and much of its properties are closer to diesel [4–6]. The decline of fossil fuel prices raises day-by-day demand for renewable fuel exploration to satisfy the world's energy demands. In contemporary times, biodiesel provides the largest energy alternative. Fossil fuel can be substituted by biodiesel. The Citrullus Colocynthis oil (CCO) is converted into biodiesel by transesterification process which in the presence of catalyst, which

K. Logesh · M. Karthick

Department of Mechanical Engineering, Vel Tech Rangarajan Dr. Sagunthala R and D Institute of Science and Technology, Avadi, Chennai, Tamil Nadu, India

S. Baskar

Department of Automobile Engineering, VELS Institute of Science, Technology and Advanced Studies (VISTAS), Chennai, Tamil Nadu, India

A. Sharma (✉)

Department of Mechanical Engineering, Manipal University Jaipur, Jaipur, India

decreases on the dependency on fossil fuel improves in the contributions towards the use of renewable fuels. Many research reports are available on the use of CCO as substitute fuel with low moisture content and durability [5, 7–9]. Many recommended a maximum yield of pancreatic lipase-based vegetable oil. The mixture of 20% biodiesel in diesel was more effective. They researched brake thermal performance and the addition of diesel-like additives for non-edible waste and bio-seeding crude.

Many studies were carried out on the use of biodiesel derived through non-edible seed to determine the effects on performance and emission properties of oxygen-additive nanoparticles, followed by a comparison of experimental results with base pure diesel [10–12]. The efficiency and emissions properties of waste oil with nano-emulsions were investigated. In another study, they evaluated nano-added bio-seed oil that results in lower oil viscosity and density. For a beneficial result, the emissions of an engine may be minimized with bio-seed such as seed oil. The efficiency and emission characteristics of various proportions of cerium oxide cotton oil and diesel with nanoparticles have been investigated by Sujesh et al. [13]. The present paper incorporates diesel for the efficiency and emission characteristics study of the various loads of a single-cylinder diesel engine with a 10% increase in the *Citrullus Colocynthis* oil at three different proportions.

2 Experimental Details

Conversion of oil into biodiesel is done through transesterification process. In our current research, Na–OH, the basic catalyst, is obtained in a pallet shape on the market and is polished very finely and combined with and well stirred to create a homogenous methanoxide mixture. Methanolysis is called this method of preparation of methanoxide. The next step is the simple catalytic raw oil transesterification. To eliminate the impurities, present in the oil the raw oil collected from the market is first filtered and then preheated to about 60 °C for about 10–15 min to remove the humidity present in the oil.

The preheated oil and the homogeneous methanoxide are then blended to a limit of 150 ml of methanol per 600 ml of oil. Then using the hot plate magnetic mixer, the mixture is mixed at 1200 rpm and the mixture is held at 65 °C for an hour. Through this one-hour method of transesterification, the triglycerides in the raw oil have been converted to glycerine. Then the glycerine produced in the transesterification phase is transferred to the separating beaker and can be positioned on top of the glycerine during the six-hour term and then extracted by the transesterified oil (Table 1).

Test fuels were produced by mixing with diesel at various percentages by volume the CCO. The preferred mixing ratio was B10, B20, B30, i.e. 10% CCO with 90% diesel, 20% CCO with 80% diesel and 30% CCO with 70% diesel to provide evidence for a broad spectrum of biodiesel. The composition of the exhaust gas has been determined using the gas analyzer. In the exhaust gases, it tests NO_x, CO₂, HC, CO. By checking the engine powered from the formulated test fuels for the output of each

Table 1 Properties of Citrullus Colocynthis oil blends

Property	Pure diesel (PD)	CCO	CCOB10	CCOB20	CCOB30
Calorific value (kJ/kg)	44,800	41,250	44,780	44,730	44,680
Density (kg/m ³)	850	885	862	870	874
Cetane number	53	57	41	45	46.8
Kinematic viscosity (mm ² /s)	2.12	4.45	1.56	1.87	2.21

fuel at the same engine load conditions, the short-term performance and the emission features were assessed.

3 Results and Discussion

3.1 Performance Parameters

The improvement in thermal brake performance in load-related test diesel. Thermal brake output of all combustibles improved as load increases as shown in Fig. 1. This could be clarified because the load raises the suction pressure, which could have contributed to the engine’s efficient combustion. At 75% load, diesel thermal brake performance, CCOB10, CCOB20 and CCOB30, respectively, was 33, 31, 30 and 29%. If the mixing rate rises to 75% of load, the brake thermal efficiency decreases. However, the thermal brake performance of the combination of CCOB20 and CCOB30 was improved by more than 20% in a load of fuel, due to the higher oxygen content in biodiesel mixtures than diesel, resulting in total combustion [14]. The CCOB20 and CCOB30 mix with higher latent vaporization heat, at 75% load,

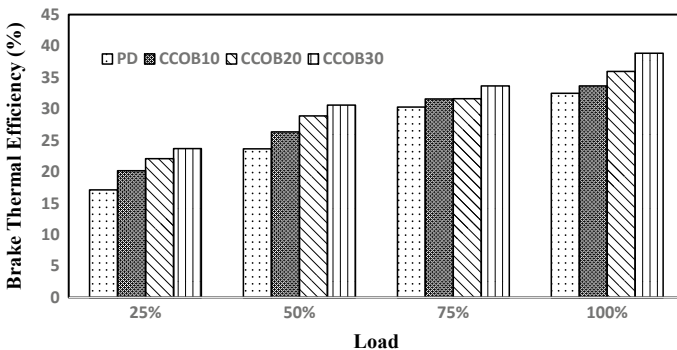


Fig. 1 Brake thermal efficiency of CCO blends

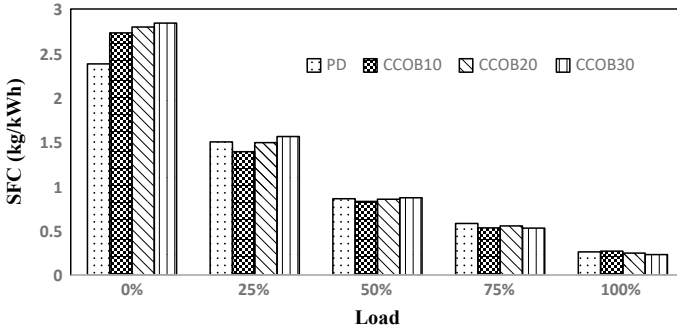


Fig. 2 Brake-specific fuel consumption of CCO blends

contributes to incomplete combustion, thus reducing the thermal performance of the brakes.

The brake-specific fuel consumption (BSFC) diesel and CCO mixtures of diesel at varying loads as shown in Fig. 2. For CCOB10, because of the lower heat quality of the blend, the BSFC is more than gasoline. At 25% load in CCOB20 and CCOB30, the oxygen content is lower than diesel as the combustion results in stronger combustion. But the BSFC of all blends was 75% higher than diesel as the burden rose.

The lower the heat value of the blend, and nonsensical combustion, lead to an increase in the amount of fuel that is injecting to retain the same engine capacity, and the lower heat value of the fuel blending is absorbed [15]. These variables would also contribute to a rise in BSFC loads.

3.2 Emission Parameters

Figure 3 shows the emissions of hydrocarbons from types of diesel and Citrullus Colocynthis oil combinations of gasoline. The increased pollution is noted for the

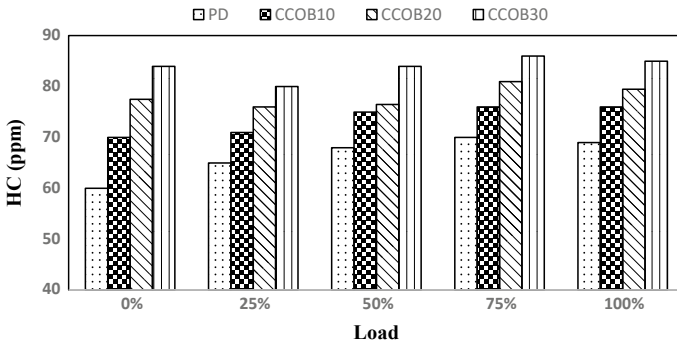


Fig. 3 Hydrocarbon emission of CCO blends

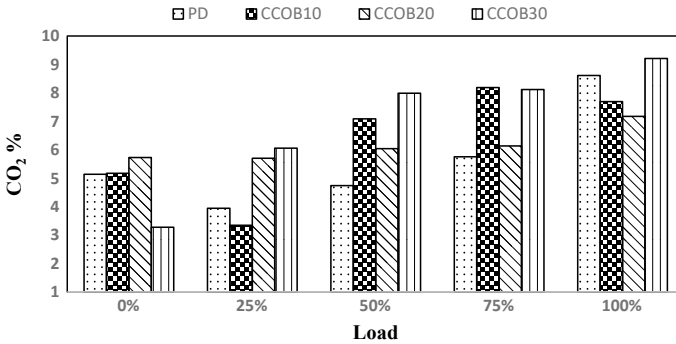


Fig. 4 Carbon dioxide emission of CCO blends

mixtures of CCOB10, CCOB20 and CCOB30 since the unburned mixture of fuel emitted into the exhaust system is not consumed. The blend of CCOB20 emits more hydrocarbon than other blends, as the unused oxygen reveals that oxygen is more emitted without combustion and additional hydrocarbon emissions. Due to the lower calorific value and delays in fuel ignition, a lot of fuel molecules are not homogeneous, and combustion happens after the energy stroke resulting in a high hydrocarbon release [16, 17]. It is noted from the literature that with the higher gas temperature and cetane number, CCO mixtures, more than 50%, show lower emissions of hydrocarbons than diesel [18].

Shift in the emission of carbon dioxide from the CI engine as shown in Fig. 4. The CCO blends' CO₂ emissions from petrol are nearly equal to minor percentage differences, with mixtures displaying an increase of up to 0.3% of CO₂ emissions relative to diesel [19]. The increase in charge raises the CO₂ emission ratio because of the consumption of additional petrol. The combustion of the fuel is easier, because of the oxygen molecules in the palm oil methyl ester blend. These concerns total fuel combustion and oxidation with the oxygen of carbon molecules by lowering CO levels of CCO blends to the atmosphere as diesel.

Figure 5 indicates the change in CO emissions for test fuels at different loads. Carbon monoxide is commonly formed if the gasoline is not oxidized by enough oxygen. Diesel is commonly run-in excess air since the diesel engine's carbon monoxide emissions are smaller than those of the petrol engine [20, 21]. At a load of 25% and a load of 75%, the CO emission of Citrullus Colocynthis oil decreased considerably relative to diesel. CCOB10, CCOB20 and CCOB30 have lower CO emissions than the represented diesel for 25%. With rising load, CO emission decreases when excess oxygen molecules oxidize CO into carbon dioxide as a result of full combustion [22].

When the engine load has stepped up to 100%, the load for mixed fuels has been lowered by marginal changes in NO_x emissions in Fig. 6. In the case of mixtures, the CCOB20 has a closer NO_x degree than the basic diesel emission. The lower fuel heat value leads to lower temperatures in the combustion chamber and lower emissions

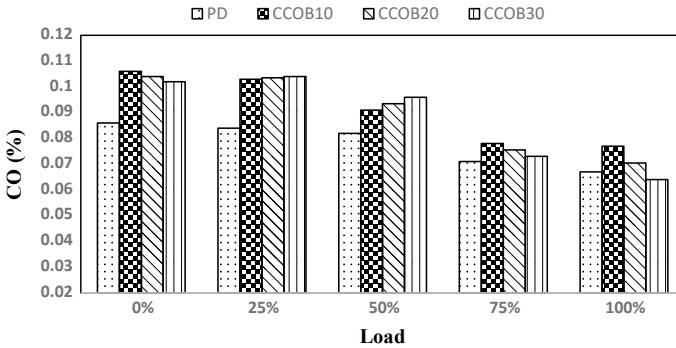


Fig. 5 Carbon monoxide emission of CCO blends

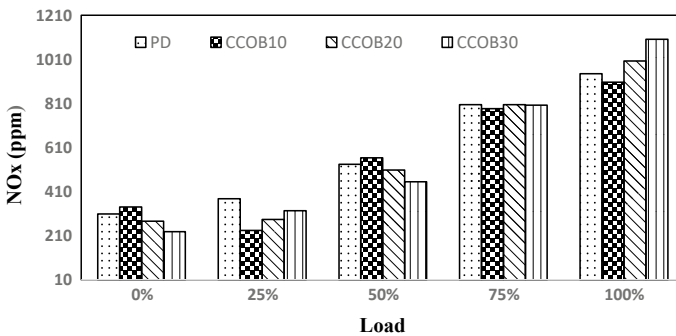


Fig. 6 Oxide of nitrogen emission of CCO blends

of NO_x in blends like CCOB20 and CCOB30. The effect of biodiesel on emissions is more obvious. The various emissions are significantly reduced due to the addition of biodiesel, but NO_x increases. The increase in the residence time and the temperature of the mixture in the cylinder may lead to raise in NO_x emission [23]. In future, the bio-diesel is playing a major role in terms of improving the performance.

4 Conclusion

The energy demand is continually increasing because of the vast number of businesses and automobiles induced by the detonation of residents. Fossil fuels, including oil, gas, coal, hydrocarbons and nuclear energy, are the available sources of energy. Greenhouse emissions are the main risks of using oil-based oils. A variety of greenhouse gases are released from the diesel ignition. This is one of the key sources of gas pollution derived from fossil fuels, including NO_x , CO and particulate substances and volatile compounds. The experimental investigations on a compression ignition

engine were carried out to test the output of *Citrullus Colocynthis* seed oil-based biodiesel and blended with zinc oxide nanoparticle diesel blends. The efficiency of the engine parameters and emissions are evaluated, and the property of biodiesel blends is checked in the laboratory. In general, we have found that the *Citrullus Colocynthis* oil, which is combined with diesel fuel, offers top quality and a major CO₂ emission reduction, making it ideal for *Citrullus Colocynthis* oil mixes CCOB20 and CCOB30.

References

1. Andres RJ, Fielding DJ, Marland G, Boden TA, Kumar N, Kearney AT (1999) Carbon dioxide emissions from fossil-fuel use, 1751–1950. *Tellus B* 51:759–765
2. Sharma A, Murugan S (2013) Investigation on the behaviour of a DI diesel engine fueled with *Jatropha Methyl Ester* (JME) and Tyre Pyrolysis Oil (TPO) blends. *Fuel* 108:699–708. <https://doi.org/10.1016/j.fuel.2012.12.042>
3. Reşitoğlu İA, Altinişik K, Keskin A (2015) The pollutant emissions from diesel-engine vehicles and exhaust aftertreatment systems. *Clean Technol Environ Policy* 17:15–27
4. Rajak U, Verma TN (2018) *Spirulina* microalgae biodiesel—A novel renewable alternative energy source for compression ignition engine. *J Clean Prod* 201:343–357
5. Rajak U, Verma TN (2018) Effect of emission from ethylic biodiesel of edible and non-edible vegetable oil, animal fats, waste oil and alcohol in CI engine. *Energy Convers Manag* 166:704–718
6. Sharma A, Dhakal B (2013) Performance and emission studies of a diesel engine using biodiesel tyre pyrolysis oil blends. *SAE Tech Pap* 2. <https://doi.org/10.4271/2013-01-1150>
7. Sivalingam A, Kandhasamy A, Kumar AS, Venkatesan EP, Subramani L, Ramalingam K, Thadhani JPJ, Venu H (2019) *Citrullus colocynthis*-an experimental investigation with enzymatic lipase based methyl esterified biodiesel. *Heat Mass Transf* 55:3613–3631
8. Bello EI, Makanju A (2011) Performance evaluation of *Egusi* melon (*Citrullus colocynthis* L.) seeds oil biodiesel. *J Emerg Trends Eng Appl Sci* 2:741–745
9. Giwa S, Abdullah LC, Adam NM (2010) Investigating “*Egusi*” (*Citrullus colocynthis* L.) seed oil as potential biodiesel feedstock. *Energies* 3:607–618
10. Sharma A, Murugan S (2017) Effect of nozzle opening pressure on the behaviour of a diesel engine running with non-petroleum fuel. *Energy* 127:236–246. <https://doi.org/10.1016/j.energy.2017.03.114>
11. Sharma A, Murugan S (2017) Durability analysis of a single cylinder DI diesel engine operating with a non-petroleum fuel. *Fuel* 191:393–402. <https://doi.org/10.1016/j.fuel.2016.11.086>
12. Shrivastava P, Verma TN, Pugazhendhi A (2019) An experimental evaluation of engine performance and emission characteristics of CI engine operated with Roselle and *Karanja* biodiesel. *Fuel* 254:115652
13. Sujesh G, Ganesan S, Ramesh S (2020) Effect of CeO₂ nano powder as additive in WME-TPO blend to control toxic emissions from a light-duty diesel engine—An experimental study. *Fuel* 278:118177
14. Sharma A, Murugan S (2017) Effect of blending waste tyre derived fuel on oxidation stability of biodiesel and performance and emission studies of a diesel engine. *Appl Therm Eng* 118:365–374. <https://doi.org/10.1016/j.applthermaleng.2017.03.008>
15. Krishania N, Rajak U, Verma TN, Birru AK, Pugazhendhi A (2020) Effect of microalgae, tyre pyrolysis oil and *Jatropha* biodiesel enriched with diesel fuel on performance and emission characteristics of CI engine. *Fuel* 278:118252
16. Sharma A (2017) Investigations of a direct injection diesel engine run on non petroleum fuel blends

17. Sharma A, Murugan S (2015) Combustion, performance and emission characteristics of a diesel engine fuelled with non-petroleum fuel: a study on the role of fuel injection timing. *J Energy Inst* 88:364–375. <https://doi.org/10.1016/j.joei.2014.11.006>
18. Anbarasu A, Saravanan M, Loganathan M (2013) The effect of ethanol addition in a biodiesel operated DI diesel engine on combustion, performance, and emission characteristics. *Int J Green Energy* 10:90–102
19. Atadashi IM, Aroua MK, Aziz AA (2010) High quality biodiesel and its diesel engine application: a review. *Renew Sustain energy Rev* 14:1999–2008
20. Chong HS, Kwon S, Lim Y, Lee J (2020) Real-world fuel consumption, gaseous pollutants, and CO₂ emission of light-duty diesel vehicles. *Sustain Cities Soc* 53:101925
21. Sullivan JL, Baker RE, Boyer BA, Hammerle RH, Kenney TE, Muniz L, Wallington TJ (2004) CO₂ emission benefit of diesel (versus gasoline) powered vehicles
22. He B-Q, Shuai S-J, Wang J-X, He H (2003) The effect of ethanol blended diesel fuels on emissions from a diesel engine. *Atmos Environ* 37:4965–4971
23. Han Z, Uludogan A, Hampson GJ, Reitz RD (1996) Mechanism of soot and NO_x emission reduction using multiple-injection in a diesel engine. *SAE Transactions*, pp 837–852

Performance and Emission Characteristics of Single-Cylinder Diesel Engine Fueled with Biodiesel Derived from Cashew Nut Shell



M. Karthick, K. Logesh, S. Baskar, and Abhishek Sharma

1 Introduction

Diesel vehicles are the primary means of transport in today's world. Its key appeal is sturdy architecture, simple service, and easy maintenance. Due to the fossil fuel shortage, maybe we cannot use its facilities for a long time. Efforts to manufacture unconventional fuels for use in diesel engines are therefore being produced around the world. Likewise, how fuel demand decreased has emphasized automotive and pressured it to manufacture modern technical engines. This led to new combustion systems being developed. Many research investigations have been done toward resolving the above problems [1–3]. The diesel engine pollution characteristics were investigated with diesel and cassava shell oil blends in different loads at constant rpm. In all the mixtures, 20% CNS was higher than all the other mixtures. It has also been found that CNS mixtures can be used without alteration in the diesel engine [4].

The liquid biodiesel CNS is mixed with this diesel fuel which acts as a biodiesel mixture. CNB20, CNB40, and CNB60 are the blends used for testing. Output testing determined the effects of the combustible fuel on the engine capacity, brake heat quality, and gas exhaustion. Emission studies tested the effect of mixtures on carbon oxides and hydrocarbon emissions. The work focuses on connection

M. Karthick · K. Logesh

Department of Mechanical Engineering, Vel Tech Rangarajan Dr. Sagunthala R and D Institute of Science and Technology, Avadi, Chennai, Tamil Nadu, India

S. Baskar

Department of Automobile Engineering, VELS Institute of Science, Technology and Advanced Studies (VISTAS), Chennai, Tamil Nadu 600117, India

A. Sharma (✉)

Department of Mechanical Engineering, Manipal University Jaipur, Jaipur, Rajasthan 303007, India

with pure diesel and the impact of doping pentanol combined with cashew nut biodiesel [5]. Cashew nut biodiesel was derived from cashew nutshell oil, and pentanol is an oxygenated product by a transesterification process. The test was done with diesel, cashew nut biodiesel, 10% pentanol, and biodiesel 20%. Researcher explores the effects of aluminum nanoparticles on the emissions and performance of the CSN fueled engine. The biodiesel nutcase of cashew prepared with the inclusion of aluminum nanoparticles is prepared through traditional and biodiesel transesterification changed [6].

The efficiency and emission properties of diesel engines depend on a range of variables, such as fuel injection, combustion chamber type, injection nozzle hole location and duration, fuel spray patterns, and air bucking. Several laboratory experiments of diesel engines have also been carried out to improve operational performance and reduce emissions [7–10]. There are two substitutes, gasoline, bioethanol, and modern adapted diesohol, which use the liquid/biodiesel-distilled cashew nutshell. The four main pollutants from diesel engines are carbon monoxide (CO), hydrocarbons (HC), particulate matter (PM), and nitrogen oxides (NO_x), and their control strategists are diesel oxidation catalyst, diesel particulate filter, and selective catalytic reduction. Biodiesel and distilled cashew noodles can be used as emulsifiers for the stabilization of diesohol and marginally for a decrease in the portion of diesel in the blend due to their molecular structure. In the last years, significant global interest was seen in the development of sustainable, waste-to-energy, and low-cost raw materials technology for diesel engine fuel and hydrocarbon bio-jet fuel [11–13]. This modern and renewable route is exciting because it requires conversion to green diesel with moderate experimental conditions with low-value residues. CNS processing of biofuels facilitates the complete use and future industrial uses in many countries of the residues of the agro-industry castaway-neutral chain. Many studies were carried out on the use of biodiesel study to determine the effects of the study and emission properties of oxygen-additive nanoparticles, followed by a comparison of experimental results with base pure diesel. Several researchers have shown to have used a variety of biodiesel to evaluate emission characteristics and to study the quality of a wide range of diesel engines with or without modification. In this study, biofuel combinations of CNS oil of its three blends B20, B40, and B60 explored and its performance analysis and emissions characteristics in a single-cylinder diesel engine are discussed in this paper.

2 Experimental Details

Cashew nut oil is a viscous reddish-brown dark liquid which is collected within the cashew from a soft structure. It is a biomaterial that is natural and organic and gives a synthetic benefit. CNS oil is also viewed as cost-effective and more advanced phenol ingredients. Cardanol oil, a commonly used commodity in the industry, has the main purpose of CNS extraction. Physically processed CNS produces 70% anacardic acid, 18% cardol, and 5% cardanol. In essence, cardanol is a single-hydroxy phenol with

Table 1 Properties of cashew nutshell blends

Property	Diesel	B20	B40	B60
Density (kg/m ³)	845	870	878	885
Calorific value (kJ/kg)	4300	41,912	41,325	40,758

a long meta-position carbon chain. It can replace phenol in phenolic resin base chemicals. Blending is characterized by the blending, to create a commodity of the desired nature of the different forms of the same material together. Biodiesel in varying amounts is mixed with renewable diesel, the names of which are B20, B40, and B60. For instance, 200 ml biodiesel is mixed with 800 ml diesel in the preparation of 1 L of B20 (20% biodiesel and 80% diesel) and is well mixed with magnet stirrer, similarly in B40 and B60 proportions. The properties of blends are given in Table 1.

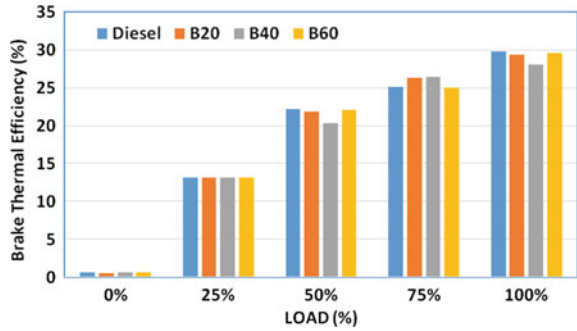
To test engine investigation and CNS oil emission requirements, the air-cooled direct injection diesel engine was used at 2.5 kW in the 1200-rpm speed rating. A dynamometer may be used manually for loading an engine from zero to maximum load, ranging from an increment of 25% based on generated engine capacity. The test rig was linked to the critical combustion pressure, diesel line pressure, and crank angle measurements computing instruments. AVL gas analyzer has observed the exhaust emission characteristics. The engine needs to start at no loading and was allowed to idle for a while. During the usage of the stopwatch and a fuel calculation desk, the time needed for 10 cc fuel consumption is noted. Now the motor is loaded steadily to the target value. The time required for fuel consumption and speed of the engine is noted after the engine has been operating at no load for some time to reach a steady state. For no loading of 25, 50, 75, and 100% of graded load, the procedure has been repeated. The reading is presented and outcomes measured. The results are current. Both mixtures are maintained with the same injection strength. For multiple loads and biodiesel blends (B20, B40, B60, and renewable diesel), the process is repeated. The results are estimated and tabled. The limitations are as the engine load increases, relative contribution of premixed combustion phase to the total heat release decreases due to the reduction in ignition delay and mixing controlled combustion phase starts to control the engine combustion and heat release process and the future work to be carried out in different blend with respect to various proportions.

3 Results and Discussion

3.1 Brake Thermal Efficiency

The transformed heat energy is called power as indicated, and the power indicated often exceeds the brake power and is used to push the piston [14]. The brake power is the engine's driving shaft's power output without loss of engine power, transfer, etc. The biodiesel also includes a quantity of the ester oxygen molecule. It also

Fig. 1 Variation of brake thermal efficiency on engine load



participates in the burning process. The brake thermal efficiency (BTE) is the brake power-to-fuel energy ratio [15]. It is found that BTE as shown in Fig. 1 is steadily decreased as the applied load is increased and brake thermal efficiency improves as the load is increased. This shows for B20 that efficient combustion exists, and energy loss reductions are made about exhaust gas [16]. The B40 and B60 also reflect this fact.

3.2 Mechanical Efficiency

The torque tests the power of a motor to spin the wheels at a certain rpm. The ratio of the brake power to the indicated power is mechanically specified [17]. Volumetric efficiency is defined as the air volume flow rate at which the device transfers volume. The efficiency, mechanical for a combination B20, B40, and B60, from the study of Fig. 2, is greater than the diesel due to the higher volumetric air flux for mixing, the volumetric efficiency is greater, and due to a rise in the specified heat power and the thermal brake efficiency is greater.

Fig. 2 Variation of mechanical efficiency on engine load

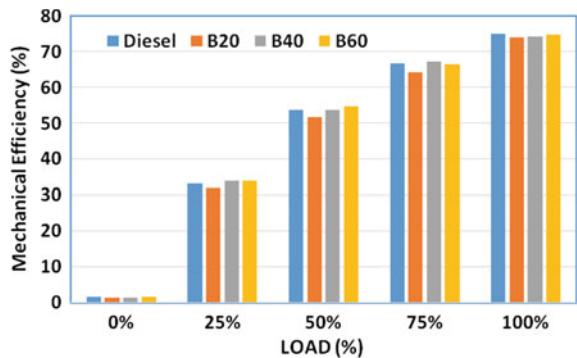
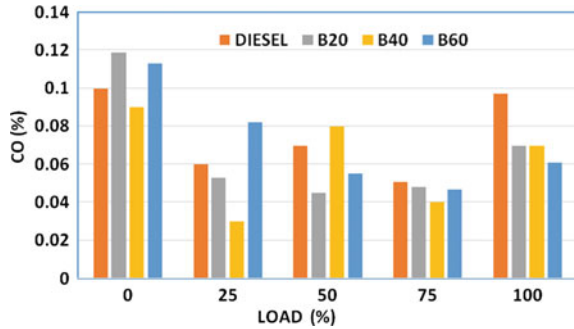


Fig. 3 Variation of carbon monoxide emission on engine load



3.3 Carbon Monoxide

The difference between carbon monoxide load and combustion is as shown in Fig. 3. The formation of CO emissions depends primarily on the physical and chemical characteristics of the fuel [18]. The CO emission of CNS biodiesel is less than the CO emission of diesel. The reduction in CO emissions for blends is due to a large amount of cetane and oxygen in the cashew nutshell’s molecular structure. The lack of oxygen primarily allows carbon monoxide to be formed. Since mixtures are oxygenated, fuel combustion increases and decreases emissions of carbon monoxide.

3.4 Unburnt Hydrocarbon

As seen in Fig. 4, hydrocarbon differences for all fuels and their mixtures have been greatly decreased by unburnt carbon emissions, but higher unburnt carbon emissions are found for the mix at low load conditions. Their emissions are substantially reduced. Under low load conditions, the fuel-injected is less and the effect is that the mixture is slight, the flame has darkened, and gas has fallen, and that the combustion is insufficient, and the hydrocarbon emissions are higher. Because of the higher

Fig. 4 Variation of unburnt hydrocarbon emission on engine load

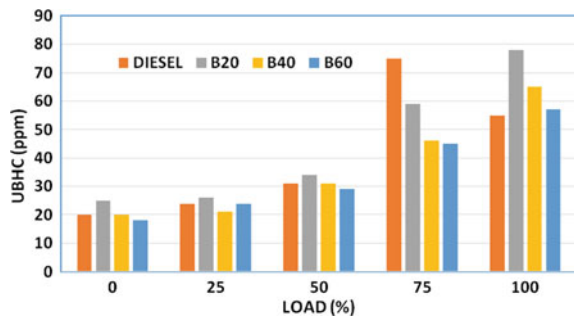
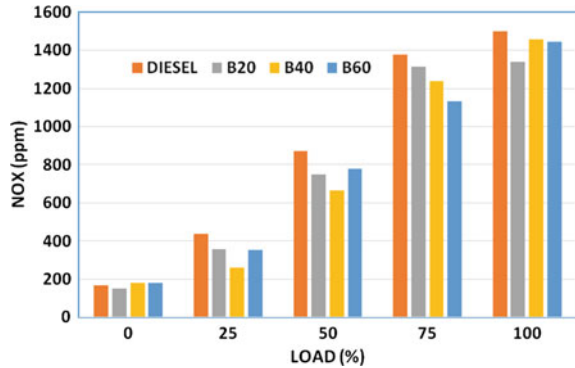


Fig. 5 Variation of nitrogen oxides emission on engine load



cetane amount and oxygen inherent in the molecular structure of CNS biodiesel, hydrocarbon pollution of the biodiesel cashew shell is less than that of diesel fuel [19].

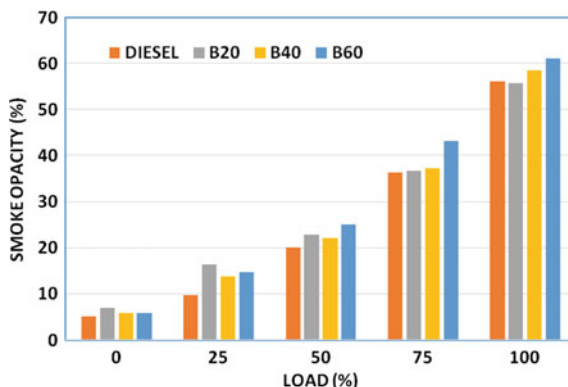
3.5 Nitrogen Oxide

As seen in Fig. 5 and the bar diagram, the shift in nitrogen oxide in comparison with both gasoline and their mixture is seen below. Results show that the engine load that encourages NO_x emissions has risen for both fuels. As the forming of NO_x is susceptible to temperature, this increased load promotes the temperature of the cylinder's loading, which is responsible for the formation of Zeldovich NO_x thermal [20]. The biodiesel CNS contains a little more NO_x than diesel [21]. The growth in NO_x is the presence of mono-unsaturated and poly-unsaturated fatty acids contained in biodiesel in the cashew nutshell. With the rise in the proportion of fuel mixtures, NO_x increases steadily. The NO_x rise can be related to the oxygen content of mixtures, and the oxygen in the gasoline can be used to generate extra NO_x oxygen.

3.6 Smoke Formation

Opacity generated from diesel engine can be explained as soot particles which are the results of unburnt fuel [22]. Opacity constitutes the degree to which smoke blocks light, and the basis on which the smoke in the diesel-powered car is measured. The opacity of smoke is somewhat equal to B20, B40, and B60 petrol, and variations are shown in Fig. 6. The smoke opacity of the B20 and B40 mixtures is similar, with the diesel fuel lower at 0–30% in addition of biodiesel, but NO_x increases. The increase in the residence time and the temperature of the mixture in the cylinder may lead

Fig. 6 Variation of smoke emission on engine load



to raise in NO_x emission [23]. In the future, the biodiesel will play a major role in terms of improvement in the behavior of the diesel engine.

4 Conclusion

Efforts to produce unconventional fuels for use in diesel engines are therefore being produced around the world. Emission and engine characteristics were studied and compared with simple diesel-driven diesel fuel for a single cylinder's direct injection diesel engine fueled with cashew nutshell biodiesel–diesel blends. With a growth in the proportion of mixtures due to lower calorific value for CNS biodiesel, the basic fuel consumption increases. The thermal efficiency of CNS oil is significantly higher than that of diesel. For engines operating on biodiesel, the fuel consumption values are higher by 10% than the engine running on conventional diesel. CO emissions are low as compared to diesel at higher loads for cashew nutshell esters. The raised NO_x emissions of the biodiesel cassava nutshell are the result of unsaturated fatty acids of mono- and polyester. Cashew nutshell biodiesel with copper oxide nanoparticle meets the essential properties of fuel in compliance with the requirements for biodiesel.

5 Limitation and Future Scope

One of the most common problems associated with biodiesel is higher viscosity than diesel. The same issues were faced with cashew nutshell biodiesel. This problem can be solved by blending CNS with fuel of lower viscosity. Also, preheating can be done to reduce the viscosity.

References

1. Sharma A, Murugan S (2013) Investigation on the behaviour of a DI diesel engine fueled with Jatropa Methyl Ester (JME) and Tyre Pyrolysis Oil (TPO) blends. *Fuel* 108:699–708. <https://doi.org/10.1016/j.fuel.2012.12.042>
2. Krishania N, Rajak U, Verma TN, Birru AK, Pugazhendhi A (2020) Effect of microalgae, tyre pyrolysis oil and Jatropa biodiesel enriched with diesel fuel on performance and emission characteristics of CI engine. *Fuel* 278:118252
3. Sharma A, Sivalingam M (2014) Impact of fuel injection pressure on performance and emission characteristics of a diesel engine fueled with Jatropa Methyl Ester Tyre Pyrolysis Blend. SAE technical paper 2014-Oct. <https://doi.org/10.4271/2014-01-2650>
4. Vedharaj S, Vallinayagam R, Yang WM, Chou SK, Chua KJE, Lee PS (2014) Experimental and finite element analysis of a coated diesel engine fueled by cashew nut shell liquid biodiesel. *Exp Therm Fluid Sci* 53:259–268
5. Devarajan Y, Nagappan BK, Munuswamy DB (2017) Performance and emissions analysis on diesel engine fuelled with cashew nut shell biodiesel and pentanol blends. *Korean J Chem Eng* 34:1021–1026
6. Radhakrishnan S, Munuswamy DB, Devarajan Y, Mahalingam A (2018) Effect of nanoparticle on emission and performance characteristics of a diesel engine fueled with cashew nut shell biodiesel. *Energy Sour Part A Recover Util Environ Eff* 40:2485–2493
7. Manigandan S, Gunasekar P, Nithya S, Devipriya J (2020) Effects of nanoadditives on emission characteristics of engine fuelled with biodiesel. *Energy Sour Part A Recover Util Environ Eff* 42:1–9
8. Rangabashiam D, Logesh K, Yashvanth U, Subbiah G, Selvam C (2019) Detailed study on the effect of nano-particle size on emission characteristics of diesel engine. *Pet Sci Technol*
9. Salam S, Choudhary T, Pugazhendhi A, Verma TN, Sharma A (2020) A review on recent progress in computational and empirical studies of compression ignition internal combustion engine. *Fuel* 279:118469. <https://doi.org/10.1016/j.fuel.2020.118469>
10. Sharma A, Murugan S (2014) Influence of fuel injection timing on the performance and emission characteristics of a diesel engine fueled with Jatropa methyl ester-tyre pyrolysis oil blend. *Appl Mech Mater* 592–594:1627–1631. <https://doi.org/10.4028/www.scientific.net/AMM.592-594.1627>
11. Crawford JT, Shan CW, Budsberg E, Morgan H, Bura R, Gustafson R (2016) Hydrocarbon bio-jet fuel from bioconversion of poplar biomass: techno-economic assessment. *Biotechnol Biofuels* 9:1–16
12. Arya S, Sharma A, Rawat M, Agrawal A (2020) Tyre pyrolysis oil as an alternative fuel: a review. *Mater Today Proc* 28:2481–2484. <https://doi.org/10.1016/j.matpr.2020.04.797>
13. Rajak U, Verma TN (2018) Spirulina microalgae biodiesel—a novel renewable alternative energy source for compression ignition engine. *J Clean Prod* 201:343–357
14. Nabi MN, Hoque SMN, Akhter MS (2009) Karanja (*Pongamia Pinnata*) biodiesel production in Bangladesh, characterization of karanja biodiesel and its effect on diesel emissions. *Fuel Process Technol* 90:1080–1086
15. Wang X, Ge Y, Yu L, Feng X (2013) Comparison of combustion characteristics and brake thermal efficiency of a heavy-duty diesel engine fueled with diesel and biodiesel at high altitude. *Fuel* 107:852–858
16. Sharma A, Murugan S (2015) Potential for using a tyre pyrolysis oil-biodiesel blend in a diesel engine at different compression ratios. *Energy Convers Manag* 93:289–297. <https://doi.org/10.1016/j.enconman.2015.01.023>
17. Agarwal D, Sinha S, Agarwal AK (2006) Experimental investigation of control of NOx emissions in biodiesel-fueled compression ignition engine. *Renew Energy* 31:2356–2369
18. Rajak U, Verma TN (2018) Effect of emission from ethylic biodiesel of edible and non-edible vegetable oil, animal fats, waste oil and alcohol in CI engine. *Energy Convers Manag* 166:704–718

19. Loganathan M, Madhavan VM, Balasubramanian KA, Thanigaivelan V, Vikneswaran M, Anbarasu A (2020) Investigation on the effect of diethyl ether with hydrogen-enriched cashew nut shell (CNS) biodiesel in direct injection (DI) diesel engine. *Fuel* 277:118165
20. Nileshkumar KD, Patel TM, Rathod GP (2015) Effect of blend ratio of plastic pyrolysis oil and diesel fuel on the performance of single cylinder CI engine. *Int J Sci Technol Eng* 1:195–203
21. Sendzikiene E, Makareviciene V, Janulis P (2006) Influence of fuel oxygen content on diesel engine exhaust emissions. *Renew Energy* 31:2505–2512
22. Yao C, Cheung CS, Cheng C, Wang Y (2007) Reduction of smoke and NO_x from diesel engines using a diesel/methanol compound combustion system. *Energy Fuels* 21:686–691
23. Han Z, Uludogan A, Hampson GJ, Reitz RD (1996) Mechanism of soot and NO_x emission reduction using multiple-injection in a diesel engine. *SAE Transaction*, pp 837–852

Investigation of Heat Transfer Characteristics in Double Tube Heat Exchanger with Helical Turbulator Using CFD



S. Padmanabhan, M. Selvamuthukumar, S. Ganesan, S. Baskar,
and Abhishek Sharma

1 Introduction

In certain applications, heat must be transmitted from fluid to fluid through a solid barrier that is used for the separation of fluids at a different temperature. The heat exchanger comprises thermal mechanics and businesses, such as air-conditioning and coolers, solar collectors, petrochemical fields, geothermal energy systems, etc. Many methods of heat transfer development are known in order to raise the heat transfer coefficient and thus increase the heat exchangers' thermal performance and to minimize running costs. Due to steep increase in energy demand, the appliance of heat exchangers to various thermal systems has been common for the past few decades. So far, many design and development modifications of heat exchangers to improve geometry and efficiency have been made. Heat exchange systems are designed to increase the heat transfer and reduce the pressure drop by developing nature-based structures. A comprehensive long-term performance calculation based on experimental heat transfer and pressure drop outcome is required for the optimal

S. Padmanabhan

School of Mechanical and Construction, Vel Tech Rangarajan Dr. Sagunthala R and D Institute of Science and Technology, Chennai, Tamil Nadu, India

M. Selvamuthukumar

Department of Applied Engineering, Vignan's Foundation for Science, Technology and Research, Vadlamudi, Andhra Pradesh, India

S. Ganesan

Sathyabama Institute of Science and Technology, Chennai, Tamil Nadu, India

S. Baskar

Department of Automobile Engineering, Vels Institute of Science, Technology and Advanced Studies, Chennai, Tamil Nadu, India

A. Sharma (✉)

Department of Mechanical Engineering, Manipal University Jaipur, Jaipur, Rajasthan, India

design of a heat exchanger. Almost all heat transfer strategies are expected to lead to a further decrease in pressure that leads to an increase in pump power consumption. Therefore, it is important to choose the technique for optimizing heat transfer with the supportable frictional loss. The modification or shift of the heated channel for the applications settled upon new techniques for heat transfer enhancement in the warming exchanger.

The heat exchanger is used for transferring thermal energy from the fluid to the solid, to the fluid, to a certain temperature, and thermal interaction. There is normally no extra fuel and collaborations in the heat exchangers. A significant difficulty in creating heat exchange systems is to improve the one-phase temperature transport, particularly when one phase of fluid flow is carried out on one side by thermal exchangers and the two-phase flows or transfers on the other. Condensing machines, evaporators, heat exchangers, and others are typical examples for a range of consumption and performance applications [1, 2]. The thermal transfer process improves the efficiency of a thermal transfer device. It normally means increasing the coefficient of heat transfer. Twisted tap inserts provide an inexpensive and effective approach for heat transfer optimization. Although the inserts can help to get the heat transferred, they can greatly decrease the inflow pressure. In any type of thermal systems, it is vital for the industry to increase thermal transmission capacity. In addition to the handling of primary oil, the weight and height often decrease [3].

Bhuiya et al. [4, 5] studied the structure of the twisted tape insert with different geometrical criteria, such as twist ratio and width ratio. In the tube, the heat propagation and friction effects are tracked single and double twisted tapes. The value of the twist ratio decreased considerably more heat transfer and friction. The twisted tape profile mainly disturbs the principal flow and therefore other geometrical variations are made use of the tweaking tape. An analysis was carried out on the turbulent forced convection with circular hole inserts in a circular vessel [6]. For a wide variety of Reynolds numbers inserts with various hole-spring ratios are investigated. Data reveal that using inserts results in an improvement between 35 and 51% in thermal transfer when evaluated with other inserts and single tube. Due to twisted tapes, Bhattacharya [7] researched the effects of swirl generators on energy transport using the SST model computationally. The analysis evaluated flow with Reynolds numbers and found that the characteristics of heat transfer usually increase, along with a higher-pressure decrease. The performance increase was found to be positive, however, only in such settings. In a second analysis, it has been concluded that it fits better than the smooth tube in a certain diameter and pitch. Thermodynamically desirable characteristics than other particles were given for the bluffing cylinders of suitable duration. Improvement techniques can be broadly categorized into passive and aggressive techniques. Passive techniques, such as raise of the roughness of tubes on the face or the attachment of swirl flow devices to a tube do not entail direct input of external force. By contrast, external inspection for required flow adjustment as well as an increasing thermal transfer rate is important for active processes [8, 9]. The thermal efficiency and fluent flow of a double pipe heat exchanger whose inner tube wall had been helically corrugated was numerically tested by Gorman et al. [10]. The results of the simulations showed that the heat transference rate in the

helically corrosive dual-level heat exchanger was increased by 3 compared to that on the smooth wall-pipe heat exchanger for both parallel and counterflow. In addition, in the former the pressure increased by a factor of 2–4 in contrast with the latter.

Helical insert is one of the most important means of heat transfer in heat exchangers. Many researchers, with the aid of finite element analysis and the computational fluid dynamics (CFD), have analyzed, calculated, and checked their findings in various mechanical heat transfer applications [11–14]. Style improvements are required to boost thermal efficiency. The purpose of the project is to test the efficiency of the ANSYS CFX by a double-pipe heat-exchanger helical inserts by using CFD analysis. For thermal exchangers without the helical insert, the convective wall heat fluid and the temperature distribution along with the tubing would be studied in a comparative examination.

2 Double Tube Heat Exchangers

A major part of modern mechanical cooling systems is double tube heat exchangers (DTHE). The thermal transfer efficiency of a heat exchanger was generally decided upon. This study aims to examine the transfer of heat and entropic generation in numerical terms in a two-pipe helical heat swap with numerous cross sections. The findings were verified and a theoretical model for laminar convective heat transfer was developed. The previous literature has been published. The entropy balance equation for the open system is used for compiling entropy production. Given the numerical data, the effect of internal tube number and the inlet mass variance ratio of the tube were studied and addressed on the eccentricities and flow of co-flow and counter flow. In relation to the geometry, the pipe area, cross-sectional annulus area and internal pipe thickness are the same. The geometrics are called equivalent. The conclusions demonstrate the most effective method for heat transfer, pressure reduction, and entropy output to be achieved by the square cross section. A concentrated setup is best suited for low flow speeds, whereas a more eccentric exterior setup is better suited for high flux rates.

Rennie and Raghavan [15, 16] conducted experimental and computing tests on the two helical heat exchangers. There were modest problems with the average heat transfer coefficient between the parallel flow and the controller flow, but the counterflow is dramatically greater. In comparison, a higher percentage of the internal dean led to the higher average heat transfer coefficient. Boonsri and Wongwises [17] theoretical study and laboratory tests investigated the heat transfer properties of helical, crimped, heat exchangers, and finned-tube heat exchangers. The flow rate of the water mass and the water inlet temperature have, however, seen to have a direct effect on the air outlet and water temperature.

3 Methodology

Research on the use of insert turbulators to maximize the transmission of heat is exponential because of positive outcomes. The literature repeatedly notes that inserting the insert in the tube has an important impact on heat transfer rate and pressure rises. From the past studies, the geometry incorporated in the region around the wall and not in the core stream can create turbulence. The most suitable types of insertions based on these results are guided wire inserts, ring inserts, and conical inserts. The decrease in pressure is also increased, but, with increasing temperature transfer rates, the belt implant can be demonstrated as effective. Due to friction with increased heat transfer rates, perforated ring inserts were found that minimize stress drop.

Twisted tape inserts provide a simple and economical way to optimize heat transfer. The flow pressure reduces considerably though inserts can be useful for thermal transfer. For the industry, the speed improvements of thermal transmission in all kinds of thermal devices are very important. Besides the savings in essential oil, size, and weight are both minimized. One of the most efficient techniques used for heat transfer in heat exchangers is the helical injection. Better thermal performance design is key [18]. The research aims to test the achievement of the heat exchanger dual tube with commercially available computer fluid dynamics (CFD) applications ANSYS CFX and the method Pro/Engineer modeling. The heat exchanger can also do a comparative study without helical inserts. For measuring of the heat transmission, heat transfer, and heat distribution coefficient along the conduit. The pressure control and flow propagation should be measured. Helical height inserts visualization of turbulence [19–21].

3.1 Modeling of Heat Exchanger

This is the first point in the continuum of study. A solid that determines the fluid flow area is the primary objective of geometry development. Current models have been compiled in dimensions and geometry descriptions. The heat exchanger would be modeled with helical inserts with the dimensions of diameter of inner and outer pipe are 12.5 and 25 mm, length of heat exchanger is 90 mm. The wire diameter of helical turbulator is 1.2 mm and length is 75 mm. Pitch distance varied at three different level in the turbulator are 4.25, 8.5, and 17 mm. Double tube heat exchangers modeling was done using Pro E Wild Fire 2.0 and exported in IGES format. The part modeling was used to construct the heat exchanger was represented in Fig. 1.

The advantages of applying geometric regions are that they are specifically related to the model and are connected with the model by moving geometry. The regions are automatically assigned when a new mesh is formed. The spatially discrete CFD model method is mesh development. Meshing is based on the discretization of the tetrahedron component. Meshed model is represented in Fig. 2. It is exported to the ICFM CFD tool in IGES format. This method used to create surface and volume

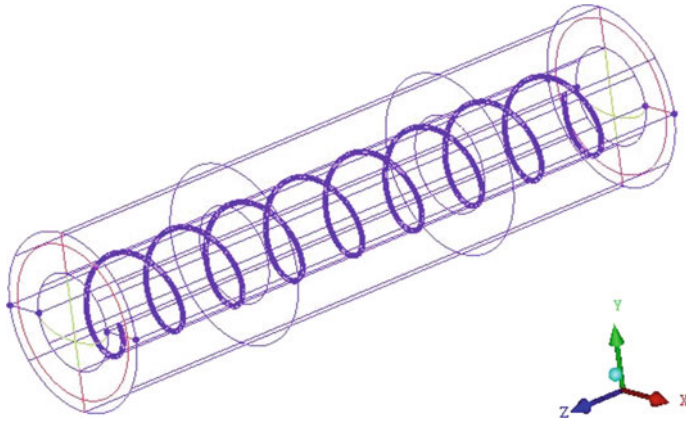


Fig. 1 Double tube heat exchanger with turbulator (pitch 8.5 mm)

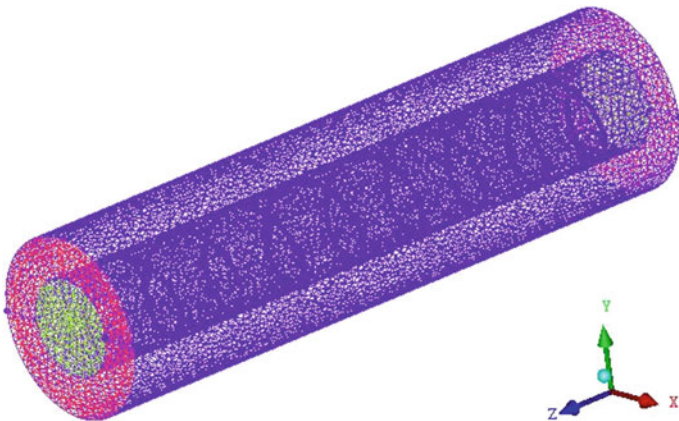


Fig. 2 Meshed Model of double tube heat exchanger with turbulator (pitch 8.5 mm)

meshes, specifying the meshing element form and mesh element type is tetrahedron, number of elements are 395,793 and nodes are 77,694.

Boundary conditions and heat exchanger specifications for CFD analysis are tabulated in Table 1, and boundary conditions and constraints are represented in Fig. 3. After defining all the conditions, the model is imported in CFX-Solver Module for doing iterative calculations and to generate result file. The solver control parameters have been specified in CFX-Pre-Module. Number of iterations performed was 75 with Auto Time scale.

Table 1 Boundary conditions and heat exchanger specifications for CFD analysis

S. No.	Heat exchanger specifications	Domain data
1	Flow type and fluid	Counter-flow with water
2	Fluid domain	Double tube
3	Solid domain	Turbulator and tube surface
4	Tube and turbulator material	Copper and Aluminum
5	Inlet boundary conditions	28° C with 0.2 m/s (Cold Fluid) 90° C with 0.2 m/s (Hot Fluid)
6	Outlet boundary condition	Pressure: 1 bar
7	Wall boundary conditions	Wall influence on flow: No slip Wall roughness: smooth wall

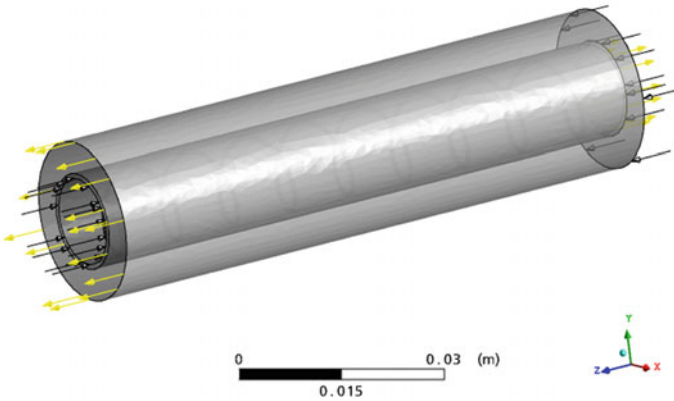


Fig. 3 Constraint of double tube heat exchanger with turbulator (pitch 8.5 mm)

4 Results and Discussion

4.1 Heat Transfer Distribution

The cold fluid heat exchanger temperature distribution with turbulators with different pitch lengths as shown in Fig. 4. Although, the fluid temperature changes in the heat exchanger outlet with the turbulator is contrasted with the heat exchanger without

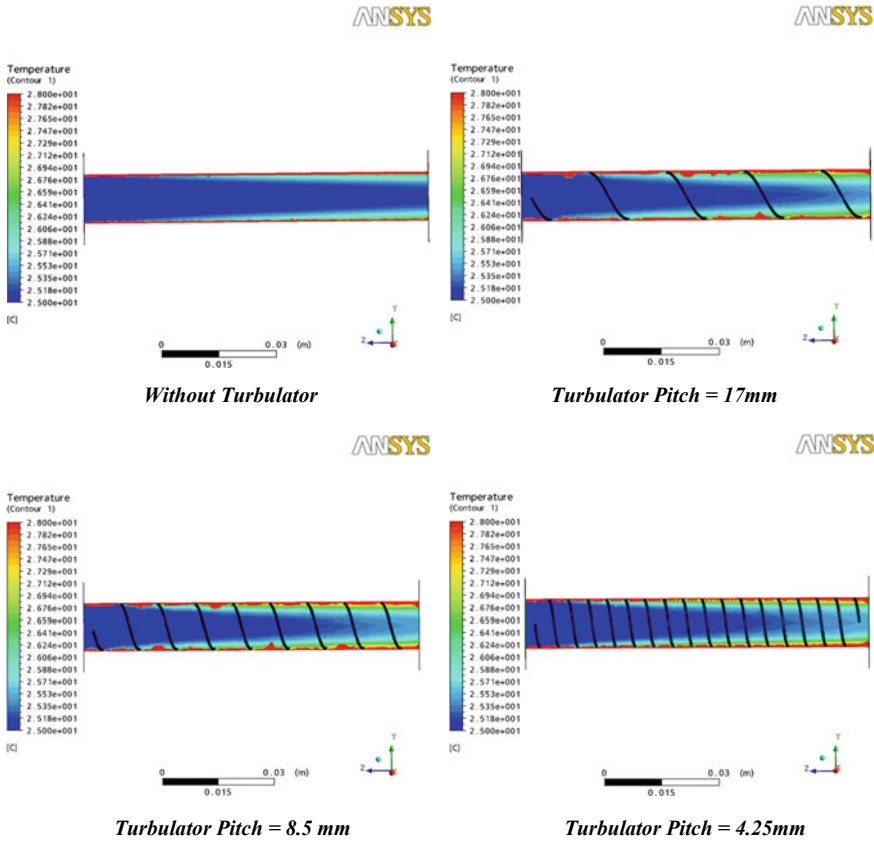


Fig. 4 Heat transfer distribution of double tube heat exchangers

the turbulator. As the fluid temperature rises further for 4.25 mm in pitch when contrasting turbulators with varying pitch lengths.

4.2 Pressure Distribution

The pressure distribution of the models as seen in Fig. 5. There is a rising pressure on the inlet and the pressure progressively reduces toward the outlet. The pressure distribution suggests that in this situation the pressure decrease is raised at the input of the turbulator pitch of 4.25 mm and when the flux begins. The other models demonstrate that the pressure at the inlet reduces.

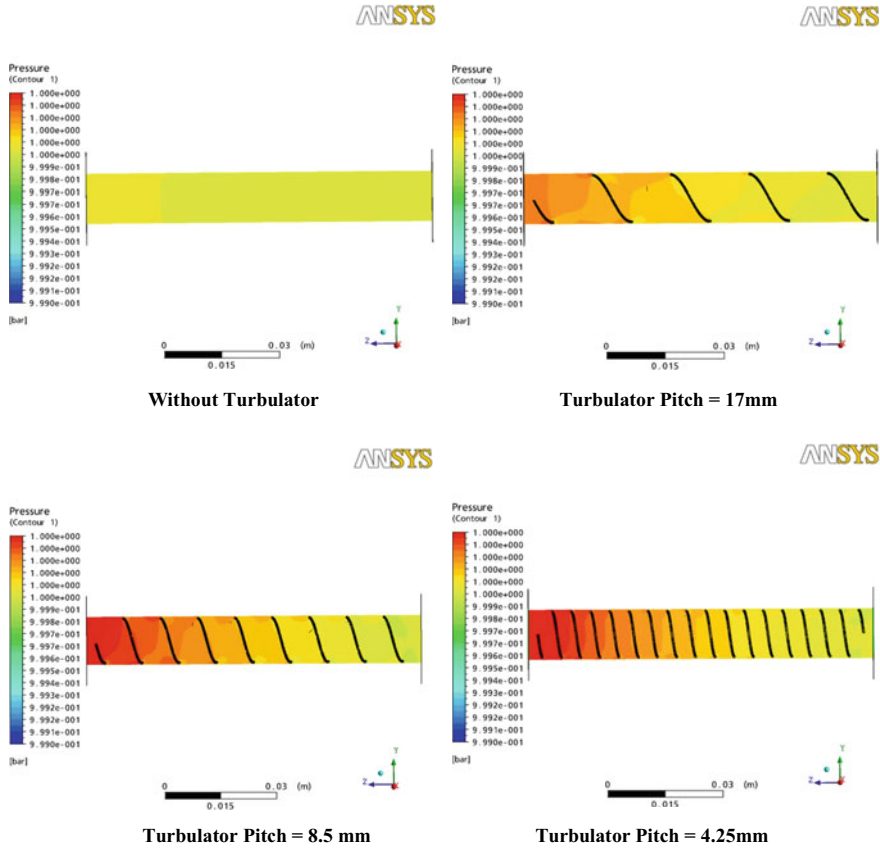


Fig. 5 Pressure distribution of double tube heat exchangers

4.3 Turbulence Eddy Dissipation

The eddy turbulence dissipation can be seen in Fig. 6. It applies to the lack of energy in the flow due to eddy. The findings indicate that turbulence dissipation at turbulator is more significant. Results suggest that turbulence eddy dissipation is more likely to occur as the flow reaches exhaust. For the turbulator pitch of 4.25 mm, improved turbulence eddy dissipation is observed.

The decreased pitch of 4.25 mm indicates the increased value from the Table 2 which contrasts all variables with a different pitch and without turbulator. The findings indicate that the heat transfer coefficient in the turbulator pipe has improved substantially. The values are high on turbulators for turbulator pitch 17 and 8.5 mm. The heat transfer coefficient has greatly improved and is above the outlet in the case of 4.25 mm pitch turbulator. There is a rising pressure on the inlet and the pressure progressively reduces toward the outlet. The pressure distribution suggests that in

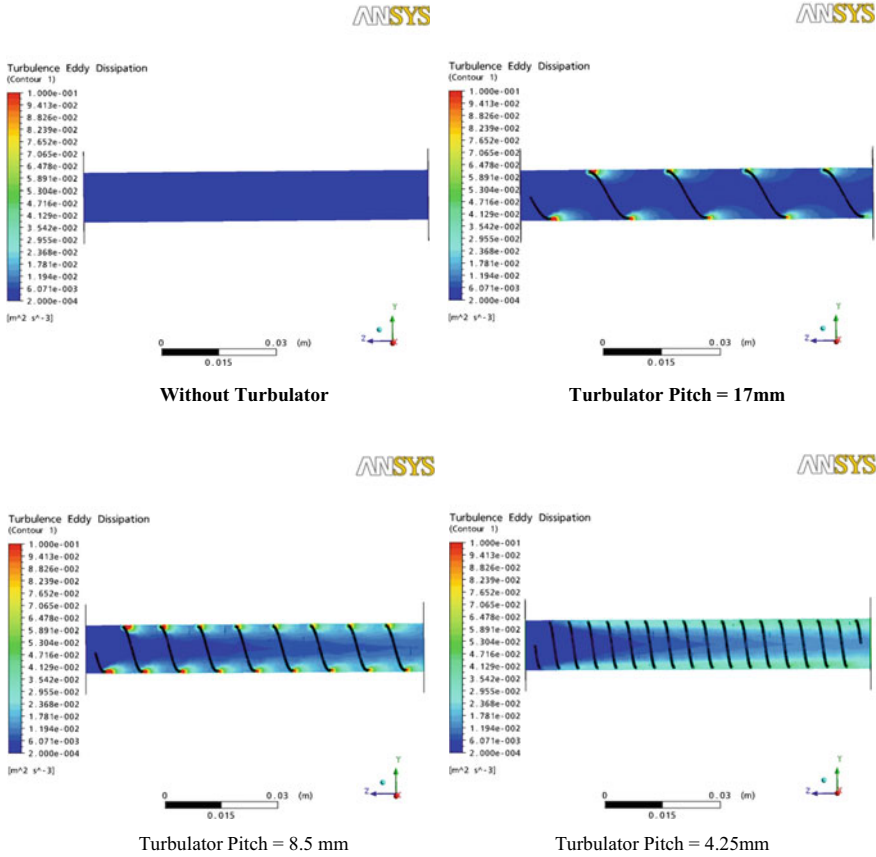


Fig. 6 Turbulence Eddy dissipation of double tube heat exchangers

Table 2 Comparative study on double tube heat exchangers with turbulator

Variable		Without turbulator	Pitch 4.25 mm	Pitch 8.5 mm	Pitch 17 mm
Heat transfer [°C]	Inlet	25.15	25.156	25.156	25.157
	Outlet	26.028	26.777	26.768	26.516
	Difference	0.874	1.621	1.612	1.359
Pressure [bar]	Inlet	1.0000	1.0000	1.0000	1.0000
	Outlet	1.00004	1.00047	1.00043	1.00025
	Difference	0.00004	0.00047	0.00043	0.00025
Turbulence Eddy dissipation [m ² s ⁻³]		0.00092	0.01719	0.01324	0.00517
Variation in Percentage		–	1778.5	1346.15	464.49

this situation the pressure decrease is raised at the input of the turbulator pitch of 4.25 mm and when the flux begins. The other models demonstrate that the pressure at the inlet reduces.

5 Conclusion

The heat transfer technique boosts the performance of thermal exchangers. For better efficiency, the heat transfer coefficient must usually be changed. Twisted tape inserts are the cost-effective and simple way to optimize heat transfer. For dual tube heat exchanger research, the CFX technique has been used. Insert helical. The improvement in the thermal transference and heat stream of the wall was observed as the pitch difference decreases. For the lower pitch helical inserts, the wall distribution heat flow coefficient is uniformly distributed. The heat transfer coefficient has significantly increased by around 80% for 4.25 mm helical inserts. The intensity of turbulence has increased significantly at the lower pitch distance. When the pitch distance decreases the pressure drop and turbulence eddy dissipation increases significantly. At lower pitch distance, the pressure drop is significant which will increase the pumping power.

6 Future Work and Limitations

The main applications of this work are to improve the heat transfer characteristics in particularly turbulent flow. The future work is going to be carried out for different flow rate. The main limitations of this work is not suitable to laminar flow due to minimum heat transfer enhancement.

References

1. Ali RK, Sharafeldeen MA, Berbish NS, Moawed MA (2016) Convective heat transfer enhancement inside tubes using inserted helical coils. *Therm Eng* 63:42–50
2. Kumar R, Chandra P (2019) Thermal analysis of compact shell and wire coil-inserted helical coil tube heat exchanger. *Int J Ambient Energy* 1–6
3. Salem MR, Eltoukhey MB, Ali RK, Elshazly KM (2018) Experimental investigation on the hydrothermal performance of a double-pipe heat exchanger using helical tape insert. *Int J Therm Sci* 124:496–507
4. Bhuiya MMK, Sayem ASM, Islam M, Chowdhury MSU, Shahabuddin M (2014) Performance assessment in a heat exchanger tube fitted with double counter twisted tape inserts. *Int Commun Heat Mass Transf* 50:25–33
5. Kumar D, Patil AK, Kumar M (2020) Experimental investigation of heat transfer and fluid flow in a circular tube with lanced ring insert. *Exp Heat Transf* 33:560–571

6. Tusar M, Noman A, Islam M, Yarlagadda P, Salam B (2019) CFD study of heat transfer enhancement and fluid flow characteristics of turbulent flow through tube with twisted tape inserts. *Energy Procedia* 160:715–722
7. Bhattacharyya S, Chattopadhyay H, Bandyopadhyay S, Roy S, Pal A, Bhattacharjee S (2016) Experimental investigation on heat transfer enhancement by swirl generators in a solar air heater duct. *Int J Heat Technol* 34:191–196
8. Bejan A, Kraus AD (2003) *Heat transfer handbook*. John Wiley & Sons
9. Andrzejczyk R, Muszynski T, Kozak P (2021) Experimental and computational fluid dynamics studies on straight and U-bend double tube heat exchangers with active and passive enhancement methods. *Heat Transf Eng* 42:167–180
10. Gorman JM, Krautbauer KR, Sparrow EM (2016) Thermal and fluid flow first-principles numerical design of an enhanced double pipe heat exchanger. *Appl Therm Eng* 107:194–206
11. Gupta V, Sharma A, Gupta KS (2017) Numerical analysis of direct type greenhouse dryer. *ASME 2017 Gas Turbine India Conference GTINDIA 2017*, vol 2, pp 5–9. <https://doi.org/10.1115/GTINDIA2017-4784>
12. Joel C, Anand S, Padmanabhan S, Prasanna Raj Yadav S (2021) Thermal analysis of carbon-carbon piston for commercial vehicle diesel engine using CAE tool. *Int J Ambient Energy* 42:163–167
13. Padmanabhan S, Ganesan S, Chandrasekaran M, Raman VS (2010) Gear pair design optimization by genetic algorithm and FEA. In: *Frontiers in Automobile and Mechanical Engineering-2010*, pp 301–307. IEEE
14. Padmanabhan S, Thiagarajan S, Kumar ADR, Prabhakaran D, Raju M (2020) Investigation of temperature distribution of fin profiles using analytical and CFD analysis. *Mater Today Proc*
15. Rennie TJ, Raghavan VGS (2005) Experimental studies of a double-pipe helical heat exchanger. *Exp Therm Fluid Sci* 29:919–924
16. Rennie TJ, Raghavan VGS (2006) Numerical studies of a double-pipe helical heat exchanger. *Appl Therm Eng* 26:1266–1273
17. Boonsri R, Wongwises S (2015) Mathematical model for predicting the heat transfer characteristics of a helical-coiled, crimped, spiral, finned-tube heat exchanger. *Heat Transf Eng* 36:1495–1503
18. Padmanabhan S, Reddy OY, Yadav KVAK, Raja VKB, Palanikumar K (2021) Heat transfer analysis of double tube heat exchanger with helical inserts. *Mater Today Proc*
19. Yang D, Guo Y, Zhang J (2016) Evaluation of the thermal performance of an earth-to-air heat exchanger (EAHE) in a harmonic thermal environment. *Energy Convers Manag* 109:184–194
20. Pourahmad S, Pesteei SM (2016) Effectiveness-NTU analyses in a double tube heat exchanger equipped with wavy strip considering various angles. *Energy Convers Manag* 123:462–469
21. Zohir AE, Habib MA, Nemitallah MA (2015) Heat transfer characteristics in a double-pipe heat exchanger equipped with coiled circular wires. *Exp Heat Transf* 28:531–545

AHP-based Identification of Tools for Sustainable Product Development



Chinmay Saraf, Sachin Agrawal, Dharmesh Barodiya, Pankaj Shrivastava, and Tikendra Nath Verma

1 Introduction

Sustainable development has become the primary focus for organizations all over the world [1]. Organizations aim to achieve low carbon emission and reduction in social and cultural impact by improving the environmental aspects of the product which they deliver and the business process which they exhibit [2]. The paper aims to address the requirement of organizations to improve sustainability at the product design level.

The basic concept of sustainable development stands on three pillars—environment, economy, and society [1]. The efforts of sustainable development encourage positive contributions to the environment, economy, and society. It was found in various studies that 80% of the sustainable impact is decided at the design stage itself [2]. Hence, the process of sustainable design becomes a prime importance to the organization, as design improvement can lead to significant improvements in sustainability [3].

One of the important aspects that improve sustainability at the design stage is the use of tools for sustainable design [4]. The tools can be classified based upon many factors. Different researchers have classified the tools based on various factors, but the common aim was to improve the utility of tools based on design needs. Case studies also show that the use of tools has resulted in significant improvements concerning sustainability [1].

C. Saraf · S. Agrawal · D. Barodiya · P. Shrivastava
Prestige Institute of Engineering Management and Research, Indore, Madhya Pradesh 452010, India

T. N. Verma (✉)
Maulana Azad National Institute of Technology, Bhopal, Madhya Pradesh 462003, India

The paper aims to identify the tools that can be applied at the design stage of the product by the product designer using the computer-aided tools and take relevant decisions to improve the sustainability of the product.

In this article, sustainable design tools are identified and ranked based upon the priority. The article identified the tools with the help of the literature review method and classified them based on the priority of the survey of experts. The method that is used to classify the tools based upon priority is analytical hierarchy process (AHP). The AHP uses a pairwise comparison with the multi-criteria decision-making process [5]. The AHP methodology will be used to compare the various product design tools to improve the sustainability of the product based upon the product designer experience. A google form was developed about the pairwise comparison and sent to the product designers, and based upon their experience, the results were evaluated to determine the priority of the tools. The outcomes of the paper can be used by design engineers to improve the sustainability [3]. It can be assumed that the tools of the highest priority will help to improve sustainability more effectively than the other tools, but the results may vary among various types of products, the experience of design engineers, and other constricting factors.

2 Literature Review

Computer-aided design is an effective tool for sustainable product design and manufacturing. According to the author, computer-aided design plays a crucial role in the product development process and also has a significant impact on the sustainability of the process. The main features of the computer-aided design such as visualization, design improvement, ease of sharing the design with the stakeholders, and improvement in the product design without the need for physical development result in improvement of the sustainability of the process. It enhances the process of the product design by integrating axiomatic design with computer-aided engineering [6].

Studied sustainability improvement concerning Indian modular switches with the help of computer-aided design and design for manufacturing [7]. The study showed that the product developed with the help of tools like computer-aided design and design for manufacturing had better sustainability scores. The methods that were used to identify the sustainability score by the author were carbon footprint analysis, energy consumption analysis, and study of air–water impacts. Based on the research, it can be inferred that both computer-aided design and design for manufacturing are significant tools for improving sustainability [7].

Further studied computer-aided design and computer-aided engineering tools can be used for improvement in the sustainability of the components of the rotary switch. The tools that were used by the author to analyze sustainability were carbon footprint analysis, energy consumption as well as air–water impact assessment. The author's study also suggests that the use of these tools leads to the development of environmentally conscious products and also improves the overall sustainability of the product [8].

Computer-aided manufacturing tools to estimate the sustainability of various manufacturing operations. In the research, the author suggested a novel framework for the application of the triple bottom theory of sustainability regarding manufacturing operations. The author also added that the new framework is integrated with the MS Excel worksheet that helps in the process of decision-making about the most sustainable manufacturing process. The research shows that sustainability in the process of manufacturing is largely related to the demand; if the demand is managed in an effective manner, then the sustainability results can be achieved. For the sustainability assessment, the authors used a novel tool called the computer-aided technologies (CAD) system [9].

Additive manufacturing is a method that is used for prototype testing and development. It also has a positive impact on the sustainability during the product development process.

Design for sustainability is an approach of product design that integrates the principles of sustainability to improve the overall sustainability of the product. The main objective of this approach is to make products more and more sustainable. The main focus during this design process is to use green materials for products and to use production methods that are more environmentally friendly. Other than this, the social and cultural impacts are also considered while designing the product. According to the author, a new product can be developed with the help of this approach, or the existing product and its production process can be re-engineered with the help of design for sustainability [4].

The other approaches for green manufacturing and the green design. According to the author, the ten basic principles for sustainable product design are—the elimination of non-essential elements, reducing the weight of the components, changing the electrical power to hydraulic power, performing the safety audit, improving the safety of the product, reducing the complexity of the human-machine interaction, modular design, better problem identification in the machine, and integrating IT and software in the machine. The author adds that the main principles of green manufacturing are reduction in emission of solid, liquid, and gaseous wastes, increase in the recyclability and reuse of the materials, reducing energy consumption, and improving the energy. The author adds that the main components of green manufacturing are the tools, raw materials, cutting fluids, and energy. Optimization of any of the four main factors results in an improvement in sustainability [10].

In another work, the author used an algorithm that optimized the machining cost, waste reduction, and the energy consumption based upon the numerical optimization method and personal health, environmentally friendly, and operational safety using the fuzzy logic [11]. The author suggested running the algorithm until and unless the desired results are obtained using the method. The main limitation of this process is that sometimes the results that come may not be applicable practically but certainly can be used to improve the all-round sustainability of the machining process [11].

Author suggested that life cycle assessment is one of the comprehensive studies that is conducted to examine the sustainability of the product or process. According to the author, in the process of life cycle assessment, the complete product life cycle is taken into consideration. The impact of the product on the environment, society,

and culture is estimated in numerical terms for better understanding of impact. Post the initial assessment, improvement is done in product design, and the life cycle assessment is done once again to evaluate the improvement. This cycle of improvement in sustainability is continued until the desired results are obtained. According to the author, the process of life cycle assessment can be done easily with the help of various software, but the data of processes may vary significantly [12].

The sustainable design is the combination of tools and frameworks that ensures that the sustainability of the product is improved. The main tools and frameworks that are studied in the paper are life cycle design of the product, reduction of material and energy consumption, reducing the overall toxicity of the product, and improving the renewability and biocompatibility of the product. Other than this, the paper also discusses the process of improvement in sustainability after the use of the product in form of disassembly and recyclability improvement of sub-assemblies [13].

Quality function deployment is a tool that is used to capture the voice of customers during the design process. The tool has been widely used in the industry by the design engineers. An advancement to the existing tools not only captures the voice of the customers but also improves the sustainability index for the product. This developed tool is known as quality function deployment for the environment. In the process of the application of quality function deployment for the environment, it is divided into four phases. In the first and the second phases, the design engineers identify the components in the products that must be focused on the environment, and in the third and fourth phases, the environmental aspects are improved for the components that were identified in the first and the second phases [14].

The process of modular design is dividing the product into sub-assemblies and systems rather than amalgamating it as a complete product. The main implications of the modular design are that the variety of the products can be developed by dividing the product into modules and then assembly of various modules to develop product variety. According to the author, there have been significant increments in the paper that connect modular design and sustainability within the decade [1]. Based on a detailed literature review, it was determined that modular design has a positive impact on the sustainability of the product and also has a positive impact on the societal and innovative aspects of sustainability. The aspects of modular design that have a positive impact on sustainability are improvement in the green supply chain, emission reduction in terms of the systems, and climate change [1] (Table 1).

3 Methodology

Analytical hierarchy process is an effective tool to develop results of a complex decision-making condition [5]. The method will be helpful in ranking the sustainability tool in order of their utility in the process of sustainable product design. The AHP method also introduces the consistency of the data to reduce the bias from the data. In AHP, pairwise comparison is done based upon the weighted score for each of the decision-making alternatives; the results of this pairwise comparison yield the

Table 1 Summary of literature review

Tool	Description	Paper
Computer-aided design	Elaborates the use of the computer-aided design such as a reduction in time for product development, better visualization, and others for improvement in the sustainability of the product	[8]
Computer-aided design and design for manufacturing	Improved the sustainability of modular switch with the help of the computer-aided design and computer-aided manufacturing processes	[7]
Computer-aided design and computer-aided engineering	Improved the sustainability of the rotary switch with the help of computer-aided design and computer-aided engineering processes	[8]
Computer-aided manufacturing	Used a novel tool cax for improvement of the sustainability of the manufacturing process	[9]
Sustainable manufacturing and design for sustainability	Elaborated the principles and application of green manufacturing and green design for sustainability	[10]
Design for sustainability	The author explained the significance of design for sustainability and various aspects that are related to it	[4]
Green manufacturing	In this paper, the author developed an algorithm to ensure green manufacturing, by reducing time and cost for machining	[11]
Life cycle assessment	The author explained the tool of life cycle assessment as an important tool for the evaluation of sustainability of the product life cycle	[12]
Design for sustainability	The author discusses the various tools and framework for the design of sustainability from birth to death of the product as an integrated approach for the design of sustainability	[13]
Quality function deployment for environment	The author explained that quality function deployment for the environment is an extension to the existing QFD tool for capturing the voice of customers and improving the sustainability of the product	[14]
Modular design	According to the author, modular design has a positive impact on the sustainability of the product. It can also be used by design engineers to improve product utility and sustainability at the same time	[1]

results. Finally, a score is generated to rank the alternatives for better decision-making [15].

The AHP method is divided into five steps; the first step is the pairwise comparison between the alternatives; the second step is the development of a comparison matrix;

the third step is the computation of the priority vectors; the fourth step is calculating the consistency ratio; and the final step is determining the ranking of the factors [5].

The first step of the AHP is a pairwise comparison, and suppose N is the total number of the factors for which priority has to be estimated, then the total number of the pairwise calculation is given by the relationship expressed in equation one.

$$C = N(N - 1)/2 \quad (1)$$

A scale is used for the pairwise comparison, which has ten ratings. The first rating is the one which is given if weightage is the equivalent to both the factors. Three is used for slightly favorable, five for strongly favorable, seven for very favorable, and nine for extremely favorable. In the next step, a comparison matrix is made from the pairwise comparison. The order of the priority matrix is equal to the number of factors. For example, if the number of the factors are six, then the priority matrix will be of size $6 * 6$. In the priority matrix, the diagonal elements are kept one and the upper triangular elements are filled with the observation of the pairwise comparison and the lower triangular matrix is the inverse of the upper triangular matrix. The results of the AHP are given by the eigenvectors of the priority matrix [5]. The eigenvectors are known as priority vectors of the calculations.

To reduce the bias in the calculation, the consistency index and the consistency ratio are calculated. The consistency index is given by the formula expressed by equation number two.

$$CI = (\lambda - N)/N - 1 \quad (2)$$

where CI is the constituency index, λ is the maximum value of the eigenvalue, and N is the number of the observation. The consistency index is used to calculate the consistency ratio for the calculations. The consistency ratio is calculated using the formula expressed in formula three.

$$CR = CI/RI \quad (3)$$

where CR is the consistency ratio and RI is the random consistency index based upon the number of observations. It must be noted that the value of the consistency ratio must be less than 10%; if it is more than 10%, then the values are rejected and new values are added for calculations [15]. The last step in the method is ranking all the observations; in the process of ranking, the priority vectors are converted into percentages, and the observations that have higher values are given higher rank as compared to those which have lower values.

Table 2 Results of AHP and ranking of tools

Rank	Tool	Priority (%)	+ (%)	- (%)
1	Design for sustainability	44.6	26.6	26.6
2	Modular design	19.0	7.8	7.5
3	Life cycle assessment (LCIA)	17.9	7.8	7.8
4	Quality function deployment for environment	8.6	4.8	4.8
5	Computer-aided engineering	4.5	1.3	1.3
6	Computer-aided design	2.8	1.2	1.2
7	Computer-aided manufacturing	3	1.1	1.1

4 Application of Methodology

Based on the literature review, the tools that were selected for application of methodology are computer-aided design, computer-aided manufacturing, computer-aided engineering, life cycle assessment (LCIA), design for sustainability, quality function deployment for environment, and modular design. The main reason for the selection of these tools was their close association with the design process and that they can be easefully applied at the design step itself.

To determine the values for pairwise comparison, a google form was sent to X numbers of the design engineers who have all the experience in product designing. The results that were received from the google forms were averaged out, and AHP method was executed on the data on an online program for AHP calculation. The results for the data are shown in Table 2.

Number of comparisons = 21.

Consistency ratio CR = 7.6%

Principal eigenvalue = 7.612.

Eigenvector solution: 6 iterations, delta = 4.1E-8.

The decision matrix based upon the eigenvalue is shown in Fig. 1, and the consolidated results are shown in Fig. 2.

5 Results

Based on the application of AHP, it can be identified that the design for sustainability is a prior tool for improvement in sustainability of the product by the design. The main implications that can be developed from this is that it mainly focuses on sustainability at core; hence, sustainability improves [11]. The tool that ranks at number two is life cycle assessment for improvement in the sustainability of the product, and post this, it is the modular design and quality function deployment for the environment. Even though computer-aided design, computer-aided manufacturing, and computer-aided engineering are significant tools for product design, they were ranked lower when

	1	2	3	4	5	6	7
1	1	6.00	3.00	6.00	7.00	8.00	9.00
2	0.17	1	1.00	4.00	6.00	5.00	6.00
3	0.33	1.00	1	4.00	7.00	6.00	4.00
4	0.17	0.25	0.25	1	2.00	7.00	4.00
5	0.14	0.17	0.14	0.50	1	2.00	2.00
6	0.12	0.20	0.17	0.14	0.50	1	1.00
7	0.11	0.17	0.25	0.25	0.50	1.00	1

Fig. 1 Decision-making matrix

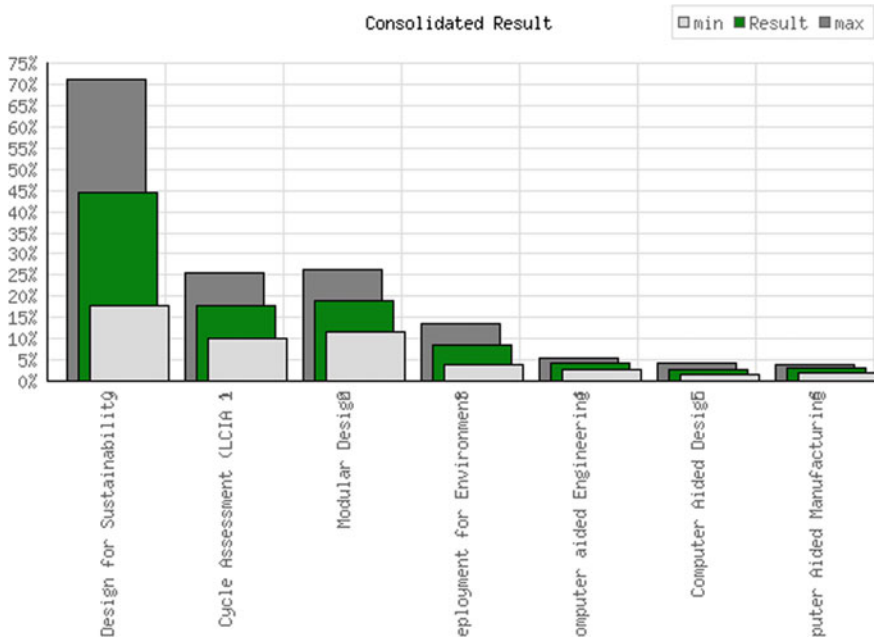


Fig. 2 Consolidated results of AHP

compared to the primary tools for improvement in sustainability. The reason behind this is that they are not primarily focused on improvement in sustainability, but the use of these tools in the process of product design has a definite impact on improvement in sustainability.

6 Conclusion

Sustainability is the main need of the hour, and it is important to integrate sustainability with the process of the product design. The paper identified the tools for sustainable product design and then ranked them based on priority using the AHP method. The data that were collected for the AHP method were based on the data from product design engineers. The outcome of the paper shows that the design for sustainability is one of the primary tools that will help in improving sustainability at the product design level and complete product life cycle. The other tools that were identified were modular design, life cycle assessment (LCIA), quality function deployment for environment, computer-aided engineering, computer-aided design, and computer-aided manufacturing. Application of these tools in the context of sustainability will have a definite improvement in the sustainability of the product.

The future scope for research is the identification of case study and quantification of the improvement in sustainability with help of each tool at the individual level. Post these studies, it can also be conducted by combining the tools and quantification of impact for better comprehension of the impact of sustainability.

References

1. Ma J, Kremer GEO (2016) A systematic literature review of modular product design (MPD) from the perspective of sustainability. *Int J Adv Manuf Technol* 86(5–8):1509–1539
2. DU CR (2016) Sustainable development goals
3. Ghoreishi M, Happonen A (2020) Key enablers for deploying artificial intelligence for circular economy embracing sustainable product design: Three case studies. In AIP conference proceedings, vol 2233, no 1, p 050008. AIP Publishing LLC
4. Bhamra T, Lofthouse V (2007) *Design for sustainability: a practical approach*. Gower Publishing, Ltd
5. Ndruru T, Riandari F (2019) Decision support system feasibility lending at KSU Mitra Karya cooperative customer unit XXVIII with analytical hierarchy process method: decision support system feasibility lending at KSU Mitra Karya cooperative customer unit XXVIII with analytical hierarchy process method. *Jurnal Mantik* 3(3):119–125
6. Murthy SR, Mani M (2012) Design for sustainability: the role of CAD. *Renew Sustain Energy Rev* 16(6):4247–4256
7. Vinodh S, Rajanayagam D (2010) CAD and DFM: enablers of sustainable product design. *Int J Sustain Eng* 3(4):292–298
8. Vinodh S (2011) Environmental conscious product design using CAD and CAE. *Clean Technol Environ Policy* 13(2):359–367
9. Saxena P, Stavropoulos P, Kechagias J, Salonitis K (2020) Sustainability assessment for manufacturing operations. *Energies* 13(11):2730

10. Jha NK (2015) Green design and manufacturing for sustainability. Crc Press
11. Jawahir IS, Wanigarathne PC, Wang X (2006) Product design and manufacturing processes for sustainability. Chapter 12 Mechanical Engineers' Handbook, pp 414–443
12. Finnveden G, Hauschild MZ, Ekvall T, Guinée J, Heijungs R, Hellweg S, Koehler A, Pennington D, Suh S (2009) Recent developments in life cycle assessment. *J Environ Manage* 91(1):1–21
13. Vezzoli C, Manzini E (2008) Design for environmental sustainability. Springer, London, p 4
14. Masui K, Sakao T, Inaba A (2001) Quality function deployment for environment: QFDE (1st report)-a methodology in early stage of DfE. In: Proceedings second international symposium on environmentally conscious design and inverse manufacturing, pp 852–857. IEEE
15. Mathivathanan D, Govindan K, Haq AN (2017) Exploring the impact of dynamic capabilities on sustainable supply chain firm's performance using Grey-Analytical Hierarchy Process. *J Clean Prod* 147:637–653

Design and Optimisation of Annulus Combustion Chamber of Gas Turbine Engine: An Analytical and Numerical Approach



Ramakrishna Balijepalli, Abhishek Dasore, Upendra Rajak, Y. Siva Kumar Reddy, and Tikendra Nath Varma

1 Introduction

Bigger and faster aircrafts operating at higher altitudes employ the gas turbine engine for the propulsion. These engines are much simpler in construction compared to the piston engine and operate at higher speeds handling much larger flow rates of air and fuel. Principal components of the gas turbine are compressor, combustion chamber and turbine. According to mass inflow rate, speed and altitude of aircrafts gas turbine engines are classified as follows; turboprop engine, turbojet engine and turbofan engine [1].

The gas turbine combustion chamber is one of the most critical components to be designed, because it must ensure a stable operation in a wide range of air/fuel ratio and load. Combustor is one of the main subsystems of the engine where the most varied and complex physical phenomena take place. Highly 3D flows, turbulent, dysphasic, mixed flows, complex chemical reactions, unsteady and multidimensional flow of heat transfer and radiative flows are some of the problems. The various applications of gas turbine engines have imposed various requirements for combustion system. Often, the various conflicting requirements placed on the combustion system can only be resolved by specialised designs. Among several calculations involved in the design of a combustion chamber, the reference area is the most important physical parameter, especially by the great impact on other dimensions. In general, this parameter must be calculated from an analysis of the limitations imposed both chemical reactions

R. Balijepalli · A. Dasore · U. Rajak · Y. Siva Kumar Reddy
Department of Mechanical Engineering, RGM College of Engineering and Technology, Nandyal,
Andhra Pradesh 518501, India

T. N. Varma (✉)
Department of Mechanical Engineering, Maulana Azad National Institute of Technology, Bhopal
462003, India

and aerodynamics, i.e. based on combustion process requirements and maximum pressure drop allowable in the combustion chamber, respectively [1, 2].

Dias et al. [3] were carried out numerical investigation of the impact of reference area of the combustion chamber on its velocity profile, temperature distribution, mixing process and flame behaviour. The results are compared with actual reference area calculated using analytical equations by Lefebvre [1]. Finally, it came to a conclusion that some modifications applied to reference area give the best results particularly by improving the combustion process and flame behaviour.

Overall design of a gas turbine and its parts works on producer gas was done by Srinivasa Sharma et al. [4]. It was observed that the energy density of producer gas with air is more than methane and other conventional liquid fuels, and the generation of NO_x is predicted at higher temperatures.

Chaudhari et al. [5] were carried out 3D numerical simulation (using Ansys CFX) of annular combustion chamber design of a 20 kW gas turbine working with kerosene as fuel. The results revealed that, as per their design, the combustion chamber may get burned due to the flame was touched the liner of it.

Three newly developed designs of combustion chamber were introduced by Ambrish Babu et al. [6] after successful trials. CFD analysis of these three models was carried out to investigate the exit temperature profile and pattern factor of a gas turbine combustion chamber. The outcomes showed that Design 3 gives the best performance results as compared to other two designs. A similar kind of work was executed by Balakrishnan et al. [7] to optimise the best design of combustion chamber of a gas turbine.

Sravan Kumar and Punna Rao [8] have been researched a 3D numerical design of complete gas turbine combustion chamber to examine various performance parameters such as temperature profiles and turbulence intensity of combustion process by choosing methane as working fuel. A maximum temperature of 2500 K is noticed during the combustion process, and also, the turbulent intensity nearer to injector was very high compared to its inlet which states that a superior air–fuel mixing and an efficient combustion process.

Alarami and Elfaghi [9] were done the theoretical design of combustion chamber of gas turbine to optimise its geometrical dimensions for achieving efficient combustion results. A similar kind of work was also done by Conrado et al. [10] to design and analyse the gas turbine.

A new mathematical model of primary area of turbojet engine was initiated, developed and tested by Davidovic [11] to determine the overall efficiency of combustion chamber. Tests agreed that the designed model can predict the operation of turbojet engine.

Theoretical design of gas turbine was studied by Hashim [12] in order to estimate various parameters such as length of flame tube, air flow distribution in the chamber, exit temperature, combustion reference area and stoichiometric air–fuel ratio. A similar kind of work is done by Priyant Mark and Selwyn [13] with the help of Ansys software.

A 3D numerical simulation of tubular-type combustion chamber of a gas turbine was carried out by Bhingade et al. [14], and the results were compared with existed experimental results and found a good agreement between them.

Effect of the dilution hole area on pattern factor of gas turbine combustor was numerically analysed by Ranjith et al. [15]. Results revealed that a decrease in dilution hole diameter is the most favourable condition improving pattern factor.

After going through a number of papers and designs for the combustion chamber, we were eager to design a combustion chamber with the least possible dimensions to cater to the need for lesser sized combustors, along with fulfilling other requirements of adequate temperature at the inlet of the turbine, so that the blades made up of expensive materials do not undergo undue thermal stress which leads to their damage, thereby increasing the turbine life which directly increases the effective life of the engine.

The main problem encountered during the reduction of the length of the liner of a combustor is the maximum exit temperature. The maximum outlet temperature remains high causing damage to turbine blades. This outlet temperature escalates to high values if the liner length is reduced even by a few units.

Pattern factor (PF) is a measure of the overall temperature distribution. It is one of the most important, at the same time, the most difficult problems in the design and development of gas turbines. A lower value of pattern factor, i.e. around 0.45–0.85, is desirable as it reflects the fact that the temperature is evenly distributed across the turbine blades without inducing much thermal stress on any particular section of the blade. In this paper, we have given major consideration in optimising the pattern factor after reducing the liner length to 152 mm, which is the least dimension in its class of combustors, and the next being 157 mm.

2 Methodology

The inlet parameters play a vital role in determining the dimension of the combustor. Apart from the inlet conditions, the exit temperature is another important consideration taken into account. The inlet conditions for the combustor, i.e. the condition of the air coming in after passing through the compressor stages is as specified in Table 1.

The most important dimension when designing a combustor is the reference area. The reference area is the effective area where the air is inlet into the annulus region

Table 1 Inlet parameters of the combustor

Parameter	Value
Temperature	743 K
Pressure	20.83 MPa
Air mass flow rate	28.71 kg/s
Fuel flow rate	0.638 kg/s

of the combustor. The shaft used to couple the turbine and the compressor passes through the centre around which an annulus combustion chamber is fitted.

The reference area (A_{ref}) is calculated using two different considerations, namely: chemical rate control and aerodynamic. The reference area is estimated using Eq. (1) by the aerodynamic consideration.

$$A_{\text{ref}} = \sqrt{\left[\frac{R}{2} \left(\frac{m_3 T_3^{0.5}}{p_3} \right) \left(\frac{\Delta p_{3-4}}{q_{\text{ref}}} \right) \left(\frac{p_3}{\Delta p_{3-4}} \right) \right]} \quad (1)$$

where R —gas constant (287 J/Kg.K), m_3 , T_3 , p_3 —combustor inlet values of mass flow rate, temperature and pressure, respectively, Δp_{3-4} —pressure loss along the combustor (usually taken as 6% of inlet pressure) and Q_{ref} —dynamic reference pressure.

Dynamic reference pressure (Q_{ref}) is calculated as using Eq. (2),

$$q_{\text{ref}} = 0.5 \rho_3 V_{\text{ref}}^2 \quad (2)$$

where V_{ref} is the reference velocity and is estimated by using Eq. (3).

$$V_{\text{ref}} = \frac{m_3}{\rho_3 A_{\text{ref}}} \quad (3)$$

An initial rough value of A_{ref} is assumed which is used to calculate the value of V_{ref} .

Reference diameter (D_{ref}) is evaluated using Eq. (4),

$$D_{\text{ref}} = \frac{\left\{ \sqrt{\left[A_{\text{ref}} + \left(\frac{\pi D_{\text{in}}^2}{4} \right) \right] \left(\frac{4}{\pi} \right)} - D_{\text{in}} \right\}}{2} \quad (4)$$

where the inner diameter of the combustor (D_{in}) is taken as 380 mm, which is a standard size. After the reference area, the liner area is calculated using Eq. (5). Liner area varies from $0.65A_{\text{ref}}$ to $0.67A_{\text{ref}}$. Hence, the liner area is taken as

$$A_L = 0.66 A_{\text{ref}} \quad (5)$$

The annulus area (A_{an}) is the difference between A_{ref} and A_L and can be evaluated from Eq. (6),

$$A_{\text{an}} = A_{\text{ref}} - A_L \quad (6)$$

After finding out the areas, the liner length is calculated followed by the other dimensions. Liner length is calculated using Eq. (7), in such a way that the temperature at exit does not exceed the temperature of 2150 °C. For this purpose, the liner length must be chosen adequately, and it must be neither too small nor too long as it will give either a higher temperature or a low value of thrust.

$$L_L = \frac{(-D_L)}{0.05 \left(\frac{\Delta p_L}{q_{ref}} \right) \ln(1 - PF)} \quad (7)$$

where D_L —liner diameter, Δp_L —pressure loss across the liner and PF—pattern factor. A liner pressure loss of about 3% is assumed. The PF used for design calculation purpose is 0.25.

PF is estimated using Eq. (8),

$$PF = \frac{(T_{max} - T_4)}{(T_4 - T_3)} \quad (8)$$

where T_4 is exit temperature and T_{max} is maximum exit temperature.

The length of each zone is calculated with the help of the formulas (Eqs. 9, 10) mentioned below: Primary zone length is estimated by Eq. (9),

$$L_{PZ} = \frac{3}{4} D_L \quad (9)$$

And, secondary zone length is evaluated by Eq. (10),

$$L_{SZ} = \frac{1}{2} D_L \quad (10)$$

The remainder length is taken as the dilution hole length and is estimated by Eq. (11),

$$L_{DZ} = D_L [3.83 - (11.83 PF) + (13.4(PF)^2)] \quad (11)$$

For calculating the number and dimensions of the main holes in each zone and also the cooling holes, the required mass flow rates and bypass ratio are critical. In a jet trainer aircraft, the bypass ratio is very low. The mass flow rate for the liner is found to be 4.2 kg/s, whereas for the casing, spacing is 7.77 kg/s. The ratio of casing mass flow rate to liner mass flow rate gives the bypass ratio, which equals to 1.8. Hence, it is a low bypass.

The air passing through the swirler is the mass flow rate through the liner inlet spacing, which is 4.2 kg/s, i.e. 14.6% of total air. The air in the casing space is the bypass air and is almost about 28% of the total air. The lower limit of air flow is taken through each zone, leaving about 25% air for the cooling purpose (shown in Table 2).

Table 2 Air flow rate through various regions

Region	Percentage of air flow (%)
Bypass	20–40
Swirler	12–20
Primary zone	15–20
Secondary zone	8–10
Dilution zone	8–10

In order to provide 15% of air in the primary zone, a total of 36 holes, on each of outer and inner liner, are taken. The diameter of each hole can be taken as 15.12 mm. Only 8% air is required in the other two zones; hence, the number of holes is taken to 20 in each zone on each liner. These holes have a diameter of 15.02 mm.

The cooling air required is 25.3%. In order to provide this quantity of cooling air, cooling holes are provided in each of the three zones. A total of 740 cooling holes are taken on each liner. These 740 holes are divided into 3 zones as: 250 + 240 + 250. The 250 holes in a primary zone are of 3.95 mm in diameter, whereas the 240 holes in the secondary zone are 2.4 mm. The remaining 250 holes in the dilution zone are of 3.29 mm in diameter.

The diffuser and the swirler are other parts that are designed as required. The length of the diffuser plays a vital role in helping the compressed air to bring to acceptable velocity levels so that the combustion takes place within the primary zone of the combustor. The diffuser length is taken as 50 mm. Generally, the diffuser angle varies from 14° to 20°. For our design, we chose the angle to be 18°, which helped us achieve an acceptable velocity of 35.83 m/s.

The swirler is responsible for creating the toroidal vortex that is necessary for the creation of turbulence to ensure the proper mixing of the air–fuel mixture. The swirler blades perform the previously said functions. These blades are given a twist of about 60°–80°. The spray cone angle which sprays the fuel in the combustor is usually taken as 75°. In our design, the blade angle taken was equal to 80°. This value of the blade twist led to a proper turbulent air–fuel mixture being created. There were 18 swirlers placed in the circular region which are equispaced to each other.

Finally, the exhaust is designed such that it mixes well with the cold jet of air coming from the bypass without adversely impacting the output thrust. To get a thrust, the combusted mixture must pass through a nozzle. If the nozzle length is too large, the thrust is reduced; if it is too small, the exit temperature remains considerably high. Therefore, a compromise between the two was achieved with an exit nozzle of 25 mm. The liner spacing at the exit was taken as 36 mm.

The first design or our base design did not give satisfactory results, which led us to make a few changes in the geometry of the combustion chamber to get the desired result. A number of changes were made in successive designs before arriving to a final geometry that gave the desired output characteristics.

The dimensions of the base design area as tabulated in Table 3.

The details about the holes of the combustor are presented in Tables 4 and 5.

Table 3 Geometric values for base design

Geometric detail	Notation	Dimension/value
Reference area	A_{ref}	0.08217 m ²
Dynamic reference pressure	Q_{ref}	6271.30 Pa
Reference velocity	V_{ref}	35.83 m/s
Internal diameter	D_{in}	380.00 mm
Reference diameter	D_{ref}	60.00 mm
Liner area	A_L	0.0524 m ²
Liner diameter	D_L	42.00 mm
Liner length	L_L	152.00 mm
Primary zone length	L_{PZ}	32.00 mm
Secondary zone length	L_{SZ}	21.00 mm
Dilution zone length	L_{DZ}	49.00 mm
Liner inlet spacing		10.00 mm
Casing inlet spacing		27.00 mm
Diffuser length		50.00 mm
Diffuser angle		180
Swirler blade angle		800
Swirler diameter		20.00 mm
Swirler length		10.00 mm
Fuel nozzle diameter		6.00 mm
No. of swirlers		18 units
Bypass ratio		1.8:1
Exhaust nozzle length		25 mm
Liner exit spacing		36 mm
Casing exit spacing		40 mm

Table 4 Main holes on each liner in base design

Zones	Number of holes	Diameter of holes (mm)
Primary	36	15.12
Secondary	20	15.02
Dilution	20	15.02

Table 5 Cooling holes on each liner in base design

Zones	Number of holes	Diameter of holes (mm)
Primary	250	3.95
Secondary	240	2.4
Dilution	250	3.29

Table 6 Geometric design values for the final design

Geometric detail	Notation	Dimension/value
Reference area	A_{ref}	0.08217 m ²
Dynamic reference pressure	Q_{ref}	6271.30 Pa
Reference velocity	V_{ref}	35.83 m/s
Internal diameter	D_{int}	380.00 mm
Reference diameter	D_{ref}	60.00 mm
Liner area	A_L	0.0524 m ²
Liner diameter	D_L	42.00 mm
Liner length	L_L	152.00 mm
Primary zone length	L_{PZ}	60.00 mm
Secondary zone length	L_{SZ}	15.00 mm
Dilution zone length	L_{DZ}	32.00 mm
Liner inlet spacing		10.00 mm
Casing inlet spacing		27.00 mm
Diffuser length		50.00 mm
Diffuser angle		18°
Swirler blade angle		80°
Swirler diameter		20.00 mm
Swirler length		10.00 mm
Fuel nozzle diameter		6.00 mm
Swirler diffuser length		30 mm
No. of swirlers		18 units
Bypass ratio		1.80:1
Exhaust nozzle length		20 mm
Liner exit spacing		34 mm
Casing exit spacing		40 mm

The major dimensions remained same in all the changed geometries, with little tweaking done to finer details like number and dimension of main holes and cooling holes. In a few designs, baffles were added to the main holes to create turbulence and ignite the fuel in the primary zone. The overall length of the combustor remained constant, while the lengths of individual zones were changed.

A major change in the final design was the removal of main holes from the secondary zone. The dimension of cooling holes was more or less the same, but the number of holes was changed. The length of primary and dilution zones was increased considerably, while the secondary zone length was reduced to a minimal. After doing the changes, the final geometry at which we arrived had the following values and presented in Table 6.

The details about the holes of the combustor are as follows: Main holes and cooling holes on each liner are represented in Tables 7 and 8, respectively.

Table 7 Main holes on each liner for final design

Zones	Number of holes	Diameter of holes (mm)
Primary	36	12
Dilution	18	15.12

Table 8 Cooling holes on each liner for final design

Zones	Number of holes	Diameter of holes (mm)
Primary	162	4
Secondary	234	2.5
Dilution	234	3

All the calculations done using the formulas gave values which became the base values of our model. These values were then later edited to suit the outlet requirements. The changes in the model were made after precisely considering all the factors and also keeping in mind the technical limitations and demands. Using all the calculations done with the help of the formulas stated above, all the design values were found out. These values were then used to model the combustion chamber in CATIA. After the design was done, the CAD model was then analysed on Ansys, with the given set of boundary conditions (shown in Fig. 1).

In order to get the desired pattern factor and exit temperature with the required liner length, a number of different designs were considered. A lot of modifications were done to the initial design, which acted as the base model on which the geometric changes were done. The boundary conditions provided for running of iteration on all the designs were same and were taken as the inlet conditions of the combustor. Since taking the entire designed model for the purpose of analysis on ANSYS would be cumbersome and time consuming, a 20° cut section was taken which could then be rotated and replicated to get the entire output profile.

Before starting the run, the designed model was meshed with a tetrahedral mesh in Ansys ICEM CFD, and all the necessary geometric clean up was done in the same on each design in consideration. After geometric clean up and meshing are done, the design is imported into Ansys CFX where the boundary conditions are given and the

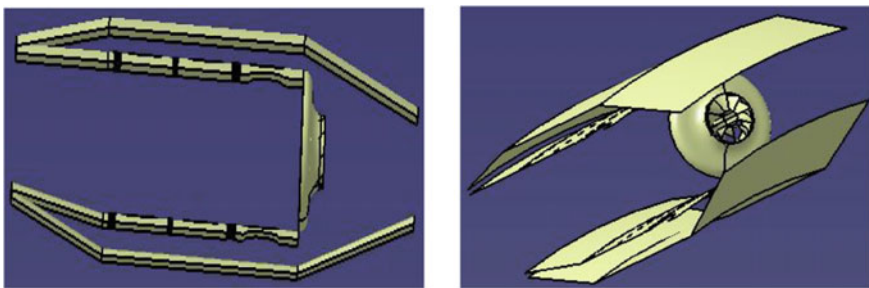


Fig. 1 a Side view and b Oblique view of cut section of combustor

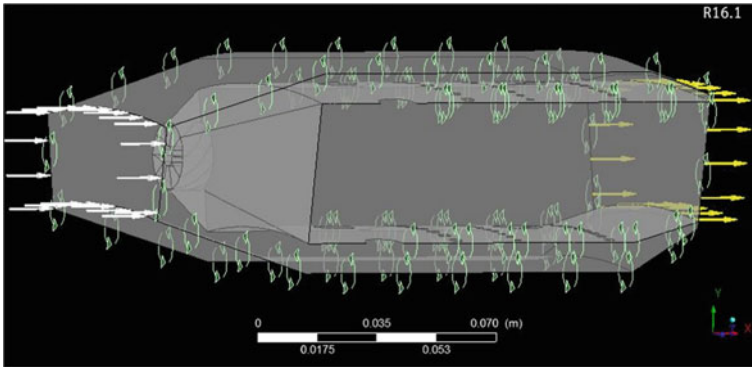


Fig. 2 Boundaries constrained and defined

fluid domain is specified. Each face of the model is given the attributes, and the test run is initiated (Fig. 2).

3 Results and Discussion

After an ample number of iterations, when the output result attains a steady state (i.e. converged), the reading of the maximum and average exit temperatures was recorded. Thus, after performing test runs on four designs (Model 1, Model 2, Model 3 and Model 4), the desired output was achieved. These recorded temperatures were used to calculate the pattern factor.

3.1 Model 1

The contours of temperature were estimated for different planes of Model 1 and shown in Figs. 3 and 4. In the first model shown in analysis, the exit profile was as follows: maximum temperature—2641.28 K, average temperature—1417.41 K and pattern factor—1.83.

The pattern factor obtained in the base model was 1.83. This is a lot higher than the desired value. The pressure loss was only 0.13% which is way to less for real purpose. In order to get a lower pattern factor, there were a few changes made to the base design. The main holes in the dilution zones were removed and instead a row of cooling holes was added. In addition to the previously mentioned changes, there were baffles that were also added to the main holes in the primary zone. This did help to reduce the pattern factor to 1.63. The pressure loss was increased to a much more suitable value of 3.58%. Though the values improved from the previous design, it was still not suitable for practical purposes.

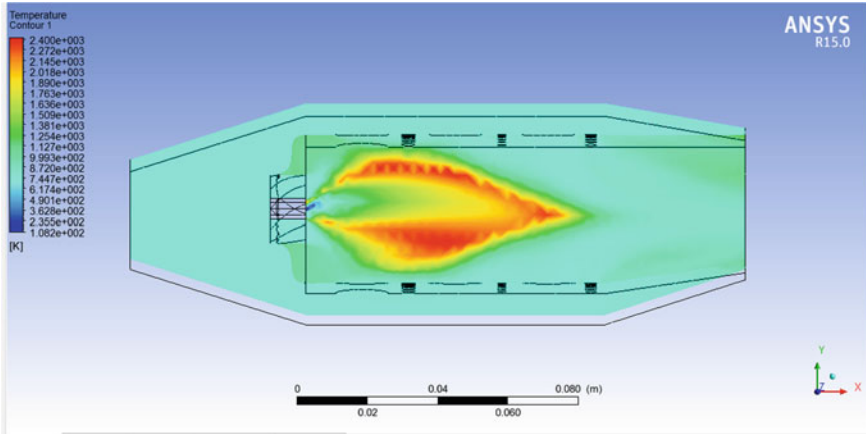


Fig. 3 Model 1 temperature contour in XY plane

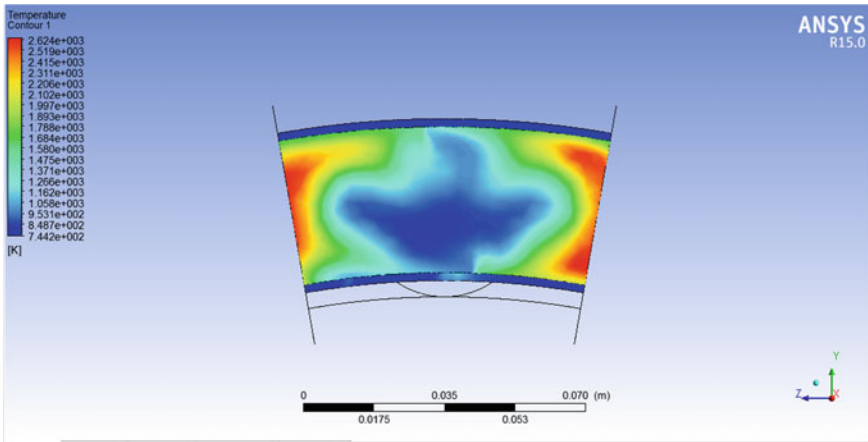


Fig. 4 Model 1 outlet temperature contour in YZ plane

3.2 Model 2

The contours of temperature were estimated for different planes of Model 2 and shown in Figs. 5 and 6. In the first model shown in analysis, the exit profile was as follows: maximum temperature—2407.07 K, average temperature—1379.02 K and pattern factor—1.63.

On further changes from the previous design, the baffles from the main holes in the primary zone were eliminated, and also, the extra row of cooling holes in dilution zone was also removed. This gave a much more desirable patter factor of 0.95. The

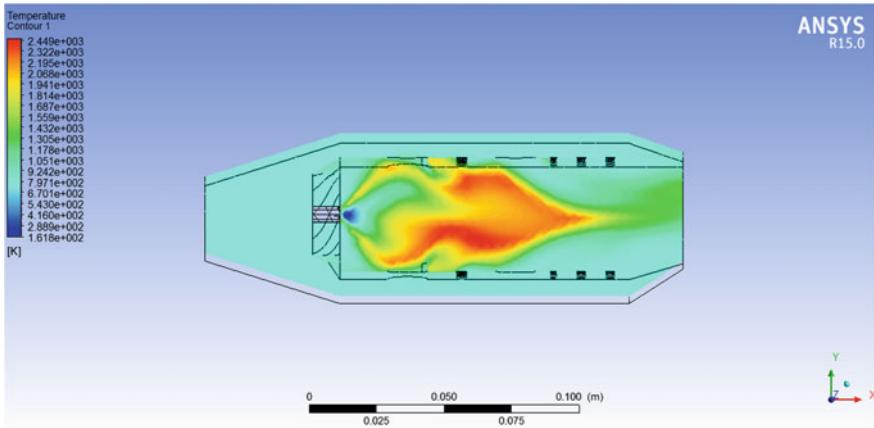


Fig. 5 Model 2 temperature contour in XY plane

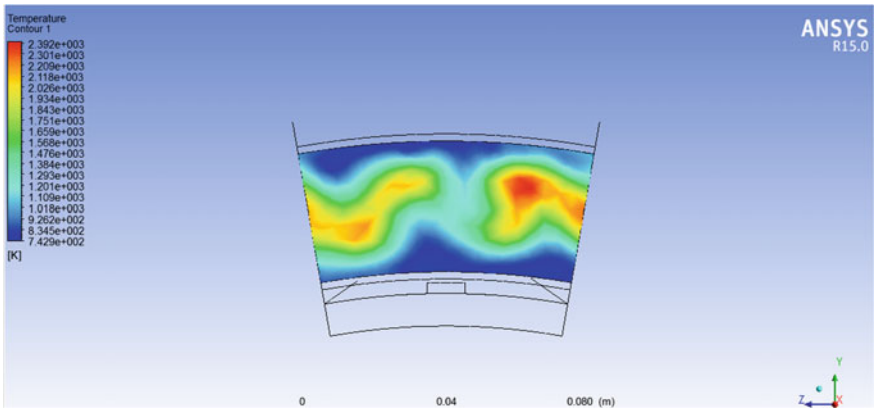


Fig. 6 Model 2 outlet temperature contour in YZ plane

average and maximum exit temperatures were also within the desired limits. The only drawback of this design was a not-so-desirable outlet profile.

3.3 Model 3

The contours of temperature were estimated for different planes of Model 3 and shown in Figs. 7, 8 and 9. In the first model shown in analysis, the exit profile was as follows: maximum temperature—2072.2 K, average temperature—1425.5 K and pattern factor—0.95.

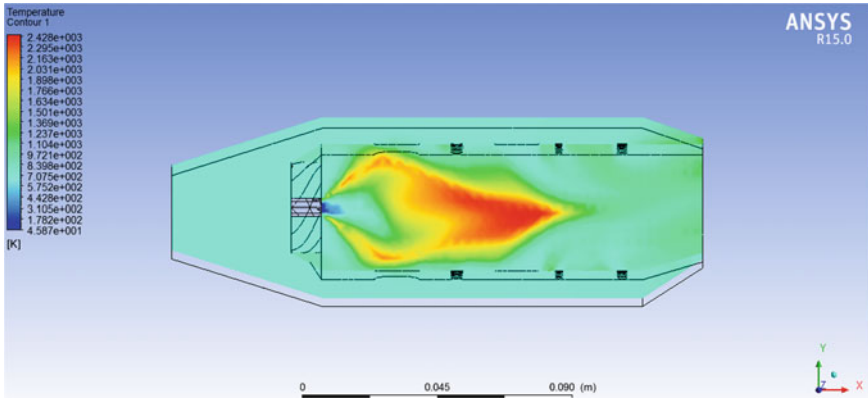


Fig. 7 Model 3 temperature contour in XY plane

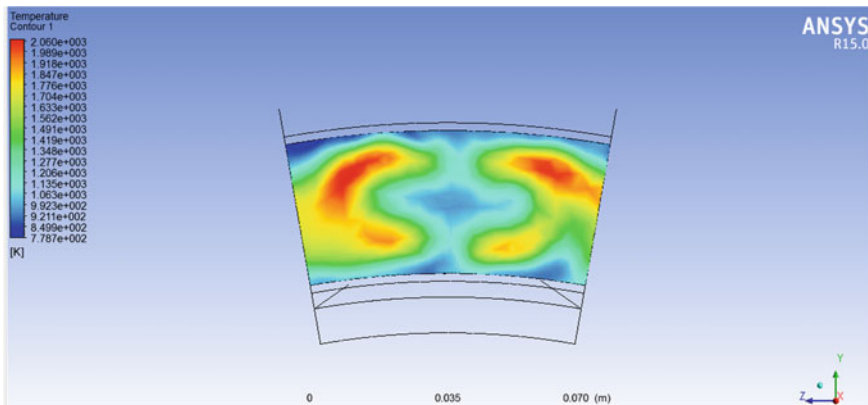


Fig. 8 Model 3 outlet temperature contour in YZ plane

In order to address the drawbacks of the previous model, a few more changes were made to the design. In this, the main holes in the secondary zone were eliminated while adding these in the dilution zone. In this model, the combustion is completed in the primary zone with the unburnt residual fuel being burnt in the secondary zone. The pattern factor achieved with this design was an exemplary 0.935. The exit temperatures were also very good. The outlet temperature profile is almost the ideal profile required for a combustor. It is evident that these results are not desirable and will cause damage to turbine blades. Hence, the final design (Model 4) taken into consideration corrects the mistakes in the previous designs and gives a more satisfactory output.

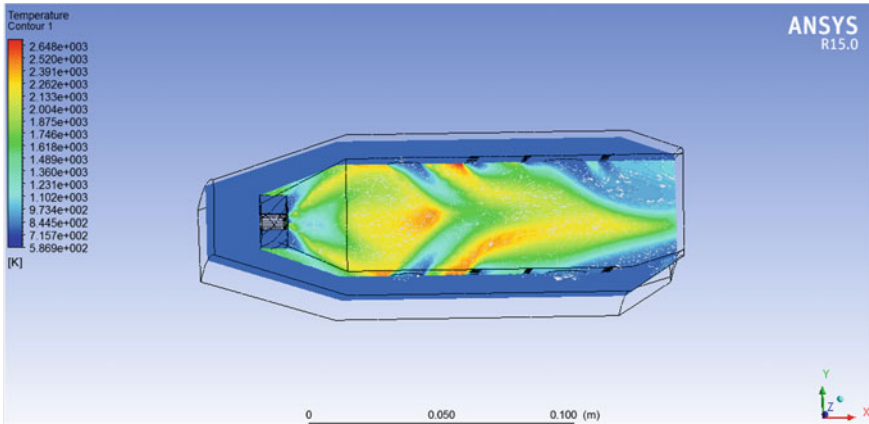


Fig. 9 Model 4 temperature contour in XY plane

3.4 Model 4

The contours of temperature were estimated for different planes of Model 4 and shown in Figs. 9 and 10. In the first model shown in analysis, the exit profile was as follows: maximum temperature—2407.07 K, average temperature—1379.02 K and pattern factor—1.63.

Therefore, it can be concluded that the design and analysis of the designed combustion chamber are successful as it optimise the designed model to a large extent to get the desired pattern factor and outlet temperature profile.

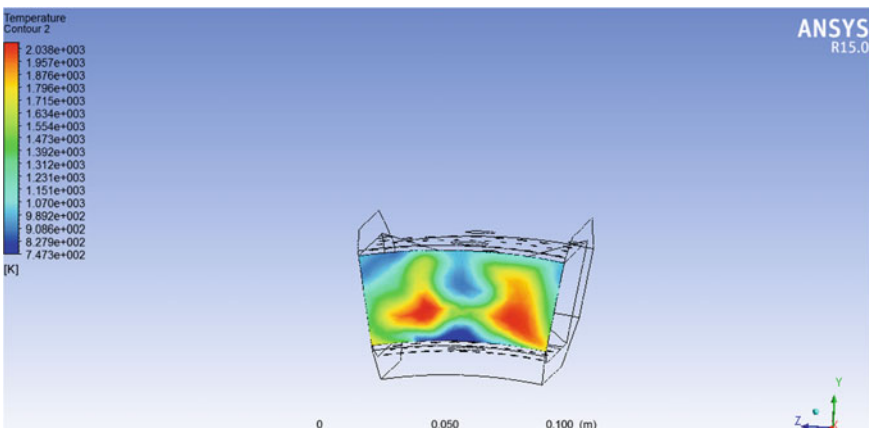


Fig. 10 Model 4 outlet temperature contour in YZ plane

4 Conclusion

The optimised design of the combustion chamber in a gas turbine is a key element of this present paper. The current methodology investigates the calculation of primary design parameters from benchmarking of ongoing industry standards and achieving optimised parameters. The several geometric dimensions of the combustion chamber are estimated dependent on various empirical equations. The entire combustion chamber is numerically simulated by using Ansys software, and results are presented. Four newly developed designs were taken into consideration to carry out CFD simulation. The maximum temperature, average temperature and pattern factor for all the four design models were estimated and concluded that Model 4 gives the best output results.

References

1. Lefebvre AH (1998) Gas turbine combustion, 2nd edn. Taylor & Francis, USA
2. Cohen, Rogers (1996) Gas turbine theory, 4th edn. Dorling Kindersley (India) Pvt. Ltd, India
3. Dias FLG, do Nascimento MAR, de Oliveira Rodrigues L (2014) Reference area investigation in a gas turbine combustion chamber using CFD. *J Mech Eng Autom* 4(2):73–82
4. Srinivasa Sharma G, Murali Krishna MVS, Reddy DN (2015) Design and analysis of gas turbine combustion chamber for producer gas as working fuel. *Int J Curr Eng Technol* 5(1):444–447
5. Chaudhari KV, Kulshreshtha DB, Channiwala SA (2012) Design and CFD simulation of annular combustion chamber with kerosene as fuel for 20 kw gas turbine engine. *Int J Eng Res Appl* 2(6):1641–1645
6. Ambrish Babu D, Arun KK, Anandanarayanan R (2012) Optimization of pattern factor of the annular gas turbine combustor for better turbine life. *IOSR J Mech Civil Eng* 5(1):30–35
7. Balakrishnan BM, Mohana Priya G, Revathi M (2016) Numerical simulation on the pattern factor of the annular combustor. *Int J Innov Res Sci Eng Technol* 5(4):6503–6509
8. Sravan Kumar P, Punna Rao P (2016) Design and analysis of gas turbine combustion chamber. *Int J Comput Eng Res* 3(12):36–40
9. Alarami AM, Elfaghi AM (2014) Optimum design procedures of turbojet combustion chamber. In: 2nd International conference on advances in engineering sciences and applied mathematics, Istanbul (Turkey)
10. Conrad A, Lacava P, Carlos A, Filho P, Departamento de Física, Milton de Souza Sanches (2004) Basic design principles for gas turbine combustors. In: Proceedings of the 10th Brazilian congress of thermal sciences and engineering—ENCIT 2004, Brazilian Society of Mechanical Sciences and Engineering—ABCm, Rio de Janeiro, Brazil
11. Davidovic N (2017) Mathematical model of turbojet engine combustion chamber primary zone. *FME Trans* 35(1):29–34
12. Hashim SA (2013) Design and fabrication of an annular combustion chamber for the micro gas turbine engine applications. *Int J Eng Res Technol* 2(8):1307–1314
13. Priyant Mark C, Selwyn A (2016) Design and analysis of annular combustion chamber of a low bypass turbofan engine in a jet trainer aircraft. *Propul Power Res* 5(2):97–107
14. Bhimgade HA, Mahatme CA, Barve PS, Gedam ND (2016) CFD approach as design optimization for gas turbine tubular combustor. *J Res Eng Appl Sci* 1(2):92–102
15. Ranjith PV, Shivashankar M, Sivaramakrishna G, Vimala N (2014) Reduction of gas turbine combustor pattern factors using CFD. *Int J Eng Res Technol* 3(6):1786–1791

Thermo-Economic Optimization of Spiral Plate HX by Means of Gradient and Gradient-Free Algorithm



Musunuru Hari Krishna, Abhishek Dasore , Upendra Rajak ,
Ramakrishna Konijeti , and Tikendra Nath Verma 

Nomenclature

A	Heat exchange area (m^2)
B	Width of the plate (m)
C_p	Specific heat (J/K)
C	Cost
D	Diameter (m)
GA	Gradient algorithm
GFA	Gradient-free algorithm
h	Heat transfer coefficient (W/m^2K)
H	Hours
K_{plate}	Thermal conductivity of the plate (W/mK)
L	Plate length (m)
\dot{m}	Mass flow rate of fluid (kg/s)
i	Annual discount rate
Δp	Pressure drop
Q	Heat flow rate (W)

M. H. Krishna

Department of Mechanical Engineering, SRK Institute of Technology, Vijayawada 521108, India

A. Dasore · U. Rajak

School of Mechanical Engineering, RGM College of Engineering and Technology, Nandyal
518501, India

M. H. Krishna · R. Konijeti

Department of Mechanical Engineering, Koneru Lakshmaiah Education Foundation,
Vaddeswaram, Guntur 522502, India

T. N. Verma (✉)

Department of Mechanical Engineering, Maulana Azad National Institute of Technology, Bhopal
462003, India

R_f	Fouling factor ($m^2 K / W$)
S	Plate spacing (m)
T	Temperature (K)
U	Overall heat transfer coefficient ($W / m^2 K$)
x	Thickness of the plate (m)
η	Pump efficiency
ρ	Density of the fluid (kg / m^3)

Subscripts

mc	Manufacturing cost
oc	Operating cost
ec	Energy
m	Mean
min	Minimum
max	Maximum
h	Hydraulic
f	Fluid
hi	Hot in
ci	Cold in
co	Cold out
ho	Hot out
Outer	Out side
Plate	Wall/plate
Hot	Hot side
Cold	Cold side

1 Introduction

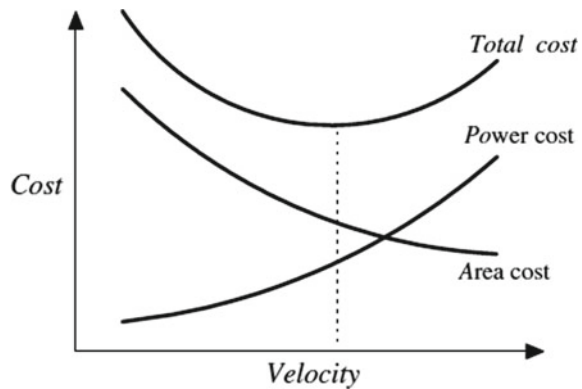
HXs are the devices utilized for the efficient transmission of heat energy from one system to the other. A basic heat exchanger consists of two flow streams of hot and cold fluids which are parted by a solid wall. The quantity of heat transfer relies on factors such as fluid flow type, heat transfer area and thermal conductivity of the wall [1]. SPHX refers to a pair of long flat plates that are looped to form two conduits in a counter-flow arrangement. SPHX is simple, sophisticated, the concentric shape of the flow passageways, and the studs generate turbulence even at the lower Reynolds number [2, 3]. SPHXs are common in petrochemical, food, paper industries for evaporation and condensation processes. These are ideal for cooling slurries and fluids with high viscosities [4, 5].

Optimization of heat exchangers is a challenging area. Optimization quest may be viewed as a design procedure, in which any number of feasible parameters will be examined according to the requisites. Diminishing the capital costs of material and running costs of energy requirements are major goals for industrial applications of heat exchangers [6]. But simultaneously, design of HXs includes intricate procedures, viz. choosing geometrical and dynamic constraints for design, cost approximation and maximization. Usually, the design job is a complex examination method (trial and error process), due to the combined values of constraints of geometry, in addition to this, the designed HX is assessed with reference to the state of specific requirements like exit temperature, heat load and pressure decrement [7]. From this viewpoint, there is a continuous scope that the intended outcomes are not the optimal. Therefore, investigators attempt to enhance thermal equipment via optimization methods and many thought-provoking and efficient works have been reported in recent time [8, 9].

Wang et al. [10] created a new procedure for optimizing HX designs, and they validated the proposed technique by an industrial circumstance application. A novel and efficient software has been developed by Jia et al. [11, 12] to optimize a heat exchanger in which data procurement and process diagrams are encompassed. Reneaume et al. [13] developed mathematics-based formulations for optimizing HXs and proposed a tool for the CAD. They also elucidated the solution approaches under several designs and working constraints. Recently, GA and GFA have gained much consideration in thermal engineering for resolving real-life problems [14]. Applications of these algorithms into HXs optimization have a robust capability of exploration and joint maximization and can effectively enhance and envisage thermal problems.

In the optimization of HXs, a trade-off between heat transmission and pressure diminution should be considered as shown in Fig. 1. In general, high flow velocities indicate a large heat transfer coefficient and hence a lesser heat transfer area and subsequently lower initial cost. However, high velocities will usually lead to large pressure fall and hence a high-power consumption and large operational costs [15, 16]

Fig. 1 Economic optimization of HXs



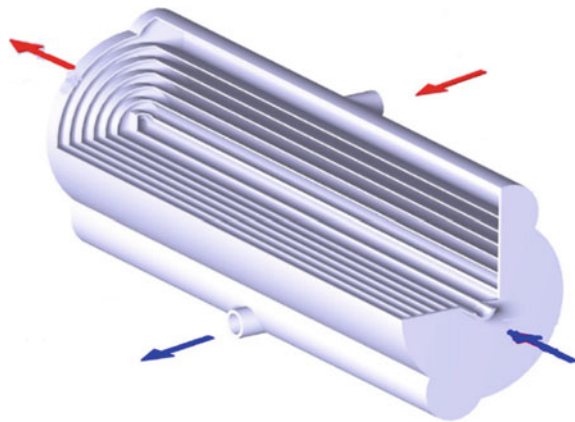
In the current examination, GA technique ‘fmincon’ and GFA method ‘genetic algorithm’ are used to obtain optimal design of the SPHE with the design variables being pressure drop on hot and cold fluids, outer spiral diameter, length and width of the plate. Minimization of the total cost, i.e. the operating cost and the initial investment, is considered as cost function. In order to demonstrate the potentiality of fmincon and genetic algorithm case, studies reported by Segundo et al. [17] were considered. The proposed methods of fmincon and genetic algorithm are not novel, but the application of these into SPHE maximizations for different objectives with various restraints is attractive, and the outcomes are expectantly interesting which are beneficial for further exploration.

2 Physical Model and Design Conditions

From the literature analysis, it is noticed that high effectual, small space, less weight and low price are the common goal in SPHX design. In practicality, there are two design prerequisites. The first one is to reduce the space and annual price of the SPHX as much as attainable under a specified efficacy and a permissible pressure loss. The second requisite is to enhance the efficacy significantly. Before the start of optimal design of SPHX is conducted, the optimization goal should be examined based on the distinct requisites. Predominately, the lowest total space and annual price are analysed in the present investigation. In addition, the lowest pressure falls of both hot and cold sides of SPHX are also taken as an objective.

In the present work, a SPHX is examined. A typical cross-sectional view of SPHX is shown in Fig. 2. For such a SPHX, the two fluids are in counter-flow arrangement with various mass flow rates under designated heat load. There are numerous geometrical constraints which may be considered as maximization variables like pressure fall on both sides, exit diameter of spiral passages, length and width of spiral plate.

Fig. 2 Schematic of SPHX with the indication of inlets and outlets for both fluids



The materials of the plate are stainless steel (*UNSS30400*) with thermal conductivity of $14W/mK$. A thumbnail description of the GA, GFA and selection of variables and constraints are elucidated in subsequent section for better understanding.

Wind-driven optimization adopted by Segundo et al. [17] uses Lagrangian description of flow process due to its infinitesimal fluid particle collection motion. In the present work, *fmincon* and genetic algorithms are adopted. The *fmincon* a GA technique is the best approach for nonlinear optimization problems, since, even if run with random start, it is still faster than other methods and often results in fewer function cells. It employs a Hessian as an optional feed in [18]. The genetic algorithm a GFA is maintained by a population of parent individuals that represent the latent solutions of a real-life problem. For example, the design engineer may inscribe the design constraints into corresponding binary string that is represented as individual [19]. An exact variety of sets of design constraints correspondingly become a population of parent individuals. Figure 3 shows the flowchart of the GFA [20]. Every individual is assigned a fitness supported on how well every individual fit a given ambient and then is assessed by survival of fitness. Fit individuals undergo the method of survival

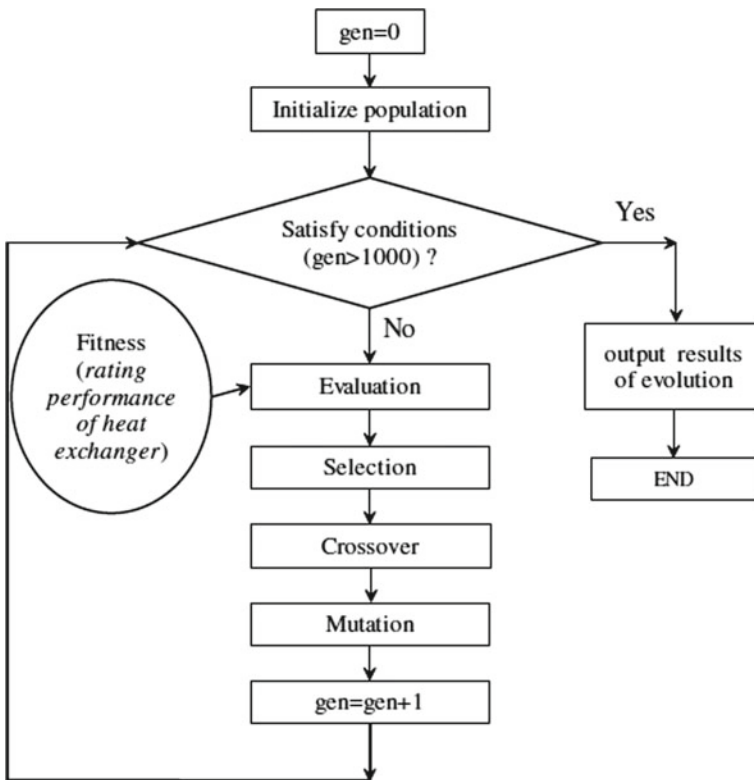


Fig. 3 Flowchart of genetic algorithm

choice, crossover and mutation, leading to make next generation, called kid individuals. A novel population is therefore established by selecting good individuals from parent and kid individuals. After some generations, the algorithm has converted to the best individual, that in all probability indicates the best resolution of the given drawback [21].

3 Optimization

3.1 Mathematical Modelling

The thermal equilibrium for a heat exchanger is given by Eq. (1).

$$Q = m_h C_h (T_{hi} - T_{ho}) = m_c C_c (T_{co} - T_{ci}) \quad (1)$$

The physical principle is law of conservation of energy, with an assumption of adiabatic boundary condition with the surrounding. When the temperatures at inlet and outlet are pre-defined, novel method to evaluate the overall heat transfer coefficient (U) is to utilize the concept of logarithmic mean temperature difference (LMTD), and the heat duty is calculated as given in Eqs. (2–5).

$$Q = U \times A \times LMTD \quad (2)$$

$$U = \frac{1}{\frac{1}{h_{hot}} + \frac{1}{h_{cold}} + \frac{x}{k_{plate}} + R_f} \quad (3)$$

$$LMTD = \frac{(T_{hi} - T_{co}) - (T_{ho} - T_{ci})}{\ln\left(\frac{T_{hi} - T_{co}}{T_{ho} - T_{ci}}\right)} \quad (4)$$

$$A = 2 \times L \times B \quad (5)$$

The Reynolds number (Re), Prandtl number (Pr) and Nusselt number (Nu) are attained from following Eqs. (6–10)

$$Re = \frac{m D_h}{B S \mu} \quad (6)$$

$$Pr = \frac{\mu C_p}{k} \quad (7)$$

$$Nu = 0.239 \times \left(1 + 5.54 \frac{D_h}{D_m}\right) Re^{0.806} Pr^{0.268} \quad (8)$$

$$D_m = \frac{D_{\min} + D_{\max}}{2} \quad (9)$$

$$D_h = \frac{2BS}{B + S} \quad (10)$$

By evaluating the Nu, it is feasible to find the heat transfer coefficient by Eq. (11)

$$h = \frac{k_f \times \text{Nu}}{D_h} \quad (11)$$

The pressure drop is obtained by Eq. (12).

$$\Delta p = 0.00085 \times \frac{Lm^2\rho}{B^2S^2} \quad (12)$$

The outer diameter of the spiral is given by Eq. (13)

$$D_o = \sqrt{[1.28L(S_h + S_c + 2x) + D_{\text{core}}^2]} \quad (13)$$

The total cost is obtained by summing up the manufacturing cost (C_{mc}) and operational cost (C_{oc}) expressed by Eq. (14)

$$C_{\text{total}} = C_{mc} + C_{oc} \quad (14)$$

The manufacturing cost (C_{mc}) is a function of surface of the heat exchanger and is given by Hall equation

$$C_{mc} = 5973 \times A^{0.59} \quad (15)$$

The operational cost can be calculated as follows

$$C_{oc} = \sum_{k=1}^{ny} \frac{C_o}{(1+i)^k} \quad (16)$$

where $C_o = P \times C_{ec} \times H$; and

$$P = \frac{1}{\eta} \left(\frac{m_{\text{hot}}}{\rho_h} \times \Delta p_h + \frac{m_{\text{cold}}}{\rho_c} \times \Delta p_c \right) \quad (17)$$

3.2 Objective Function

The total of a SPHE includes the manufacturing and operating cost, and this is to be minimized.

$$\text{Minimize } J = C_{\text{total}} = C_{mc} + C_{oc} \tag{18}$$

The following are the four constraints in this optimization study, and they are with regard to the pressure drop that occurs as the fluid stream through hot and cold sides, the total heat load limitation and the size limitation of the SPHE.

$$\Delta p_{\text{hot}} - 0.00085 \times \frac{(Lm_{\text{hot}}^2 \rho)}{B^2 S^2} = 0 \tag{19}$$

$$\Delta p_{\text{cold}} - 0.00085 \times \frac{(Lm_{\text{cold}}^2 \rho)}{B^2 S^2} = 0 \tag{20}$$

$$D_{\text{outer}} - [1.28L(S_h + S_c + 2x) + D_{\text{core}}^2]^{0.5} = 0 \tag{21}$$

$$Q - (U \times 2LB \times LMTD) = 0 \tag{22}$$

All these constraints are highly nonlinear. The design constraints in the investigation to be optimized are pressure drop in the hot as well as cold fluids, outer diameter, length and width of SPHE. The values of their upper and lower limits of all the design parameters are given in Table 1.

The optimized results from the present study are compared with the wind-driven optimized results. The physical properties of hot and cold streams are adapted from Moretta et al. [22] and cross-verified in Bidabadi [23] and are mentioned in Table 2.

Additional information needed to calculate the operating costs and heat transfer coefficients are mentioned in Table 3.

Table 1 Upper and lower limits of the design constraints

Property	Hot fluid stream	Cold fluid stream
Pressure drop in hot fluid	127.75	18.92
Pressure drop in cold side	298.60	273.15
Outer diameter	298.15	285.93
Length	4186.80	3786.12
Width	0.05	2.3

Table 2 Property values of hot and cold fluid streams

Property	Hot fluid stream	Cold fluid stream
Mass flow rate (Kg/s)	127.75	18.92
Inlet temperature (K)	298.60	273.15
Outlet temperature (K)	298.15	285.93
Specific heat capacity (J/kgK)	4186.80	3786.12
Density (kg/m^3)	1350	1000
Viscosity ($Pa.s$)	0.10353	0.00122
Velocity (m/s)	4.4006	3.2597

Table 3 Details for optimization

Parameter	Value
Number of years, N_y	15
Discount rate, I	0.1
Energy cost per watt hour	0.00012
Annual work hours ($h/year$)	8000
Thermal conductivity of material (W/mK)	14.532
Fouling factor (m^2K/W)	0.000347
Core diameter (m)	0.3048

4 Results and Discussion

For a specified heat duty (Q), gradient and gradient-free optimization techniques ‘fmincon and genetic algorithm’, respectively are used to obtain the optimized design variables stated in Table 1. The stream properties for the simulation were taken from case study Moretta et al. [22] as stated in Table 2. MATLAB optimization toolbox was used to perform optimization, and tolerance for constraints was set to $1e^{-06}$.

It can be noticed from Table 4 that GFA outperformed wind-driven algorithm and fmincon. GA converges to a cost of 20, 572 where a fmincon converges to a cost of

Table 4 Comparison of present results with reported works

Parameter	Moretta et al. [22] (case study)	Segundo et al. [17] (WDO)	Present work (fmincon)	Present work (genetic algorithm)
$(\Delta P)_{hot}$	110.190	111.198	107.254	163.78
$(\Delta P)_{cold}$	85.430	45.195	43.592	66.56
D_s	0.849	2.280	1.5	1.5
L	7.8170	5	5	7.367
B	0.9144	0.6720	0.855	0.56
U	1113	75	1551.314	1606.6
C_{total}	44,813	18,186	20,941.279	20,572

20941.279, which is about 13.5 and 11.5% higher than the wind-driven algorithm. Even though the goal of the optimization was to minimize the cost, it can be observed that the overall heat transfer coefficient (U) which signifies the physical process of interest is about 95% higher than WDO and 30.7% higher than the case study.

The increase in the cost in the GA as compared to WDO can be quantified to the increased overall heat transfer coefficient. However, the computation time for genetic algorithm is higher than fmincon. For a preliminary analysis with constraint on computation time and facility, it is advisable to utilize gradient-based optimizer fmincon.

From Figs. 4, 5 and 6, it can be observed that fmincon converges to optimized value in two iterations but iterations continued up to four in order to satisfy the specified tolerance constraints on functional and constraint values, whereas GA searches for

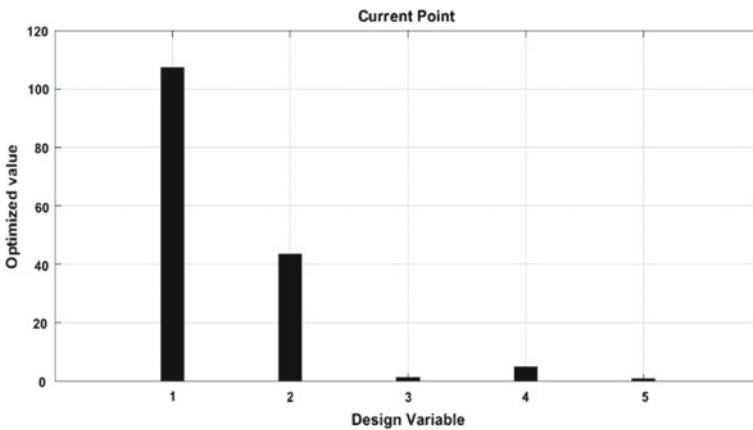


Fig. 4 Optimized parameter plot for fmincon

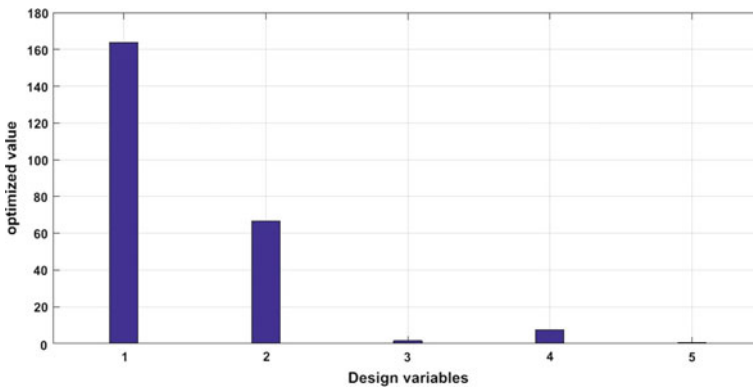


Fig. 5 Optimized parameter plot for GA

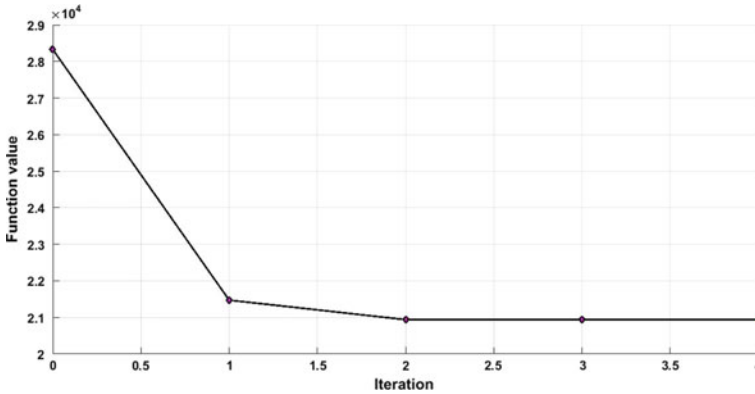


Fig. 6 Variation of objective function with iteration for fmincon

the optimized values in the complete range with random updates of design variables, thereby increasing the number of functional evaluations.

5 Conclusions

In the current investigation, thermo-economic modelling and maximization techniques are employed to attain the optimum values of design constraints of SPHX. Therefore, the extensive thermodynamic modelling of this SPHX is carried out utilizing MATLAB software program and subsequent inferences are drawn:

1. A novel objective function which comprises manufacturing and operating costs is defined.
2. The fmincon and gradient algorithm are applied effectively to the multi-objective maximization of SPHX.
3. The cost of SPHX obtained by fmincon is 53.2% lesser than the ones reported in case study and 13.1% higher than WDO.
4. The cost of SPHX attained by GA is 54% lesser than the one reported in case study and 11.5% higher than WDO.
5. It is concluded that the genetic algorithm can be employed in optimizing the design configurations of SPHX according to various design constraints, viz. minimum surface area and cost.
6. The present analysis can form a basic paradigm in optimizing the designs of various types of HXs.

References

1. Sarma PK, Ramakrishna K, Subramanyam T, Prasad LSV, Korada VS, Srinivas V, Dharma Rao V, Prasad VSRK (2017) Fouling and its effect on the thermal performance of heat exchanger tubes. *Int J Heat Tech* 35(3):509–519
2. Madhuri CR, Ramakrishna K, Abhishek D (2019) Heat transfer enhancement using hybrid nanofluids in spiral plate heat exchangers. *Heat Transf Asian Res* 48:3128–3143
3. Fraas A (1989) *Heat Exchanger Design*. Wiley-Interscience, New York
4. Metta VR, Ramakrishna K, Abhishek D (2018) Thermal design of spiral plate heat exchanger through numerical modeling. *Int J Mech Eng Tech* 9(7):736–745
5. Bebs T, Roetzel W (1992) Distribution of heat flux density in spiral heat exchangers. *Int J Heat Mass Transf* 35(6):1331–1347
6. Bes T, Roetzel W (1993) Thermal theory of the spiral heat exchanger. *Int J Heat Mass Transf* 36(3):765–773
7. Saravanan K, Rajavel R (2008) An experimental investigation of heat transfer coefficients for spiral plate heat exchanger. *Mod Appl Sci* 2(5):14–20
8. Muralikrishna K, Shenoy UV (2000) Heat exchanger design targets for minimum area and cost. *Trans Inst Chem Eng* 78:161–167
9. Jafari Nasr MR, Polley GT (2000) An algorithm for cost comparison of optimized shell-and-tube heat exchangers with tube inserts and plain tubes. *Chem Eng Technol* 23:267–272
10. Wang L, Sunden B (2001) Design methodology for multistream plate–fin heat exchangers in heat exchanger networks. *Heat Transf Eng* 22:3–11
11. Jia R, Sunden B, Xuan Y (2001) Design and optimization of compact heat exchangers. In: Shah RK (ed), 3rd international conference on compact heat exchangers and enhancement technology for the process industries, Davos, Switzerland, pp 135–142
12. Jia R, Sunden B (2003) Optimal design of compact heat exchangers by an artificial neural network method. In: Proceedings of HT2003, ASME summer heat transfer conference, Paper No HT2003-47141
13. Reneaume JM, Niclout N (2003) MINLP optimization of plate fin heat exchangers. *Chem Biochem Eng Q* 17:65–76
14. Unuvar A, Kargici S (2004) An approach for the optimum design of heat exchangers. *Int J Energy Res* 28:1379–1392
15. Traverso A, Massardo AF (2005) Optimal design of compact recuperators for micro-turbine application. *Appl Therm Eng* 25:2054–2071
16. Sachin G, Narasimha KK, Ramakrishna K, Abhishek D (2018) Thermodynamic analysis and effects of replacing HFC by fourth generation refrigerants in VCR systems. *Int J Air-conditioning Refrig* 26(1):1850013-1–1850013-12
17. Segundo EHV, Mariani VC, Coelho LDH (2015) Spiral heat exchanger optimization using wind driven algorithm, In: XII Brazilian symposium of smart intelligent automation (SBAI) Natal-RN
18. Byrd RH, Mary EH, Nocedal J (1999) An interior point algorithm for large-scale nonlinear programming. *SIAM J Optim* 9(4):877–900
19. Coleman TF, Li Y (1996) An interior, trust region approach for nonlinear minimization subject to bounds. *SIAM J Optim* 6:418–445
20. Wu R, Zhang X, Fan Y, Hu R, Luo X (2019) A Bi-Layer compact thermal model for uniform chip temperature control with non-uniform heat sources by genetic-algorithm optimized microchannel cooling. *Int J Therm Sci* 136:337–346
21. Konda JR, Madhusudhana Reddy NP, Konijeti R, Dasore A (2019) Effect of non-uniform heat source/sink on MHD boundary layer flow and melting heat transfer of Williamson nanofluid in porous medium. *Multidiscip Model Mater Struct* 15(2):452–472

22. Moretta AA (2010) Spiral plate heat exchangers: Sizing units for cooling non-Newtonian slurries. *Chem Eng. (New York—Mcgraw Hill Incorporated then Chemical Week Publishing Llc)* 117(5):44–49
23. Bidabadi M, Sadaghiani AK, Azad AV (2013) Spiral heat exchanger optimization using genetic algorithm. *Sci Iran* 20(5):1445–1454

Numerical Investigation to Study the Effect of Inlet Inclination on the Turbulence Intensity of the Naturally Ventilated Room Using CFD



Ghogare Abhijeet Ganesh, Shobha Lata Sinha, Tikendra Nath Verma, and Satish Kumar Dewangan

1 Introduction

The study of indoor thermal comfort deals with the effect of various factors that contribute to maintaining a favorable environment for an indoor human being. The term comforts in indoor environment quality studies psychological sensations and physiological factors such as the combination of acoustics, thermal conditions, and visual and indoor air quality with the help of a mechanically controlled heating/cooling ventilation system [1]. Indoor environmental quality defines the combination of all the above factors. For many years, these factors were studied separately by different experts in the field. Studies show that there is a direct relationship between indoor environment quality (IEQ), occupant health, comfort, and productivity [2]. The four major components of IEQ are thermal comfort, indoor air quality, acoustic comfort, and visual comfort. Thermal comfort is the situation of the mind that expresses gratification with the thermal environment. Many factors influence the thermal comfort of the building occupants. These factors are: metabolic rate, mean radiant temperature, air temperature, clothing insulation, operative temperature, airspeed, relative humidity, and turbulence intensity [3]. All the above factors were studied carefully by many of the researchers but the effect of turbulence intensity is paid less attention by the many studies. The inlet boundary conditions get affected by the turbulence intensity [4]. In this study, efforts have been made to study the effect of inlet fresh air inclination on indoor turbulence intensity of airflow. This paper focuses on the following important sections.

G. A. Ganesh · S. L. Sinha · S. K. Dewangan
Department of Mechanical Engineering, National Institute of Technology, Raipur 492013, India

T. N. Verma (✉)
Department of Mechanical Engineering, Maulana Azad National Institute of Technology, Bhopal 462003, India

2 Physical Problem

2.1 CFD Model and Case Description

The 3D CFD model of the office with a size of $4.8 \times 2.6 \times 2.4$ m (L \times H \times W) was created with ICEM CFD software. The same office design was previously used in Oleson et al. in experimental work [5] and numerical work in Ganesh et al. [6]. The paper can refer to the details of the geometry. The room modeled by CFD is an empty office room with a double-panel radiator. The empty room was considered to study the indoor environmental conditions. Figure 1 shows the empty room, which consists of a double-panel radiator used for cold air heating purposes, window, insulated walls including the ceiling and flooring, a modifiable inlet, and an exhaust vent. The complete description of the geometric model is discussed in detail in the previous study [6]. The occupied zone has been created in the modeled empty office. The occupied zone in the office is the area 0.6 m away from every wall and up to the height of 1.8 m, which is generally the preferred zone for a human being for occupation. To analyze the comfort parameters in the occupied zone, four observation lines (l_1 , l_2 , l_3 , and l_4) were drawn at a distance of $X = 0.6, 1.8, 3.0, 4.2$ m in the modeled fluid field of the office. The median plane that passes through the origin and is upright to

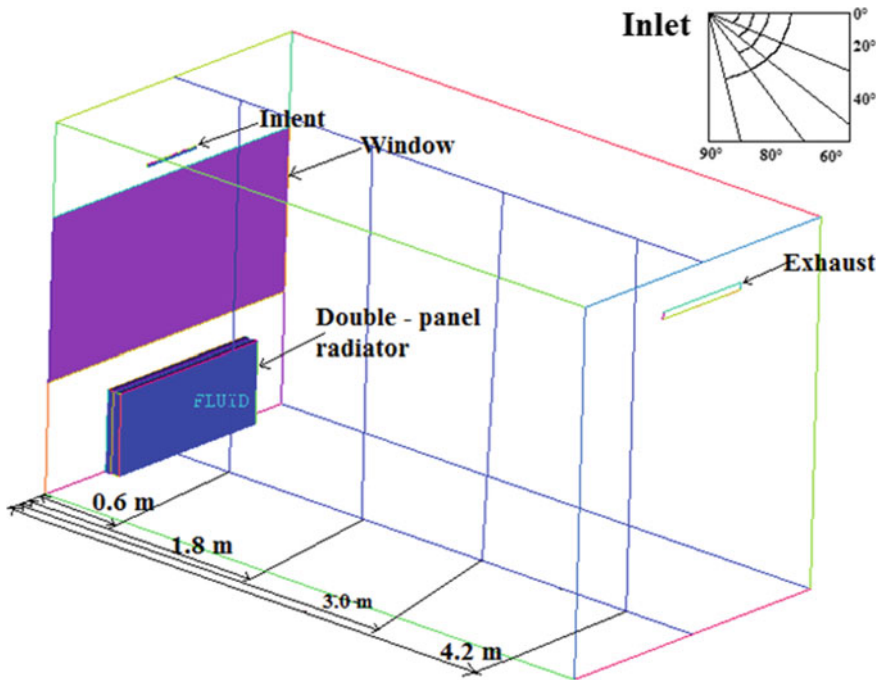


Fig. 1 Schematic representation of 3D modeled office

Table 1 Case study table

Case no	Inlet inclination (Degrees)
Inclination angle (1)	0
Inclination angle (2)	20
Inclination angle (3)	40
Inclination angle (4)	60
Inclination angle (5)	80

the YZ plane ($Z = 0$) was likewise traced to study the overall comfort condition in the room (Fig. 1).

The above office was modeled to analyze the indoor comfort environment required for the modeled room in cold weather conditions. Ambient thermal conditions in winter can be very cold, and therefore, the fresh $-5\text{ }^{\circ}\text{C}$ inlet air stream was taken from a modifiable inlet. The initial indoor air temperature was patched to $16\text{ }^{\circ}\text{C}$. All the walls were perfectly delimited and isolated to avoid the interface of heat between the interior and exterior environment of the room. For a favorable indoor environment, the temperature in the occupied zone should be kept in the range of $20\text{--}23\text{ }^{\circ}\text{C}$ [3]. The constant heat flux for the dual panel radiator was provided to retain indoor thermal comfort. For a required indoor environment, the inlet air change rate kept constant at 7.3 l/s (0.8 h^{-1}) [7].

2.2 Case Description and Boundary Conditions

The detailed case studies performed are listed in Table 1. The present study carried out numerically using the following five cases. The five independent models were used to study the effect of inlet air inclination on turbulence intensity of airflow. The basic boundary conditions used in the study are listed in Table 2.

3 Numerical Methodology

Numerical study of the above problems needs to solve the governing equations of mass, momentum, and energy listed below, in Eqs. (1–5) [8]. For all types of flows, ANSYS FLUENT resolves conservation equations for mass and momentum. The problems involving heat interaction, energy conservation equations must be solved. Different types of turbulent models are available in Ansys fluent, the suitable turbulent model needs to be selected for the flow field analysis.

$$\frac{\partial \rho}{\partial t} + \nabla \cdot (\rho \vec{V}) = 0 \tag{1}$$

Table 2 Boundary conditions

Geometry	Boundary conditions
Inlet (1) Temperature (2) Air velocity	$T_{\text{air}} = -5 \text{ }^\circ\text{C}$ $v_{\text{air}} = 0.7 \text{ m/s}$
Exhaust	Outflow
Window surface temperature	$T_w = 14 \text{ }^\circ\text{C}$
Walls	Insulated
Double-panel radiator	Constant heat flux To maintain 40–42 °C surface temperature
Turbulent model	k–ε Standard
Radiation scheme	DO Radiation
Pressure scheme	SIMPLE algorithm, 2nd order

$$\frac{\partial(\rho u)}{\partial t} + \nabla \cdot (\rho u \vec{v}) = -\frac{\partial p}{\partial x} + \frac{\partial \tau_{xx}}{\partial x} + \frac{\partial \tau_{yz}}{\partial y} + \frac{\partial \tau_{zx}}{\partial z} + \rho f_x \tag{2}$$

$$\frac{\partial(\rho v)}{\partial t} + \nabla \cdot (\rho v \vec{v}) = -\frac{\partial p}{\partial y} + \frac{\partial \tau_{xy}}{\partial x} + \frac{\partial \tau_{yy}}{\partial y} + \frac{\partial \tau_{yz}}{\partial z} + \rho f_y \tag{3}$$

$$\frac{\partial(\rho w)}{\partial t} + \nabla \cdot (\rho w \vec{v}) = -\frac{\partial p}{\partial z} + \frac{\partial \tau_{xz}}{\partial x} + \frac{\partial \tau_{yz}}{\partial y} + \frac{\partial \tau_{zz}}{\partial z} + \rho f_z \tag{4}$$

$$\frac{\partial}{\partial t}(\rho E) + \nabla \cdot (\vec{v}(\rho E + p)) = \nabla \cdot \left(k_{eff} \nabla T - \sum_j h_j \vec{J}_j + \left(\vec{\tau}_{eff} \cdot \vec{v} \right) \right) \tag{5}$$

Reynolds averaged Navies–Stokes equation was solved using k–ε turbulence model. The DO radiation model was employed to analyze the effect of thermal bands of the radiator.

4 Result and Discussion

The thermal comfort in the office room has been obtained using the heating double-panel radiator. The cold air entering the office is being heated by a double-panel radiator. The room air temperature was maintained at 23 °C for the thermal comfort of the indoor occupants. Figure 2 indicates the turbulent intensity variation due to the inlet air inclination. As the cold air enters from the inlet located exactly above the radiator, the cold air current tries to settle down on the ground due to its high density. Subsequently, the inlet cold air near the radiator gets heated and tries to move upward toward the ceiling. This flow of cold and downward flow of indoor air occurs due to the buoyancy effect. The buoyancy effect is stronger near the heating radiator

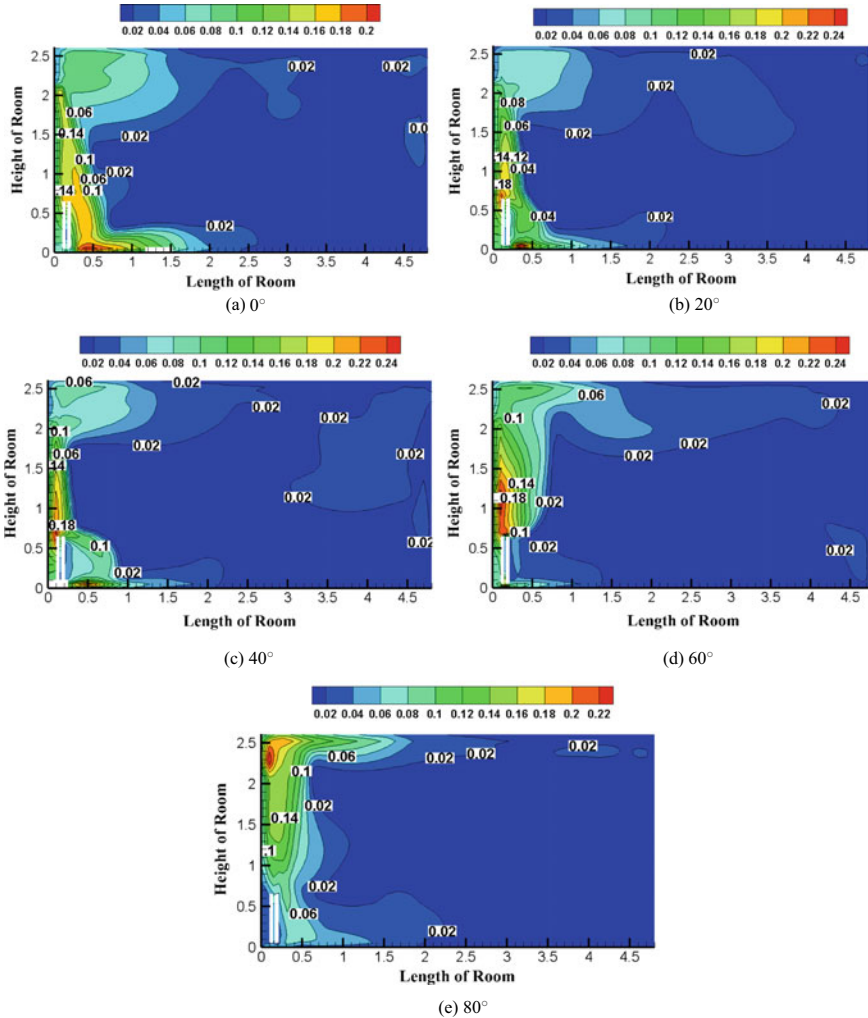


Fig. 2 Turbulent intensity outlines at mid-plane ($Z = 0$) in an office with different inlet vent angles **a** 0°, **b** 20°, **c** 40°, **d** 60°, **e** 80°

and inlet vent location. This mixing of hot and cold air in this region results in air circulations and swirl. The area of this region can be termed as a mixing area. This high-intensity circulation of air in the mixing area is measured in terms of turbulence. The turbulence also affects the thermal comfort of an occupant. The higher amount of turbulence of indoor air results in intense cold sensation to occupant and creates discomfort. For acceptable thermal comfort, the turbulence region should not interact with the occupied zone. Hence in this study, to control and reduce the mixing area various inlet vent inclinations were analyzed. From Fig. 2a–e, it can be seen that the area of the mixing region varies as the inlet inclination increases. It is observed that as

the inlet inclination increases the mixing region contracts at floor level and increases in the ceiling region. An increase in inlet inclination results in the mixing area since the cold air directly impinges on the radiator surface and gets heated immediately and reduces the mixing region length. From Fig. 2a–e, we can see that, as the inlet inclination increases the region of high turbulence (red-colored) of the fractional value of more than 0.2 shifts continuously upward in the y-direction. The higher turbulence in the ceiling region is acceptable as compared to the floor level. From Fig. 2e, we can see that the turbulence is minimum in the floor level and maximum in the ceiling region. This arrangement of inlet flow inclination is most favorable for thermal comfort as compared to the other inlet inclination settings.

5 Conclusions

Controlling only the turbulent intensity does not guarantee acceptable thermal comfort but there must be a proper balance between all the major thermal comfort parameters such as thermal comfort and air velocity [9]. But when analyzing the effect of inlet inclination on turbulence intensity the following outcomes can be drawn,

- The inclination of inlet flow affects the turbulence intensity in the mixing zone only.
- The buoyancy effect is predominant in the turbulence intensity.
- The increase in inlet inclination results in direct contact of cold and hot air, and it reduces the mixing zone.
- The occupancy in the mechanically controlled office should be away from the inlet vent and heating equipment to avoid discomfort due to turbulent intensity.
- For higher inlet inclination, the region of occupancy is larger and can be closer to the inlet vent and heating equipment.

References

1. Yang R, Wang L (2012) Multi-objective optimization for decision-making of energy and comfort management in building automation and control. *Sustain Cities Soc* 2(1):1–7. <https://doi.org/10.1016/j.scs.2011.09.001>
2. Yang W, Moon HJ (2019) Combined effects of acoustic, thermal, and illumination conditions on the comfort of discrete senses and overall indoor environment. *Build Environ* 148:623–633. <https://doi.org/10.1016/j.buildenv.2018.11.040>
3. International Standard Organization, ISO 7730 (2005) Ergonomics of the thermal environment—Analytical determination and interpretation of thermal comfort using calculation of the PMV and PPD indices and local thermal comfort criteria
4. Cao S-J, Meyers J (2013) Influence of turbulent boundary conditions on RANS simulations of pollutant dispersion in mechanically ventilated enclosures with transitional slot Reynolds number. *Build Environ* 59:397–407. <https://doi.org/10.1016/j.buildenv.2012.09.004>

5. Olesen BW, Mortensen E, Thorshauge J, Berg-Munch B (1980) Thermal comfort in a room heated by different methods, ASHRAE Transactions, Los Angeles Meeting, vol 86, Tech Paper no 2556
6. Ganesh GA, Sinha SL, Verma TN (2020) Numerical simulation for optimization of the indoor environment of an occupied office building using double-panel and ventilation radiator. *J Build Eng.* <https://doi.org/10.1016/j.jobe.2019.101139>
7. Al Assaad D, Ghali K, Ghaddar N (2018) The effectiveness of intermittent personalized ventilation assisting a chilled ceiling for enhanced thermal comfort and acceptable indoor air quality. *Build Environ* 144:9–22. <https://doi.org/10.1016/j.buildenv.2018.08.005>
8. ANSYS FLUENT 13 User's Guide. 2013. "Ansys Fluent Theory Guide." ANSYS Inc.,15317 (November): 724–746
9. Ganesh GA, Sinha SL, Verma TN (2020) Effect of inlet airflow direction on the indoor environment of a naturally ventilated room using CFD. ISSN: 2249-8958, vol 9, issue 3. <https://doi.org/10.35940/ijeat.C5112.029320>

Analysis of Solar Photovoltaic-Based Water Pumping System in Sehore, India



Shubham Mishra, Shrey Verma, Ambar Gaur, Subhashree Mohapatra, Subhankar Chowdhury, and Gaurav Dwivedi

1 Introduction

In rural areas and remote places where electrical energy supplied from the grid is minimal or unavailable due to various constraints [1], solar photovoltaic (SPV) system can be utilized to meet the energy requirement of the growing population all across the world as the availability of solar energy is abundant in almost all regions [2–4]. Earlier in the absence of energy from the grid to power the water pumping system, diesel generators were used which are not only expensive but also causes harmful emission to the environment [4]. Solar photovoltaic-based water pumping system (SPBWPS) requires no fuel for its operation and is environment friendly [5–7].

Energy generation from the SPV system depends on climatic conditions and energy from it is generated only during the availability of sunlight only [6]. Hence to ensure a reliable operation of water pumping system, battery energy storage unit, biodiesel-based generator, etc., are required [7]. The biodiesel-based generator has lower emissions levels as compared to the conventional diesel generator system [8].

The efficiency of SPBWPS depends on several factors including climatic conditions, SPV panels, energy storage energy backup units, power controllers, power converters and inverters, and pumps and motors [9–12]. The software used for simulation helps in system design and optimization of the available energy resources to get the best results [10]. Analysis of design and simulation results gives a brief view of the performance of the system and problems that needed to be rectified before deploying it on the field [11]. There are a lot of software options available to design SPBWPS including PVsyst software [13, 14]. The designing of the system is easy in PVsyst, and performance study of the system based on several parameters can be done using the graphical approach [15].

S. Mishra · S. Verma · A. Gaur · S. Mohapatra · S. Chowdhury · G. Dwivedi (✉)
Energy Centre, Maulana Azad National Institute of Technology, Bhopal 462003, India

In this work, PVsyst 7.1 is used to design the system for a location in Sehore, Madhya Pradesh, India. The groundwater information of the selected location is taken from [14]. The paper is divided into four sections. Section 2 contains the theoretical analysis of system design and simulation of the system using PVsyst 7.1, and Sect. 3 has a detailed discussion of the results. This work is done to perform design and simulation analysis of a SPBWPS. This work can be further extended to on-field implementation of the system and evaluate the difference between design performance and on-field performance of the system.

2 Methodology

2.1 Theoretical Analysis

This includes analysis of hydraulic power, sizing of PV array, sizing of the motor, and calculation of the system efficiency. Figure 1 shows the generalized representation of SPWPS [15]. As all the systems are interconnected in SPWPS with feedback using water level sensors in tank and groundwater, to control the working of whole system to make it more efficient. Controller unit controls the level of water in tank to avoid overflow, has maximum power point tracker (MPPT) to maximize the output of PV system with the variation of solar irradiance level, and controls the ON/OFF of pump based on the solar irradiance presence and water level in both ground and tank.

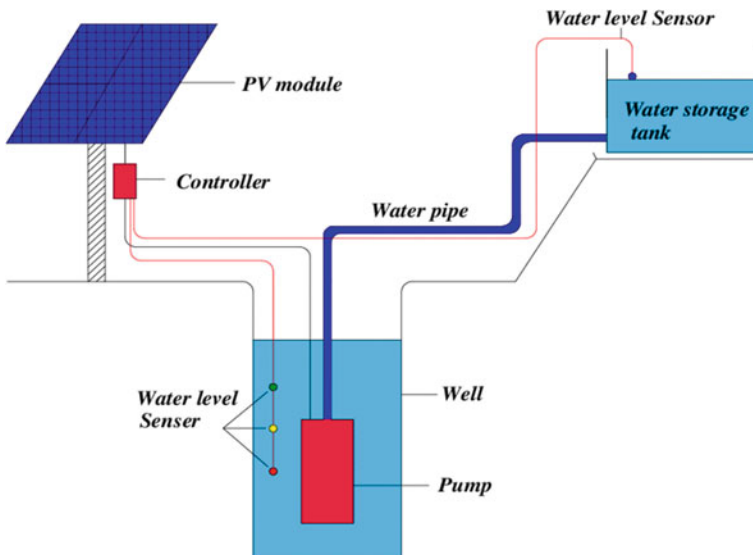


Fig. 1 Generalized representation of solar-powered water pump

Calculation of required Hydraulic power. Ideally, the hydraulic power required to drive the pump depends on.

- Mass flow rate of liquid
- Liquid density
- Differential height.

$$\text{Hydraulic power } P_H(\text{kW}) = \frac{\rho * Q * g * h}{3.6 * 10^6} \quad (1)$$

where

ρ = water density (kg/m³).

Q = discharge of water (m³/h).

g = acceleration due to gravity (9.8 m/s).

h = differential head (m), which is the difference in level of groundwater and tank upper level with the addition of frictional loss.

Motor sizing. The power generated by the PV array is fed directly to the DC motor with the help of controller that operates the pump. The amount of power required for the driving of (direct current) DC motor is depending on the pump efficiency as the motor drive the pump.

$$\text{Power required by motor } P_M(\text{kW}) = \frac{\text{Hydraulic power required by pump}}{\text{Efficiency of the pump}} \quad (2)$$

PV array sizing. The PV array sizing defines the total size of the solar PV system. The total power required also depends upon the system's efficiency.

$$\text{Total power required from PV array} = \frac{\text{Power required by motor}}{\text{Efficiency of the system}} \quad (3)$$

The input power to the system is calculated with the help of incident solar radiation of the solar panel surface.

$$P_i = G_i * A_c \quad (4)$$

where

G_i = Incident solar irradiance (W/m²).

A_c = Effective area covered by cells in module (m²).

The unit PV module power output is given by

$$P_o = V_{OC} * I_{SC} \quad (5)$$

No. of PV module required for array

$$\text{Total no PV module in array} = \frac{\text{Power output required from PV array}}{\text{Power output form unit module}} \quad (6)$$

PV array efficiency η_p is given by

$$\eta_p = \frac{\text{Total power used from PV array}}{\text{PV array capacity}} * 100 \quad (7)$$

PV array input power depends on the area covered by the array and the average total solar irradiance incident on the plane surface of the PV.

Theoretical mathematical calculation. Approximate water requirement for the day is 40m^3 for agriculture use, taking peak sun hour of 8 h/day. Duration of pumping = 6 h.

$$\text{Flow rate } Q(\text{m}^3/\text{h}) = 40/6 = 6.66 = 7 \text{ m}^3/\text{h}$$

$g = 9.8 \text{ m/s}^2$, $\rho = 1000 \text{ kg/m}^3$, $h = 33 \text{ m}$ (static head of 30 m with 10% of friction loss = total head of 33 m)

$$P_H = \frac{1000 * 9.8 * 7 * 33}{3.6 * 10^6} = 628.833 \text{ W} = 0.628 \text{ KW}$$

Pump power requirement (if pump efficiency is 49%) = $628.833/0.49 = 1283.33 \text{ W}$.

Total power required from PV array (if system efficiency is 81.4%) = $1283.33/0.814 = 1576.57 \text{ W} = 1.576 \text{ kW}$.

Input power to the system from annual solar irradiance, where $G_i = 5.18 \text{ W/m}^2/\text{day}$ and $A_c = 16 \text{ m}^2$.

Then $P_i = 5.18 * 16 = 82.88 \text{ kWh/day}$.

The unit PV module power output, where $V_{OC} = 14.7 \text{ V}$ and $I_{SC} = 8.84\text{A}$.

Then $P_o = 14.7 * 8.84 = 130 \text{ W}$.

No of PV module required = $2000/130 = 15.38 \approx 16$ panels approx.

Efficiency of PV array = $1576/2000 = 0.788 = 78.8\%$.

2.2 Simulation of Design Using PVsyst 7.1

Details of water well location. The detailed location of the water well is presented in Table 1. Water level and depth of the well are decided based on the data Ground Water

Table 1 Location and water well information

Name of location for system installation	Sehore, Bhopal, Madhya Pradesh
Latitude	23.21° N
Longitude	77.08° E
Altitude	496 m
Name of water resource	Deep well to storage
Application	Irrigation
Diameter of well	15 cm
Static level depth	30 m
Pump level	50 m

Information Booklet, Sehore District, Madhya Pradesh. Sehore District is nearby of Chambal and Narmada river basin, which makes the predominately agriculture-based economy in this district. As the major of the irrigation sources are groundwater either by tube wells or dug wells [14].

Details of the pump, water storage, and piping network. There are variety of pumps available in market such as submersible, floating and surface water pump which is further divided into helical, diaphragm type, centrifugal, positive displacement type, divided shaft pump type, whose efficiency varies from 40 to 60% [16]. Table 2 represents the details of the pump, water storage, and piping network. In simulation, a centrifugal multistage-type pump is used powered by DC brushless motor of 1500 W with a head of 20–70 m, flow rate at 7.7–4.07 m³/h. Water tank is assumed made up of fibreglass reinforced plastic of capacity 45m³ and kept at height of 1 foot, to make gravity flow of water to the irrigation fields, connected with a polyethylene (PE50) category of 2-inch piping system.

Details of PV array. PV array made up of silicon cells system utilizes the visible length spectrum rays of sun ranging from 300 to 1100 nm (nanometres) to generate electricity. PV array is made up of by combining various modules in series and

Table 2 Pumping system details

Type of pump	Centrifugal multistage
Supply type	DC, brushless
Power rating	1500 W
Name of manufacture	Generic
Volume of storage tank	45 m ³
Water requirement	40 m ³
Diameter	4.4 m
Height	3.0 m
Feeding altitude	4 m
Size of pipe	2"

Table 3 Information about PV array

Name of manufacture	Vikram solar
Model name	Generic Mono 130Wp 36 cells
Type of cell	Si-mono
No of modules	16
Power rating per unit module	130 Wp
Voltage rating	14.7 V
Current rating	8.84 A
Total power capacity of PV array	2 kW

parallel connections as per voltage and current requirements at converter level [6]; here we have used 8 modules in series and 2 modules in parallel covering an area of 16m². Table 3 describes the detail of the PV array used.

Monthly climatic data of the location. The climatic data include global horizontal radiation, diffuse, direct radiation, and temperature of the SPWPS site location in Table 4. Data is collected from Sehore_MN73.SIT Meteorom 7.3 (1981–2010), Sat = 100%. With the help of metrological data, the annual solar irradiance level of 5.18 W/m²/day is assumed. And based on the variation in season, a seasonal tilt adjustment of 20° in summer and 50° in winter with 0° azimuths is assumed.

Table 4 Monthly climatic data

Month	Global horizontal radiation (kWh/m ² /mth)	Diffuse radiation (kWh/m ² /mth)	Direct radiation (kWh/m ² /mth)	Ambient temperature (°C)
January	137.5	38.70	98.8	17.7
February	147.8	45.41	102.39	20.9
March	195.6	57.84	137.76	26.6
April	200.8	72.27	128.53	31.2
May	211.1	85.48	125.62	33.6
June	169.8	96.01	73.79	30.4
July	131.5	89.66	41.01	27.0
August	121.0	79.99	41.01	25.7
September	145.4	79.00	66.4	26.4
October	165.1	57.79	107.31	26.1
November	138.1	43.59	94.51	21.1
December	126.4	41.92	84.48	19.1
Total	1890.3	787.64	1102.66	25.6

Table 5 Main results obtained from simulation

Main simulation results		
System production	Water pumped—14,210 m ³	Specific—1945 m ³ /kWp/bar
	Energy at pump—2898 kWh	Specific—0.20 kWh/m ³
	Water needs—14,600 m ³	Missing water—2.7%
	Unused PV energy—539 kWh	Unused fraction—15.1%
	System efficiency—81.4%	Pump efficiency—48.5%
Investment	Global (incl. of 5% GST)—553,686 INR	Specific—266 INR/Wp
Yearly cost	Annuities (loan at 6% for 20 years)—19,309 INR/year	Running cost—10,100 INR/year
Water cost	2.06 INR/m ³	

3 Results and Discussion

3.1 Output of System Design Calculation

The system efficiency for the designed system from PVsyst7 is 81.4%. This result shows that most of the energy generated through PV strings is utilized by the submersible pump set and only 15.7% of generated energy is not utilized. The water pumping cost from the designed system is 2.06 INR/m³, which is very feasible in comparison with a conventional diesel engine water pumping set. Table 5 describes the result obtained from the simulation of PV-based water pumping set.

3.2 Performance Ratio

The performance ratio (PR) is the ratio of the measured output energy of the PV system to the expected output energy with the standard term and condition based on the system nameplate rating. For the designed system, PR is 0.656. Here for the calculation of PR includes the optical losses (Shadings, IAM, soiling), the array losses (PV conversion, ageing, module quality, mismatch, wiring, etc.), and the system losses (inverter efficiency in grid-connected, or storage/battery/unused losses in stand-alone, etc.). Figure 2 shows the PR for the year.

3.3 Normalized Production

Figure 3 shows the energy balance of the proposed solar water pumping system for the Sehore region, Bhopal site. As the figure explains, there is very low unused

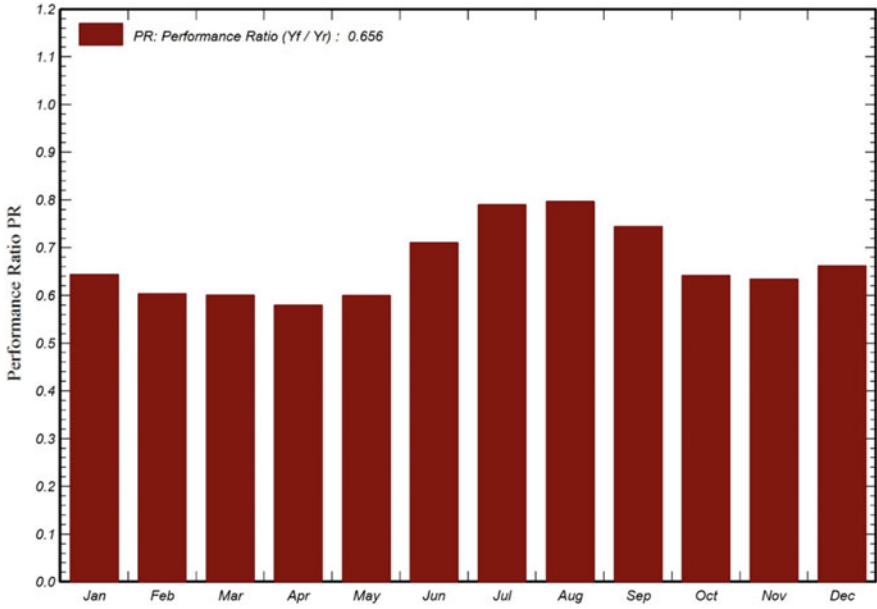


Fig. 2 Performance ratio of the system

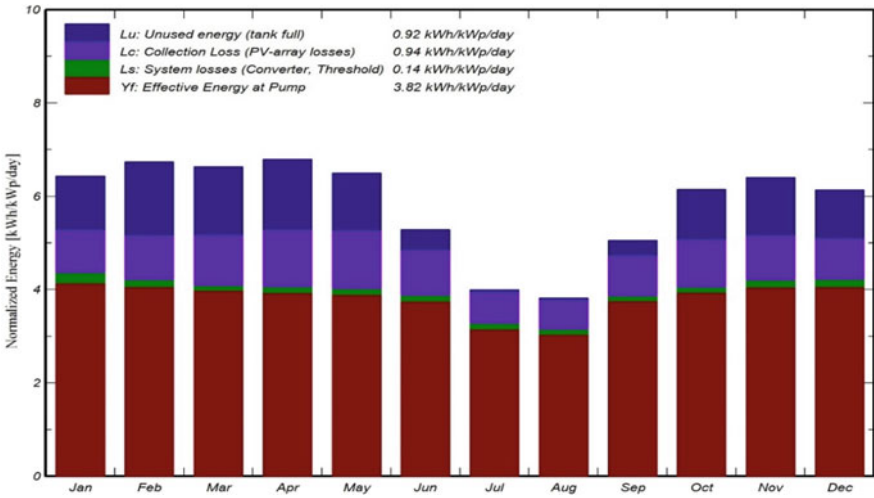


Fig. 3 Energy balance of the SPWPS for Sehore site: Nominal power 2080 Wp

energy for the given site, due to the system is designed based on the maximum water production volume within a year. It shows the normalized value of unused energy (tank full), collection loss (PV array loss), system loss and the effective energy at the pump. Unused energy in the system is minimum in comparison with the addition of collection and system loss, as the system is designed to deliver the maximum amount of water per day using all available energy resources. When it is desired to maximize the water, the output is subject to high losses, but if all of the losses are minimized, it will reduce the water output on a per-day basis and unused energy will be maximized.

3.4 Flow Rate Function of the Pump

Figure 4 shows the relationship between energy available at the pump and the average flow rate of the pump. It shows the almost linear relationship between the flow rate and the available energy at the pump. It shows how the flow rate, size of the pump depends on the availability of power. As there is a requirement for the pump controller for adjusting the size of the pump according to the available power at the pump.

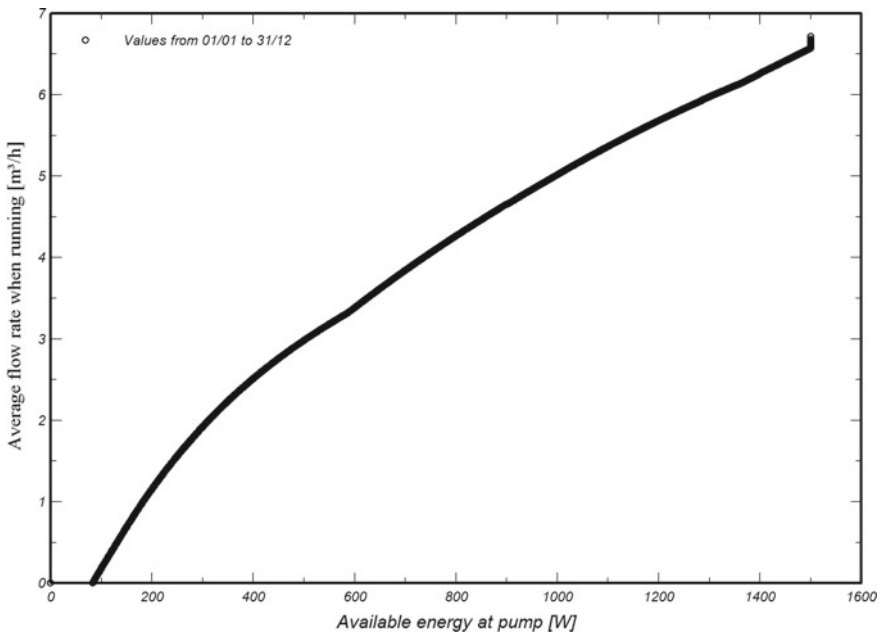


Fig. 4 Flow rate function of pumps power

Table 6 System summary, water and energy cost

Total installation cost	553,686 INR
Operating cost	10,000 INR/year
Energy used for pumping	2898 kWh/year
Excess energy (tank full)	539 kWh/year
Water pumped	14,210 m ³
Cost of pumped water	

3.5 Economic Calculation

Economic calculation of SPWPS has been accessed using PVsyst software to calculate the energy and water cost. The factors used for economic evaluation are installation cost, operating cost, depreciation and financial cost. Table 6 describes the system summary, water and energy cost.

Installation cost:

PV modules: 16 units * 5000 INR/unit = 80,000 INR.

Support for modules: 16 units * 145 INR/unit = 2320 INR.

Pump including controller (with a life span of 20 years): 1 unit = 35,000 INR.

Tank and hydraulic system: 260,000 INR.

Transport, engineering and drilling cost: 150,000 INR.

Overall cost (5% GST) = 553,686 INR.

Financing: It includes the depreciation cost, loan amount and interest.

Depreciation assets cost: 117,320 INR.

Subsidy: 332,211 INR (govt. provide 60% subsidy to promote the PV pump set for approaching towards renewable energy adoption).

Loan: 221,474 INR (at 6% interest rate for 20 years).

Water is a sale at the rate of 4 INR/m³.

Return on investment: As the pumped water is sold to the villages for irrigation at the rate of 4 INR/m³, as assumed the 20 years of project lifetime period.

Payback period: 15 years.

Net present value: 550,612.39 INR is the difference between the present value of cash inflows and the present value of cash outflows over a period of time.

Return of investment: 99.4%.

4 Conclusion

The present work shows an excellent and simplified approach for design optimization of the SPBWPS by employing a theoretical approach and using simulation software (PVsyst 7.1). The efficiency of the system which is designed on simulation software is calculated to be 81.4%. Also, the cost of water pumping from the designed system is 2.06 INR/m³, which highly feasible when compared with a conventional diesel engine water pumping set. The design analysis part plays a very crucial role in evaluating the system efficiency and cost of pumping the water. The simulation results help in understanding the system's performance before deploying it on the field. This study will be very helpful for budding scholars and researchers working in the field of SPBWPS. This work can be further extended to employing a tracking system for solar PV to increase the energy output and analysing the impact of using an energy storage system on increased operating hours of pumping operation.

Credit authorship contribution statement Shrey Verma: Simulation and writing the original draft. Shubham Mishra: Writing—review and editing. Ambar Gaur: Investigation, Subhashree Mohapatra: Data curation, Subhankar Chowdhury: Data curation Gaurav Dwivedi: Final drafting and conceptualization.

References

1. Rawat R, Kaushik SC, Lamba R (2016) A review on modeling, design methodology and size optimization of photovoltaic based water pumping, standalone and grid connected system. *Renew Sustain Energy Rev* 57:1506–1519. <https://doi.org/10.1016/j.rser.2015.12.228>
2. Mishra S, Verma S, Chowdhury S, Dwivedi G (2020) Materials today : proceedings analysis of recent developments in greenhouse dryer on various parameters—a review. *Mater Today Proc*, no. xxxx. <https://doi.org/10.1016/j.matpr.2020.07.429>
3. Korpale VS, Kokate DH, Deshmukh SP (2016) Performance assessment of solar agricultural water pumping system. *Energy Procedia* 90: 518–524. <https://doi.org/10.1016/j.egypro.2016.11.219>
4. Oyedokun OA, Achara N, Muhammed SU, Ishaq OO (2017) Design and simulation of solar powered water pumping system for irrigation purpose in Kaduna, Nigeria. *Int J Sci Eng Technol* 6(10):342. <https://doi.org/10.5958/2277-1581.2017.00053.5>
5. Yadav K, Kumar A, Sastry OS, Wandhare R (2019) An assessment for the selection of weather profiles for performance testing of SPV pumps in Indian climate. *Sol Energy* 179:11–23. <https://doi.org/10.1016/j.solener.2018.12.021>
6. Verma S, Mohapatra S, Chowdhury S, Dwivedi G (2020) Cooling techniques of the PV module: a review. *Mater Today Proc*, no xxxx. <https://doi.org/10.1016/j.matpr.2020.07.130>
7. Biswas S, Iqbal MT (2018) Dynamic modelling of a solar water pumping system with energy storage. *J Sol Energy* 2018:1–12. <https://doi.org/10.1155/2018/8471715>
8. Gaur A, Mishra S, Chowdhury S, Baredar P, Verma P (2020) Materials today : proceedings a review on factor affecting biodiesel production from waste cooking oil : An Indian perspective. *Mater Today Proc*, no xxxx. <https://doi.org/10.1016/j.matpr.2020.09.432>
9. Ba A, Aroudam E, Chighali OE, Hamdoun O, Mohamed ML (2018) Performance optimization of the PV pumping system. *Procedia Manuf* 22:788–795. <https://doi.org/10.1016/j.promfg.2018.03.112>

10. Sharma R, Sharma S, Tiwari S (2020) Design optimization of solar PV water pumping system. *Mater Today Proc* 21(xxxx):1673–1679. <https://doi.org/10.1016/j.matpr.2019.11.322>
11. Yahyaoui I, Tina G, Chaabene M, Tadeo F (2015) Design and evaluation of a renewable water pumping system. *IFAC-PapersOnLine* 48(30):462–467. <https://doi.org/10.1016/j.ifacol.2015.12.422>
12. Kumar Lodha N, Sudhakar K (2013) Theoretical design and simulation analysis of PV based pumping system for domestic applications in Bhopal, M.P, India. *Int J Sci Res* ISSN 4(4):2293–2297. www.ijsr.net
13. Mermoud A (2004) Pump behaviour modelling. *Univ Geneva* 19
14. Pradesh M (2013) SEHORE DISTRICT ministry of water resources central ground water board north central region BHOPAL SEHORE DISTRICT AT A GLANCE
15. Girma M, Assefa A, Molinas M (2015) Feasibility study of a solar photovoltaic water pumping system for rural Ethiopia. *AIMS Environ Sci* 2(3):697–717. <https://doi.org/10.3934/environsci.2015.3.697>
16. Verma S et al (2020) Solar PV powered water pumping system—a review. *Mater Today Proc*, no xxxx. <https://doi.org/10.1016/j.matpr.2020.09.434>

Vibro-Acoustics of a Mandar



Pradip Gorai, Pankaj Kumar, N. P. Choudhry, and Ajay Kr. Gupta

1 Introduction

Mandar is a percussion musical instrument used in the eastern part of India. It is popular among the tribe people and is similar to Mridangam and Dhol. This is widely used in Jharkhand, West Bengal, and its near border region. Tribe community uses this instrument in their social events such as wedding, jagran, and dance. As per expert players, this is the oldest musical instrument in their community. Mandar has two popular versions: One is used by Santhali community and other one used is by Bengali community. Till now very few people have explored the acoustics property of mandar, and no one have any documentation on it. But there are plenty of documents available on percussion instrument such as Mridangam, Tabla, Dhol, and Katteldrum. In 1934, Raman published his experimental observation that Mridangam follows harmonicity. It is worth noting that almost all the tuned drums of India have a central black patch (e.g., Mridangam, Tabla, Pakhavaj).

P. Gorai · N. P. Choudhry
Department of Mechanical Engineering, B.I.T Sindri, Dhanbad, Jharkhand, India

P. Kumar (✉)
Department of Mechanical Engineering, GMRIT, Rajam, Andra Pradesh, India
e-mail: pankajkumar@gmr.it.edu.in

A. Kr. Gupta
Department of Mechanical Engineering, SRU, Raipur, India

© The Author(s), under exclusive license to Springer Nature Singapore Pte Ltd. 2022
P. Verma et al. (eds.), *Advancement in Materials, Manufacturing and Energy Engineering*,
Vol. II, Lecture Notes in Mechanical Engineering,
https://doi.org/10.1007/978-981-16-8341-1_51

2 Literature Review

Musical drums with harmonic overtones

Sir C. V. Raman [1] (Raman 1920). He made important observations about the sustained intensity of the first three harmonics of tuned Indian drums. He had also commented on the importance of the heterogeneous composite membranes and the central mass loading.

The acoustical knowledge of ancient Hindus

Sir C. V. Raman [2] (1922). In this paper, he finds that the Indian musical instrument like Mridangam flute is more acoustically in nature than the Western musical instrument and concluded that ancient Hindus have sound knowledge of acoustics.

Effect of air cavity on the annular drum

Gottlieb [3] (1981) has presented a numerical investigation on full circular kettledrum: the effect of air cavity on the annular drum. In this study, he found that the effect of a closed backing cavity is confined to a slight increase in the fundamental frequency. He observed that other modes do not go through any considerable change. However, it is worth noting that the analytical method considered only axisymmetrical modes of the membrane.

Acoustics of a cavity-backed membrane: The Indian musical drum

Bhat [4] (1991) has presented that the acoustics of a cavity-backed composite membrane is analyzed under the assumptions that the cavity air pressure on the membrane is uniform and hence sustains only axisymmetric membrane modes under impact excitation of the membrane. Axisymmetric modes of the membrane possess a harmonic relationship among themselves under certain parameter combinations.

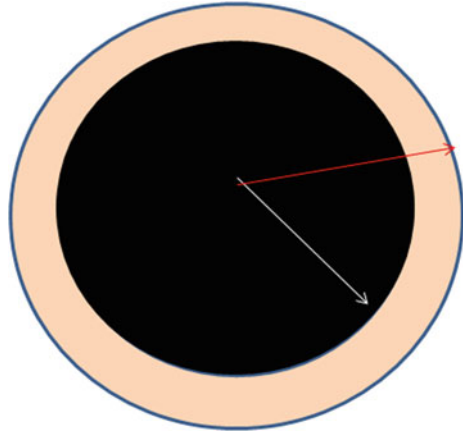
And he concluded that the composite nature of the membrane, the mass loading, and the kettledrum effect all play a role in bringing the axisymmetric modes into a harmonic relationship in a mandar.

Vibro-acoustics of a Mridangam

Sooraj [5] (2017) has presented the vibro-acoustic model of a Mridangam was developed from the structural models of the membranes and acoustic model of the enclosed cavity. And he found that the membrane has highest influence in the dynamics and thereby the sound of Mridangam.

The eigenspectra of Indian musical drums

Sathej and Adhikari [6] (2009) have presented an analytical model which uses a high-resolution numerical method (Fourier–Chebyshev collection) to model the membranes of Tabla.

Fig. 1 Mandar membrane

3 Description of Mandar Membrane

There are two membranes in the mandar one in the right side (Dishana) and another is in the left side (Chana). I have worked only in the left side membrane (Chana) of Mandar. The membrane consists of leather and patch layer and acts like a composite membrane (Fig. 1).

Inner diameter = 24.4cm

Outer diameter = 27.5cm

Thickness of black region (gangat patch) = 3mm

Thickness of leather = 1mm

Density of leather = 882

Density of gangat patch = 1920.

4 Numerical Analysis

The numerical model of mandar membrane is constructed in the FEA Software (Simulia Abaqus 6.14) with the following assumptions

1. Membrane is isotropic and homogeneous in nature.
2. There is a negligible effect of moisture (mandar is completely dry).
3. Tension is uniform over the membrane (Fig. 2 and Table 1).

These analyses had done on Simulia Abaqus 6.14. S4R elements in Abaqus which are used to model the membrane and it is selected as a shell. The boundary of the membrane is assumed to be constrained like a fixed support the natural frequencies and mode shape are extracted using inbuilt Lanczos solver.

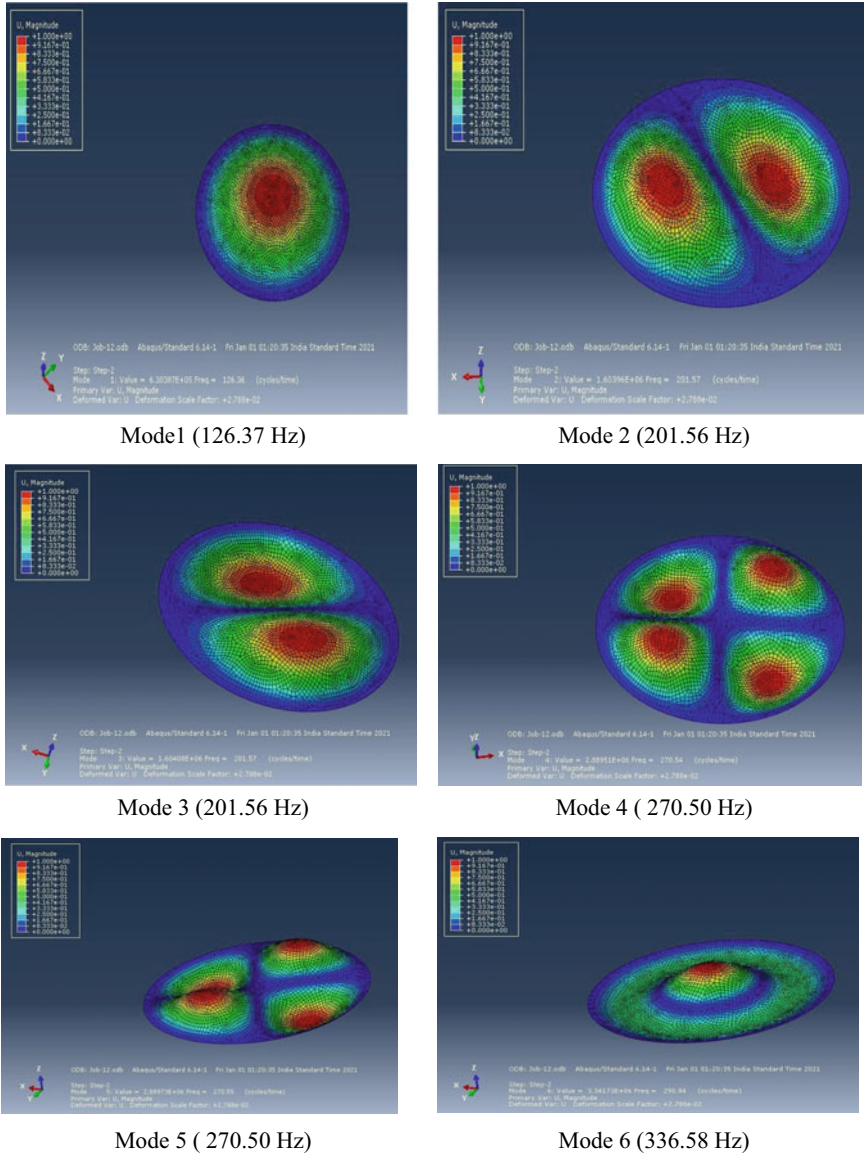
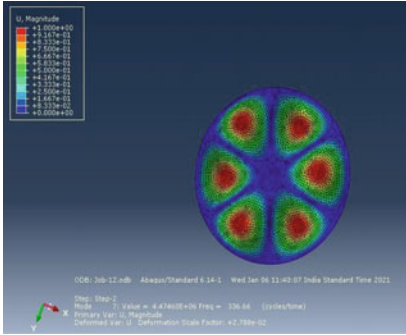


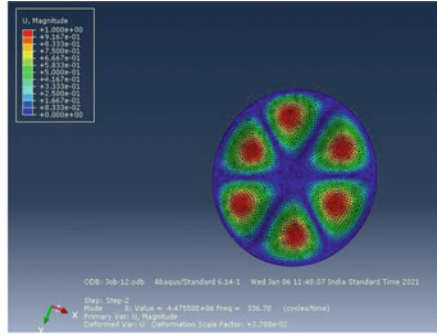
Fig. 2 Numerical analysis model of mandar membrane in Abaqus 6.14 software

5 Experimental Setup

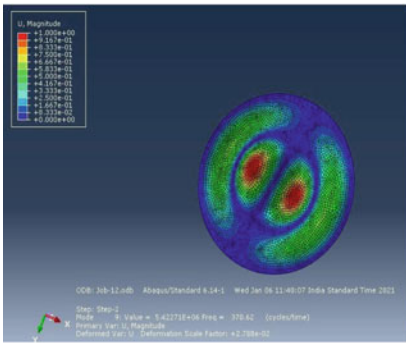
In this study, the natural frequencies of mandar membrane and its mode shape are found out using the concept of Chladni’s patterns. To perform the experiment, we made a setup whose schematic diagram is shown in Figs. 3 and 4.



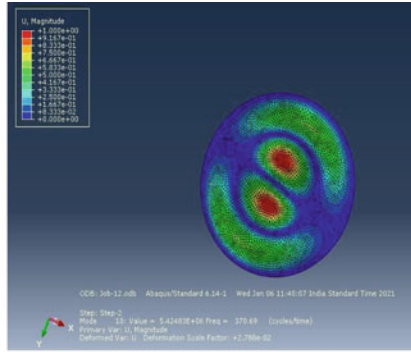
Mode 7 (336.58 Hz)



Mode 8 (336.59 Hz)



Mode 9 (370.48 Hz)



Mode 10 (370.48 Hz)

Fig. 2 (continued)

Table 1 Mesh convergence study of mandar membrane numerical model natural frequencies (in Hz)

Mesh	Coarse	Fine	Super fine
Approximate global size (mm)	4	2	1
No of element	4527	18,042	73,273
Mode 1	126.36	126.37	126.36
Mode 2	201.57	201.56	201.54
Mode 3	201.57	201.56	201.54
Mode 4	270.54	270.50	270.46
Mode 5	270.55	270.50	270.46
Mode 6	290.94	290.59	290.84
Mode 7	336.66	336.58	336.53
Mode 8	336.70	336.59	336.53
Mode 9	370.62	370.48	370.39
Mode 10	370.69	370.48	370.39

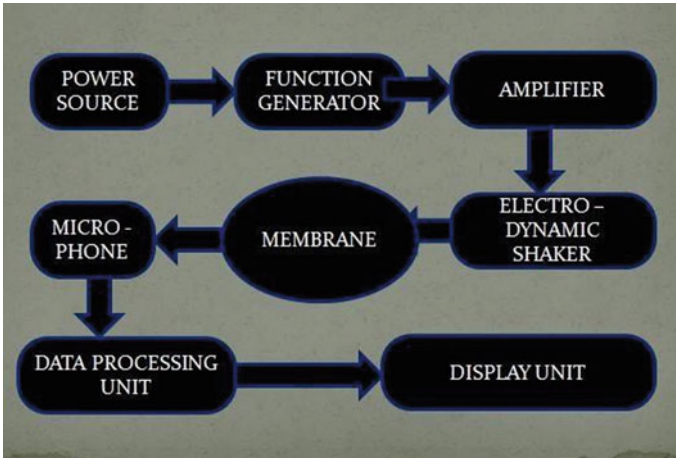


Fig. 3 Schematics diagram of experimental setup



Fig. 4 Experimental setup

Our main aim is to know the frequency and mode shape of the vibrating mandar membrane for that we excite the membrane by electrodynamic shaker plunger. The frequency of electrodynamic shaker is controlled by function generator. In the mode extraction process, membrane vibrates at particular frequencies and shows their respective mode shape. A point force excitation is using an electrodynamic shaker. A single microphone measurement using a free-field microphone (kept at a distance of 100 mm from the plane of the membrane) is used to identify resonance frequencies with the help of data processing and display unit. This is done by FFT analyzer that installed into the laptop. The tuning of electrodynamic shaker is done with the help of function of generator by changing the input frequency, and at the particular

frequency membrane starts vibrate and sand particles show vigorous movement and settle down at nodal diameter and depict mode shape for each resonance frequency.

6 Results and Discussion

The result presented here a mandar Dishana membrane tuned to 150 Hz. The plunger of the electrodynamic shaker is in contact with a point of 10 mm radially inward from the inner edge of the mandar rim (Figs. 5, 6, and 7 and Table 2).

As per data that we found from numerical analysis and experiment, there are variations between them it might be due to the following reasons

- Nescient about the exact mechanical property of membrane material
- Amount of tension applied in the membrane
- In scaling of the material property.

Fig. 5 Mode 1 (150 Hz)



Fig. 6 Mode 2 (202.5 Hz)



Fig. 7 Mode 3 (260 Hz)**Table 2** Mandar membrane experiment: natural frequencies comparison with numerical

Mode combination	Expt (Hz)	Numerical (Hz)	Expt ratio	Nume ratio
(0, 1)	150	126.36	1	1
(1, 1)	202.5	210.57	1.35	1.66
(1, 2)	260	270.55	1.733	2.14

In this project, we found that the mode shape frequency is not in harmonic so we can conclude that mandar is not an acoustically harmonic instrument. If we want to make it harmonic, then we have to change some parameters such as

- tension in the membrane
- re-paste the patch
- tuned the mandar by expert.

7 Conclusion and Future Work

By Ramakrishna and Sondhi [7] (1954) analytical analysis: Tension plays an important role in the composite membrane for that we have to devolve a setup to find the tension in membrane. In numerical analysis, we have to know the exact behavior of the mandar membrane. It is hoped that this work will give a new direction to the analyses of Indian musical instruments and thus aid in their future engineering.

References

1. Raman CV (1920) Musical drums with harmonic overtones. *Nature* (London) 104:500
2. Raman CV (1922) The acoustical knowledge of ancient Hindus. *Ashutosh Mookerjee Silver Jubilee* 2:179–185. <https://doi.org/10.1121/1.387654>

3. Gottlieb HPW (1982) Effect of air cavity on the annular drum. *J Acoustical Soc Am* 71(4):1025–1027
4. Bhat RB (1991) Acoustics of a cavity backed membrane: The Indian musical drum. *J Acoustical Soc Am* 90(3):1469–1474. <https://doi.org/10.1121/1.401886>
5. Sooraj G, Padmanabhan C (2017) Vibro-acoustics of the South Indian drum: Mandar In: Proceedings of 24th international congress on sound and vibration, London, p 216 (23–27 July 2017)
6. Sathej G, Adhikari R (2009) The eigenspectra of Indian musical drums. *J Acoustical Soc Am* 125(2):831–838. <https://doi.org/10.1121/1.3058632>
7. Ramakrishna BS, Sondhi MM (1954) Vibrations of Indian musical drums regarded as composite membranes. *J Acoustical Soc Am*